FRONTIERS IN SILK SCIENCE AND TECHNOLOGY

EDITED BY: Nicola Maria Pugno, Antonella Motta and David Kaplan
PUBLISHED IN: Frontiers in Materials and Frontiers in Bioengineering and Biotechnology

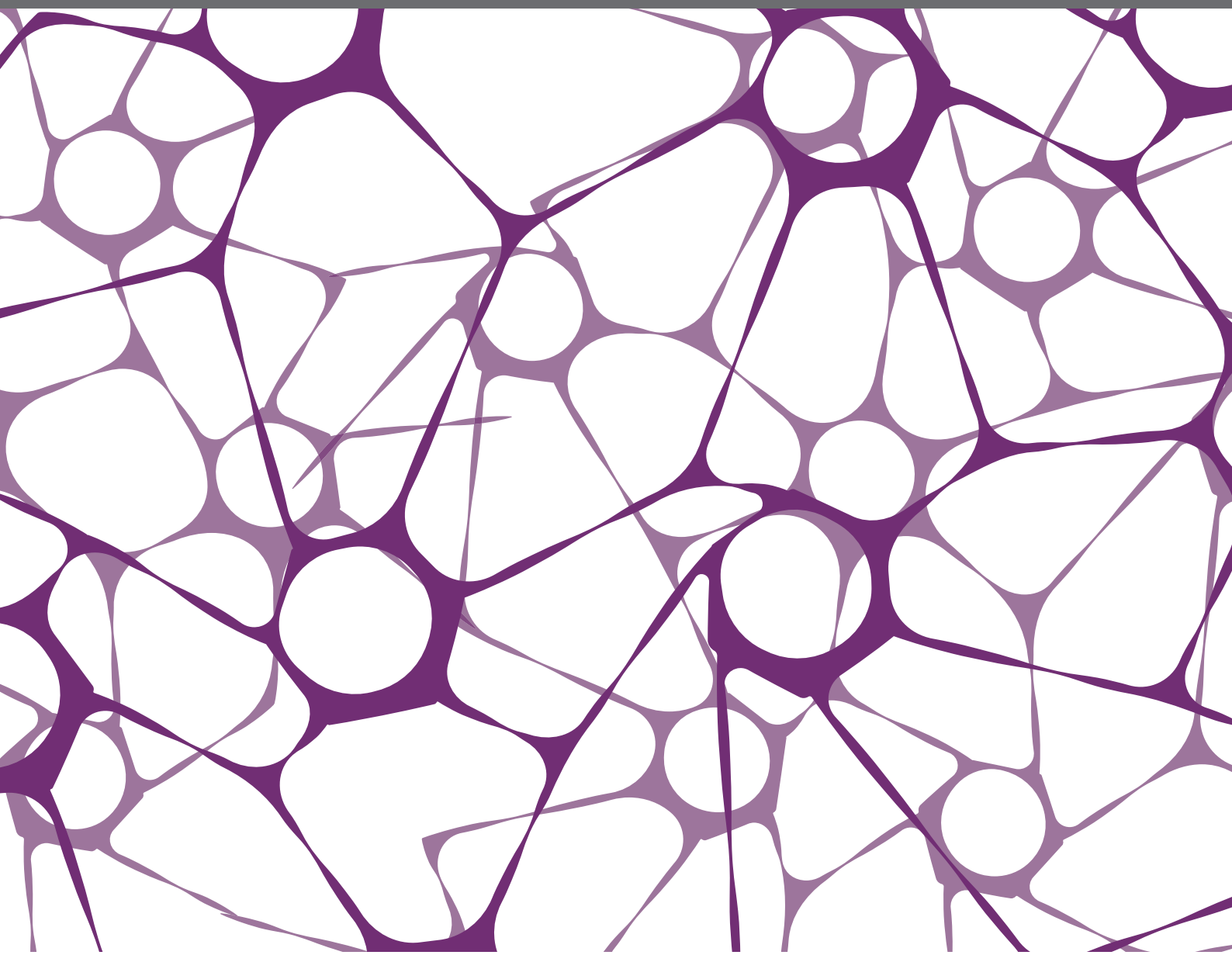

frontiers Research Topics

ISSN 1664-8714
ISBN 978-2-88971-087-4
DOI 10.3389/978-2-88971-087-4

About Frontiers

Frontiers is more than just an open-access publisher of scholarly articles: it is a pioneering approach to the world of academia, radically improving the way scholarly research is managed. The grand vision of Frontiers is a world where all people have an equal opportunity to seek, share and generate knowledge. Frontiers provides immediate and permanent online open access to all its publications, but this alone is not enough to realize our grand goals.

Frontiers Journal Series

The Frontiers Journal Series is a multi-tier and interdisciplinary set of open-access, online journals, promising a paradigm shift from the current review, selection and dissemination processes in academic publishing. All Frontiers journals are driven by researchers for researchers; therefore, they constitute a service to the scholarly community. At the same time, the Frontiers Journal Series operates on a revolutionary invention, the tiered publishing system, initially addressing specific communities of scholars, and gradually climbing up to broader public understanding, thus serving the interests of the lay society, too.

Dedication to Quality

Each Frontiers article is a landmark of the highest quality, thanks to genuinely collaborative interactions between authors and review editors, who include some of the world's best academicians. Research must be certified by peers before entering a stream of knowledge that may eventually reach the public - and shape society; therefore, Frontiers only applies the most rigorous and unbiased reviews.
Frontiers revolutionizes research publishing by freely delivering the most outstanding research, evaluated with no bias from both the academic and social point of view. By applying the most advanced information technologies, Frontiers is catapulting scholarly publishing into a new generation.

What are Frontiers Research Topics?

Frontiers Research Topics are very popular trademarks of the Frontiers Journals Series: they are collections of at least ten articles, all centered on a particular subject. With their unique mix of varied contributions from Original Research to Review Articles, Frontiers Research Topics unify the most influential researchers, the latest key findings and historical advances in a hot research area! Find out more on how to host your own Frontiers Research Topic or contribute to one as an author by contacting the Frontiers Editorial Office: frontiersin.org/about/contact

FRONTIERS IN SILK SCIENCE AND TECHNOLOGY

Topic Editors:
Nicola Maria Pugno, University of Trento, Italy
Antonella Motta, University of Trento, Italy
David Kaplan, Tufts University Medford, United States

Citation: Pugno, N. M., Motta, A., Kaplan, D., eds. (2021). Frontiers in Silk Science and Technology. Lausanne: Frontiers Media SA. doi: 10.3389/978-2-88971-087-4

Table of Contents

frontiers in Materials

EDITORIAL
published: 26 May 2021
doi: 10.3389/fmats.2021.685538

Editorial: Frontiers in Silk Science and Technology

Nicola Maria Pugno[1,2]*, *Antonella Motta*[3,4] *and David Kaplan*[5]

[1] *Laboratory of Bio-inspired, Bionic, Nano, Meta Materials & Mechanics, Department of Civil, Environmental and Mechanical Engineering, University of Trento, Trento, Italy,* [2] *School of Engineering and Material Science, Queen Mary University of London, London, United Kingdom,* [3] *Department of Industrial Engineering and BIOtech Research Center, University of Trento, Trento, Italy,* [4] *European Institute of Excellence on Tissue Engineering and Regenerative Medicine, Trento, Italy,* [5] *Department of Biomedical Engineering, School of Engineering, Tufts University, Science and Technology Center, Medford, MA, United States*

Keywords: silk, spider, silkworm, mechanics, biomaterials, spiderweb

Editorial on the Research Topic

Frontiers in Silk Science and Technology

Silks from both spiders and silkworms have emerged as useful materials for addressing new challenges in materials science. These protein-based materials are often superior to many other polymers from a mechanical point of view and provide the possibility to realize composites with remarkable biological properties. Thus, studying raw silks, as well as silk-based natural and artificial composites, while controlling and manipulating processing conditions, is important to achieve advances in silk utility for materials science and technology. In doing this, a multidisciplinary and multiscale approach is crucial for studying silk and its derivatives.

This themed article collection focuses on some of the latest advances in silk science and technology, and topics include:

- Protein structure and intermolecular interactions
- Characterization in the liquid and solid states
- Self-assembly in silk proteins
- Standardization of processing
- New uses for silks—e.g., optical and electronic materials
- Spider silk properties, uses, processing
- Recombinant silk
- Fabrication of bio-inspired materials with superior properties
- Silk from genetically modified organisms
- Silk mechanics
- Silk composites
- Silk bionanocomposites

This themed article collection features high-quality research from the 2019 edition of the Frontiers in Silk Sciences and Technologies conference (Trento, Italy), as well as significant contributions from experts worldwide working on the topic, across academia and industry, with a total of 17 contributions, as briefly summarized below reporting nearly verbatim the related abstracts.

In Riekel et al. the authors focused on "Nanoscale X-Ray Diffraction of Silk Fibers." This report focuses on current possibilities and perspectives of scanning X-ray nanodiffraction for probing nanoscale heterogeneities in silk fibers such as nanofibrils, skin-core morphologies, nanocrystalline inclusions and fine fibers down to submicron diameters.

In Pérez-Rigueiro et al. the authors focused on "Lessons From Spider and Silkworm Silk Guts." The results presented in previous work on the formation of fibers from silkworm and spider silk guts are reviewed and new information is included on the glands that allow the formation of

OPEN ACCESS

Edited and reviewed by:
Gennady Mishuris, Aberystwyth University, United Kingdom

***Correspondence:**
Nicola Maria Pugno
nicola.pugno@unitn.it

Specialty section:
This article was submitted to Mechanics of Materials, a section of the journal Frontiers in Materials

Received: *25 March 2021*
Accepted: *20 April 2021*
Published: *26 May 2021*

Citation:
Pugno NM, Motta A and Kaplan D (2021) Editorial: Frontiers in Silk Science and Technology. Front. Mater. 8:685538. doi: 10.3389/fmats.2021.685538

these fibers. Silk gut fibers were obtained directly from the silk glands by immersion in a mild acid solution and subsequent stretching. The fibers produced were characterized in terms of their microstructure and mechanical properties. The comparison of silk gut fibers with their natural counterparts allows for new insights into processing, microstructure and properties of silkworm and spider silks.

In Sogawa et al. the authors focused on "Surface Analysis of Native Spider Draglines by FE-SEM and XPS." Although the physical and biological functions of the skin layer of spider dragline silk fibers have been studied and partially clarified, the morphology and elemental contents of these skin layer of silk fibers have not been investigated in detail. Here, the surface of *Nephila clavata* spider dragline was evaluated by field emission scanning electron microscopy (FE-SEM) and X-ray photoelectron spectroscopy (XPS) to obtain surface morphological and molecular information. The FE-SEM images of the spider dragline indicated that it forms a bundle of microfibrils. This hierarchical structure induces faint fibrillar and network-like patterns on the surface of the dragline. XPS analysis revealed the presence of Na, P, and S, which are reasonably explained considering the biological components of the major ampullate gland of spiders. The results will be important to consider in terms of the molecular transition of silk proteins to form hierarchical structures during spider dragline spinning.

In Xu et al. the authors focused on "Use of Silk Proteins to Form Organic, Flexible, Degradable Biosensors for Metabolite Monitoring." The development of sustainable and degradable biosensors and bioelectronics has implications for implantable systems, as well in addressing issues of electronic waste. Mechanically flexible and bioresorbable sensors can find applications at soft biological interfaces. While devices typically use metallic and synthetic components and interconnects that are non-degradable or have the potential to cause adverse tissue reactions, the use of nature-derived materials and conducting polymers can provide distinct advantages. In particular, silk fibroin and sericin can provide a unique palette of properties, providing both structural and functional elements. Here, a fully organic, mechanically flexible biosensor in an integrated 3-electrode configuration is demonstrated. Silk sericin conducting ink is micropatterned on a silk fibroin substrate using a facile photolithographic process. Next, using a conducting polymer wire sheathed in silk fibroin, organic interconnects are used to form the electrical connections. This fully organic electrochemical system has competitive performance metrics for sensing in comparison to conventional systems, as verified by detection of a model analyte—ascorbic acid. The stability of the silk biosensor through biodegradation was observed, showing that the sensors can function for several days prior to failure. Such protein-based systems can provide a useful tool for biomonitoring of analytes in the body or the environment for controlled periods of time, followed by complete degradation, as transient systems for various applications.

In Veiga et al. the authors focused on "Recent Advances in Silk Sericin/Calcium Phosphate Biomaterials." Calcium phosphates (CaPs) have been widely used in the field of biomedical engineering as bone graft substitutes or as carriers for drug delivery applications. Recent developments have focused on combining CaPs with proteins to obtain functional biomaterials that accommodate a broader spectrum of functional requirements. Silk sericin was considered an unutilized protein by-product from the textile industry, generating tons of residues every year. However, much effort has been dedicated to its recovery after being associated with numerous biological properties such as antioxidant, antibacterial, anti-coagulation and regenerative activities. In the past years, sericin has also demonstrated to be suitable as a template for CaP mineralization. The present review focuses on the recent developments for the production of sericin/CaP composites, exploring their potential applications in bioengineering and opening new avenues in other research fields such as in the cosmetic, food and environmental sectors. In addition, this paper can also be useful as a guideline to design future research based on sericin/CaP biomaterials.

In Jeong et al. the authors focused on "Progress in Silk Fibroin Based Composite Scaffold/Hydrogel: Silk Fibroin/PEG Hydrogel for the RPE Regeneration a Promising Biomaterial for Clinical Application." Retinal pigment epithelium (RPE) plays a decisive role in the normal function of the retina, especially in the maintenance of photoreceptors. RPE dysfunction, loss of sight, and degeneration has been implicated as the cause of many retinal diseases including pigmented retinitis and age-related macular degeneration (AMD). Silk fibroin (SF) is a biodegradable natural polymer with biocompatibility, non-toxic, and non-immunological properties. In this study, hydrogel material was prepared by mixing it with PEG [poly (ethylene glycol)] a synthetic polymer. SF hydrogel (SH) and with PEG (SPH) were prepared with different sonication times and were physio chemically characterized by SEM, FTIR, compressive strength, porosity. In addition *in vitro* cytocompatibility was analyzed. As a result, the 20s SPH hydrogel exhibited superior cytocompatibility, cell adhesion, and improved cell growth compared to pure SH. Their respective genes expression for retinal function and matrix production was also positively influenced by 20s SPH with an increase in gene expression of RPE65, CRALBP. The obtained results suggest that the 20s SPH hydrogel can be used as an alternative material for the application of retinal regeneration and delivery.

In Lopes et al. the authors focused on "Phase Diagram and Estimation of Flory-Huggins Parameter of Interaction of Silk Fibroin/Sodium Alginate Blends." Silk fibroin (SF) and sodium alginate (SA) are natural polymers used to produce biomaterials. One of the strategies to improve the properties of these products is to prepare blends, which are partially miscible. Phase separation is observed, therefore, the thermodynamic analysis of this system is important to predict the final state and composition of this blends. This study explored blends with a different initial composition of SF, SA, and water (WA) at 25°C and neutral pH. After phase separation, two phases were identified, one rich in SF and other rich in SA. The Flory-Huggins parameters of interaction of polymer-solvent and polymer-polymer were estimated using the extended equation and data of phase equilibrium, their values indicates the partial miscibility of the polymers.

In Blamires et al. the authors focused on "Spider Silk Biomimetics Programs to Inform the Development of New Wearable Technologies." Wearable fabrics are predominantly produced from synthetic polymer fibers derived from petrochemicals. These have negative effects on the natural environment as a consequence of the manufacturing process, insurmountable waste production, and persistence of the fibers in ecosystems. With the use of wearables worldwide set to increase exponentially, more environmentally friendly fibers are sought. Natural fibers such as spider silk are produced using proteins in a water solvent, yet they have many superior qualities to synthetic fibers. Moreover, spiders can tune their silk properties as their ecological circumstances demand it. Research focused on the biomimetic potential of spider silks with an eye on the development of smart wearable fibers is accordingly a potentially lucrative area of research. There are nonetheless major challenges associated, including recovering the original mechanical performance within the fibers developed, scaling up production, keeping the production costs of the silk building blocks to a minimum, elucidating, and understanding the different silk genome sequences, and creating precision artificial spinning processes. The authors outline herein a template for a working framework for a spider silk biomimetics program that can inform designers and biological researchers alike. It suggests that an objective-focused research program utilizing a cross-disciplinary toolbox of top-down and bottom-up techniques is required. They close by providing some speculative examples stemming from current activities in their laboratories.

In Ferreira et al. the authors focused on "3D Structure and Mechanics of Silk Sponge Scaffolds Is Governed by Larger Pore Sizes." Three-dimensional scaffolds play an essential role in tissue engineering. Although essential, the tunability of the 3D scaffolds mechanical and transport properties remains a challenge. In this work, the authors present new approaches to advance the field. First, they applied their progressive pH acidification to mimic the natural silk gelation process before ice-templating (−20 and −80°C); second, they fitted the mechanical properties using a connectivity model; third, they fitted the scaffolds mechanical relaxation to understand the transport properties; and fourth they used micro-CT to correlate the process parameters to the scaffolds' performances. Their results suggested that the free shrinkage of the scaffolds determined their final properties. They found, however, that the porosity (above 90%) was anisotropic, similarly the tortuosity (between 1 and 1.3). They identified two major pore dimensions, the first one between 10 and 20 μm, and the second between 50 and 130 μm. Mechanically, their model suggested that the bulk modulus captured the elastic contribution and was controlled predominantly by the silk concentration. They tentatively associated the fractional modulus 1 to the collapse of the larger pores structures and was controlled mostly by the process temperature. They assigned the slow relaxation to the transport of fluid in the silk sponge scaffolds; and the fast relaxation with a viscoelastic relaxation. The silk concentration and process temperatures did not influence the latter. Overall, their use of the tomography, mechanical test, and detailed statistical analysis provides inroads into the interplay between process parameters (silk concentration and process temperature) and the multiple responses of the silk sponge scaffolds. The development of a new mechanical fitting for the compression test helped capture simply the different failure modes in the sponge scaffolds as well as correlating those events to relaxation and eventually transport properties.

In Silva et al. the authors focused on "Green Pathway for Processing Non-mulberry Antheraea pernyi Silk Fibroin/Chitin-Based Sponges: Biophysical and Biochemical Characterization." Silk protein fibroin (SF)-based matrices from non-mulberry, and mulberry silkworms are used for different applications in regenerative medicine. Silk fiber spun by the wild non-mulberry silkworm *Antheraea pernyi* (Ap) is also a promising biomedical material, due to the presence of the inherent tripeptide sequence of Arginine-Glycine-Aspartic acid (RGD) on the protein fibroin sequences. However, SF derived from the Ap cocoons still lacks exploitation in the healthcare field due to its poor solubility in the conventional solvents. This work addresses the application of green chemistry principles, namely the use of ionic liquids (ILs, 1-butyl-imidazolium acetate) and renewable resources such as *Antheraea pernyi* silk fibroin (ApSF) and chitin (Ch), for the fabrication of sponges from the blends of ApSF and Ch (APC). The formation of β-sheet in different contents during ApSF/Ch/IL was acquired by exposing gels to methanol/water and ethanol/water. The sponges were then obtained by freeze-drying. This approach promotes the formation of both stable and ordered ApSF/Ch-based sponges. The developed sponges show suitable porosity and interconnectivity, appreciable swelling degree, and tuneable viscoelastic compressive properties for tissue engineering. Collectively, the structural properties of these ApSF/Ch-based sponges make them promising candidates for biomedical applications, namely cartilage regeneration.

In Brancato et al. the authors focused on "Tumor-Stroma Interactions Alter the Sensitivity of Drug in Breast Cancer." Flat cell cultures or xenografts are inadequate tools to unravel cancer complex biology. 3D *in vitro* tumor models garnered interest since they recapitulate better dynamic mechanisms of cancer, but a gold standard model that faithfully mimics solid cancer is not available yet. A 3D breast cancer model is fabricated using freeze-dried silk fibroin scaffolds. Breast cancer cell lines (MCF-7 and MDA-MB231) are seeded with normal mammary fibroblasts onto silk fibroin scaffolds (1 and 2 mm thick). Cell proliferation is monitored by Alamar blue assay, the 3D breast cancer model morphology is observed by confocal microscopy, and gene expression modulation concerning extracellular matrix markers is evaluated. Further, 3D bioengineered breast cancer models are treated with doxorubicin. Silk fibroin scaffolds allow the proliferation of cancer cells and fibroblasts. Cells growth is enhanced when cancer cells and fibroblasts are seeded together. Histological staining shows 3D cell organization. MMP-1, MMP-2, MMP-3, Col-1, and fibronectin expression are upregulated in co-culture. After doxorubicin treatment, stronger reduction in cell activity is observed in 2 mm SF scaffold in comparison to 1 mm. The 3D *in vitro* breast cancer model obtained can easily be scaled-up and translated to the preclinical testing of novel chemotherapeutics.

In Ribeiro et al. the authors focused on "Hierarchical HRP-Crosslinked Silk Fibroin/ZnSr-TCP Scaffolds for Osteochondral

Tissue Regeneration: Assessment of the Mechanical and Antibacterial Properties." The biomaterials requirements for osteochondral (OC) defects restoration simultaneously include adequate mechanical behavior, and the prevention of bacterial adherence and biofilm formation, without impairing local tissue integration. Bilayered and hierarchical scaffolds combining a cartilage-like layer interconnected to an underlying subchondral bone-like layer appeared as innovative technological solutions able to mimic the native OC tissue hierarchical architecture. This study is focused on the assessment of the combined compression-shear stresses and possible bacterial biofilm formation of hierarchical scaffolds prepared from a horseradish peroxidase-crosslinking reaction of silk fibroin (SF) combined with zinc (Zn) and strontium (Sr)-doped β-tricalcium phosphate (β-TCP) for OC tissue regeneration. Scaffolds with undoped-β-TCP incorporation were used as control. Results showed that the bilayered scaffolds presented suitable aptitude to support compression and shear loading for OC tissue, with better mechanical properties for the ZnSr-containing structures. Young and shear moduli presented values close to 0.01 MPa in the region 10–20% strain. The investigation of biomaterials surface ability to prevent biofilm formation showed reduced bacterial adhesion of *Escherichia coli* (*E. coli*, gram-negative) and *Staphylococcus aureus* (*S. aureus*, gram-positive) on both scaffolds, thus suggesting that the proposed hierarchical scaffolds have a positive effect in preventing gram-positive and gram-negative bacteria proliferation.

In Pantano et al. the authors focused on "Doubling the Mechanical Properties of Spider Silk by C60 Supersonic Molecular Beam Epitaxy." Spider silk is one of the most fascinating natural materials, owing to its outstanding mechanical properties. In fact, it is able to combine usually self-excluding properties, like strength and toughness that synthetic fibers fail to replicate. Here, the authors report a method to further enhance the already excellent mechanical properties of spider's silk, producing nanocomposite fibers where the matrix of spider silk is reinforced with C_{60} molecules. These are deposited by Supersonic Molecular Beam Epitaxy (SuMBE) and are able to efficiently interact with silk, as evidenced by XPS analysis. As a consequence, upon proper adjustment of the fullerene kinetic energy, the treated fibers show improved strength, Young's modulus and toughness.

In Lee et al. the authors focused on "Recent Advances in Fluorescent Silk Fibroin." Silk is a natural macromolecular protein consisting of fibroin and sericin. Silk fibroin (SF), derived from *Bombyx mori*, is a representative fibrous protein that has been used mainly in fashion textiles and surgical sutures. Also, SF has been extensively applied as a potential biomaterial in a number of biomedical and biotechnological fields, as SF can be reconstituted in various forms through physical and chemical processes. In addition to direct use of SF with intrinsic structure and properties, there are many attempts to insert more novel functional properties into SF, retaining its favorable natural characteristics. In recent years, fluorescent silk obtained through various methods, such as the genetic modification or dye feeding, has been applied in a variety of medical fields. These functionalized silks have properties that can be applied to new and versatile fields such as drug delivery, and monitoring surgical and wound healing processes. This review focuses on the preparation methods and the latest technological advances on the use of fluorescent SF materials, especially their biomedical applications.

In Eom et al. the authors focused on "Multiscale Hybridization of Natural Silk–Nanocellulose Fibrous Composites With Exceptional Mechanical Properties." Because of the crisis of the petrochemical era, environmentally friendly natural polymers and related material processes are receiving great attention. Cellulose and silk are typical fibrous materials that consist of polysaccharides and proteins, respectively, and have excellent mechanical properties and high physicochemical stabilities due to their unique self-assembly-based hierarchical structures. In this study, highly stable high-strength silk fiber (HSF)–cellulose nanofibril (CNF) composites were prepared by the hierarchical fusion of micrometer-scale HSFs and nanometer-scale CNFs. This manufacturing process is cost-effective because the raw materials (HSFs and CNFs) are used as is. It is an eco-friendly process because it does not require the use of organic solvents or toxic reagents. In addition, it is an energy-efficient process because heat fusion (120°C) takes only 10 min. The results of the Direct Red 80 staining experiments confirm that up to 15 wt.% CNFs were added to the HSF nonwoven. With the increase in the CNF amount, the nanometer-scale CNFs form a coating on the micro-scale HSFs. At the same time, the CNFs form bonds with the HSFs and increase the interfibrillar bonding strength of the CNF-coated HSFs. Therefore, the mechanical properties of the HSF/CNF composite and its stability in the water environment rapidly increase with increasing CNF concentration. In the case of HSF/CNF15, the mechanical and impact strengths increase by 110 and 228%, respectively, compared with HSF non-woven without CNF. In addition, as CNFs are introduced, hydrophobicity of the surface and bulk of the HSF/CNF composite can be impacted, thereby maintaining structural stability in the water environment. This eco-friendly HSF/CNF composite can be widely used as reinforcement for fiber-reinforced plastics as well as for other applications in the fibrous composite industry.

In Puerta et al. the authors focused on "Effects of Chemical Post-treatments on Structural and Physicochemical Properties of Silk Fibroin Films Obtained From Silk Fibrous Waste." Silk fibroin (SF) is a protein polymer claimed to have outstanding potential for medical applications. However, because of the manufacturing process, materials from regenerated SF exhibit a higher percentage of amorphous structures. The amorphous structures cause the material to be water soluble and can significantly limit its applications in wet biological environments. In order to increase the amount of crystalline structures and decrease the water solubility of SF materials, post-treatment with alcohols is usually employed. SF can be obtained from silk fibrous wastes (SFW), usually discarded in silk textile processes. This represents an opportunity to produce materials with high added value from low-cost natural sources. In this study, SF was obtained from SFW, and films were made thereof followed by a post-treatment by immersion or in a saturated atmosphere of methanol (MeOH) or ethanol (EtOH), using different

exposure times. The resulting films were analyzed according to crystallinity, the percentage of crystalline and amorphous structures, and thermal stability. Also, water absorption and weight loss in aqueous media were determined. The results showed a significant increase in crystalline structures in all treated samples, varying according to the type and time of exposure to post-treatment conducted. The highest increase was shown in the case of the post-treatment by immersion in MeOH for 1 h, with a 23% increase over the untreated sample. This increase in crystallinity was reflected in an increase in the degradation temperature and a degradation rate of 5.3% on day 7. The possibility of tuning the degree of crystallinity, as well as thermal stability and aqueous integrity of thin films of SFW, can be applied to adjust these materials to the requirements of specific biomedical applications.

Finally, in Greco et al. the authors focused on "Strong and Tough Silk for Resilient Attachment Discs: The Mechanical Properties of Piriform Silk in the Spider Cupiennius salei (Keyserling, 1877)." Spiders are able to produce different types of silk with different mechanical and biological properties. Piriform silk is produced to secure spiders and their webs to surfaces by using a nano-fibril network embedded in a cement-like matrix. Despite their fundamental role, the mechanical properties and function of these anchorages are still poorly understood due to the practical difficulties in nano-fibril sample preparation, the complexity of the system, and the high variation of attachment disc structures. Here the authors estimated the mechanical properties of this nano-fibril silk and those of the whole silk membrane in the large wandering spider *Cupiennius salei* through a combination of nanoindentation and nanotensile techniques and with the support of a simple analytical model. The results highlight the mechanical properties of the piriform silk, facilitating the modeling of silk composite mechanics. This could inspire the design of more efficient bio-inspired adhesives and fabrics.

AUTHOR CONTRIBUTIONS

All authors listed have made a substantial, direct and intellectual contribution to the work, and approved it for publication.

Conflict of Interest: The authors declare that the research was conducted in the absence of any commercial or financial relationships that could be construed as a potential conflict of interest.

frontiers in Materials

ORIGINAL RESEARCH
published: 04 December 2019
doi: 10.3389/fmats.2019.00315

Nanoscale X-Ray Diffraction of Silk Fibers

Christian Riekel, Manfred Burghammer and Martin Rosenthal*

The European Synchrotron Radiation Facility (ESRF), Grenoble, France

This report focuses on current possibilities and perspectives of scanning X-ray nanodiffraction for probing nanoscale heterogeneities in silk fibers such as nanofibrils, skin-core morphologies, nanocrystalline inclusions and fine fibers down to submicron diameters.

Keywords: silk fibers, X-ray nanodiffraction, synchrotron radiation, skin-core structure, nanocrystallites, radiation damage

OPEN ACCESS

Edited by:
Nicola Maria Pugno, University of Trento, Italy

Reviewed by:
Domenico De Tommasi, Politecnico di Bari, Italy
Dongchan Jang, Korea Advanced Institute of Science and Technology (KAIST), South Korea

****Correspondence:***
Christian Riekel
riekel@esrf.fr

Specialty section:
This article was submitted to Mechanics of Materials, a section of the journal Frontiers in Materials

Received: *20 August 2019*
Accepted: *20 November 2019*
Published: *04 December 2019*

Citation:
Riekel C, Burghammer M and Rosenthal M (2019) Nanoscale X-Ray Diffraction of Silk Fibers. Front. Mater. 6:315. doi: 10.3389/fmats.2019.00315

INTRODUCTION

Progress in mimicking biological silk production and designing advanced functional materials relies on understanding silks hierarchical organization and its relation to macroscopic function. While mechanics trends across the spider phylogeny for major ampullate silks (MaS) can be deduced from protein sequence (Blackledge et al., 2012), detailed modeling of specific mechanical properties requires information on silks functional elements and their hierarchical organization. Here we will consider functional elements up to the nanoscale, which are accessible to X-ray scattering techniques. Indeed, β-sheet nanodomains of several nm size, embedded in an amorphous matrix of protein chains, are basic functional elements of MaS fibers observed by wide-angle X-ray scattering (WAXS) (Fraser and MacRae, 1973). This two-phase model is used in various molecular modeling approaches based on phenomenological or molecular dynamics approaches for simulating protein chain behavior in the amorphous phase (Termonia, 1994; Papadopoulos et al., 2009; Su and Buehler, 2016; Puglisi et al., 2017). Morphological features such as protein chain self-assembly into nanofibrils (see below) can be simulated by assuming nanodomains interconnected by pre-strained chains (Papadopoulos et al., 2009). Lamellar distributions of nanodomains are also obtained from bottom-up molecular dynamics simulations (Cetinkaya et al., 2011). Interestingly a skin-core morphology is assumed for balancing prestressed chains in the core, experimentally observed by infrared spectroscopy (Papadopoulos et al., 2009).

The experimental observation of nanofibrils relies principally on scattering (e.g., X-ray and neutron small-angle scattering, SAXS/SANS) and imaging (e.g., transmission electron microscopy, TEM, and others) techniques. SAXS/SANS data provide shape information but have to be transformed into real space assuming usually cylindrical objects (Yang et al., 1997; Sapede et al., 2005). For highly crystalline bagworm silk several levels of nanofibrillar assembly have been revealed (Yoshioka et al., 2019). The local distribution and interactions of nanoscale functional elements including skin-core morphologies cannot, however, be obtained from such studies which are usually performed on fiber bundles. X-ray microbeam diffraction (microXRD) allows probing single, μm-sized silk fibers (Riekel and Vollrath, 2001), paving the way for studying silks available only in small quantities (Craig, 2003), but has a limited reciprocal space (SAXS) resolution (see also conclusions) and cannot resolve skin-core morphologies. In contrast, high resolution imaging techniques such as transmission electron microscopy (TEM) and atomic force microscopy (AFM) allow local imaging of nanoscale functional elements from single nanofibrils to skin-core morphologies

but only for very thin samples, which may require embedding, sectioning and staining. Indeed, a skin-core morphology has been revealed by TEM for *Nephila's* MaS fibers (Frische et al., 1998) and single recluse spider nanofibrils of 20 × 7 nm^2 cross-section have been imaged by AFM (Wang and Schniepp, 2018). Arguably there is, however, insufficient knowhow on dimensional aspects, volume density and spatial distribution of nanofibrils and other nanoscale functional elements in silk fibers, limiting the development of mechanical models (Wang and Schniepp, 2019).

Here we will discuss the scope of scanning X-ray nanodiffraction (nanoXRD) combining bulk sensitivity with nanoscale lateral resolution. Specifically, we will provide an update on *Argiope's* MaS skin-core morphology (Riekel et al., 2017) and extend it to *B. mori's* cocoon silk. Radiation damage issues will be discussed for the smallest focal spots used. We will show for the case of *Argiope's* stabilimentum that scanning nanoXRD allows probing down to subμm diameter silk fibers and provide an outlook on R&D opportunities enabled by the ongoing upgrade of the ESRF source brightness.

METHODS

NanoXRD experiments were performed at the ID13 undulator beamline at *The European Synchrotron* (ESRF: www.esrf.eu) (Riekel et al., 2017). Monochromatic focal spots of 170–180 nm fwhm (full-width-half-maximum) with a flux density of ∼1.5*10^5 photons/s/nm^2 were generated by refractive lenses (Riekel et al., 2017) and of 40–50 nm fwhm with a flux density of ∼1.3*10^7 photons/s/nm^2 by multilayer Laue lenses (Kubec et al., 2017). X-ray transparent Si_3N_4 membranes provide stable sample supports (**Figures 1C–E**) (Riekel et al., 2017). Local structural information is obtained by step-scanning samples through the focal spot and recording diffraction patterns in transmission geometry at each position by a single photon counting pixel detector (Dectris®) at a calibrated distance (**Figures 1A,B**). Typical exposure times used were 2 s for the ∼180 nm and 0.1 s for the ∼40 nm focal spots. The sequence of patterns obtained in a mesh-scan (**Figures 1A,B**) is transformed into a composite diffraction image (called here: "composite image") corresponding to a real space projection of local reciprocal space variations. Selecting the angular range of pixels extending into the wide-angle scattering (WAXS) or small-angle X-ray scattering (SAXS) range allows visualizing atomic-scale or morphological-scale features (Riekel et al., 2009, 2017).

APPLICATIONS

NanoXRD Patterns

NanoXRD patterns for *Argiope bruennichi's* MaS bridge-thread with the ∼180 nm focus (Riekel et al., 2017) and an untreated

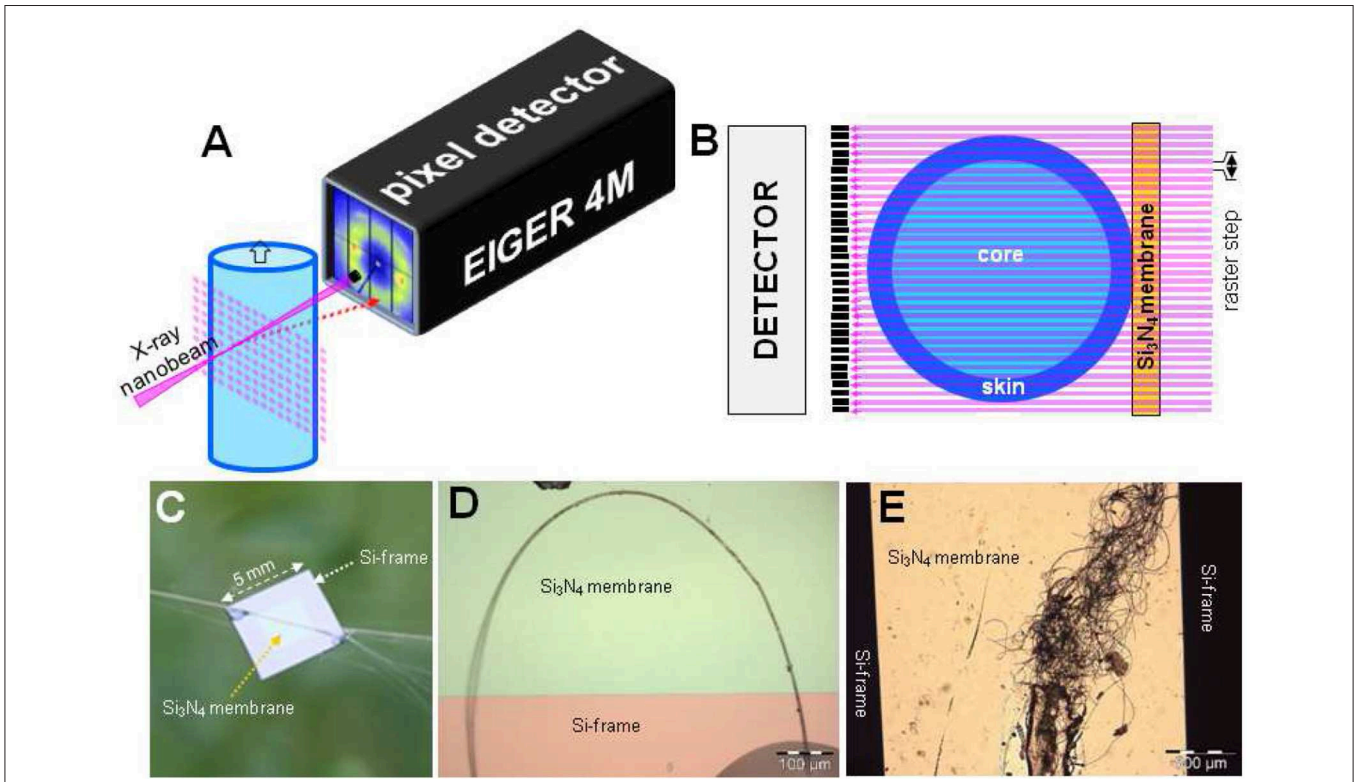

FIGURE 1 | Methodological aspects of scanning nanoXRD. **(A)** Mesh-scan of fiber through X-ray focal spot. Diffraction patterns are recorded at each step. **(B)** View normal to beam direction of mesh-scan through fiber section with skin-core morphology. The depth-of-focus guarantees a quasi-constant spot diameter across the fiber. **(C)** *A. bruennichi's* bridge-thread bundle glued to Si_3N_4 membrane supported by a Si-frame; **(D)** Bridge-thread bent into a loop for probing local deformation (not reported below). **(E)** Decorating fibers from *A. bruennichi's* stabilimentum. **(B,C)** Reproduced/adapted from Riekel et al. (2017) with permission from ACS.

Bombyx mori's cocoon bave with the ∼40 nm focus are shown in **Figures 2A–D**. The fiber texture (observed also for single patterns) is due to a preferential axial alignment of the polypeptide chains in the <5 nm size nanodomains. Indeed, for ∼180 nm focus at the center of a 5 μm diameter *B. mori* fiber of ∼50% crystallinity ∼10^8 unit cells contribute to the Bragg peaks and ∼$5*10^6$ unit cells for a 40 nm focus, decreasing by factor 20 for a 100 nm thick layer at the rim. The equatorial WAXS profiles agree to those obtained by X-ray microdiffraction (microXRD) (Riekel et al., 1999; Martel et al., 2007; **Figures 2E,F**), holding also for derived crystallographic parameters (e.g., peak position, particle size) (Riekel et al., 2017). The beam divergence of the ∼180 nm focus allows resolving the MaS ∼10 nm SAXS correlation peak from the beamstop (inset **Figure 2B**) (Riekel et al., 2017). A broadened correlation peaks is just visible for the ∼40 nm focus at the edge of the beamstop (**Figure 2C**; red arrow). The geometry (e.g., beamstop size, sample-detector distance) was, however, not optimized for SAXS.

MaS Fibers

Biochemical and spectroscopic studies suggest a skin-core morphology with two proteneous and a very thin lipidic coat surrounding the core (Sponner et al., 2007). Scanning nanoXRD suggests that the inner proteneous coat is amorphous, consisting of nanofibrillar bundles (Riekel et al., 2017). Indeed, the WAXS composite image appears to be homogeneous (**Figures 3A,B**). This holds also for the SAXS composite image based on the meridional correlation peak, attributed to the nanodomains stacks making up the nanofibrils (**Figures 3C,D**). A skin-layer is, however, revealed in the SAXS composite image based on the equatorial streak (**Figures 3E,F**). The modulated intensity profile of one of the streaks (inset **Figure 3G**) can be modeled by scattering from cylindrical rods (**Figure 3G**). Streaks from different locations within the skin suggest a variability in rod diameters from about 40–140 nm (**Figure 3H**) which was also observed by AFM for nanofibrils from the skin-layer of *B. mori* and wild silk fibers (Putthanarat et al., 2000).

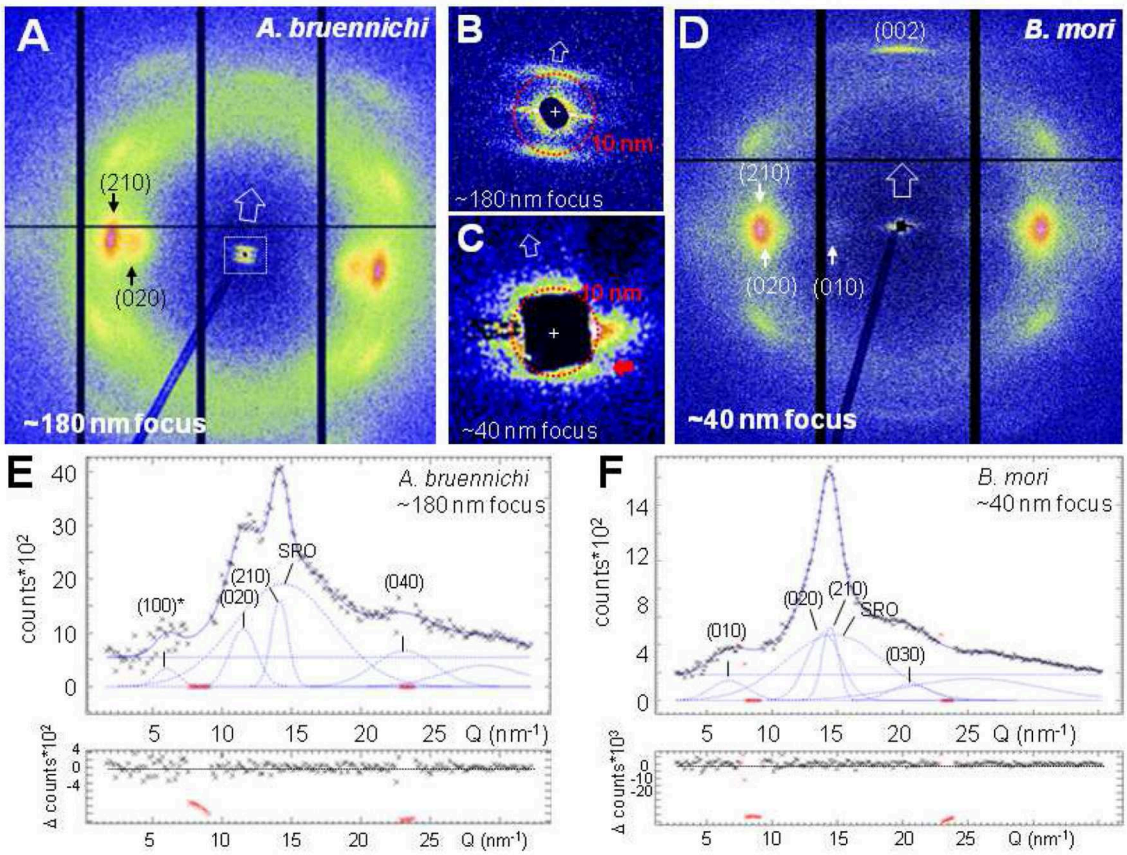

FIGURE 2 | NanoXRD patterns of silk fibers. 20 patterns were averaged for the ∼180 nm focus and 201 patterns for the ∼40 nm focus. **(A)** *A. bruennichi's* MaS fiber pattern for 190 nm_{hor} × 170$_{ver}$ nm^2 (fwhm) focus. Black vertical and horizontal lines correspond to inactive detector areas. **(B)** SAXS-range for ∼180 nm focus. Open arrow along (meridional) fiber axis. **(C)** SAXS-range for ∼40 nm focus; red arrow points to correlation peak at the edge of the beamstop. **(D)** *B. mori's* pattern for 50$_{hor}$ × 35$_{ver}$ nm^2 (fwhm) focus. **(E,F)** Equatorial intensity profiles (black crosses) and fitted curves by Gaussians for Bragg/SRO peaks; 0-order polynomial for random background ($Q = 2\pi/d$; d: lattice spacing); individual Gaussians shown after subtraction of polynomial. Lower plots: differences of observed minus simulated profiles. Inactive detector areas (in red) masked for the fits. Millers indices correspond to poly(L-alanine) or poly(L-alanylglycine) lattices (Marsh et al., 1955a,b). The forbidden (100)* reflection is discussed in Riekel et al. (2017).

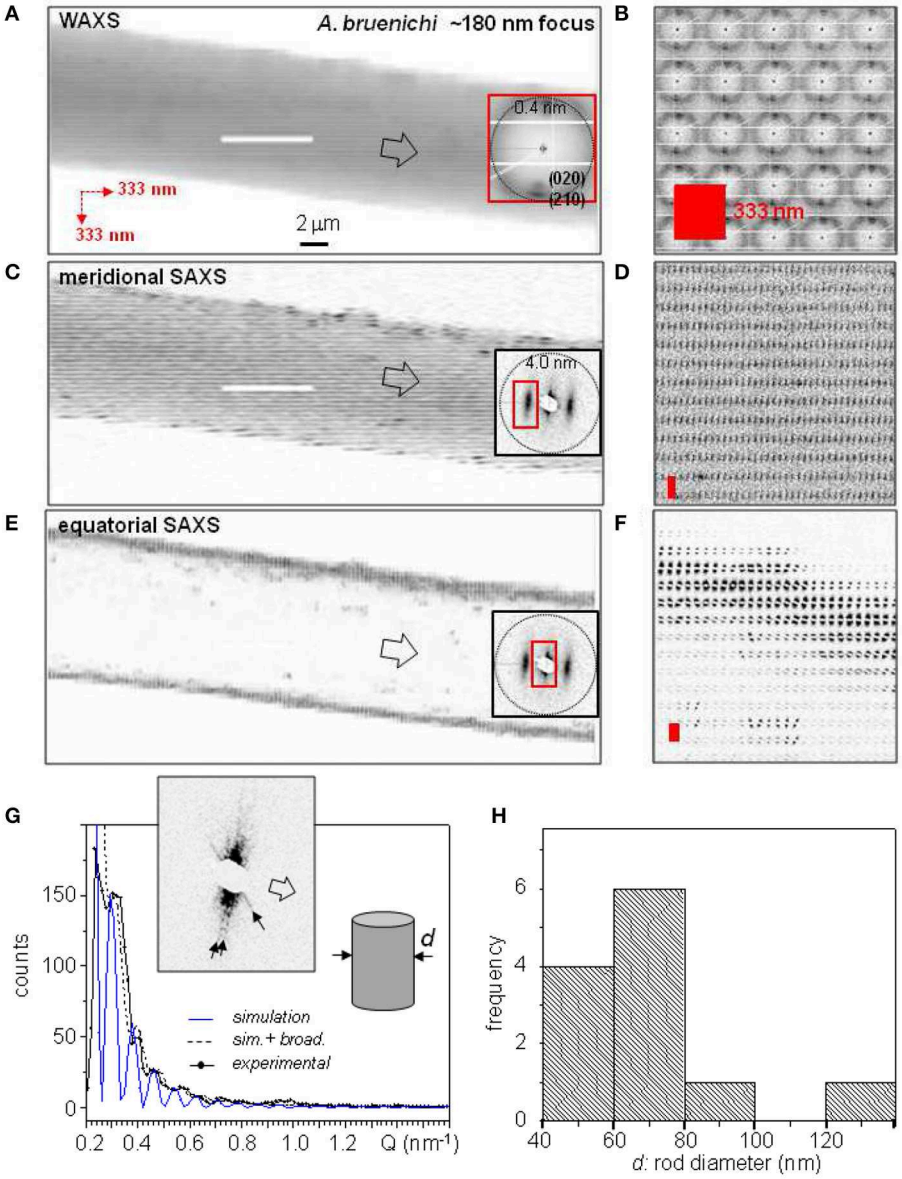

FIGURE 3 | Composite images of *A. bruennichi's* bridge-thread based on 333 nm_{hor} × 333 nm_{ver} raster-steps through 170 nm_{hor} × 170 nm_{ver} (fwhm) focus. The insets show patterns from the center of the fiber. **(A)** Based on strongest WAXS peaks and SRO scattering. **(C)** Based on meridional SAXS correlation peak. **(E)** Based on equatorial SAXS streak. **(B,D,F)** Zooms of composite images to the left; red rectangles correspond to step-increments. **(G)** Simulation of scattering from nanofibrils in the skin-layer by cylindrical model. **(H)** Histogram of skin-layer cylinder diameters. Reproduced/adapted from Riekel et al. (2017) with permission from ACS.

The smallest rod diameters for the MaS thread are observed for positions close to the inner interface of the skin-layer. Individual streaks from nanofibrils observed at this location support the suggestion of a less densely packed layer at the inner interface of the skin-layer (Frische et al., 1998). The local nanofibrillar orientation agrees to the model of a nanofibrillar layer wound around the core (Vollrath et al., 1996).

Evidence for a fragile glycoprotein skin-layer covering the protein coat (Sponner et al., 2007) has not been clearly established as only amorphous patches covered by a thin lipidic layer -possibly due to a degraded glycoprotein coat- were observed (Riekel et al., 2017). A partially peeled-off layer provides, however evidence for a further skin-layer (**Figure 4A**). Indeed, the WAXS composite image reveals powder-like scattering (**Figure 4B**). Averaged patterns show two textured powder rings from Bragg peaks with $d = 0.415$ (± 0.001) nm, $d = 0.375$ (± 0.003) nm lattice spacings which do not correspond to β-sheet peaks (**Figures 4C,D**). Additional SRO scattering supports the model of a thin disordered proteneous layer decorated by nanocrystalline inclusions. The Bragg peaks

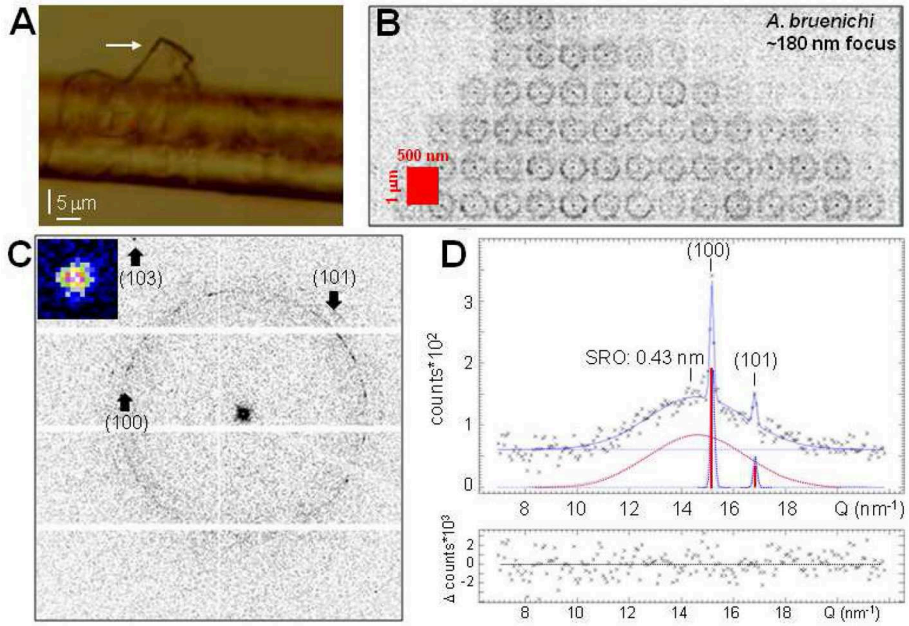

FIGURE 4 | Polyglycine-II (PG-II) nanocrystallites in MaS skin-layer. **(A)** Optical microscopy of thin layer (white arrow) detaching from *A. bruennichi's* MaS thread's surface. **(B)** WAXS composite image based on 500 nm_{hor} × 1 μm_{ver} raster-steps (red rectangle) from the tip of the layer in **(A)** through a 190_{hor} × 170_{ver} nm^2 (fwhm) focus. The pixels are 16× binned to enhance weak scattering. **(C)** Average of patterns from the composite image; positions of (100)/(101) PG-II reflections indicated. A (103) peak with $d = 0.254$ nm (zoom) is indicated at the edge. The limited amount of higher order PG-II reflections is due to the preferred [001] texture, reducing the probability of Bragg scattering. **(D)** Radial intensity profile of **(C)**. Gaussians fitted to Bragg peaks (dotted-blue) and SRO scattering (dotted-red); 0-order polynomial fitted to random background. The calculated intensities of the PG-II (100)/(101) Bragg peaks (Crick and Rich, 1955) are indicated as red bars, scaled to the height of the (100) Gaussian.

can be related to clusters of nanocrystals of about 40 nm size derived from their peak-width using Scherrer's equation (Klug and Alexander, 1974). The peak positions and calculated intensities agree to hexagonal polyglycine II (PG-II) (Crick and Rich, 1955) with a = b = 0.481 (±0.001) nm, c = 0.960 (±0.003) nm. We note that a skin-layer decorated by ∼3.5 nm PG-II nanocrystallites has also been observed by scanning nanoXRD for thin flag silk fibers (Riekel et al., 2019). Although the topic will not be discussed in this article, PG-II reflections can provide an alternative explanation for the S,S* peaks and their intensity ratio observed in MaS fibers (Riekel et al., 1999, 2017; Trancik et al., 2006), which were discussed previously only in the context of the non-periodic lattice (NPL) model (Thiel et al., 1994, 1997).

Silkworm Fibers

Composite images from a *B. mori* bave were obtained for the ∼40 nm focus. WAXS composite images based on the equatorial (210/020) and meridional (002) reflections show a homogeneous matrix as for the MaS thread (**Figures 5A–D**). The weak SAXS streaks are oriented normal to the fiber axis implying axially oriented nanofibrils. A slight intensity increase of the streaks is only observed at the rim (**Figures 5E,F**). Three nanofibrillar fractions of $\pm 48^\circ/0^\circ$ with respect to the fiber axis in a supposedly layered morphology were deduced from AFM images of peeled, degummed *B. mori* fibers and correlated with WAXS data (Putthanarat et al., 2000). We tested this model by averaging all patterns in every horizontal scan-line to increase counting statistics, resulting in a pseudo line-scan normal to the bave axis. A continuous intensity increase of the (020)/(210) Bragg peak from the interface is observed as the fiber volume probed by the focal spot increases while the SAXS streak intensity shows an anomalous increase for 3–4 patterns near the interface (**Figure 5G**). The azimuthal intensity profile at the (020) position can best be simulated by an overlap of two Gaussians with different width (**Figure 5H**). Three Gaussians simulating three nanofibrillar fractions splitting the peak (Putthanarat et al., 2000) do, however, not fit the profile. The narrow peak is attributed to scattering from nanodomains while the broader peak -extending outside the Bragg peaks along the equator- is probably due to a more ordered SRO fraction overlapping the SRO powder ring. We determined the nanodomains orientation function as f_c∼0.93 from the (002) reflections azimuthal width of 12.76° fwhm, corresponding to *A. bruennichi's* MaS f_c-value (Riekel et al., 2017). A ribbon-like nanofibrillar layer wound around the core would imply a variation of the streaks orientations (e.g., **Figure 3G**) which is not observed for *B. mori*. The anomalous intensity of the streaks near the interface could be due to an increase in scattering density contrast due to sericin penetrating the outer fibroin layers (Mueller and Hentschel, 2004), analog to water penetrating MaS fibers (Riekel and Vollrath, 2001). In summary, there is no evidence for a significant fraction of

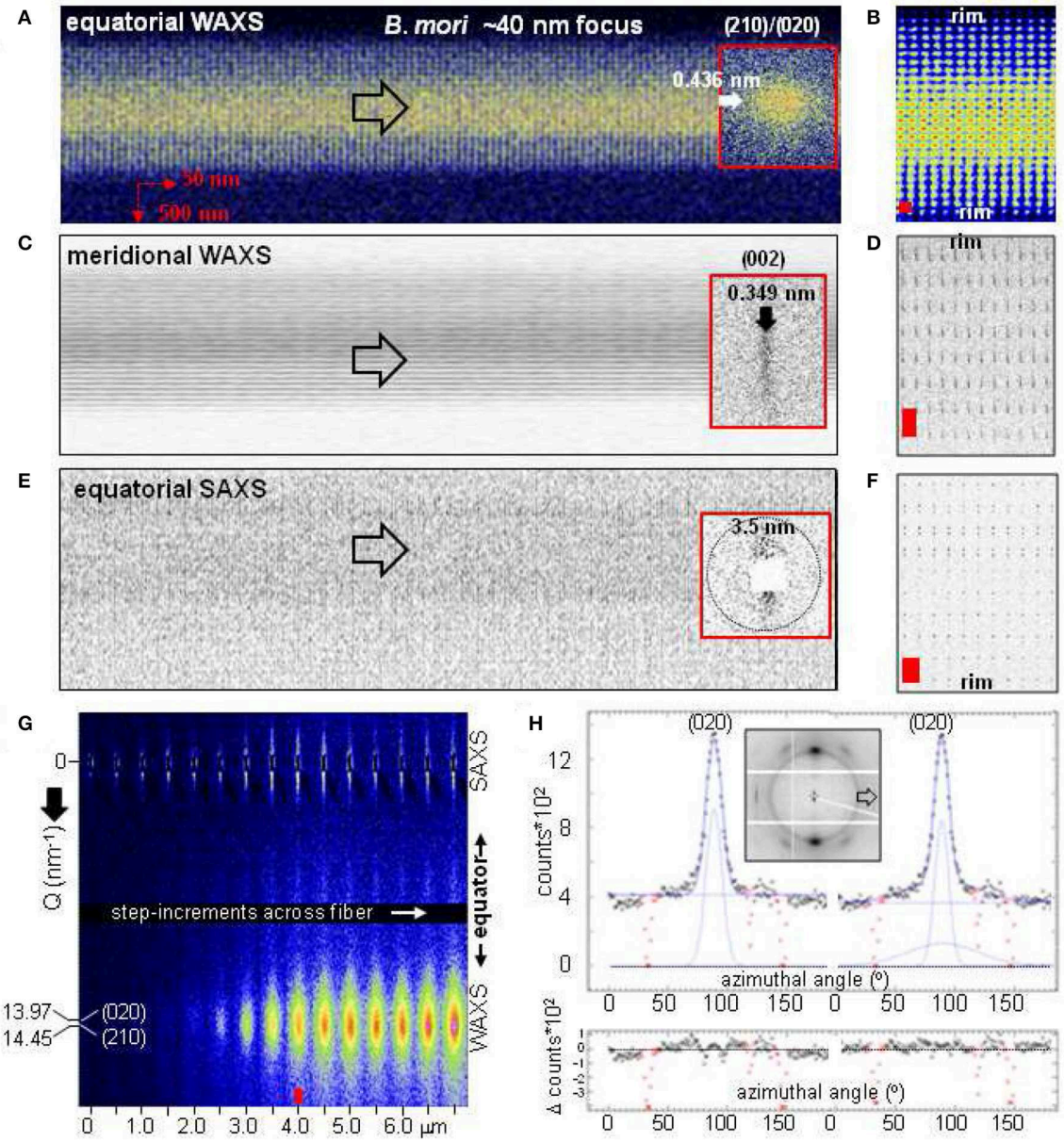

FIGURE 5 | Composite images of *B. mori* bave based on 50 nm_{hor} × 500 nm_{ver} raster-steps through a 50 nm_{hor} × 35 nm_{ver} focus. Note that the two fibers are nearly overlapping in projection. Insets: patterns from the center of the bave. **(A)** Based on (210)/(020) Bragg peaks. **(C)** Based on the (002) Bragg peak. **(E)** Based on the equatorial SAXS streak. Open arrows along fiber axis. **(B,D,F)** Zooms of composite images to the left (distorted for better viewing). Red rectangles correspond to step-increments. **(G)** Pseudo line-scan across part of the bave covering the equatorial SAXS streak and the (020)/(210) peaks. The upper part of the streak is partially extinguished due to a scattering artifact (image expanded vertically by about factor 5). **(H)** Fit of azimuthal profile through (020) peak (inset) for pattern indicated by red arrow in **(G)** by Gaussian and 0-order polynomial functions. Fit by single Gaussian to the left; fit by two Gaussians with different width to the right. Inactive detector areas (in red) masked for the fits.

nanofibrils differing from a unique axial orientation distribution. While it cannot be excluded that the three fractions differing in orientation deduced by AFM (Putthanarat et al., 2000) are related to the degumming process, caution is necessary when correlating surface sensitive AFM with bulk sensitive XRD results.

X-Ray Radiation Damage

X-ray radiation damage due to radicals generated from residual water molecules affects the crystallinity of unexposed neighboring scan-points in a scanning nanoXRD experiment (Riekel et al., 2017). This loss in order increases as the step-width is reduced and affects particularly experiments with the

smallest focal spots. We determined radiation damage effects for a ∼50 nm focal spot by performing consecutive line-scans normal to *A. bruennichi's* MaS fiber axis at 1 μm distance for 500, 250, 100, and 50 nm step-increments (**Figure 6A**).

The patterns were averaged for each line-scan and integrated radially (**Figures 6B,C**). An increase in SRO with reduction of Bragg peak intensities is observed for 100/50 nm step-increments. This is also reflected in the variation of the crystallinity (X) and is accompanied by a reduction of the radial peak width of the equatorial reflections corresponding to a particle size (L) increase (**Figure 6D**). L-values for 250/500 nm step-increments correspond within errors to those obtained for a 170 nm focus (Riekel et al., 2017). As the L-values correspond to an average over all crystalline nanodomain sizes we assume that a preferential destruction of the smaller nanodomains explains the shift to larger L-values with increasing radiation damage. This conclusion was also derived from mesh scans through a 170 nm focus suggesting that the step increment has to be in

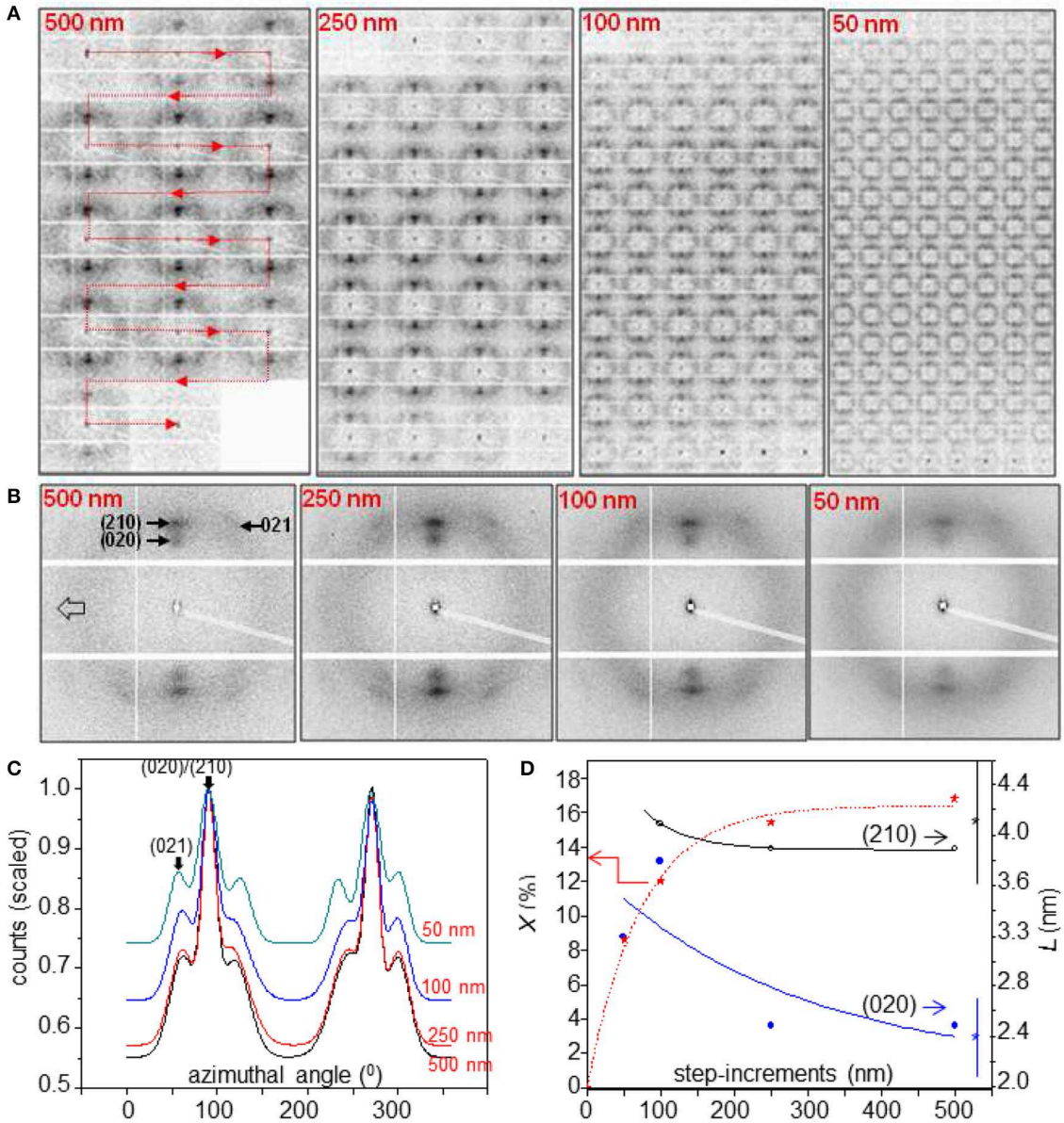

FIGURE 6 | Radiation damage effects during line-scans of *A. bruennichi's* MaS fiber through a ∼50 nm focus. **(A)** Linear scans normal to fiber axis for step-increments indicated as red insets; 1 s exposure per pattern. The red line for 500 nm step-increments indicates the succession of patterns in a line-scan across the fiber. **(B)** Averaged patterns for each line-scan. **(C)** Radially integrated averaged patterns up to the 1st layer-line scaled to the maximum intensity of the (210) reflections (=1.0). **(D)** Variation of crystallinity (X; red stars) and particle size (L) for (020) (blue circles) and (210) (black circles) peaks as a function of step-increments. Exponential functions fitted as guides-to-the eye, assuming $X = 0\%$ for 0 nm focal spot size. L-values with 2σ error bars to the right were obtained for a 170 nm focus (Riekel et al., 2017).

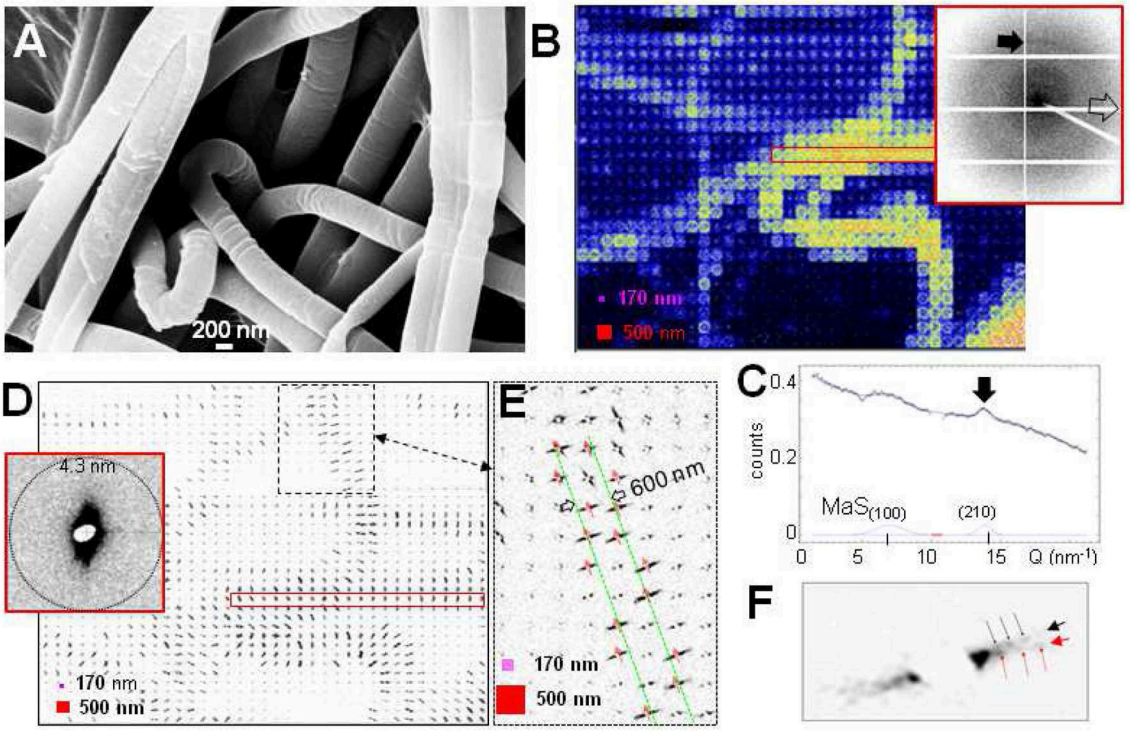

FIGURE 7 | Scanning nanoXRD of *A. bruennichi's* decorating fibers with 500 nm_{hor} × 500 nm_{ver} raster-steps through a 170 nm_{hor} × 170 nm_{ver} focus. **(A)** Scanning electron microscopy (SEM) image of decorating fibers (Zeiss Leo SEM: 10 KV, 10 nm sputtered gold layer). **(B)** WAXS composite image covering diffuse powder ring in inset-pattern; pink square: focus size; red square: step-increments (also in **D,E**). Inset: averaged scattering from patterns within red, open rectangle. Black arrow indicates a weak equatorial peak; open arrow along local fiber axis. **(C)** Equatorial WAXS profile fitted by 2 Gaussians for Bragg peaks and a 1st-order polynomial for the overall diffuse scattering. Black arrow as for inset-pattern in **(B)**. $MaS_{(100)/(210)}$ positions: (Riekel et al., 2017). **(D)** SAXS composite image based on equatorial streak. Inset shows averaged scattering from within red rectangle. **(E)** Zoom of dashed area in **(D)**; SAXS streaks define the contours (in green) of an about 600 nm diameter fiber (or thread); red arrows: local fiber axes. **(F)** Zoom into streak at rim of the fiber in **(E)** revealing two intensity-modulated streaks with ~10^0 angular separation (black/red arrows).

the order of ≥500 nm to minimize radiation damage effects for current scanning nanoXRD conditions (Riekel et al., 2017). For qualitative work a certain extent of radiation damage can be accepted when reducing step-increments. To reduce radiation damage effects, mesh-scans are often performed as successive line-scans with as small as possible step-increment while the separation of neighboring scan-lines is increased to ≥500 nm (**Figures 5A–F**). Radiation damage effects are generally less important for higher crystalline *B. mori* fibers allowing line-scans with down to 50 nm step-increments.

Fine Silk Fibers

Fine silk fibers down to subμm diameters are becoming accessible to scanning nanoXRD as shown for decorating fibers composing the stabilimentum of *Argiope* spiders (**Figure 7A**) which are attributed to aciniform silk (Herberstein et al., 2000; Foelix, 2011). Indeed, composite images reveal the contours of the fibers (**Figures 7B,D,E**). The WAXS pattern is dominated by diffuse scattering from a disordered fraction with additional weak intensity modulations resembling MaS SRO scattering (**Figure 7C**). A narrow equatorial peak at the MaS (210) position suggests a fraction of β-type nanodomains of about 5 nm particle size. The relatively strong peak at the position of the forbidden MaS (100) reflection (Riekel et al., 2017) could be due to side-group disorder of polypeptide chains. We estimate the volume fraction of the β-type material <5% from the ratio of the β-type scattering to the broad diffuse scattering background. The focal spot size is, however, too large for determining the local distribution of β-type scattering and verifying the possibility of a skin-core structure. The rim of the fibers is revealed by equatorial SAXS streaks (**Figures 7D,E**) with intensity modulations implying a nanofibrillar morphology (**Figure 7F**). Analysis of the intensity modulations for a rod-like objects (see **Figure 3G**) suggests a rod diameter of about 50 nm.

CONCLUSIONS AND OUTLOOK

The skin-core morphology of MaS fibers has been investigated by scanning nanoXRD and the presence of two proteneous layers -suggested by biochemical and spectroscopic studies (Sponner et al., 2007)—has been confirmed. No evidence for skin-core morphology has, however, been obtained for a silkworm fiber. One of the MaS layers appears to be amorphous with nanofibrillar morphology. The other layer, which is probably formed by

glycoproteins (Sponner et al., 2007), is decorated by PG-II nanocrystallites. This type of skin-layer covering an amorphous core has also been observed for *A. marmoreus* flagelliform silk (Riekel et al., 2019). We note that morphologies based on ordered skin-layers and a more disordered core, providing a balance of strength and toughness, are well-known for synthetic polymeric fibers (Müller et al., 2000; Liu et al., 2014). PG-II nanodomains have only recently been suggested as functional elements, reinforcing flagelliform silk fibers (Perea et al., 2013). S,S* reflections observed for MaS fibers are probably also based on PG-II nanodomains. Systematic studies of nanoscale heterogeneities across the spider phylogeny should shed light on the presence and local distribution of β-sheet, PG-II and possibly other nanocrystalline inclusions. Potential targets are β-type nanodomains in *Argiope* decorating fibers (**Figure 7B**), the probably ribbon-like morphology of *Eriophora* MiS fibers (Riekel et al., 2001) and PG-II nanodomains in several flagelliform silks probed by microXRD (Craig, 2003; Perea et al., 2013). Such studies could also contribute to an understanding of the nature of graphene and single-walled carbon nanotubes inclusions in spiders MaS and silkworm fibroin fibers (Wang et al., 2014, 2016; Lepore et al., 2017).

The ESRF is currently being upgraded in the context of the "Extremely Bright Source" (EBS) project from a 3rd to a 4th generation synchrotron radiation source with an expected increase in brightness by more than an order in magnitude (Dimper et al., 2015). This should allow scanning nanoXRD techniques evolving into providing enhanced reciprocal space (SAXS) resolution for focal spots down to around 100 nm or aim at very small focal spots in the 10–30 nm range with a limited SAXS resolution. Both types of focal spots will likely provide new insights into silks hierarchical organization and will also require exploring advanced sectioning approaches such as focused ion beam (FIB) techniques. Increasing the composite image spatial resolution (pixel-density) will require, however, new data collection approaches for reducing radiation damage, enabling also tomographic approaches. Indeed, cryocooling techniques adapted to the high positional sample stability requirements would allow blocking radical propagation. The aim of correlating microstructure with macroscopic (e.g., mechanical) properties will continue, however, requiring room temperature experiments. It will be interesting exploring whether more intense nanobeams would allow outrunning radical propagation into unexposed scan-points by faster scan-modes enabled by high readout-frequency pixel detectors. This could provide access to nanoscale resolution composite images of parts of orb-webs comprising functionally different fibers including junctions and of dynamic processes related to crystallization or aggregation.

DATA AVAILABILITY STATEMENT

All datasets generated for this study are included in the article/supplementary material.

AUTHOR CONTRIBUTIONS

All authors listed have made a substantial, direct and intellectual contribution to the work, and approved it for publication.

ACKNOWLEDGMENTS

We thank Dr. Irina Snigireva (ESRF microimaging lab) for providing the SEM image of decorating fibers.

REFERENCES

Blackledge, T. A., Pérez-Rigueiro, J., Plaza, G. R., Perea, B., Navarro, A., Guinea, G. V., et al. (2012). Sequential origin in the high performance properties of orb spider dragline silk. *Sci. Rep*. 2:782. doi: 10.1038/srep00782

Cetinkaya, M., Xiao, S., Markert, B., Stacklies, W., and Gräter, F. (2011). Silk fiber mechanics from multiscale force distribution analysis. *Biophys. J*. 100, 1298–1305. doi: 10.1016/j.bpj.2010.12.3712

Craig, C. L. (2003). *Spiderwebs and Silk: Tracing Evolution From Molecules to Genes to Phenotypes*. New York, NY: Oxford University Press.

Crick, F. H., and Rich, A. (1955). Structure of polyglycine II. *Nature* 176, 780–781. doi: 10.1038/176780a0

Dimper, R., Reichert, H., Raimondi, P., Sánchez Ortiz, L., Sette, F., and Susini, J. (2015). *Orange Book: ESRF Upgrade Programme Phase II (2015-2022)-Technical Design Study*. Grenoble: ESRF; The European Synchrotron.

Foelix, R. F. (2011). *Biology of Spiders*. New York, NY: Oxford University Press.

Fraser, R. D. B., and MacRae, T. P. (1973). *Conformations of Fibrous Proteins*. New York, NY: Academic Press.

Frische, S., Maunsbach, A., and Vollrath, F. (1998). Elongate cavities and skin-core structure in *Nephila* spider silk observed by electron microscopy. *J. Microscopy* 189, 64–70. doi: 10.1046/j.1365-2818.1998.00285.x

Herberstein, M. E., and Craig, C. L., Coddington, J. A., and Elgar, M. A. (2000). The functional significance of silk decorations of orb-web spiders: a critical review of the empirical evidence. *Biol. Rev*. 75, 649–669. doi: 10.1111/j.1469-185X.2000.tb00056.x

Klug, H. P., and Alexander, L. E. (1974). *X-ray Diffraction Procedures for Polycrystalline and Amorphous Materials*. New York, NY: Wiley Interscience.

Kubec, A., Melzer, K., Gluch, J., Niese, S., Braun, S., Patommel, J., et al. (2017). Point focusing with flat and wedged crossed multilayer laue lenses. *J. Synchotron Rad*. 24, 413–421. doi: 10.1107/S1600577517001722

Lepore, E., Bosia, F., Bonaccorso, F., Bruna, M., Taioli, S., Garberoglio, G., et al. (2017). Spider silk reinforced by graphene or carbon nanotubes. *2D Mater*. 4:031013. doi: 10.1088/2053-1583/aa7cd3

Liu, Q., Gao, H., Zha, L., Hu, Z., Ma, Y., Yu, M., et al. (2014). Tuning bio-inspired skin–core structure of nascent fiber via interplay of polymer phase transitions. *Phys.Chem.Chem.Phys*. 16, 15152–15157. doi: 10.1039/C4CP00792A

Marsh, R. E., Corey, R. B., and Pauling, L. (1955a). An investigation of the structure of silk fibroin. *Biochim. Biophys. Acta* 16, 1–34. doi: 10.1016/0006-3002(55)90178-5

Marsh, R. E., Corey, R. B., and Pauling, L. (1955b). The Structure of Tussah Silk Fibroin. *Acta Cryst*. 8, 710–715. doi: 10.1107/S0365110X5500217X

Martel, A., Burghammer, M., Davies, R. J., and Riekel, C. (2007). Thermal degradation of *Bombyx mori* silk: evolution of molecular dtructure, crystalline parameters and mechanical properties. *Biomacromolecules* 8, 3548–3556. doi: 10.1021/bm700935w

Mueller, B. R., and Hentschel, M. P. (2004). Synchrotron radiation refraction tomography for characterization of lightweight materials. *X-ray Spectr*. 33, 402–406. doi: 10.1002/xrs.736

Müller, M., Riekel, C., Vuong, R., and Chanzy, H. (2000). Skin/core micro-structure in viscose rayon fibres analysed by X-ray microbeam

and electron diffraction mapping. *Polymer* 41, 2627–2632. doi: 10.1016/S0032-3861(99)00433-4

Papadopoulos, P., Soelter, J., and Kremer, F. (2009). Hierarchies in the structural organization of spider silk - a quantitative model. *Colloid Polym. Sci.* 287, 231–236. doi: 10.1007/s00396-008-1968-x

Perea, G. B., Riekel, C., Guinea, G. V., Madurga, R., Daza, R., Burghammer, M., et al. (2013). Identification and dynamics of polyglycine II nanocrystals in *Argiope trifasciata* flagelliform silk. *Sci. Rep.* 3:3061. doi: 10.1038/srep03061

Puglisi, G., De Tommasi, D., Pantano, M. F., Pugno, N. M., and Saccomandi, G. (2017). Micromechanical model for protein materials: from macromolecules to macroscopic fibers. *Phys. Rev. E* 96:042407. doi: 10.1103/PhysRevE.96.042407

Putthanarat, S., Stribeck, N., Fossey, S. A., Eby, R. K., and Adams, W. W. (2000). Investigation of the nanofibrils of silk fibers. *Polymer* 41, 7735–7747. doi: 10.1016/S0032-3861(00)00036-7

Riekel, C., Braenden, C., Craig, C., Ferrero, C., Heidelbach, F., and Müller, M. (1999). Aspects of X-ray diffraction on single spider fibers. *Int. J. Biol. Macrom.* 24, 179–186. doi: 10.1016/S0141-8130(98)00084-1

Riekel, C., Burghammer, M., Dane, T. J., Ferrero, C., and Rosenthal, M. (2017). Nanoscale structural features in spider bridge thread fibres. *Biomacromolecules* 18, 231–241. doi: 10.1021/acs.biomac.6b01537

Riekel, C., Burghammer, M., Davies, R., Gebhardt, R., and Popov, P. (2009). "Fundaments of soft condensed matter scattering and diffraction with microfocus techniques," in *Applications of Synchrotron Light to Scattering and Diffraction in Materials*, Vol. 776, eds T. A. Ezquerra, M. Garcia-Gutierrez, A. Nogales, and M. Gomez. Heidelberg: Springer. 91–104. doi: 10.1007/978-3-540-95968-7_4

Riekel, C., Burghammer, M., and Rosenthal, M. (2019). Skin-core morphology in spider flagelliform silk. *Appl. Phys. Lett.* 115:123702. doi: 10.1063/1.5110268

Riekel, C., Craig, C. L., Burghammer, M., and Müller, M. (2001). Microstructural homogeneity of support silk spun by *Eriophora fuliginea* (C.L. Koch) determined by scanning X-ray microdiffraction. *Naturwissenschaften* 88, 67–72. doi: 10.1007/s001140000197

Riekel, C., and Vollrath, F. (2001). Spider silk fibre extrusion: combined wide- and small-angle X-ray microdiffraction experiments. *Int. J. Biol. Macrom.* 29, 203–210. doi: 10.1016/S0141-8130(01)00166-0

Sapede, D., Seydel, T., Forsyth, V. T., Koza, M., Schweins, R., Vollrath, F., et al. (2005). Nanofibrillar structure and molecular mobility in spider dragline silk. *Macromolecules* 38, 8447–8453. doi: 10.1021/ma0507995

Sponner, A., Vater, W., Monajembashi, S., Unger, E., Grosse, F., and Weisshart, K. (2007). Composition and hierarchical organisation of a spider silk. *PLOS One* 10:e998. doi: 10.1371/journal.pone.0000998

Su, I., and Buehler, M. J. (2016). Nanomechanics of silk: the fundamentals of a strong, tough and versatile material. *Nanotechnolohy* 27:302001. doi: 10.1088/0957-4484/27/30/302001

Termonia, Y. (1994). Molecular modelling of spider silk elasticity. *Macromolecules* 27, 7378–7381. doi: 10.1021/ma00103a018

Thiel, B. L., Guess, K. B., and Viney, C. (1997). Non-periodic lattice crystals in the hierarchical microstructure of spider (major ampullate) silk. *Biopolymers* 41, 703–719. doi: 10.1002/(SICI)1097-0282(199706)41:7<703::AID-BIP1>3.0.CO;2-T

Thiel, B. L., Kunkel, D., and Viney, C. (1994). Physical and chemical microstructure of spider dragline: a study by analytical transmission electron microscopy. *Biopolymers* 34, 1089–1097. doi: 10.1002/bip.360340812

Trancik, J. E., Czernuszka, J. T., Bell, F. I., and Viney, C. (2006). Nanostructural features of a spider dragline silk as revealed by electron and X-ray diffraction studies. *Polymer* 47, 5633–5642. doi: 10.1016/j.polymer.2005.01.110

Vollrath, F., Holtet, T., Thøgersen, H. C., and Frische, S. (1996). Structural organization of spider silk. *Proc. R. Soc. Lond. B* 263, 147–151. doi: 10.1098/rspb.1996.0023

Wang, J. T., Li, L. L., Zhang, M. Y., Liu, S. L., Jiang, L. H., and Shen, Q. (2014). Directly obtaining high strength silk fiber from silkworm by feeding carbon nanotubes. *Mat Sci Eng C* 34, 417–421. doi: 10.1016/j.msec.2013.09.041

Wang, Q., and Schniepp, H. C. (2018). Strength of recluse spider's silk originates from nanofibrils. *ACS MacroLett.* 7, 1364–1370. doi: 10.1021/acsmacrolett.8b00678

Wang, Q., and Schniepp, H. C. (2019). Nanofibrils as building blocks of silk fibers: critical review of the experimental evidence. *JOM* 71, 1248–1263. doi: 10.1007/s11837-019-03340-y

Wang, Q., Wang, C., Zhang, M., Jian, M., and Zhang, Y. (2016). Feeding single-walled carbon nanotubes or graphene to silkworms for reinforced silk fibers. *Nano Lett.* 16, 6695–6700. doi: 10.1021/acs.nanolett.6b03597

Yang, Z., and Grubb, D. T., and Jelinski, L. W. (1997). Small-angle X-ray scattering of spider dragline silk. *Macromolecules* 30, 8254–8261. doi: 10.1021/ma970548z

Yoshioka, T., Tsubota, T., Tashiro, K., Jouraku, A., and Kameda, T. (2019). A study of the extraordinarily strong and tough silk produced by bagworms. *Nat. Commun.* 10:1469. doi: 10.1038/s41467-019-09350-3

Conflict of Interest: The authors declare that the research was conducted in the absence of any commercial or financial relationships that could be construed as a potential conflict of interest.

frontiers in Materials

ORIGINAL RESEARCH
published: 18 December 2019
doi: 10.3389/fmats.2019.00331

Use of Silk Proteins to Form Organic, Flexible, Degradable Biosensors for Metabolite Monitoring

Meng Xu[1], *Yanke Jiang*[1,2], *Sayantan Pradhan*[1] *and Vamsi K. Yadavalli*[1]*

[1] Department of Chemical and Life Science Engineering, Virginia Commonwealth University, Richmond, VA, United States, [2] College of Environment and Resources, Chongqing Technology and Business University, Chongqing, China

The development of sustainable and degradable biosensors and bioelectronics has implications for implantable systems, as well in addressing issues of electronic waste. Mechanically flexible and bioresorbable sensors can find applications at soft biological interfaces. While devices typically use metallic and synthetic components and interconnects that are non-degradable or have the potential to cause adverse tissue reactions, the use of nature-derived materials and conducting polymers can provide distinct advantages. In particular, silk fibroin and sericin can provide a unique palette of properties, providing both structural and functional elements. Here, a fully organic, mechanically flexible biosensor in an integrated 3-electrode configuration is demonstrated. Silk sericin conducting ink is micropatterned on a silk fibroin substrate using a facile photolithographic process. Next, using a conducting polymer wire sheathed in silk fibroin, organic interconnects are used to form the electrical connections. This fully organic electrochemical system has competitive performance metrics for sensing in comparison to conventional systems, as verified by detection of a model analyte—ascorbic acid. The stability of the silk biosensor through biodegradation was observed, showing that the sensors can function for several days prior to failure. Such protein-based systems can provide a useful tool for biomonitoring of analytes in the body or environment for controlled periods of time, followed by complete degradation, as transient systems for various applications.

Keywords: organic electronics, flexible biosensor, silk fibroin, silk sericin, conductive polymers, biodegradable, metabolite monitoring

OPEN ACCESS

Edited by:
Antonella Motta,
University of Trento, Italy

Reviewed by:
PaYaM ZarrinTaj,
Oklahoma State University, United States
Ahmed El-Fiqi,
Dankook University, South Korea

***Correspondence:**
Vamsi K. Yadavalli
vyadavalli@vcu.edu

Specialty section:
This article was submitted to Biomaterials, a section of the journal Frontiers in Materials

Received: *15 September 2019*
Accepted: *03 December 2019*
Published: *18 December 2019*

Citation:
Xu M, Jiang Y, Pradhan S and Yadavalli VK (2019) Use of Silk Proteins to Form Organic, Flexible, Degradable Biosensors for Metabolite Monitoring. Front. Mater. 6:331. doi: 10.3389/fmats.2019.00331

INTRODUCTION

Devices with properties of biocompatibility, flexibility, and degradability can function as on-body (e.g., wearables) or *in vivo* (e.g., implantables) monitoring systems for human health, soft robotics, or human-machine interfaces (Wang et al., 2017a,b, 2018; Feiner and Dvir, 2018; Xu et al., 2018). The use of mechanically compliant substrates allows function in contact with delicate biological interfaces and physical deformation. Components that can break down functionally and/or physically at the end of their operational period with programmable lifetime and functionality, can potentially resolve risks associated with chronic implants, or the need for additional extractive surgery (Tan et al., 2016; Lei et al., 2017). Concurrently, there is an increasing desire for "green electronics" with sustainable fabrication and lifecycle, with the objective of reducing e-waste (Irimia-Vladu, 2014). Qualities of sustainability, miniaturization, flexibility, biodegradability, and

biocompatibility can therefore provide great utility. This class of devices is being enabled by an evolution in organic electronic materials (Balint et al., 2014; Liao et al., 2015), as well as advanced synthetic or bio-derived/inspired substrates (Zhu et al., 2016; Liu et al., 2017). Natural, intrinsically flexible and mechanically robust biomaterials have been proposed as structural components for a wide variety of devices (Suginta et al., 2013; Zhu et al., 2016; Liu et al., 2017). In particular, silk proteins (fibroin and sericin) provide a unique ensemble of properties that make them ideal for these applications. In comparison to synthetic polymers, they can provide controllable biodegradability, and mild immune and inflammatory responses (Enomoto et al., 2010; Thurber et al., 2015). We posit the ability of silk proteins to provide not just the *structural* components of biodegradable devices, but also the *functional* constituents therein (Kim et al., 2010; Hwang et al., 2013).

In this work, we show the use of silk proteins to fabricate electrochemical biosensors as well as their interconnects, demonstrating how fibroin and sericin can provide viable and competitive alternatives. Specifically the goal is to outline the substitution of inorganic/metallic materials at sensor-biological interfaces (Rivnay et al., 2014). In conventional electrochemical systems, a 3-electrode configuration with metal electrodes (e.g., Pt, Ag/AgCl) is used. Conducting or semiconducting fibers/wires are needed to connect various components and external power sources. While metals present high conductivity and low cost, they tend to be oxidized under ambient and especially, physiological conditions, and can possess a mechanical mismatch in terms of weight and modulus at soft tissue interfaces (Geddes and Roeder, 2003). Often, they have low biocompatibility, cytotoxicity, and foreign body reaction (Voskerician et al., 2005; Gong et al., 2016). With a few exceptions, they are not biodegradable (Yun et al., 2009). In some cases, electrodes have to be coated with soft materials to minimize inflammatory responses or blocking due to protein adsorption (Hanssen et al., 2016). However, there have been relatively few studies in the development of fully organic, flexible functional devices, typically owing to lower performance metrics, leading to the need to incorporate metallic elements. Here we show how silk proteins in conjunction with conducting polymers can be used for the fabrication of functional fully organic, flexible, degradable biosensors.

In this system, conductive electrodes are micropatterned on a silk fibroin support substrate to form biosensing elements. The electrodes are formed using an ink comprising the conducting polymer poly (3,4-ethylenedioxythiophene):poly(styrene sulfonate) (PEDOT:PSS) dispersed within a silk sericin protein matrix. We utilize photocrosslinkable variants of both silk fibroin and sericin, that permits the use of a facile photolithographic technique to fabricate a flexible device (Kurland et al., 2013, 2014). Using these biomaterials, our group has earlier shown the fabrication of flexible biosensors for electroactive targets (e.g., ascorbic acid, dopamine, glucose), biomacromolecules such as vascular endothelial growth factor (VEGF), and microsupercapacitors for energy storage (Pal et al., 2016b, 2018; Xu and Yadavalli, 2019). Here, for the first time, we show a 3-electrode electrochemical cell using only the silk conductive ink + flexible silk substrate, without metal components. This implies that the working (WE), reference (RE), and counter electrodes (CE) are formed using the organic ink. We further show the use of core-sheath PEDOT:PSS-silk fibroin conductive wires to connect the devices. Conductive polymers constituting "organic wiring," offer advantages in terms of biocompatibility, low cytotoxicity, and ease of biochemical modification (Liao et al., 2015; Aydemir et al., 2016; Pappa et al., 2018). Polymer sheathing can protect their connections with external power sources or readouts. Protective sheaths around the wires can improve flexibility and operational life by providing shielding from the external environment, as well as protecting the surrounding tissue from damage (Green et al., 2008). In this work, ascorbic acid is used as a model small molecule analyte to demonstrate the function of the sensor. Fully organic silk biosensors with organic wiring can potentially permit real-time, continuous monitoring of health parameters in a minimally- or non-invasive manner, while providing mechanical conformability to the intrinsically curvy body or tissue interface. The system is stable in a liquid environment, but can be proteolytically degraded. These studies lay the groundwork for the use of silk biomaterials toward mechanically flexible, functionally transient devices that can provide highly biocompatible, and degradable systems for healthcare or environmental applications.

MATERIALS AND METHODS

Materials

All analytical grade reagents were used unless stated otherwise. Silk fibroin was extracted and purified from *Bombyx mori* silkworms following a well-established protocol (Rockwood et al., 2011). Silk sericin was used as received from Wako Chemicals (Richmond, VA). PEDOT:PSS (dry re-dispersible pellets) was purchased from Sigma-Aldrich (St. Louis, MO) and made into 1% solution in DI-water. The PEDOT:PSS solution was homogenized by ultrasonication (20 kHz, Cole-Parmer, Vernon Hills, IL) for 30 min, and filtered through a 0.45 μm-pore-size filter. A conductive ink composite consisting of PEDOT:PSS suspension in photosericin was stored at room temperature for later use. For the chemical modification of silk proteins, 2-isocyanatoethyl methacrylate (IEM, 98% with ≤0.1% BHT as inhibitor) and anhydrous lithium chloride (LiCl) (Sigma-Aldrich) were used. Anhydrous dimethyl sulfoxide (DMSO) and formic acid (FA) were from Thermo Fisher Scientific (Waltham, MA). L-ascorbic acid powder was purchased from Duda Energy LLC (Decatur, AL).

Synthesis of Photoreactive Silk Proteins

Photoreactive fibroin and sericin were synthesized according previously reported protocols (Kurland et al., 2013; Pal et al., 2016a). Briefly, the silk protein (fibroin or sericin) was dissolved in 1 M LiCl in DMSO to form 1% (w/v) solution. The proteins were conjugated with photoreactive methacrylate moieties by reaction with IEM at 60°C for 5 h with continuous N_2 purge. The modified proteins were precipitated in excess cold ethanol overnight. The precipitate was washed with cold ethanol/acetone (1:1) solution and centrifuged (4,000 rpm, 20 min, 4°C), and this

process was repeated 3 times. Finally, the product was lyophilized to obtain photocrosslinkable fibroin and sericin powder (referred to herewith as photofibroin and photosericin).

PEDOT:PSS Spinning Solution and Conductive Fiber Fabrication

PEDOT:PSS pellets were dispersed in water followed by ultrasonication to form a homogeneous stock solution of 10% (w/w). Fiber spinning was carried out using a wet-spinning method (Zhang et al., 2019). PEDOT:PSS solution was extruded via a syringe pump (Harvard Apparatus PHD 2000) into a 98% H_2SO_4 coagulation bath. Extrusion was performed from the bottom of the bath. Optimizing for the processing conditions, the fiber diameter (strength), and conductivity, fibers with 10 wt.% PEDOT:PSS were used, which were extruded using a blunt 27G needle at 0.25 μl/min. This composition resulted in highly stable fibers ∼50 μm diameter that can be easily handled, with a conductivity of ∼140 S/cm. The spun fibers were directly washed using an ethanol/water mixture (3:1 v/v) to remove any residual H_2SO_4. PEDOT:PSS fibers were collected on a reel then dried at room temperature.

Fabrication of Sheathed Single or Multiple PEDOT:PSS Fibers

Silk-sheathed PEDOT:PSS wires were formed by coating the conductive fibers in photofibroin via photocrosslinking at an ambient environment. Formic acid was used as the solvent with 13.2% (w/v) of photofibroin and 4.4% of Irgacure 2959 photoinitiator (BASF, Germany). The photoreactive, optically transparent coating solution was applied on a glass microchannel support to form a bottom layer. PEDOT:PSS fibers were then straightened and anchored on the bottom. A top layer was then formed by drop-casting. Following evaporation of the excess solvent, the sheathed fiber was crosslinked using UV light for 5 s (OmniCure S1000 UV Spot Curing lamp (Lumen Dynamics, Ontario, Canada) at 365 nm (2 mW cm^{-2}). Free-standing, sheathed, conducting wires were obtained by separating from the glass support using water immersion.

Fabrication of the Flexible Biosensor

Flexible silk fibroin substrates and conductive microelectrodes were formed using contact photolithography with designed features (**Figure 1**) (Xu et al., 2019). The substrate was formed from a solution composed of 7.5% (w/v) of photofibroin and 1.5% of Irgacure 2959 photoinitiator in formic acid (FA). The solution was drop-cast on a clean glass substrate. To avoid adhesion between the photoresist and the photomask, the excess solvent was allowed to completely evaporate in a fume hood. The cast fibroin thin films were polymerized by UV exposure using an OmniCure S1000 UV Spot Curing lamp (Lumen Dynamics, Ontario, Canada). The entire film was exposed at 365 nm UV (2 mW cm^{-2}) for 2 s to form the flexible substrates. The conductive ink is a water-based biocomposite with a formulation of 2.5% (w/v) of photosericin, 1% (w/v) PEDOT:PSS, and 0.5% (v/v) of Darocur 1173 photoinitiator. The ink was drop-cast on the fibroin substrates. After the conductive ink was completely dried under dark in the fume hood, microelectrodes were patterned under UV light for 1.5 s through a chrome photomask. The microelectrodes were developed in DI-water under sonication, followed by rinsing with excess water to remove any residual ink.

Silk fibroin sheathed PEDOT: PSS wires were then connected to the electrodes using a conductive ink composite of 6.25% (w/w) PEDOT:PSS in photosericin. The conductive ink was cast at the junction between the wires and the electrodes and dried slowly under ambient conditions. This was followed by photocrosslinking of the junction using UV. A 7.25% (w/v) solution of photofibroin in HFIP was used to further seal the junction. The solution was cast on the junction, dried and crosslinked under UV light. The presence of residual acrylate groups on the surface of the electrodes in the conductive ink and in the photofibroin solution allows the covalent attachment of the entire system on the substrate. Therefore, the connection of the wire with the electrode do not easily get damaged under mechanical deformation. Finally, the system was connected to a potentiostat for electrochemical measurements.

Electrochemical Characterization and Measurement

Electrochemical measurements were conducted using a Gamry Interface 1010E Potentiostat (Gamry Instruments, Warminster, PA). The electrical conductivity of uncoated PEDOT:PSS fibers and sheathed fibers were characterized by cyclic voltammetry (CV) using a two-electrode configuration. In order to test if the coating was successful, Cu tape was attached to the exposed portion of the fiber and different positions on the sheath. The ability of the silk fibroin to form an electrically insulating sheath on the conductive fibers was also tested. The experimental set up and the conductivity of the bare and sheathed wires are shown in **Figure S1**. In order to compare the performance of the designed all-organic electrodes, a standard three-electrode cell configuration was used (organic electrode as the working electrode, Ag/AgCl as the standard reference electrode and Pt as the counter electrode). Cyclic voltammetry (CV) and the chronoamperometry were carried out to characterize the biosensor and to conduct the electrochemical detection. The scanning range was −1 to 1 V at the rate of 50 mV s^{-1}. In amperometric measurements, the potential was set to 0.5 V.

Performance of Biosensor Under Proteolytic Degradation

To determine the response of the biosensor as they degrade, the organic microelectrodes were immersed in 3 ml of PBS solution containing 1 mg ml^{-1} protease (Protease XIV from *Streptomyces griseus,* ≥3.5 U mg^{-1}, Sigma Aldrich) and stored at 37°C. As a control, PBS buffer without protease was used. Samples were extracted at regular intervals and investigated under an optical microscope for degradation. In addition, the function of the biosensors was studied over this period. The sensors were taken out at Day 1, 4, and 7, cleaned with DI-water, and dried using N_2. The sensors were then used for sensing of ascorbic acid. The degradation evaluation was tested by cyclic voltammetry (CV) using a standard three-electrode cell configuration as noted above.

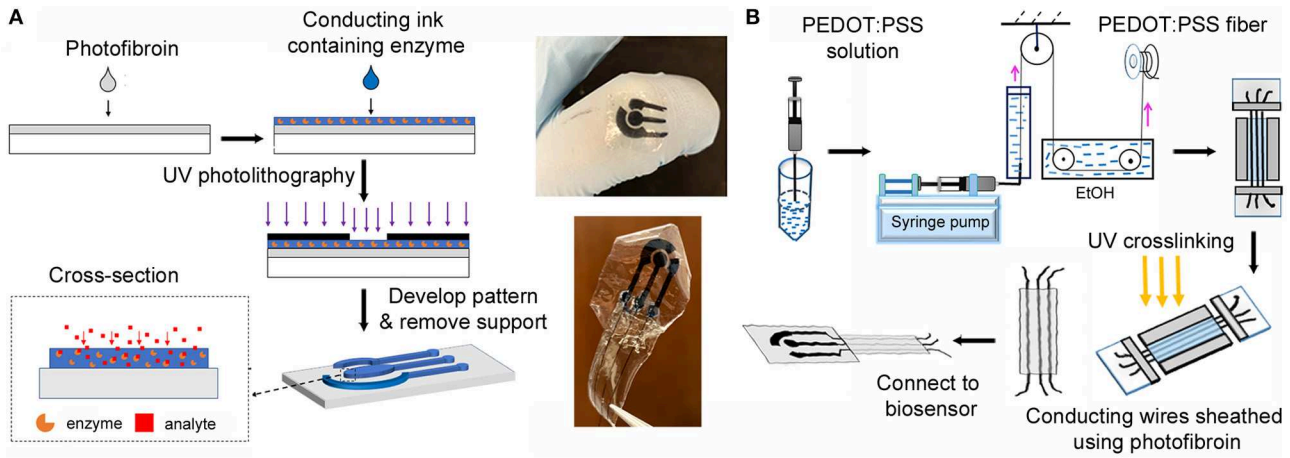

FIGURE 1 | (A) Fabrication of the fully-organic, flexible 3-electrode silk biosensor using photolithography. **(B)** Fabrication of the fibroin sheathed conducting wires. The images in the center show the biosensor and the connected device.

RESULTS AND DISCUSSION

In comparison to their rigid counterparts, mechanically flexible sensors are designed to function at non-planar, soft, and even non-stationary bio-interfaces. They can be useful for the accurate detection and quantification of specific biomarkers in clinical diagnosis toward evaluating biological and pathological activities, or response to therapeutic interventions (Xu et al., 2018). Biosensors and bioelectronics characterized by the ability to fully or partially dissolve, disintegrate, or physically or chemically decompose in a controlled fashion in a working environment, can further enhance the applications of flexible devices. These biodegradable or bioresorbable systems would provide a "transient" function useful in a number of spheres of operation e.g., implantable devices, devices that minimize waste, and platforms for data security (Kang et al., 2018; Li et al., 2018; Chatterjee et al., 2019). Our objective in this work is to show that silk proteins can enable such flexible (bio)sensors without the need for either metallic electrodes or interconnects. We discuss the fabrication and characterization of a fully-organic biosensor that is also mechanically flexible and compliant, and can be completely degraded under the action of proteolytic enzymes. Further we show that connections to external devices can be facilitated by long, highly conductive PEDOT:PSS fibers. The fibers are coated with optically transparent silk fibroin to form sheathed, insulated, fully organic conducting wires. Dopamine, a neurotransmitter, ascorbic acid (vitamin C), and glucose are three model analytes monitored using the developed organic bioelectrodes to demonstrate direct electrochemical biosensing. While the results for ascorbate is shown in the manuscript, the data for dopamine and glucose are shown in the **Supplementary Information** in the interest of brevity.

Fabrication of Flexible, Organic Electrodes

The proposed system is based on photocrosslinkable silk proteins which are compatible with, and can be functionalized by the commercially available conducting polymer PEDOT:PSS to form an integrated functional and structural device. The underlying substrate is formed from silk fibroin that can provide strong support to the functional sensing patterns as well as be mechanically compliant to a curvy biological surface. The electrochemical cell is fabricated using a sericin/PEDOT:PSS biocomposite. As a photocrosslinkable conducting ink, this can be micropatterned to form a 3-electrode design on the flexible support (**Figure 1A**). The sensor design is shown in detail in **Figure 2a**. The sensors are around 1 cm^2 in area with electrode patterns 1,000 μm wide. In contrast to earlier reported silk-based biosensors in which only the working electrode was fabricated from the organic ink (necessitating Pt, Ag/AgCl counter and reference electrodes), here the working, reference, and counter electrodes are all fabricated from the same material (silk biocomposite). Photolithography remains a desirable technique to fabricate structures of high complexity over large areas in a fast and reproducible fashion. As a high-resolution technique, it is possible to fabricate multiplexed microsensors with patterns on the order of 10 s of micrometers.

In order to connect the devices, core-sheath PEDOT:PSS-silk fibroin conductive wires are used to form a fully organic design (**Figure 1B**). Conductive polymers represent "organic wiring" with biocompatibility and low cytotoxicity (Liao et al., 2015; Aydemir et al., 2016; Pappa et al., 2018). Sheathed multifunctional fibers have been previously reported in tissue engineering (e.g., PCL/PPy and PLA/PPy core-sheath nanofibers) to improve flexibility and operational life (Wei et al., 2005; Xie et al., 2009). Silk-PEDOT-PSS composites have also been previously reported (Müller et al., 2011; Tsukada et al., 2012). However, PEDOT:PSS/fibroin core-sheath configurations and/or connection to a biosensor have not been shown. In this work, fibers optimized for diameter and conductivity were used. The use of silk fibroin to form a protective sheath around the fiber not only improves the operation of the wires, but also protect the connections from the external environment, while minimizing any auxiliary damage to surrounding tissue (Green et al., 2008). These integrated organic sensors are mechanically flexible and

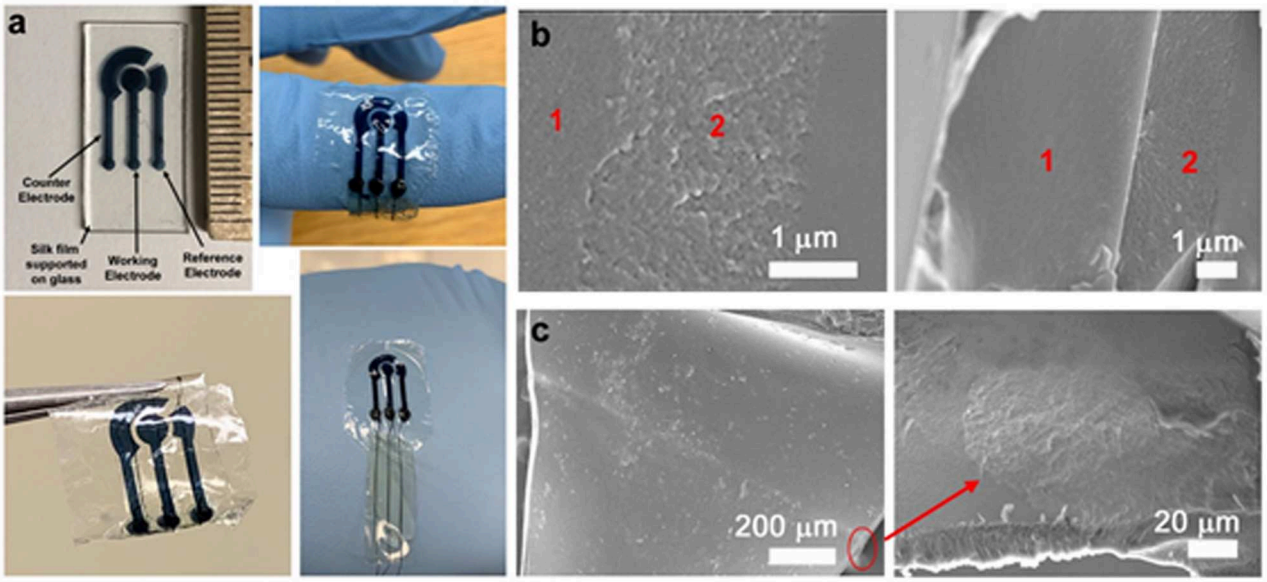

FIGURE 2 | (a) Sensor design showing the position of the working, reference, and counter electrodes. The biosensors with the core-sheath PEDOT:PSS wires/fibroin sheaths are conformable, flexible and can be subjected to mechanical deformation. **(b)** SEM images of the cross section of the organic electrodes, showing the underlying fibroin substrate (1) and sericin-PEDOT:PSS conductive microelectrodes (2). **(c)** SEM images of the sheathed wire showing the cross-section and the PEDOT:PSS wire (red circle), a closeup of which can be seen in the bottom right panel.

can be wrapped, twisted, or otherwise conform to soft tissue interfaces (**Figure 2a**). As a thin sheet (∼20–40 μm thick), they can easily conform to an underlying curvy and soft surface (including soft tissue—**Figure S2**). The protein micro-matrix can entrap the conductive polymers and prevent them leaching out, while allowing small metabolites such as glucose or ascorbic acid to diffuse into the film and trigger the electrochemical reaction. SEM imaging of the electrode surface on the flexible substrate shows the porous electrode surface (**Figure 2b, Figure S3**).

Electrochemical Characterization of the Electrodes

Electrochemical characterization was conducted using cyclic voltammetry to clarify the difference in performance between the developed fully-organic biosensor and a conventional organic electrochemical system. Conventional electrochemical biosensors for the monitoring of metabolites usually utilize Ag/AgCl as the standard reference electrode (RE) and Pt as the counter electrode (CE). These are well-investigated systems known to provide steady current flow and stable signal output. In earlier reports, we demonstrated the use of this organic electrode for the detection of various analytes including glucose, ascorbic acid, and vascular endothelial growth factor (Pal et al., 2016b; Xu and Yadavalli, 2019). Ag/AgCl and Pt were employed as independent reference and counter electrodes, respectively. In considering bioresorbable biosensors or electronics, the goal is to provide diagnostic or monitoring function while avoiding extended device load on the body, or requiring secondary surgical procedures for removal. Therefore, using separate standard and counter electrodes is not optimal. However, in comparison to their metallic counterparts, organic electrodes face problems of current stability due to the fact that the continuous electrochemical reaction of PEDOT:PSS affects performance [i.e., oxidized state (conductive) vs. neutral state (non-conductive)].

The electrochemical behavior of organic electrodes used as RE and CE (free of metallic components) was studied to clarify feasibility for sensing. We will refer to the system with all organic electrodes (WE, CE, and RE) as O3E. In comparison, the system with only one organic electrode but with any conventional RE and CE will be referred as OE. For this work, the same material (sericin/PEDOT:PSS conducting ink) was used to fabricate the working electrodes (WE). For the OE, a standard Ag/AgCl reference electrode (RE), and the Pt counter electrode (CE) was used. Cyclic voltammetry (CV) was conducted on both systems. Over a scan range of −1 to 1 V, the O3E system yielded −83.8 and 122 μA at −1 and 1 V, respectively, whereas the OE system exhibited −22.8 and 83.2 μA at the same potentials. CVs are shown in the **Figure S4**. Interestingly, the O3E sensor had a higher current response than the OE sensor, presumably due to the electrochemical redox reaction occurring in the O3E that can be summarized as the oxidation/reduction of PEDOT:PSS at WE, RE, and CE (Marzocchi et al., 2015).

$$PEDOT^{+} : PSS^{-} + C^{+} + e^{-} \leftrightarrow PEDOT^{0} + C^{+} : PSS^{-} \quad (1)$$

where C^{+} and e^{-} represent cations and electrons, respectively. On the other hand, the electrochemical redox reaction in the OE is the Equation (1) at the WE, the reaction:

$$AgCl\,(s) + e^{-} \leftrightarrow Ag\,(s) + Cl^{-}(aq) \quad (2)$$

Occurs at the reference electrode (RE). When the PEDOT:PSS is polarized anodically/cathodically from the neutral state by the applied potential, it is more conductive at both the WE and RE. Therefore, with all three electrodes formed using the PEDOT:PSS ink (O3E), the developed biosensor would be more sensitive to the changes of electrochemical potential than the OE system that only uses PEDOT:PSS as WE. In order to present a miniaturized biosensor, we used the design shown in **Figure 2** which allows connections of all electrodes to an external potentiostat.

Detection of Ascorbic Acid Using Different Electrochemical Sensor Configurations

Following electrochemical analysis, the O3E system was tested as a biosensor. The electroactive species ascorbic acid (AA) was used as a model metabolite in order to demonstrate electrochemical performance and compare to OE configurations. AA, widely known as vitamin C, plays an important role in the formation of collagen in the development of bones, muscles and blood vessels (Rawat et al., 2015). The performance metrics of the O3E are competitive as seen in **Figure 3**. In all figures, the sensor response is presented as a normalized current (normalized to the baseline signal in pure PBS $-I_{nor} = I_{AA}/I_{PBS} \times 100\%$). This allows comparison across different sensors (at least three sensors were tested in each case). The inset shows a rapid response time of the sensor on the order of a few seconds. It can be seen that a higher *sensitivity* to the addition of AA was observed with a correspondingly higher slope in the calibration curve in comparison to the OE configuration. This is because the redox reactions of AA occur not only at the WE, but also at the RE and CE, implying that the O3E biosensor displays an amplified current response toward the addition of the analyte. The detection limits (LODs) of the developed O3E biosensor and the OE are 49.2 and 50.2 μM, respectively. The close LODs for the two configurations are expected given the identical compositions of the working electrodes for both systems. The OE value is consistent with our earlier report (Pal et al., 2016b). While these values are higher than previously reported LODs for ascorbate biosensors which have been reported to be ∼5–10 μM (Pakapongpan et al., 2012; Csiffáry et al., 2016), the ability to be within the same order of magnitude despite the lack of metals is very promising for use as organic, degradable, and flexible biosensors.

Despite the higher current response, the OE configuration (organic electrodes as WE, the standard Ag/AgCl reference electrode and the Pt counter electrode) yields a higher sensor signal. Therefore, the conductivity of the O3E configuration is not as good as metallic electrodes or even OE. This is likely because the direct electron transfer from the analyte through the PEDOT:PSS is much slower and limited in comparison to Ag or Pt electrodes. This further indicates that these kinds of fully organic (O3E) biosensors would have a narrower detection range in comparison. Since the microfabrication process is conducted at room temperature using only water as the solvent, it is possible to immobilize enzymes and antibodies in the conducting ink, thereby forming biosensors for a wide variety of target metabolites. Detection of glucose (via the enzyme glucose oxidase) and the neurotransmitter, dopamine was demonstrated (**Figures S6, S7**). In both cases, detection of these targets was achievable over physiologically relevant concentrations, showing the versatility of this approach. The overall area of the electrodes also plays a role in determining the dynamic range with smaller surface areas having similar sensitivities and limits of detection but lower range. Thus, the design of the sensors would have to be optimized depending on the application.

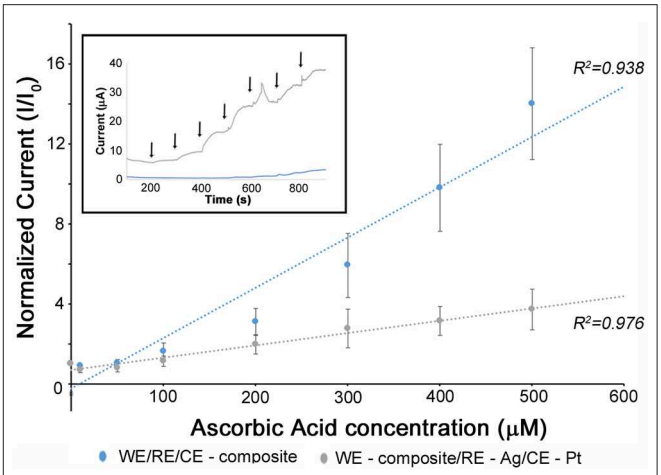

FIGURE 3 | The detection of ascorbic acid using different electrode combinations. The blue represents the electrochemical biosensor using sericin/PEDOT:PSS organic electrodes as Working Electrode (WE), Reference Electrode (RE), and Counter Electrode (CE) (O3E). The gray represents the electrochemical cell setup using sericin/PEDOT:PSS organic electrode as WE, Ag/AgCl electrode as RE, Pt as CE (OE). The inset figure is the calibration curve (normalized current vs. concentration of ascorbic acid) for the detection of ascorbic acid using the two electrical setups. The control sample was PBS ($I_{nor} = 1$). The addition of AA occurred at 100 s intervals. In all experiments, at least three different sensors were studied.

Electrochemical Performance of the Biosensors During Degradation

The primary advantage of using a fully-organic biosensor without metallic components is the potential to be controllably degradable (e.g., *in vivo* or in nature). *In vitro*, this process may be replicated by the use of proteolytic enzymes. Silk-based materials have demonstrated their utility in this regard and have been extensively studied for their controllable biodegradation (Lu et al., 2011), an important property in their applications in tissue engineering. While resorbable and degradable sensors have been proposed, their performance over time in their working environment has not been fully characterized. Here, the organic devices were examined for sensing of AA under proteolytic biodegradation.

The O3E biosensors were immersed in a solution containing 1 unit ml^{-1} protease at 37°C over a 1 week period to provide an *in vitro* simulation of an *in vivo* environment. The electrochemical sensing for performance is shown in **Figure 4**.

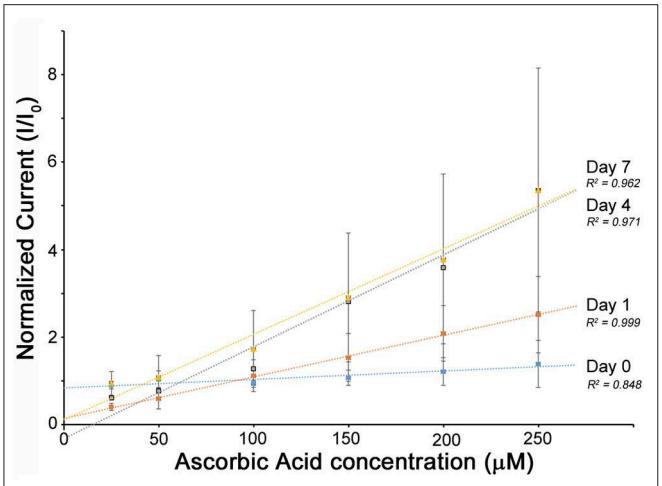

FIGURE 4 | The electrochemical performance of the O3E flexible biosensor when stored in 1 unit ml^{-1} of protease solution at 37°C. The sensors were monitored over a period of 1 week. The control sample was PBS ($I_{nor} = 1$). It may be noted that after 10 days, the sensors begin to lose mechanical integrity at the macroscale and are not easily connected for reliable measurements. The relatively high error bars can be explained by sensor-to-sensor variability obtained during averaging of the signals from three separate sensors.

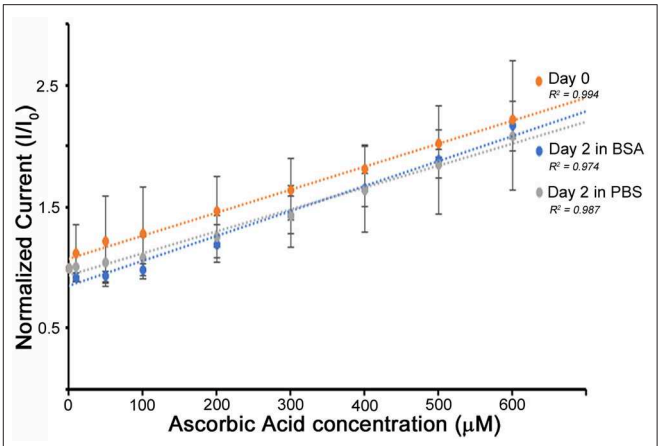

FIGURE 5 | The O3E biosensor was evaluated in the presence of a blocking agent (BSA). The biosensors were immersed in 40 mg/ml BSA solution (in 0.1 M PBS, pH 7.4) (blue line), or PBS buffer (as control) (gray line) over 2 days. A linear response is maintained over 2 days, with very small change in comparison to the starting biosensors (Day 0–orange).

The sensors maintain a linear response I_{nor} to ascorbic acid during the entire process (1 week). Over a period of 24 h, there is no change in the sensor function. Interestingly, from Day 1 to Day 4, the slopes of the calibration curves increased slightly, indicating the sensitivity of the developed biosensor to the addition of AA was improved. While this appears counterintuitive, this is likely due to the biodegradation of the silk matrix causing an exposure of the entrapped PEDOT:PSS, which in turn improves the direct electron transfer from the electrolyte to the conductive polymers. From Day 4 to Day 7, the slope of the calibration curve remains the same. Following around 10 days, the sensor connections degrade, making it impossible to get an accurate reading. Therefore, we can specify a working life-time for the devices as studied in this work to be ∼1 week. Given that the linear response of the sensors is unaffected by the degradation, it is therefore possible to envision a simple mathematical relationship to provide the accurate concentrations on a given day from the calibration curves shown.

At the macroscale, the biosensors lose structural integrity over ∼1 month (Images showing the electrode surface degradation are shown in **Figure S5**). It may be noted that the PEDOT:PSS itself is not biodegradable. However, due to the degradation of the matrix, causes the entire sensor to break down. This was earlier shown by our group (Pal et al., 2016a,b). In these experiments, the sensors tested are formed on fibroin films ∼20 μm thick with the electrodes themselves being ∼20 μm thick. By carefully controlling the material thickness and crosslinking, it is possible to form devices that can function for longer periods of time (e.g., months), which provides interesting possibilities. However, as designed, these sensors can be used for "transient" devices to monitor wound healing for instance, wherein a short timeframe of operation is required.

Performance of the Flexible Biosensor Against Biofouling

One of the possible applications of using such flexible, fully organic biosensors is *in vivo* monitoring of metabolites. However, sensor fouling continues to be one of the major challenges facing biosensors. Non-specific absorption of proteins or cells results in sensor occlusion and therefore a loss in performance (Wang et al., 2015). It has been suggested that a layer of membrane from naturally derived materials (e.g., silk fibroin, cellulose, chitosan) could help reduce biofouling and prolong the lifetime of implanted biosensors (Wisniewski and Reichert, 2000). We observed that interestingly, the developed silk biosensor possesses a natural resistance to biofouling owing to its protein-based structural composition. Given the reference range for albumin concentrations in serum is ∼35–50 mg/ml, the O3E biosensor was testing by immersing in a 0.1 M PBS buffer containing 40 mg/ml BSA. The control group was immersed in 0.1 M PBS buffer. Both groups were examined for their performance in detecting ascorbic acid following 2 days of immersion (**Figure 5**). The linear response of the biosensors is maintained in both PBS even in the presence of the strong challenge of BSA blocking. An O3E biosensor was also tested against glucose in similar conditions with PBS control and 40 mg/ml BSA. A slight reduction in sensitivity was observed, but the sensor again maintained a linear response (**Figure S7**). It is therefore hypothesized that the BSA can absorb to the electrode surface, but is isolated by the silk protein matrix from insulating the conductive materials (PEDOT:PSS) in the matrix and therefore does not affect the diffusion to the electrodes. However, it could potentially affect the encapsulated enzymes, thereby reducing performance. It may

be noted that typically much lower concentrations of BSA are studied (2–5 mg/ml) for such sensors, which reflects that these sensors display good promise for the next series of experiments (i.e., translation to animal models and longer-term investigations). Even though the tested solution containing BSA is a simplified system and does not fully represent a complex biofluid system, the performance of the developed organic flexible biosensor was able to exhibit good stability against protein absorption. Future studies are focused on studying the function of biosensors in a working environment of such complex fluids that can present biodegradation and biofouling challenges along with the presence of other chemical interferents.

CONCLUSIONS

In summary, here we demonstrate the feasibility of using silk proteins to construct a fully-organic, flexible biosensor for the monitoring of metabolites. The entire fabrication process is based on contact photolithography which is simple, rapid, and can be performed under ambient conditions. Using a combined 3-electrode configuration, the working, reference, and counter electrodes are fabricated from an organic conducting ink. The developed biosensors display excellent performance in terms of sensitivity and detection range for the sensing of analytes. Thus, these biosensors can be considered for *in vivo* implantation whereby they can function in challenging biological environments. Most interestingly, these biosensors display a transient function whereby they can function for a period of 1 week after which they begin to degrade. They display a stable linear performance even during proteolytic biodegradation. The target repertoire of the biosensors can be expanded by adding different enzymes in the basic formulation of sericin/PEDOT:PSS conductive ink. This concept of fully-organic devices can therefore provide a pathway for the development of next-generation, ease-to-use, and degradable flexible biosensors for health monitoring.

DATA AVAILABILITY STATEMENT

The datasets generated for this study are available on request to the corresponding author.

AUTHOR CONTRIBUTIONS

MX, YJ, and VY conceptualized and designed the study. MX and SP performed the integrated device fabrication and biosensing. YJ performed the experiments of PEDOT:PSS fiber sheathing. All authors contributed to data analysis and writing the manuscript.

FUNDING

This research was partly funded by the National Science Foundation (CBET-1704435), the State Scholarship Fund (No. 201808505099), and National Science Foundation of China (No. 31402144).

SUPPLEMENTARY MATERIAL

The Supplementary Material for this article can be found online at: https://www.frontiersin.org/articles/10.3389/fmats.2019.00331/full#supplementary-material

REFERENCES

Aydemir, N., Malmstrom, J., and Travas-Sejdic, J. (2016). Conducting polymer based electrochemical biosensors. *Phys. Chem. Chem. Phys.* 18, 8264–8277. doi: 10.1039/C5CP06830D

Balint, R., Cassidy, N. J., and Cartmell, S. H. (2014). Conductive polymers: towards a smart biomaterial for tissue engineering. *Acta Biomater.* 10, 2341–2353. doi: 10.1016/j.actbio.2014.02.015

Chatterjee, S., Saxena, M., Padmanabhan, D., Jayachandra, M., and Pandya, H. J. (2019). Futuristic medical implants using bioresorbable materials and devices. *Biosens. Bioelectron.* 142:111489. doi: 10.1016/j.bios.2019.111489

Csiffáry, G., Futo, P., Adányi, N., and Kiss, A. (2016). Ascorbate oxidase-based amperometric biosensor for L-ascorbic acid determination in beverages. *Food Technol. Biotechnol.* 54, 31–35. doi: 10.17113/ftb.54.01.16.4135

Enomoto, S., Sumi, M., Kajimoto, K., Nakazawa, Y., Takahashi, R., Takabayashi, C., et al. (2010). Long-term patency of small-diameter vascular graft made from fibroin, a silk-based biodegradable material. *J. Vasc. Surg.* 51, 155–164. doi: 10.1016/j.jvs.2009.09.005

Feiner, R., and Dvir, T. (2018). Tissue-electronics interfaces: from implantable devices to engineered tissues. *Nat. Rev. Mater.* 3:17076. doi: 10.1038/natrevmats.2017.76

Geddes, L., and Roeder, R. (2003). Criteria for the selection of materials for implanted electrodes. *Ann. Biomed. Eng.* 31, 879–890. doi: 10.1114/1.1581292

Gong, C.-S. A., Syu, W.-J., Lei, K. F., and, Hwang, Y.- S. (2016). Development of a flexible non-metal electrode for cell stimulation and recording. *Sensors* 16:1613. doi: 10.3390/s16101613

Green, R. A., Lovell, N. H., Wallace, G. G., and Poole-Warren, L. A. (2008). Conducting polymers for neural interfaces: challenges in developing an effective long-term implant. *Biomaterials* 29, 3393–3399. doi: 10.1016/j.biomaterials.2008.04.047

Hanssen, B. L., Siraj, S., and Wong, D. K. (2016). Recent strategies to minimise fouling in electrochemical detection systems. *Rev. Anal. Chem.* 35, 1–28. doi: 10.1515/revac-2015-0008

Hwang, S. W., Kim, D. H., Tao, H., Kim, T. I., Kim, S., Yu, K. J., et al. (2013). Materials and fabrication processes for transient and bioresorbable high-performance electronics. *Adv. Funct. Mater.* 23, 4087–4093. doi: 10.1002/adfm.201300127

Irimia-Vladu, M. (2014). "Green" electronics: biodegradable and biocompatible materials and devices for sustainable future. *Chem. Soc. Rev.* 43, 588–610. doi: 10.1039/C3CS60235D

Kang, S.-K., Koo, J., Lee, Y. K., and Rogers, J. A. (2018). Advanced materials and devices for bioresorbable electronics. *Acc. Chem Res.* 51, 988–998. doi: 10.1021/acs.accounts.7b00548

Kim, D. H., Viventi, J., Amsden, J. J., Xiao, J. L., Vigeland, L., Kim, Y. S., et al. (2010). Dissolvable films of silk fibroin for ultrathin conformal bio-integrated electronics. *Nat. Mater.* 9, 511–517. doi: 10.1038/nmat2745

Kurland, N. E., Dey, T., Kundu, S. C., and Yadavalli, V. K. (2013). Precise patterning of silk microstructures using photolithography. *Adv. Mater.* 25, 6207–6212. doi: 10.1002/adma.201302823

Kurland, N. E., Dey, T., Wang, C., Kundu, S. C., and Yadavalli, V. K. (2014). Silk protein lithography as a route to fabricate sericin microarchitectures. *Adv. Mater.* 26, 4431–4437. doi: 10.1002/adma.201400777

Lei, T., Guan, M., Liu, J., Lin, H. C., Pfattner, R., Shaw, L., et al. (2017). Biocompatible and totally disintegrable semiconducting polymer for ultrathin and ultralightweight transient electronics. *Proc. Natl. Acad. Sci. U.S.A.* 114, 5107–5112. doi: 10.1073/pnas.1701478114

Li, R. F., Wang, L., Kong, D. Y., and Yin, L. (2018). Recent progress on biodegradable materials and transient electronics. *Bioact. Mater.* 3, 322–333. doi: 10.1016/j.bioactmat.2017.12.001

Liao, C., Zhang, M., Yao, M. Y., Hua, T., Li, L., and Yan, F. (2015). Flexible organic electronics in biology: materials and devices. *Adv. Mater.* 27, 7493–7527. doi: 10.1002/adma.201402625

Liu, Y., He, K., Chen, G., Leow, W. R., and Chen, X. (2017). Nature-inspired structural materials for flexible electronic devices. *Chem. Rev.* 117, 12893–12941. doi: 10.1021/acs.chemrev.7b00291

Lu, Q., Zhang, B., Li, M., Zuo, B., Kaplan, D. L., Huang, Y., et al. (2011). Degradation mechanism and control of silk fibroin. *Biomacromolecules* 12, 1080–1086. doi: 10.1021/bm101422j

Marzocchi, M., Gualandi, I., Calienni, M., Zironi, I., Scavetta, E., Castellani, G., et al. (2015). Physical and electrochemical properties of PEDOT:PSS as a tool for controlling cell growth. *ACS Appl. Mater. Interfaces* 7, 17993–18003. doi: 10.1021/acsami.5b04768

Müller, C., Hamedi, M., Karlsson, R., Jansson, R., Marcilla, R., Hedhammar, M., et al. (2011). Woven electrochemical transistors on silk fibers. *Adv. Mater.* 23, 898–901. doi: 10.1002/adma.201003601

Pakapongpan, S., Mensing, J. P., Lomas, T., and Tuantranont, A. (2012). "Electrochemical sensor for ascorbic acid based on graphene/CuPc/PANI nanocomposites," in *2012 IEEE International Conference on Electron Devices and Solid State Circuit (EDSSC)* (Bangkok: IEEE).

Pal, R. K., Farghaly, A. A., Collinson, M. M., Kundu, S. C., and Yadavalli, V. K. (2016a). Photolithographic micropatterning of conducting polymers on flexible silk matrices. *Adv. Mater.* 28, 1406–1412. doi: 10.1002/adma.201504736

Pal, R. K., Farghaly, A. A., Wang, C., Collinson, M. M., Kundu, S. C., and Yadavalli, V. K. (2016b). Conducting polymer-silk biocomposites for flexible and biodegradable electrochemical sensors. *Biosens. Bioelectron.* 81, 294–302. doi: 10.1016/j.bios.2016.03.010

Pal, R. K., Kundu, S. C., and Yadavalli, V. K. (2018). Fabrication of flexible, fully organic, degradable energy storage devices using silk proteins. *Acs Appl. Mater. Interfaces* 10, 9620–9628. doi: 10.1021/acsami.7b19309

Pappa, A.-M., Parlak, O., Scheiblin, G., Mailley, P., Salleo, A., and Owens, R. M. (2018). Organic electronics for point-of-care metabolite monitoring. *Trends Biotechnol.* 36, 45–59. doi: 10.1016/j.tibtech.2017.10.022

Rawat, K., Sharma, A., Solanki, P. R., and Bohidar, H. B. (2015). Potential of gelatin-zinc oxide nanocomposite as ascorbic acid sensor. *Electroanalysis.* 27, 2251–2491. doi: 10.1002/elan.201500090

Rivnay, J., Owens, R. M., and Malliaras, G. G. (2014). The rise of organic bioelectronics. *Chem. Mater.* 26, 679–685. doi: 10.1021/cm4022003

Rockwood, D. N., Preda, R. C., Yücel, T., Wang, X., Lovett, M. L., and Kaplan, D. L. (2011). Materials fabrication from Bombyx mori silk fibroin. *Nat. Protoc.* 6, 1612–1631. doi: 10.1038/nprot.2011.379

Suginta, W., Khunkaewla, P., and Schulte, A. (2013). Electrochemical biosensor applications of polysaccharides chitin and chitosan. *Chem. Rev.* 113, 5458–5479. doi: 10.1021/cr300325r

Tan, M. J., Owh, C., Chee, P. L., Kyaw, A. K., Kai, D., and Jun Loh, X. (2016). Biodegradable electronics: cornerstone for sustainable electronics and transient applications. *J. Mater. Chem. C* 4, 5531–5558. doi: 10.1039/C6TC00678G

Thurber, A. E., Omenetto, F. G., and Kaplan, D. L. (2015). *In vivo* bioresponses to silk proteins. *Biomaterials* 71, 145–157. doi: 10.1016/j.biomaterials.2015.08.039

Tsukada, S., Nakashima, H., and Torimitsu, K. (2012). Conductive polymer combined silk fiber bundle for bioelectrical signal recording. *PLoS ONE* 7:e33689. doi: 10.1371/journal.pone.0033689

Voskerician, G., Chung-Chiun, L., and Anderson, J. M. (2005). Electrochemical characterization and *in vivo* biocompatibility of a thick-film printed sensor for continuous *in vivo* monitoring. *IEEE Sens. J.* 5, 1147–1158. doi: 10.1109/JSEN.2005.857877

Wang, C., Wang, C., Huang, Z., and Xu, S. (2018). Materials and structures toward soft electronics. *Adv. Mater.* 30:1801368. doi: 10.1002/adma.201801368

Wang, L., Chen, D., Jiang, K., and Shen, G. (2017a). New insights and perspectives into biological materials for flexible electronics. *Chem. Soc. Rev.* 46, 6764–6815. doi: 10.1039/C7CS00278E

Wang, X. W., Liu, Z., and Zhang, T. (2017b). Flexible sensing electronics for wearable/attachable health monitoring. *Small* 13:1602790. doi: 10.1002/smll.201602790

Wang, Y., Vaddiraju, S., Gu, B., Papadimitrakopoulos, F., and Burgess, D. J. (2015). Foreign body reaction to implantable biosensors: effects of tissue trauma and implant size. *J. Diabetes Sci. Technol.* 9, 966–977. doi: 10.1177/1932296815601869

Wei, M., Lee, J., Kang, B., and Mead, J. (2005). Preparation of core-sheath nanofibers from conducting polymer blends. *Macromol. Rapid Comm.* 26, 1127–1132. doi: 10.1002/marc.200500212

Wisniewski, N., and Reichert, M. (2000). Methods for reducing biosensor membrane biofouling. *Colloids Surf. B Biointerfaces* 18, 197–219. doi: 10.1016/S0927-7765(99)00148-4

Xie, J., MacEwan, M. R., Willerth, S. M., Li, X., Moran, D. W., Sakiyama-Elbert, S. E. et al. (2009). Conductive core–sheath nanofibers and their potential application in neural tissue engineering. *Adv. Funct. Mater.* 19, 2312–2318. doi: 10.1002/adfm.200801904

Xu, M., Obodo, D., and Yadavalli, V. K. (2018). The design, fabrication, and applications of flexible biosensing devices. *Biosens. Bioelectron.* 124–125, 96–114. doi: 10.1016/j.bios.2018.10.019

Xu, M., Pradhan, S., Agostinacchio, F., Pal, R. K., Greco, G., Mazzolai, B., et al. (2019). Easy, scalable, robust, micropatterned silk fibroin cell substrates. *Adv. Mater. Interfaces* 6:801822. doi: 10.1002/admi.201801822

Xu, M., and Yadavalli, V. K. (2019). Flexible biosensors for the impedimetric detection of protein targets using silk-conductive polymer biocomposites. *ACS Sensors* 4, 1040–1047. doi: 10.1021/acssensors.9b00230

Yun, Y., Dong, Z., Lee, N., Liu, Y., Xue, D., Guo, X., et al. (2009). Revolutionizing biodegradable metals. *Mater. Today* 12, 22–32. doi: 10.1016/S1369-7021(09)70273-1

Zhang, J., Seyedin, S., Qin, S., Lynch, P. A., Wang, Z., Yang, W., et al. (2019). Fast and scalable wet-spinning of highly conductive PEDOT: PSS fibers enables versatile applications. *J. Mater. Chem. A* 7, 6401–6410. doi: 10.1039/C9TA00022D

Zhu, B., Wang, H., Leow, W. R., Cai, Y., Loh, X. J., Han, M.-Y., et al. (2016). Silk fibroin for flexible electronic devices. *Adv. Mater.* 28, 4250–4265. doi: 10.1002/adma.201504276

Conflict of Interest: The authors declare that the research was conducted in the absence of any commercial or financial relationships that could be construed as a potential conflict of interest.

frontiers in Materials

MINI REVIEW
published: 18 February 2020
doi: 10.3389/fmats.2020.00029

Spider Silk Biomimetics Programs to Inform the Development of New Wearable Technologies

Sean J. Blamires[1], Patrick T. Spicer[2] and Patricia J. Flanagan[3]*

[1] The Spider Silk Research Lab, Evolution & Ecology Research Centre, School of Biological, Earth & Environmental Sciences, The University of New South Wales, Sydney, NSW, Australia, [2] Complex Fluids Group, School of Chemical Engineering, The University of New South Wales, Sydney, NSW, Australia, [3] Faculty of Art and Design, The University of New South Wales, Sydney, NSW, Australia

Wearable fabrics are predominantly produced from synthetic polymer fibers derived from petrochemicals. These have negative effects on the natural environment as a consequence of the manufacturing process, insurmountable waste production, and persistence of the fibers in ecosystems. With the use of wearables worldwide set to increase exponentially, more environmentally friendly fibers are sought. Natural fibers such as spider silk are produced using proteins in a water solvent, yet they have many superior qualities to synthetic fibers. Moreover, spiders can tune their silk properties as their ecological circumstances demand it. Research focused on the biomimetic potential of spider silks with an eye on the development of smart wearable fibers is accordingly a potentially lucrative area of research. There are nonetheless major challenges associated, including recovering the original mechanical performance within the fibers developed, scaling up production, keeping the production costs of the silk building blocks to a minimum, elucidating, and understanding the different silk genome sequences, and creating precision artificial spinning processes. We outline herein a template for a working framework for a spider silk biomimetics program that can inform designers and biological researchers alike. It suggests that an objective-focused research program utilizing a cross-disciplinary toolbox of top-down and bottom-up techniques is required. We close by providing some speculative examples stemming from current activities in our laboratories.

Keywords: biomimetics, spider silk, environmentally sustainable manufacturing, structure-function properties, wearable technology

OPEN ACCESS

Edited by:
Nicola Maria Pugno, University of Trento, Italy

Reviewed by:
Johnny De Nardi Martins, Federal University of Santa Catarina, Brazil
Philippe Boisse, Institut National des Sciences Appliquées de Lyon (INSA Lyon), France

****Correspondence:***
Sean J. Blamires
sean.blamires@unsw.edu.au

Specialty section:
This article was submitted to Polymeric and Composite Materials, a section of the journal Frontiers in Materials

Received: *17 October 2019*
Accepted: *28 January 2020*
Published: *18 February 2020*

Citation:
Blamires SJ, Spicer PT and Flanagan PJ (2020) Spider Silk Biomimetics Programs to Inform the Development of New Wearable Technologies. Front. Mater. 7:29. doi: 10.3389/fmats.2020.00029

The way that wearable materials are currently designed and produced is not sustainable (Carr and Gibson, 2016). Given the inevitable rise in global population and the associated expansion in wearables consumption over the next 30–50 years (Franklin, 2018), there is an urgent need to reduce the environmental impact associated with the production of wearable fabrics across product life cycles (Le Quéré et al., 2009; Myers, 2014).

Man-made and synthetic materials such as rayon and polyester have predominated wearable designs since the 1950's (Franklin, 2018). These materials are primarily derived from the polymerization of petrochemical monomers, which involves high temperatures and treatments that use noxious solvents, before spinning them through syringes, valves, microspinnerets, electrospinners, or 3D printing devices (Damiati et al., 2018). Post-spinning treatments with

additional noxious chemicals is often required to dry and fix the polymers into solid fibers. The primary advantage of developing fibers this way is that vast quantities can be produced for a wide variety of purposes at a relatively low cost (Wu et al., 2017). The problem nevertheless with creating materials this way is that it is extremely environmentally harmful due to the handling and disposal of the solvents used during spinning and fixing, and the energy input required to treat and fix the materials. The post-production environmental damage is, however, more striking. A 5 kg wash of polyester fabrics for instance releases over 6,000,000 microfibers that remain in the environment and can act as reservoirs for organic pollutants (De Falco et al., 2018). Additionally, the mass production of materials for fast-fashion results in textile wastes contributing to 5% of the world's landfill (Nguyen-Robertson and Byrne, 2019). Furthermore, the substantial overstock of fabrics gets either burnt or contributes further to landfill. Once in landfill or drainage systems the fibers seep into soil and ocean ecosystems where they persist for 10–1,000 s of years (Szostak-Kotowa, 2004). Even more disturbing, the fibers can become rapidly incorporated into ecological and human food webs (Browne et al., 2008).

There is evidently a growing market for sustainable, reclaimed, organic, textiles and a renewed interest in merging traditional crafting skills with new technologies (Quinn, 2010). Natural materials such as silks, elastin, resilin, byssus, and wool are examples of fibers derived from natural proteins, which are synthesized and secreted by animals using water as the solvent (Waite, 1992; Abascal and Regan, 2018). Although they are made from biological macromolecules, such as polypeptides, polysaccharides, and lipids, and treated with water and air, many natural materials have superior properties on multiple measures of performance than synthetic material (Liu and Zhang, 2011). For instance, spider dragline silk (Liu and Zhang, 2011; Blamires et al., 2017) has greater strength, elasticity, and toughness than most natural or synthetic materials (**Table 1**). Particularly important is the fact that silks are easily degraded by natural enzymes after relatively short periods of time (Gellynck et al., 2008), removing the persistent accumulation effect associated with synthetic fibers. Accordingly, if we could replicate the production processes of these natural fibers we might be able to circumvent much of the environmental damage associated with using synthetic polymers for wearable technologies (Eadie and Ghosh, 2011; Lapidot et al., 2012).

Despite great urgency being placed on the development of new environmentally benign materials, there have been few examples of the successful development of processes producing materials that mimic silks or other animal products (Wolff et al., 2017). Biomimetics, or the transfer of functional principles from living systems to engineering applications offer one way forward (Sanchez et al., 2005; Pawlyn, 2011; Wegst et al., 2015; Wolff et al., 2017).

Traditionally an engineer, or designer, might have sought a solution to a particular design problem by examining similar mechanisms in living systems. Indeed, there are examples of successful biomimetic technological processes that have this kind of top-down approach. These include the development of superhydrophobic surfaces based on the lotus leaf, and the "shark skin" drag-resistant swim suit (Hwang et al., 2015). Researchers in the biological and other sciences, nonetheless, generally solve problems using bottom-up approaches, i.e., they start by observing a function and then ask questions of its significance and application (Speck et al., 2017; **Figure 1**). These seemingly disparate approaches can lead to disconnections between the endeavors of designers and scientific researchers and may obstruct our capacity to incorporate advanced technologies into new materials.

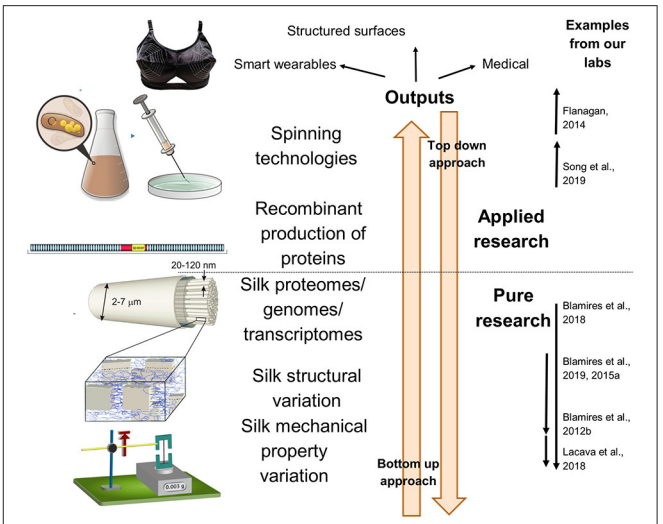

FIGURE 1 | An overview of the components and working principals of a complete and multidiscipline biomimetics research program aiming to develop wearable technologies, and other marketable materials, based on the structures, and functions of spider silks. It shows how combining pure and applied research can produce outcomes and the distinctions between taking top down (starting at the application to search for a natural function) and bottom up (i.e., observing a function and then ask questions of its application) approaches. Examples of research from our laboratories is given for each level.

How might research programs grounded in pure science ever inform the development of new wearables? Flanagan (2014) advocates a "toolbox" methodology (i.e., adopting tools from different disciplines) to form successful interdisciplinary research programs. In addition to using such a methodology the various participants must clearly define their objectives and working principals if quality biomimetic outcomes are to be realized (Myers, 2014; Wolff et al., 2017). Nevertheless, it is exceptionally difficult for biologists, engineers and designers from their various sub-disciplines to speak with each other using a common vernacular, so the capacity for researchers across the arts and sciences to communicate effectively with those from outside their respective discipline seems ill-fated at the outset. To circumvent this we establish herein a template for a spider silk biomimetics program that informs designs while remaining grounded within a biological research paradigm (see **Figure 1**).

The first objective of any biomimetics research program is to identify the problems that the disparate disciplines might have in common despite approaching them from different working principals (Wolff et al., 2017). The most common

TABLE 1 | A comparison of the various properties of natural and synthetic materials.

Property	Natural materials							Synthetic materials					
	Spider dragline silk	Silkworm cocoon silk	Wool	Resilin	Elastin	Byssus	Cotton	Viscose rayon	Polyester fiber composite	Nylon fiber	Synthetic rubber	Kevlar	Carbon fiber
Strength (GPa)	0.2–1.6[a]	0.6[b]	0.2[b]	0.003[b]	0.002[b]	0.06–0.12[c]	0.4[d]	0.03[e]	0.02–0.07[e]	0.95[b]	0.05[b]	3.6[b]	4[b]
Toughness (MJ m^{-3})	10–350[a]	70[b]	60[b]	4[b]	2[b]	20–40[c]	100–150[d]	4[e]	0.6–20[e]	80[b]	100[b]	50[b]	25[b]
Extensibility (mm mm^{-1})	0.05–0.5[a]	0.1–0.3[b]	0.5[b]	1.9[b]	1.5[b]	0.7–1.0[c]	0.55[d]	0.3[e]	0.02–0.18[f]	0.18[b]	8.5[b]	0.027[b]	0.013[b]
Stiffness/ Elastic modulus (GPa)	1–15[a]	7–15[b]	0.5[b]	0.002[b]	0.001[b]	0.13–0.4[c]	2.0–3.7[d]	0.05[e]	0.1–3[f]	5[b]	0.001[b]	130[b]	300[b]
Density (g cm^{-3})	1.3[g]	1.4[h]	1.5[i]	1.3[j]	–	–	1.54[d]	1.5[f]	1.1[f]	1.2[f]	0.9[f]	1.5[f]	2[f]

[a]*Agnarsson et al. (2010);* [b]*Omenetto and Kaplan (2010);* [c]*Bouhlel et al. (2017);* [d]*Gordon and Hseih (2011);* [e]*Morton and Hearle (2008);* [f]*Belaid et al. (2015);* [g]*Heim et al. (2009);* [h]*Chen et al. (2012);* [i]*Dmitrievich et al. (2014);* [j]*Elvin et al. (2005).*

difficulty in the instance of programs intending to produce spider silk-like fibers is producing fibers with the same mechanical performance as natural silk fibers, as developing large quantities of fibers of inferior performance is somewhat futile (Bini et al., 2006; Heidebrecht and Scheibel, 2013). Nevertheless, all fibers developed within the various laboratories have thus far not been of similar quality as naturally spun spider silks (Koh et al., 2015); even when complete or near complete gene or amino acid sequences had been replicated. There are obviously secretory, assembly and spinning functions that we do not fully understand and need to investigate further.

There are numerous studies documenting how dragline silk performance influences the evolutionary ecology of the spider that secretes it (e.g., Blamires et al., 2012a,b; Lacava et al., 2018; Viera et al., 2019). These studies show that spiders can tune the properties of their silks to accommodate different uses of the silk across different ecological circumstances. They thus provide a basis for bioprospecting for extremely high performing silks for biomimetics programs (Agnarsson et al., 2010), and might be used to pinpoint the most flexible mechanical properties of a particular silk to show us how to better control property variability (Blamires et al., 2017). Nonetheless, few studies have documented all of the relevant property variations across macro- to nano scales (but see Blamires et al., 2018; Lacava et al., 2018). A deeper exploration of this largely untapped research space will enable the development of biomimetic protocols with more precise control of property variability.

The next common problem for the development of spider silk biomimetics programs is that of scaled production. Just as we eventually moved from large-scale harvesting and processing of natural fibers like cellulose to the production of synthetic fiber materials with exceptional strength like Rayon (regenerated cellulose) and Kevlar (polyaraphenylene terephthalamide) (see Morgan, 1981), a significant shift in paradigm is needed to move to large-scale manufacture of silk fibers. Biomimetic approaches hold promise for such a shift, as there are existing parallels between synthetic polymer fiber production and processes developed through evolutionary adaptations. For example, synthetic fibers are routinely produced by pumping highly viscous polymer melts through small spinneret openings. The polymer melts used for synthetic fibers have unique flow behavior that is also similar to spider silk precursors, as they are quite viscous when immobile but become more than 10 times thinner as they are pushed through the spinneret opening (Kojic et al., 2006; Porter and Vollrath, 2009). Another similarity between synthetic fiber and natural silk production is the shape of the entrance region in some natural and industrial spinnerets; both having a hyperbolic tapering that is advantageous for uniformity of flow (Lefèvre and Auger, 2016). Clearly the engineering of such processes will need to take advantage of the expertise gained from synthetic material processes, while closely studying natural processes and their properties.

From the design viewpoint, large amounts of fibers with desirable qualities built into them are needed to construct fibrous yarns on a commercially viable scale. Biological researchers thus must be able to produce large masses of extremely high quality spider silk fibers using existing recombinant or polymer engineering technologies (Bini et al., 2006; Xia et al., 2010; Heidebrecht and Scheibel, 2013; Jastrzebska et al., 2016; Blamires et al., 2017). We consider it imperative to set about identifying the obstacles to scaling through research that follows bottom-up and top-down approaches (exemplified by **Figure 1** and discussions within Tarakanova and Buehler, 2012).

Studies of natural spider silk variability indicate that producing silk involves a complex relationship between competing ecological cost to the animal and silk performance (Craig et al., 2000; Wilder, 2011; Blamires et al., 2012a, 2015a,b). There is speculation among researchers as to what this cost(s) might be, including metabolic or nutritional stress (Craig et al., 2000; Guehrs et al., 2008; Blamires et al., 2012a), but there is no

clear consensus. Identifying the cost(s) is nonetheless worthy of further investigation as undue costs can adversely affect the ability to significantly scale up production of biomimetic processes (Wolff et al., 2017).

The suppression of key nutrients and/or metabolic rates in spiders under dietary stress leads to a compromised investment in key amino acids and other building blocks of the silk proteins (Craig et al., 2000; Guehrs et al., 2008; Blamires et al., 2012a), leading to a compromise in properties (Zax et al., 2004; Blamires et al., 2015a, 2018). It thus seems like the investment costs are most prominent and identifiable when the spider is under dietary stress (Blamires et al., 2017). It also seems that metabolic and/or nutritional stresses are not the only factors limiting the quantity and quality of silks produced by spiders (Su and Buehler, 2016; Blamires et al., 2017). To uncover these other limitations cross-disciplinary research utilizing a "toolbox" methodology are required to systematically assess spider metabolism, nutrition, gene expression, silk structures, and mechanical properties.

Another problem we recognize here is our general incomplete or disjointed understanding of the underlying gene and/or amino acid sequences of most of the spidroins (the technical name for silk proteins). The consequence of this is that incomplete or partially complete sequences are often used in cloning and recombinant development programs, leading to the production of significantly smaller (20–50 kDa as opposed to 200+kDa) proteins that behave differently (Rammensee et al., 2008; Liu and Zhang, 2011; Heidebrecht and Scheibel, 2013). For instance, they coagulate at high concentrations and/or polymerize under different conditions than do full length protein sequences (Heim et al., 2009). The recent determination of full-length spider silk genomes (e.g., Garb et al., 2019; Kono et al., 2019) provides valuable information on the size and sequence of the various spidroins, as well as insights into the way they are secreted, stored, and spun *in vivo*. According to Carlson's Curve (Carlson, 2010) the ability to sequence and synthesize full genomes are becoming exponentially more cost effective over time. We are accordingly confident that the opportunity to develop and utilize full length spidroin sequences will be soon realized.

Even if the full gene sequences of the spidroins that we want cloned are known, producing spidroins *en mass* in up to 80% concentration (as in spider silk glands; Chaw et al., 2015), still presents an additional challenge. Recombinant technologies, i.e., the transferral of the silk genes to bacterial or yeast hosts to express the proteins, appears to be the cheapest and most reliable way to develop silk proteins (Torakeva et al., 2013). Attaining full length recombinant spider silk proteins is nevertheless still difficult because the length and size of the various spidroins render them difficult for bacterial hosts to synthesize and secrete, and for researchers to isolate and purify in solution (Heidebrecht and Scheibel, 2013; Wolff et al., 2017). The storage of the spidroins at high concentration facilitates the formation of micellar structures promoted by the alternating hydrophobic and hydrophilic regions across the protein terminal and core domains (Vollrath and Knight, 2001; Nova et al., 2010; Beun et al., 2014). Nevertheless, spidroins constructed in the lab using recombinant and other technologies tend to self-assemble and/or aggregate in high concentrations rather than forming micelles in solution (Hoffmann et al., 2018). Hence the storage capacity of laboratory synthesized spidroins is severely limited, which affects the shear stresses that the proteins experience within the spinning column, thereby hindering sol development, thus affecting the physical properties of the spun fibers (Heidebrecht and Scheibel, 2013; Wolff et al., 2017; Hoffmann et al., 2018). Nonetheless, when solubilized in high concentration under precise pH and ionic conditions, spidroins can form liquid crystallites (Vollrath and Knight, 2001). Knowledge of analogous processes, such as the natural bacterial production of nanocellulose fibers by *Aceobacter xylinum* (Iguchi et al., 2000) may accelerate the development of silk-like materials by similar means, as well as exemplifying processes to engineer the use of such materials (Song et al., 2019).

Finally, we contemplate whether it is possible to fully re-create all of the natural production processes associated within spider silk and, if not, which ones should biomimetic programs harness (Naik and Stone, 2005)? Evolution by natural selection modifies organismal processes over 1,000s of generations with the reproductive successes of the organism's progeny being the measure of its success. Spiders have evolved a toolkit of secretions that interact across scales; from gene expression to the formation of proteins, protein structures, fibers and, ultimately, webs and other extended phenotypes that perform specific biological functions (Blamires et al., 2017). Accounting for all of the physiological, biochemical, and ecological processes acting pre- and post-spinning to affect silk performance is nonetheless not easily replicable in the laboratory (Blamires et al., 2012b).

Biodesign is the use of organisms to enhance the function or production systems, where the border between mechanical and biological processes merge (Myers, 2014; Oxman, 2015). The challenge is to accommodate methodologies that combine top-down design procedures with bottom-up processes. Biodesigns have proven scalable and their applications are complementary with biological principles (Speck et al., 2017). Biodesign and biomimetic systems could then potentially be combined in a way to provide a wearables development framework based on spider silks and other high-performance natural materials. A key aspect of scalability of fiber manufacturing processes is an understanding of the parameters needed to produce specific product attributes and developing the models to link material properties to optimized manufacture. Such models exist for synthetic polymer spinning processes (Doufas et al., 2000) and can be re-applied to silk spinning using mechanical property characterization techniques specific to the stretching flows required for fiber production (Tripathi et al., 2000). Insights gained from such measurements will enable rapid feedback during material formation, process development, and scaled up biomanufacturing, as demonstrated by recent innovations (Boulet-Audet et al., 2019).

The objective of our prospective research is to develop new environmentally-friendly yet robust and light-weight wearable technologies from spider silk-like fibers that we develop by combining biomimetics research programs with a biodesign framework. This objective is ambitious, but we believe it is achievable utilizing the multidiscipline research toolbox approach. We thus provide some speculative examples

about how current research projects in the Spider Silk Research Lab might proceed to the development of new wearable technologies.

Example 1: We recently found the dry cribellate capture silk of the Tasmanian cave spider, *Hickmania troglodytes*, to combine hydrophobic and hydrophilic properties that vary in a multitude of ways both as the spider ages and across habitats. We speculate that a closer examination of the biological mechanisms facilitating the hydrophobic-hydrophilic switching in this type of silk will make it possible to biomimetically engineer silk-like fibers woven into micro-encapsulated white graphene to provide an on-off switch for the incorporation in smart celluloses and other wearable fibers and fabrics.

Example 2: Our work on the optical properties of spider dragline silk has shown that the silk's textured surface and crystalline structures primarily influences its colouration (Blamires et al., 2019). Examining the surface features of the silk more closely might thus enable us to copy the fibers' surface textures to create chromogenic fabrics incorporating micro-scale weave structures and knots to create unique colourations without using dyes or pigments.

Example 3: We know that the flexibility and toughness of spider dragline silk are adaptive across a web or fiber, and can be tailored to suit a particular purpose. Accordingly, an engineered material that can replicate the selective flexibility of spider silk may be a useful "smart" material that can vary in property and compliance across environments. Since human skin needs to adapt its functionality across the human body, a deeper investigation of dragline silk's variability across environments might facilitate the development of more biocompatible synthetic skins, skin grafts, garments, patches, threads, biomembranes, or buttresses (Foo and Kaplan, 2002; Scheibel, 2004; Lee et al., 2007).

AUTHOR CONTRIBUTIONS

SB and PF conceptualized the manuscript, and all authors wrote and approved the manuscript.

REFERENCES

Abascal, N. C., and Regan, L. (2018). The past, present and future of protein based materials. *Open Biol.* 8:180113. doi: 10.1098/rsob.180113

Agnarsson, I., Kuntner, M., and Blackledge, T. A. (2010). Bioprospecting finds the toughest biological material: extraordinary silk from a giant riverine orb spider. *PLoS ONE* 5:e11234. doi: 10.1371/journal.pone.0011234

Belaid, S., Chabira, S. F., Ballard, P., Sebaa, M., and Belhouide, S. (2015). Thermal aging effect on the mechanical properties of polyester fiberglass composites. *J. Mater. Env. Sci.* 6, 2795–2803.

Beun, L. H., Storm, I. N., Werten, M. W. T., de Wolf, F. A., Cohen Stuart, F. A., and de Vries, R. (2014). From micelles to fibers: balancing self-assembling and random coiling domains in pH-responsive silk-collagen-like protein-based polymers. *Biomacromolecules* 15, 3349–3357. doi: 10.1021/bm500826y

Bini, E., Foo, C. W. P., Huang, J., Karageorgiou, V., Kitchel, B., and Kaplan, D. L. (2006). RGD-functionalized bioengineered spider dragline silk biomaterial. *Biomacromolecules* 7, 3139–3145. doi: 10.1021/bm0607877

Blamires, S. J., Blackledge, T. A., and Tso, I. M. (2017). Physicochemical property variation in spider silk: ecology, evolution, and synthetic production. *Annu. Rev. Entomol.* 62, 443–460. doi: 10.1146/annurev-ento-031616-035615

Blamires, S. J., Cerexhe, G., White, T. E., Herberstein, M. E., and Kasumovic, M. M. (2019). Spider silk colour covaries with thermal properties but not protein structure. *J. Roy. Soc. Interf.* 16:20190199. doi: 10.1098/rsif.2019.0199

Blamires, S. J., Liao, C. P., Chang, C. K., Chuang,Y. C., Wu, C. L., Blackledge, T. A., et al. (2015a). Mechanical performance of spider silk is robust to nutrient-mediated changes in protein composition. *Biomacromolecules* 16, 1218–1225. doi: 10.1021/acs.biomac.5b00006

Blamires, S. J., Nobbs, M., Martens, P. J., Tso, I. M., Chuang, W. S., Chang, C. K., et al. (2018). Multiscale mechanisms of nutritionally induced property variation in spider silks. *PLoS ONE* 13:e0192005. doi: 10.1371/journal.pone.0192005

Blamires, S. J., Piorkowski, D., Chuang, A., Tseng, Y. H., Toft, S., and Tso, I. M. (2015b). Can differential nutrient extraction explain property variations in a predatory trap? *Roy. Soc. Open Sci.* 2:140479. doi: 10.1098/rsos.140479

Blamires, S. J., Wu, C. L., Blackledge, T. A., and Tso, I. M. (2012b). Environmentally induced post-spin property changes in spider silks: influences of web type, spidroin composition and ecology. *Biol. J. Linn. Soc.* 106, 580–588. doi: 10.1111/j.1095-8312.2012.01884.x

Blamires, S. J.,Wu, C. L., and Tso, I. M. (2012a). Variation in protein intake induces variation in spider silk expression. *PLoS ONE* 7:e31626. doi: 10.1371/journal.pone.0031626

Bouhlel, Z., Genard, B., Ibrahim, N., Carrington, E., Babarro, J. M. F., Lok, A., et al. (2017). Interspecies comparison of the mechanical properties and biochemical composition of byssal threads. *J. Exp. Biol.* 220, 984–994. doi: 10.1242/jeb.141440

Boulet-Audet, M., Rice, G. W., Moody, K. M., Bainbridge, J. M., Tom, S., Davijani, A. A. B., et al. (2019). *Methods of Generating Recombinant Spider Silk Protein Fibers*. Emeryville, CA: U.S. Patent Application 16/176,939, 1–55.

Browne, M. A., Dissanayake, A., Galloway, T. S., Lowe, D. M., and Thompson, R. C. (2008). Ingested microscopic plastic translocates to the circulatory system of the mussel, *Mytilus edulis* (L.). *Env. Sci. Technol.* 42, 5026–5031. doi: 10.1021/es800249a

Carlson, R. (2010). *Biology Is Technology: The Promise, Peril, and New Business of Engineering Life*. Cambridge, MA: Harvard University Press. doi: 10.4159/9780674053625

Carr, C., and Gibson, C. (2016). Geographies of making: rethinking materials and skills for volatile futures. *Progr. Human Geogr.* 40, 297–315. doi: 10.1177/0309132515578775

Chaw, R. C., Correa-Garhwal, S. M., Clarke, T. H., Ayoub, N. A., and Hayashi, C. Y. (2015). Proteomic evidence for components of spider silk synthesis from black widow silk glands and fibers. *J. Proteom. Res.* 14, 4223–4231. doi: 10.1021/acs.jproteome.5b00353

Chen, P. Y., McKittrick, J., and Meyers, M. A. (2012). Biological materials: functional adaptations and bioinspired designs. *Prog. Mater. Sci.* 57, 1492–1704. doi: 10.1016/j.pmatsci.2012.03.001

Craig, C. L., Riekel, C., Herberstein, M. E., Weber, R. S., Kaplan, D., and Pierce, N. E. (2000). Evidence for diet effects on the composition of silk proteins produced by spiders. *Mol. Biol. Evol.* 17, 1904–1913. doi: 10.1093/oxfordjournals.molbev.a026292

Damiati, S., Mhanna, R., Kodzius, R., and Ehmoser, E. K. (2018). Cell-free approaches in synthetic biology utilizing microfluidics. *Genes* 9:144. doi: 10.3390/genes9030144

De Falco, F., Gullo, M. P., Gentile, G., Di Pace, E., Cocca, M., Gelabert, L., et al. (2018). Evaluation of microplastic release caused by textile washing processes of synthetic fabrics. *Env. Poll.* 236, 916–925. doi: 10.1016/j.envpol.2017.10.057

Dmitrievich, Z. A., Viktorovna, S. T., Borisovich, Z. D., and Olegovna, K. A. (2014). Thermal treatment of the mineral wool mat. *Adv. Mater. Res.* 838, 196–200. doi: 10.4028/www.scientific.net/AMR.838-841.196

Doufas, A. K., McHugh, A. J., and Miller, C. (2000). Simulation of melt spinning including flow-induced crystallization: part I. Model development and predictions. *J. Non-Newt. Fluid Mech.* 92, 27–66. doi: 10.1016/S0377-0257(00)00088-4

Eadie, L., and Ghosh, T. K. (2011). Biomimicry in textiles: past, present and potential. An overview. *J. Roy. Soc. Interf.* 8, 761–775. doi: 10.1098/rsif.2010.0487

Elvin, M. E., Carr, A. G., Huson, M. G., Maxwell, J. M., Pearson, R. D., Vuocolo, T., et al. (2005). Synthesis and properties of crosslinked recombinant pro-resilin. *Nature* 437, 999–1002. doi: 10.1038/nature04085

Flanagan, P. J. (2014). "A vibrant evolution: from wearable devices to objects as mediators of experience," in *Design, User Experience and Usability: User Experience Design for Everyday Life Applications and Services*, ed A. Marcus (Cham, SZ: Springer), 675–686. doi: 10.1007/978-3-319-07635-5_64

Foo, C. W. P., and Kaplan, D. L. (2002). Genetic engineering of fibrous proteins: spider dragline silk and collagen. *Adv. Drug Deliv. Rev.* 54, 1131–1143. doi: 10.1016/S0169-409X(02)00061-3

Franklin, K. (2018). *Radical Matter: Rethinking Materials for a Sustainable Future*. London: Thames & Hudson.

Garb, J. E., Haney, R. A., Schwager, E. E., Gregoric, M., Kuntner, M., Agnarsson, I., et al. (2019). The transcriptome of Darwin's bark spider silk glands predicts proteins contributing to dragline silk toughness. *Comm. Biol.* 2:275. doi: 10.1038/s42003-019-0496-1

Gellynck, K., Verdonk, P., Forsyth, R., Almqvist, K. F., Van Nimmen, E., Gheysens, T., et al. (2008). Biocompatibility and biodegradability of spider egg sac silk. *J. Mat. Sci.* 19, 2963–2970. doi: 10.1007/s10856-007-3330-0

Gordon, S., and Hseih, Y. L. (2011). *Cotton: Science and Technology*. Boca Raton: CRC Press.

Guehrs, K. H., Schlott, B., Grosse, F., and Weisshart, K. (2008). Environmental conditions impinge on dragline silk protein composition. *Ins. Mol. Biol.* 17, 553–564. doi: 10.1111/j.1365-2583.2008.00826.x

Heidebrecht, A., and Scheibel, T. R. (2013). Recombinant production of spider silk proteins. *Adv. Appl. Microbiol.* 82, 115–152. doi: 10.1016/B978-0-12-407679-2.00004-1

Heim, M., Keerl, D., and Scheibel, T. R. (2009). Spider silk: from soluble protein to extraordinary fiber. *Ang. Chem. Int. Ed.* 48, 3584–3596. doi: 10.1002/anie.200803341

Hoffmann, B., Gruat-Henry, C., Mulitini, P., Jiang, L., Brooks, B. D., and Brooks, A. E. (2018). Using hydrodynamic focusing to predictably alter the diameter of synthetic silk fibers. *PLoS ONE* 13:e0195522. doi: 10.1371/journal.pone.0195522

Hwang, J., Jeong, Y., Park, J. M., Hong, J. W., and Choi, J. (2015). Biomimetics: forecasting the future of science, engineering, and medicine. *Inter. J. Nanomed.* 10, 5701–5713. doi: 10.2147/IJN.S83642

Iguchi, M., Yamanaka, S., and Budhiono, A. (2000). Bacterial cellulose—a masterpiece of nature's arts. *J. Mater. Sci.* 35, 261–270. doi: 10.1023/A:1004775229149

Jastrzebska, K., Felcyn, E., Kozak, M., Szybowicz, M., Buchwald, T., Pietralik, Z., et al. (2016). The method of purifying bioengineered spider silk determines the silk sphere properties. *Sci. Rep.* 6:28106. doi: 10.1038/srep28106

Koh, L. D., Cheng, Y., Teng, C. P., Khin, Y. W., Lo, X. J., Tee, S. Y., et al. (2015). Structures, mechanical properties and applications of silk fibroin materials. *Prog. Polym. Sci.* 46, 86–110. doi: 10.1016/j.progpolymsci.2015.02.001

Kojic, N., Bico, J., Clasen, C., and McKinley, G. H. (2006). *Ex vivo* rheology of spider silk. *J. Exp. Biol.* 209, 4355–4362. doi: 10.1242/jeb.02516

Kono, N., Nakamura, H., Ohtoshi, R., Pedrazzoli Moran, D. A., Shinohara, A., Yoshida, Y., et al. (2019). Orb-weaving spider *Araneus ventricosus* genome elucidates the spidroin gene catalogue. *Sci. Rep.* 9:8380. doi: 10.1038/s41598-019-44775-2

Lacava, M., Camargo, A., Garcia, L. F., Benamu, M., Santana, M., and Fang, J., et al. (2018). Web building and silk properties functionally covary among species of wolf spider. *J. Evol. Biol.* 31, 968–978. doi: 10.1111/jeb.13278

Lapidot, S., Meirovitch, S., Sharon, S., Heyman, A., Kaplan, D. L., and Shoseyov, O. (2012). Clues for biomimetics from natural composite materials. *Nanomedicine* 7, 1409–1423. doi: 10.2217/nnm.12.107

Le Quéré, C., Raupach, M. R., Canadell, J. G., Marland, G., Bopp, L., Ciais, P., et al. (2009). Trends in the sources and sinks of carbon dioxide. *Nature Geosci.* 2, 831–836. doi: 10.1038/ngeo689

Lee, K. S., Kim, B. Y., Je, Y. H., Woo, S. D., Sohn, H. D., and Jin, B. R. (2007). Molecular cloning and expression of the C-terminus of spider flagelliform silk protein from *Araneus ventricosus*. *J. Biosci.* 32, 705–712 doi: 10.1007/s12038-007-0070-8

Lefèvre, T., and Auger, M. (2016). Spider silk inspired materials and sustainability: perspective. *Mater. Technol.* 31, 384–399. doi: 10.1179/1753555715Y.0000000065

Liu, X., and Zhang, K. Q. (2011). "Silk fiber — molecular formation mechanism, structure- property relationship and advanced applications," in *Oligomerization of Chemical and Biological Compounds*, ed. C. Lesieur (Rejika, Croatia: In Tech), 69–101.

Morgan, P. W. (1981). Brief history of fibers from synthetic polymers. *J. Macromol. Sci.* 15, 1113–1131. doi: 10.1080/00222338108066456

Morton, W. E., and Hearle, J. W. S. (2008). *Physical Properties of Textile Fibres, 4th Edn.* Cambridge, UK: Woodhead. doi: 10.1533/9781845694425

Myers, W. (2014). *Biodesign: Nature, Science, Creativity*. London: Thames and Hudson.

Naik, R. R., and Stone, M. O. (2005). Integrating biomimetics. *Mater. Today* 8, 18–26. doi: 10.1016/S1369-7021(05)71077-4

Nguyen-Robertson, C. V., and Byrne, N. (2019). *Circular Fashion: Turning Old Clothes Into Everything From New Cotton to Fake Knees*. Melbourne, VIC: The Conversation.

Nova, A., Keten, S., Pugno, N. M., Redaelli, A., and Buehler, M. J. (2010). Molecular and nanostructural mechanisms of deformation, strength and toughness of spider silk fibrils. *Nano Lett.* 10, 2626–2634. doi: 10.1021/nl101341w

Omenetto, F. G., and Kaplan, D. L. (2010). New opportunities for an ancient material. *Science* 329, 528–531. doi: 10.1126/science.1188936

Oxman, N. (2015). Templating design for biology and biology for design. *Archit. Design* 85, 100–107. doi: 10.1002/ad.1961

Pawlyn, M. (2011). *Biomimicry in Architecture*. London: RIBA Publishing.

Porter, D., and Vollrath, F. (2009). Silk as a biomimetic ideal for structural polymers. *Adv. Mater.* 21, 487–492. doi: 10.1002/adma.200801332

Quinn, B. (2010). *Textile Futures: Fashion, Design and Technology*. Berg: Oxford NY.

Rammensee, S., Slotta, U., Scheibel, T. R., and Bausch, A. R. (2008). Assembly mechanism of recombinant spider silk proteins. *Proc. Nat. Acad. Sci. U.S.A.* 105, 6590–6595. doi: 10.1073/pnas.0709246105

Sanchez, C., Arribath, H., and Guille, M. M. (2005). Biomimetism and bioinspiration as tools for the design of innovative materials and systems. *Nat. Mater.* 4, 277–288. doi: 10.1038/nmat1339

Scheibel, T. R. (2004). Spider silks: recombinant synthesis, assembly, spinning, and engineering of synthetic proteins. *Microbial Cell Fact.* 3:14. doi: 10.1186/1475-2859-3-14

Song, J., Babayekhorasani, F., and Spicer, P. T. (2019). Soft bacterial cellulose microcapsules with adaptable shapes. *Biomacromolecules* 20, 4437–4446. doi: 10.1021/acs.biomac.9b01143

Speck, O., Speck, D., Horn, R., Gantner, J., and Sedlbauer, K. P. (2017). Biomimetic bio-inspired biomorph sustainable? An attempt to classify and clarify biology-derived technical developments. *Bioinspir. Biomim.* 12:011004. doi: 10.1088/1748-3190/12/1/011004

Su, I., and Buehler, M. J. (2016). Nanomechanics of silk: the fundamentals of a strong, tough and versatile material. *Nanotechnology* 27:302001. doi: 10.1088/0957-4484/27/30/302001

Szostak-Kotowa, J. (2004). Biodeterioration of textiles. *Int. Biodeter. Biodegrad.* 53, 165–170. doi: 10.1016/S0964-8305(03)00090-8

Tarakanova, A., and Buehler, M. J. (2012). The role of capture spiral silk properties in the diversification of orb webs. *J. Roy. Soc. Interf.* 9, 3240–3248. doi: 10.1098/rsif.2012.0473

Torakeva, O., Michalczechen-Lacerda, V. A., Rech, E. L., and Kaplan, D. L. (2013). Recombinant DNA production of spider silk proteins. *Microb. Biotech.* 6, 651–663. doi: 10.1111/1751-7915.12081

Tripathi, A., Whittingstall, P., and McKinley, G. H. (2000). Using filament stretching rheometry to predict strand formation and "processability" in adhesives and other non-Newtonian fluids. *Rheol. Acta* 39, 321–337. doi: 10.1007/s003970000072

Viera, C., Garcia, L. F., Lacava, M., Fang, J., Wang, X., Kasumovic, M. M., et al. (2019). Silk physico-chemical variability and mechanical robustness facilitates intercontinental invasibility of a spider. *Sci. Rep.* 9:13273. doi: 10.1038/s41598-019-49463-9

Vollrath, F., and Knight, D. P. (2001). Liquid crystalline spinning of spider silk. *Nature* 410, 541–548. doi: 10.1038/35069000

Waite, J. H. (1992). "The formation of mussel byssus: anatamoy of a natural manufacturing processes," in *Structure, Cellular Synthesis and Assembly of Biopolymers*, ed S. T. Case (Berlin: Springer-Verlag), 27–54. doi: 10.1007/978-3-540-47207-0_2

Wegst, U. G., Bai, H., Saize, E., Tomsia, A., and Ritchie, R. O. (2015). Bioinspired structural materials. *Nat. Mater.* 14, 23–36. doi: 10.1038/nmat4089

Wilder, S. M. (2011). Spider nutrition: an integrative perspective. *Adv. Ins. Physiol.* 40, 87–136. doi: 10.1016/B978-0-12-387668-3.00002-7

Wolff, J. O., Wells, D., Reid, C. R., and Blamires, S. J. (2017). Clarity of objectives and working principles enhances the success of biomimetic programs. *Bioinspir. Biomim.* 12:051001. doi: 10.1088/1748-3190/aa86ff

Wu, Y., Shah, D. U., Liu, C., Yu, Z., Ren, X., Rowland, M. J., et al. (2017). Bioinspired supramolecular fibers drawn from a multiphase self-assembled hydrogel. *Proc. Nat. Acad. Sci. U.S.A.* 114, 8163–8168. doi: 10.1073/pnas.1705380114

Xia, X. X., Qian, Z. G., Ki, C. S., Park, Y. H., Kaplan, D. L., and Lee, S. Y. (2010). Native-sized recombinant spider silk protein produced in metabolically engineered *Escherichia coli* results in a strong fiber. *Proc. Nat. Acad. Sci. U.S.A.* 107, 14059–14063. doi: 10.1073/pnas.1003366107

Zax, D. B., Armanios, D. E., Horak, S., Malowniak, C., and Yang, Z. (2004). Varaition of mechanical properties with amino acid content in the silk of *Nephila clavipes*. *Biomacromolecules* 5, 732–738. doi: 10.1021/bm034309x

Conflict of Interest: The authors declare that the research was conducted in the absence of any commercial or financial relationships that could be construed as a potential conflict of interest.

frontiers in Materials

MINI REVIEW
published: 18 February 2020
doi: 10.3389/fmats.2020.00024

Recent Advances in Silk Sericin/Calcium Phosphate Biomaterials

Anabela Veiga[1,2], *Filipa Castro*[1]*, *Fernando Rocha*[1] and *Ana L. Oliveira*[2]*

[1] LEPABE – Laboratory for Process Engineering, Environment, Biotechnology and Energy, Faculty of Engineering, University of Porto, Porto, Portugal, [2] Universidade Católica Portuguesa, CBQF - Centro de Biotecnologia e Química Fina - Laboratório Associado, Escola Superior de Biotecnologia, Porto, Portugal

Calcium phosphates (CaPs) have been widely used in the field of biomedical engineering as bone graft substitutes or as carriers for drug delivery applications. Recent developments have focused on combining CaPs with proteins to obtain functional biomaterials that accommodate a broader spectrum of functional requirements. Silk sericin was considered an unutilized protein by-product from the textile industry, generating tons of residues every year. However, much effort has been dedicated to its recovery after being associated with numerous biological properties such as antioxidant, antibacterial, anti-coagulation and regenerative activities. In the past years, sericin has also demonstrated to be suitable as a template for CaP mineralization. The present review focuses on the recent developments for the production of sericin/CaP composites, exploring their potential applications in bioengineering and opening new avenues in other research fields such as in the cosmetic, food and environmental sectors. In addition, this paper can also be useful as a guideline to design future research based on sericin/CaP biomaterials.

Keywords: biomaterials, bone tissue engineering (bone-TE), calcium phosphates (CaPs), drug delivery, hydroxyapatite (HAp), sericin

OPEN ACCESS

Edited by:
Antonella Motta,
University of Trento, Italy

Reviewed by:
Vamsi Yadavalli,
Virginia Commonwealth University, United States
Biman B. Mandal,
Indian Institute of Technology Guwahati, India
Pornanong Aramwit,
Chulalongkorn University, Thailand

***Correspondence:**
Filipa Castro
filipaj@fe.up.pt
Ana L. Oliveira
aloliveira@porto.ucp.pt

Specialty section:
This article was submitted to Biomaterials, a section of the journal Frontiers in Materials

Received: *19 September 2019*
Accepted: *21 January 2020*
Published: *18 February 2020*

Citation:
Veiga A, Castro F, Rocha F and Oliveira AL (2020) Recent Advances in Silk Sericin/Calcium Phosphate Biomaterials. Front. Mater. 7:24. doi: 10.3389/fmats.2020.00024

INTRODUCTION

Bone matrix consists of both a non-mineralized organic component (∼20% of the wet weight) and a mineralized inorganic component (∼65–70%), composed mainly by collagen and carbonated calcium phosphate (CaP) crystals, respectively. Crystallographic c-axis of these crystals are arranged parallelly to the longitudinal axis of the fibrous protein, forming a tough and flexible nanocomposite structure (Fuchs et al., 1997; Amini et al., 2012).

Accordingly, calcium phosphates (CaPs) from natural or synthetic nature, are widely used in bone-related applications due to their biocompatibility, low density, chemical stability and crystallinity (Vallet-Regí and González-Calbet, 2004). Among existing CaPs, hydroxyapatite (HAp) is the most studied biomaterial due to its close similarity to human hard tissue in terms of morphology and composition (Habraken et al., 2016).

In a quest to mimic bone tissue, several studies have focused on the synthesis of CaP composites using synthetic polymers [polyglycolic acid (PGA), poly L-lactic acid (PLLA), polylactic-coglycolic acid (PLGA), and polycaprolactone (PCL)] (Rezwan et al., 2006; Lee and Yuk, 2007; Chen et al., 2014), natural polymers (alginate, chitosan, cellulose) (Pighinelli and Kucharska, 2013; Cardoso et al., 2014; Salama, 2019), proteins (collagen, fibrin, keratin, and silk fibroin) (Dias et al., 2010; Bleek and Taubert, 2013; Brown and Barker, 2014; Liu, 2015; Farokhi et al., 2018),

or combinations of the foregoing (Chen et al., 2014). Synthetic polymers may induce local and systemic host reactions due to the release of chemicals and monomers from polymer degradation, while natural polymers may lead to products with different characteristics due to the differences in raw materials (Chen et al., 2014).

Proteins have demonstrated to regulate the size, particle size distribution, morphology, and assembly method of nanostructured CaPs, being thus used to fabricate novel materials with biomimetic characteristics for hard tissue repair (Cai and Yao, 2010; Chen et al., 2014). Further, their natural origin confers unique biocompatibility, versatility, and biodegradability properties (Swetha et al., 2010). Collagen has been conventionally used in the synthesis of organic/CaP composites. Although collagen/CaP composites have a greater similarity to natural bone, the clinical application of collagen-type biomaterials is still limited due to its high cost, increased risk of cross-infection and fast degradability (Chen et al., 2014). Alternative protein systems can play a pivotal role during the mineralization of CaP, as a binding-matrix. Keratin/CaP and fibrin/CaP composites have biocompatibility and bioactivity properties suitable for bone tissue engineering. However, these biomaterials lack mechanical properties and processing properties, and have fast biodegrability (Gsib et al., 2017; Shavandi et al., 2017).

In this context silk is a valuable alternative due to its excellent intrinsic properties such as non-toxicity, biodegradability, self-assembly, mechanical stability and controllable structure (Altman et al., 2003; Ha et al., 2013). In nature, silk-like proteins are produced by several organisms such as silkworms, spiders, mollusks, scorpions, bees, and ants (Holland et al., 2019). The use of silk from the domesticated silkworm *Bombyx mori* is well-established as suitable for biomedical applications due to its abundance, batch-to-batch stability, and clinical track record (Ude et al., 2014). This type of silk comprises a fibrous semi-crystalline silk core, silk fibroin, which is mainly responsible for the load-bearing capacity, and an outer layer of a globular protein, sericin, which serves as gluing agent and has a protective function. While fibroin is processed in large scale in the textile industry, sericin is a by-product generated during this process, in the so-called degumming procedure (Mondal et al., 2006).

Silk fibroin has been widely used and investigated for applications such as sutures (Saxena et al., 2014), artificial ligaments (Farè et al., 2013), tissue engineering constructs (Kasoju and Bora, 2012), and substrates for cell culture (Liu et al., 2012). Fibroin/CaP composites have been reported and are considered suitable for load bearing applications (Yan et al., 2013; Farokhi et al., 2018).

Silk sericin, on the other hand, was until recently considered unfit for biomedical use. Of 1 million tons of silkworm cocoons produced each year worldwide, ∼50,000 t of sericin are generated, leading to environmental and economic concerns (Aramwit et al., 2012b). This protein, in its native state, was found to elicit immune and allergic responses when present in virgin silk sutures (Soong and Kenyon, 1984). However, emerging evidence suggests that extracted sericin *per se* is biocompatible, similarly to silk fibroin or collagen (Chirila et al., 2013; Lamboni et al., 2015). Therefore it has been gaining reputation in the biomedical field with several works showing its potential, as revised elsewhere (Kunz et al., 2016; Ahsan et al., 2018). Thus, the use of sericin/CaP composites not only reduces the inherent environmental impact of sericin disposal but also allows the development of new functional biomaterials. This silk protein increases antioxidant, anti-tyrosinase and anti-inflammatory activity; stimulates collagen production, tumor inhibitory effects; induces the nucleation of bone-like CaPs; and promotes stability and prolonged release in drug delivery systems (Aramwit, 2014; Lamboni et al., 2015).

The molecular weight distribution and even the amino acid composition of sericin were found to be dependent on the extraction method used (Yang et al., 2014c; Kunz et al., 2016). Sericin consists of 18 amino acids, among which serine, histidine, glutamic acid, aspartic acid, threonine, and tyrosine are normally present in higher percentages. Thus, this protein is highly hydrophilic and its molecular weight can range from 20 to 400 kDa (Kunz et al., 2016). Its polar side chains have several functional groups (carboxyl, amine, hydroxyl) responsible for moisturizing and oxidizing properties, allowing the interaction with other compounds through crosslinking, copolymerization or blending to form improved biomaterials (Ahsan et al., 2018). According to the literature, amino acids can highly influence the mineralization process of CaPs. Glutamic acid and aspartic acid play a critical role in controlling HAp nucleation and growth, by attracting calcium and phosphate ions and consequently increasing the local supersaturation, which results in the development of crystals. Histidine and other negatively charged amino acids are involved in HAp nucleation within extracellular matrix proteins (George and Veis, 2008; Tavafoghi and Cerruti, 2016).

Sericin mainly adopts the form of an amorphous random spiral and may also present the form of a β-sheet organized structure. The random spiral easily acquires β-sheet conformation as a consequence of moisture absorption and mechanical elongation, forming a denser, organized, crystalline and less soluble structure. If the protein is dissolved in hot water and subsequently undergoes a temperature decrease, its random coil structure becomes β-sheet, acquiring a gelatinous form (Chen et al., 2015). That is, with the change in temperature the conformation of the protein changes. Upon heating the sericin dissolves in solution, upon cooling the sericin solution jellifies (Sol-Gel properties; Kunz et al., 2016).

SILK SERICIN/CALCIUM PHOSPHATE-BASED MATERIALS

Recently, sericin has demonstrated to be suitable as a template for CaP mineralization. In the literature, sericin/CaP biomaterials are usually synthetized by wet mechanochemical processes, where mineralization occurs by spontaneous nucleation (Cai et al., 2009, 2010) or using a surface as template (Takeuchi et al., 2005b; Yang et al., 2014a). The resulting composites generally present a poor crystallinity and the size of the particles generated can range from 20 to 500 nm in length to 3–80 nm

in width (Cai et al., 2009, 2010; Veiga et al., 2019). The influence of several experimental conditions on the formation of these sericin/CaPs has been studied by several authors, namely different sericin extraction and storage procedures, mineralization time, sericin concentration, and temperature (**Table 1**). In the works of Takeuchi et al. (2003a, 2005b), sericin was obtained by extraction in boiling water, using different temperatures and storage procedures. It was found that high molecular weight sericin and β-sheet structure induces apatite deposition. These conditions were achieved for higher extraction temperatures and sericin storage. It is well-known that the extraction method used influences the molecular weight and the amino acid concentration of sericin, which results in different physical and biological properties (Kunz et al., 2016). According to Aramwit et al. (2010), extraction in boiling water is the least toxic procedure to cells and activates the highest collagen production. Acid, alkaline, and urea extraction methods can also be used to obtain sericin that promotes the formation of bone organic matrix. However, these approaches can result in toxicity at higher sericin concentrations (Padamwar and Pawar, 2004). Moreover, acid and alkaline methods have a degrading effect on proteins and considerably increase its solubility. Although urea and enzymatic methods can be used to obtain unchanged sericin, the procedures are expensive and time consuming. On the other hand, hot-water extraction is a simple and environmentally friendly method that preserves the main characteristics of silk sericin (Gulrajani et al., 2000; Dash et al., 2008).

As for the influence of the mineralization time on apatite deposition, it was found that the optimum days for growth of nano HAp crystals with low crystallinity is 7 days. In contrast, after 30 days, the size of HAp crystals increases, and other CaP phases are formed (Sukjai et al., 2012). Further, it was also shown that nucleation of HAp mediated by sericin is a gradual process, since nanoneedle crystals with low crystallinity are only grown after at least 24 h of mineralization (Yang et al., 2014b). In the work of Zhang et al. (2014), the same conclusions were drawn for ethanol-treated sericin films immersed in SBF. A three-dimensional (3D) structure with globular carbonate apatite particles was observed after 7 days. Further, rigid and brittle properties of the film increased with mineralization time, since apatite particles were increasingly being deposited. While the elastic modulus increased significantly after 5 and 7 days (23.027 $\pm$ 0.83 to 57.02 $\pm$ 1.04 MPa), the tensile strength (day 1: 1.58 $\pm$ 0.53, day 7: 0.24 $\pm$ 0.18) and the elongation at break of the 3D film decreased (day 1: 112.83 $\pm$ 49.02%, day 7: 2.01 $\pm$ 1.81%). The increase of the mineralization time and sericin concentration was also reported to lead to an increase in the mean particle size of the particles synthetized (Cai et al., 2009). The recent developments in sericin/CaP composites and its potential for biomedical applications is presented in the next section.

RESEARCH APPLICATIONS

Biomineralization

Although proteins play a crucial role during mineral formation in biological systems, the biomineralization process is still far from being understood (Subburaman et al., 2006). Therefore, most studies on sericin/CaP composites focus on contributing to the understanding of this phenomenon. Sericin/CaP nanoparticle systems obtained are generally nanorod-like crystals with poor crystallinity. Further, sericin promotes crystal growth of HAp along the c-axis, resembling natural biomineralization. Although in the work of Cai et al. (2010), HAp particles similar to mineral bone were achieved in the absence of sericin, this was only verified for specific temperature and pH conditions. Other works argue that the presence of sericin promotes a homogeneous assembly of HAp, under several experimental conditions (Cai et al., 2009; Yang et al., 2014b). The proposed mechanisms for the assembly of CaP crystals in the presence of sericin are usually based on changes in the protein conformation. When dissolved, sericin adopts an amorphous structure in which the hydrophilic sidechains are exposed. However, when submitted to different triggers (e.g., mechanical stretching properties, moisture absorption, temperature, dehydration, or using crosslinking agents), changes in random coil structure for β-sheet easily occur (Teramoto and Miyazawa, 2003; Nayak et al., 2012; Kunz et al., 2016).

According to Takeuchi, the induction sites for HAp nucleation in sericin films are governed by the arrangement of carboxyl groups on the protein (Takeuchi et al., 2005b). When a protein acquires a β-sheet conformation, the amino acid side chains alternate between the two faces of the sheet. Hydrophobic side-chains point in one direction and polar side-chains in the other, which can explain orientation of functional groups in β-sheet sericin (Boyle, 2018). For sericin/HAp particles, the presence of chelated calcium ions in the precipitation medium provides nucleation sites. The formed HAp crystals are rearranged along their c-axis by attaching to the sericin molecular chains (Cai et al., 2009).

The understanding of the biomineralization process can lead to numerous applications in biomedical engineering, namely for the development of advanced bone substitutes (Chen et al., 2019; Veiga et al., 2019). Even though pure sericin has poor mechanical properties, which hinders its utilization in bone tissue engineering (bone-TE), its biological properties can promote bone formation and induce the nucleation of bone-like HAp. In fact, sericin/CaP materials have shown the ability to promote cell differentiation and proliferation of bone marrow-derived mesenchymal stem cells (BMSCs) and of human osteosarcoma cells (MG-63; **Table 1**). Therefore, most of the developed works on sericin/CaP focus on demonstrating the potential of these composites in the field of bone-TE, as biomaterials for bone filling and repair or as drug delivery systems for tumor therapy, as illustrated in **Figure 1**.

Bone Tissue Engineering

Although some authors mention the potential of sericin/CaP as scaffolds for TE (Takeuchi et al., 2003b; Yang et al., 2014b), an ideal 3D scaffold should not only act as a template for tissue growth and has controlled resorbability, but should also elicit a regenerative effect and present adequate mechanical performance over time (Canillas et al., 2017). As previously mentioned, the last requirement is not fulfilled by using only sericin (Ahsan et al., 2018).

TABLE 1 | Articles on sericin/CaP biomaterials.

Objectives	Methodology	Experimental conditions	Studied variables	Physicochemical properties	Biological properties	Applications	References
Investigate the ability of natural silk and its related materials to facilitate apatite deposition under biomimetic conditions.	- Sericin extraction was performed in boiling water (105°C, 1 h); Soaking method: - Cloths made of raw silk, normal silk fiber, and sericin films were soaked in 1.5 SBF.	pH = 7.25; T = 36.5°C; Mineralization time: 7 days.	–	- The deposition of apatite microspheres was observed on both the surface of cloth made from raw silk fiber and in the sericin films; - CaP particles were not obtained on cloth made from normal silk fibers; - The apatite deposition on the raw silk fiber cloth was accelerated by presence of calcium ions (treatment with $CaCl_2$).	–	Present the potential of sericin/HAp composites in the field of bone tissue engineering (as bone substitutes and scaffolds).	Takeuchi et al., 2003b
Study the structural effect of sericin on its apatite-forming ability using 1.5 SBF.	Soaking method: - Sericin films were immersed in 1.5 SBF.		Four Different types of sericin films were obtained: Extraction/Storage of sericin 105°C 1 h/none: 105–0 d; 120°C 1 h/none: 120–0 d; 105°C 1 h/4°C for 2 weeks: 105–2 w; 120°C 1 h/4°C for 2 weeks: 120–2 w.	- Molecular weight: 134, 106, 42, and 43 kDa for 105–0 d, 105–2 w, 120–0 d, and 120–2 w, respectively; - After storage for 2 weeks at 4°C, β-sheet structure became dominant; - Spherical HAp particles with low crystallinity were only observed on the surface of 105–2 w film after 7 days.	–	Contributing for the understanding of biological mineralization.	Takeuchi et al., 2003a, 2005b
Investigate the optimum day for the growth of HAp in sericin-coated silk fibers using SBF.	Soaking method: - Sericin coated silk fibers and non-sericin coated silk fibers were used were soaked in SBF of various concentrations.	T = 37°C.	Mineralization time: 7 and 30 days. SBF concentration (1.5 and 1.0 SBF).	- In non-sericin coated silk fibers, flat shape CaP crystals were formed after 7 days. With the increase in SBF concentration, cauliflower shape HAp crystals were obtained; - In sericin coated silk fibers only cauliflower shape HAp crystals were formed for 1.0 SBF concentrations (1–4 μm) and 1.5 SBF (0.1–0.2 μm).	–	Contributing for the understanding of biological mineralization.	Sukjai et al., 2012
Investigate the mineralization of sericin by alternative soaking in calcium and phosphate.	- Sericin (wt.%) = 8, extraction was performed in boiling water for 30 min; - The sericin film was soaked in 90% (v/v) ethanol; - Alternative soaking of the sericin film in calcium and phosphate solutions: 1°) [$CaCl_2$] (100 mM); 2°) [$NaHCO_3$] (60mM).	pH = 8.7; T = 37 °C.	Immersion cycles: 5, 10, 15 cycles.	- When the cycles of dip coating were set to be 5, 10, and 30, respectively, aggregation appeared on the coating and apatite spherical crystals were increased; - The coating thickness increased by increasing cycles of dip coating.	- *In vitro* assays showed that the HAp/sericin composites obtained have higher cell adhesion and growth activity of MG-63 cells, when compared to HAp.	Present the potential of HAp/sericin composites in the field of bone tissue engineering (for bone regeneration).	Yang et al., 2014a

(Continued)

TABLE 1 | Continued

Objectives	Methodology	Experimental conditions	Studied variables	Physicochemical properties	Biological properties	Applications	References
Study the mineralizing of ethanol-treated sericin film in SBF.	Sericin (wt.%) = 9, extraction was performed in boiling water for 30 min; - The sericin film was soaked in 40% (v/v) ethanol; Soaking method: - The sericin/ethanol film was immersed in 1.5 SBF.	pH 7.4; T = 37 °C.	Mineralization time =1, 3, 5, or 7 days.	- With the increase in mineralization time, the quantity of the deposited inorganic substance increased, showing a 3D aggregated structure; - After 7 days globular carbonate apatite particles with low crystallinity were observed (initial thickness = 93.5 ± 728.7 μm; thickness after 7 days: 6.22 ± 2.13 mm).	*In vitro* assays showed that the sericin/HAp composites obtained have higher cell viability of human osteosarcoma MG-63 cells, when compared to sericin.	Present the potential of sericin/HAp composites in the field of bone tissue engineering (as 3D materials).	Zhang et al., 2014
Study the effect sericin concentration and mineralization time on HAp assembly.	Co-precipitation method: [Na_2HPO_4] (12 mM); [$CaCl_2$] (20 mM) + sericin.	pH=9.5; T= 25 °C.	Mineralization time: 0, 20, and 60 min; Sericin (w/v%) = 0.001, 0.1, 0.5, and 1, purchased from Aotesi Biochemicals Co. Ltd (Huzhou, China).	- Rod-like sericin/HAp composites were obtained; - The crystallinity of the composites is lower when compared to HAp; - Higher concentration of sericin led to the synthesis of larger HAp particles—sericin 0.001% had the smallest size of 50–100 nm in length and <20 nm in diameter, while sericin 1% possessed the largest size of 300–500 nm in length and 50–80 nm in diameter; - Longer mineralization time led to an increase of the crystallinity and size of the composites; - Size of the crystals goes from 50 to 100 nm in length and <20 nm in diameter; to 300–500 nm in length and 50–80 nm in diameter.	*In vitro* assays showed that the composites obtained have higher cell differentiation and proliferation of MG-63 cells, when compared to HAp. Further, composites with higher sericin concentrarion had the highest ability to accelerate cell proliferation and differentiation.	Contributing for the understanding of biological mineralization.	Cai et al., 2009
Study the effect of the solution pH value on HAp assembly.	Sericin (w/v%) = 0.625, purchased from Aotesi Biochemicals Co. Ltd (Huzhou, China). Co-precipitation method: [Na_2HPO_4] (30mM); [$CaCl_2$] (12.5 mM) + sericin.	T=50 °C; Mineralization time: 320 min.	pH: 7.4, 10, and 12.	- A homogeneous assembly of HAp with an enamel prism-like structure could be obtained both in the presence of sericin and in its absence (T =50°C and pH 10); - At pH 7.4, few aggregated nanoplates were formed; - When the pH value increased to 10, a large amount of nanoparticle bundles was obtained. - At pH 12 the particles have a size of 150–250 nm in length and 50–80 nm in width. The particles obtained have rod-like morphology; - All the particles have low crystallinity, being the samples with sericin more amorphous.	–	Contributing for the understanding of biological mineralization.	Cai et al., 2010

(Continued)

TABLE 1 | Continued

Objectives	Methodology	Experimental conditions	Studied variables	Physicochemical properties	Biological properties	Applications	References
Study the effect of sericin concentration and mineralization time on HAp assembly and its osteogenic potential.	Sericin (mg/mL) = 0.5, 2, and 8; extraction was performed in boiling water (120 °C for 30 min). Co-precipitation method: [Na_2HPO_4] (12 mM); $CaCl_2$ (20 mM) + sericin.	pH = 9.5; T = room temperature.	Mineralization time: 2, 6, 12, and 24 h.	- A higher concentration of sericin promotes the formation of nanoneedle-like crystals; - Nucleation of HAp mediated by sericin is a gradual process; - After 2 h, a clump of starfish- like crystals was randomly scattered; - After 6 h, spherical crystals were formed and aggregated; - After 12 h, spindly crystals were heavily aggregated; - After 24 h nanoneedle crystals with 20–40 nm in length and 3–5 nm in width were obtained.	*In vitro* assays showed that the mineralized sericin/HAp composites obtained have higher osteogenic differentiation of BMSCs, when compared to non-mineralized composites.	Present the potential of sericin/HAp composites in the field of bone tissue engineering (as scaffolds).	Yang et al., 2014b
Present a new simple method to synthetize sericin/HAp composites and study the effect of SS concentration on HAp assembly.	Co-precipitation method: [Na_2HPO_4] (0.012 M); [$CaCl_2.2H_2O$] (0.02 M) + sericin.	T= 37°C; pH ≈ 6; Mineralization time: ≈ 2 h 30 min.	Sericin (g/L) = 0.1, 1, extraction was performed in boiling water (1 h, 150 rpm).	- The synthesized particles are single-phased nanometric HAp with low crystallinity; - The increase in sericin concentration is associated with decreased crystallinity; - Sericin/HAp composites have a higher mean particle size when compared to HAp. Further, the increase in sericin concentration leads to a size increase (Hap-−0.070 μm; sericin 0.1 g/L-−0.105 μm; sericin 1 g/L-−0.116 μm.); - The increase in sericin concentration also leads to the formation of more particles with a plate-like structure.	*In vitro* assays showed that the sericin/HAp composites obtained do not elicit a cytotoxic response on human primary cells (HNDFs) and that at high concentrations (100 mg/mL) elicit a lower cytotoxic response than a commercially available HAp.	Contributing for the understanding of biological mineralization.	Veiga et al., 2019
Use sericin to regulate the mineralization of $CaCO_3$.	Sericin (g/L) = 2, purchased from Aotesi Biochemicals Co. Ltd (Huzhou, China). Co-precipitation method: [Na_2CO_3] (0.2 mol/L); $CaCl_2$ (0.2 mol/L) + sericin.	T = 20°C.	Mineralization time = 10, 20, 30, 40, and 50 min.	- With the increase in the mineralization time, the crystal phase of $CaCO_3$ transferred from calcite dominated to vaterite dominated mixtures; - The morphology of $CaCO_3$ changed from disk-like calcite crystal to spherical vaterite crystal, the products with the reaction time of 10 min are mainly disk-like crystals and little spherical and cube-like crystals (5–15 μm). After 20 min small thorn spherical aggregates of rhombic crystal (with the diameter of 6–7 μm) and lamellar structured crystal (with the size of 3–4 μm) are formed. After 30 and 40 min flower-like crystals with the size of 4–5 μm and partly ellipsoidal crystals 5–6 μm in length and 2–3 μm in width and polyhedral structure of 3–4 μm are formed. After 50 min 4–5 μm sized spherical crystals assembled are obtained.	–	Contributing for the understanding of biological mineralization.	Zhao et al., 2013

(Continued)

TABLE 1 | Continued

Objectives	Methodology	Experimental conditions	Studied variables	Physicochemical properties	Biological properties	Applications	References
Obtain HAp microspheres using $CaCO_3$ as the template under the assistance of microwave irradiation.	Sericin = 2 g/L, purchased from Aotesi Biochemicals Co. Ltd (Huzhou, China). Precipitation method: 1°) Synthesis of $CaCO_3$ particles through a co-precipitation method: - $[CaCl_2]$ (0.2 M) + sericin; 1°) Synthesis of HAp particles: Addition of $[Na_2HPO_4]$ (0.2 M).	1°) Mixture was stirred for 50 min; T = 25°C and pH = 7; 2°) Mixture was stirred for 180 min: T = 40°C; pH = 10.	Ca and P ratios of 1:0.15, 1:0.3, 1:0.45, 1:2.5; Mineralization time = 1, 3, 5, 10, 15 min; Microwave powers = 160, 320, 480, 640, and 800 W.	- Weight percentages of HAp in the composites are 19, 25, 40, 45, and 56% corresponding to the microwave power values of 160, 320, 480, 640, and 800 W, respectively; - With the increase of Ca/P ratio in the reaction solution from 1:0.15, 1:0.30, 1:0.45, 1:2.5 to 1:7, the content of HAp in the composite increases from 0.8, 1.4, 12.3, 50.0 to 99.0%; - The composite with higher HAp content showed a slower degradation speed; - The average diameter of the spherical particles is about 6.7 μm, which is close to the size of $CaCO_3$ template.	–	Present the potential of sericin/HAp composites in the field of bone tissue engineering (for bone repair and regeneration).	Yang et al., 2016
Obtain HAp using spherical $CaCO_3$ fabricated in the presence of sericin.	Sericin (g/L) = 2, purchased from Aotesi Biochemicals Co. Ltd (Huzhou, China); 1°) Synthesis of $CaCO_3$ particles through a co-precipitation method: - $[CaCl_2]$ (0.2 M) + sericin; 2°) Addition of $[Na_2HPO_4]$ (0.2 M); 3°) Synthesis of HAp particles using a hydrothermal method: • $CaCO_3$ powder was added into $[Na_2HPO_4]$ (0.1 M).	1°) Mixture was stirred for 30 min at room temperature; 2°) Mixture was stirred at 40°C for 180 min and dried at 60°C for 48 h. 2°) Mixture was maintained in na autoclave at 140°C for different times; Precipitate was dried at 60°C for 48 h.	Time in the autoclave = 2, 4, 8, and 16 h.	- The sericin/$CaCO_3$/HAp particles obtained are homogeneous microspheres with a size distribution from 3 to 10 μm; - Uniform porous HAp microspheres with high crystallinity were obtained: - Increasing time in the autoclave has little impact on morphology of sample but results in more rough surfaces.	- *In vitro* assays showed that the sericin/$CaCO_3$/HAp composites obtained are not toxic to MG-63 cells and have similar proliferation rates. Further, with the increase in HAp content higher cell viability was observed. - *In vivo* assays showed that sericin/$CaCO_3$/HAp composites are biodegradable and biocompatible when implanted into the groin subcutaneous tissue, using colloidal sodium alginate solution as a carrier. Additionaly, sericin/$CaCO_3$ have a higher degradation rate.	Present the potential of sericin/$CaCO_3$/HAp composites in the field of bone tissue engineering (for bone repair).	Zhong et al., 2016
Prepare sericin/monite composites using a cost-effective method.	- Sericin was obtained by extraction in boiling water. - Sericin was treated with ethanol, subjected to membrane dialysis and lyophilized. Co-precipitation method: $[Na_2HPO_4]$ (Sigma-Aldrich Chemicals Pvt Ltd; CAS Number 7558794) + sericin; $[CaCl_2{\cdot}2H_2O]$ (1 M).	Misture was stirred for 3 h.	–	- The particles obtained have a heterogeneous size distribution and different morphologies.	- *In vitro* assays showed that the sericin/monite composites do not elicit hemolysis of human blood. Further, the composites present cell viability and osteogenic properties and increase cell proliferation of MG-63 cells.	Present the potential of sericin/monite composites in the field of bone tissue engineering (as bone grafts).	Vedakumari et al., 2019

(Continued)

TABLE 1 | Continued

Objectives	Methodology	Experimental conditions	Studied variables	Physicochemical properties	Biological properties	Applications	References
Investigate the distribution and degradation of CaP/sericin nanoparticles *in vivo.*	- Sericin (mg/mL) = 10, purchased from Aotesi Biochemicals Co. Ltd (Huzhou, China). Co-precipitation method: [Na_2HPO_4] (30 mM); [$CaCl_2$] (50 mM) + sericin.	pH = 9–10; T = 50°C.	–	- The sericin/CaP materials obtained adopt a spherical morphology with an average diameter of 80 nm; - The particles have a smooth surface and a low degree of crystallinity.	*In vivo* tests evaluated the distribution, degradability and tumor targeting of the sericin/CaP composites; - Distribution of sericin/CaP nanoparticles *in vivo* were mostly verified in the liver of mice; - The degradation time did not increase linearly with the amount of sericin/CaP nanoparticles injected *in vivo;* - Nanoparticles with an average size of 80 nm can achieve tumor localization at 7 days after the intravenous injection.	Present the potential of sericin/CaP composites in the field of bone tissue engineering (for tumor therapy as a vehicle to deliver therapeutic medicine).	Zhao et al., 2017
Study the stability of sericin/CaP microcapsules for stability release.	Sericin (w/v%) = 0.2, purchased from Aotesi Biochemicals Co. Ltd (Huzhou, China). - Sericin microcapsules were obtained mixing the sericin solution with [CaCl2] (30 mM) and by the posterior addition of amylum (0.5%); Soaking method: - The sericin microcapsules were added to a supersaturated calcium phosphate solution [Ammonium phosphate solution (5 mM); calcium nitrate solution (10 mM); citric acid (2.5 mM)].	–	Mineralization time: 3, 5, 6.5, and 12 h; *In vitro* amylum release at different pH values: 3, 5, 7, and 9; T = 37°C; *In vitro* amylum release at different ionic strengths: Sodium chloride solutions with 0, 0.1, 0.4, and 0.7 M.	- An increase in the mineralization time led to an increase of the crystallinity and thickness of the microcapsules; Particles in the surface of the microparticles with a CaP salt-based composition and flake-like morphology after 12 h; - When the pH value was 3 the amylum release rate was slow for the sericin microcapsules and the release amount increased gradually. After 100 h, the release rate decreased, and the release amount did not increase. pH 5 and 7 with similar behavior, characterized by a faster release rate. At pH 9, the composite became unstable; - The release rate was very fast when the concentration of NaCl in the controlled-releasing solution was 0.7 M at 37°C, being slower for other concentrations. Further, at lower pH values sericin/CaP microspheres release rate was rather slower when compared to sericin microspheres.	*In vitro* assays showed the composites promote the viability and proliferation of HapG-2 cells, when compared to sericin microcapsules.	Present the potential of sericin/HAp composites in the field of bone tissue engineering (for drug delivery and encapsulating bioactive molecule systems).	Li et al., 2016
In vivo biodegradation evaluation of the α-TCP porous body coated with SS.	Sericin was extracted from raw silk fiber by an autoclave at 105°C for 60 min and stored at 4°C for 2 weeks. Soaking method: - A α-TCP block was soaked into a sericin solution.	–	–	–	*In vivo* tests showed that after 4 weeks of implantation on bone defects made in rabbit tibiae and subcutaneous sites of rabbit backs, higher density of cortical bone was estimated for α-TCP coated with sericin than for mere α-TCP.	Present the potential of sericin/HAp composites in the field of bone tissue engineering (for bone repair as a biodegradable materials).	Takeuchi et al., 2005a

(Continued)

TABLE 1 | Continued

Objectives	Methodology	Experimental conditions	Studied variables	Physicochemical properties	Biological properties	Applications	References
Fabrication of hierarchical bio-hybrid architectures through a green and facile method.	Sericin (mg/mL) = 0.1, purchased from Wako Chemicals, Japan. Co-precipitation method: [$CaCl_2$] (100 mM) + sericin PBS.	T = 25°C; Mineralization time: 24 h.	–	- Porous, uniformly grown flower-like composites were obtained (average size 2–5 μm); - The composites have highly crystalline characteristics when compared to pure sericin; - These composites have a large surface area and show excellent adsorption activity for the toxic heavy metal ions of Lead (II), cadmium (II), and mercury (II) from wastewater.	–	Present the potential of sericin/HAp composites for multimodal possible applications such as adsorption of toxic heavy metals and hazardous dye from wastewater.	Koley et al., 2016

The objectives and suggested applications of the reviewed papers, as well as the methodology, experimental conditions, studied variables, and main results are highlighted.

Therefore, sericin/CaP biomaterials can better perform as, for instances, a particulate system for bone filling rather than as a 3D regenerative material (Jones, 2013). Accordingly, studies focus on the synthesis of sericin/CaP nanoparticles (Cai et al., 2009), and films (Jones, 2013; Zhang et al., 2014). Sericin/CaP nanoparticles have been described as suitable for bone filling applications due to their biocompatibility, biodegradation, strong ability to promote cell differentiation and proliferation and possibility to deliver therapeutic medicine. Sericin/CaP composite films have also potential in bone-related applications, being biocompatible and promoting cell viability. Further, both particles and films can be used to for fundamental studies of cell–matrix interactions (**Table 1**).

HAp is a relatively inert material that is retained *in vivo* for prolonged periods of time due to its slow reabsorption rate (Campana et al., 2014). Thus, sericin/HAp composites have potential as coating in orthopedic or dental implants. This is in agreement with the studies of Klein et al. (1991) and Dhert et al. (1993) where it was found that, when used as a coating material, HAp exhibits excellent bone contact with implanted titanium prosthesis. By comparison, tricalcium phosphate (TCP) materials give rise to more bone remodeling lacunae along the implant surface (Klein et al., 1991). Additionally, it has also been reported that the use of sericin can improve the osseointegration and osteoconduction of orthopedic titanium implants (Nayak et al., 2013), and that sericin/HAp composites have excellent biocompatibility and cell viability (Yang et al., 2014a; Zhang et al., 2014).

In contrast to HAp, TCP-based scaffolds are resorbable, making TCP composites specially suitable for the treatment of small bone defects (Bohner, 2000). In the study of Chasono et al., a TCP-based material led to complete new bone formation after 13–20 weeks of implantation (Chazono et al., 2004). Also, TCP appears to have superior osteoconductivity and bone remodeling, when compared to HAp (Ogose et al., 2005). The co-precipitation of sericin with TCP is demonstrated to decrease the degradation rate and improve the biological performance. According to the results of Takeuchi et al. (2005a), sericin/α-TCP materials show slower degradation in bone defect of rabbits, when compared to pure α-TCP. Other sericin/CaP composites, such as sericin/HAp/calcium carbonate ($CaCO_3$), have also showed controllable degradability properties (Zhao et al., 2013; Yang et al., 2016). In published works, the formation of sericin/HAp composites, was achieved through the conversion of sericin/$CaCO_3$ particles using the assistance of microwave irradiation (Yang et al., 2016) or via a hydrothermal method (Zhong et al., 2016). A higher HAp content was also associated with a slower degradation rate, being therefore appropriate for bone regeneration.

In vivo experiments showed that dicalcium phosphate anhydrous (DCPA), also known as monetite, can resorb faster than most CaP, supporting implant replacement by newly formed tissue (Tamimi et al., 2012). Thus, the sericin/monetite synthetized by Vedakumari et al. (2019) has potential as biodegradable materials.

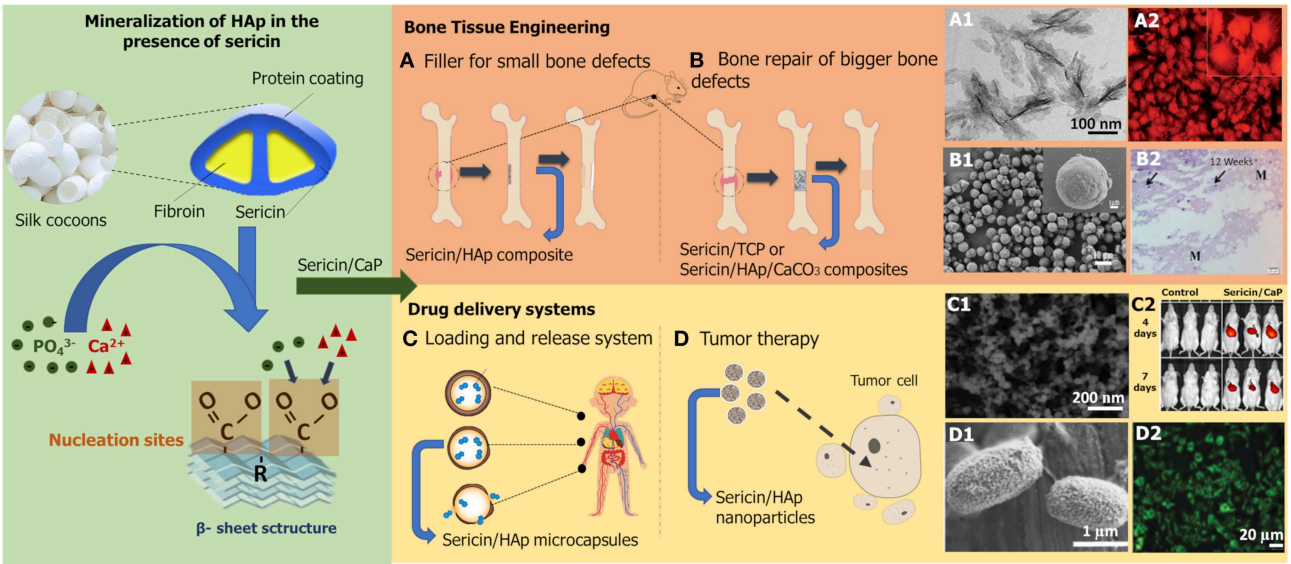

FIGURE 1 | Schematic representation of CaP mineralization process in the presence of sericin and research applications of sericin/CaP composites. Proposed biomineralization mechanism based on the works of Takeuchi et al. (2005b), Cai et al. (2009), and Veiga et al. (2019). **(A1)** Sericin/HAp composite particles, **(A2)** cell morphology and differentiation of MG-63 cells after 5 days of contact with the composite reproduced from Cai et al. (2009) with permission from Royal Society of Chemistry; **(B1)** sericin/$CaCO_3$ composite particles, **(B2)** mice tissue after 12 weeks of composite implantation reproduced from Zhong et al. (2016) with permission from Elsevier Science & Technology Journals; **(C1)** sericin/CaP composite nanoparticles, **(C2)** distribution of the composite *in vivo* reproduced from Zhao et al. (2017) with permission from John Wiley and Sons; **(D1)** sericin/HAp composite microcapsules, **(D2)** cell adhesion activity on HapG-2 cells after 7 days of contact with the composite reproduced from Li et al. (2016) with permission from Royal Society of Chemistry.

Drug Delivery Systems

Sericin/CaPs materials have also been proposed as drug delivery systems. Due to their biodegradability and hydrophilicity sericin-based materials may be used as a vehicle to deliver therapeutic medicine (Wang et al., 2015). Ideally, these systems should have controlled degradation, enable easy binding of other molecules and have pH responsiveness (Kunz et al., 2016). Sericin/CaP composites can be designed as microsystems with a good loading and release capability for bioactive molecules to be applied in TE or as an anti-tumor therapeutic system (**Table 1**). The drug release potential of sericin/CaP microcapsules was studied in a paper by Li et al. (2016), by incubating sericin microcapsules with a supersaturated calcium phosphate solution containing citric acid. The CaP shell protected the inner sericin structure, and consequently the stored bioactive molecules until a pH change occurs. Not only did the capsules showed an improved stability and a longer storage time capability, but also increased cell viability.

In the work of Zhao et al. (2017), sericin/CaP nanoparticles were developed and injected into mice by intravenous injection, to allow particle distribution through the whole body. Analysis of the *ex vivo* organs showed that 80 nm spherical sericin/CaP nanoparticles are almost completely distributed in the liver cells of mice (≈90%) and can be biodegraded within 2 weeks. However, the degradation rate is not proportional to the amount of composites injected, as 100 and 200 μg of nanoparticles were degraded after 48 h and 13 days, respectively. The targeting percentage was 30% at 7 days post-injection. As no particles were found in other organs, it was concluded that these composites can target specific solid tumors *in vivo*.

Nowadays, nanoparticle pharmaceutical carriers are probably amongst the most studied sericin/CaP composites, making these very interesting composites in this field. The large surface area/volume ratio provides the capability to load large amounts of biomolecules and the ability to go across the cellular membrane (Jia et al., 2013).

Other Applications

As the study of sericin/CaP composite materials is relatively recent, there are still several areas to be explored, taking advantage of the individual properties of sericin and CaP. For instance, calcium has an important role in maintaining homeostasis in mammalian skin, promoting wound healing (Lansdown, 2002; Kawai et al., 2011). In particular calcium-based nanoparticles have shown to have therapeutic benefits when used in cutaneous wound repair (Kawai et al., 2011). On the other hand, sericin has high antioxidant potential (Prasong, 2011; Kumar and Mandal, 2017), antibacterial activity (Ramesan et al., 2016), mitogenic effect on cells (Terada et al., 2005), potential to inhibit inflammation (Aramwit et al., 2012a), and ability to retain hydration (Padamwar et al., 2005). In the study of Aramwit et al., a sericin-based therapeutic cream formulation improved healing by promoting collagen production and rapid re-epithelialization in rat skin wounds (Aramwit et al., 2009, 2013). Both two-dimensional (films) and three-dimensional (scaffolds) sericin matrices, obtained using different blending methods, have been reported for skin tissue repair (Nayak et al., 2012; Lamboni et al., 2015; Karahaliloglu et al., 2017). Therefore, a sericin/CaP biomaterial could significantly accelerate and improves wound healing and soft tissue replacement. While sericin has been used

in many cosmetic products over the years, CaP-based materials are only recently being explored in this area. CaP particles can be used as a bone filler in esthetical treatments for diminishing wrinkles by stimulating conjunctive tissue formation (Lopes et al., 2009). Due to its affinity for biopolymers, crystallites of HAp in the dermis can promote the self-assembly of collagen fibers, smoothing fine lines and even deeper wrinkles (Bell, 2012; Gupta et al., 2019). CaP-based sunscreens have also been studied due to their biocompatible nature that does not generate allergies and other skin irritations, contrary to many organic sunscreens (de Araujo et al., 2010). These properties coupled with sericin strong suppressing activity against UVB-induced acute damage and tumor promotion (Zhaorigetu et al., 2003; Kumar et al., 2018), anti-wrinkle effect and anti-tyrosinase characteristics (Chlapanidas et al., 2013; Kumar and Mandal, 2019) justify the development of sericin/CaP biomaterials for the cosmetic industry.

Different CaP phases are used in food applications, as a supplement to increase calcium and phosphorus intake or as food additives to thicken and stabilize firm foods (Eliaz and Metoki, 2017). Phosphate additives are widely used in processed foods as preservatives, acidifying agents, acidity buffers, and emulsifying agents. Despite their applications, the use of non-naturally occurring phosphates in food can negatively affect the general health of the consumer. Synthetically produced phosphates are effectively absorbed in the gastrointestinal tract, whereas in "organic" phosphates, the absorption percentage ranges between 40 and 60%. This can lead to calcification in blood vessels and organs, being also potentially harmful for patients with chronic kidney disease (Sherman, 2007; Ritz et al., 2012). Studies show that sericin can be used to prevent functional gastrointestinal disorders, improving ion absorption and consequent bioavailability of these elements (zinc, iron, magnesium, and calcium ions) and improving constipation (Sasaki et al., 2000a,b). These characteristics can inspire the synthesis of sericin/CaP materials also for the food industry.

Recent applications of sericin/CaP composites include the removal of micro-pollutants from wastewater. In the work of Koley et al. (2016), sericin/HAp materials were used to purify water, exhibiting excellent adsorption of toxic heavy metal ions. While HAp has stability, sericin is a water-soluble material, capable of forming hydrogen bonds and with strong metal binding properties (Khosa et al., 2014).

RECENT ADVANCES

Despite their properties of interest and numerous applications, sericin/CaP composites still have disadvantages to circumvent such as poor mechanical resistance under complex stress states. CaPs and pure sericin have a low mechanical profile when compared to bone tissue, which limits the application of sericin/CaP composites as 3D biomaterials for load-bearing applications (Kunz et al., 2016; Canillas et al., 2017). Of the reviewed papers, only Zhang et al. (2014) reported the mechanical properties of sericin/HAp composites, obtained by mineralization of a flexible ethanol-treated sericin film. Other explored alternatives to enhance these characteristics include the integration of other components in the composite. Adding a structural organic component such as collagen (Griffanti et al., 2019; Jang et al., 2019), chitosan (Chen et al., 2015), and alginate (Zhang et al., 2015); or a synthetic polymer such as polymethyl methacrylate (PMMA) (Tontowi et al., 2017) are examples of some of the most recent approaches. Structural integrity of the constructs can also be obtained by cross-linking the components with glutaraldehyde (GTA) (Bhowmick et al., 2016).

CONCLUSIONS

Up to recently, silk sericin was traditionally disposed during silk processing. Nowadays, there has been a growing interest in its recovery due to both its beneficial properties and environmental impact caused by its generation. Works on sericin/CaP composites focus mainly on understanding the biomineralization process, through the study of the effect of sericin in HAp nucleation. Other studies dedicate to the synthesis of these biomaterials for the substitution and regeneration of hard tissues and to the development of new drug delivery systems. Apart from the biomedical field, there are other areas where these composites have a lot of potential, such as in the cosmetic, food an environmental sector.

In the last decade, the number of published papers on sericin/CaP composites has increased substantially. Thus, in the near future, it is clear that the integration of silk sericin in CaP biomaterials will result in advanced composite systems with evident benefits on several research fields, particularly in biomedical and pharmaceutic-related applications.

AUTHOR CONTRIBUTIONS

All authors contributed to the analysis and writing of the manuscript, and approved it for publication.

FUNDING

This work was financially supported by: Base Funding – UIDB/00511/2020 of the Laboratory for Process Engineering, Environment, Biotechnology and Energy – LEPABE – funded by national funds through the FCT/MCTES (PIDDAC). The authors also acknowledge Portuguese National Funds from FCT—Fundação para a Ciência e a Tecnologia through project UID/Multi/04044/2019. This work was supported by project Biotherapies-Bioengineered Therapies for Infectious Diseases and Tissue Regeneration and Interreg V-A POCTEP Programme through FEDER funds from the European Union [0245_IBEROS_1_E] C. A.

ACKNOWLEDGMENTS

The authors also extend their deep appreciation to Department of Chemical Engineering at Faculty of Engineering of the University of Porto, and Centre for Biotechnology and Fine Chemistry at School of Biotechnology of the Portuguese Catholic University.

REFERENCES

Ahsan, F., Ansari, T., Usmani, S., and Bagga, P. (2018). An insight on silk protein sericin: from processing to biomedical application. *Drug Res.* 68, 317–327. doi: 10.1055/s-0043-121464.

Altman, G., Diaz, F., Jakuba, C., Calabro, T., Horan, R. L., Chen, T., et al. (2003). Silk-based biomaterials. *Biomaterials* 24, 401–416. doi: 10.1016/S0142-9612(02)00353-8

Amini, A., Laurencin, C., and Nukavarapu, S. (2012). Bone tissue engineering: recent advances and challenges. *Crit. Rev. Biomed. Eng.* 40, 363–408. doi: 10.1615/CritRevBiomedEng.v40.i5.10.

Aramwit, P. (2014). "Bio-response to silk sericin," in *Silk Biomaterials for Tissue Engineering and Regenerative Medicine*, ed S. C. Kundu (England, Woodhead Publishing; Elsevier), 299–329. doi: 10.1533/9780857097064.2.299

Aramwit, P., Kanokpanont, S., De-Eknamkul, W., and Srichana, T. (2009). Monitoring of inflammatory mediators induced by silk sericin. *J. Biosci. Bioeng.* 107, 556–561. doi: 10.1016/j.jbiosc.2008.12.012.

Aramwit, P., Kanokpanont, S., Nakpheng, T., and Srichana, T. (2010). The effect of sericin from various extraction methods on cell viability and collagen production. *Int. J. Mol. Sci.* 11, 2200–2211. doi: 10.3390/ijms11052200.

Aramwit, P., Keongamaroon, O., Siritientong, T., Bang, N., and Supasyndh, O. (2012a). Sericin cream reduces pruritus in hemodialysis patients: a randomized, double-blind, placebo-controlled experimental study. *BMC Nephrol.* 13:119. doi: 10.1186/1471-2369-13-119.

Aramwit, P., Palapinyo, S., Srichana, T., Chottanapund, S., and Muangman, P. (2013). Silk sericin ameliorates wound healing and its clinical efficacy in burn wounds. *Arch. Dermatol. Res.* 305, 585–594. doi: 10.1007/s00403-013-1371-4.

Aramwit, P., Siritientong, T., and Srichana, T. (2012b). Potential applications of silk sericin, a natural protein from textile industry by-products. *Waste Manage. Res.* 30, 217–224. doi: 10.1177/0734242X11404733.

Bell, S. (2012). *Therapeutic Calcium Phosphate Particles in Use for Aesthetic of Cosmetic Medicine, and Methods of Manufacture and Use*. U.S. Patent No 2012/0207803. Washington, DC: U.S. Patent and Trademark Office.

Bhowmick, S., Scharnweber, D., and Koul, V. (2016). Co-cultivation of keratinocyte-human mesenchymal stem cell (HMSC) on sericin loaded electrospun nanofibrous composite scaffold (cationic gelatin/hyaluronan/chondroitin sulfate) stimulates epithelial differentiation in HMSCs: *in vitro* study. *Biomaterials* 88, 83–96. doi: 10.1016/j.biomaterials.2016.02.034.

Bleek, K., and Taubert, A. (2013). New developments in polymer-controlled, bioinspired calcium phosphate mineralization from aqueous solution. *Acta Biomater.* 9, 6283–6321. doi: 10.1016/j.actbio.2012.12.027.

Bohner, M. (2000). Calcium orthophosphates in medicine: from ceramics to calcium phosphate cements. *Int. J. Care Injured.* 31: D37–D47. doi: 10.1016/S0020-1383(00)80022-4.

Boyle, L. (2018). "Applications of *de novo* designed peptides," in *Peptide Applications in Biomedicine, Biotechnology and Bioengineering*, ed S. Koutsopoulos (England: Woodhead Publishing; Elsevier), 51–86. doi: 10.1016/B978-0-08-100736-5.00003-X

Brown, C., and Barker, T. (2014). Fibrin-based biomaterials: modulation of macroscopic properties through rational design at the molecular level. *Acta Biomater.* 10, 1502–1514. doi: 10.1016/j.actbio.2013.09.008.

Cai, Y., Jin, J., Mei, D., Xia, N., and Yao, J. (2009). Effect of silk sericin on assembly of hydroxyapatite nanocrystals into enamel prism-like structure. *J. Mater. Chem.* 19:5751. doi: 10.1039/b901620a.

Cai, Y., Mei, D., Jiang, T., and Yao, J. (2010). Synthesis of oriented hydroxyapatite crystals: effect of reaction conditions in the presence or absence of silk sericin. *Mater. Lett.* 64, 2676–2678. doi: 10.1016/j.matlet.2010.08.071

Cai, Y., and Yao, J. (2010). Effect of proteins on the synthesis and assembly of calcium phosphate nanomaterials. *Nanoscale* 2:1842. doi: 10.1039/c0nr00092b

Campana, V., Milano, G., Pagano, E., Barba, M., Cicione, C., Salonna, G., et al. (2014). Bone substitutes in orthopaedic surgery: from basic science to clinical practice. *J. Mater. Sci.* 25, 2445–2461. doi: 10.1007/s10856-014-5240-2

Canillas, M., Pena, P., de Aza, A. H., and Rodríguez, M. A. (2017). Calcium phosphates for biomedical applications. *Boletín de La Sociedad Española de Cerámica y Vidrio* 56, 91–112. doi: 10.1016/j.bsecv.2017.05.001

Cardoso, D., Beucken, J., Both, L., Bender, J., Jansen, J., and Leeuwenburgh, S. C. (2014). Gelation and biocompatibility of injectable alginate-calcium phosphate gels for bone regeneration. *J. Biomed. Mater. Res. Part A* 102, 808–817. doi: 10.1002/jbm.a.34754.

Chazono, M., Tanaka, T., Komaki, H., and Fujii, K. (2004). Bone formation and bioresorption after implantation of injectable β-tricalcium phosphate granules-hyaluronate complex in rabbit bone defects. *J. Biomed. Mater. Res.* 70A, 542–549. doi: 10.1002/jbm.a.30094

Chen, L., Hu, J., Ran, J., Shen, C., and Tong, H. (2015). A novel nanocomposite for bone tissue engineering based on chitosan-silk sericin/hydroxyapatite: biomimetic synthesis and its cytocompatibility. *RSC Adv.* 5, 56410–56422. doi: 10.1039/C5RA08216A

Chen, L., Hu, J., Ran, J., Shen, X., and Tong, H. (2014). Preparation and evaluation of collagen-silk fibroin/hydroxyapatite nanocomposites for bone tissue engineering. *Int. J. Biol. Macromol.* 65, 1–7. doi: 10.1016/j.ijbiomac.2014.01.003

Chen, Y., Feng, Y., Deveaux, J., Masoud, M., Chandra, F., Chen, H., et al. (2019). Biomineralization forming process and bio-inspired nanomaterials for biomedical application: a review. *Minerals* 9:68. doi: 10.3390/min9020068

Chirila, T., Suzuki, S., Bray, L., Barnett, N., and Harkin, D. (2013). Evaluation of silk sericin as a biomaterial: *in vitro* growth of human corneal limbal epithelial cells on *Bombyx mori* sericin membranes. *Progr. Biomater.* 2:14. doi: 10.1186/2194-0517-2-14

Chlapanidas, C., Faragò, S., Lucconi, G., Perteghella, S., Galuzzi, M., Mantelli, M., et al. (2013). Sericins exhibit ROS-scavenging, anti-tyrosinase, anti-elastase, and *in vitro* immunomodulatory activities. *Int. J. Biol. Macromol.* 58, 47–56. doi: 10.1016/j.ijbiomac.2013.03.054

Dash, R., Mandal, M., Ghosh, S., and Kundu, S. C. (2008). Silk sericin protein of tropical tasar silkworm inhibits UVB-induced apoptosis in human skin keratinocytes. *Mol. Cell. Biochem.* 311, 111–119. doi: 10.1007/s11010-008-9702-z

de Araujo, T. S., Souza, S. O., and Sousa, E. M. B. (2010). Effect of Zn^{2+}, Fe^{3+} and Cr^{3+} addition to hydroxyapatite for its application as an active constituent of sunscreens. *J. Phys.* 249:012012. doi: 10.1088/1742-6596/249/1/012012.

Dhert, W. J. A., Klein, C. P. A. T., Jansen, J. A., Velde, E. A., Vriesde, R. C., Rozing, P. M., et al. (1993). A histological and histomorphometrical investigation of fluorapatite, magnesiumwhitlockite, and hydroxylapatite plasma-sprayed coatings in goats. *J. Biomed. Mater. Res.* 27, 127–138. doi: 10.1002/jbm.820270116

Dias, G., Mahoney, P., Swain, M., Kelly, R., Smith, R., and Ali, M. A. (2010). Keratin-hydroxyapatite composites: biocompatibility, osseointegration, and physical properties in an ovine model. *J. Biomed. Mater. Res.* 95, 1084–1095. doi: 10.1002/jbm.a.32908.

Eliaz, N., and Metoki, N. (2017). Calcium phosphate bioceramics: a review of their history, structure, properties, coating technologies and biomedical applications. *Materials* 10:334. doi: 10.3390/ma10040334

Farè, S., Torricelli, P., Giavaresi, G., Bertoldi, S., Alessandrino, A., Villa, T., et al. (2013). *In vitro* study on silk fibroin textile structure for anterior cruciate ligament regeneration. *Mater. Sci. Eng. C* 33, 3601–3608. doi: 10.1016/j.msec.2013.04.027

Farokhi, M., Mottaghitalab, F., Samani, S., Shokrgozar, M., Kundu, S. C., Reis, R. L., et al. (2018). Silk fibroin/hydroxyapatite composites for bone tissue engineering. *Biotechnol. Adv.* 36, 68–91. doi: 10.1016/j.biotechadv.2017.10.001

Fuchs, K., Thompson, W., and Warden, S. (1997). "Bone biology," in *Bone Repair Biomaterials, Vol. 11*, eds K. M. Pawelec and J. A. Planell (England: Woodhead Publishing; Elsevier), 1–22. doi: 10.1016/S0950-351X(97)80473-9

George, A., and Veis, A. (2008). Phosphorylated proteins and control over apatite nucleation, crystal growth, and inhibition. *Chem. Rev.* 108, 4670–4693. doi: 10.1021/cr0782729

Griffanti, G., Jiang, W., and Nazhat, S. (2019). Bioinspired mineralization of a functionalized injectable dense collagen hydrogel through silk sericin incorporation. *Biomater. Sci.* 7, 1064–1077. doi: 10.1039/C8BM01060A

Gsib, O., Egles, C., and Bencherif, S. (2017). Fibrin: an underrated biopolymer for skin tissue engineering. *J. Mol. Biol. Biotechnol.* 2, 1–4.

Gulrajani, M. L., Agarwal, R., and Chand, S. (2000). Degumming of silk with a fungal protease. *Indian J. Fibre Text. Res.* 25, 138–142.

Gupta, N., Spiegel, O. L., and Spiegel, J. H. (2019). "Radiesse™ calcium hydroxylapatite injectable filler," in *Neurotoxins and Fillers in Facial Esthetic Surgery* (Hoboken, NJ: John Wiley & Sons, Inc.), 71–74. doi: 10.1002/9781119294306.ch5

Ha, T., Quan, T., Vu, D., and Si, D. (2013). "Naturally derived biomaterials: preparation and application," in *Regenerative Medicine and Tissue Engineering*, ed J. Andrades (Rijeka: InTech), 247–269. doi: 10.5772/55668

Habraken, W., Habibovic, P., Epple, M., and Bohner, M. (2016). Calcium phosphates in biomedical applications: materials for the future? *Mater. Today* 19, 69–87. doi: 10.1016/j.mattod.2015.10.008

Holland, C., Numata, K., Rnjak-Kovacina, J., and Seib, F. (2019). The biomedical use of silk: past, present, future. *Adv. Healthc. Mater.* 8:1800465. doi: 10.1002/adhm.201800465

Jang, J., Lee, E., Kwon, G., and Seo, Y. (2019). The effect of coated nano-hydroxyapatite concentration on scaffolds for osteogenesis. *J. Biomater. Appl.* 34, 827–839. doi: 10.1177/0885328219875275

Jia, F., Liu, X., Li, L., Mallapragada, S., Narasimhan, B., and Wang, Q. (2013). Multifunctional nanoparticles for targeted delivery of immune activating and cancer therapeutic agents. *J. Control. Rel.* 172, 1020–1034. doi: 10.1016/j.jconrel.2013.10.012

Jones, J. (2013). "Scaffolds for Tissue Engineering," in *Biodegradable Polymer-Based Scaffolds for Bone Tissue Engineering*, ed N. Sultana (Berlin; Heidelberg; Germany: Springer-Verlag; SpringerBriefs in Applied Sciences and Technology), 201–213. doi: 10.1007/978-3-642-34802-0_1

Karahaliloglu, Z., Kilicay, E., and Denkbas, E. (2017). Antibacterial chitosan/silk sericin 3D porous scaffolds as a wound dressing material. *Artif. Cells Nanomed. Biotechnol.* 45, 1172–1185. doi: 10.1080/21691401.2016.1203796

Kasoju, N., and Bora, U. (2012). Silk fibroin in tissue engineering. *Adv. Healthc. Mater.* 1, 393–412. doi: 10.1002/adhm.201200097

Kawai, K., Larson, B., Ishise, H., Carre, A., Nishimoto, S., Longaker, M., et al. (2011). Calcium-based nanoparticles accelerate skin wound healing. *PLoS ONE* 6:e27106. doi: 10.1371/journal.pone.0027106

Khosa, M., Shah, S., and Feng, X. (2014). Metal sericin complexation and ultrafiltration of heavy metals from aqueous solution. *Chem. Eng. J.* 244, 446–456. doi: 10.1016/j.cej.2014.01.091

Klein, C. P., Patka, P., van der Lubbe, H. B., Wolke, J. G., and de Groot, K. (1991). Plasma-sprayed coatings of tetracalciumphosphate, hydroxyl-apatite, and β-TCP on titanium alloy: an interface study. *J. Biomed. Mater. Res.* 25, 53–65. doi: 10.1002/jbm.820250105

Koley, P., Sakurai, M., Takei, T., and Aono, M. (2016). Facile fabrication of silk protein sericin-mediated hierarchical hydroxyapatite-based bio-hybrid architectures: excellent adsorption of toxic heavy metals and hazardous dye from wastewater. *RSC Adv.* 6, 86607–86616. doi: 10.1039/C6RA12818A

Kumar, J., Alam, S., Jain, A., Ansari, K., and Mandal, B. (2018). Protective activity of silk sericin against UV radiation-induced skin damage by downregulating oxidative stress. *ACS Appl. Biomater.* 1, 2120–2132. doi: 10.1021/acsabm.8b00558

Kumar, P., and Mandal, B. (2017). Antioxidant potential of mulberry and non-mulberry silk sericin and its implications in biomedicine. *Free Radic. Biol. Med.* 108, 803–818. doi: 10.1016/j.freeradbiomed.2017.05.002

Kumar, P., and Mandal, B. (2019). The inhibitory effect of silk sericin against ultraviolet-induced melanogenesis and its potential use in cosmeceutics as an anti-hyperpigmentation compound. *Photochem. Photobiol. Sci.* 18, 2497–2508. doi: 10.1039/C9PP00059C

Kunz, R., Brancalhão, R., Ribeiro, L., and Natali, M. (2016). Silkworm sericin: properties and biomedical applications. *Biomed Res. Int.* 2016:8175701. doi: 10.1155/2016/8175701

Lamboni, L., Gauthier, M., Yang, G., and Wang, Q. (2015). Silk sericin: a versatile material for tissue engineering and drug delivery. *Biotechnol. Adv.* 33, 1855–1867. doi: 10.1016/j.biotechadv.2015.10.014

Lansdown, B. G. (2002). Calcium: a potential central regulator in wound healing in the skin. *Wound Rep. Regener.* 10, 271–285. doi: 10.1046/j.1524-475X.2002.10502.x

Lee, Y., and Yuk, S. (2007). Polymeric protein delivery systems. *Prog. Polym. Sci.* 32, 669–697. doi: 10.1016/j.progpolymsci.2007.04.001

Li, W., Cai, Y., Zhong, Q., Yang, Y., Kundu, C., and Yao, J. (2016). Silk sericin microcapsules with hydroxyapatite shells: protection and modification of organic microcapsules by biomimetic mineralization. *J. Mater. Chem. B* 4, 340–347. doi: 10.1039/C5TB02328A

Liu, C. (2015). "Hydroxyapatite (HAp) for biomedical applications," in *Structure and Properties of Hydroxyapatite for Biomedical Applications*, ed M. Mucalo (England: Woodhead Publishing; Elsevier), 3–19. doi: 10.1016/B978-1-78242-033-0.00010-9

Liu, J., Lawrence, B., Liu, A., Schwab, I., Oliveira, L., and Rosenblatt, M. I. (2012). Silk fibroin as a biomaterial substrate for corneal epithelial cell sheet generation. *Invest. Opthalmol. Vis. Sci.* 53:4130. doi: 10.1167/iovs.12-9876

Lopes, B., Dias, M., Silva, V., Santos, P., Monteiro, F., and Gomes, P. (2009). *Production Method for Calcium Phosphate Nano-Particles With High Purity and Their Use*. U.S. Patent No 2009/0263497 A1. Washington, DC: U.S. Patent and Trademark Office.

Mondal, M., Trivedy, K., and Kumar, S. (2006). The silk proteins, sericin and fibroin in silkworm, bombyx mori linn., - a review. *Caspian J. Environ. Sci.* 25, 77–84.

Nayak, S., Dey, T., Naskar, D., and Kundu, S. (2013). The promotion of osseointegration of titanium surfaces by coating with silk protein sericin. *Biomaterials* 34, 2855–2864. doi: 10.1016/j.biomaterials.2013.01.019

Nayak, S., Talukdar, S., and Kundu, S. (2012). Potential of 2D crosslinked sericin membranes with improved biostability for skin tissue engineering. *Cell Tissue Res.* 347, 783–794. doi: 10.1007/s00441-011-1269-4

Ogose, A., Hotta, T., Kawashima, H., Kondo, N., Gu, W., Kamura, T., et al. (2005). Comparison of hydroxyapatite and beta tricalcium phosphate as bone substitutes after excision of bone tumors. *J. Biomed. Mater. Res.* 72B, 94–101. doi: 10.1002/jbm.b.30136

Padamwar, M., Pawar, A., Daithankar, A., and Mahadik, K. R. (2005). Silk sericin as a moisturizer: an *in vivo* study. *J. Cosmet. Dermatol.* 4, 250–257. doi: 10.1111/j.1473-2165.2005.00200.x

Padamwar, M. N., and Pawar, A. P. (2004). Silk sericin and its application : a review. *J. Sci. Ind. Res.* 63, 323–329.

Pighinelli, L., and Kucharska, M. (2013). Chitosan-hydroxyapatite composites. *Carbohydr. Polym.* 93, 256–262. doi: 10.1016/j.carbpol.2012.06.004

Prasong, S. (2011). Screening of antioxidant activity of some samia ricini (eri) silks: comparison with *Bombyx mori*. *J. Biol. Sci.* 11, 336–339. doi: 10.3923/jbs.2011.336.339

Ramesan, M. T., Athira, V. K., Jayakrishnan, P., and Gopinathan, C. (2016). Preparation, characterization, electrical and antibacterial properties of sericin/poly(vinyl alcohol)/poly(vinyl pyrrolidone) composites. *J. Appl. Polym. Sci.* 43535. doi: 10.1002/app.43535

Rezwan, K., Chen, Q. Z., Blaker, J. J., and Boccaccini, A. (2006). Biodegradable and bioactive porous polymer/inorganic composite scaffolds for bone tissue engineering. *Biomaterials* 27, 3413–3431. doi: 10.1016/j.biomaterials.2006.01.039

Ritz, E., Hahn, K., Ketteler, M., Kuhlmann, M., and Mann, J. (2012). Phosphate additives in food. *Deutsches Aerzteblatt Online* 109, 49–55. doi: 10.3238/arztebl.2012.0049

Salama, A. (2019). Cellulose/Calcium phosphate hybrids: new materials for biomedical and environmental applications. *Int. J. Biol. Macromol.* 127, 606–617. doi: 10.1016/j.ijbiomac.2019.01.130.

Sasaki, M., Yamada, H., and Kato, N. (2000a). A resistant protein, sericin improves atropine-induced constipation in rats. *Food Sci. Technol. Res.* 6, 280–283. doi: 10.3136/fstr.6.280

Sasaki, M., Yamada, H., and Kato, N. (2000b). Consumption of silk protein, sericin elevates intestinal absorption of zinc, iron, magnesium and calcium in rats. *Nutr. Res.* 20, 1505–1511. doi: 10.1016/S0271-5317(00)80031-7

Saxena, T., Karumbaiah, L., and Valmikinathan, C. (2014). "Proteins and poly(amino acids)," in *Natural and Synthetic Biomedical Polymers*, eds S. Kumbar and M. Deng (Netherlands: Elsevier Science; ScienceDirect), 43–65. doi: 10.1016/B978-0-12-396983-5.00003-X

Shavandi, A., Silva, T.i., Bekhit, A., and Bekhit, A. (2017). Keratin: dissolution, extraction and biomedical application. *Biomater. Sci.* 5, 1699–1735. doi: 10.1039/c7bm00411g

Sherman, R. (2007). Dietary phosphate restriction and protein intake in dialysis patients: a misdirected focus. *Semin. Dial.* 20, 16–18. doi: 10.1111/j.1525-139X.2007.00204.x

Soong, K., and Kenyon, K. (1984). Adverse reactions to virgin silk sutures in cataract surgery. *Ophthalmology* 91, 479–483. doi: 10.1016/S0161-6420(84)34273-7

Subburaman, K., Pernodet, N., Kwak, S. Y., DiMasi, E., Ge, S., Zaitsev, V., et al. (2006). Templated biomineralization on self-assembled protein fibers. *Proc. Natl. Acad. Sci. U.S.A.* 103, 14672–14677. doi: 10.1073/pnas.0602952103

Sukjai, O., Asanithi, P., Limsuwan, S., and Limsuwan, P. (2012). Growth of hydroxyapatite on sericin coated and non- sericin coated silk fibers using simulated body fluid. *Int. J. Sci. Res. Publ.* 3, 69–72. doi: 10.1016/j.proeng.2012.02.059

Swetha, M., Sahithi,. K., Moorthi, A., Srinivasan, N., Ramasamy, K., and Selvamurugan, N. (2010). Biocomposites containing natural polymers and hydroxyapatite for bone tissue engineering. *Int. J. Biol. Macromol.* 47, 1–4. doi: 10.1016/j.ijbiomac.2010.03.015

Takeuchi, A., Ohtsuki, C., Kamitakahara, M., Ogata, S., Tanihara, M., Miyazaki, T., et al. (2003a). Apatite deposition on silk sericin in a solution mimicking extracellular fluid: effects of fabrication process of sericin film. *Key Eng. Mater.* 254–256, 403–406. doi: 10.4028/www.scientific.net/KEM.254-256.403

Takeuchi, A., Ohtsuki, C., Kamitakahara, M., Ogata, S., Tanihara, M., Miyazaki, T., et al. (2005a). Biodegradation of porous alpha-tricalcium phosphate coated with silk sericin. *Key Eng. Mater.* 284–286, 329–32. doi: 10.4028/www.scientific.net/KEM.284-286.329

Takeuchi, A., Ohtsuki, C., Miyazaki, T., Kamitakahara, M., Ogata, S., Yamazaki, M., et al. (2005b). Heterogeneous nucleation of hydroxyapatite on protein: structural effect of silk sericin. *J. R. Soc. Interface* 2, 373–78. doi: 10.1098/rsif.2005.0052

Takeuchi, A., Ohtsuki, C., Miyazaki, T., Tanaka, H., Yamazaki, M., and Tanihara, M. (2003b). Deposition of bone-like apatite on silk fiber in a solution that mimics extracellular fluid. *J. Biomed. Mater. Res.* 65A, 283–289. doi: 10.1002/jbm.a.10456

Tamimi, F., Le Nihouannen, D., Eimar, H., Sheikh, Z., Komarova, S., and Barralet, J. (2012). The effect of autoclaving on the physical and biological properties of dicalcium phosphate dihydrate bioceramics: brushite vs. monetite. *Acta Biomater.* 8, 3161–3169. doi: 10.1016/j.actbio.2012.04.025

Tavafoghi, M., and Cerruti, M. (2016). The role of amino acids in hydroxyapatite mineralization. *J. R. Soc. Interface* 13:20160462. doi: 10.1098/rsif.2016.0462

Terada, S., Sasaki, M., Yanagihara, K., and Yamada, H. (2005). Preparation of silk protein sericin as mitogenic factor for better mammalian cell culture. *J. Biosci. Bioeng.* 100, 667–671. doi: 10.1263/jbb.100.667

Teramoto, H., and Miyazawa, M. (2003). Analysis of structural properties and formation of sericin fiber by infrared spectroscopy. *J. Insect Biotecnol. Sericol.* 72, 157–163. doi: 10.11416/jibs.72.157

Tontowi, E., Raharjo, K., Sihaloho, R., and Baroroh, D. (2017). Comparison of design method for making composite of (PMMA/HA/Sericin). *Mater. Sci. Forum* 901, 85–90. doi: 10.4028/www.scientific.net/MSF.901.85

Ude, A. U., Eshkoor, R. A., Zulkifili, R., Ariffin, A. K., Dzuraidah, A. W., Azhari, C. H., et al. (2014). Bombyx mori silk fibre and its composite: a review of contemporary developments. *Mater. Des.* 57, 298–305. doi: 10.1016/j.matdes.2013.12.052

Vallet-Regí, M., and González-Calbet, J. (2004). Calcium phosphates as substitution of bone tissues. *Progr. Solid State Chem.* 32, 1–31. doi: 10.1016/j.progsolidstchem.2004.07.001

Vedakumari, S., Jayalakshmi, W., Sanjayan, C. G., Jayavardhini, B., Arya, K., Murugesan, R., et al. (2019). Fabrication of microcomposites based on silk sericin and monetite for bone tissue engineering. *Polym. Bull.* 77, 475–481. doi: 10.1007/s00289-019-02754-7

Veiga, A., Castro, F., Reis, C., Sousa, A., Oliveira, A. L., and Rocha, F. (2019). Hydroxyapatite/sericin composites: a simple synthesis route under near-physiological conditions of temperature and pH and preliminary study of the effect of sericin on the niomineralization process. *Mater. Sci. Eng.* 108:110400. doi: 10.1016/j.msec.2019.110400

Wang, Z., Zhang, Y., Zhang, J., Huang, L., Liu, J., Li, Y., et al. (2015). Exploring natural silk protein sericin for regenerative medicine: an injectable, photoluminescent, cell-adhesive 3D hydrogel. *Sci. Rep.* 4:7064. doi: 10.1038/srep07064

Yan, P., Oliveira, J., Oliveira, A., and Reis, R. (2013). Silk fibroin/nano-CaP bilayered scaffolds for osteochondral tissue engineering. *Key Eng. Mater.* 587, 245–248. doi: 10.4028/www.scientific.net/kem.587.245

Yang, M., Mandal, N., Shuai, Y., Zhou, G., Min, S., and Zhu, L. (2014a). Mineralization and biocompatibility of *Antheraea pernyi* (*A. pernyi*) silk sericin film for potential bone tissue engineering. *Biomed. Mater. Eng.* 24, 815–824. doi: 10.3233/BME-130873

Yang, M., Shuai, Y., Zhang, S., Chen, C., Zhu, Y., Mao, C., et al. (2014b). Biomimetic nucleation of hydroxyapatite crystals mediated by antheraea pernyi silk sericin promotes osteogenic differentiation of human bone marrow derived mesenchymal stem cells. *Biomacromolecules* 15, 1185–1193. doi: 10.1021/bm401740x

Yang, M., Shuai, Y., Zhou, G., Mandal, N., Zhu, L., and Mao, C. (2014c). Tuning molecular weights of *Bombyx mori* (*B. mori*) silk sericin to modify its assembly structures and materials formation. *ACS Appl. Mater. Interfaces* 6, 13782–13789. doi: 10.1021/am503214g

Yang, N., Zhong, Q., Zhou, Y., Kundu, S., Yao, J., and Cai, Y. (2016). Controlled degradation pattern of hydroxyapatite/calcium carbonate composite microspheres. *Microsc. Res. Tech.* 79, 518–524. doi: 10.1002/jemt.22661

Zhang, H. P., Wang, X. Y., Min, S. J., Mandal, M., Yang, M. Y., and Zhu, L. J. (2014). Hydroxyapatite/sericin composite film prepared through mineralization of flexible ethanol-treated sericin film with simulated body fluids. *Ceram. Int.* 40, 985–991. doi: 10.1016/j.ceramint.2013.06.095

Zhang, Y., Liu, J., Huang, L., Wang, Z., and Wang, L. (2015). Design and performance of a sericin-alginate interpenetrating network hydrogel for cell and drug delivery. *Sci. Rep.* 5:12374. doi: 10.1038/srep12374

Zhao, R., Han, H., Ding, S., Li, Z., and Kong, X. (2013). Effect of silk sericin on morphology and structure of calcium carbonate crystal. *Front. Mater. Sci.* 7, 177–183. doi: 10.1007/s11706-013-0202-z

Zhao, R., Ren, X., Xie, C., and Kong, X. (2017). Towards understanding the distribution and tumor targeting of sericin regulated spherical calcium phosphate nanoparticles. *Microsc. Res. Tech.* 80, 321–330. doi: 10.1002/jemt.22800

Zhaorigetu, S., Yanaka,. N., Sasaki, M., Hiromitsu, W., and Kato, N. (2003). Inhibitory effects of silk protein, sericin on UVB-induced acute damage and tumor promotion by reducing oxidative stress in the skin of hairless mouse. *J. Photochem. Photobiol. B Biol.* 71, 11–17. doi: 10.1016/S1011-1344(03)00092-7

Zhong, Q., Li, W., Su, X., Li, G., Zhou, Y., Kundu, S. C., et al. (2016). Degradation pattern of porous $CaCO_3$ and hydroxyapatite microspheres *in vitro* and *in vivo* for potential application in bone tissue engineering. *Colloids Surfaces B* 143, 56–63. doi: 10.1016/j.colsurfb.2016.03.020

Conflict of Interest: The authors declare that the research was conducted in the absence of any commercial or financial relationships that could be construed as a potential conflict of interest.

frontiers in Materials

ORIGINAL RESEARCH
published: 28 February 2020
doi: 10.3389/fmats.2020.00046

Lessons From Spider and Silkworm Silk Guts

José Pérez-Rigueiro[1,2,3], Víctor Ruiz[1,2], José Luis Cenis[4], Manuel Elices[2] and Gustavo Víctor Guinea[1,2,3]*

[1] Centro de Tecnología Biomédica, Universidad Politécnica de Madrid, Madrid, Spain, [2] Departamento de Ciencia de Materiales, ETSI Caminos, Canales y Puertos, Universidad Politécnica de Madrid, Madrid, Spain, [3] Biomedical Research Networking Center in Bioengineering, Biomaterials and Nanomedicine (CIBER-BBN), Madrid, Spain, [4] Departamento de Biotecnología, Instituto Murciano de Investigación y Desarrollo Agrario y Alimentario (IMIDA), Murcia, Spain

The results presented in previous works on the formation of fibers from silkworm and spider silk guts are reviewed and new information is included on the glands that allow the formation of these fibers. Silk gut fibers are obtained directly from the silk glands by immersion in a mild acid solution and subsequent stretching. The fibers so produced were characterized in terms of their microstructure and mechanical properties. The comparison of silk gut fibers with their natural counterparts allows gaining new insights in the processing, microstructure and properties of both silkworm and spider silks.

Keywords: biomimetics, mechanical characterization, silkworm silk, spider silk, spinning

OPEN ACCESS

Edited by:
Nicola Maria Pugno, University of Trento, Italy

Reviewed by:
Giuseppe Puglisi, Politecnico di Bari, Italy
Domenico De Tommasi, Politecnico di Bari, Italy

****Correspondence:***
José Pérez-Rigueiro
jose.perez@ctb.upm.es

Specialty section:
This article was submitted to Mechanics of Materials, a section of the journal Frontiers in Materials

Received: *09 September 2019*
Accepted: *12 February 2020*
Published: *28 February 2020*

Citation:
Pérez-Rigueiro J, Ruiz V, Cenis JL, Elices M and Guinea GV (2020) Lessons From Spider and Silkworm Silk Guts. Front. Mater. 7:46. doi: 10.3389/fmats.2020.00046

INTRODUCTION

Silkworm and spider silks represent a fascinating biological system at the frontier between Materials Science, Biology and Biotechnology (Heim et al., 2009). In spite of originating from two independent evolutionary events (Craig and Riekel, 2002), the concurrence of many of their defining features points to the robustness and universality of their design principles. In this regard, both systems are based on the conversion of a protein solution into high performance solid fibers under extremely mild processing conditions (Vollrath and Knight, 2001; Jin and Kaplan, 2003).

Consequently, the study of silks and the development of artificial processes and new materials inspired in these fibers has represented one of the major driving forces in the field of biomimetics (Schmitt, 1969). The implementation of the biomimetic approach, however, requires unveiling the basic principles of the natural system that, in the case of silks, is hampered by the subtle interplay of all the contributing elements to the spinning process. Thus, discriminating between the basic principles of the process and those accidental to couple the system with the living spinning organism, either worm or spider, proved a most difficult task. As a result of this difficulty and although significant advances were made on the understanding of the system (Iizuka, 1985; Askarieh et al., 2010; Hagn et al., 2010), the development of biomimetic spinning systems and fibers is still an intensive area of research (Madurga et al., 2017).

In this context, the possibility of producing fibers directly from the silk glands offers a clear opportunity to explore the elements of the process following a route that differs from the natural spinning system. The fibers produced from the silk glands, known as silk gut fibers or, briefly, silk guts ("hijuelas" in Spanish and "crins de Florence" in French) were a traditional craftsmanship product in southern Europe, especially in the Región de Murcia (Spain), during the XVIII and XIX centuries (Humphries, 1949; Marden, 1951; Martin, 1991). Silkworm silk gut fibers were produced by immersing the worms in a vinegar solution and by subsequently stretching the glands, leading

to what were the best fibers of its time. The production of silk guts was discontinued in the 1950s due to the impossibility to compete in the market with the new polymeric fibers, such as nylon.

In spite of its long history, no detailed characterization of the microstructure and mechanical behavior of silkworm silk gut was available until 2015 (Cenis et al., 2015), when it was found that the comparison of the silk guts with the natural materials allowed a deep insight on the spinning process and on the microstructure and mechanical properties of both materials. In addition, it was also found that a similar process leads to the formation of spider silk gut fibers from spider silk glands (Jiang et al., 2014; Ruiz et al., 2019). This work reviews the main findings obtained from the comparison of silkworm and spider silk gut fibers with their natural counterparts, and highlights those aspects deemed more relevant for the study of these material from a biomimetic perspective.

EXPERIMENTAL WORK

The details on the experimental work on the formation of silkworm and spider silk guts and their subsequent microstructural and mechanical characterization are provided elsewhere (Jiang et al., 2014; Cenis et al., 2015; Ruiz et al., 2019). Briefly, glands were retrieved from the spinning organisms after being anesthetized. Silk gland extraction is straightforward with worms, but requires the careful assessment of the gland to be used when working with spiders. This assessment was performed through mass spectroscopy by identifying peptides characteristics of each spidroin as found from Genetic analysis (Babb et al., 2017). After being retrieved, the glands were immersed in Ringer's solution for a period no longer than 30 min. Glands were then submerged into a mild acetic acid solution, typically with a concentration in the range 1–5%, and removed after a period of time between 1 and 6 min. The excess of water was gently removed and the glands were stretched either with a tensile testing machine or by hand.

Stretching the gland in a tensile testing machine allows measuring the forces that appear during the formation of the silk gut. These forces were converted to engineering stress vs. engineering strain curves. The *engineering strain* sustained by the gland during the formation process was defined as the increment in length of the gland divided by the initial length of the gland (typically 60 mm for silkworm silk and 5 mm for major ampullate gland silk). The *engineering stress* to which the gland is subjected during the formation process of the silk gut fiber were calculated as the ratio between the measured force and the maximum cross sectional area of the silk gut as measured in an optical or scanning electron microscope. Usage of the maximum cross sectional area in this case corresponds to calculating the minimum stress required for completing the transition of protein solution into solid fiber.

Silk guts were mounted on aluminum foil frames with gauge lengths between 10 and 60 mm, and micrographs were obtained either in an optical microscope or in a scanning electron microscope in order to determine the apparent diameter of the fibers. The cross sectional area was calculated from the apparent diameter of the silk gut by assuming a circular cross section. Engineering stresses of the silk gut fibers were calculated by taking the minimum diameter of the silk gut, and true stresses were calculated from engineering stresses under the assumption of volume constancy (Guinea et al., 2006). In this case, the usage of the minimum cross sectional area of the silk gut fiber is intended to provide the value for the maximum stress that the fiber may sustain. The microstructural characterization of the silk guts was performed through Fourier transform infrared spectroscopy (FTIR) and X-ray diffraction (XRD).

RESULTS AND DISCUSSION

Silk Guts From Silkworm and Spider Silk Glands

The historical process for making fibers from silk guts was developed with silkworms and thrust by the practical applications of the material. Silkworm silk guts were formed traditionally in a two-step process that required immersion in a vinegar solution and subsequent manual stretching (Humphries, 1949; Marden, 1951). An example of a fiber obtained following this process, although the vinegar solution is substituted by an acetic acid solution, is shown in **Figure 1A**. Extending this process to obtain fibers from silk guts from spider silk glands had to face with two main difficulties. Firstly, orb-web spiders present up to seven different silk glands, from which up to five different types of fibers are spun (Heim et al., 2009). Since each fiber is endowed with a characteristic set of tensile properties (Blackledge and Hayashi, 2006), it was likely that spider silk guts produced from different glands might exhibit different properties. Consequently, it was necessary to get a proper identification of the glands being employed. Secondly, the size of spider silk glands is much smaller than that of silkworms, even if working with specimens from the *Nephila* genus, that includes some of the largest orb-web spiders. This smaller size renders the manipulation of the gland and, especially, the stretching step much more difficult than for silkworm silk gut. Fortunately, these drawbacks were overcome

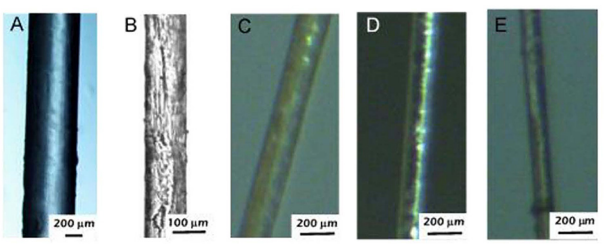

FIGURE 1 | Optical micrographs of different spider and silkworm silk gut fibers produced by immersion in an acetic acid solution and subsequent stretching by hand. The details of the formation process for each silk gut are shown in **Table 1**. **(A)** Silkworm silk gut. **(B)** Major ampullate gland silk gut. **(C)** Tubuliform gland silk gut. **(D)** Minor ampullate gland silk gut. **(E)** Flagelliform silk gut. Major ampullate glands were retrieved from *Nephila inaurata* specimens. Tubuliform, minor ampullate and flagelliform spider gland silks were retrieved from *Nephila clavipes* specimens.

in most cases and **Figures 1B–E** show optical micrographs of spider silk guts obtained from the major ampullate gland, the tubuliform gland, the minor ampullate gland and the flagelliform gland, respectively. All glands were retrieved from *Nephila clavipes* specimens, except for the major ampullate gland that was retrieved from a *Nephila inaurata* spider. Attempts to produce silk gut from the acciniform gland failed due its small size and the impossibility to stretch the gland after being immersed in the acetic acid solution. The detailed conditions for the formation of each silk gut shown in **Figure 1** are indicated in **Table 1**.

The possibility of producing fibers from silk guts of all the spider silk glands amenable to being manipulated suggest the existence of a common spinning process that is likely to have appeared in the ancestral silk gland (Blackledge et al., 2009). In this regard, it is more surprising that a similar process leads to the formation of silkworm silk glands. Silkworm and spider silks are thought to be the result of two independent evolutionary events. Consequently, the parallelism in the processing of both materials may be understood as an indication of the robustness of a process that allows the conversion of a protein solution into high performance solid fibers. As indicated above, the difficulty in obtaining silk guts increases when the size of the gland decreases. Consequently, the most complete microstructural and mechanical characterization of silk guts is limited up to date to the larger glands: silkworm silk, and spider major ampullate and tubuliform glands. For this reason, these are the materials on which the discussion below will be based.

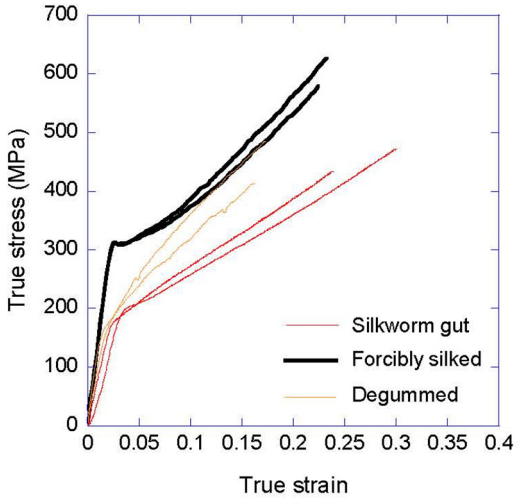

FIGURE 2 | Comparison of the true stress-true strain curves of natural silkworm silk and silkworm silk gut. The tensile properties of silkworm silk fibers obtained by forced silking and after being subjected to a degumming treatment are shown. Silkworm silk gut was produced by immersion in a 2% acetic acid solution for 2 min and subsequent stretching.

Silkworm Silk and Silkworm Silk Gut Fibers

The tensile properties of natural silkworm and silk gut fibers are compared in **Figure 2**. Since the properties of natural silkworm silk depend on the treatment that the material undergoes before being tested, representative true stress-true strain curves of fibers either obtained by forced silking or subjected to a subsequent degumming treatment are presented. Both conditions were shown to summarize the large variability in the tensile properties that is characteristic of the natural material (Belen Perea et al., 2016). Although the qualitative mechanical behavior of all fibers is comparable, there are significant quantitative differences between silk gut fibers and natural fibers that preclude the identification of the former with their natural counterparts. In other words, the silk gut formation process applied to silkworm silk glands does not lead to the formation of proper silkworm silk, so that the differences between silkworm natural silk, and silk gut are deeper than the mere variation in the cross sectional area of the fibers obtained by both processing methods. Differences are observed very clearly when comparing the elastic modulus of the natural silk, that ranges between E = 14 GPa (forcibly silked) and E = 12 GPa (degummed) for the natural material, and the value of E = 7 GPa, measured for silkworm silk gut. Differences are also apparent when the regions at high strains beyond the yield point are compared. In this region the average slope of the silkworm silk gut stress-strain curves is significantly smaller than those of the natural silk fibers, either forcibly silked or after being subjected to degumming.

The XRD analysis of silkworm silk gut has revealed some microstructural features that justify the differences in the mechanical behavior observed between natural fibers and silk gut fibers. Representative XRD patterns of natural silkworm silk and silkworm silk gut fibers are presented in **Figures 3A,B**, respectively. It was found that both materials share a common unit cell, but significant variations are observed in terms of crystallinity and in the size of the β-nanocrystals. Thus, crystallinity in silkworm silk gut reaches a value of ∼30%, that is half of the value found in silkworm silk. This reduction in crystallinity accounts for the reduction in the elastic modulus of silkworm silk gut fibers compared with the natural fibers. In addition, a two-state polymer model (Puglisi et al., 2017) may account for the reduction in the average slope of the silkworm silk gut stress-strain curve in the high strain region when compared with the natural material. The two-state polymer model assumes that the micromechanism responsible for the deformation of the polymeric fiber is the transition from rigid folded to entropic folded domains. The higher crystallinity of the natural silk

TABLE 1 | Processing conditions of the silk guts shown in **Figure 1**.

Silk gland	Acetic acid concentration (%)	Immersion time (min)
Silkworm (*Bombyx mori*)	2	2
Major ampullate gland (*Nephila inaurata*)	1	3
Tubuliform gland (*Nephila clavipes*)	1	1
Minor ampullate gland (*Nephila clavipes*)	1	1
Flagelliform gland (*Nephila clavipes*)	5	3(+2)

Flagelliform silk gut was formed after immersion in the acetic acid solution for 3 min, and stretched 2 min later after being removed from the acetic acid solution.

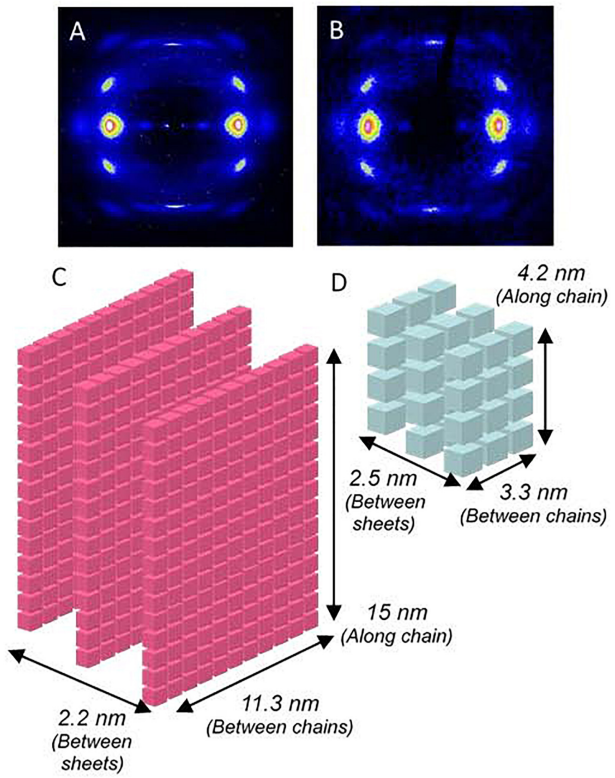

FIGURE 3 | Microstructural analysis of silkworm silk and silkworm silk gut fibers. **(A)** X-ray diffraction pattern of a natural silkworm silk fiber. **(B)** X-ray diffraction pattern of a silkworm silk gut. **(C)** Schematic representation of the average β-nanocrystal in natural silkworm silk. **(D)** Schematic representation of the average β-nanocrystal in silkworm silk gut fibers. In panels **(C,D)** each cube represents a unit cell of the nanocrystalline phase.

fibers implies the existence of a larger fraction of rigid folded domains, whose unfolding requires higher values of stress, as observed experimentally.

The differences between the natural material and silk guts are even more significant when the size of the nanocrystals is considered. A schematic representation of the β-nanocrystals as found in silkworm silk and silk gut is shown in **Figures 3C,D**, in which each cube represents a unit cell. From these schemes it is apparent that the volume of a β-nanocrystal in natural silkworm silk is much larger than that of a β-nanocrystal in silk gut. This result suggests that the appearance of the highly crystalline structure of silkworm silk is dependent on the details of the natural spinning process in the worm. Some of the processing conditions must not be reproduced in the process that leads to the formation of the silk gut fibers and, consequently, the microstructure of the latter does not reach such a high value for the crystalline fraction. The deviation of the natural silkworm silk fiber cross section from a circular shape might be a clue, since it indicates that the fiber must be subjected to significant shear stresses during its processing in the silk gland.

Another interesting aspect raised by the comparison of the β-nanocrystals in natural silk and silk guts is the formation of the nanocrystals from the piling up of exactly three β-pleated sheets in both cases. The persistence of this microstructural feature in contrast with the large overall differences between the nanocrystalline phases in both materials might reflect a deep design principle of silkworm silk. A similar piling up of exactly three β-pleated sheets that make up the nanocrystalline phase was also found in an extensive analysis of the microstructure of MA spider silk retrieved from different species (Madurga et al., 2015).

Major Ampullate and Tubuliform Silks and Silk Guts

In spite of the parallelisms in the formation process of silkworm and spider silk guts, the comparison of the latter with natural spider silk fibers points to the existence of profound divergences in some design principles between silk spinning in worms and spiders. As indicated above, although spider silk gut fibers were obtained from four different spider silk glands: major ampullate gland, tubuliform gland, minor ampullate gland, and flagelliform gland, only silk guts produced from the two largest glands (MA and Tub) were amenable for a detailed mechanical and microstructural characterization. The comparison of MA and Tub silk guts with their natural counterparts is presented in **Figures 4A,B**.

Figure 4A compares the tensile properties of natural MA silk and MA silk gut fibers obtained from *N. inaurata* spiders. The large variability shown by MA silk, even when a single spider species is considered has represented a major challenge for the characterization of the material (Madsen et al., 1999; Perez-Riguero et al., 2001). In this regard, the application of techniques based on the supercontraction of MA silk (Work, 1977; Perez-Rigueiro et al., 2003) allows a relatively straightforward procedure for the comparison of MA fibers spun under different experimental conditions or spun by different species (Madurga et al., 2016). Consequently, the possible supercontraction ability of MA silk gut fibers was assessed and it was found that, as with the natural material, MA silk gut fibers exhibit a ground state to which the fiber can revert by immersion in water. The existence of this ground state is considered as the defining property of a supercontracting fiber (Perez-Rigueiro et al., 2019).

From **Figure 4A** it is apparent that MA silk gut fibers subjected to maximum supercontraction concur with the natural MA fibers, also subjected to maximum supercontraction, up to the breaking point of the former. The similarity between both fibers was also supported by the concurrence of their FTIR spectra and XRD patterns (Jiang et al., 2014). Consequently, MA silk gut fibers can be identified with natural MA spider silk, so that the only essential difference between both fibers is the large divergence between their cross sectional areas. This difference in the cross sectional area might also account for the reduced tensile strength of MA silk gut fibers, since it is a well-established principle of Materials Science that tensile strength is inversely proportional to the cross sectional area of a fiber. Although this principle is mainly supported by data obtained from artificial materials, it is reasonable to assume that a larger area also allows the existence of larger defects in natural materials, leading to a reduced strength. In contrast with the extreme variability

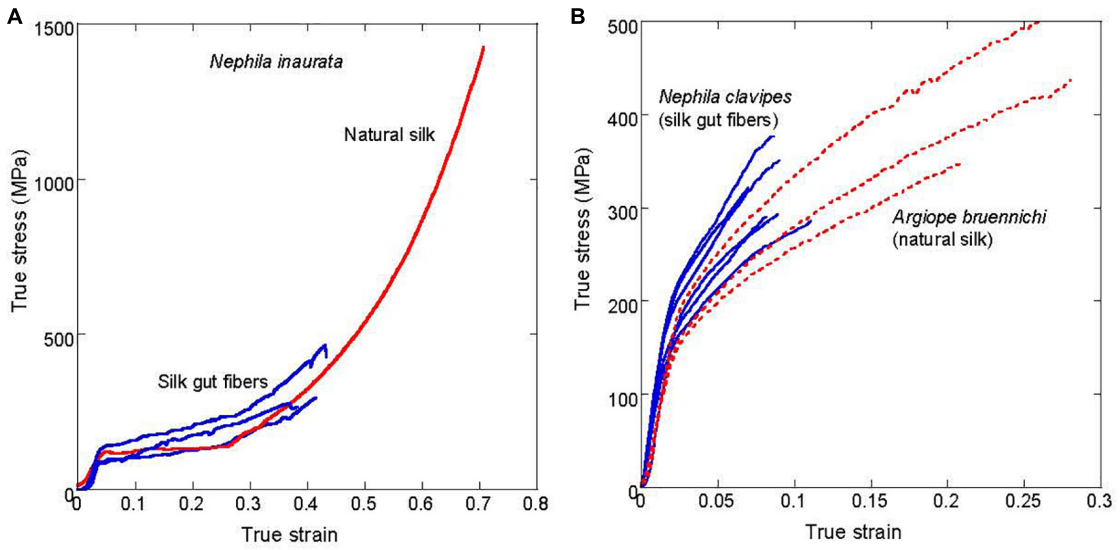

FIGURE 4 | Comparison of the true stress-true strain curves of natural spider silk and spider silk gut fibers. **(A)** Comparison of the major ampullate gland silk natural fibers and major ampullate silk gut fibers of *Nephila inaurata*. **(B)** Comparison of the tubuliform natural fibers spun by *Argiope bruennichi* spiders and tubuliform silk gut fibers produced from *Nephila clavipes* spiders.

characteristic of MA fibers, **Figure 4B** illustrates the extreme conservation of tubuliform silk. In this case, the tensile behavior of natural Tub silk and Tub silk gut fibers is shown to concur even when fibers from two species that diverged over 120 Mya (Elices et al., 2009) (*Argiope bruennichi* and *N. clavipes*) are compared.

The previous results highlight two profound principles in the design of the spider silk spinning system. First of all, it is apparent that the instructions required for forming the solid fiber from a protein solution are contained in the spidroin solution in the gland and are independent of the detailed spinning mechanism, in particular from the spider gland silk. It is found that the formation of spider silk gut fibers, either MA or Tub, only requires a change in the pH of the solution and subsequent stretching, and a material with the same microstructure and mechanical properties of the natural spun fibers is obtained. In addition, it also shows the intriguing contrast between the extreme variability observed in MA silk and the extreme conservation of Tub silk. In spite of sharing a common organization based on large proteins constituted by a small number of repetitive amino acid motifs, the large differences observed between both silk fibers opens the question of which evolutionary pressures may have led to these two divergent behaviors.

Process of Silk Fibers Formation From a Protein Solution

The capacity to produce silk gut fibers with properties comparable to their natural counterparts also allows access to some features of the transition between protein solution and solid fiber that are usually hidden in the silk glands of the spinning organisms. Thus, it is feasible to measure the forces (and stresses) involved in the formation of the silk gut fibers and, in addition, it is also possible to follow the early microstructural changes associated with the formation of the solid fiber.

Figure 5A illustrates the forces involved in the formation process of silkworm and MA silk gut fibers expressed as engineering stress-engineering strain curves. It is again striking the concurrence between both curves in spite of the differences in evolutionary origin between the spinning organisms. There are, however, some remarkable differences in the details of both curves, that point to differences in some of the deformation mechanisms of both silk guts. Thus, the recorded mechanical properties obtained during the formation MA silk do correspond to an elastomer (Gosline et al., 1984), and is consistent with the importance of the elastomeric behavior of the protein chains in the mechanical properties of MA silk (Termonia, 1994, 2000). In contrast, silkworm silk gut exhibits an initial stiffer region followed by a more compliant behavior at larger values of strain. A comparable tensile behavior was observed in silkworm (*Bombyx mori*) silk fibers tested in water (Perez-Rigueiro et al., 2000) and is not compatible with an elastomeric behavior of the protein chains in the initial steps of silkworm silk gut formation.

It was found that both glands were solidified at an engineering strain of ∼100% (i.e., the gland is stretched up to a length that doubles its initial length) and this value is shown on each curve by a solid circle. The combination of the stress–strain curve during the silk gut formation process and the observation that the fiber is formed at this value of strain allows determining the minimum force, or equivalently, the minimum stress required to complete the transition between protein solution and solid fiber. From **Figure 5A** a value of ∼1 MPa is obtained, which is significantly lower than previous estimations on the stresses involved in the spinning of natural silks obtained from the rheological study of the protein solution (Holland et al., 2006; Kojic et al., 2006) or

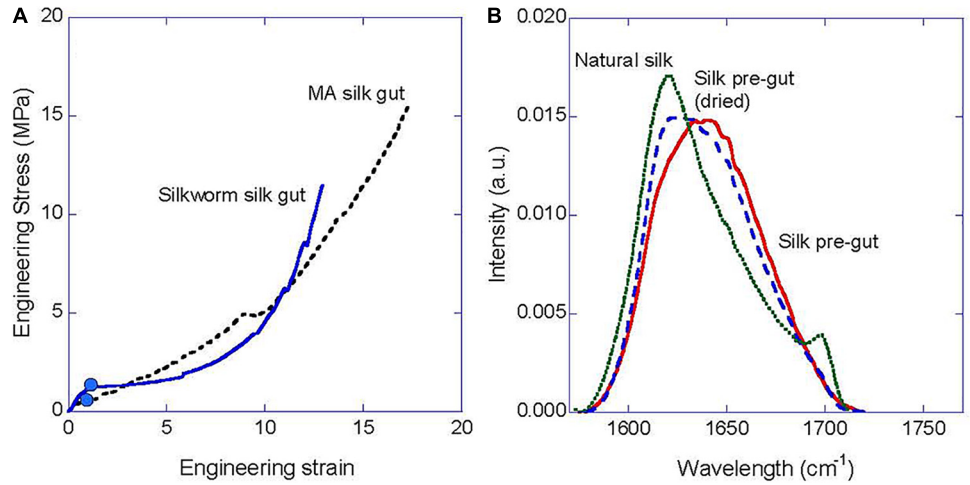

FIGURE 5 | Characterization of the silk gut formation process. **(A)** Illustrative engineering stress-engineering strain curve measured during the silk gut formation process from the gland of a silkworm (*B. mori*) and of a MA gland (*N. inaurata*). **(B)** Comparison of the FTIR spectra of natural *B. mori* silk fiber, a pre-gut fiber formed by stretching the gland up to a strain of 100%, and a pre-gut fiber formed by stretching the gland up to a strain of 100% and being allowed to dry in air for 1 h.

by measuring the forces exerted on the fiber during forced silking (Elices et al., 2006). Both experimental procedures had estimated a value of the spinning stresses between 20 and 40 MPa. The results obtained from the analysis of the forces involved in the formation of silk gut suggest that these larger values might be related with other processes in the spinning of the natural fiber [i.e., friction of the fiber with the valve in the spinning of MA silk (Ortlepp and Gosline, 2004)] different from the transition between protein solution to solid material.

Figure 5B shows the amide I peak of silkworm (*B. mori*) silk obtained by FTIR and compares it with the amide I peaks of a silkworm silk pre-gut (see below for the definition of pre-gut) and a silkworm silk pre-gut subjected to drying for 1 h. Silkworm silk pre-gut was formed by stretching the gland up to an engineering strain of e = 100% (initial length of the gland: 60 mm, final length: 120 mm), stopping the process at that value of strain and recording the FTIR spectrum immediately. Alternatively, other pre-guts were produced under the same conditions and allowed to dry for 1 h before being characterized by FTIR. A clear shift of the maximum of the peak from ∼1640 cm^{-1} in the silk pre-gut, to 1620 cm^{-1} in the dried silk pre-gut and in the natural silkworm is observed. This shift is the result of the increasing contribution of β-pleated sheets to the secondary structure of the proteins (Pellerin et al., 2005). It is remarkable, however, that a significant fraction of β-pleated sheet is observed in the silk pre-gut fiber, which supports the hypothesis that the appearance of this secondary structure and, possibly, the piling up of the β-sheets into β-nanocrystals are very early events in the formation of the solid fiber. Drying of the pre-gut leads to an increase in the content of the β-pleated and to the formation of 3_1 helices (Chen et al., 2001; Teramoto and Miyazawa, 2005), and illustrates the order in which the microstructure of silkworm silk is formed during the formation process of the fiber. A similar study was not possible on MA silk guts due to experimental difficulties related with the much smaller size of the MA gland (∼5 mm).

CONCLUSION

Silk gut fibers can be produced from the silk glands of silkworm (*B. mori*) and from the major ampullate gland silk, tubuliform gland silk, minor ampullate gland silk, and flagelliform gland silk of *Nephila* spiders by immersion of the glands in a mild acidified solution and subsequent stretching.

The stress-strain curves of silkworm silk gut fibers are qualitatively similar to those of the natural silkworm silk fibers, but differ in the value of the mechanical parameters, such as the elastic modulus. These differences can be traced back to variations in the crystalline phase between both materials. Crystallinity of silkworm silk gut fibers is half of that measured from the natural fibers. Besides, the size of the β-nanocrystals in silkworm silk gut fibers is much smaller than that of native silk. However, in spite of the differences between the crystalline phases of both materials, there is a persistence in the number of β-pleated sheets that form the nanocrystals, suggesting that this might be a design principle in the formation of the fiber.

In contrast to silkworm silk, MA and Tub spider silk gut fibers are shown to be the same material as their natural counterparts. MA spider silk gut fibers are endowed with the ability to supercontract and their properties concur with those of the natural material if both, silk gut fibers and native silk, are retrieved from the same species. The concurrence of the tensile behavior of Tub silk gut fibers and Tub native fibers of different species points to the persistence of these silk fibers throughout evolution. The identification of spider silk gut fibers and native fibers in this case indicates that the processing instructions for forming the fibers from the protein solution are contained in the spidroins and are independent of the natural gland system.

The possibility of producing silk gut fibers also offers a unique opportunity to monitor the early events leading to the formation of the fiber. In this regard, it is found that the major microstructural change leading to the formation of the solid

material is the appearance of β-pleated secondary structure at a strain of ∼100%. In addition, it is also found that the mechanical stresses required to complete the transition from the protein solution to the fibers are in the range of ∼1 MPa, which is a much smaller value than previous estimations suggested. Differences between these previous values and the one found from the analysis of the silk might arise from other forces that appear in the natural spinning process, but which are not directly involved in the liquid-solid transition. All these findings highlight the insights that can be gained from the comparison of silk guts and natural silk fibers and should encourage the making of new studies that might follow this rationale in the future.

DATA AVAILABILITY STATEMENT

The datasets generated for this study are available on request to the corresponding author.

AUTHOR CONTRIBUTIONS

VR prepared the spider silk guts. JP-R and JC prepared the silkworm silk guts and coordinated the research. All authors have discussed the results and revised the manuscript.

FUNDING

This work was funded by the Ministry of Economy and Competitiveness in Spain through projects MAT2016-75544-C2 and MAT2016-79832-R, and Comunidad de Madrid (Spain) through grants NEUROCENTRO-B2017/BMD-3760 and IND2018/BMD-9804.

ACKNOWLEDGMENTS

Spiders were reared in Reptil Madrid S.L. by Oscar Campos.

REFERENCES

Askarieh, G., Hedhammar, M., Nordling, K., Saenz, A., Casals, C., Rising, A., et al. (2010). Self-assembly of spider silk proteins is controlled by a pH-sensitive relay. *Nature* 465, 236–239. doi: 10.1038/nature08962

Babb, P. L., Lahens, N. F., Correa-Garhwal, S. M., Nicholson, D. N., Kim, E. J., Hogenesch, J. B., et al. (2017). The Nephila clavipes genome highlights the diversity of spider silk genes and their complex expression. *Nat. Genet.* 49, 895–903. doi: 10.1038/ng.3852

Blackledge, T. A., and Hayashi, C. Y. (2006). Silken toolkits: biomechanics of silk fibers spun by the orb web spider *Argiope argentata* (Fabricius 1775). *J. Exp. Biol.* 209, 2452–2461. doi: 10.1242/jeb.02275

Blackledge, T. A., Scharff, N., Coddington, J. A., Szuts, T., Wenzel, J. W., Hayashi, C. Y., et al. (2009). Reconstructing web evolution and spider diversification in the molecular era. *Proc. Natl. Acad. Sci. U.S.A.* 106, 5229–5234. doi: 10.1073/pnas.0901377106

Cenis, J. L., Madurga, R., Aznar-Cervantes, S. D., Abel Lozano-Perez, A., Mari-Buye, N., Meseguer-Olmo, L., et al. (2015). Mechanical behaviour and formation process of silkworm silk gut. *Soft Matter* 11, 8981–8991. doi: 10.1039/c5sm01877c

Chen, X., Knight, D. P., Shao, Z. Z., and Vollrath, F. (2001). Regenerated Bombyx silk solutions studied with rheometry and FTIR. *Polymer* 42, 9969–9974.

Craig, C. L., and Riekel, C. (2002). Comparative architecture of silks, fibrous proteins and their encoding genes in insects and spiders. *Comp. Biochem. Physiol. B Biochem. Mol. Biol.* 133, 493–507. doi: 10.1016/s1096-4959(02)00095-7

Elices, M., Guinea, G. V., Plaza, G. R., Real, J. I., and Perez-Rigueiro, J. (2006). Example of microprocessing in a natural polymeric fiber: role of reeling stress in spider silk. *J. Mater. Res.* 21, 1931–1938. doi: 10.1557/jmr.2006.0240

Elices, M., Plaza, G. R., Arnedo, M. A., Pérez-Rigueiro, J., Torres, F. G., and Guinea, G. V. (2009). Mechanical Behaviour of Silk during the evolution of Orb-web spinning spiders. *Biomacromolecules* 10, 1904–1910. doi: 10.1021/bm900312c

Gosline, J. M., Denny, M. W., and Demont, M. E. (1984). Spider silk as rubber. *Nature* 309, 551–552. doi: 10.1038/309551a0

Guinea, G. V., Perez-Rigueiro, J., Plaza, G. R., and Elices, M. (2006). Volume constancy during stretching of spider silk. *Biomacromolecules* 7, 2173–2177. doi: 10.1021/bm060138v

Hagn, F., Eisoldt, L., Hardy, J. G., Vendrely, C., Coles, M., Scheibel, T., et al. (2010). A conserved spider silk domain acts as a molecular switch that controls fibre assembly. *Nature* 465, 239–242. doi: 10.1038/nature08936

Heim, M., Keerl, D., and Scheibel, T. (2009). Spider silk: from soluble protein to extraordinary fiber. *Angew. Chem. Int. Ed Engl.* 48, 3584–3596. doi: 10.1002/anie.200803341

Holland, C., Terry, A. E., Porter, D., and Vollrath, F. (2006). Comparing the rheology of native spider and silkworm spinning dope. *Nat. Mater.* 5, 870–874. doi: 10.1038/nmat1762

Humphries, A. M. C. (1949). The story of silk and silkworm gut. *Post Grad. Med. J* 25, 483–488. doi: 10.1136/pgmj.25.288.483

Iizuka, E. (1985). Silk thread - mechanism of spinning and its mechanical-properties. *Appl. Polym. Symp.* 41, 173–185.

Jiang, P., Mari-Buye, N., Madurga, R., Arroyo-Hernandez, M., Solanas, C., Ganan-Calvo, A., et al. (2014). Spider silk gut: development and characterization of a novel strong spider silk fiber. *Sci. Rep.* 4, 7326. doi: 10.1038/srep07326

Jin, H. J., and Kaplan, D. L. (2003). Mechanism of silk processing in insects and spiders. *Nature* 424, 1057–1061. doi: 10.1038/nature01809

Kojic, N., Bico, J., Clasen, C., and McKinley, G. H. (2006). Ex vivo rheology of spider silk. *J. Exp. Biol.* 209, 4355–4362. doi: 10.1242/jeb.02516

Madsen, B., Shao, Z. Z., and Vollrath, F. (1999). Variability in the mechanical properties of spider silks on three levels: interspecific, intraspecific and intraindividual. *Int. J. Biol. Macromol.* 24, 301–306. doi: 10.1016/s0141-8130(98)00094-4

Madurga, R., Blackledge, T. A., Perea, G. B., Plaza, G. R., Riekel, C., Burghammer, M., et al. (2015). Persistence and variation in microstructural design during the evolution of spider silk. *Sci. Rep.* 5:14820. doi: 10.1038/srep14820

Madurga, R., Ganan-Calvo, A. M., Plaza, G. R., Guinea, G. V., Elices, M., and Perez-Rigueiro, J. (2017). Production of high performance bioinspired silk fibers by straining flow spinning. *Biomacromolecules* 18, 1127–1133. doi: 10.1021/acs.biomac.6b01757

Madurga, R., Plaza, G. R., Blackledge, T. A., Guinea, G. V., Elices, M., and Perez-Rigueiro, J. (2016). Material properties of evolutionary diverse spider silks described by variation in a single structural parameter. *Sci. Rep.* 6:18991. doi: 10.1038/srep18991

Marden, L. (1951). Spain's silkworm gut. *Natl. Geogr. Mag.* 100, 100–108.

Martin, L. H. H. (1991). The history of silkworm gut. *Am. Fly Fish.* 17, 3–7.

Ortlepp, C., and Gosline, J. (2004). Consequences of forced silking. *Biomacromolecules* 5, 727–731. doi: 10.1021/bm034269x

Pellerin, C., Rousseau, M. E., Cote, M., and Pezolet, M. (2005). Study of molecular orientation by vibrational spectroscopy: from polymers to silk. *Macromol. Symp.* 220, 85–98. doi: 10.1002/masy.200550207

Perea, G. B., Solanas, C., Mari-Buye, N., Madurga, R., Agullo-Rueda, F., Muinelo, A., et al. (2016). The apparent variability of silkworm (*Bombyx mori*) silk and its relationship with degumming. *Eur. Polym J.* 78, 129–140. doi: 10.1016/j.eurpolymj.2016.03.012

Perez-Rigueiro, J., Elices, M., and Guinea, G. V. (2003). Controlled supercontraction tailors the tensile behaviour of spider silk. *Polymer* 44, 3733–3736. doi: 10.1016/s0032-3861(03)00245-3

Perez-Rigueiro, J., Madurga, R., Ganan-Calvo, A. M., Elices, M., Guinea, G., Tasei, Y., et al. (2019). Emergence of supercontraction in regenerated silkworm (*Bombyx mori*) silk fibers. *Sci. Rep.* 9:2398. doi: 10.1038/s41598-019-38712-6

Perez-Rigueiro, J., Viney, C., Llorca, J., and Elices, M. (2000). Mechanical properties of silkworm silk in liquid media. *Polymer* 41, 8433–8439. doi: 10.1016/s0032-3861(00)00179-8

Perez-Riguero, J., Elices, M., Llorca, J., and Viney, C. (2001). Tensile properties of Argiope trifasciata drag line silk obtained from the spider's web. *J. Appl. Polym. Sci.* 82, 2245–2251. doi: 10.1002/app.2072

Puglisi, G., De Tommasi, D., Pantano, M. F., Pugno, N. M., and Saccomandi, G. (2017). Micromechanical model for protein materials: from macromolecules to macroscopic fibers. *Phys. Rev. E* 96:042407. doi: 10.1103/PhysRevE.96.042407

Ruiz, V., Jiang, P., Mueller, C., Jorge, I., Vazquez, J., Ridruejo, A., et al. (2019). Preparation and characterization of Nephila clavipes tubuliform silk gut. *Soft Matter* 15, 2960–2970. doi: 10.1039/c9sm00212j

Schmitt, O. H. (1969). "Some interesting and useful biomimetic transforms," in *Proceedings of the Third International Biophysics Congress*, Boston, MA, 297.

Teramoto, H., and Miyazawa, M. (2005). Molecular orientation behavior of silk sericin film as revealed by ATR infrared spectroscopy. *Biomacromolecules* 6, 2049–2057. doi: 10.1021/bm0500547

Termonia, Y. (1994). Molecular modeling of spider silk elasticity. *Macromolecules* 27, 7378–7381. doi: 10.1021/ma00103a018

Termonia, Y. (2000). "Molecular modelling of the stress/strainbehaviour of spider dragline," in *Structural Biological Materials*, ed. M. Elices (Amsterdam: Pergamon Press), 335–349.

Vollrath, F., and Knight, D. P. (2001). Liquid crystalline spinning of spider silk. *Nature* 410, 541–548. doi: 10.1038/35069000

Work, R. W. (1977). Dimensions, birefringences, and force-elongation behavior of major and minor ampullate silk fibers from orb-web-spinning spiders - effects of wetting on these Properties. . *Text. Res. J.* 47, 650–662. doi: 10.1177/004051757704701003

Conflict of Interest: The authors declare that the research was conducted in the absence of any commercial or financial relationships that could be construed as a potential conflict of interest.

frontiers in Materials

ORIGINAL RESEARCH
published: 10 March 2020
doi: 10.3389/fmats.2020.00049

Hierarchical HRP-Crosslinked Silk Fibroin/ZnSr-TCP Scaffolds for Osteochondral Tissue Regeneration: Assessment of the Mechanical and Antibacterial Properties

Viviana P. Ribeiro[1,2†], Sandra Pina[1,2*†], Sabina Gheduzzi[3], Ana C. Araújo[1,2], Rui L. Reis[1,2,4] and Joaquim M. Oliveira[1,2,4]*

[1] 3B's Research Group, Research Institute on Biomaterials, Biodegradables and Biomimetics, Headquarters of the European Institute of Excellence on Tissue Engineering and Regenerative Medicine, University of Minho, Guimarães, Portugal, [2] ICVS/3B's – PT Government Associate Laboratory, Braga/Guimarães, Portugal, [3] Centre for Orthopaedic Biomechanics, Department of Mechanical Engineering, University of Bath, Bath, United Kingdom, [4] The Discoveries Centre for Regenerative and Precision Medicine, Headquarters at University of Minho, Guimarães, Portugal

OPEN ACCESS

Edited by:
Antonella Motta,
University of Trento, Italy

Reviewed by:
Francesco Grassi,
Rizzoli Orthopedic Institute (IRCCS), Italy
José Pérez-Rigueiro,
Polytechnic University of Madrid, Spain

***Correspondence:**
Viviana P. Ribeiro
viviana.ribeiro@i3bs.uminho.pt
Sandra Pina
sandra.pina@i3bs.uminho.pt

[†] These authors have contributed equally to this work

Specialty section:
This article was submitted to Mechanics of Materials, a section of the journal Frontiers in Materials

Received: 23 October 2019
Accepted: 18 February 2020
Published: 10 March 2020

Citation:
Ribeiro VP, Pina S, Gheduzzi S, Araújo AC, Reis RL and Oliveira JM (2020) Hierarchical HRP-Crosslinked Silk Fibroin/ZnSr-TCP Scaffolds for Osteochondral Tissue Regeneration: Assessment of the Mechanical and Antibacterial Properties. Front. Mater. 7:49. doi: 10.3389/fmats.2020.00049

The biomaterials requirements for osteochondral (OC) defects restoration simultaneously include adequate mechanical behavior, and the prevention of bacterial adherence and biofilm formation, without impairing local tissue integration. Bilayered and hierarchical scaffolds combining a cartilage-like layer interconnected to an underlying subchondral bone-like layer appeared as innovative technological solutions able to mimic the native OC tissue hierarchical architecture. This study is focused on the assessment of the combined compression-shear stresses and possible bacterial biofilm formation of hierarchical scaffolds prepared from a horseradish peroxidase-crosslinking reaction of silk fibroin (SF) combined with zinc (Zn) and strontium (Sr)-doped β-tricalcium phosphate (β-TCP) for OC tissue regeneration. Scaffolds with undoped-β-TCP incorporation were used as control. Results showed that the bilayered scaffolds presented suitable aptitude to support compression and shear loading for OC tissue, with better mechanical properties for the ZnSr-containing structures. Young and shear moduli presented values close to 0.01 MPa in the region 10–20% strain. The investigation of biomaterials surface ability to prevent biofilm formation showed reduced bacterial adhesion of *Escherichia coli* (*E. coli,* gram-negative) and *Staphylococcus aureus* (*S. aureus*, gram-positive) on both scaffolds, thus suggesting that the proposed hierarchical scaffolds have a positive effect in preventing gram-positive and gram-negative bacteria proliferation.

Keywords: silk fibroin, horseradish peroxidase, ZnSr-tricalcium phosphate, hierarchical scaffolds, mechanical strength, antibacterial adhesion, osteochondral regeneration

INTRODUCTION

Irreversible injuries of the hierarchical osteochondral (OC) tissue, triggered by different pathological conditions, can affect both the articular cartilage and the subchondral bone. Currently, autografts or allografts, bone marrow stimulation, cell-based therapy with autologous chondrocytes implantation, and intra-articular injections of mesenchymal stem cells with platelet-rich plasma

(PRP), are the most common surgical methods used for OC tissue treatment (Zhang et al., 2016; Devitt et al., 2017; Bastos et al., 2019). Nevertheless, these treatments are able to reduce pain and cannot warrant the complete regenerative process of the tissue and the articular cartilage healing (De L'Escalopier et al., 2015). Advanced personalized therapies that possibly creating a microenvironment that mimics the OC tissue architecture at the host site may contribute to a faster regeneration (Yousefi et al., 2015). Three-dimensional (3D) scaffolds, with complex, porous and stratified heterogeneous structures, have been renowned as the crucial goal to treat OC damaged tissue, thus serving the mechanical and biological support of the articular cartilage, the subchondral bone and its interface (Drury and Mooney, 2003; Hutmacher, 2006). These structures should hold suitable macro- and micro-porosity, with interconnected and open porosity, thus help cell growth, proliferation, and migration for ECM production (Kang et al., 2018). The degradation and biocompatibility are also imperative attentions for 3D scaffolds manufacturing, assuring their stability, safety, and cost-efficiency (Wang et al., 2008; Ji et al., 2012).

Distinct materials have been emerging as the next generation for scaffolding fabrication, as the case of natural-based polymers (e.g., silk fibroin, collagen, gelatin, chitosan, elastin, fibrin, and albumin), which present superior biocompatibility and low risk of toxicity from the metabolized degradation products (Malafaya et al., 2007; Oliveira and Mano, 2015). Besides, the possibility of combining these biopolymers with inorganic materials [e.g., hydroxyapatite (HAp) and β-tricalcium phosphate (β-TCP)] extend their mechanical performance and osteogenic capacity (Pina et al., 2018). Amongst biopolymers, *Bombyx mori* silk produced by silkworms, as source of silk fibroin (SF) has been attracting great deal of attention in the biomedical field due to its mechanical properties, *in vivo* biocompatibility and biodegradability (Kundu et al., 2013). Furthermore, the hydrophilic and semi-amorphous regions of the SF β-sheet structure can mimic the anionic structure of non-collagenous proteins, acting as deposits of HAp nanoparticles (Marelli et al., 2012). On the other side, β-TCP is one of the calcium phosphate (CaP) compound significantly used as bone grafting substitute material, owed its biocompatibility and resorbability instigating the replacement of implants by the tissues. It is also an adequate ionic carrier, thus playing an essential part in the biological action course, namely enhanced production of bone morphogenetic protein-2 and vascular endothelial growth factors (Bose et al., 2013; Fielding and Bose, 2013). Indeed, many studies have reported the contribution of bioactive inorganic materials functionalized with ionic doping (e.g., strontium, zinc, magnesium, manganese, silicon) to the bone health and to exhibit enhanced biocompatibility and antibacterial properties, while keeping the mechanical properties of the implants (Pina et al., 2010; Mestres et al., 2012). For instance, strontium (Sr) has a bone-seeking behavior encouraging bone formation by osteoblasts, and inhibiting bone resorbtion by osteoclast cells (Saidak and Marie, 2012). Zinc (Zn) has antibacterial properties and is able to stimulate osteoblasts proliferation and differentiation, while stopping the resorption process by osteoclasts (Kandaz et al., 2009). Some works have also reported the use of Sr and Zn as antibacterial agents. Sr-doped HAp exhibited antibacterial activity against *Escherichia coli (E. coli)*, *Staphylococcus aureus (S. aureus)*, and *Lactobacillus* (Lin et al., 2008), and a reduction of bacterial *E. coli*, *S. aureus*, *Candida albicans,* and *Streptococcus mutans* was observed after in contact with HAp incorporating Zn (Chung et al., 2006; Stanić et al., 2010; Thian et al., 2013).

In order to address the OC regeneration challenges, SF combined with ZnSr-doped β-TCP scaffolds has been recently reported (Pina et al., 2017; Ribeiro et al., 2019b). As a first approach, SF were mixed with β-TCP incorporating Sr, Zn, and Mn, to produce biofunctional scaffolds with adequate micro- and macro-porosity for bone tissue regeneration (Pina et al., 2017). *In vitro* assays using human adipose-derived stem cells (hASCs) demonstrated different cellular responses by varying the ionic doping elements in the scaffolds, namely when combined with Sr and Zn in comparison to the single ions. Then, we have proposed a new approach by developing bilayered and hierarchical scaffolds with controlled porosity at the macro- and micro-scale, and improved stability for short- to long-term OC implantation purposes (Ribeiro et al., 2019b). For that, a horseradish peroxidase (HRP)-mediated approach was used to crosslink SF (HRP-SF) combined with ZnSr-doped β-TCP (ZnSrTCP). HRP-SF was used as articular cartilage-like layer, while HRP-SF/ZnSrTCP was used to produce the subchondral bone layer. The scaffolds presented adequate structural integrity, resilient and viscoelastic properties that can be easily adjusted to the OC defect. *In vitro* response of co-cultured human osteoblasts and human chondrocytes indicated osteogenic activity and chondrogenic inducement, respectively in the subchondral and chondral-like layers. The appropriateness of using HRP-crosslinked SF scaffolds was already demonstrated in previous works for cartilage tissue showing the features of enzymatically crosslinked SF hydrogels (Yan et al., 2016; Ribeiro et al., 2018a,b).

In the present study, complementary structural, mechanical properties, and antibacterial activity of the hierarchical scaffolds were investigated. Hence, the failure behavior of the scaffolds was evaluated under combined compression and shear loading, aiming to obtain its strengths for different mode loading conditions. Some concerns with regards to the implant-associated infections, have been reported as one of the most common surgical problems after orthopedic surgeries (Neut et al., 2003; Darouiche, 2004). Therefore, the bacterial adhesion and biofilm formation of the monolayered scaffolds against *E. coli* and *S. aureus* were screened. In particular, it was assessed the antibacterial properties of the scaffolds containing ZnSr as antibacterial agents.

MATERIALS AND METHODS

Preparation of Aqueous SF Solution

Silk fibroin (SF) was extracted from *Bombyx mori* cocoons (Portuguese Association of Parents and Friends of Mentally Disabled Citizens, APPACDM, Castelo Branco, Portugal) by boiling for 1 h in 0.02M sodium carbonate solution (Sigma-Aldrich, St. Louis, MO, United States), to remove the glue-like

sericin protein, and rinsed with distilled water to completely extract the degumming solution. The degummed SF was dissolved in a 9.3M lithium bromide solution (Sigma-Aldrich, St. Louis, MO, United States) for 1 h at 70°C, and dialyzed in distilled water using a benzoylated dialysis tubing (MWCO: 2 kDa) (Sigma-Aldrich, St. Louis, MO, United States) for 48 h. Afterward, the SF solution was concentrated with poly(ethylene) glycol solution (Sigma-Aldrich, St. Louis, MO, United States) to yield a solution of ∼16 wt.%, determined by weighting the dry SF. The SF solution was then stored at 4°C until further use.

Synthesis and Characterization of ZnSr-Doped β-Tricalcium Phosphate (β-TCP) Powders

β-TCP powders doped with 10 mol.% of Sr + Zn (ZnSrTCP) were synthesized using wet chemical precipitation, with a molar ratio of (Ca + Sr + Zn)/P = 1.48, as previously reported (Pina et al., 2017). Calcium nitrate tetrahydrate [$Ca(NO_3).4H_2O$, Sigma-Aldrich, St. Louis, MO, United States], diammonium hydrogen phosphate [$(NH_4)_2HPO_4$, Sigma-Aldrich, St. Louis, MO, United States], strontium nitrate [$Sr(NO_3)$, Sigma-Aldrich, St. Louis, MO, United States] and zinc nitrate [$Zn(NO_3)$, Sigma-Aldrich, St. Louis, MO, United States] were used as starting chemical precursors, respectively for Ca, P, Sr, and Zn. The precipitated suspension was kept for 4 h under constant stirring conditions and ripened for further 20 h under rest conditions, at 50°C and pH ∼7, by adding required amounts of NH_4OH solution. The precipitate was vacuum filtered, dried at 100°C, and heat-treated for 2 h at 1100°C. Then, the powders were ground to fine powders and sieved by a mesh size of 63 μm, showing a final average particle size of 1–10 μm. Pure β-TCP (TCP) powder was also produced for comparison purposes. The crystalline phases presented on the powders were analyzed by X-ray diffraction (XRD) using a conventional Bragg–Brentano diffractometer (Bruker D8 Advance DaVinci, Germany), equipped with CuKα radiation, produced at 40 kV and 40 mA. Data sets were collected in the 2θ range of 10–70° with a step size of 0.02° and 1 s per step. The phase composition of the powders was calculated based on XRD patterns through Rietveld analysis with TOPAS 5.0 software (Bruker, Germany), using the structural model of ICSD card numbers #97500 for β-TCP and #73712 for calcium pyrophosphate ($Ca_2P_2O_7$, β-CPP). Refined parameters were scale factor, sample displacement, background as Chebyshev polynomial of fifth order, crystallite size, and lattice parameters.

Preparation of Hierarchical HRP-Crosslinked SF/ZnSr-Doped β-Tricalcium Phosphate Scaffolds

Hierarchical scaffolds comprising 80/20 (w/w) of HRP-SF/ZnSrTCP as subchondral bone layer and HRP-SF as articular cartilage layer, were fabricated using particulate leaching followed by freeze-drying techniques, as described elsewhere (Ribeiro et al., 2019a,b). Firstly, 1 mL SF (16 wt.%), 50 μL HRP solution (HRP type VI, 0.84 mg/mL) and 65 μL hydrogen peroxide solution (H_2O_2, 0.36 wt.%; Panreac, Barcelona, Spain) (1/0.26‰/1.45‰) was mixed to obtain HRP-SF solution. The subchondral bone-like layer was produced by means of mixing HRP-SF and ZnSrTCP powders. The solution was moved to cylindrical molds (9 mm inner diameter; Deltalab, Barcelona, Spain), and 2 g of granular sodium chloride (low in endotoxins; EMPROVE, VWR BDH Prolabo, Briare, France) with 500-1000 μm (Analytic Sieve Shaker; AS 200 Digit, Retsch, Germany) was added, and left for gelling at 37°C. After that, the molds were immersed in distilled water for salt extraction, for 72 h. The subchondral bone scaffolds were taken out from the molds with a punch (8 mm inner diameter; Smith & Nephew, Portugal). Secondly, HRP-SF solution was placed on the top of the subchondral bone scaffolds, in new silicon molds (8 mm inner diameter) to obtain the articular cartilage-like layer. Then, 2 g of granular sodium chloride (500-1000 μm) was added to the solution and left at 37°C until complete gelation. Then, the bilayered scaffolds were punched (8 mm inner diameter), kept at −80°C and freeze-dried (Telstar Cryodos-80, Barcelona, Spain) for 7 days. Monolayered HRP-SF, HRP-SF/ZnSrTCP, and HRP-SF/TCP scaffolds were also produced for bacteria growth tests. The monolayered scaffolds were denominated as MdTCP and MTCP, respectively for HRP-SF/ZnSrTCP and HRP-SF/TCP scaffolds, while the bilayered scaffolds appear as BdTCP and BTCP, respectively for HRP-SF| HRP-SF/ZnSrTCP and HRP-SF| HRP-SF/TCP scaffolds.

Combined Compression-Shear Properties of the Bilayered Scaffolds

Mechanical testing of the bilayered scaffolds was performed after immersing them in PBS solution (1.37 mM NaCl, 27 mM KCl, 80.6 mM Na_2HPO_4, 19.4 mM KH_2PO_4). Prior to testing samples were stored at 37°C overnight. On the day of testing, samples were blotted dry and their height and diameter were measured three times with repositioning with a digital caliper. Average dimensions were used for subsequent data manipulation. Each sample was secured between two steel compression plates and loaded under simultaneous compression and shear. The loading ramps were synchronized and applied at a rate of 1 mm/min up to a strain of 30% using a custom designed multi-axis testing machine (**Figure 1**) (Holsgrove et al., 2017). Load and displacement data were converted into nominal stress and strain and plotted for each of the five samples tested. Young (E) and shear (G) moduli were evaluated in the region 10–20% strain by fitting experimental data using the least squares technique. Results are presented as mean ± SD.

Antibacterial Properties

Bacterial Cultivation and Inoculums Preparation

Escherichia coli (*E. coli*, gram-negative bacteria; ATCC 25922, US) and *Staphylococcus aureus* (*S. aureus*, gram-positive bacteria; ATCC 25923, US) were used as bacterial models to evaluate the antibacterial performance of the scaffolds. Bacterial cultures were grown in Tryptic Soy broth (TSB) medium, overnight at 37°C incubation. The cultures were centrifuged (9000 rpm), washed in PBS solution and bacteria pellet was then, re-suspended in PBS solution at a concentration adjusted to 1–2 × 10^6 CFU/mL.

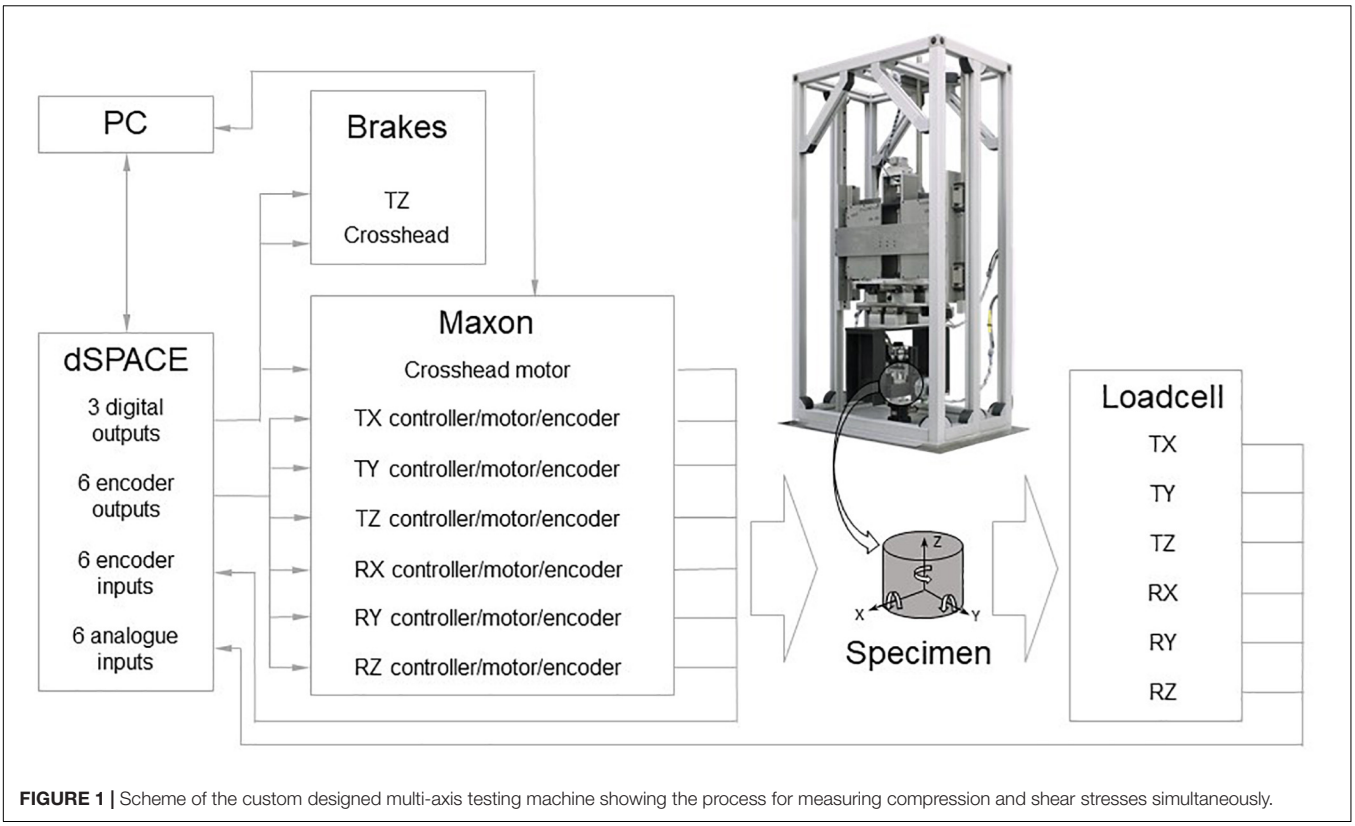

FIGURE 1 | Scheme of the custom designed multi-axis testing machine showing the process for measuring compression and shear stresses simultaneously.

Bacterial Adhesion and Biofilm Formation on the Scaffolds

The *E. coli* and *S. aureus* adherence and biofilm formation on the surface of the portioned HRP-SF, MdTCP, and MTCP scaffolds (8 mm diameter and 3 mm height) were evaluated by seeding the bacteria in a 10 μL suspension of 10^6 CFU/mL on the surface of the scaffolds for 24 h at 37°C incubation. Scaffolds were sterilized by ethylene oxide (Gas Sterilizer/Aerator, Steri-Vac 5XL, 3M Company, Saint Paul, MN, United States). Prior bacteria seeding, all scaffolds were hydrated in PBS solution and keep overnight in the incubator at 37°C.

Bacterial Culture in Liquid Medium

The effects of the HRP-SF, MdTCP and MTCP scaffolds (8 mm diameter and 3 mm height) on *E. coli* and *S. aureus* growth were assessed. Scaffolds were sterilized by ethylene oxide (Gas Sterilizer/Aerator, Steri-Vac 5XL, 3M Company, Saint Paul, MN, United States). First, bacterial liquid cultures were prepared as described above, and then the pre-hydrated scaffolds (incubated overnight at 37°C in PBS solution) were immersed in 1.5 mL of TSB medium containing 10^6 CFU/mL of *E. coli* and *S. aureus*. Scaffolds were incubated with the bacteria for additional 24 h, under agitation. Afterward, the Optical Density (OD; 620 nm) of bacterial suspensions were quantified in a Visible Spectrophotometer (Genesys 30, Thermo Fisher Scientific, Waltham, MA, United States) using gray filters, in order to determine the percentage of bacteria reduction in suspension medium, in the presence of the scaffolds and as a function of the OD in the positive control. Scaffolds without bacterial inoculation were used as negative control, and bacterial cultures without scaffolds were used as positive control. Each experiment was performed in triplicate.

Scanning Electron Microscopy

A high-resolution field emission scanning electron microscope (SEM) with Focused Ion Beam (FIB-SEM; Auriga Compact; Zeiss, Oberkochen, Germany) was used to evaluate bacteria adhesion and the initial formation of biofilm on the scaffolds. The HRP-SF, MdTCP, and MTCP scaffolds recovered after 24 h of direct bacterial seeding and after bacteria culture in liquid medium were first washed with PBS solution and fixed with 2.5% (v/v) glutaraldehyde solution in PBS for 1 h at 4°C in the dark. Afterward, the glutaraldehyde solution was removed, and samples were washed in PBS solution before dehydration in series of ethanol concentrations (30, 50, 70, 90, and 100% v/v). After drying, all samples were platinum sputtered (EM ACE600; Leica, Wetzlar, Germany) and visualized by SEM. Micrographs were taken at an accelerating voltage of 5 kV at different magnifications.

Statistical Analysis

The numerical results are presented as mean ± standard deviation (SD). The GraphPad Prism 5.0 software (GraphPad Software, La Jolla, CA, United States) was used to perform statistical analysis, where a Shapiro–Wilk normality test was first performed to evaluate the data normality. The results indicated

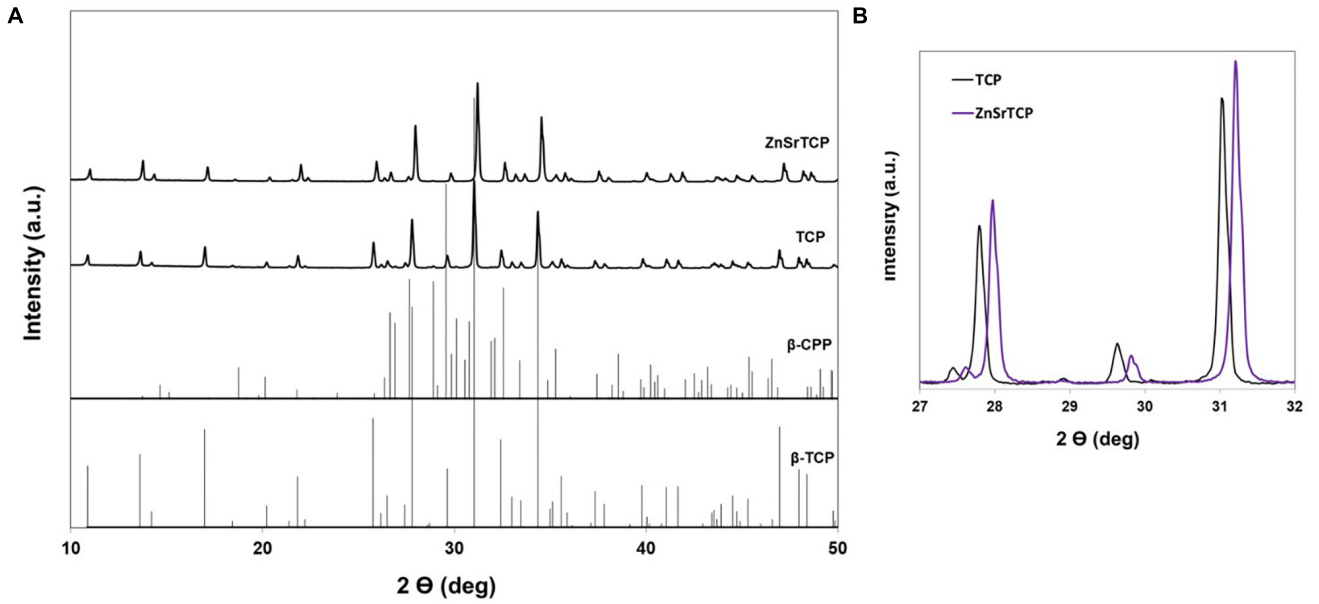

FIGURE 2 | X-ray diffraction patterns of pure TCP and ZnSrTCP powders **(A)**; Zoomed area of **(A)** within the 2θ range from 27 to 32° to show the shift of XRD peaks to higher 2θ angles with ionic incorporation **(B)**. The standard β-TCP (ICDD PDF 04-014-2292) and β-CPP (ICDD PDF 04-009-3876) are also presented for comparison.

that a non-parametric test should be applied for compression-shear mechanical properties results, whereas a parametric test should be used to compare the results of percentage reduction in OD of bacterial suspensions. The results from compression-shear mechanical properties were analyzed by means of a Mann–Whitney test. Five specimens for each composition were tested. A one-way analysis of variance (ANOVA) followed by Tukey's test was used to analyze the percentage reduction in OD of bacterial suspensions. Three independent experiments were performed, using at least two replicates for each condition.

RESULTS

ZnSr-Doped β-TCP Powders

The XRD patterns of pure and ZnSr-doped β-TCP powders are displayed in **Figure 2**. The crystallographic phases were identified based on the standards ICDD PDF 04-014-2292 of β-TCP and 04-009-3876 of β-CPP. It can be seen that the powders consist of β-TCP phase and traces amount of β-CPP, with no amorphous phases. The incorporation of ZnSr into TCP structure is set by a gradual peak shifting (zoomed area **Figure 1B**) of the β-TCP peak to higher angles, thus meaning that the lattice parameters of β-TCP have decreased. The quantitative phase analysis obtained by Rietveld refinement supported the formation of β-TCP as the main crystalline phase with 91 and 9 wt.% of b-CPP in the powders. The refined lattice parameters obtained for standard pure β-TCP were $a = b = 10.439(8)$ Å, $c = 37.395(0)$, $a = \beta = 90°$, and $\gamma = 120°$ in the hexagonal setting (space group R3c) with structural parameters reported by Yashima et al. (2003). These parameters were used as the starting values to refine the data of ZnSrTCP powder. **Table 1** shows a clear decreasing in both lattice parameters along *a*-axis and *c*-axis with ZnSr incorporated, in comparison with TCP powder, thus proving the effective ionic incorporation into β-TCP structure.

Mechanical Properties of the Bilayered Scaffolds

Nominal stress-strain plots for simultaneous axial and shear loading were obtained from load displacement data (**Figure 3**). Young and shear moduli were evaluated for each sample in the region 10–20% strain and then averaged. Neither the Young modulus (0.008 ± 0.006 and 0.009 ± 0.002 MPa for BTCP and BdTCP, respectively) nor the shear one (0.002 ± 0.002 and 0.002 ± 0.001 MPa for BTCP and BdTCP, respectively) showed statistically significant difference when the significance level was set at 0.5. However, a weak tendency of slightly improved mechanical properties was identified for BdTCP scaffolds (**Figure 4**). Besides, the scaffolds were able to preserve their integrity at different loadings.

TABLE 1 | Lattice parameters of β-TCP and β-CPP phases of TCP and ZnSrTCP powders.

	Lattice parameters (Å)			
	β-TCP		β-CPP	
Samples	a	c	a	c
TCP	10.439	37.395	6.690	24.135
ZnSrTCP	10.408	37.302	6.715	23.949

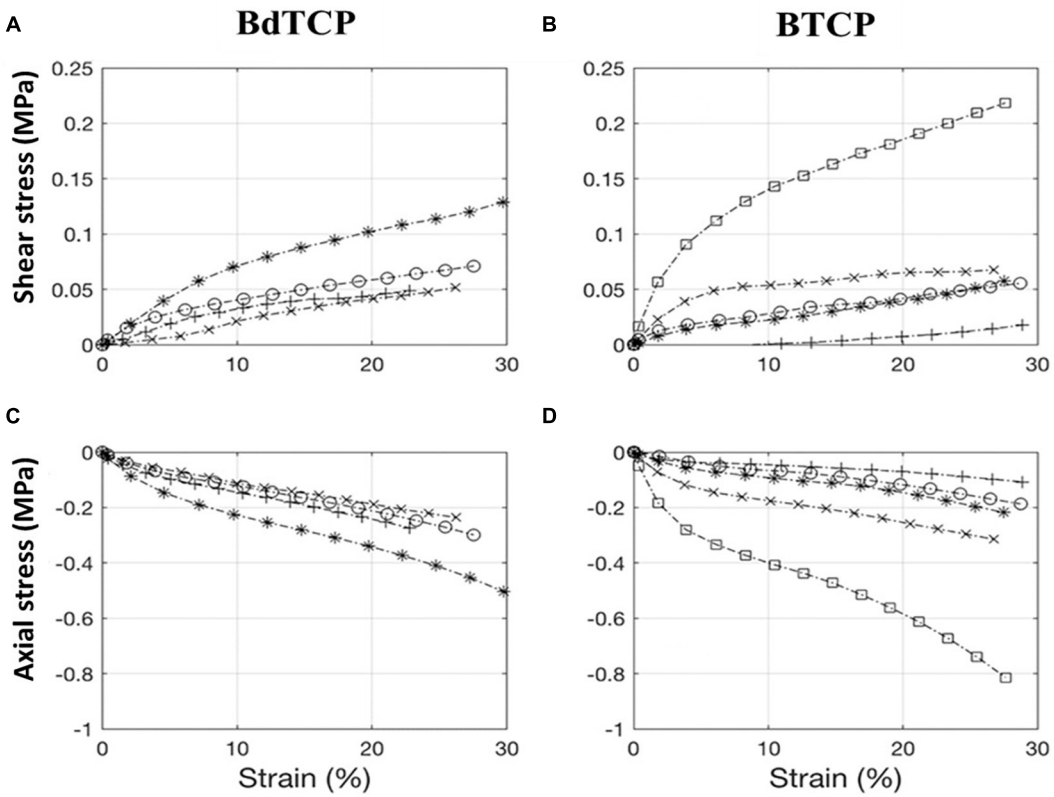

FIGURE 3 | Stress-strain plots for bilayered BTCP and BdTCP scaffolds. Axial compression and shear were applied simultaneously both at a rate of 1 mm/min up to a strain of 30%. BdTCP shear stress and strain **(A)**, BTCP shear stress and strain **(B)**, BdTCP axial stress and strain **(C)**, and BTCP axial stress and strain **(D)**. Results are the mean ± SD of 5 independent experiments. Each curve corresponds to an individual test. The two-curve in **(A–D)** were obtained simultaneously on the same sample, and same symbol refers to the same sample.

Analysis of Bacterial Adherence, Morphology, and Biofilm Formation

SEM Observation After Direct Contact Assay

The adhesion and biofilm formation of *E. coli* and *S. aureus* on the HRP-SF, MdTCP, and MTCP scaffolds was first evaluated by direct contact assay (**Figure 5**). After 24 h of culturing, both bacteria adhered to the HRP-SF scaffolds surface (**Figures 5A,B**) and cross-sections (**Figures 5C,D**), although no biofilm formation was detected. As for the MdTCP (**Figures 5E–H**) and MTCP (**Figures 5I–L**) scaffolds, some poorly distributed bacteria adhered to the scaffolds but at lower levels as compared to the pure HRP-SF scaffolds (**Figures 5A–D**). *E. coli* and *S. aureus* morphology showed cells with regular and smooth shapes and others exhibiting wrinkling, flattening and rupture of the membranes structure. Some cell debris were also detected, which indicates damages of the bacterial walls and loss of cellular content.

Bacterial Viability and Release Profile in Liquid Medium

Bacterial viability in the presence of the HRP-SF, MdTCP, and MTCP scaffolds was evaluated after 24 h of culturing in liquid medium (**Figure 6**). Scaffolds showed no inhibitory effects against *E. coli* growth, presenting a non-significant reduction in OD as compared to the positive control (**Figure 6A**). As for *S. aureus*, a significant reduction (P-value = 0.0098) in OD was detected in the presence of the HRP-SF (72.68 ± 15.14%) and MTCP (73.83 ± 13.71%) scaffolds, in relation to the controls without scaffolds. Even though, both bacteria presented a high viability in the presence of the structures after 24 h of inoculation.

When observed the *E. coli* and *S. aureus* adhesion to the surface of the scaffolds (**Figure 6B**), only a few bacteria were able to adhere while keeping their regular and smooth morphology. Cell debris were observed (red arrows), resulting from the bacterial walls collapse and loss of cellular components. No biofilm formation was observed, and scaffolds were able to maintain their structural integrity during the inoculation period.

DISCUSSION

In the last few years, OC tissue engineering has arisen as an excellent approach to repair and regenerate damaged tissues, avoiding all the limitations of allogenic, autologous, and other available treatments for the tissue healing. Henceforth, 3D scaffolds owing specific structural, mechanical and osteogenic features have been developed addressing articular cartilage

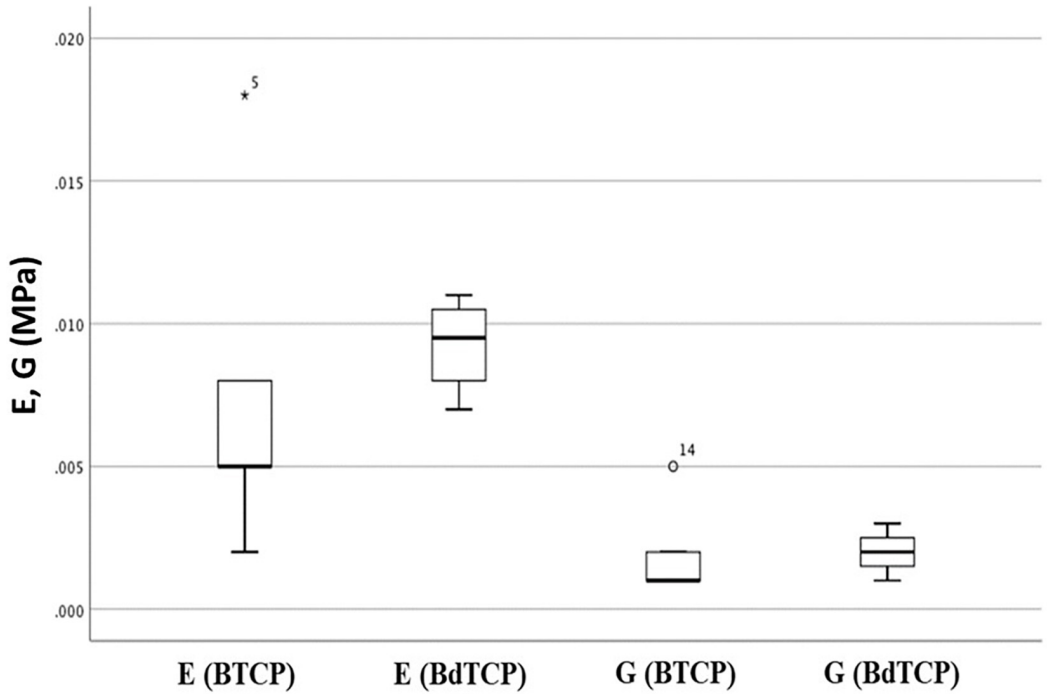

FIGURE 4 | Young (E) and shear (G) moduli for the bilayered pure (BTCP) and doped (BdTCP) scaffolds. Results presented are the mean ± SD of 5 independent experiments.

and subchondral bone regeneration (Drury and Mooney, 2003; Hutmacher, 2006). As aforementioned, our group have recently followed a different approach to produce hierarchically structured scaffolds by using HRP to crosslink SF and to combine it with ZnSr-doped β-TCP nanoparticles as a subchondral bone layer, and HRP-SF as articular cartilage-like layer (Ribeiro et al., 2019b). These scaffolds showed a suitable porous structure with macro-pores larger than 500 μm and micro-pores that reached only 10 μm. The porosity distribution profile showed that in each layer of the hierarchical scaffolds, the pores were evenly distributed, with a mean porosity of 89.1 ± 1.4% in the HRP-SF layer, 31.4 ± 8.4% in the HRP-SF/ZnSrTCP layer and 21.6 ± 8.8% in the HRP-SF/TCP layer. The interface region presented an intermediate porosity of 76.4 ± 2.8 and 71.7 ± 14.6%, respectively in BdTCP and BTCP scaffolds. The scaffolds were able to support human osteoblasts and chondrocytes activity in co-culture conditions, through an extensive cell proliferation profile and ECM production. The *in vivo* response of those scaffolds, after implantation for 8 weeks in rabbit critical size OC defects, exhibited cartilage and calcified tissues repair and regeneration (Ribeiro et al., 2019a). The exceptional assets of using SF namely, the *in vivo* biocompatibility and biodegradability, and excellent mechanical elasticity, illustrate its importance for scaffolds manufacturing (Melke et al., 2016). Particularly, the fibrous structure comparable to collagen type I and type II, brings interest to use SF in orthopedic repair applications (Wang et al., 2006). Furthermore, SF can act as deposition sites of HAp due to its hydrophilic and semi-amorphous sections between the β-sheets, thus mimicking the structure of non-collagenous proteins (Marelli et al., 2012). Different studies have also reported that the crystalline phase of SF may nucleate the deposition of HAp (Vetsch et al., 2015), inducing conformational variations to the protein and presenting superior mechanical properties (Jin et al., 2015). Although SF protein has poor ability for bone regeneration, its blending with inorganic biomaterials by forming a composite material, can improve the final mechanical properties and enhance their osteogenic capacity, thus mimicking the structure of bone tissue. For that reason, the number of publications and annual citations of peer-review original articles related with SF/CaPs composite scaffolds for bone and OC TE applications increased exponentially over the last 20 years, according to the Web of Knowledge database (**Figure 7**). Therefore, joining SF and CaP-based nanopowders result in mechanically stable and osteoconductive scaffolds, thus promoting new OC tissue formation.

In this study, the HRP-SF, pure and HRP-SF/ZnSr-doped β-TCP hierarchical scaffolds were characterized in terms of structural, mechanical and antibacterial properties. Firstly, pure and ZnSr-doped β-TCP were obtained through wet chemical precipitation method, which has the advantage of producing homogeneous powders, and easiness of controlling parameters (i.e., precipitation temperature, and pH) resulting in uniform particles size and morphology, with adequate bioresorbability (Fomin et al., 2008). From XRD patterns and respective refined lattice parameters, the formation of crystalline β-TCP phase and traces of β-CPP on the powders was observed (**Figure 2**). The peak shifts toward higher angles confirmed the successful incorporation of Zn and Sr ions into β-TCP structure. Those

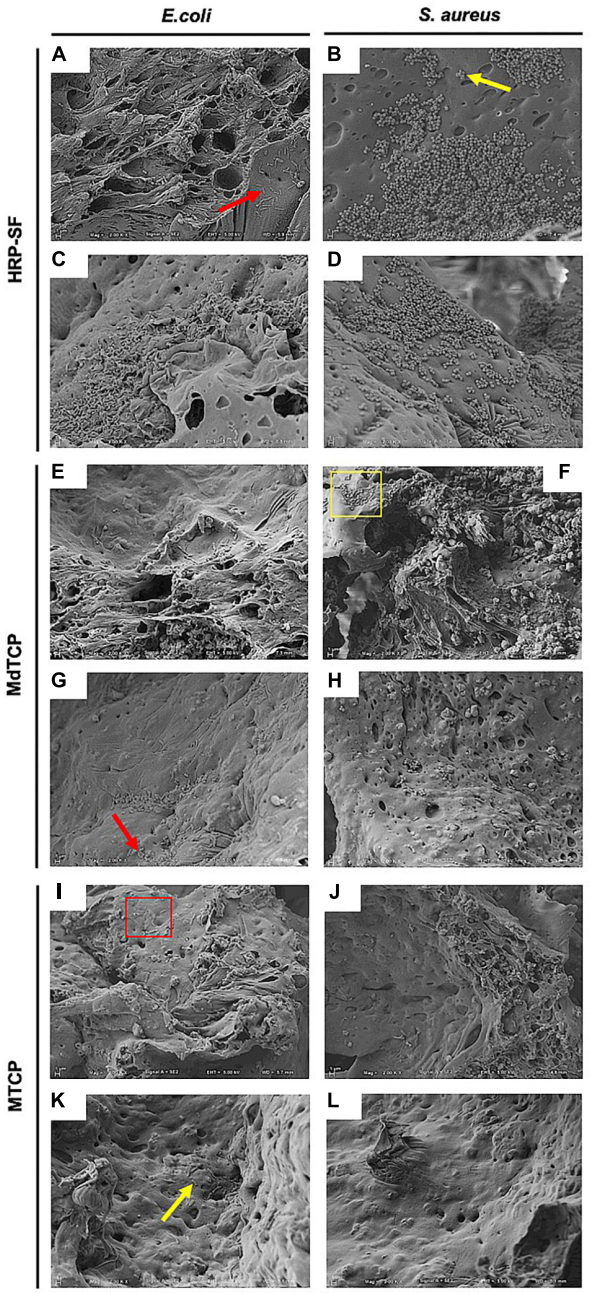

FIGURE 5 | Representative SEM images of *E. coli* and *S. aureus* adhesion and biofilm formation on the **(A–D)** HRP-SF scaffolds, **(E–H)** MdTCP scaffolds, and **(I–L)** MTCP scaffolds after seeding for 24 h. Bacteria adhesion at the **(A,B,E,F,I,J)** surface and **(C,D,G,H,K,L)** cross-sections of the scaffolds. The yellow square and arrows indicate a group of bacteria and individual bacteria with normal surface morphology, respectively. The red square and arrows indicate a group of bacteria or individual bacteria with shape modifications and cell debris, respectively.

changes observed in the lattice parameters unit are ascribed to the ionic radii of Zn (0.74 Å) and Sr (1.12 Å) in comparison to Ca (0.99 Å). Therefore, both *a*-axis and *c*-axis refined lattice parameters increase with higher ionic radii (as Sr), and decrease with smaller (as Zn) ionic radii, than Ca, as reported elsewhere (Kannan et al., 2008, 2009, 2010; Mayer et al., 2008).

Osteochondral lesions are frequently associated with mechanical instability of the joints, thus inducing osteoarthritic degenerative dissimilarities (Martin et al., 2007). Consequently, the mechanical properties of an ideal OC scaffold are of crucial importance, in order to allow the implanted scaffold to bear the physiological loading of the joint without failure or fatigue (Guilak et al., 2001). As previously reported by Ribeiro et al. (2019b), the compressive strengths of BdTCP and BTCP scaffolds were evaluated until a 60% deformation showing respectively, 124.8 ± 23.4 and 92 ± 6.1 kPa. However, considering that human routine activities are subjected to compression, shear and combined compression-shear loading, it is therefore essential the evaluation of the scaffold's strengths, under these combined loadings. Thus, the wet strengths of pure and ZnSr-doped bilayered scaffolds were herein tested under combined compression and shear loading for different mode loading conditions. Results showed Young and shear moduli close to 0.01 MPa, with a tendency of slightly improved mechanical properties for BdTCP, with both keeping their integrity at different mode loading, owing to the binding strength of HRP-SF (**Figures 3**, **4**). The achieved mechanical properties have a small range of values in comparison to the reported ones for natural bone (Young modulus of 1–20 GPa for cortical bone; Young modulus of 10–100 MPa for trabecular bone; shear modulus of 0.2–2 MPa) and for normal human articular cartilage (Young modulus of 0.2–0.3 GPa; shear modulus of 0.1–2 MPa) (Blaker et al., 2005; Sabree et al., 2015). It has been reported that temporary and porous scaffolds may possess compressive modulus of few MPa, which is enough to allow cellularity for ECM mineralization and ingrowth, thus supporting the initial regenerative process (Blaker et al., 2005).

The antibacterial effects and biofilm formation provoked by bacteria adhesion and proliferation on the implants surface may cause acute and chronic infections of the underlying cartilage and bone tissues (Wang et al., 2011). Besides, those effects on biomaterials containing Zn and Sr have been demonstrated on the growth of pathogenic bacteria like *E. coli* and *S. aureus* (Lin et al., 2008; Matsumoto et al., 2009; Wang et al., 2012; Huo et al., 2013). CaPs-based cements and powders have been recognized for having considerable potential for the fully restoration of bone defects in combination with antibacterial properties essential to prevent bacterial infections during implantation procedures (Ewald et al., 2011; Gokcekaya et al., 2017). Although silk sericin has superior antibacterial properties (Karahaliloglu et al., 2017), it has been shown that SF-based materials can be successfully used as supporting matrices for blending with antibacterial polymers in different biomedical applications, including wound dressing (Çalamak et al., 2014, Calamak et al., 2015). Herein, the objective was to evaluate if the monolayered scaffolds are capable of preventing bacterial adhesion to its surfaces and biofilm formation, which is known as a clinical issue involving biomedical devices implantation (O'hara et al., 2018). In fact, alternative biomaterial implants possessing both osteogenic/chondrogenic potential and capable of inhibit

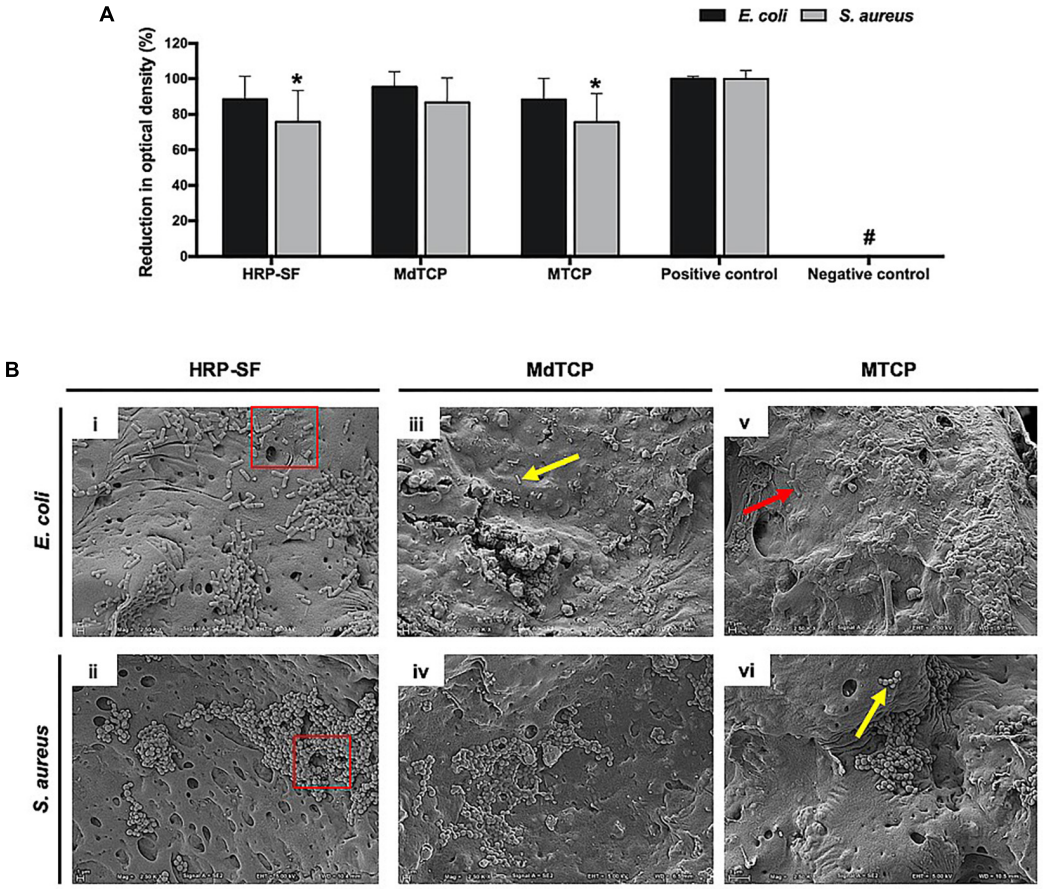

FIGURE 6 | *Escherichia coli* and *S. aureus* cultured in liquid medium, in the presence of HRP-SF, MdTCP, and MTCP scaffolds for the period of 24 h. **(A)** Percentage of bacteria reduction in suspension medium as a function of the OD in the positive control. Data expressed as mean ± standard deviation (SD). *Statistically significant when compared with positive control (*P*-value = 0.0098). HRP-SF (*n* = 7); MdTCP (*n* = 7); MTCP (*n* = 7). # indicate zero-order OD values. **(B)** Representative SEM images of bacteria adhesion and biofilm formation on the (i, ii) HRP-SF scaffolds, (iii, iv) MdTCP scaffolds, and (v, vi) MTCP scaffolds. The yellow arrows indicate normal surface morphology of bacteria. The red squares and arrows indicate a group of bacteria or individual bacteria with shape modifications and cell debris, respectively.

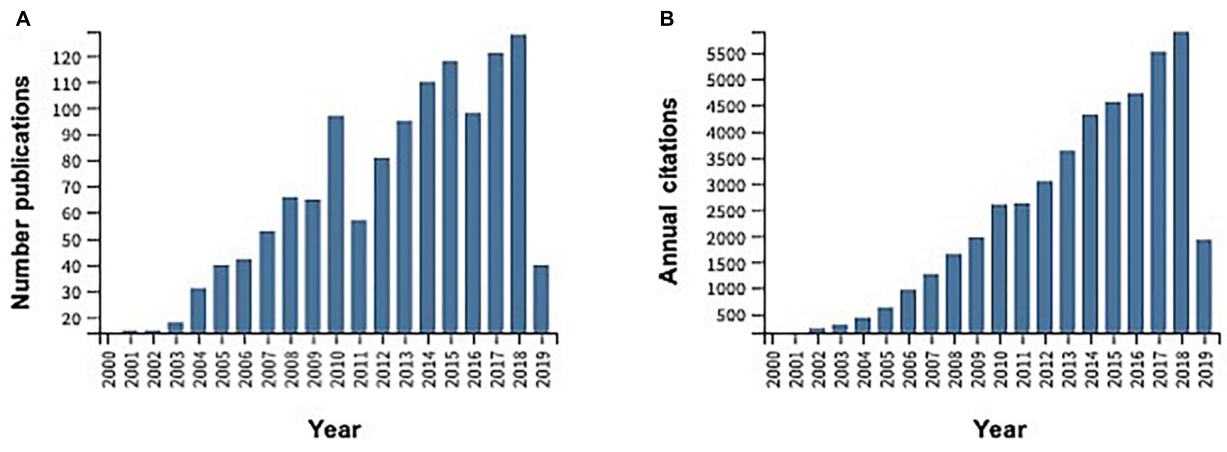

FIGURE 7 | Evolution of the total number of publications per year **(A)** and annual citations **(B)** obtained through a survey in ISI Web of Knowledge under the topic "Silk fibroin and calcium phosphate scaffolds for bone and OC tissue engineering" over the last 20 years.

bacterial colonization have been explored by researchers in the orthopedic community (Zhang et al., 2017; Wang et al., 2019). Although some bacterial adherence was observed in the HRP-SF, MdTCP and MTCP scaffolds after 24 h of cell seeding (**Figure 5**) and culture in liquid medium (**Figure 6B**), all scaffolds were able to prevent biofilm formation of *E. coli* and *S. aureus*. However, the behavior of bacteria adhesion in the cell seeded HRP-SF scaffolds (**Figures 5A–D**) and HRP-SF scaffolds incorporating TCP particles (**Figures 5E–L**) was different. The superior bacterial adhesion observed on the pure HRP-SF scaffolds can be explained by the antibacterial properties of β-TCP (Gokcekaya et al., 2017), and Zn and Sr ions (Lin et al., 2008; Wang et al., 2012), which had a negative effect on *E. coli* and *S. aureus* adherence. Such differences were not observed on the scaffolds cultured in liquid medium, which can be related to the type of bacterial culture used in each assay, namely the different proximity of cells to the scaffolds surface at the time of incubation. Also, the different scaffolds composition had no effects on the adherence of the different bacterial species, despite their distinctive morphologies and cell membranes (Sonohara et al., 1995). However, the shape modifications and cell debris detected in some the adhered bacteria indicate that at some point the proposed scaffolds may play a desired antibacterial effect. Despite the significant reduction in OD of *S. aureus* incubated in the presence of the HRP-SF and MTCP scaffolds (**Figure 6A**), both bacteria presented a high viability (>70% OD) after 24 h of culture in liquid medium and in the presence of the structures (Sonohara et al., 1995). This result can be related to the low release profile from the scaffolds, as shown by the zero-order OD values detected in the controls without bacteria and confirmed that within 24 h no clear biocide effects were induced by the structures despite the bacterial adherence and biofilm formation was prevented. Thus, this can be a valuable approach when hierarchical scaffolds envisioning orthopedic applications are needed, since it can possibly prevent the initial bacterial adhesion to the implanted devices.

CONCLUSION

In this study, the failure behavior under combined compression-shear loading and antibacterial properties of hierarchical scaffolds fully integrating a HRP-SF cartilage-like layer and a HRP-SF/ZnSrTCP subchondral bone-like layer, were assessed. The hierarchical scaffolds presented appropriate ability to support compression and shear loading for OC tissue, with a tendency of improved mechanical properties for the ZnSr-doped scaffolds. The low adherence and absence of biofilm formation on the scaffolds surface using *E. coli* and *S. aureus* have shown that the proposed scaffolds are able to prevent bacterial infections associated with surgical implants. Further studies are necessary to optimize the amount of ZnSr-doped β-TCP on the scaffolds in order to yield more pronounced anti-bacterial effects.

DATA AVAILABILITY STATEMENT

The datasets generated for this study are available on request to the corresponding author.

AUTHOR CONTRIBUTIONS

VR and SP: conceptualization and writing – original draft preparation. VR, SP, AA, and SG: methodology and investigation. SP, SG, RR, and JO: writing – review and editing. JO: supervision. RR and JO: funding administration. All authors agreed to be accountable for the work and to ensure that any questions relating to the accuracy and integrity of the manuscript are investigated and properly resolved.

FUNDING

This research was funded by the Portuguese Foundation for Science and Technology for the Hierarchitech project (M-era-Net/0001/2014), and by the Research and Innovation Staff Exchanges (RISE) action (H2020 Marie Skłodowska-Curie actions) for the BAMOS project (H2020-MSCA-RISE-2016-734156). The authors also thank the funds provided under the distinctions attributed to JO (IF/01285/2015) and SP (CEECIND/03673/2017).

REFERENCES

Bastos, R., Mathias, M., Andrade, R., Amaral, R. J. F. C., Schott, V., Balduino, A., et al. (2019). Intra-articular injection of culture-expanded mesenchymal stem cells with or without addition of platelet-rich plasma is effective in decreasing pain and symptoms in knee osteoarthritis: a controlled, double-blind clinical trial. *Knee Surg. Sports Traumatol. Arthrosc.* doi: 10.1007/s00167-019-05732-8 [Epub ahead of print].

Blaker, J. J., Maquet, V., Jérôme, R., Boccaccini, A. R., and Nazhat, S. N. (2005). Mechanical properties of highly porous PDLLA/Bioglass® composite foams as scaffolds for bone tissue engineering. *Acta Biomater.* 1, 643–652. doi: 10.1016/j.actbio.2005.07.003

Bose, S., Fielding, G., Tarafder, S., and Bandyopadhyay, A. (2013). Trace element doping in calcium phosphate ceramics to understand osteogenesis and angiogenesis. *Trends Biotechnol.* 31, 594–605. doi: 10.1016/j.tibtech.2013.06.005

Calamak, S., Aksoy, E. A., Ertas, N., Erdogdu, C., Sagıroglu, M., and Ulubayram, K. (2015). Ag/silk fibroin nanofibers: effect of fibroin morphology on Ag+ release and antibacterial activity. *Euro. Polym. J.* 67, 99–112. doi: 10.1016/j.eurpolymj.2015.03.068

Çalamak, S., Erdoğdu, C., Özalp, M., and Ulubayram, K. (2014). Silk fibroin based antibacterial bionanotextiles as wound dressing materials. *Mater. Sci. Eng. C Mater. Biol. Appl.* 43, 11–20. doi: 10.1016/j.msec.2014.07.001

Chung, R.-J., Hsieh, M.-F., Huang, C.-W., Perng, L.-H., Wen, H.-W., and Chin, T.-S. (2006). Antimicrobial effects and human gingival biocompatibility of hydroxyapatite sol–gel coatings. *J. Biomed. Mater. Res. B Appl. Biomater.* 76, 169–178. doi: 10.1002/jbm.b.30365

Darouiche, R. O. (2004). Treatment of infections associated with surgical implants. *New Engl. J. Med.* 350, 1422–1429. doi: 10.1056/nejmra035415

De L'Escalopier, N., Barbier, O., Mainard, D., Mayer, J., Ollat, D., and Versier, G. (2015). Outcomes of talar dome osteochondral defect repair using

osteocartilaginous autografts: 37 cases of Mosaicplasty®. *Orthop. Traumatol. Surg. Res.* 101, 97–102. doi: 10.1016/j.otsr.2014.11.006

Devitt, B. M., Bell, S. W., Webster, K. E., Feller, J. A., and Whitehead, T. S. (2017). Surgical treatments of cartilage defects of the knee: systematic review of randomised controlled trials. *Knee* 24, 508–517. doi: 10.1016/j.knee.2016.12.002

Drury, J. L., and Mooney, D. J. (2003). Hydrogels for tissue engineering: scaffold design variables and applications. *Biomaterials* 24, 4337–4351. doi: 10.1016/s0142-9612(03)00340-5

Ewald, A., Hösel, D., Patel, S., Grover, L. M., Barralet, J. E., and Gbureck, U. (2011). Silver-doped calcium phosphate cements with antimicrobial activity. *Acta Biomater.* 7, 4064–4070. doi: 10.1016/j.actbio.2011.06.049

Fielding, G., and Bose, S. (2013). SiO(2) and ZnO Dopants in 3D Printed TCP scaffolds enhances osteogenesis and angiogenesis in vivo. *Acta Biomater.* 9, 9137–9148. doi: 10.1016/j.actbio.2013.07.009

Fomin, A., Barinov, S., Ievlev, V., Smirnov, V., Mikhailov, B., Belonogov, E., et al. (2008). Nanocrystalline hydroxyapatite ceramics produced by low-temperature sintering after high-pressure treatment. *Doklady Chem.* 418, 22–25. doi: 10.1134/s0012500808010084

Gokcekaya, O., Ueda, K., Ogasawara, K., Kanetaka, H., and Narushima, T. (2017). In vitro evaluation of Ag-containing calcium phosphates: effectiveness of Ag-incorporated β-tricalcium phosphate. *Mater. Sci. Eng. C* 75, 926–933. doi: 10.1016/j.msec.2017.02.059

Guilak, F., Butler, D. L., and Goldstein, S. A. (2001). Functional tissue engineering: the role of biomechanics in articular cartilage repair. *Clin. Orthop. Relat. Res.* 391, S295–S305.

Holsgrove, T. P., Miles, A. W., and Gheduzzi, S. (2017). The application of physiological loading using a dynamic, multi-axis spine simulator. *Med. Eng. Phys.* 41, 74–80. doi: 10.1016/j.medengphy.2016.12.004

Huo, K., Zhang, X., Wang, H., Zhao, L., Liu, X., and Chu, P. K. (2013). Osteogenic activity and antibacterial effects on titanium surfaces modified with Zn-incorporated nanotube arrays. *Biomaterials* 34, 3467–3478. doi: 10.1016/j.biomaterials.2013.01.071

Hutmacher, D. W. (2006). "Scaffolds in tissue engineering bone and cartilage," in *The Biomaterials: Silver Jubilee Compendium*, ed. D. F. Williams (Amsterdam: Elsevier).

Ji, W., Yang, F., Seyednejad, H., Chen, Z., Hennink, W. E., Anderson, J. M., et al. (2012). Biocompatibility and degradation characteristics of PLGA-based electrospun nanofibrous scaffolds with nanoapatite incorporation. *Biomaterials* 33, 6604–6614. doi: 10.1016/j.biomaterials.2012.06.018

Jin, Y., Kundu, B., Cai, Y., Kundu, S. C., and Yao, J. (2015). Bio-inspired mineralization of hydroxyapatite in 3D silk fibroin hydrogel for bone tissue engineering. *Colloids Surf. B Biointerfaces* 134, 339–345. doi: 10.1016/j.colsurfb.2015.07.015

Kandaz, M., Ertekin, M. V., Erdemci, B., Kı Zı ltunç, A., Koçer, Í, Özmen, H. K., et al. (2009). The effects of zinc sulfate on the levels of some elements and oxidative stress occurring in lenses of rats exposed to total cranium radiotherapy. *Eurasian J. Med.* 41, 110–115.

Kang, H., Zeng, Y., and Varghese, S. (2018). Functionally graded multilayer scaffolds for in vivo osteochondral tissue engineering. *Acta Biomater.* 78, 365–377. doi: 10.1016/j.actbio.2018.07.039

Kannan, S., Goetz-Neunhoeffer, F., Neubauer, J., and Ferreira, J. M. F. (2008). Ionic substitutions in biphasic hydroxyapatite and beta-tricalcium phosphate mixtures: structural analysis by rietveld refinement. *J. Am. Ceram. Soc.* 91, 1–12. doi: 10.1111/j.1551-2916.2007.02117.x

Kannan, S., Goetz-Neunhoeffer, F., Neubauer, J., and Ferreira, J. M. F. (2009). Synthesis and structure refinement of zinc-doped beta-tricalcium phosphate powders. *J. Am. Ceram. Soc.* 92, 1592–1595. doi: 10.1111/j.1551-2916.2009.03093.x

Kannan, S., Goetz-Neunhoeffer, F., Neubauer, J., Pina, S., Torres, P. M. C., and Ferreira, J. M. F. (2010). Synthesis and structural characterization of strontium- and magnesium-co-substituted β-tricalcium phosphate. *Acta Biomater.* 6, 571–576. doi: 10.1016/j.actbio.2009.08.009

Karahaliloglu, Z., Kilicay, E., and Denkbas, E. B. (2017). Antibacterial chitosan/silk sericin 3D porous scaffolds as a wound dressing material. *Artif. Cells Nanomed. Biotechnol.* 45, 1172–1185. doi: 10.1080/21691401.2016.1203796

Kundu, B., Rajkhowa, R., Kundu, S. C., and Wang, X. (2013). Silk fibroin biomaterials for tissue regenerations. *Adv. Drug Deliv. Rev.* 65, 457–470. doi: 10.1016/j.addr.2012.09.043

Lin, Y., Yang, Z., Cheng, J., and Wang, L. (2008). Synthesis, characterization and antibacterial property of strontium half and totally substituted hydroxyapatite nanoparticles. *J. Wuhan Univ. Technol. Mater. Sci. Ed.* 23, 475–479. doi: 10.1007/s11595-006-4475-2

Malafaya, P. B., Silva, G. A., and Reis, R. L. (2007). Natural–origin polymers as carriers and scaffolds for biomolecules and cell delivery in tissue engineering applications. *Adv. Drug Deliv. Rev.* 59, 207–233. doi: 10.1016/j.addr.2007.03.012

Marelli, B., Ghezzi, C. E., Alessandrino, A., Barralet, J. E., Freddi, G., and Nazhat, S. N. (2012). Silk fibroin derived polypeptide-induced biomineralization of collagen. *Biomaterials* 33, 102–108. doi: 10.1016/j.biomaterials.2011.09.039

Martin, I., Miot, S., Barbero, A., Jakob, M., and Wendt, D. (2007). Osteochondral tissue engineering. *J. Biomech.* 40, 750–765.

Matsumoto, N., Sato, K., Yoshida, K., Hashimoto, K., and Toda, Y. (2009). Preparation and characterization of β-tricalcium phosphate co-doped with monovalent and divalent antibacterial metal ions. *Acta Biomater.* 5, 3157–3164. doi: 10.1016/j.actbio.2009.04.010

Mayer, I., Cuisinier, F. J. G., Gdalya, S., and Popov, I. (2008). Tem study of the morphology of Mn2+-doped calcium hydroxyapatite and β-tricalcium phosphate. *J. Inorg. Biochem.* 102, 311–317. doi: 10.1016/j.jinorgbio.2007.09.004

Melke, J., Midha, S., Ghosh, S., Ito, K., and Hofmann, S. (2016). Silk fibroin as biomaterial for bone tissue engineering. *Acta Biomater.* 31, 1–16. doi: 10.1016/j.actbio.2015.09.005

Mestres, G., Le Van, C., and Ginebra, M.-P. (2012). Silicon-stabilized α-tricalcium phosphate and its use in a calcium phosphate cement: characterization and cell response. *Acta Biomater.* 8, 1169–1179. doi: 10.1016/j.actbio.2011.11.021

Neut, D., Van Horn, J. R., Van Kooten, T. G., Van Der Mei, H. C., and Busscher, H. J. (2003). Detection of biomaterial-associated infections in orthopaedic joint implants. *Clin. Orthop. Relat. Res.* 413, 261–268. doi: 10.1097/01.blo.0000073345.50837.84

O'hara, L. M., Thom, K. A., and Preas, M. A. (2018). Update to the centers for disease control and prevention and the healthcare infection control practices advisory committee guideline for the prevention of surgical site infection (2017): a summary, review, and strategies for implementation. *Am. J. Infect. Control* 46, 602–609. doi: 10.1016/j.ajic.2018.01.018

Oliveira, M. B., and Mano, J. F. (2015). "Natural—based and stimuli—responsive polymers for tissue engineering and regenerative medicine," in *Polymers in Regenerative Medicine: Biomedical Applications from Nano-to Macro-Structures*, eds M. M. Pradas and M. J. Vicent (Hoboken, NJ: John Wiley & Sons, Inc.), 49–90. doi: 10.1002/9781118356692.ch2

Pina, S., Canadas, R., Jiménez, G., Perán, M., Marchal, J., Reis, R., et al. (2017). Biofunctional ionic-doped calcium phosphates: silk fibroin composites for bone tissue engineering scaffolding. *Cells Tissues Organs* 204, 150–163. doi: 10.1159/000469703

Pina, S., Rebelo, R., Correlo, V. M., Oliveira, J. M., and Reis, R. L. (2018). "Bioceramics for osteochondral tissue engineering and regeneration," in *Osteochondral Tissue Engineering: Nanotechnology, Scaffolding-Related Developments and Translation*, eds J. M. Oliveira, S. Pina, J. S. Roman, and R. L. Reis (New York, NY: Springer International Publishing AG), 53–75. doi: 10.1007/978-3-319-76711-6_3

Pina, S., Vieira, S. I., Rego, P., Torres, P. M. C., Goetz-Neunhoeffer, F., Neubauer, J., et al. (2010). Biological responses of brushite-forming Zn- and ZnSr-substituted β-TCP bone cements. *Eur. Cell Mater.* 20, 162–177. doi: 10.22203/ecm.v020a14

Ribeiro, V. P., Da Silva Morais, A., Maia, F. R., Canadas, R. F., Costa, J. B., Oliveira, A. L., et al. (2018a). Combinatory approach for developing silk fibroin scaffolds for cartilage regeneration. *Acta Biomater.* 72, 167–181. doi: 10.1016/j.actbio.2018.03.047

Ribeiro, V. P., Pina, S., Canadas, R. F., Morais, A. D. S., Vilela, C., Vieira, S., et al. (2019a). In vivo performance of hierarchical HRP-crosslinked silk fibroin/β-TCP scaffolds for osteochondral tissue regeneration. *Regen. Med. Front.* 1:e190007. doi: 10.20900/rmf20190007

Ribeiro, V. P., Pina, S., Costa, J. B., Cengiz, I. F., García-Fernández, L., Fernaìndez-Gutieìrrez, M. D. M., et al. (2019b). Enzymatically cross-linked silk fibroin-based hierarchical scaffolds for osteochondral regeneration. *ACS Appl. Mater. Interfaces* 11, 3781–3799. doi: 10.1021/acsami.8b21259

Ribeiro, V. P., Silva-Correia, J., Gonçalves, C., Pina, S., Radhouani, H., Montonen, T., et al. (2018b). Rapidly responsive silk fibroin hydrogels as an artificial matrix for the programmed tumor cells death. *PLoS One* 13:e0194441. doi: 10.1371/journal.pone.0194441

Sabree, I., Gough, J. E., and Derby, B. (2015). Mechanical properties of porous ceramic scaffolds: influence of internal dimensions. *Ceram. Int.* 41, 8425–8432. doi: 10.1016/j.ceramint.2015.03.044

Saidak, Z., and Marie, P. J. (2012). Strontium signaling: molecular mechanisms and therapeutic implications in osteoporosis. *Pharmacol. Ther.* 136, 216–226. doi: 10.1016/j.pharmthera.2012.07.009

Sonohara, R., Muramatsu, N., Ohshima, H., and Kondo, T. (1995). Difference in surface properties between *Escherichia coli* and *Staphylococcus aureus* as revealed by electrophoretic mobility measurements. *Biophys. Chem.* 55, 273–277. doi: 10.1016/0301-4622(95)00004-h

Stanić, V., Dimitrijević, S., Antić-Stanković, J., Mitrić, M., Jokić, B., Plećaš, I. B., et al. (2010). Synthesis, characterization and antimicrobial activity of copper and zinc-doped hydroxyapatite nanopowders. *Appl. Surf. Sci.* 256, 6083–6089. doi: 10.1016/j.apsusc.2010.03.124

Thian, E. S., Konishi, T., Kawanobe, Y., Lim, P. N., Choong, C., Ho, B., et al. (2013). Zinc-substituted hydroxyapatite: a biomaterial with enhanced bioactivity and antibacterial properties. *J. Mater. Sci. Mater. Med.* 24, 437–445. doi: 10.1007/s10856-012-4817-x

Vetsch, J. R., Paulsen, S. J., Müller, R., and Hofmann, S. (2015). Effect of fetal bovine serum on mineralization in silk fibroin scaffolds. *Acta Biomater.* 13, 277–285. doi: 10.1016/j.actbio.2014.11.025

Wang, C., Liu, L.-L., Zhang, A.-T., Xie, P., Lu, J.-J., and Zou, X.-T. (2012). Antibacterial effects of zinc oxide nanoparticles on *Escherichia coli* K88. *Afr. J. Biotechnol.* 11, 10248–10254.

Wang, L., Cao, W., Wang, X., Li, P., Zhou, J., Zhang, G., et al. (2019). Biodegradable silver-loaded polycation modified nanodiamonds/polyurethane scaffold with improved antibacterial and mechanical properties for cartilage tissue repairing. *J. Mater. Sci. Mater. Med.* 30:41. doi: 10.1007/s10856-019-6244-8

Wang, W., Ouyang, Y., and Poh, C. K. (2011). Orthopaedic implant technology: biomaterials from past to future. *Ann. Acad. Med. Singapore* 40, 237–244.

Wang, X., Kim, H. J., Wong, C., Vepari, C., Matsumoto, A., and Kaplan, D. L. (2006). Fibrous proteins and tissue engineering. *Mater. Today* 9, 44–53. doi: 10.1016/s1369-7021(06)71742-4

Wang, Y., Rudym, D. D., Walsh, A., Abrahamsen, L., Kim, H.-J., Kim, H. S., et al. (2008). In vivo degradation of three-dimensional silk fibroin scaffolds. *Biomaterials* 29, 3415–3428. doi: 10.1016/j.biomaterials.2008.05.002

Yan, L.-P., Silva-Correia, J., Ribeiro, V. P., Miranda-Gonçalves, V., Correia, C., Da Silva Morais, A., et al. (2016). Tumor growth suppression induced by biomimetic silk fibroin hydrogels. *Sci. Rep.* 6:31037. doi: 10.1038/srep31037

Yashima, M., Sakai, A., Kamiyama, T., and Hoshikawa, A. (2003). Crystal structure analysis of β-tricalcium phosphate Ca3(Po4)2 by neutron powder diffraction. *J. Solid State Chem.* 175, 272–277. doi: 10.1016/s0022-4596(03)00279-2

Yousefi, A. M., Hoque, M. E., Prasad, R. G., and Uth, N. (2015). Current strategies in multiphasic scaffold design for osteochondral tissue engineering: a review. *J. Biomed. Mater. Res. A* 103, 2460–2481. doi: 10.1002/jbm.a.35356

Zhang, W., Ouyang, H., Dass, C. R., and Xu, J. (2016). Current research on pharmacologic and regenerative therapies for osteoarthritis. *Bone Res.* 4:15040. doi: 10.1038/boneres.2015.40

Zhang, Y., Zhai, D., Xu, M., Yao, Q., Zhu, H., Chang, J., et al. (2017). 3D-printed bioceramic scaffolds with antibacterial and osteogenic activity. *Biofabrication* 9:025037. doi: 10.1088/1758-5090/aa6ed6

Conflict of Interest: The authors declare that the research was conducted in the absence of any commercial or financial relationships that could be construed as a potential conflict of interest.

frontiers in Bioengineering and Biotechnology

ORIGINAL RESEARCH
published: 20 March 2020
doi: 10.3389/fbioe.2020.00231

Surface Analysis of Native Spider Draglines by FE-SEM and XPS

Hiromitsu Sogawa[1†], Kyohei Nakano[2†], Ayaka Tateishi[1], Keisuke Tajima[2] and Keiji Numata[1]*

[1] Biomacromolecules Research Team, RIKEN Center for Sustainable Resource Science, Saitama, Japan, [2] Emergent Functional Polymers Research Team, RIKEN Center for Emergent Matter Science, Saitama, Japan

Although the physical and biological functions of the skin layer of spider dragline have been studied and partially clarified, the morphology and elemental contents of the skin layer of silk fibers have not been investigated in detail to date. Here, the surface of *Nephila clavata* spider dragline was evaluated by field emission scanning electron microscopy (FE-SEM) and X-ray photoelectron spectroscopy (XPS) to obtain clear surface morphological and molecular information. The FE-SEM images of the spider dragline indicate that the spider dragline forms a bundle of microfibrils. This hierarchical structure might induce faint fibrilar and network-like patterns on the surface of the dragline. XPS analysis revealed the presence of Na, P, and S, which are reasonably explained by considering the biological components of the major ampullate gland of spiders. The results obtained here are preliminary but will be important to consider the molecular transition of silk proteins to form excellent hierarchical structures during the spider dragline spinning process.

Keywords: spider dragline, silkworm, silk fiber, FE-SEM, XPS, surface analysis

OPEN ACCESS

Edited by:
Nicola Maria Pugno, University of Trento, Italy

Reviewed by:
Joanna Mystkowska, Białystok Technical University, Poland
Gregory P. Holland, San Diego State University, United States

***Correspondence:**
Keiji Numata
keiji.numata@riken.jp

† These authors have contributed equally to this work

Specialty section:
This article was submitted to Biomaterials, a section of the journal Frontiers in Bioengineering and Biotechnology

Received: *14 September 2019*
Accepted: *05 March 2020*
Published: *20 March 2020*

Citation:
Sogawa H, Nakano K, Tateishi A, Tajima K and Numata K (2020) Surface Analysis of Native Spider Draglines by FE-SEM and XPS. Front. Bioeng. Biotechnol. 8:231. doi: 10.3389/fbioe.2020.00231

INTRODUCTION

Silk fibers are well known as tough biomaterials, especially spider dragline silk, which possesses excellent toughness due to a combination of great tensile strength and ductility (Blackledge, 2012; Holland et al., 2018). The physical properties of dragline silk fibers depend not solely on protein constituents but also on the hierarchical microstructure (Sponner et al., 2007; Heim et al., 2010). Previously, it was hypothesized that the hierarchical structure of spider silk fiber is similar to that of silkworm silk fiber (Gosline et al., 1986; Vollrath, 1992). However, a highly organized skin-core structure of spider silk fiber was observed by atomic force microscopy (Li S.F. et al., 1994; Li S.F.Y. et al., 1994; Brown et al., 2012; Faugas et al., 2013) and light and electron microscopy (Thiel et al., 1994; Vollrath et al., 1996; Frische et al., 1998; Shao et al., 1999; Augsten et al., 2000), and this structure was different from the proposed structure of silkworm silk fiber (Gosline et al., 1986; Vollrath, 1992). Supercontracted spider silk fiber and the phenomenon of "supercontraction" were also used to investigate a structural hypothesis consisting of a fibril core surrounding an outer thin layer (Vollrath et al., 1996; Faugas et al., 2013). An experimental procedure to separate the different skin layers of dragline fibers has been developed (Sponner et al., 2007; Yazawa et al., 2019), and the results indicate that the order of the multilayer organization from exterior to interior is as follows: lipid coat, glycoprotein, skin, outer core, and inner core (Sponner et al., 2007). Additionally, Riekel et al. reported that the surface of the spider dragline consists of highly oriented protein chains

forming an approximately 100 nm skin layer based on scanning transmission X-ray diffraction measurements (Rousseau et al., 2007; Riekel et al., 2017).

The skin layer is also important for the gas barrier properties of silk fibers. The mechanical and physical properties of spider dragline and silkworm silk fibers are known to depend on the humidity; namely, the amorphous and crystalline regions are influenced by water molecules (Fu et al., 2009; Yazawa et al., 2016; Malay et al., 2017). Spider dragline is a composite of multiple biopolymers that consists of a protein core surrounded by outer skin layers. Recently, we investigated the skin layer of *Nephila* spider dragline, especially the biological and physical functions of the skin layers (Yazawa et al., 2019). The mechanical/physical properties as well as the crystal structures do not depend significantly on the skin constituents, suggesting that the protein core region of spider dragline determines the structural and mechanical properties. Surprisingly, the skin layer does not influence supercontraction, i.e., the layer does not have water vapor barrier properties, but does protect the fiber from protease degradation activity. This result implies that the skin layer is more important as a biological barrier than a physical barrier.

Although the physical and biological functions of the skin layer of spider dragline have been studied and partially clarified, the morphological and elemental characterizations of the skin layer of silk fibers have not been investigated in detail to date. Here, the surface of the *Nephila clavata* spider dragline was evaluated by field emission scanning electron microscopy (FE-SEM) and X-ray photoelectron spectroscopy (XPS) to obtain clear surface morphological and molecular information.

EXPERIMENTAL

Collection and Preparation of Spider Dragline

Spider draglines (silk fibers) were collected from *Nephila clavata* females (body sizes: approximately 25 mm). Draglines were reeled at 21 mm/s and kept in lightproof boxes at a relative humidity from 30 to 50% to prevent UV damage and drying of the silk fibers.

Preparation of Spider Silk Fibers Without a Skin Layer

The removal of the skin layer was conducted according to a previously reported method (Sponner et al., 2007; Yazawa et al., 2019). Briefly, *N. clavata* spider dragline silk fibers were immersed twice in diethyl ether for 10 min. To remove the diethyl ether, the fibers were dried overnight in a vacuum oven at 40°C.

Field Emission Scanning Electron Microscopy

The surface morphology of the spider dragline was observed and characterized by field emission scanning electron microscopy (FE-SEM, GeminiSEM, Carl Zeiss, Oberkochen, Germany). The silk fiber samples were mounted on an aluminum stub with conductive tape without sputter-coating prior to FE-SEM visualization. For the observation, the acceleration voltage and working distance were set at 0.5–1.0 kV and 2.0 mm, respectively.

Enzymatic Treatment

For the enzymatic treatment, we used the native draglines without the diethyl ether wash. The native draglines were immersed in 0.1 M phosphate buffer (pH = 7.4) containing 0.5 mg/mL of proteinase K. Less than 1 mg of spider dragline was immersed in 1 mL of the enzyme solution at 37°C for 24 h. The enzymatic degradation conditions were determined based on previous reports on enzymatic degradation (Li et al., 2003; Numata et al., 2005, 2008, 2010; Numata and Kaplan, 2010). After the enzymatic treatment, the sample was washed with 0.1 M phosphate buffer and Milli-Q water twice and dried for 1 day under vacuum conditions.

XPS Measurements

X-ray photoelectron spectroscopy (XPS) was performed with a photoelectron spectroscopy system (PHI 5000 Versa Probe II, ULVAC-PHI). Monochromated Al Kα (1486.6 eV) radiation with an operating power of 50 W (15 kV voltage) was used in all the XPS measurements. The analyzed area was 200 μm. The XPS survey spectra (**Figure 3B**) were measured with a pass energy of 117.4 and 0.125 eV energy step. For the measurement of each atomic element, pass energy of 23.5 and 0.025 eV energy steps were used. The recorded signals were accumulated eight times for C1s, O1s, and twelve times for other elements. A take-off angle was 45° to the sample substrate. During the measurement, the samples were neutralized using both a low-energy ion beam and a low-energy electron beam.

For data analysis, we used PHI MultiPak software (ULVAC-PHI). The signal background of each component was subtracted using the Shirley method. The atomic concentration was calculated by considering the relative sensitivity factor for each element corrected with the sensitivity factor of the system. The

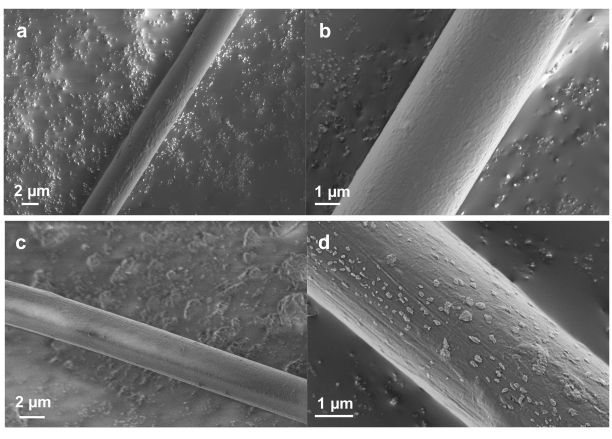

FIGURE 1 | FE-SEM images showing the surface of silk fibers at different magnifications. **(a,b)** Native *Nephila* spider dragline. **(c,d)** *Nephila* spider dragline after ether extraction.

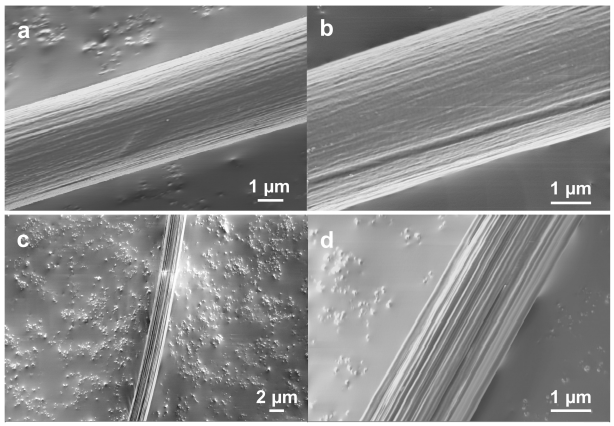

FIGURE 2 | FE-SEM images showing the surface of *Nephila* spider dragline after proteinase-K treatment. **(b,d)** Are enlarged images of **(a,c)**, respectively.

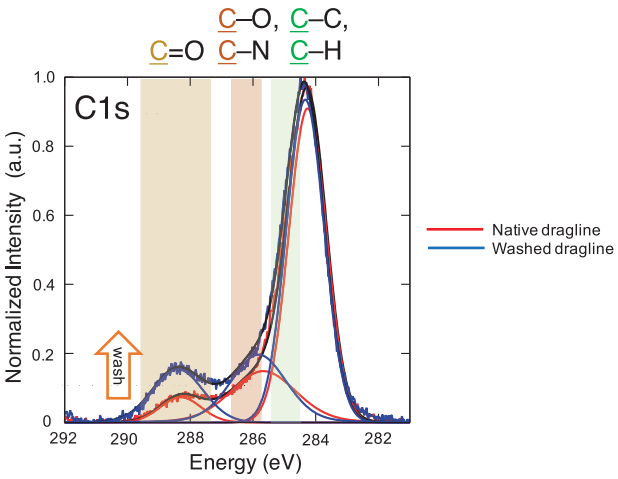

FIGURE 4 | XPS spectra of the native spider dragline (red) and spider dragline after washing with ether (blue). The peak fitting results are also shown in the same color. The details on the peak fitting is described in Experimental section.

fitting protocol used the Gaussian-Lorentzian function, but the best fit results were obtained with Gaussian 100%.

RESULTS AND DISCUSSION

FE-SEM Observations of Silk Fibers

FE-SEM observations have several advantages over general SEM imaging. In this study, direct imaging of a single dragline without a sputter-coating process was conducted to observe the surface morphology at high resolution. **Figure 1** shows the typical FE-SEM images of the native *Nephila* dragline and the dragline without a skin layer. In previous literature with SEM imaging (Lin et al., 2017; Yazawa et al., 2019), the surface of spider draglines has been reported to be smooth and clean. However, we found with FE-SEM that the surface of the *Nephila* spider dragline has fibril and network-like patterns (**Figure 1b**). Once the silk layer was washed out with ether, the patterns disappeared, but debris from the skin layer was observed at the fiber surface (**Figures 1c,d**). The white spots indicate the residues of the lipid layer, which is the outermost layer of dragline silk. As a comparison, the surface morphologies of silkworm silk, which were previously reported and summarized, were referenced (Malay et al., 2016). In many cases, inorganic compounds have been observed on the surface of silkworm cocoon silk fibers (Numata et al., 2015). These previous reports on the surface morphologies of silkworm silks differ from the patterns found on the surface of the spider dragline. In this study, the silk fibers were not pretreated for FE-SEM imaging, and hence, the surface morphologies should not be induced by the sample treatment. Therefore, the natural spider dragline seems to show characteristic fibril and network-like patterns. The patterns might be related to the spinning process of spiders, especially the final part around the spinneret.

Enzymatic Treatment

To further examine the surface morphologies, especially the fibril and network-like patterns, we studied the morphological changes of the native *Nephila* spider dragline after enzymatic treatment with proteinase K. We treated the spider dragline with

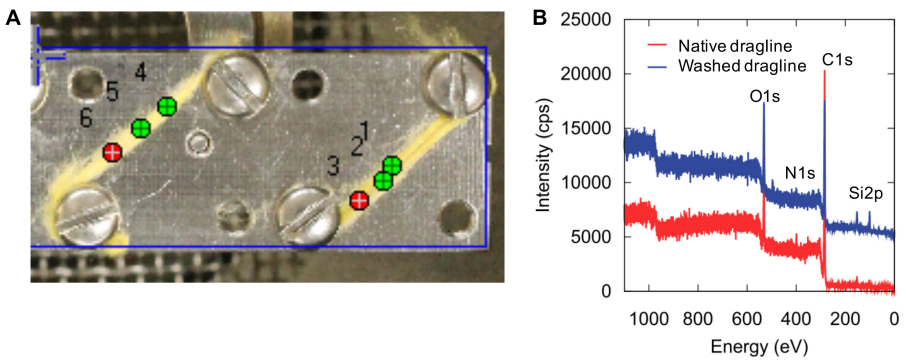

FIGURE 3 | XPS sample setting **(A)** and wide-scan spectra **(B)** of native spider dragline (red) and spider dragline after ether wash (blue).

proteinase K (without any diethyl ether treatment), an efficient protease, and subsequently observed the dragline by FE-SEM (**Figure 2**). To avoid misunderstanding of the biodegradability of the spider dragline, we need to clear the biodegradability of spider dragline, according to the previous study (Yazawa et al., 2019). Yazawa et al. (2019) reported that the skin layer of the dragline can protect the dragline from the enzymatic attacks. Proteinase K, which was found in extracts of the fungus *Engyodontium album*, is a serine protease with a broad substrate specificity and high activity against aliphatic and aromatic amino acids. The biodegradation of the spider dragline by proteinase K is not expected in the natural environments, because *Nephila* spider does not prefer to construct web and territories in the environments contaminated with fungi.

The enzymatic degradation behavior of the dragline was not consistent, as **Figures 2a,c** show different degradation degrees of the draglines. **Figures 2a,b** clearly shows that the dragline consists of a bundle of microfibrils. Furthermore, **Figures 2c,d** indicates that the bundle structures of microfibrils are maintained even inside of the dragline. Thus, both FE-SEM images indicate that the spider dragline forms a structure similar to a bundle of microfibrils. The enzymatic treatment degraded the skin layer and silk fibroins of the native draglines, resulting that these microfibrils were exposed and observed by FE-SEM. This hierarchical structure might induce faint fibril patterns at the surface of the dragline, however, we need to further study the effect of the natural spinning process with spider spinnerets.

XPS Measurements

XPS is a powerful method for characterizing the surface chemical composition and chemical states of each element. An XPS study of recombinant silk protein during a thermal degradation process was reported previously (Dao et al., 2017), but natural spider draglines have not been investigated to date. **Figure 3** shows the setting of the fiber samples and the wide-range XPS spectra of the native dragline and the dragline washed with diethyl ether for skin layer removal. The peaks originating from silicon were

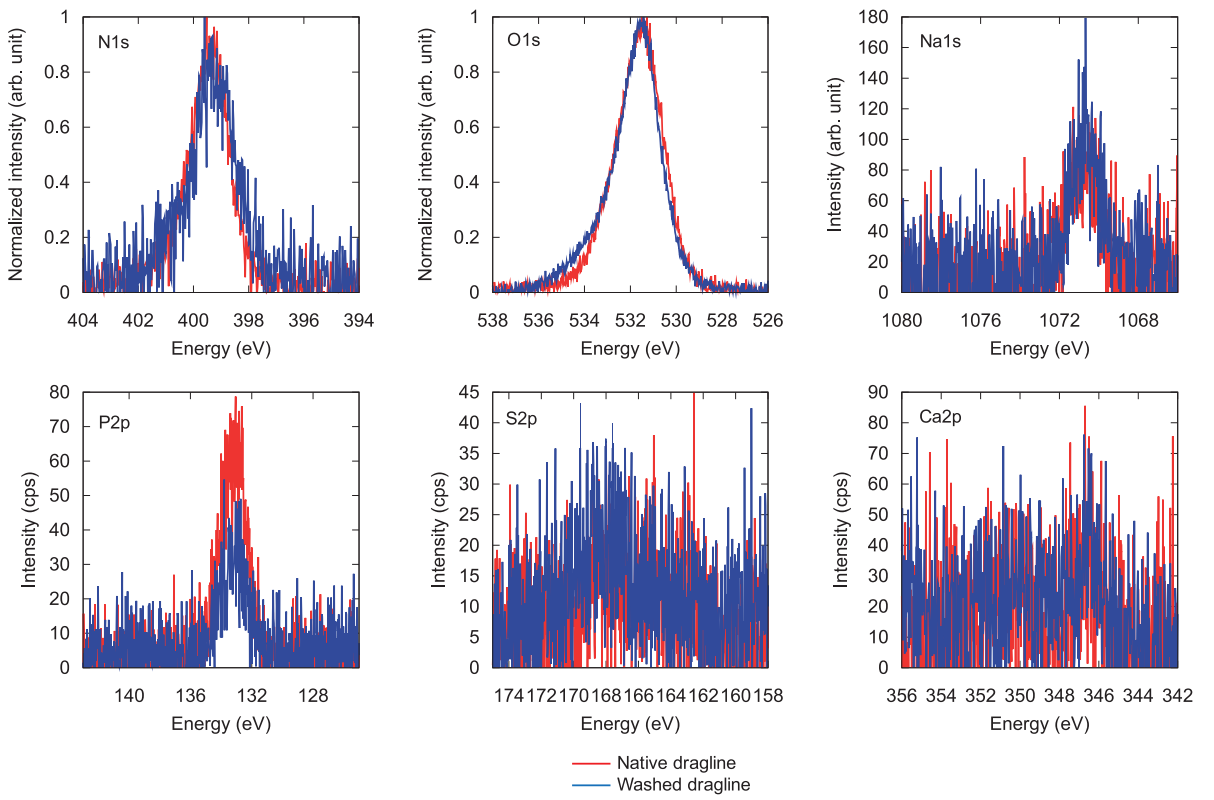

FIGURE 5 | XPS spectra for different elements in native spider dragline (red) and spider dragline after an ether wash (blue).

TABLE 1 | XPS characterization of different elements and components of native spider dragline and spider dragline after an ether wash.

% (Standard deviation)	C 1s C-H	C 1s C = O	C 1s C-O	N 1s	O 1s	Na 1s	P 2p	S 2p	Ca 2p
Native dragline	60.1 (6.3)	6.8 (2.3)	16.0 (2.5)	2.8 (1.4)	8.8 (2.7)	1.2 (0.7)	0.68 (0.06)	0.53 (0.16)	0.75 (0.45)
Washed dragline	50.1 (2.6)	8.2 (2.1)	16.3 (3.2)	2.4 (0.1)	13.5 (3.7)	1.4 (0.5)	0.48 (0.25)	0.74 (0.08)	1.0 (0.53)

Numbers in parentheses are standard deviations in results obtained three different measurement positions.

unexpected contamination from the washing experiment. We could not detect potassium in the wide-range XPS spectra, even though the presence of potassium is expected according to the previous ionic elemental analyses of the major ampullate glands (Knight and Vollrath, 2001; Andersson et al., 2014; Oktaviani et al., 2019). Perhaps, potassium might not be localized at the surface of the dragline. On the other hand, O 1s, C 1s, and N 1s were obviously detected as shown in **Figures 4**, **5**.

The spectra concerning C 1s were further assigned as shown in **Figure 4**, namely, C = O, C-O/C-N, and C-C/C-H. The XPS spectra were deconvoluted with the Gaussian–Lorentzian mixed function to resolve multiple chemical states, as listed in **Table 1**. The standard deviations of the contents include all the errors from the variation of the atomic concentration of the samples, positional accuracy of the fitting, and also from the equipment itself. We think the primary origin of the deviation might be the variation of the samples themselves because our samples are natural ones. The increase in C = O content suggests the appearance of peptide bonds at the surface after the washing process. The removal of the lipid layer via the diethyl ether treatment was successfully detected by XPS. Thus, the XPS measurements with spider draglines indicated sufficient quantification to discuss the surface chemical compositions.

Figure 5 shows each spectrum corresponding to N 1s, O 1s, Na 1s, P 2p, S 2p, and Ca 2p. Only phosphate, P 2p, decreased in intensity after the skin layer removal. Considering that phosphate ions exist in the overall ampullate gland of spiders (Andersson et al., 2014; Oktaviani et al., 2019), the skin layer may contain more phosphate ions than the protein core inside the dragline. The peak corresponding to calcium, Ca 2p, could be background noise because of the abundant presence of calcium ions in the natural environment. The other elements, N 1s, O 1s, Na 1s, and S 2p, did not show any significant change before and after the skin removal treatment. Sodium should be related to the ionic conditions of the spider ampullate gland, but we could not find any related difference between the skin layer and core regions. The S 2p peak, which can be related to sulfate ions and the cysteines of spider silk proteins, was detected even though its intensity and signal-to-noise ratio were very low. The sulfate ion is kosmotropic and can be present at the end of the spider major ampullate gland to form the dragline; hence, it is reasonable to detect the S 2p peak by XPS. However, we gave up discussing more details of the S 2p peak, due to the relatively low intensity. The Ca 2p peak can be related to Ca ions, which are predominantly present under the natural environments. Similar to the S 2p peak, we avoid to discuss the more details of the Ca 2p based on the current signal-to-noise ratios.

CONCLUSION

We evaluated the surface of *Nephila clavata* spider dragline by FE-SEM and XPS to obtain clear surface morphological and chemical information. This is the first surface analysis of natural spider draglines by both powerful techniques. The FE-SEM images of the spider dragline indicate that the spider dragline forms a bundle of microfibrils. This hierarchical structure might induce faint fibril and network-like patterns at the surface of the dragline, however, we need to further study the origin of the patterns. Perhaps, we need to consider the effect of the natural spinning process with spider spinnerets to explain the surface patterns found in this study. XPS analysis revealed the presence of Na, P, and S, which are reasonably explained by considering the biological components of the major ampullate gland of spiders. The information obtained here is preliminary but will be important and essential to consider the molecular transition of silk proteins to form excellent hierarchical structures during the spider dragline spinning process.

DATA AVAILABILITY STATEMENT

The raw data supporting the conclusions of this article will be made available by the authors, without undue reservation, to any qualified researcher.

AUTHOR CONTRIBUTIONS

HS prepared the samples. AT conducted the FE-SEM measurements. KNa performed the XPS experiments. KT and KNu conceptualized and oversaw the project. All the authors co-wrote the manuscript.

FUNDING

This work was financially supported by the Impulsing Paradigm Change through Disruptive Technologies Program (ImPACT) of the Japan Science and Technology Corporation (JST) and RIKEN Engineering Network.

REFERENCES

Andersson, M., Chen, G., Otikovs, M., Landreh, M., Nordling, K., Kronqvist, N., et al. (2014). Carbonic anhydrase generates CO2 and H+ that drive spider silk formation via opposite effects on the terminal domains. *PLoS Biol.* 12:e1001921. doi: 10.1371/journal.pbio.1001921

Augsten, K., Muhlig, P., and Herrmann, C. (2000). Glycoproteins and skin-core structure in *Nephila clavipes* spider silk observed by light and electron microscopy. *Scanning* 22, 12–15. doi: 10.1002/sca.4950220103

Blackledge, T. A. (2012). Spider silk: a brief review and prospectus on research linking biomechanics and ecology in draglines and orb webs. *J. Arachnol.* 40, 1–12. doi: 10.1636/M11-67.1

Brown, C. P., Harnagea, C., Gill, H. S., Price, A. J., Traversa, E., Licoccia, S., et al. (2012). Rough fibrils provide a toughening mechanism in biological fibers. *ACS Nano* 6, 1961–1969. doi: 10.1021/nn300130q

Dao, A. T. N., Nakayama, K., Shimokata, J., and Taniike, T. (2017). Multilateral characterization of recombinant spider silk in thermal degradation. *Polym. Chem.* 8, 1049–1060. doi: 10.1039/c6py01954d

Faugas, B., Ellison, M. S., Dean, D., and Kennedy, M. S. (2013). Surface characterization of as-spun and supercontracted *Nephila clavipes* dragline silk. *J. Surf. Eng. Mater. Adv. Technol.* 03, 18–26. doi: 10.4236/jsemat.2013.33A004

Frische, S., Maunsbach, A. B., and Vollrath, F. (1998). Elongate cavities and skin–core structure in *Nephila* spider silk observed by electron microscopy. *J. Microsc.* 189, 64–70. doi: 10.1046/j.1365-2818.1998.00285.x

Fu, C. J., Porter, D., and Shao, Z. Z. (2009). Moisture effects on *Antheraea pernyi* silk's mechanical property. *Macromolecules* 42, 7877–7880. doi: 10.1021/Ma901321k

Gosline, J. M., DeMont, M. E., and Denny, M. W. (1986). The structure and properties of spider silk. *Endeavour* 10, 37–43. doi: 10.1016/0160-9327(86)90049-9

Heim, M., Romer, L., and Scheibel, T. (2010). Hierarchical structures made of proteins. The complex architecture of spider webs and their constituent silk proteins. *Chem. Soc. Rev.* 39, 156–164. doi: 10.1039/b813273a

Holland, C., Numata, K., Rnjak-Kovacina, J., and Seib, F. P. (2018). The biomedical use of silk: past, present, future. *Adv. Healthc. Mater.* 8:e1800465. doi: 10.1002/adhm.201800465

Knight, D. P., and Vollrath, F. (2001). Changes in element composition along the spinning duct in a *Nephila* spider. *Naturwissenschaften* 88, 179–182. doi: 10.1007/s001140100220

Li, M., Ogiso, M., and Minoura, N. (2003). Enzymatic degradation behavior of porous silk fibroin sheets. *Biomaterials* 24, 357–365. doi: 10.1016/s0142-9612(02)00326-5

Li, S. F., McGhie, A. J., and Tang, S. L. (1994). New internal structure of spider dragline silk revealed by atomic force microscopy. *Biophys. J.* 66, 1209–1212. doi: 10.1016/s0006-3495(94)80903-8

Li, S. F. Y., McGhie, A. J., and Tang, S. L. (1994). Comparative study of the internal structures of Kevlar and spider silk by atomic force microscopy. *J. Vac. Sci. Technol. A* 12, 1891–1894. doi: 10.1116/1.578978

Lin, T. Y., Masunaga, H., Sato, R., Malay, A. D., Toyooka, K., Hikima, T., et al. (2017). Liquid crystalline granules align in a hierarchical structure to produce spider dragline microfibrils. *Biomacromolecules* 18, 1350–1355. doi: 10.1021/acs.biomac.7b00086

Malay, A. D., Arakawa, K., and Numata, K. (2017). Analysis of repetitive amino acid motifs reveals the essential features of spider dragline silk proteins. *PLoS One* 12:e0183397. doi: 10.1371/journal.pone.0183397

Malay, A. D., Sato, R., Yazawa, K., Watanabe, H., Ifuku, N., Masunaga, H., et al. (2016). Relationships between physical properties and sequence in silkworm silks. *Sci. Rep.* 6:27573. doi: 10.1038/srep27573

Numata, K., Cebe, P., and Kaplan, D. L. (2010). Mechanism of enzymatic degradation of beta-sheet crystals. *Biomaterials* 31, 2926–2933. doi: 10.1016/J.Biomaterials.2009.12.026

Numata, K., Finne-Wistrand, A., Albertsson, A. C., Doi, Y., and Abe, H. (2008). Enzymatic degradation of monolayer for poly(lactide) revealed by real-time atomic force microscopy: effects of stereochemical structure, molecular weight, and molecular branches on hydrolysis rates. *Biomacromolecules* 9, 2180–2185. doi: 10.1021/Bm800281d

Numata, K., and Kaplan, D. L. (2010). Mechanisms of enzymatic degradation of amyloid beta microfibrils generating nanofilaments and nanospheres related to cytotoxicity. *Biochemistry* 49, 3254–3260. doi: 10.1021/bi902134p

Numata, K., Kikkawa, Y., Tsuge, T., Iwata, T., Doi, Y., and Abe, H. (2005). Enzymatic degradation processes of poly[(R)-3-hydroxybutyric acid] and poly[(R)-3-hydroxybutyric acid-co-(R)-3-hydroxyvaleric acid] single crystals revealed by atomic force microscopy: effects of molecular weight and second-monomer composition on erosion rates. *Biomacromolecules* 6, 2008–2016. doi: 10.1021/bm0501151

Numata, K., Sato, R., Yazawa, K., Hikima, T., and Masunaga, H. (2015). Crystal structure and physical properties of *Antheraea yamamai* silk fibers: long poly(alanine) sequences are partially in the crystalline region. *Polymer* 77, 87–94. doi: 10.1016/j.polymer.2015.09.025

Oktaviani, N. A., Matsugami, A., Hayashi, F., and Numata, K. (2019). Ion effects on the conformation and dynamics of repetitive domains of a spider silk protein: implications for solubility and beta-sheet formation. *Chem. Commun.* 55, 9761–9764. doi: 10.1039/c9cc03538a

Riekel, C., Burghammer, M., Dane, T. G., Ferrero, C., and Rosenthal, M. (2017). Nanoscale structural features in major ampullate spider silk. *Biomacromolecules* 18, 231–241. doi: 10.1021/acs.biomac.6b01537

Rousseau, M.-E., Hernández Cruz, D., West, M. M., Hitchcock, A. P., and Pézolet, M. (2007). *Nephila clavipes* spider dragline silk microstructure studied by scanning transmission X-ray microscopy. *J. Am. Chem. Soc.* 129, 3897–3905. doi: 10.1021/ja067471r

Shao, Z., Hu, X. W., Frische, S., and Vollrath, F. (1999). Heterogeneous morphology of *Nephila edulis* spider silk and its significance for mechanical properties. *Polymer* 40, 4709–4711. doi: 10.1016/s0032-3861(99)00072-5

Sponner, A., Vater, W., Monajembashi, S., Unger, E., Grosse, F., and Weisshart, K. (2007). Composition and hierarchical organisation of a spider silk. *PLoS One* 2:e998. doi: 10.1371/journal.pone.0000998

Thiel, B. L., Kunkel, D. D., and Viney, C. (1994). Physical and chemical microstructure of spider dragline: a study by analytical transmission electron microscopy. *Biopolymers* 34, 1089–1097. doi: 10.1002/bip.360340812

Vollrath, F. (1992). Spider webs and silks. *Sci. Am.* 266, 70–77.

Vollrath, F., Holtet, T., Thogersen, H. C., and Frische, S. (1996). Structural organization of spider silk. *Proc. R. Soc. Lond. B* 263, 147–151. doi: 10.1098/rspb.1996.0023

Yazawa, K., Ishida, K., Masunaga, H., Hikima, T., and Numata, K. (2016). Influence of water content on the beta-sheet formation, thermal stability, water removal, and mechanical properties of silk materials. *Biomacromolecules* 17, 1057–1066. doi: 10.1021/acs.biomac.5b01685

Yazawa, K., Malay, A. D., Masunaga, H., and Numata, K. (2019). Role of skin layers on mechanical properties and supercontraction of spider dragline silk fiber. *Macromol. Biosci.* 19:e1800220. doi: 10.1002/mabi.201800220

Conflict of Interest: The authors declare that the research was conducted in the absence of any commercial or financial relationships that could be construed as a potential conflict of interest.

frontiers in Materials

REVIEW
published: 20 March 2020
doi: 10.3389/fmats.2020.00050

Recent Advances in Fluorescent Silk Fibroin

Ok Joo Lee[1†], Md. Tipu Sultan[1†], Heesun Hong[1], Young Jin Lee[1], Ji Seung Lee[1], Hanna Lee[1], Soon Hee Kim[1] and Chan Hum Park[1,2]*

[1] *Institute of Nano Bio Regenerative Medicine, Hallym University, Chuncheon, South Korea,* [2] *Department of Otorhinolaryngology-Head and Neck Surgery, Chuncheon Sacred Heart Hospital, School of Medicine, Hallym University, Chuncheon, South Korea*

Silk is a natural macromolecular protein consisting of fibroin and sericin. Silk fibroin (SF), derived from *Bombyx mori,* is a representative fibrous protein that has been used mainly in fashion textiles and surgical sutures. Also, SF has been extensively applied as a potential biomaterial in a number of biomedical and biotechnological fields, as SF can be reconstituted in various forms through physical and chemical processes. In addition to direct use of SF with intrinsic structure and properties, there are many researchers attempt to insert more novel functional properties into SF, despite retaining its favorable natural characteristics. In recent years, fluorescent silk obtained through various methods, such as the genetic modification or dye feeding method, has been applied in a variety of medical fields. These functionalized silks have properties that can be applied to new and versatile fields more than currently existing fields such as drug delivery, monitoring surgical and wound healing processes. This review focuses on the preparation methods and the latest technological advances on the use of fluorescent SF materials, especially their biomedical applications.

Keywords: fluorescent, silk, bio-imaging, sensing materials, medical application

OPEN ACCESS

Edited by:
Antonella Motta, University of Trento, Italy

Reviewed by:
Keiji Numata, RIKEN, Japan
Vamsi Yadavalli, Virginia Commonwealth University, United States

****Correspondence:***
Chan Hum Park
hlpch@paran.com

† These authors have contributed equally to this work

Specialty section:
This article was submitted to Mechanics of Materials, a section of the journal Frontiers in Materials

Received: *07 December 2019*
Accepted: *18 February 2020*
Published: *20 March 2020*

Citation:
Lee OJ, Sultan MT, Hong H, Lee YJ, Lee JS, Lee H, Kim SH and Park CH (2020) Recent Advances in Fluorescent Silk Fibroin. Front. Mater. 7:50. doi: 10.3389/fmats.2020.00050

INTRODUCTION

SF from the *Bombyx mori* silkworm is a block copolymer and consists of 26 kDa light and 390 kDa heavy chain joined by a disulfide bridge (Yang et al., 2004; Vepari and Kaplan, 2007). The sequence of SF amino acid includes repetitive Gly–Ala–Gly–Ala–Gly–Ser repeats that can be self-assembled into aa β-sheet structure (Heslot, 1998; Zhou et al., 2001). SF has been highlighted as a functional biomaterial with excellent biocompatibility, remarkable mechanical properties such as low inflammation-inducing effect, excellent water vapor with oxygen permeability, blood compatibility, and controllable degradation.

Until now, SF has been fabricated into various forms for different applications. For example, SF has been used to make films, sponges, electrospun mats, nano- or microparticles, and hydrogels (Rockwood et al., 2011; Sultan et al., 2018). Because of these features, SFs are increasingly being studied for biomedical uses, including bone, tendon, ligament, cartilage, skin, nerve, cornea, tympanic membrane, dental, artificial kidney, and bladder (Altman et al., 2003; Vepari and Kaplan, 2007; Kim et al., 2010; Rockwood et al., 2011; Lee et al., 2014; Font Tellado et al., 2017; Lee et al., 2017; Park et al., 2018; Tang et al., 2018; Yeon et al., 2018; Sultan et al., 2019). Recently, to outfit a number of applications, SF has been chemically modified through several aqueous or organic solvent-processing methods, resulting in the change of its chemical, physical, and mechanical properties (Murphy and Kaplan, 2009; Li et al., 2012). Chemical modifications of SF through

coupling reactions, amino acid modification, grafting reactions have been displayed to change characteristics of silk material, including hydrophilicity, beta-sheet self-assembly, materials structure, and solution feature.

During the last decade, several efforts have been conducted for the modification of the surface and functionalization of SF using a vast wide range of technology and materials with functional properties to meet the worldwide market demands of natural and smart materials. Successful surface modification of silk can be overcome its intrinsic shortcomings with enhanced end-user performance. Surface modifications of SF are achieved through physical techniques (such as UV, Gas, Plasma treatment), chemical approaches (such as grafting copolymerization techniques, and chemical agents including acid anhydrides and polycarboxylic acids) (Li et al., 2012). Through surface modification, silk products with improved performance in the field of fibers and biomaterials can be obtained. This technology allows us to regulate cell response and improve cell adhesion to silk substrates.

UV irradiation is a very effective method of surface alteration for industrial uses, owing to its big excitation spectrum, multiple wavelengths availabilities, and cost-effective (Bergonzo et al., 1992; Ying Zhang et al., 1993; Periyasamy et al., 2007a). Surface modification of the SF has been achieved using UV treatment to enhance adhesion and wettability without any significant losses in crystallinity, mass, and strength (Park et al., 2007; Periyasamy et al., 2007a,b). An adequate increment of hydrophilicity of SF materials would be feasible for cell proliferation and adhesion. Simultaneously, some of the essential properties of silk clothes could be altered by UV irradiation.

Gas cures can impart various properties to SF dependent on the gas species used. For instance, ozone treatment has been used to increase the flexibility and yellowness indices of both fresh and degummed silk materials (Sargunamani and Selvakumar, 2006). Under atmospheric pressure, the use of ammonia-gas to treat SF materials increased the softness without any change of the apparent dyeing rate and crystallinity (Lee et al., 2006). Plasma, a hot ionized gas consisting of a mixture of electrons, also has been used to surface modification of SF materials. For example, the hydrophobicity of SF was increased when SF was treated with hexafluoropropene (C3F6) plasma (Li and Jinjin, 2007).

Chemical modifying agents such as acid anhydrides and polycarboxylic acids can produce chemical bonds by reacting with basic amino acids in SF. These chemical linkages can advance the hydrophobicity, thermal stability, and increase recovery of the SF materials without any significant effect on mechanical properties (Arai et al., 2001a, 2003; Davarpanah et al., 2009). Like these chemical agents can also use to graft other materials onto SF fibers create a novel silk material completely new properties. Acid anhydrides and polycarboxylic acids have also been used as bridge linkages to graft polysaccharide chitosan onto SF. This chitosan grafted SF demonstrated antibacterial activity and increased dyeability (Marsh et al., 1955; Arai et al., 2003). Other chemical agents, including EPSIA (a silicone-containing epoxy crosslinking agent) and isocyanates, have also been used to surface modifications of SF materials (Otterburn, 1977; Maclaren, 1981; Arai et al., 2001b; Cai et al., 2001).

Over several decades, fluorescent proteins have been used as a biotechnological tool to explore the function of a particular gene of interest through directly monitoring, visualizing, and measuring protein expression in living cells. Fluorescent SF has gained numerous attention for its applicability in various biotechnological and medical applications due to its inherent fluorescence property achieved through the insertion of the fluorescence gene into silk cocoons. The addition of the fluorescence properties into SF via gene insertion escapes the conjugation step to insert a fluorescently tagged protein such as green fluorescent protein (GFP). Therefore, the introduction of fluorescent properties in SF offers several potential advantages over the fluorescently tagged protein.

In the past decade, many studies have been reported to make silkworm silk with special characteristics for its application in new fields. Dyeing methods for obtaining silk of various colors are typically harsh conditions involving high temperature and pH changes and require additional steps to restore the original properties of silk. Recently, a method has been developed that produces functional silks that biologically introduce dyes into SF (Tansil et al., 2011b). Otherwise, the modification of silk proteins by genetic engineering has attracted much attention (Kikuchi et al., 1992; Yamao et al., 1999; Zhang et al., 1999; Zhao et al., 2001). Typically, a GFP is gene-targeted with the fibroin gene to obtain green fluorescent silkworm cocoons (Zhao et al., 2001). Bulk production of three colors (red, green, and orange) of fluorescent silks has been achieved through transgenic silkworms (Iizuka et al., 2013). These fluorescent silks of different colors can be potentially useful in medical applications and as silk fiber for clothing.

Therefore, in the current review, we summarize the preparation approaches of several fluorescent silk materials, present an updated review of the cutting-edge methodological advances on the use of fluorescent silk in biomedical applications. Fluorescent SF with properties and utility unattainable with conventional silk materials would have enormous potential and will offer biomedical applications, including drug delivery, bio-imaging, and sensing.

PREPARATION METHODS OF FLUORESCENT SILK MATERIALS

Natural (Autofluorescence)

When silkworms eat mulberry leaves, various pigments are absorbed into the silkworm body, including various nutrients. Silkworms can produce yellow fluids and cocoons by binding the yellow carotenoid (among the pigments absorbed into the silkworm body) pigment to the intracellular carotenoid-binging protein (CBP). The Y (Yellow blood) gene is the determinant of the cocoon color in the silkworm *Bombyx mori* and controls the uptake of carotenoids into the intestinal mucosa and the silk gland. Sakudoh et al. (2007) reported that colorless hemolymph and white cocoons resulted in the Y recessive strain, due to an improper mRNA splicing that appeared by a transposon-associated genomic omission, creates an incompetent CBP mRNA. Mainly, the pigments are integrated into the sericin with

a little absorption into fibroin. White SF produced due to the removal of sericin by a degumming process. However, there is considerable confirmation presenting that silk cocoons have a fluorescent nature, generally due to the existence of flavonoids, including quercetin derivatives (Tamura et al., 2002; Daimon et al., 2010; Kusurkar et al., 2013) and carotenoid compounds (Harizuka, 1953). It has been evident that like silk cocoons, SF-derived scaffolds exhibit a fluorescence index in UV, green, and blue, lights (Mandal and Kundu, 2009; Zhang et al., 2010; Kundu et al., 2012; Hodgkinson et al., 2014; Bhardwaj et al., 2015). Since the SF scaffold releases fluorescence at wavelengths identical in color to the fluorescent dyes themselves, the intrinsic fluorescence of SF can interfere with the signal from such fluorescent dyes (Georgakoudi et al., 2007).

Amirikia et al. (2018) fabricated an SF scaffold using the freeze-drying method and examined the fluorescence of the SF scaffold both prior and after cell seeding and fluorescent labeling using confocal microscopy. They subsequently explored the fluorescent index of the SF scaffold chemically. Cells labeled with fluorophore seeded into the scaffold exhibited a similar fluorescent color as the scaffold itself when stimulated by a similar wavelength of light. SF solution showed absorption maxima at 277 nm while emission maxima 345 nm, in the UV-Vis and fluorescence spectroscopy, which is a typical protein-derived signal. Thus, they concluded that the fluorescence of the SF scaffold related to intrinsic protein fluorescence and not to flavonoid constituents of cocoons from which the SF protein was derived. In addition, Kusurkar et al. (2013) applied a "water glass" based approach to obtain the fluorophores from silk cocoons.

Feeding Method Using a Dye-Containing Diet

There is an early attempt to serving coloring matter to silkworms in the twentieth century (Edwards, 1921). This kind of study was to examine the persistence of mulberry leaves in the gut of silkworms (Lombardi, 1920) or the toxicity associated with particular dyes to silkworms (Campbell, 1932). Various studies demonstrated that orcein was up taken to silk cocoons from silkworm's food, some other dyes were absorbed by guts or even traveled into eggs of the silkworm (Jucci and Ponsevernoi, 1930; Goris and Muehlemann, 1936). Numerous other tested dyes, including gentian violet, berlin blue, safranin, Nile blue, methylene blue, neutral red, alizarin, fuchsin, indigo carmine, and methyl orange were not taken up in silk (Jucci and Ponsevernoi, 1930). Due to the absence of proper and accurate characterization techniques, these above-mentioned studies results were not conclusive regards to the incorporation of the dyes into silk, particularly in SF. The molecular effect of these dyes or other additives into silk was not also correlated.

For the first time, rhodamine B as a dye uptake into the SF has been shown by Tansil et al. They fed silkworms on a dye-containing food, and confirmed via advanced characterization (Tansil et al., 2011a,b). Fluorescent silk cocoons and fibers were obtained by serving silkworms with a mixture of mulberry leaf powder and fluorescent molecules such as rhodamine B, rhodamine 101, and rhodamine 110. It was evident that SF can interact with rhodamine B, rhodamine 101, and rhodamine 110 by molecular recognition (Tansil et al., 2011b).

Genetic Modification

Recently genetically altered silks derived from engineered silkworms have been demonstrated (Yamao et al., 1999). Once the silkworm strain is developed, transgenic silkworms can be easily multiplied and retained. Transformed silkworm was first successfully developed by Tamura et al. (2000) using a constructed vector with a Piggy Bac transposon system derived from Trichoplusiani, a Lepidoptera insect. Also, the Piggy Bac transfer vector has been used to conduct many silkworm transformation studies so far. Among them, a transgenic silkworm produced recombinant silkworm cocoon containing human collagen protein has been reported in 2003 (Tomita et al., 2003). Expression systems were established to produce recombinant proteins using fibroin and sericin, respectively. Currently, fluorescent transgenic silkworms have been developed using various transformation vectors (Liu et al., 2009). The insertion of the transgene into the genome of silkworm allows obtaining specific desired characteristics via altering the silk protein (Tamura et al., 2000; Iizuka et al., 2013).

Several kinds of transformation vectors have been constructed using silk genes for the alteration of silk (Tomita, 2011). The vector using the fibroin L chain gene and the fibroin H chain gene is suitable for the fabrication of modified silks among the constructed vectors. Numerous useful silks with functional properties are produced using the vector and have been revealed to retain useful properties for medicines and fabrics. For instance, recombinant silkworm/spider silk produced by the transgenic silkworm is harder than normal silk fibers and as hard as a natural dragline (Teule et al., 2012). Recently biologically active silk constituted a chimeric protein of human fibroblast growth factor, and fibroin L chain has been stated to be applicable as a novel biomaterial for tissue engineering (Hino et al., 2006). The film derived from silk comprising with a chimeric protein of the fibroin L chain, and fibronectin sequence or a partial collagen peptide has been exhibited to have improved cell adhesion activity in comparison to original silk (Yanagisawa et al., 2007). It is crucial to develop a cost-effective production approach that produced enormous quantities of modified silk to expand the utility of transgenic silkworm silks. Iizuka et al. (2013) developed a transgenic silkworm that produces fluorescent silk and set up an isolation method to remove sericin at low temperatures to develop it into a suitable material that can be applied to various industrial fields. Fluorescent silk dresses and lights were produced based on this technology (**Figure 1**). Kim et al. developed a microcarrier by inserting EGFP of jellyfish into exon 2 of the heavy chain gene of silkworm fibroin. The green fluorescence remains intact, and the green fluorescence gene is transmitted to the next generation. They also have developed transgenic silkworm expressing the red and blue fluorescent protein (Kim et al., 2012, 2013, 2014).

Post-treatment

Fixation of inorganic solvent particles on silk fibers is another method for obtaining fluorescent SF. Chu and Liu demonstrated

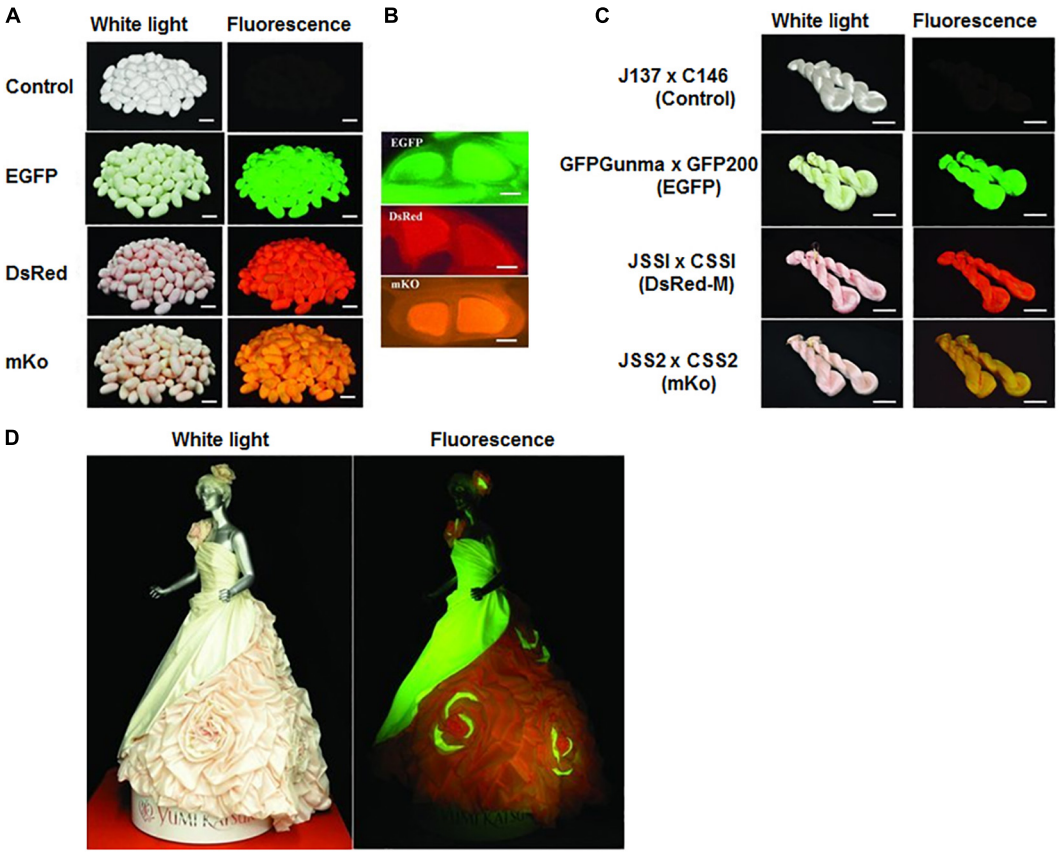

FIGURE 1 | Colored Fluorescent Silk Made by Transgenic Silkworms. **(A)** Colored fluorescent cocoons and **(B)** cross-section of the cocoon silk produced by the hybrid races. **(C)** Fluorescent silks. **(D)** Wedding dress made by the colored fluorescent silks. Reproduced from Iizuka et al. (2013) with permission from John Wiley and Sons.

TABLE 1 | A brief summary of fluorescent SF-based materials and their potential biomedical applications.

Preparation method	Genes/Dyes	Emission wavelength colors	Forms of SF materials	Applications	References
Genetic modification	EGFP, mKate2, EYEF	Green, Red, Yellow	Scaffold, Solution, Membrane	Bio-imaging, Biomedical application	Kim et al., 2015
	EGFP	Green	Silk gland		Tamura et al., 2000; Uchino et al., 2007
	EGFP, DsRed mKO	Green, Red, Orange	Raw silk	Biomedical application	Iizuka et al., 2013
Natural (auto-fluorescence)		Green, Red	Scaffold	Tissue engineering	Amirikia et al., 2018
Post-treatment	quantum dots (QDs)		Particle Hydrogel, microsphere Film	Bio-imaging	Chu and Liu, 2008; Zheng et al., 2015; Ko et al., 2018
Feeding	Rhodamine B	Pink	fiber		Tansil et al., 2011b
	Rhodamine 101	Faint-pink		Tissue engineering	
	Rhodamine 110	Green			

a novel method of preparing fluorescent silkworm silks by integrating semiconductor nanocrystals quantum dots (QDs) into the silks through electrostatic absorption using a fixer of a polyelectrolyte (PE) (Chu and Liu, 2008). Therefore, silkworm silks incorporated with QDs had adjustable colors from green to near-infrared, which penetrated via an opaque pigskin of ∼3.5 mm in thickness. Ko et al. fabricated a novel SF-based carbon quantum dots (SF-CQDs), which was synthesized over a short time (20 min) via a facile microwave-irradiation method (Ko et al., 2018). These SF-CQDs exhibited good crystallinity, water dispersity, low toxicity, photoluminescence stability, optical properties, and biocompatibility.

Recently, several studies have been used the addition of dye into the SF solution method to develop dye-doped SF in the

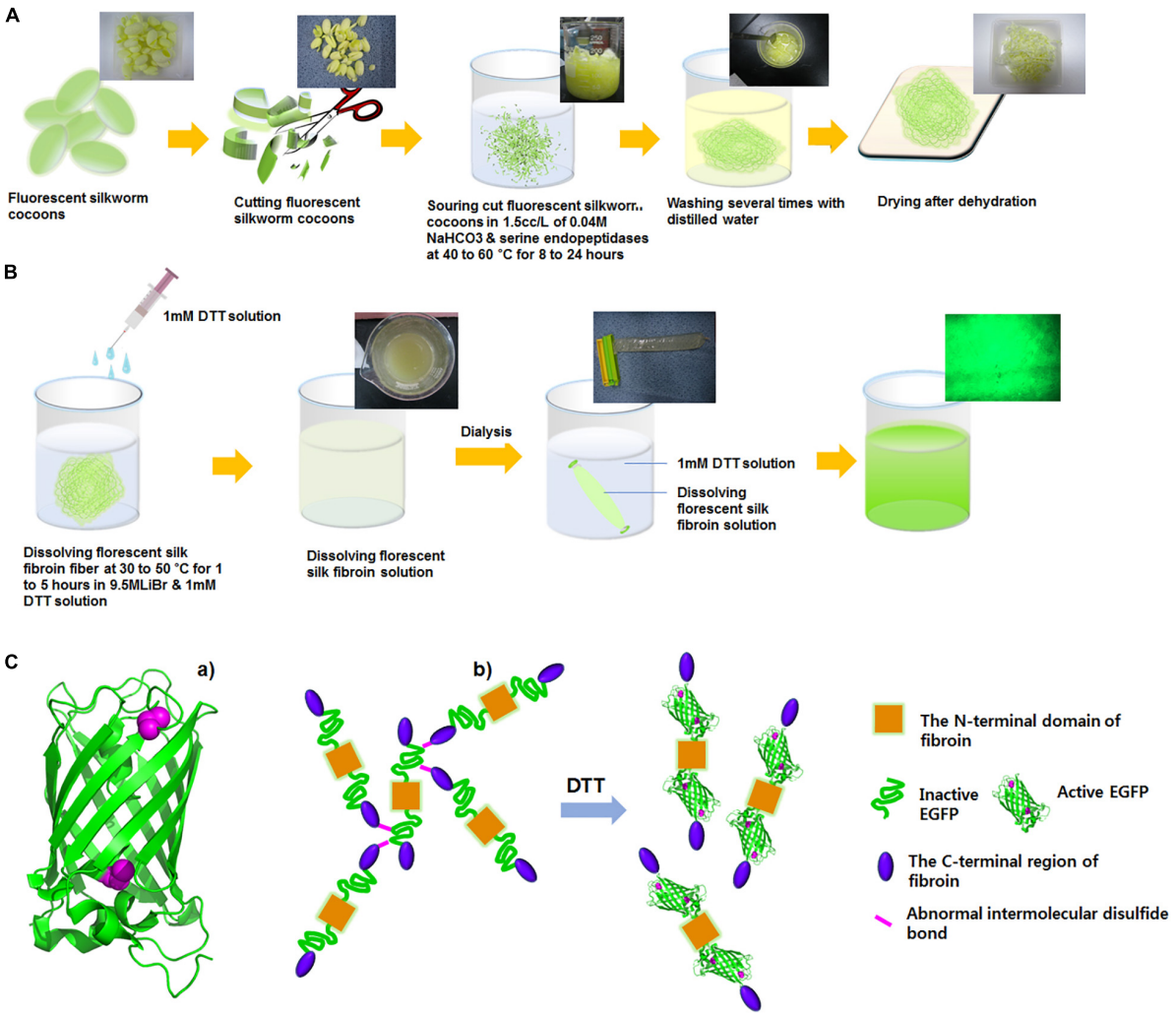

FIGURE 2 | Preparation of fluorescent silk fibroin solution. **(A)** Fluorescent silk was degummed with 0.5% (w/w) Na_2CO_3 with 1 mM DTT solution at 45°C for overnight and then washed with distilled water. **(B)** Degummed fluorescent SF was dissolved in 9.5 M LiBr for 4 h at 45°C and dialyzed to remove salts in a cellulose tube against distilled water for 2 days at room temperature. **(C)** The critical role of DTT in the improvement of fluorescent activity of the fluorescent fibroin. (a) The EGFP structure (green ribbons) with two cysteine residues (magenta spheres). EGFP, EYFP, and mKate2 contain cysteine residues that are not involved in disulfide bonds. (b) A model for the improvement of fluorescence activity of the fluorescent fibroin in the presence of DTT. DTT would allow EGFP to be properly folded and to exert fluorescent activity by preventing the formation of abnormal intermolecular disulfide bonds. Reproduced from Kim et al. (2015) with permission from ELSEVIER.

forms of nanoparticles, films, and electrospun (Kaneko et al., 1991; Myung et al., 2008; Min et al., 2017). Kaneko et al. (1991) incorporated luminescence from the excitation state of Ru $(bpy)_3^{2+}$ (bpy, 2,2′-bipyridine) into an SF membrane by casting a mixture of aqueous solutions of a 1 mM Ru $(bpy)_3^{2+}$ and 2.8 wt.% SF. The excitation lifetime of the incorporated dye complex into an SF membrane exhibited lengthier (1700 ns) than the value (598 ns) in aqueous solution, suggesting the existence of an active site for the complex binding. Four water-soluble dyes, including riboflavin, sodium fluorescein, rhodamine B, and stilbene 420, were used to develop fluorescent silk nanofibers (FSNs) mat through the electrospinning method. This red-green-blue (RGB) fluorescent nanofibrous mats were successfully used for acid vapor detection and nutrition delivery (Min et al., 2017).

Although several methods, including feeding, genetic modification, and post-processing, have been successfully applied to obtain florescent SF, there are some advantages and disadvantages of each method. The feeding method using a dye-containing diet is simple but not conclusive regards to the addition of the dyes into SF. Numerous studies have been effectively utilized the genetic modification method to obtain fluorescent SF as this method offers the addition of the desired properties correctly. However, this transgenic method suffers from several limitations, including low efficiency, high cost, and the complexity of the process. Moreover, transgenic silkworms sometime fail to spin silks (Zhang et al., 1999). The post-processing technique offers several advantages, for example, a profoundly productive and effectively reproducible

procedure with low cost in contrast with the dye feeding method or transgenic strategy. However, the post-processing method also suffers from some drawbacks due to the release of some toxic ions from the inserted molecules into the SF such as QDs (Chu and Liu, 2008).

APPLICATIONS OF FLUORESCENT SILK MATERIALS

SF-based biomaterials have been extensively explored in biomedical fields, including cartilage and bone, drug delivery, vascular grafts, skin tissue, wound dressings, ligaments, cornea, tympanic membrane, and artificial kidney. SF has been incorporated with different materials or been modified by chemically/genetically to produce fluorescence SF materials for a wide range of applications (**Table 1**). There have been numerous studies on the applications of fluorescent SF in the biomedical and biotechnological fields.

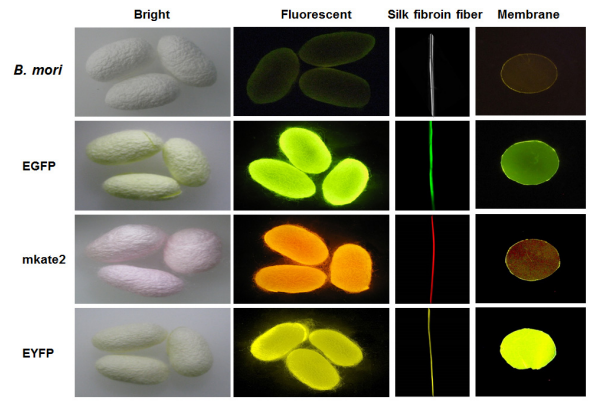

FIGURE 3 | Fluorescent cocoons, silk fibroin fibers, and membranes. The fluorescent cocoons produced by transgenic silkworms had various fluorescent proteins, including EGFP, mKate2, and EYFP. Reproduced from Kim et al. (2015) with permission from ELSEVIER.

Bio-Imaging

The distribution or degradation of biomaterials tracking is vital for tissue engineering and drug delivery. In the recent past, the use of fluorescent polymeric nanoparticles (PNPs) for bio-imaging has received ample attention for non-invasive tracking (Win et al., 2015). In an early study, QDs containing SF hydrogels were prepared from CdTe QDs (MPA-QDs) incorporated SF solution (Zheng et al., 2015). The integration of QDs into SF hydrogels considerably reduced the cytotoxicity with the significantly stable fluorescent property. This QDs containing silk hydrogels with established and robust fluorescence have prospective applications in tracking the distribution and degradation of SF-based biomaterials, and also as a suitable diagnostic tool. Nanodiamonds (NDs) have also been applied for bio-imaging due to its bright extensive fluorescence emission feature (Khalid et al., 2014; Xu et al., 2019).

In recent times, the use of Two-Photon Fluorescence (TPF) microscopy for bio-imaging has gained an ample interest due to numerous significant benefits over currently existing detection technologies, including and transmission electron microscopy (TEM) and scanning electron microscopy (SEM) (He et al., 2008). In biological imaging, silk films integrated with TPF properties could be applied as a film scaffold. To achieve this objective, the uniform distribution of the TPF QDs are essential in the silk

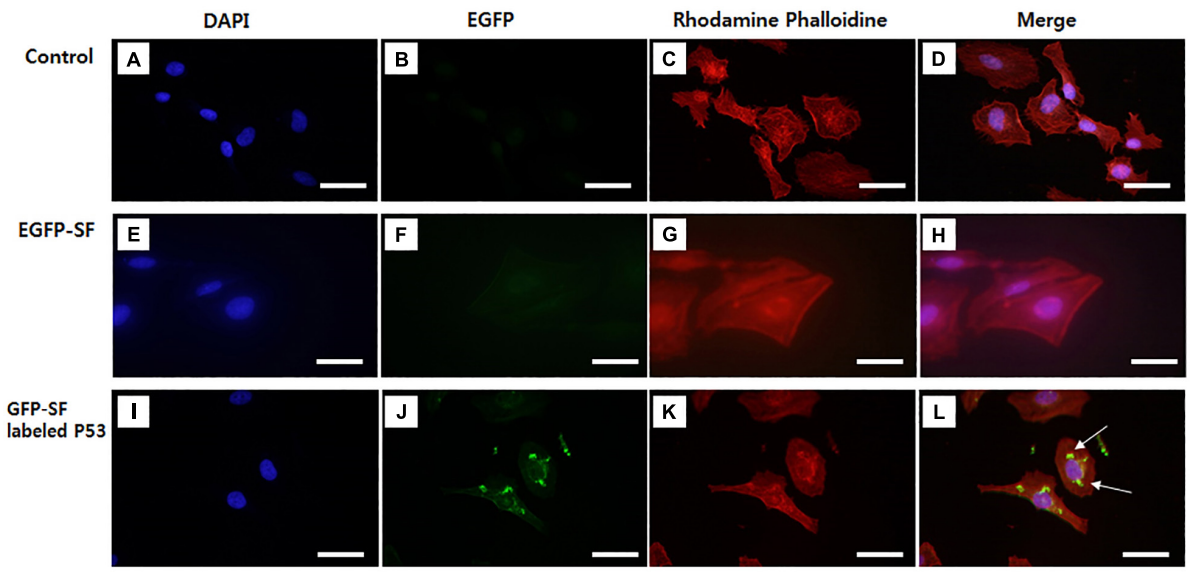

FIGURE 4 | Images of p53 localization using EGFP fluorescent SF labeled p53 antibody in HeLa cell. **(A–D)** Control, **(E–H)** EGFP fluorescent SF solution, **(I–L)** EGFP fluorescent SF labeled p53. HeLa cells were stained with **(A,E,I)** DAPI and **(C,G,K)** Rhodamine Phalloidin and imaged under fluorescence microscopy, **(D,H,L)** DAPI, GFP, and Rhodamine Phalloidin images were merged. White arrows are the image of EGFP-SF labeled P53 in Hela cell. Scale bar = 50 μm. Not published.

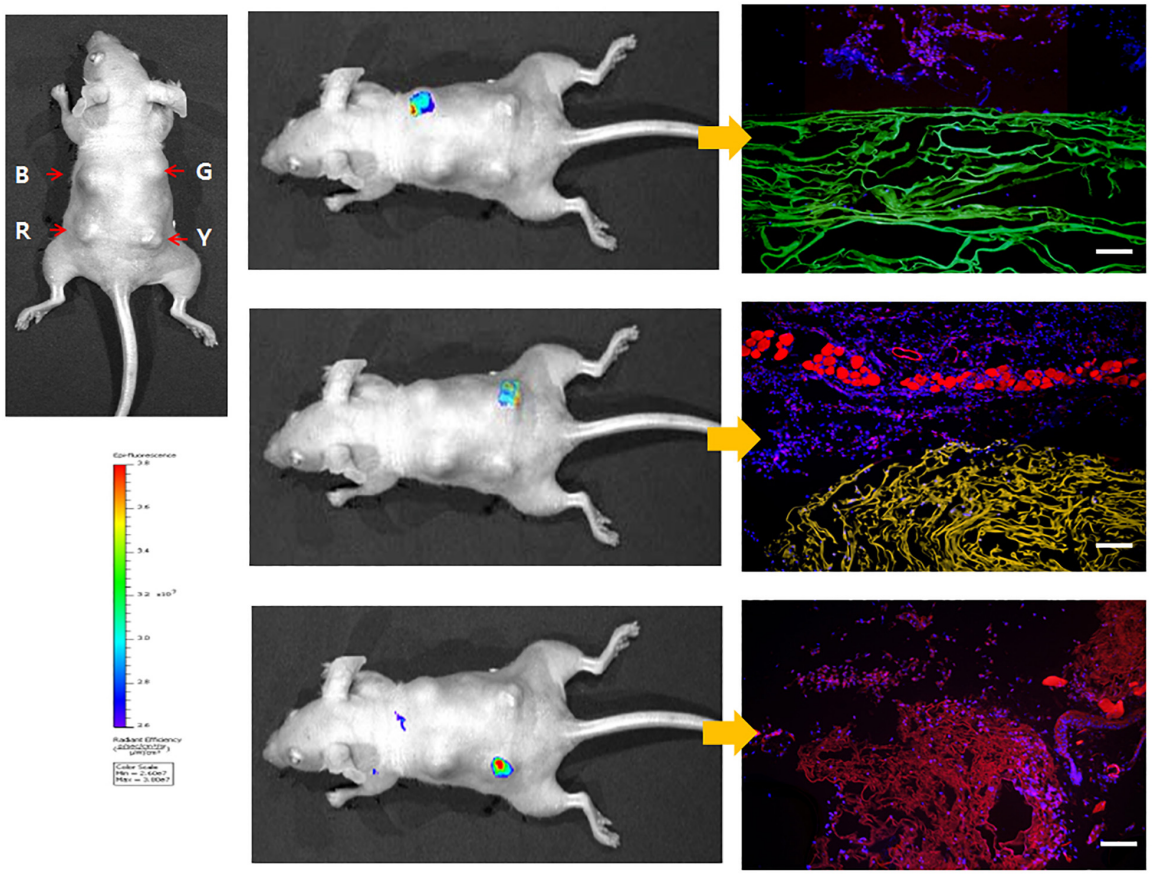

FIGURE 5 | Whole-body imaging of fluorescent SF sponges in the dorsal region of nude mouse at 7 days. The color bar indicates relative signal intensity. (B) *B. mori,* (G) EGFP, (R) mKate2, (Y) EYFP. Reproduced from Kim et al. (2015) with permission from ELSEVIER.

film. The silk films composite with QDs could be used to observe activities underneath the deep tissue in a non-invasive and real-time manner (Lin et al., 2015). Lin et al. (2015) have also been developed a novel and versatile material-assembly approach to achieve fluorescent release SF biocomposite materials that could be used in non-invasive scaffold imaging.

Kim et al. (2015) have shown, for the first time, a fluorescent SF solution preparation method for biomedical applications (**Figure 2**). This work stated an approach of preparing a fluorescent SF solution and various forms, including membrane, sponge, particle, and electrospun fiber (**Figure 3**). The transgenic fluorescent cocoons exhibited the fluorescent protein's color when exposed to a blue LED light. The fluorescent cocoons were treated at 60°C overnight in an aqueous solution of 3% NaHCO3 with a proteolytic enzyme alcalase and then washed several times with distilled water to remove the sericin proteins. Then the extracted silk was melted in 1 mM DTT containing 9.5 M LiBr solution at 40°C. After that, the solution was filtered through a miracloth and dialyzed against distilled water to remove the salt for 2 days. The final concentration of the aqueous SF solution was 4 wt.%. The fluorescence studies were performed with the cocoons and the SF solution, and the fluorescence was captured at excitation wavelengths of 488 nm for EGFP, 514 nm for EYFP) and 588 nm for mKate2 and maximum emission wavelengths were detected at 507 nm for EGFP, 527 nm for EYFP, and 633 nm for mKate2, respectively. Similar excitation and emission characteristics were detected for the cocoons and solution. Soluble fluorescent SF was conjugated with anti p53 antibodies and used to detect the p53 (an early cancer biomarker) expression in HeLa cells (**Figure 4**). Cells were adhered to and grew well on the membranes, which were fabricated from the fluorescence SF solutions by casting them on polystyrene plates. The sponges prepared from the SF solutions were subcutaneously transplanted into the dorsal regions of the nude mice and shown to retain their fluorescence over 1 year, demonstrating the long-term biocompatibility of these biomaterials (**Figure 5**). Intraoperative use of EGFP fluorescent SF was also found in animal models to identify small esophageal and stomach perforation (**Figure 6**). Therefore, it can be imagining that functional fluorescent SF materials can be applied in a wide range of areas, such as optoelectronics, biomedical, and chemical science, in the future.

Sensing Materials

Biosensing devices with excellent biocompatibility, sensitivity, multi-stimuli-responsivity, and low weight having great attention since health monitoring and early diagnosis are more critical

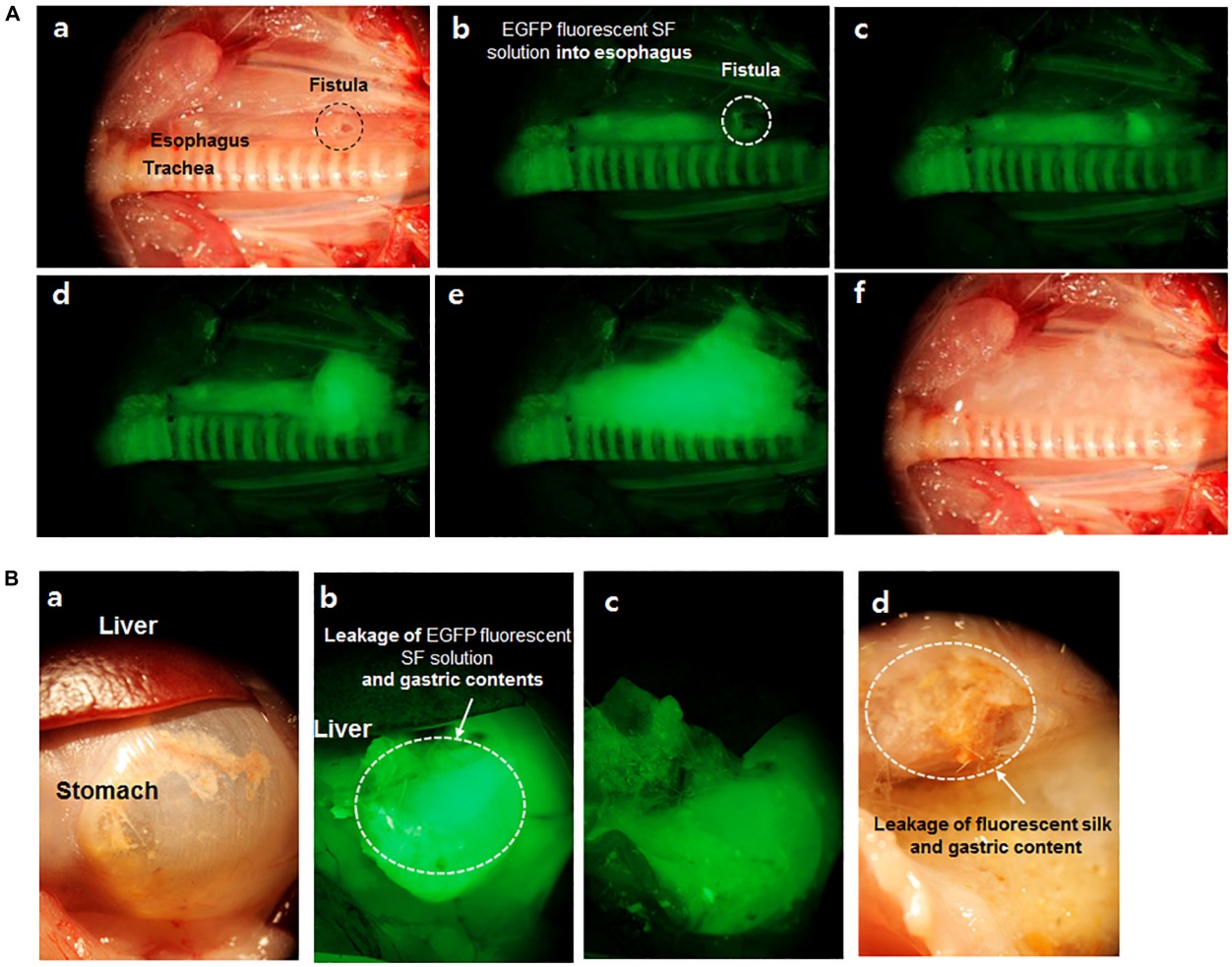

FIGURE 6 | Images of EGFP fluorescent SF solution in esophageal **(A)** and stomach **(B)** fistula of the rat. (a) Esophageal fistula (0.5 mm) image with white light reflectance, (b–e) EGFP fluorescent captured images per 0.3 s. EGFP fluorescent was detected at esophageal fistula according to time passed under fluorescent light, (f) Image of leaked EGFP fluorescent SF from fistula with white light reflectance. **(B**,a**)** Stomach and liver image with white light reflectance light (b,c) Leakage image of EGFP fluorescent SF solution and gastric contents from fistula site after feeding of EGFP fluorescent SF solution under fluorescent light, (d) Leakage image of EGFP fluorescent SF solution and gastric contents with white light reflectance light. Reproduced from Kim et al. (2015) with permission from ELSEVIER.

than the treatment of diseases. Silk-derived materials have been applied as the support material to create pressure sensors with very high sensitivity. SF can be fabricated into numerous forms of hydrogels, ultra-fine, and thick films (Parker et al., 2009) and also can form flexible interfaces with biological recognition elements such as enzymes, and aptamers while retaining its functional properties for sensing applications (Pal et al., 2016). SF protein has been used as a sensor material for the detection of vitamin B12 by Chakravarty et al. Their SF-based sensing platform was developed for the dual-mode tracking of B12 in human blood serum (HBS) and solution using photoluminescence (PL) and electrical methods to enhances the strength and operative lifespan of the device. The autofluorescence of SF solution exhibited a high fluorescence quenching, while a micro-patterned film of SF showed a sharp increase in current intensity in the presence of B12 (Chakravarty et al., 2018).

In a previous study, electrospun fluorescent silk nanofibers (FSNs) have been applied as a very sensitive chemosensor and a nutrient releaser with a physically transient form. Among these, the sodium fluorescein doped FSN could be used as an extremely sensitive fluorescent chemosensor for acid fumes in the air. In this study, FSN sensors reacted to the acid vapor of the hydrochloric (HCl) instantly at a lethal concentration of > 300 ppm and could also be detected at low concentrations of $\sim$5 ppm. FSNs could be disappeared at a set period by regulating the silk fibers' crystallinity. Depend on this property, FSNs mat was used as an indicator or water-disposable skin-type patch to be attached to protective equipment and clothing. The reduction of the fluorescence of nanofiber mats was defined to measure the quantity of vitamin B2 transported to the skin (Min et al., 2017). Complete control of fluorescence release by introducing mesoscopic ordered structures and its applications will be

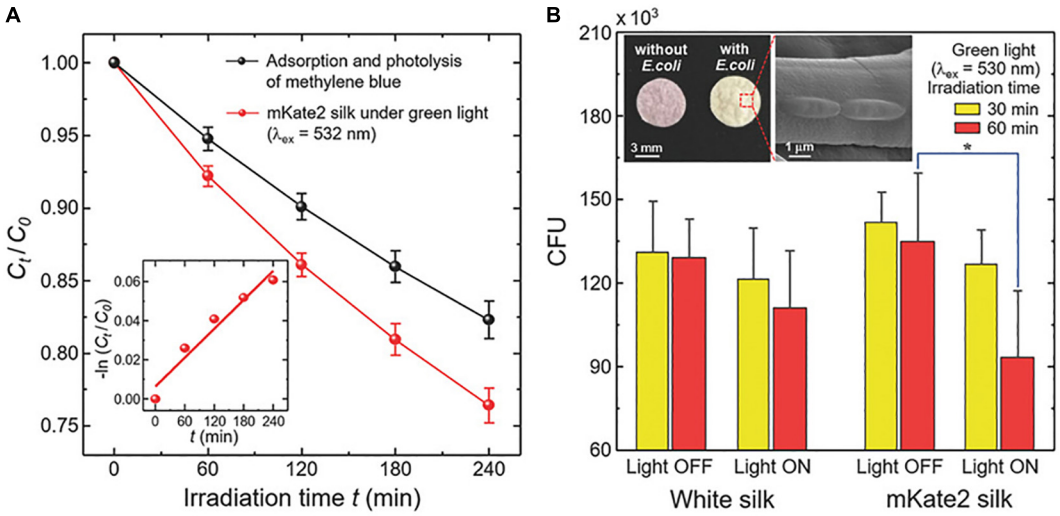

FIGURE 7 | Photocatalytic activity of mKate2 silk for degrading methylene blue and deactivating bacteria under green light excitation at ambient temperature. **(A)** Photodegradation of methylene blue in aqueous solutions by mKate2 silk under green light activation. **(B)** Colony-forming units (CFU) of live *E. coli* (DH5α). Reproduced from Leem et al. (2018) with permission from WILEY-VCH.

significantly extended the usefulness of fluorescence in several fields, including optical systems, optoelectronic technology, and biological sensors. Furthermore, considering that SF-based sensors emerged only in recent years, innovative sensors with highly sensitive, flexible, durable, biocompatible, and portable can be predicted in the future.

Drug Delivery

Silk is well known as a suitable carrier for the delivery of different drugs due to its excellent biocompatibility, non-toxicity, high binding capacity, controlled drug release properties, and relatively slow degradability *in vivo* (Hofmann et al., 2006; Murphy and Kaplan, 2009). Fluorescent dyes have been applied to monitor and visualize the internalization of carriers or measure the loading and release of drugs in controlled release/delivery systems (Wang et al., 2007; Ren et al., 2011). Khalid et al. have been demonstrated the drug release kinetics of the nanodiamond-SF-doxorubicins (NDSX) spheres by loading spheres with anthracycline DoX. Degradable SF spheres stabilize and release the drug in a precise manner while ND provides a fluorescent modality for imaging. Degradability of SF and the following release of DoX was monitored through the fluorescence of ND inside the spheres. These NDSX spheres have the potential to a role as dual-functional nanomaterials for drug delivery and succeeding imaging within biological structures and could be useful in targeted drug delivery (Khalid et al., 2016).

A versatile FSN has been prepared using a novel combination of optically active organic dyes and silk polymer. FSNs produced through the electrospinning approach shows striking functions of the fixed organic dyes along with encoding the system that physically disappears at a preset time. Fluorescent nanofibrous mats with red-green-blue (RGB) color, disposable membranes for nutrition delivery, and ecofriendly and transient fluorescent chemosensors for acid vapor recognition, were adequately demonstrated using FSNs. A drug delivery model using membranes of silk nanofiber fixed with vitamin B2 was also recommended (Min et al., 2017).

Antibacterial Effect

SF with novel properties can be fabricated by the immobilization of nanomaterials to SF materials. Silver nanoparticles (AgNPs) applied as antimicrobial agents are effective against approximately 650 strains of bacteria, including antibiotic-resistant strains, have gained enormous interest in the functionalization of silk. Recently, antibacterial SF scaffolds with green synthesized AgNPs have been developed for human mesenchymal stem cell differentiation and osteoblast proliferation. The antimicrobial activity of AgNPs immobilized-SF films was evaluated against gram-negative bacteria and antibiotic-resistant bacteria, and it was found to be effective against both (Nadiger and Shukla, 2016). Fluorescent proteins often result in cytotoxicity and phototoxicity due to the production and release of reactive oxygen species (ROS) by some red fluorescent proteins. The photo-generation of ROS is actively used for removing cancerous tissue. It has been demonstrated that silk with a transgenic fusion of far-red fluorescent probe in (mKate2) offers a photosensitizer hybridization platform for photo inducible control of ROS. ROS are active radicals for breaking down organic contaminants that were generated when the resulting hybrid was illuminated with a green light. The survival rate of E. coli dropped to 45 percent when E. coli on the fluorescent silk was activated for 60 min under a weak green light (**Figure 7**; Leem et al., 2018).

Optical Systems

SF in film form has been applied for numerous high-performance optical devices (Omenetto and Kaplan, 2008; Parker et al., 2009; Ling et al., 2016). Based on several vital physical properties,

biocompatible SF has potential as an optical biomaterial (Perry et al., 2008). The optical properties of SF films can be adjusted by changing the coating rate and varying their response to humidity (Li et al., 2017), which would make SF as a suitable humidity indicator. SF has been utilized to develop an ultrathin active moiré chiral metamaterials (MCMs) as a novel optical sensor in which SF use as a spacer layer (Wu et al., 2018). However, there is no study about the application of fluorescence SF in the optical systems. Therefore, further research needed to be performed to explore the applicability of fluorescent SF in the optical system.

CONCLUSION

Silkworm silks have been applied as a luxurious textile material for over 4000 years. Typically, raw silkworm silk comprises two kinds of self-assembled proteins, fibroin and sericin. The fibroin is a significant constituent of silk fiber serving as the core, while the sericin is a minor constituent serving as a coating protein. SF, which has undergone the degumming for removal of sericin, provides an essential set of material options for biomaterials such as coatings for cell culture and drug delivery matrices and scaffolds for tissue engineering, including bone, cartilage, skin, tympanic membrane, vasculature, and the esophagus because of the impressive mechanical properties, biocompatibility, and biodegradability. SF can be transformed into various forms, including films, hydrogels, nanoparticles, nanofibers for various biomedical applications. Transformed SF into these different forms depends on formulating a solution form of SF as a precursor. Several properties of fluorescent SF are similar to those of natural SF. Iizuka et al. (2013) revealed that the mechanical properties of the fluorescent SF regards to the maximum strain tolerated and Young's modulus was similar to those of ordinary silk. However, the maximum stress value of the natural silk was slightly higher than that of the fluorescent silk (Iizuka et al., 2013). Super strong fluorescent silk, which was produced through feeding *Bombyx mori* silkworms with carbon nanodots, showed super-strong mechanical properties than that of the natural silk (Chu and Liu, 2008). In our previous study, we exhibited similar cell viability on both the fluorescent SF membrane and wild type SF membrane (Kim et al., 2015). This finding indicated that the fluorescent properties did not alter the biocompatibility of the fluorescent SF. Photostability is one of the fundamental properties of the fluorescent SF for functional silk fiber for fabricating fabrics and for biomedical applications. An early study showed that the fluorescent color of the fabrics with the recombinant silk persisted for over 2 years. Therefore, if fluorescent SF can be produced in various forms, it can also be used in various biomedical fields. The multifunctional SF-based materials with fluorescent can use to *in vitro* and *in vivo* imaging purposes and other biomedical applications due to their excellent fluorescent properties and biocompatibility. Aside from the biomedical applications, the derivatives of fluorescence SF, such as films, gels, fibers offer the possibility in electronics and photonics. In the future, we believe fluorescent SF will be created by the fusion of various advanced technology and will further expand the biomedical applications.

AUTHOR CONTRIBUTIONS

OL and MS wrote the manuscript. HH, YL, JL, HL, and SK contributed to collect references. CP designed and supervised to organize the manuscript. All authors carefully read the manuscript and commented on the article.

FUNDING

This work was supported by the National Research Foundation of South Korea (NRF) grant funded by the Korea Government (MSIP; Grant Nos. NRF-2015R1D1A3A01020100 and NRF-2018R1D1A1B07050927), Republic of Korea and by the Hallym University Research Fund.

REFERENCES

Altman, G. H., Diaz, F., Jakuba, C., Calabro, T., Horan, R. L., Chen, J., et al. (2003). Silk-based biomaterials. *Biomaterials* 24, 401–416.

Amirikia, M., Shariatzadeh, S. M. A., Jorsaraei, S. G. A., and Mehranjani, M. S. (2018). Auto-fluorescence of a silk fibroin-based scaffold and its interference with fluorophores in labeled cells. *Eur. Biophys. J.* 47, 573–581. doi: 10.1007/s00249-018-1279-1

Arai, T., Freddi, G., Innocenti, R., Kaplan, D. L., and Tsukada, M. (2001a). Acylation of silk and wool with acid anhydrides and preparation of water-repellent fibers. *J. Appl. Polym. Sci.* 82, 2832–2841. doi: 10.1002/app.2137

Arai, T., Ishikawa, H., Freddi, G., Winkler, S., and Tsukada, M. (2001b). Chemical modification of Bombyx mori silk using isocyanates. *J. Appl. Polym. Sci.* 79, 1756–1763. doi: 10.1002/1097-4628(20010307)79:10<1756::aid-app30>3.0.co;2-g

Arai, T., Freddi, G., Innocenti, R., and Tsukada, M. (2003). Preparation of water-repellent silks by a reaction with octadecenylsuccinic anhydride. *J. Appl. Polym. Sci.* 89, 324–332. doi: 10.1002/app.12081

Bergonzo, P., Patel, P., Boyd, I. W., and Kogelschatz, U. (1992). Development of a novel large area excimer lamp for direct photo deposition of thin films. *Appl. Surf. Sci.* 54, 424–429. doi: 10.1016/0169-4332(92)90081-8

Bhardwaj, N., Devi, D., and Mandal, B. B. (2015). Tissue-engineered cartilage: the crossroads of biomaterials, cells and stimulating factors. *Macromol. Biosci.* 15, 153–182. doi: 10.1002/mabi.201400335

Cai, Z., Jiang, G., and Yang, S. (2001). Chemical finishing of silk fabric. *Color. Technol.* 117, 161–165. doi: 10.1111/j.1478-4408.2001.tb00056.x

Campbell, F. L. (1932). Preliminary experiments on the toxicity of certain coal-tar dyes for the silkworm. *J. Econ. Entomol.* 25, 905–917. doi: 10.1093/jee/25.4.905

Chakravarty, S., Gogoi, B., Mandal, B. B., Bhardwaj, N., and Sarma, N. S. (2018). Silk fibroin as a platform for dual sensing of vitamin B12 using photoluminescence and electrical techniques. *Biosens. Bioelectron* 112, 18–22. doi: 10.1016/j.bios.2018.03.057

Chu, M., and Liu, G. (2008). Fluorescent silkworm silk prepared via incorporation of green, yellow, red, and near-infrared fluorescent quantum dots. *IEEE Trans. Nanotechnol.* 7, 308–315. doi: 10.1109/TNANO.2008.917836

Daimon, T., Hirayama, C., Kanai, M., Ruike, Y., Meng, Y., Kosegawa, E., et al. (2010). The silkworm Green b locus encodes a quercetin 5-O-glucosyltransferase that produces green cocoons with UV-shielding properties. *Proc. Natl. Acad. Sci. U.S.A.* 107, 11471–11476. doi: 10.1073/pnas.1000479107

Davarpanah, S., Mahmoodi, N. M., Arami, M., Bahrami, H., and Mazaheri, F. (2009). Environmentally friendly surface modification of silk fiber: chitosan

grafting and dyeing. *Appl. Surf. Sci.* 255, 4171–4176. doi: 10.1016/j.apsusc.2008.11.001

Edwards (1921). Feeding dye stuffs to silkworms. *Textile World* 60, 1111–1113.

Font Tellado, S., Bonani, W., Balmayor, E. R., Foehr, P., Motta, A., Migliaresi, C., et al. (2017). (*) Fabrication and characterization of biphasic silk fibroin scaffolds for tendon/ligament-to-bone tissue engineering. *Tissue Eng. Part A* 23, 859–872. doi: 10.1089/ten.TEA.2016.0460

Georgakoudi, I., Tsai, I., Greiner, C., Wong, C., Defelice, J., and Kaplan, D. (2007). Intrinsic fluorescence changes associated with the conformational state of silk fibroin in biomaterial matrices. *Opt. Express* 15, 1043–1053. doi: 10.1364/oe.15.001043

Goris, A., and Muehlemann. (1936). Coloration of silkworm gut. *Bull. Acad. Med.* 116, 268–273.

Harizuka, M. (1953). Physiological genetics of the carotenoids in Bombyx mori, with special reference to the pink cocoon. *Bull. Seric Exp. Stn. Jpn.* 14, 141–156.

He, G. S., Tan, L. S., Zheng, Q., and Prasad, P. N. (2008). Multiphoton absorbing materials: molecular designs, characterizations, and applications. *Chem. Rev.* 108, 1245–1330. doi: 10.1021/cr050054x

Heslot, H. (1998). Artificial fibrous proteins: a review. *Biochimie* 80, 19–31. doi: 10.1016/s0300-9084(98)80053-9

Hino, R., Tomita, M., and Yoshizato, K. (2006). The generation of germline transgenic silkworms for the production of biologically active recombinant fusion proteins of fibroin and human basic fibroblast growth factor. *Biomaterials* 27, 5715–5724. doi: 10.1016/j.biomaterials.2006.07.028

Hodgkinson, T., Yuan, X. F., and Bayat, A. (2014). Electrospun silk fibroin fiber diameter influences in vitro dermal fibroblast behavior and promotes healing of ex vivo wound models. *J. Tissue Eng.* 5, 2041731414551661. doi: 10.1177/2041731414551661

Hofmann, S., Foo, C. T., Rossetti, F., Textor, M., Vunjak-Novakovic, G., Kaplan, D. L., et al. (2006). Silk fibroin as an organic polymer for controlled drug delivery. *J. Control Release* 111, 219–227. doi: 10.1016/j.jconrel.2005.12.009

Iizuka, T., Sezutsu, H., Tatematsu, K. I., Kobayashi, I., Yonemura, N., Uchino, K., et al. (2013). Colored fluorescent silk made by transgenic silkworms. *Adv. Funct. Mater.* 23, 5232–5239. doi: 10.1002/adfm.201300365

Jucci, N., and Ponsevernoi. (1930). Migration in to cocoon and eggs of dyes administered to silkworms. *Boll. Soc. Italiana Biol. Speriment.* 5, 1056–1060.

Kaneko, M., Iwahata, S., and Asakura, T. (1991). Luminescence from excited tris(2,2'-bipyridine)-ruthenium(II) incorporated into a silk fibroin membrane. *J. Photochem. Photobiol. A Chem.* 61, 373–380. doi: 10.1016/1010-6030(91)90020-T

Khalid, A., Lodin, R., Domachuk, P., Tao, H., Moreau, J. E., Kaplan, D. L., et al. (2014). Synthesis and characterization of biocompatible nanodiamond-silk hybrid material. *Biomed. Opt. Express* 5, 596–608. doi: 10.1364/BOE.5.000596

Khalid, A., Mitropoulos, A. N., Marelli, B., Tomljenovic-Hanic, S., and Omenetto, F. G. (2016). Doxorubicin loaded nanodiamond-silk spheres for fluorescence tracking and controlled drug release. *Biomed. Opt. Express* 7, 132–147. doi: 10.1364/BOE.7.000132

Kikuchi, Y., Mori, K., Suzuki, S., Yamaguchi, K., and Mizuno, S. (1992). Structure of the Bombyx mori fibroin light-chain-encoding gene: upstream sequence elements common to the light and heavy chain. *Gene* 110, 151–158. doi: 10.1016/0378-1119(92)90642-3

Kim, D. W., Lee, O. J., Kim, S. W., Ki, C. S., Chao, J. R., Yoo, H., et al. (2015). Novel fabrication of fluorescent silk utilized in biotechnological and medical applications. *Biomaterials* 70, 48–56. doi: 10.1016/j.biomaterials.2015.08.025

Kim, J., Kim, C. H., Park, C. H., Seo, J. N., Kweon, H., Kang, S. W., et al. (2010). Comparison of methods for the repair of acute tympanic membrane perforations: silk patch vs. paper patch. *Wound Repair Regen.* 18, 132–138. doi: 10.1111/j.1524-475X.2009.00565.x

Kim, S. W., Yun, E. Y., Choi, K.-H., Kim, S. R., Park, S. W., Kang, S. W., et al. (2012). Construction of fluorescent red silk using fibroin H-chain expression system. *J. Seric Entomol. Sci.* 50:8792.

Kim, S. W., Yun, E. Y., Choi, K.-H., Kim, S. R., Park, S. W., Kang, S. W., et al. (2013). Production of fluorescent green silk using fibroin H-chain expression system. *J. Seric Entomol. Sci.* 51, 153–158. doi: 10.7852/jses.2013.51.2.153

Kim, S. W., Yun, E. Y., Choi, K.-H., Kim, S. R., Park, S. W., Kang, S. W., et al. (2014). Expression of the blue fluorescent protein in fibroin H-chain of transgenic silkworm. *J. Seric Entomol. Sci.* 52, 25–32. doi: 10.7852/jses.2014.52.1.25

Ko, N. R., Nafiujjaman, M., Cherukula, K., Lee, S. J., Hong, S.-J., Lim, H.-N., et al. (2018). Microwave-assisted synthesis of biocompatible silk fibroin-based carbon quantum dots. *Part. Part. Syst. Charact.* 35:1700300. doi: 10.1002/ppsc.201700300

Kundu, S. C., Kundu, B., Talukdar, S., Bano, S., Nayak, S., Kundu, J., et al. (2012). Invited review nonmulberry silk biopolymers. *Biopolymers* 97, 455–467. doi: 10.1002/bip.22024

Kusurkar, T. S., Tandon, I., Sethy, N. K., Bhargava, K., Sarkar, S., Singh, S. K., et al. (2013). Fluorescent silk cocoon creating fluorescent diatom using a "Water glass-fluorophore ferry". *Sci. Rep.* 3:3290. doi: 10.1038/srep03290

Lee, J. M., Sultan, M. T., Kim, S. H., Kumar, V., Yeon, Y. K., Lee, O. J., et al. (2017). Artificial auricular cartilage using silk fibroin and polyvinyl alcohol hydrogel. *Int. J. Mol. Sci.* 18:E1707. doi: 10.3390/ijms18081707

Lee, M. S., Lee, M., Tokuyama, T., Wakida, T., Inoue, G., and Ishida, S. (2006). Ammonia-gas and liquid ammonia treatments of silk fabric. *J. Appl. Polym. Sci.* 101, 3487–3492. doi: 10.1002/app.24520

Lee, O. J., Ju, H. W., Kim, J. H., Lee, J. M., Ki, C. S., Kim, J. H., et al. (2014). Development of artificial dermis using 3D electrospun silk fibroin nanofiber matrix. *J. Biomed. Nanotechnol.* 10, 1294–1303. doi: 10.1166/jbn.2014.1818

Leem, J. W., Park, J., Kim, S. W., Kim, S. R., Choi, S. H., Choi, K. H., et al. (2018). Green-light-activated photoreaction via genetic hybridization of far-red fluorescent protein and silk. *Adv. Sci. (Weinh)* 5:1700863. doi: 10.1002/advs.201700863

Li, G., Liu, H., Li, T., and Wang, J. (2012). Surface modification and functionalization of silk fibroin fibers/fabric toward high performance applications. *Mater. Sci. Eng. C* 32, 627–636. doi: 10.1016/j.msec.2011.12.013

Li, Q., Qi, N., Peng, Y., Zhang, Y., Shi, L., Zhang, X., et al. (2017). Sub-micron silk fibroin film with high humidity sensibility through color changing. *RSC Adv.* 7, 17889–17897. doi: 10.1039/C6RA28460D

Li, S., and Jinjin, D. (2007). Improvement of hydrophobic properties of silk and cotton by hexafluoropropene plasma treatment. *Appl. Surf. Sci.* 253, 5051–5055. doi: 10.1016/j.apsusc.2006.11.027

Lin, N., Meng, Z., Toh, G. W., Zhen, Y., Diao, Y., Xu, H., et al. (2015). Engineering of fluorescent emission of silk fibroin composite materials by material assembly. *Small* 11, 1205–1214. doi: 10.1002/smll.201402079

Ling, S., Li, C., Jin, K., Kaplan, D. L., and Buehler, M. J. (2016). Liquid exfoliated natural silk nanofibrils: applications in optical and electrical devices. *Adv. Mater.* 28, 7783–7790. doi: 10.1002/adma.201601783

Liu, J. M., David, W. C., Ip, D. T., Li, X. H., Li, G. L., Wu, X. F., et al. (2009). High-level expression of orange fluorescent protein in the silkworm larvae by the Bac-to-Bac system. *Mol. Biol. Rep.* 36, 329–335. doi: 10.1007/s11033-007-9183-2

Lombardi, P. L. (1920). The duration of the stay of the ingested leaf in the intestine of the silkworm. *Ann. Scuola Agr. Portici* 2, 1–10.

Maclaren, J. A. (1981). *Wool Science: The Chemical Reactivity of the Wool Fibre/John A. Maclaren and Brian Milligan*. Marrickville, NSW: Science Press.

Mandal, B. B., and Kundu, S. C. (2009). Cell proliferation and migration in silk fibroin 3D scaffolds. *Biomaterials* 30, 2956–2965. doi: 10.1016/j.biomaterials.2009.02.006

Marsh, R. E., Corey, R. B., and Pauling, L. (1955). An investigation of the structure of silk fibroin. *Biochim. Biophys. Acta* 16, 1–34.

Min, K., Kim, S., Kim, C. G., and Kim, S. (2017). Colored and fluorescent nanofibrous silk as a physically transient chemosensor and vitamin deliverer. *Sci. Rep.* 7:5448.

Murphy, A. R., and Kaplan, D. L. (2009). Biomedical applications of chemically-modified silk fibroin. *J. Mater. Chem.* 19, 6443–6450. doi: 10.1039/b905802h

Myung, S. J., Kim, H.-S., Kim, Y., Chen, P., and Jin, H.-J. (2008). Fluorescent silk fibroin nanoparticles prepared using a reverse microemulsion. *Macromol. Res.* 16, 604–608. doi: 10.1007/bf03218567

Nadiger, V. G., and Shukla, S. R. (2016). Antibacterial properties of silk fabric treated with silver nanoparticles. *J. Text. Inst.* 107, 1543–1553. doi: 10.1080/00405000.2015.1129756

Omenetto, F. G., and Kaplan, D. L. (2008). A new route for silk. *Nat. Photon.* 2:641. doi: 10.1038/nphoton.2008.207

Otterburn, M. S. (1977). "The chemistry and reactivity of silk," in *Chemistry of Natural Protein Fibers*, ed. R. S. Asquith (Boston, MA: Springer US), 53–80. doi: 10.1007/978-1-4613-4109-3_2

Pal, R. K., Farghaly, A. A., Wang, C., Collinson, M. M., Kundu, S. C., and Yadavalli, V. K. (2016). Conducting polymer-silk biocomposites for flexible and biodegradable electrochemical sensors. *Biosens. Bioelectron.* 81, 294–302. doi: 10.1016/j.bios.2016.03.010

Park, B. J., Takatori, K., Sugita-Konishi, Y., Kim, I.-H., Lee, M.-H., Han, D.-W., et al. (2007). Degradation of mycotoxins using microwave-induced argon plasma at atmospheric pressure. *Surf. Coat. Technol.* 201, 5733–5737. doi: 10.1016/j.surfcoat.2006.07.092

Park, Y. R., Sultan, M. T., Park, H. J., Lee, J. M., Ju, H. W., Lee, O. J., et al. (2018). NF-kappaB signaling is key in the wound healing processes of silk fibroin. *Acta Biomater.* 67, 183–195. doi: 10.1016/j.actbio.2017.12.006

Parker, S. T., Domachuk, P., Amsden, J., Bressner, J., Lewis, J. A., Kaplan, D. L., et al. (2009). Biocompatible silk printed optical waveguides. *Adv. Mater.* 21, 2411–2415. doi: 10.1002/adma.200801580

Periyasamy, S., Gulrajani, M. L., and Gupta, D. (2007a). Preparation of a multifunctional mulberry silk fabric having hydrophobic and hydrophilic surfaces using VUV excimer lamp. *Surf. Coat. Technol.* 201, 7286–7291. doi: 10.1016/j.surfcoat.2007.01.038

Periyasamy, S., Gupta, D., and Gulrajani, M. L. (2007b). Modification of one side of mulberry silk fabric by monochromatic VUV excimer lamp. *Eur. Polym. J.* 43, 4573–4581. doi: 10.1016/j.eurpolymj.2007.07.014

Perry, H., Gopinath, A., Kaplan, D. L., Dal Negro, L., and Omenetto, F. G. (2008). Nano- and micropatterning of optically transparent, mechanically robust, biocompatible silk fibroin films. *Adv. Mater.* 20, 3070–3072. doi: 10.1002/adma.200800011

Ren, D., Kratz, F., and Wang, S. W. (2011). Protein nanocapsules containing doxorubicin as a pH-responsive delivery system. *Small* 7, 1051–1060. doi: 10.1002/smll.201002242

Rockwood, D. N., Preda, R. C., Yucel, T., Wang, X., Lovett, M. L., and Kaplan, D. L. (2011). Materials fabrication from Bombyx mori silk fibroin. *Nat. Protoc.* 6, 1612–1631. doi: 10.1038/nprot.2011.379

Sakudoh, T., Sezutsu, H., Nakashima, T., Kobayashi, I., Fujimoto, H., Uchino, K., et al. (2007). Carotenoid silk coloration is controlled by a carotenoid-binding protein, a product of the Yellow blood gene. *Proc. Natl. Acad. Sci. U.S.A.* 104, 8941–8946. doi: 10.1073/pnas.0702860104

Sargunamani, D., and Selvakumar, N. (2006). A study on the effects of ozone treatment on the properties of raw and degummed mulberry silk fabrics. *Polym. Degrad. Stabil.* 91, 2644–2653. doi: 10.1016/j.polymdegradstab.2006.05.001

Sultan, M. T., Lee, O. J., Kim, S. H., Ju, H. W., and Park, C. H. (2018). Silk fibroin in wound healing process. *Adv. Exp. Med. Biol.* 1077, 115–126. doi: 10.1007/978-981-13-0947-2_7

Sultan, M. T., Moon, B. M., Yang, J. W., Lee, O. J., Kim, S. H., Lee, J. S., et al. (2019). Recirculating peritoneal dialysis system using urease-fixed silk fibroin membrane filter with spherical carbonaceous adsorbent. *Mater. Sci. Eng. C Mater. Biol. Appl.* 97, 55–66. doi: 10.1016/j.msec.2018.12.021

Tamura, T., Thibert, C., Royer, C., Kanda, T., Abraham, E., Kamba, M., et al. (2000). Germline transformation of the silkworm Bombyx mori L. using a piggyBac transposon-derived vector. *Nat. Biotechnol.* 18, 81–84. doi: 10.1038/71978

Tamura, Y., Nakajima, K., Nagayasu, K., and Takabayashi, C. (2002). Flavonoid 5-glucosides from the cocoon shell of the silkworm, Bombyx mori. *Phytochemistry* 59, 275–278. doi: 10.1016/s0031-9422(01)00477-0

Tang, L., Yang, Y., Li, Y., Yang, G., Luo, T., Xu, Y., et al. (2018). Knitted silk mesh-like scaffold incorporated with sponge-like regenerated silk fibroin/collagen I and seeded with mesenchymal stem cells for repairing Achilles tendon in rabbits. *Acta Bioeng. Biomech.* 20, 77–87.

Tansil, N. C., Li, Y., Koh, L. D., Peng, T. C., Win, K. Y., Liu, X. Y., et al. (2011a). The use of molecular fluorescent markers to monitor absorption and distribution of xenobiotics in a silkworm model. *Biomaterials* 32, 9576–9583. doi: 10.1016/j.biomaterials.2011.08.081

Tansil, N. C., Li, Y., Teng, C. P., Zhang, S., Win, K. Y., Chen, X., et al. (2011b). Intrinsically colored and luminescent silk. *Adv. Mater.* 23, 1463–1466. doi: 10.1002/adma.201003860

Teule, F., Miao, Y. G., Sohn, B. H., Kim, Y. S., Hull, J. J., Fraser, M. J., et al. (2012). Silkworms transformed with chimeric silkworm/spider silk genes spin composite silk fibers with improved mechanical properties. *Proc. Natl. Acad. Sci. U.S.A.* 109, 923–928. doi: 10.1073/pnas.1109420109

Tomita, M. (2011). Transgenic silkworms that weave recombinant proteins into silk cocoons. *Biotechnol. Lett.* 33, 645–654. doi: 10.1007/s10529-010-0498-z

Tomita, M., Munetsuna, H., Sato, T., Adachi, T., Hino, R., Hayashi, M., et al. (2003). Transgenic silkworms produce recombinant human type III procollagen in cocoons. *Nat. Biotechnol.* 21, 52–56. doi: 10.1038/nbt771

Uchino, K., Imamura, M., Shimizu, K., Kanda, T., and Tamura, T. (2007). Germ line transformation of the silkworm, Bombyx mori, using the transposable element Minos. *Mol. Genet. Genomics* 277, 213–220. doi: 10.1007/s00438-006-0176-y

Vepari, C., and Kaplan, D. L. (2007). Silk as a biomaterial. *Prog. Polym. Sci.* 32, 991–1007. doi: 10.1016/j.progpolymsci.2007.05.013

Wang, X., Hu, X., Daley, A., Rabotyagova, O., Cebe, P., and Kaplan, D. L. (2007). Nanolayer biomaterial coatings of silk fibroin for controlled release. *J. Control Release* 121, 190–199. doi: 10.1016/j.jconrel.2007.06.006

Win, K. Y., Teng, C. P., Ye, E., Low, M., and Han, M. Y. (2015). Evaluation of polymeric nanoparticle formulations by effective imaging and quantitation of cellular uptake for controlled delivery of doxorubicin. *Small* 11, 1197–1204. doi: 10.1002/smll.201402073

Wu, Z., Chen, X., Wang, M., Dong, J., and Zheng, Y. (2018). High-performance ultrathin active chiral metamaterials. *ACS Nano* 12, 5030–5041. doi: 10.1021/acsnano.8b02566

Xu, Z., Shi, L., Yang, M., and Zhu, L. (2019). Preparation and biomedical applications of silk fibroin-nanoparticles composites with enhanced properties – A review. *Mater. Sci. Eng. C Mater. Biol. Appl.* 95, 302–311. doi: 10.1016/j.msec.2018.11.010

Yamao, M., Katayama, N., Nakazawa, H., Yamakawa, M., Hayashi, Y., Hara, S., et al. (1999). Gene targeting in the silkworm by use of a baculovirus. *Genes Dev.* 13, 511–516. doi: 10.1101/gad.13.5.511

Yanagisawa, S., Zhu, Z., Kobayashi, I., Uchino, K., Tamada, Y., Tamura, T., et al. (2007). Improving cell-adhesive properties of recombinant Bombyx mori silk by incorporation of collagen or fibronectin derived peptides produced by transgenic silkworms. *Biomacromolecules* 8, 3487–3492. doi: 10.1021/bm700646f

Yang, Y., Shao, Z., Chen, X., and Zhou, P. (2004). Optical spectroscopy to investigate the structure of regenerated Bombyx mori silk fibroin in solution. *Biomacromolecules* 5, 773–779. doi: 10.1021/bm0343848

Yeon, Y. K., Park, H. S., Lee, J. M., Lee, J. S., Lee, Y. J., Sultan, M. T., et al. (2018). New concept of 3D printed bone clip (polylactic acid/hydroxyapatite/silk composite) for internal fixation of bone fractures. *J. Biomater. Sci. Polym. Ed.* 29, 894–906. doi: 10.1080/09205063.2017.1384199

Ying Zhang, J., Esrom, H., Kogelschatz, U., and Emig, G. (1993). Large area photochemical dry etching of polyimide with excimer UV lamps. *Appl. Surf. Sci.* 69, 299–304. doi: 10.1016/0169-4332(93)90522-D

Zhang, F., Zhao, Y., Chen, X., Xu, A., Huang, J., and Lu, C. (1999). Fluorescent transgenic silkworm. *Acta Biochim. Biophys. Sin.* 31, 119–123.

Zhang, Y., Fan, W., Ma, Z., Wu, C., Fang, W., Liu, G., et al. (2010). The effects of pore architecture in silk fibroin scaffolds on the growth and differentiation of mesenchymal stem cells expressing BMP7. *Acta Biomater.* 6, 3021–3028. doi: 10.1016/j.actbio.2010.02.030

Zhao, Y., Chen, X., Peng, W. P., Dong, L., Huang, J. T., and Lu, C. D. (2001). Altering fibroin heavy chain gene of silkworm Bombyx mori by homologous recombination. *Sheng Wu Hua Xue Yu Sheng Wu Wu Li Xue Bao (Shanghai)* 33, 112–116.

Zheng, Z. Z., Liu, M., Guo, S. Z., Wu, J. B., Lu, D. S., Li, G., et al. (2015). Incorporation of quantum dots in silk biomaterials for fluorescence imaging. *J. Mater. Chem. B* 3, 6509–6519. doi: 10.1039/C5TB00326A

Zhou, C. Z., Confalonieri, F., Jacquet, M., Perasso, R., Li, Z. G., and Janin, J. (2001). Silk fibroin: structural implications of a remarkable amino acid sequence. *Proteins* 44, 119–122. doi: 10.1002/prot.1078

Conflict of Interest: The authors declare that the research was conducted in the absence of any commercial or financial relationships that could be construed as a potential conflict of interest.

frontiers in Materials

ORIGINAL RESEARCH
published: 15 May 2020
doi: 10.3389/fmats.2020.00098

Multiscale Hybridization of Natural Silk–Nanocellulose Fibrous Composites With Exceptional Mechanical Properties

Jungju Eom[1], Subong Park[2], Hyoung-Joon Jin[1] and Hyo Won Kwak[3,4]**

[1] Department of Polymer Science and Engineering, Inha University, Incheon, South Korea, [2] Fisheries Engineering Division, National Institute of Fisheries Science, Busan, South Korea, [3] Department of Forest Sciences, Seoul National University, Seoul, South Korea, [4] Research Institute of Agriculture and Life Sciences, College of Agriculture and Life Sciences, Seoul National University, Seoul, South Korea

Because of the crisis of the petrochemical era, environmentally friendly natural polymers and related material processes are receiving great attention. Cellulose and silk are typical fibrous materials that consist of polysaccharides and proteins, respectively, and have excellent mechanical properties and high physicochemical stabilities due to their unique self-assembly-based hierarchical structures. In this study, highly stable high-strength silk fiber (SF)–cellulose nanofibril (CNF) composites were prepared by the hierarchical fusion of micrometer-scale SFs and nanometer-scale CNFs. This manufacturing process is cost-effective because the raw materials (SFs and CNFs) are used as is. It is an eco-friendly process because it does not require the use of organic solvents or toxic reagents. In addition, it is an energy-efficient process because heat fusion (120°C) takes only 10 min. The results of the Direct Red 80 staining experiments confirm that up to 15 wt.% CNFs were added to the SF nonwoven. With the increase in the CNF amount, the nanometer-scale CNFs form a coating on the micro-scale SFs. At the same time, the CNFs form bonds with the SFs and increase the interfibrillar bonding strength of the CNF-coated SFs. Therefore, the mechanical properties of the SF/CNF composite and its stability in the water environment rapidly increase with increasing CNF concentration. In the case of SF/CNF15, the mechanical and impact strengths increase by 110 and 228%, respectively, compared with SF nonwoven without CNF. In addition, as CNFs are introduced, hydrophobicity of the surface and bulk of the SF/CNF composite can be imparted, thereby maintaining its structural stability in the water environment. This eco-friendly SF/CNF composite can be widely used as reinforcement preform of fiber-reinforced plastics as well as for other applications in the fibrous composite industry.

Keywords: silk fibroin, cellulose nanofiber, fibrous composite, nonwoven, adhesion

OPEN ACCESS

Edited by:
Antonella Motta, University of Trento, Italy

Reviewed by:
Marina Scarpa, University of Trento, Italy
Veronique Michaud, Federal Institute of Technology in Lausanne, Switzerland

****Correspondence:***
Hyoung-Joon Jin
hjjin@inha.ac.kr
Hyo Won Kwak
bk0502@snu.ac.kr

Specialty section:
This article was submitted to Polymeric and Composite Materials, a section of the journal Frontiers in Materials

Received: *20 December 2019*
Accepted: *30 March 2020*
Published: *15 May 2020*

Citation:
Eom J, Park S, Jin H-J and Kwak HW (2020) Multiscale Hybridization of Natural Silk–Nanocellulose Fibrous Composites With Exceptional Mechanical Properties. Front. Mater. 7:98. doi: 10.3389/fmats.2020.00098

INTRODUCTION

Silk is an attractive natural fibrous material with a unique hierarchical composite structure (Shao and Vollrath, 2002; Vollrath et al., 2013; Koh et al., 2015). Its molecular structure consists of repetitive amino acid sequences (Malay et al., 2016), which form a secondary β-sheet-driven protein structure by the surrounding environment to form silk nanofibrils. The self-assembled nanofibrils

agglomerate to produce fibroin microfibers and, finally, a bicomponent nonwoven cocoon fabric in which sericin surrounds two fibroin strands (Keten et al., 2010; Omenetto and Kaplan, 2010; Asakura et al., 2015; Malay et al., 2016; Wang et al., 2018b). Based on its unique hierarchical structure, silk has excellent mechanical properties (Chen et al., 2012; Shah et al., 2014; Sanjay et al., 2018) and is resistant to physical attacks and harsh environmental conditions. In addition, silk cocoons produced by silkworms have the advantage that they occur under environmentally friendly process conditions such as room temperature and atmospheric pressure.

Because of their excellent biocompatibility and biodegradability as well as intrinsic mechanical rigidity, various regenerated silk materials have received increased attention (Han et al., 2017; Magaz et al., 2018; Yazawa et al., 2018; Zhang et al., 2018). However, regenerated silk materials have a significant disadvantage in that they are difficult to scale up (Lee et al., 2018). During the regeneration process, environmental problems occur because of the use of organic solvents. In addition, molecular weight decomposition occurs in natural silk, leading to the deterioration of its physical properties (Cho et al., 2012; Kim et al., 2014; Lee et al., 2018; Yin et al., 2019). To overcome the above-mentioned disadvantages and effectively utilize silk materials, untreated (no regeneration) natural silk fibers (SFs) should be used (Peng et al., 2019).

Fibrous and fiber preform composites, which are produced by using natural SF as raw material, consist of SFs and additional chemical binders that increase the bonding between the SFs (Song et al., 2009; Yuan et al., 2010; Shubhra et al., 2011; Guang et al., 2015). Their mechanical properties greatly depend on the interaction between the binder and fibers. To improve the interaction between the binder and fiber, chemical modifications (Dányádi et al., 2010; Guo et al., 2016; Lee et al., 2019) (i.e., ionic, electrostatic, polar, and van der Waals forces exerted on the fiber and adhesive) and physical modifications of the fiber surfaces (Song et al., 2010), which increase the roughness and specific surface area of the fibers, have been widely used (Adekunle, 2015). However, these modifications lead to the physicochemical damage of the fibers and thus the mechanical weakness of the product if the modification time is extensive (Baiardo et al., 2004; Carvalho et al., 2010; Favaro et al., 2010; Das et al., 2015; Pandey et al., 2015). Another approach to increasing the interaction between the fibers is to fabricate hairy and fuzzy fibers based on the adhesion of finely sized nanomaterials to the surface of the fibers (Juntaro et al., 2008; Pommet et al., 2008; Lee et al., 2012; Arévalo and Peijs, 2016; Fortea-Verdejo et al., 2016).

Multiscale hybridized materials have received great attention by the scientific and industrial communities during the last decade due to their synergistic effects originating from different morphological scales (Duan et al., 2017; Lin et al., 2017; Toprakcioglu et al., 2017; Hadadi et al., 2018). In the composite materials approach, multiscale hybridization is an important key to solve inherent weaknesses such as the deterioration of the mechanical properties due to the poor reinforcement and structural dismantling in wet or aqueous environments (Fortea-Verdejo et al., 2016). In the biomedical fields, the production of multiscale materials can be used to create an effective drug delivery system (Numata et al., 2012; Gao et al., 2019), enabling sustainable and ultrafast drug delivery. At the same time, based on the nano-topologies of the microsurfaces (Mozumder et al., 2011), superhydrophobic materials can be produced. In addition, injectable scaffolds with reinforced mechanical strengths can be prepared by incorporating nano and microparticles into three-dimensional hydrogels (Xiao et al., 2017). Therefore, the fabrication of multiscale hybridizing fibrous composites using natural micro- and nanoscale fibrous materials is a simple and environmentally friendly fabrication method with a synergistic structure–property relationship.

Wood is the most abundant natural resource on Earth and a cellular hierarchical biocomposite (Eichhorn et al., 2010). The self-assembly of hydrogen bond-based repetitive glucose units results in the formation of elemental fibrils, which develop into microcrystalline cellulose (MCC) (Tayeb et al., 2018). The MCC forms a macroscopic biocomposite structure that reinforces the matrix consisting of lignin, hemicellulose, and wax, eventually forming a whole tree with a scale of tens of meters. Various natural raw materials can be obtained from such a complex hierarchical structure of woody biomass (Klemm et al., 2005, 2011; Cervin et al., 2013). Such raw materials have been used to manufacture paper, (Song et al., 2009) pulp, (Theng et al., 2015) and fiber, which greatly contributed to human development. Recently, the development of advanced materials using nanocellulose has been actively attempted because of the robust physicomechanical properties of nanocellulose, which are based on its unique morphology and crystalline structure (Theng et al., 2015; Amini et al., 2017; Saba et al., 2017b,a; Tayeb et al., 2018; Feng et al., 2019; Kwak et al., 2019b).

To fabricate such a natural multiscale hybridizing polymer fibrous composite, SFs produced by silkworms and cellulose nanofibrils (CNFs) obtained from the woody biomass were used as natural micro and nanoscale fibrous raw materials, respectively. In this study, natural polymeric hierarchical fibrous composites were fabricated by using filtration and thermal fusion methods typically used in conventional paper manufacturing. The successful fabrication of hierarchal nano and microscale hybridization structures was verified using dye stains and the interactions between the nano and microscale fibers were confirmed using disintegration observations. Finally, the mechanical properties and water stability depending on the CNF concentrations of the natural multiscale hybridized fibrous composites were determined.

MATERIALS AND METHODS

Materials

Silk cocoons of the *Bombyx mori* silkworm were kindly provided by the National Academy of Agricultural Science (NAAS, Korea). Bamboo fibers were obtained from Damyang (2–3 years old, Phyllostachys, Korea) and used as native cellulose fibers. Direct Red 80 was obtained from Tokyo Chemical Industry Co., Ltd., Japan. Na_2CO_3 was purchased from Sigma-Aldrich (Korea).

Degumming of Silk Fibers (SF)

The silkworm cocoons were boiled for 30 min in an aqueous solution containing 0.02 M sodium carbonate (Na_2CO_3, >99.0%, Sigma-Aldrich) to remove sericin and other impurities. After washing the samples several times with deionized water (DI) water, the resulting protein SFs were dried for 3 days at 25°C. Next, the degummed SF fibers were wound onto a small mandrel to yield 6 cm long aligned fibers.

Preparation of Cellulose Nanofibril (CNF)

To remove the waxy material from the bamboo, 2 g of the bamboo fiber was dewaxed on a Soxhlet equipment (SE-Series, Vinci Technologies, France) with a benzene/ethanol [2: 1 (v/v) mixture of] for 6 h. The lignocellulosic material in the sample was then removed using a sodium chlorite ($NaClO_2$) solution at 75°C for 1 h and repeated same process five times until the color of the sample became white. The residual hemicellulose, starch and pectin were further removed at 90°C for 2 h with 2 wt% potassium hydroxide (KOH). Thereafter, bamboo cellulose dispersion (0.05 wt%) was prepared by adjusting the concentration of the dispersion with distilled water. About 200 mL of the bamboo cellulose dispersion was placed in an ultrasonic generator (Kyungil Ultrasonic Co., Korea), and subsequent sonication (800 W, 4 s on/off pulse) was performed for 1 h to obtain disintegrated cellulose nanofibrils. In order to avoid temperature elevation during high intensity ultrasonic processing, sonication was performed in an ice/water cooling bath system. In order to confirm nanofibril preparation, morphological image of bamboo CNF was obtained using field emission scanning electron microscopy (FE-SEM, AURIGA, Carl Zeiss, Germany), and determination of nanofibers diameters were performed with "Image J" software.

Fabrication of SF/CNF Fibrous Composites

To obtain a homogeneous CNF dispersion, 1 wt.% CNF solution was sonicated at 300 W, 4 s on/off pulse under the ice/water bath condition. Then, 0–1 wt.% of CNF solutions were prepared by dilution with the distilled water. SF fibers (1.6 g) were added to the desired CNF solution and incubated for 10 min to fully wet the CNF dispersed solution within the SF fibers. The SF/CNF suspension was poured into a metal mold and homogenously distributed. Thereafter, a paper towel was used to remove excessive water from the SF/CNF mixture in the mold (six times). The moisture-free SF/CNF mixture was placed onto a hot press machine (HLP-12H, Han tech, Korea) and the metal mold was removed. Subsequently, the SF/CNF mixture was pressed at 120°C for 10 min to fabricate a SF/CNF fibrous composite. A polyester nonwoven was placed on the top and bottom of the SF/CNF mixture to avoid the adhesion of the SF/CNF to the plate of the hot press. The overall process of manufacturing SF/CNF composites is shown in **Scheme 1**. As a control, untreated nonwoven silk was prepared using the above-mentioned pressing method at room temperature. The resultant SF–CNF composite was labeled SF/CNF-n, where "*n*" corresponds to the initial CNF content (*n* = 5, 10, and 15 wt.% of SF, respectively).

Characterization

To determine the CNF distribution on the SF surface, the prepared SF/CNF fibrous composite was immersed in 60 mL of Direct Red 80 dye solution (0.0025 wt.%) and incubated for 30 min. Thereafter, distilled water was used to remove the unreacted dye molecules from the sample until no red color was observed on the paper towel, which was pressed onto the SF/CNF fibrous composite sample. The washed fibrous composite was incubated in the oven at 60°C for 1 day and images of the dried sample were obtained. To obtain the Direct Red 80-dyed CNF sample, 1 wt.% of CNF solution was casted on a Petri dish and lyophilized using a freeze dryer. Subsequently, sponge-type CNFs were obtained by pressing at 120°C for 10 min. The above-mentioned dyeing process was also used for this sample and an image was obtained.

Optical images of the prepared SF/CNF composites were obtained using a digital camera (D7200, Nikon, Japan). The morphologies of the SF/CNF composites were analyzed using field emission scanning electron microscopy (FE-SEM, AURIGA, Carl Zeiss, Germany). To obtain cross-sectional images of the SF/CNF composites, the samples were placed in a liquid nitrogen chamber for 6 h and then cut using a cryo-blade. To find out coating and interfacial adhesion behavior of nanocellulose onto the SF fibers, 1.6 g of SF fibers were immersed onto the 40 ml of cellulose nanocrystal (CNC) and CNF solution (0.5 wt%) and it dried 60°C for 24 h. The prepared SF/CNC and SF/CNF composites were immersed the 50 ml of distilled water and it sonicated 200 W for 20 min to detach CNC and CNF from the SF fibers. Then morphology of the SF/CNC and SF/CNF before and after ultrasonication treatment were analyzed using FE-SEM.

The X-ray diffraction (XRD, Rigaku, DMAX 2500) analyses were conducted over a 2θ range of 5°–60° at 40 kV and 100 mA using Cu Kα radiation (λ = 0.154 nm). An attenuated total reflectance Fourier transform infrared (ATR-FTIR) spectrometer was used to examine the chemical structures of the SF/CNF composites. The scan range, scan number, and resolution of the measurements were 4000–700 cm^{-1}, 128, and 2 cm^{-1}, respectively. The absolute density (ρm) of the manufactured SF/CNF composites was measured with a He pycnometer (AccuPyc 1330, Micromeritics, United States). The samples were weighed and then loaded in the measurement chamber. The envelope density (ρe) of the fibrous composites was calculated from the mass and envelope volume of the nonwoven samples. The porosity of the fibrous composite was calculated using Eq. (1):

$$\text{Porosity (\%)} = \left\{ \frac{1 - (\textit{Enveloped density})}{\textit{Absolute Density}} \right\} \times 100 \qquad (1)$$

To determine the mechanical properties of the SF/CNF composite, tensile tests were performed using a universal testing machine (CS225, Lloyd Instruments, Ltd., United Kingdom). The experiment was conducted by applying a tensile force in accordance with the main arrangement direction of the SF fibers. The gauge length and width of the samples were fixed to 50 and 25 mm, respectively, and tensile tests were performed using a 1000 N load cell at an extension rate of

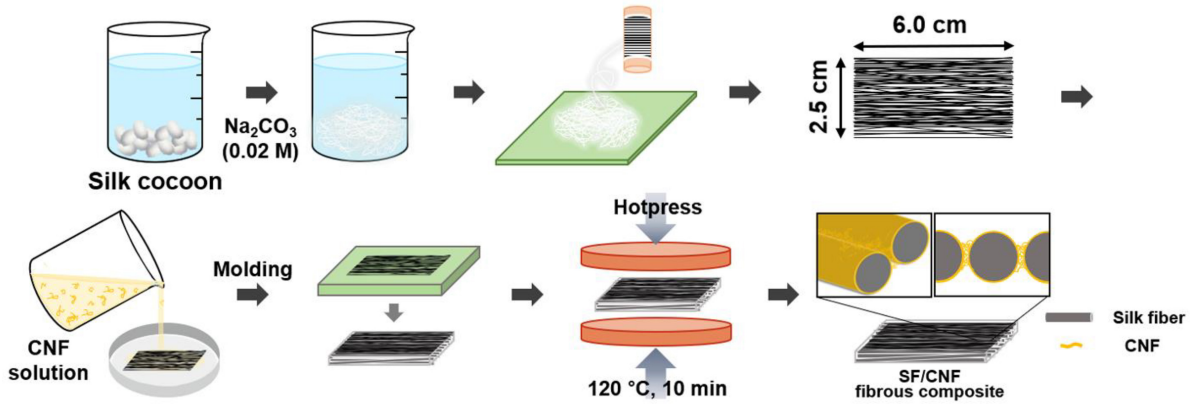

SCHEME 1 | Schematic of the fabrication of SF/CNF composites.

10 mm/min. All samples were preconditioned at 20°C and a relative humidity of 65%. The Izod impact strength of the unnotched fibrous composite specimens was measured with a (QM700A, Qmesys, Korea) machine at a strike velocity of 2.5 m/s according to the ASTMD256 test method. The experiment was conducted by applying an impact force to vertical direction of SF fiber's alignment. At least five samples were tested under each condition and the averages and standard deviations of the tensile strength, elongation at break, and initial Young's modulus were evaluated. To study the physical stability of the SF/CNF composites in a water environment, water droplet images were obtained 1 s after placing a water droplet on the fibrous composite surface. To investigate the stability under hydrolytic conditions, the SF/CNF composites were immersed in 60 mL distilled water for 21 days. Subsequently, optical images of the fibrous composites were obtained.

To determine the moisture absorption behavior of the SF/CNF composites, a water uptake test was performed (de Campos et al., 2013). The sample size was fixed to 60 mm (length) and 25 mm (width). All samples were preconditioned at 25°C and a relative humidity of 51%. Thereafter, the samples were immersed in distilled water. Their weights were determined before and after immersion. At least five samples were tested under each condition and the averages and standard deviations were obtained. The water uptake was calculated using Eq. (2). The parameters W_0 and W_t are the initial weight and the weight after immersion for 24 h, respectively.

$$\text{Water uptake (\%)} = \frac{(W_t - W_o)}{W_o} \times 100 \qquad (2)$$

RESULTS AND DISCUSSION

Using the chemical purification and high intensity ultrasonication process, bamboo-derived cellulose nanofibril (CNF) was successfully prepared. As a result of morphology confirming through the FE-SEM and FE-TEM image, the formation of high aspect ratio CNFs having 15–35 nm of diameter (average diameter: 26.1 nm) was observed (**Figure 1**).

In order to examine the effect of nonwoven fabrication processing on the silk fibroin (SF) fiber, SF nonwoven fabric was prepared by simply pressing without treatment. **Figure 2A** shows the image of the degummed SF (sericin removed) and pressed SF nonwoven without heat treatment. The degummed SF shows a three-dimensional cotton candy shape, and it can be confirmed that such SF can be manufactured as a two-dimensional like nonwoven fabric through a simple pressing process. It was found that the pressing process did not change the color of the SF fibers themselves. Meanwhile, images of SF nonwoven and CNF added SF/CNF composite nonwoven prepared by hot pressing method are shown in **Figure 2B**. In the case of CNF, the hot-pressed CNF film remains white color even though manufactured by the hot-pressing method. However, in the case of SF, prepared hot-pressed silk non- woven is converted to pale yellow. Generally, a yellowing phenomenon can mainly be observed when protein crosslinking (both self-crosslinking and crosslinking with a chemical crosslinker) occurs. During the fabrication of nonwoven SFs, protein self-crosslinking occurs, resulting in a yellowing phenomenon (Lee et al., 2018). Urreaga and de la Orden (2006) prepared chitosan treated cotton cellulose fibers to examine the interaction between amino group of chitosan and cellulose carbonyl groups and found that the higher the amount of added chitosan, the more conjugated imine groups produced, resulting in yellowing behavior of cellulose. However, it is difficult to observe a significant color difference in the SF/CNF composite compared to the SF heat-treated nonwoven. Therefore, the yellowing phenomenon occurring in the SF/CNF composite is largely affected by the crosslinking of the SF fiber itself.

To confirm the effect of CNF concentration on the residual CNF contents in the SF/CNF composites, the weight gain ratio of SF/CNF were calculated based on the dry weight and the obtained result was shown in **Figure 2C**. As shown in the figure, as the CNF content increases to 15% of the SF weight, the weight gain ratio of the SF/CNF composite also increases proportionally. However, it can be seen that there is a limit to the amount of CNF that can penetrate into the SF nonwoven

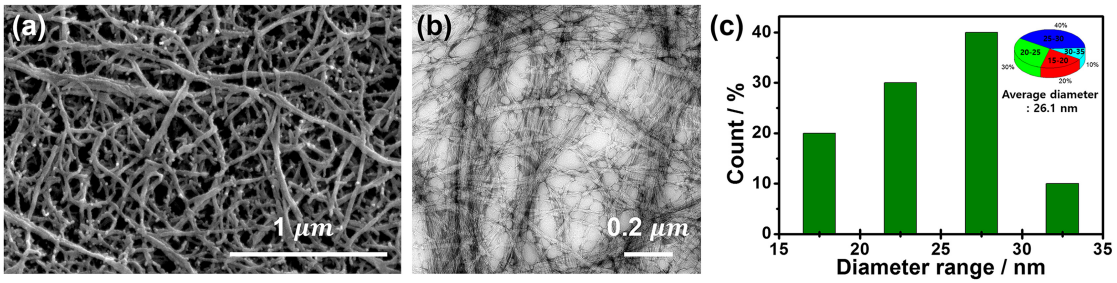

FIGURE 1 | FE-SEM **(a)**, FE-TEM **(b)** images, and nanofibril diameter distribution **(c)** of bamboo cellulose nanofibril (CNF).

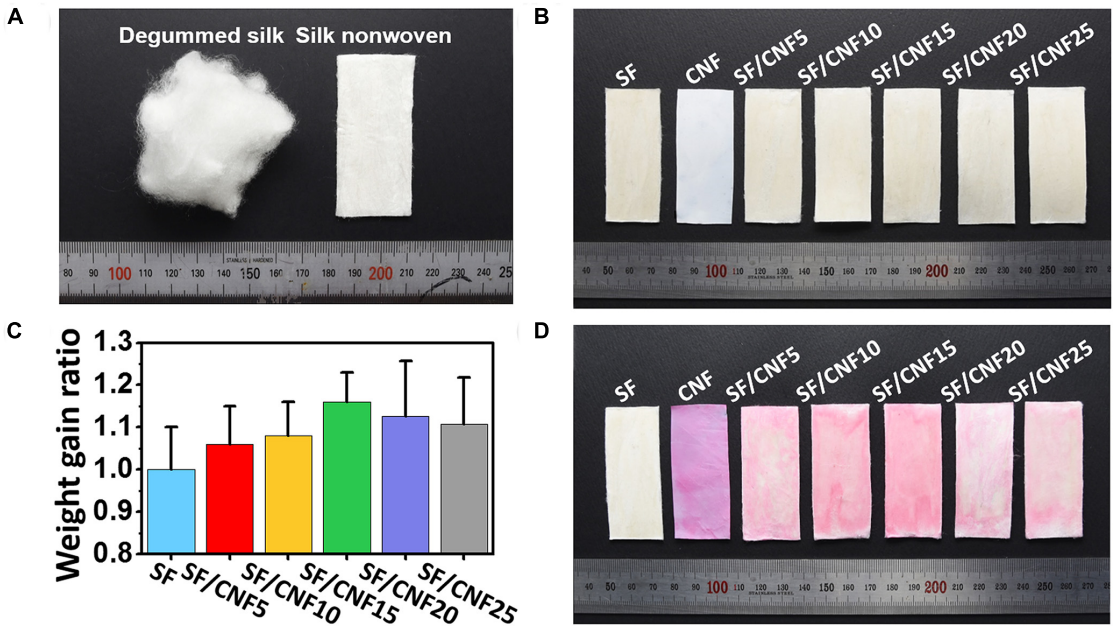

FIGURE 2 | Effect of CNF addition on the visual inspection of SF/CNF composites. Optical images of degummed SF fibers and prepared SF nonwoven without heat treatment **(A)**, hot-pressed SF/CNF composites **(B)**, weight gain ratio of SF/CNF composites **(C)**, and optical images of Direct Red 80 dyed SF/CNF composites **(D)**.

fabric by reduced weight gain ratio of SF/CNF20 and SF/CNF25 compared to SF/CNF15.

In the degumming process, which is the removal of silk sericin from cocoon silk, a Direct Red 80 staining test is widely used to confirm the removal of the gummy sericin protein (Nisal et al., 2014; Kwak et al., 2017). Depend on the hydrophilicity of silk proteins (fibroin and sericin), Direct Red 80 easily stains the gummy and hydrophilic sericin protein, while degummed hydrophobic fibroin fiber cannot be dyed (Kwak and Lee, 2015). In addition, (Saleem et al., 2007) confirmed that the Direct Red 80 dye is easily dyed to cellulose cotton fibers. By using the different dyeability between cellulose and silk fibroin, the distribution of CNF in SF/CNF composite was visualized and the optimal CNF content was found. The Direct Red 80 dyed fibrous SF/CNF composite samples are shown in **Figure 2D**. As shown in the figure, Direct Red 80 does not dye nonwoven SF, probably because the SFs are hydrophobic and the dye molecules do not penetrate the β-sheet-dominated SF structure. On the other hand, in the case of the nonwoven CNF fabric, the Direct Red 80 dye penetrates the fabric and a vivid pink color can be observed. This is the result of dyeing through hydrogen bond with cellulose chain after the Direct Red 80 dye dissociates under neutral aqueous conditions. The CNF concentration of the SF/CNF composite can be simply determined based on the dyeing performance observed during the Direct Red 80 staining test. As the CNF content of the SF/CNF composites increases from 5 to 15 wt.%, the color of the fibrous composite surfaces becomes more vivid (pink). In the case of the SF/CNF5 composite, a white part can be observed because the amount of CNF between the SFs is not high enough. In the case of SF/CNF10 and SF/CNF15, the surfaces of the SF fibrous composites are fully covered with CNF molecules, which results in uniform pink layers. In addition, as the CNF weight increases, the color becomes more vivid, indicating that the CNF concentration of the SF nonwoven is higher. However, SF/CNF20 and SF/CNF25 are partially pale pink similar with SF/CNF5 despite the increase in the CNF

weight. Resulted concentration effect of CNF may be related to the rheological properties of CNF dispersion. Lasseuguette et al. (2008) investigated the rheological properties of CNF solution according to the concentration. At low or diluted concentration region (>>0.25 wt%), the viscosity increased linearly with concentration, whereas at higher concentration the viscosity followed a power law equation. In this study, to consider the water absorption capacity of SF fibers, a higher concentration of CNF dispersion was used to add more CNF to the SF nonwovens. As a result, as the concentration of CNF increases, the viscosity of the CNF dispersion increases, which makes it difficult for CNF to sufficiently penetrate between the SF fiber surface and the between the SF pores. The penetration tendency of CNF into the SF nonwovens can also be clearly seen in cross sectional images of the SF/CNF composite (**Supplementary Figure S1**).

To investigate the macroscopic changes of the nonwoven SF structure after the combination of the CNFs with SFs, the envelope and absolute densities of the SF/CNF composites were measured. The porosities of the SF/CNF composites were calculated based on the relationship between the envelope and absolute densities, as shown in **Figures 3A–C** and **Supplementary Table S1**.

The absolute density (ρ_m), commonly referred to as bulk density, is the ratio between the mass and the unit volume of a sample. Voids or pores in the material are not considered. The absolute density insignificantly changes, even if CNF is added to the SF structure. On the other hand, the envelope density (ρ_e), defined as the ratio between the mass of the material and the sample volume, includes voids or pores in the material. As the CNF content increases, the envelope density of the SF/CNF composite increases from 0.79 ± 0.03 for nonwoven SF to 1.02 ± 0.02 for the SF/CNF15 composite. The calculated porosity was obtained based on the results of two density measurements. The CNF content increases; porosity decreases from 40.91 ± 1.08 (sf nonwoven) to 25.91 ± 1.36 (SF/CNF15). Kwak et al. (2019a) fabricated jute fiber–sericin preform composites using sericin as bio-adhesive for the adhesion of jute fibers and observed a similar offset phenomenon of the porous structure of the jute fiber composites due to the void filling effect of the sericin proteins. The decrease in the porosity of the SF/CNF composite with increasing CNF concentration is due to the fact that the CNF does not only form a coating on the SF but also fills the space between the SFs.

To identify the effect of the CNF binder on the morphological changes of the SF/CNF composites, surface and cross-sectional FE-SEM images were obtained. The results are shown in **Figure 4**. All samples of the SF/CNF composites were found to be well aligned in certain direction even after the hot-pressing process. In the case of SF nonwoven, the SF surface is smooth and the space between the SFs is clearly visible. On the other hand, as CNFs are introduced, the CNF forms a coat on the SFs; at the same time, it fills the space between the SFs. This phenomenon becomes more apparent as the CNF content increases. In the case of the SF/CNF15 composite, CNFs cover the whole SF surface and fill almost all pores between the SFs. This pore filling effect can also be observed in the cross-sectional images (as shown in **Figures 4e–h**). As the CNF content increases, the gaps between the SFs are filled and the sizes of the pores decrease. This effect can be clearly observed in the FE-SEM cross-sectional images with higher magnification. In the case of SF nonwoven, the boundary between the SFs can be clearly observed, whereas in the case of the SF/CNF15 composite, CNFs are observed between SFs, which makes the boundary between fibers unclear. Nevertheless, pores between the SFs can be observed, indicating that the CNFs reduce the porosity of the SF structure but do not fill the entire pore structure of the SF matrix.

To investigate the chemical structure and crystalline properties of SF/CNF composites after CNF addition, FTIR spectra and XRD patterns were obtained. The results are shown in **Figure 5**. The FTIR spectra of the SF/CNF composites are shown in **Figure 5A**. In the spectrum of neat CNF, an O-H stretching mode at 3300 cm^{-1}, C-H stretching mode at 2800 cm^{-1}, and C-O stretching peak at 1013 cm^{-1} can be observed, which are typically associated with cellulose structures. In the case of SF/CNF composites, the SF shows a crystalline secondary β-sheet structure typical for SF proteins. Regardless of the CNF content, the spectra of all SF/CNF composites show amide I (C = O stretching) and amide II (N-H bending and C-N stretching) peaks at 1620 and 1510 cm^{-1}, respectively, which are associated with the secondary β-sheet structure of SF (Jackson and Mantsch, 1995; Lu et al., 2010; Nagarkar et al., 2010; Boulet-Audet et al., 2015). This means that the CNFs do not induce the conformational transition of the β-sheet structure of SF, even if CNFs are introduced to the SF structure. In general, silk-based materials, including natural and regenerated SFs, have excellent mechanical properties when the silk materials exhibit a β-sheet structure. Therefore, maintaining the secondary

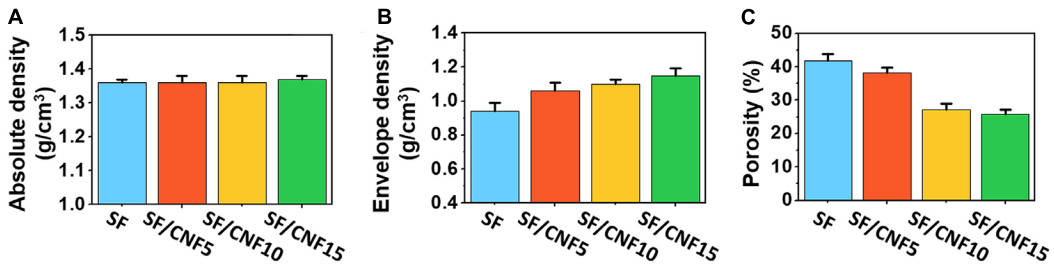

FIGURE 3 | Absolute density **(A)**, envelope density **(B)**, and calculated porosity **(C)** of the SF/CNF composites with various amounts of CNFs.

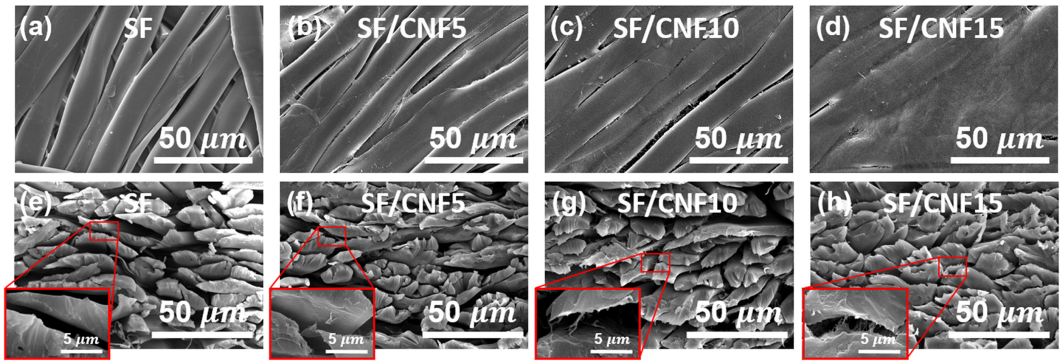

FIGURE 4 | FE-SEM images of the SF/CNF composites with various CNF concentrations. Surface **(a–d)** and cross section **(e–h)** images; **(a,e)**: SF nonwoven, **(b,f)**: SF/CNF5, **(c,g)**: SF/CNF10, **(d,h)**: SF/CNF15. The insets represent high-magnitude images.

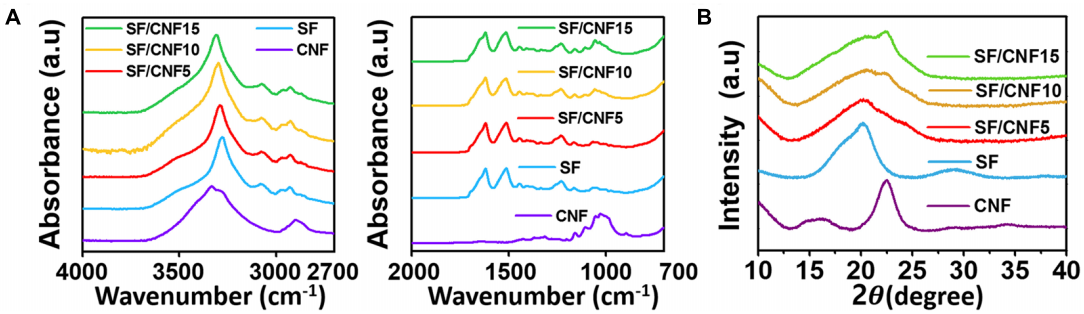

FIGURE 5 | Characteristics of CNF, nonwoven SF, and SF/CNF composites with various amounts of CNFs: **(A)** FTIR spectra, **(B)** XRD pattern.

β-sheet structure of the SF, even when CNF is added, will have a positive effect on the mechanical properties. On the other hand, as the CNF content increases, the intensity of the C-O stretching absorption peak at 1013 cm^{-1} increases,(Morán et al., 2008; Han et al., 2013; Feng et al., 2019) implying the settling of CNF on the surface of the SF. Furthermore, in the spectra of the SF/CNF composites, the O-H peak of SF merges with that of CNF. The spectra exhibit a blue-shifted broader peak, indicating the interaction between SFs and CNFs through the hydrogen bonds (Lee et al., 2013).

The XRD patterns of the SF/CNF composites are shown in **Figure 5B**. The nonwoven SF exhibits a peak at 20.2°, which corresponds to the silk II β-sheet crystallite structure (Lee, 2004; Cheng et al., 2015; Guang et al., 2015; Ming et al., 2015). In the case of CNF, characteristic peaks at 2θ = 16.3° and 22.6° are observed, representative for the typical cellulose type I structure (Morán et al., 2008; Han et al., 2013; Kwak et al., 2019b). Based on the XRD patterns of the SF/CNF composites, the CNF binder affects their crystalline structures. In the case of SF/CNF5, because the CNF does not cover the whole SF surface, the crystal structure of SF appears to be sharp. On the other hand, in the case of SF/CNF10, the crystal structure appears to be mixed, but the peak at 20.2°, which represents the crystal structure of silk, is more dominant. In the case of SF/CNF15 with a higher CNF content, the peak at 22.6°, which corresponds to CNF, is more prevalent. Based on the FTIR and XRD results, the introduction of CNF does not lead to the transfer of the β-sheet structure of SF, but the crystal structure of the entire SF/CNF composite changes.

To visually identify the interaction between CNF and SF, a ultrasonication detaching test was applied using nanocellulose coated SF fibers. To find out the effect of nanocellulose morphology on the interaction between SF and nanocellulose, cellulose nanocrystal (CNC) with a low aspect ratio and CNF with a high aspect ratio were used as a SF coating agent. Thereafter, bonded nanocellulose onto SF fibers were detached by ultrasonic treatment, which is a strong physical treatment technique. **Figure 6a** shows the morphology of a freeze-dried CNC. It can be seen that the aspect ratio of CNC is lower than that of CNF as shown above image (**Figure 1a**). Also, as shown in **Figure 6b**, neat silk fibers have a smooth surface. **Figure 6d** show that the SF has a smooth surface, while the CNC-coated SF has a rough surface. This smooth surface of SF changed to rough with a short aspect ratio of CNC covering (**Figure 6c**). The rough surface of the CNC-coated SF indicates that the CNC covers the surface of the SF and forms a core–shell-like structure. Although the roughness decreases after sonication, the CNC-coated SF surface is rougher than that of the conventional SFs. This means that more than just physical adsorption occurs between CNC and SF. Compared with CNC, CNF has a longer aspect ratio, so it can be applied not only for simple coating but also for interfacial adhesion between SF fibers. In order to confirm the adhesion behavior of CNF, CNF coating was applied

to SF fibers, and FE-SEM images of SF/CNF fibers subjected to sonication to separate them are shown in **Figures 6e,f**. As can be seen in the figure, the CNF bundle wraps around the SF fibers, so the SF fibers have a rough surface. Not only this, you can clearly observe the presence of CNF bundles between SF fibers. Through this, when the CNF is introduced onto the SF fibers, CNF can play not only the simple coating reagent but also the interfacial adhesive of the SF fibers. On the other hand, similar to the CNC, defibrillation and detachment of CNF from the SF fibers occurred by strong ultrasonication treatment, but nanoscaled CNF bundles exist, indicating that there is a certain binding force between CNF and SF. However, further consideration of the exact mechanism between CNF and SF is needed.

Based on the introduction of CNF, which allows the simultaneous coating and binding of SFs, SF/CNF composites with excellent mechanical properties can be easily fabricated. To confirm this effect, the mechanical properties of SF/CNF composites with various amounts of CNFs were investigated using impact and tensile tests. The results are shown in **Figure 7** and **Supplementary Table S2**. **Figures 7A,B** present the average tensile strength and modulus of SF/CNF composites with the various amounts of CNFs, respectively, and indicate the improved tensile behavior of the SF/CNF composites. The SF/CNF fibrous composite with 5 wt.% CNF (SF/CNF5) exhibits a 60 and 61% increase in the tensile strength and modulus, respectively, compared with nonwoven SF. The mechanical reinforcement further enhances with increasing CNF content. The SF/CNF15 composite shows a 110% and 150% increase in the tensile strength and modulus, respectively. The impact strength test results (**Figure 7C**) confirm the mechanical reinforcement effect of CNF. Based on the impact tests, the SF/CNF5 displays a ∼53% increase in the impact strength compared with SF nonwoven, whereas SF/CNF10 and SF/CNF15 show an increase in the impact strength of ∼109 and ∼228%, respectively. These data prove that CNF can reinforce the low impact strength of nonwoven SF and that higher CNF concentrations can accentuate this trend. The mechanical reinforcement phenomenon of SF/CNF composites can be explained as follows. First, because the introduction of CNF does not affect the secondary β-sheet structure of SF, the mechanical properties of the SFs can be maintained, even after the preparation of the SF/CNF composites. In addition, by coating CNF onto the SF surface, a core–shell-structured SF/CNF fiber forms, which promotes the hydrogen bonding between the microscale SFs and nanoscale CNFs. In addition, as the amount of CNF increases, high-aspect ratio CNFs can form an interfibrillar bridges between the hybrid fibers of the SF/CNF composites,

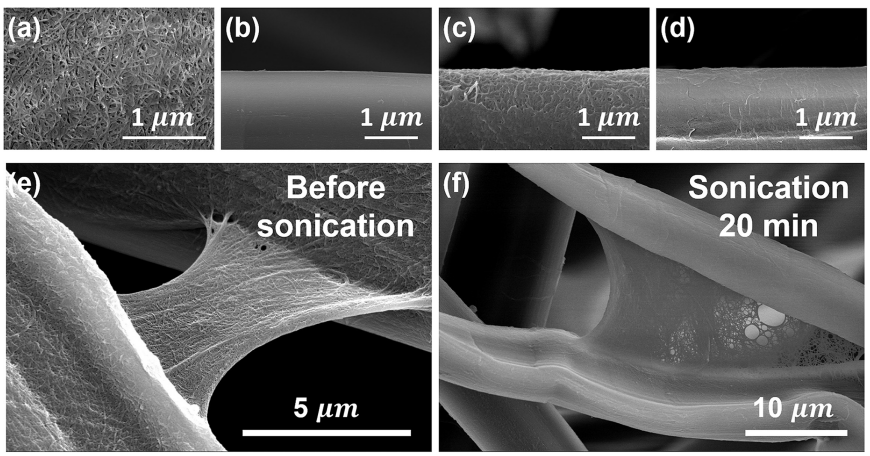

FIGURE 6 | FE-SEM image of **(a)** neat CNC, **(b)** neat silk, SF/CNC, SF/CNF before **(c,e)** and after **(d,f)** sonication treatment for 20 min.

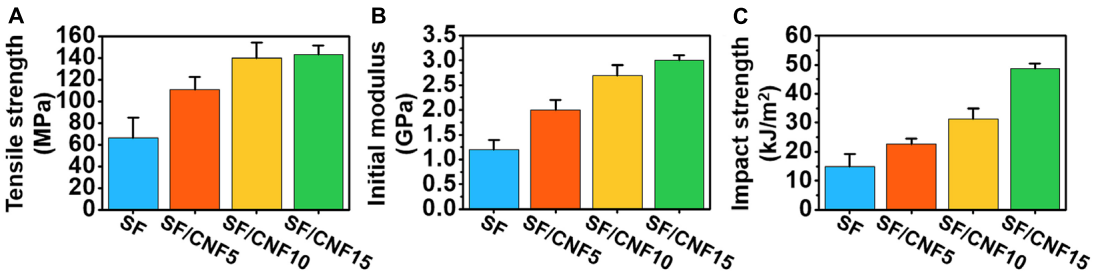

FIGURE 7 | Mechanical properties of nonwoven SF and SF/CNF composites with various amounts of CNFs: **(A)** tensile strength, **(B)** tensile modulus, and **(C)** impact strength.

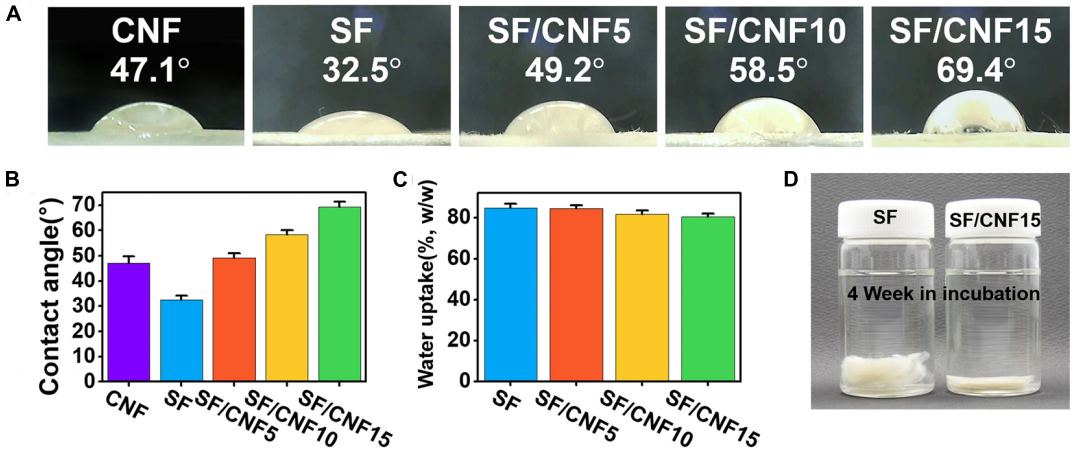

FIGURE 8 | (A,B) Initial water contact angles of the SF/CNF composites with various amounts of CNFs, **(C)** water uptake of SF/CNF composites with various amounts of CNFs after 24 h, and **(D)** nonwoven SF and SF/CNF15 composite after 4 weeks of incubation.

thereby improving the interfacial adhesion characteristics of the SF/CNF composites.

The stability of the fibrous structure including the nonwoven fabric in wet or high-humidity environments is a very important property. Because most of the natural fibers are hydrophilic, composite materials with natural fibers as reinforcing agents often have disadvantages in that they are more vulnerable to moisture environments than materials without a reinforced matrix (Fages et al., 2013; Theng et al., 2015, 2017). Many natural polymer-based CNF-reinforced composites fabricated using common blending methods show hydrophilic properties such as a decrease in the water contact angle (WCA) (Kwak et al., 2018; Wang et al., 2018a), increasing water uptake or absorption capacity, and higher swelling ratio with increasing CNF concentration. On the other hand, when the surface coating and layer-by-layer coating method are used, the CNF-reinforced composite materials have hydrophobic properties because CNF actively affects the surface morphologies or topologies of the composite materials. The WCA is used as an indicator for the degree of surface hydrophobicity or hydrophilicity of film, textile, and membrane materials. Water droplet images representative of the SF/CNF fibrous composites and the average WCA results are shown in **Figures 8A,B**. Generally, a film with a WCA above 65° is considered as hydrophobic (Vogler, 1998). The WCA of the nonwoven SF without CNF is ∼32.5°, which indicates that the nonwoven SF is hydrophilic. In contrast, when CNF is added to the SF structure, the WCA significantly increases. In the case of SF/CNF15, the contact angle is ∼69.4°, which means that the CNF coating on the SF surface and CNF bonding with SFs sufficiently hydrophobizes the surfaces of the SF/CNF composites. The hydrophobic effect of CNF is due to the change in the surface topology of the entire SF/CNF composite.

In addition, the hydrostability of SF/CNF composites in wet environments was also examined using a water uptake test. The results are shown in **Figure 8C**. As the CNF content increases, the water uptake of the SF/CNF composites decreases (Fages et al., 2013; Theng et al., 2015, 2017). This might have the following reasons: (1) the initial diffusion rate of the water molecules decreases because of the aforementioned surface hydrophobicity, and (2) by introducing CNF into SF fibrous systems, the porosity of the SF/CNF composites decreases, thus reducing the space for water impregnation. Finally, the increase in the hydrogen bonding between SF–CNF and CNF–CNF reduces the affinity to water molecules. The hydrophobic effect of CNF greatly contributes to the morphological stability of the SF/CNF composites in wet environments. As shown in **Figure 8D**, nonwoven SF without CNF shows that each SF disintegrates in a 4-week stirring environment, causing the loss of the dense SF structure. In contrast, the dense nonwoven structure of the SF/CNF15 composite can be well maintained, even after 4 weeks of stirring in an aqueous environment.

CONCLUSION

In this study, natural micro- and nano-fiber fused fibrous composites were fabricated using silk and cellulose as green raw materials. Robust SF/CNF composites were fabricated using a simple short-term thermal bonding process. This process is eco-friendly and energy-efficient because it does not require an organic solvent, additional chemical reagents, long processing time, and high energy consumption. The introduction of CNF to SF increases the interfibrillar bonding of SFs as well as the coating on the SF surface. As the CNF content increases, the coating and bonding effects of CNF rapidly increase. Therefore, the mechanical properties and structural stability of the SF/CNF composites increase compared with that of nonwoven SF without CNF. A maximum of 15 wt.% CNF can be added to the SF/CNF composite. The SF/CNF15 composite shows a 110 and 225% increase in the impact and tensile strength, respectively, compared with nonwoven SF. The results also show that the hydrophobicity of the SF/CNF composite

surface and bulk materials can be imparted. Such green and facile SF/CNF composites have immense potential for a wide range of applications, particularly in the nonwoven and fiber-reinforced plastics industries.

DATA AVAILABILITY STATEMENT

All datasets generated for this study are included in the article/**Supplementary Material**.

AUTHOR CONTRIBUTIONS

The manuscript was written through contributions of all authors. All authors have given approval to the final version of the manuscript.

FUNDING

This work was supported by the National Research Foundation of Korea (NRF) grant funded by the Korea government (MSIT) (NRF-2020R1C1C1012623), by Basic Science Research Program through the National Research Foundation of Korea (NRF) funded by the Ministry of Education (NRF-2019R1A2B5B01070270), and by a grant from the National Institute of Fisheries Science, South Korea (R2020038).

SUPPLEMENTARY MATERIAL

The Supplementary Material for this article can be found online at: https://www.frontiersin.org/articles/10.3389/fmats.2020.00098/full#supplementary-material

REFERENCES

Adekunle, K. F. (2015). Surface treatments of natural fibres—a review: part 1. *OJPChem.* 05, 41–46. doi: 10.4236/ojpchem.2015.53005

Amini, E., Tajvidi, M., Gardner, D. J., and Bousfield, D. W. (2017). Utilization of cellulose nanofibrils as a binder for particleboard manufacture. *Bio Resour.* 12, 4093–4110. doi: 10.15376/biores.12.2.4093-4110

Arévalo, R., and Peijs, T. (2016). Binderless all-cellulose fibreboard from microfibrillated lignocellulosic natural fibres. *Compos. Part A Appl. Sci. Manuf.* 83, 38–46. doi: 10.1016/j.compositesa.2015.11.027

Asakura, T., Okushita, K., and Williamson, M. P. (2015). Analysis of the Structure of *Bombyx mori* silk fibroin by NMR. *Macromolecules* 48, 2345–2357. doi: 10.1021/acs.macromol.5b00160

Baiardo, M., Zini, E., and Scandola, M. (2004). Flax fibre–polyester composites. *Compos. A Appl. Sci. Manuf.* 35, 703–710. doi: 10.1016/j.compositesa.2004.02.004

Boulet-Audet, M., Vollrath, F., and Holland, C. (2015). Identification and classification of silks using infrared spectroscopy. *J. Exp. Biol.* 218, 3138–3149. doi: 10.1242/jeb.128306

Carvalho, K. C. C., Mulinari, D. R., Voorwald, H. J. C., and Cioffi, M. O. H. (2010). Chemical modification effect on the mechanical properties of hips/ coconut fiber composites. *Bio Resour.* 5, 1143–1155.

Cervin, N. T., Andersson, L., Ng, J. B. S., Olin, P., Bergström, L., and Wågberg, L. (2013). Lightweight and strong cellulose materials made from aqueous foams stabilized by nanofibrillated cellulose. *Biomacromolecules* 14, 503–511. doi: 10.1021/bm301755u

Chen, F., Porter, D., and Vollrath, F. (2012). Structure and physical properties of silkworm cocoons. *J. R. Soc. Interface* 9, 2299–2308. doi: 10.1098/rsif.2011.0887

Cheng, G., Wang, X., Tao, S., Xia, J., and Xu, S. (2015). Differences in regenerated silk fibroin prepared with different solvent systems: from structures to conformational changes. *J. Appl. Polym. Sci.* 132, 1–8. doi: 10.1002/app.41959

Cho, H. J., Yoo, Y. J., Kim, J. W., Park, Y. H., Bae, D. G., and Um, I. C. (2012). Effect of molecular weight and storage time on the wet- and electro-spinning of regenerated silk fibroin. *Polym. Degrad. Stab.* 97, 1060–1066. doi: 10.1016/j.polymdegradstab.2012.03.007

Dányádi, L., Móczó, J., and Pukánszky, B. (2010). Effect of various surface modifications of wood flour on the properties of PP/wood composites. *Compos. Part A Appl. Sci. Manuf.* 41, 199–206. doi: 10.1016/j.compositesa.2009.10.008

Das, O., Sarmah, A. K., and Bhattacharyya, D. (2015). A sustainable and resilient approach through biochar addition in wood polymer composites. *Sci. Total Environ.* 51, 326–336. doi: 10.1016/j.scitotenv.2015.01.063

de Campos, A., Tonoli, G. H. D., Marconcini, J. M., Mattoso, L. H. C., Klamczynski, A., Gregorski, K. S., et al. (2013). TPS/PCL composite reinforced with treated sisal fibers: property. *J. Polym. Environ.* 21, 1–7. doi: 10.1007/s10924-012-0512-8

Duan, B., Shou, K., Su, X., Niu, Y., Zheng, G., Huang, Y., et al. (2017). Hierarchical microspheres constructed from chitin nanofibers penetrated hydroxyapatite crystals for bone regeneration. *Biomacromolecules* 18, 2080–2089. doi: 10.1021/acs.biomac.7b00408

Eichhorn, S. J., Dufresne, A., Aranguren, M., Marcovich, N. E., Capadona, J. R., Rowan, S. J., et al. (2010). Review: current international research into cellulose nanofibres and nanocomposites. *J. Mater Sci.* 45, 1–33. doi: 10.1007/s10853-009-3874-0

Fages, E., Cano, M., Gironés, S., Boronat, T., Fenollar, O., and Balart, R. (2013). The use of wet-laid techniques to obtain flax nonwovens with different thermoplastic binding fibers for technical insulation applications. *Textile Res. J.* 83, 426–437. doi: 10.1177/0040517512454183

Favaro, S. L., Ganzerli, T. A., de Carvalho Neto, A. G. V., da Silva, O. R. R. F., and Radovanovic, E. (2010). Chemical, morphological and mechanical analysis of sisal fiber-reinforced recycled high-density polyethylene composites. *Express Polym. Lett.* 4, 465–473. doi: 10.3144/expresspolymlett.2010.59

Feng, Y., Li, X., Zhang, Q., Ye, D., Li, M., You, R., et al. (2019). Fabrication of porous silk fibroin/cellulose nanofibril sponges with hierarchical structure using a lithium bromide solvent system. *Cellulose* 26, 1013–1023. doi: 10.1007/s10570-018-2149-9

Fortea-Verdejo, M., Lee, K.-Y., Zimmermann, T., and Bismarck, A. (2016). Upgrading flax nonwovens: nanocellulose as binder to produce rigid and robust flax fibre preforms. *Compos. Part A App. Sci. Manuf.* 83, 63–71. doi: 10.1016/j.compositesa.2015.11.021

Gao, Y., Hou, M., Yang, R., Zhang, L., Xu, Z., Kang, Y., et al. (2019). Highly porous silk fibroin scaffold packed in PEGDA/sucrose microneedles for controllable transdermal drug delivery. *Biomacromolecules* 20, 1334–1345. doi: 10.1021/acs.biomac.8b01715

Guang, S., An, Y., Ke, F., Zhao, D., Shen, Y., and Xu, H. (2015). Chitosan/silk fibroin composite scaffolds for wound dressing. *J. Appl. Polym. Sci.* 132, 1–7. doi: 10.1002/app.42503

Guo, F., Wang, N., Cheng, Q., Hou, L., Liu, J., Yu, Y., et al. (2016). Low-cost coir fiber composite with integrated strength and toughness. *ACS Sustainable Chem. Eng.* 4, 5450–5455. doi: 10.1021/acssuschemeng.6b00830

Hadadi, A., Whittaker, J. W., Verrill, D. E., Hu, X., Larini, L., and Salas-de la Cruz, D. (2018). A hierarchical model to understand the processing of polysaccharides/protein-based films in ionic liquids. *Biomacromolecules* 19, 3970–3982. doi: 10.1021/acs.biomac.8b00903

Han, C., Yao, Y., Cheng, X., Luo, J., Luo, P., Wang, Q., et al. (2017). Electrophoretic deposition of gentamicin-loaded silk fibroin coatings on 3d-printed porous cobalt–chromium–molybdenum bone substitutes to prevent orthopedic implant infections. *Biomacromolecules* 18, 3776–3787. doi: 10.1021/acs.biomac.7b01091

Han, J., Zhou, C., Wu, Y., Liu, F., and Wu, Q. (2013). Self-assembling behavior of cellulose nanoparticles during freeze-drying: effect of

suspension concentration, particle size, crystal structure, and surface charge. *Biomacromolecules* 14, 1529–1540. doi: 10.1021/bm4001734

Jackson, M., and Mantsch, H. H. (1995). The use and misuse of ftir spectroscopy in the determination of protein structure. *Crit. Rev. Biochem. Mol. Biol.* 30, 95–120. doi: 10.3109/10409239509085140

Juntaro, J., Pommet, M., Kalinka, G., Mantalaris, A., Shaffer, M. S. P., and Bismarck, A. (2008). Creating hierarchical structures in renewable composites by attaching bacterial cellulose onto sisal fibers. *Adv. Mater.* 20, 3122–3126. doi: 10.1002/adma.200703176

Keten, S., Xu, Z., Ihle, B., and Buehler, M. J. (2010). Nanoconfinement controls stiffness, strength and mechanical toughness of β-sheet crystals in silk. *Nat. Mater* 9, 359–367. doi: 10.1038/nmat2704

Kim, H.-J., Jeong, Y.-H., Choe, H.-C., and Brantley, W. A. (2014). Hydroxyapatite formation on biomedical Ti–Ta–Zr alloys by magnetron sputtering and electrochemical deposition. *Thin Solid Films* 572, 119–125. doi: 10.1016/j.tsf.2014.07.058

Klemm, D., Heublein, B., Fink, H.-P., and Bohn, A. (2005). Cellulose: fascinating biopolymer and sustainable raw material. *Angew. Chem. Int. Ed.* 44, 3358–3393. doi: 10.1002/anie.200460587

Klemm, D., Kramer, F., Moritz, S., Lindström, T., Ankerfors, M., Gray, D., et al. (2011). Nanocelluloses: a new family of nature-based materials. *Angew. Chem. Int. Ed.* 50, 5438–5466. doi: 10.1002/anie.201001273

Koh, L.-D., Cheng, Y., Teng, C.-P., Khin, Y.-W., Loh, X.-J., Tee, S.-Y., et al. (2015). Structures, mechanical properties and applications of silk fibroin materials. *Prog. Polym. Sci.* 46, 86–110. doi: 10.1016/j.progpolymsci.2015.02.001

Kwak, H. W., Eom, J., Cho, S. Y., Lee, M. E., and Jin, H.-J. (2019a). High-toughness natural polymer nonwoven preforms inspired by silkworm cocoon structure. *Int. J. Biol. Macromol.* 127, 146–152. doi: 10.1016/j.ijbiomac.2019.01.005

Kwak, H. W., You, J., Lee, M. E., and Jin, H.-J. (2019b). Prevention of cellulose nanofibril agglomeration during dehydration and enhancement of redispersibility by hydrophilic gelatin. *Cellulose* 26, 4357–4369. doi: 10.1007/s10570-019-02387-z

Kwak, H. W., Ju, J. E., Shin, M., Holland, C., and Lee, K. H. (2017). Sericin promotes fibroin silk i stabilization across a phase-separation. *Biomacromolecules* 18, 2343–2349. doi: 10.1021/acs.biomac.7b00549

Kwak, H. W., Lee, H., Lee, M. E., and Jin, H.-J. (2018). Facile and green fabrication of silk sericin films reinforced with bamboo-derived cellulose nanofibrils. *J. Cleaner Prod.* 200, 1034–1042. doi: 10.1016/j.jclepro.2018.07.289

Kwak, H. W., and Lee, K. H. (2015). Monitoring of phase separation between silk fibroin and sericin using various dye system. *Int. J. Ind. Entomol.* 30, 1–5. doi: 10.7852/ijie.2015.30.1.1

Lasseuguette, E., Roux, D., and Nishiyama, Y. (2008). Rheological properties of microfibrillar suspension of TEMPO-oxidized pulp. *Cellulose* 15, 425–433. doi: 10.1007/s10570-007-9184-2

Lee, J., Le Boulicaut, N., Kwon, O. H., Park, W. H., and Cho, D. (2019). Electron beam irradiation effect on the mechanical and thermal properties of 2-D silk fibroin fabric/poly(lactic acid) biocomposites. *J. Ind. Eng. Chem.* 71, 150–159. doi: 10.1016/j.jiec.2018.11.017

Lee, J. H., Bae, C. H., Park, B.-D., and Um, I. C. (2013). Preparation of cellulose nanofibril/regenerated silk fibroin composite fibers. *Int. J. Ind. Entomol.* 26, 81–88. doi: 10.7852/IJIE.2013.26.2.81

Lee, J. H., Bae, Y. S., Kim, S. J., Song, D. W., Park, Y. H., Bae, D. G., et al. (2018). Preparation of new natural silk non-woven fabrics by using adhesion characteristics of sericin and their characterization. *Int. J. Biol. Macromol.* 106, 39–47. doi: 10.1016/j.ijbiomac.2017.07.179

Lee, K. H. (2004). Silk sericin retards the crystallization of silk fibroin. *Macromol. Rapid Commun.* 25, 1792–1796. doi: 10.1002/marc.200400333

Lee, K.-Y., Bharadia, P., Blaker, J. J., and Bismarck, A. (2012). Short sisal fibre reinforced bacterial cellulose polylactide nanocomposites using hairy sisal fibres as reinforcement. *Compos. Part A Appl. Sci. Manuf.* 43, 2065–2074. doi: 10.1016/j.compositesa.2012.06.013

Lin, T.-Y., Masunaga, H., Sato, R., Malay, A. D., Toyooka, K., Hikima, T., et al. (2017). Liquid crystalline granules align in a hierarchical structure to produce spider dragline microfibrils. *Biomacromolecules* 18, 1350–1355. doi: 10.1021/acs.biomac.7b00086

Lu, Q., Hu, X., Wang, X., Kluge, J. A., Lu, S., Cebe, P., et al. (2010). Water-insoluble silk films with silk I structure. *Acta Biomaterialia* 6, 1380–1387. doi: 10.1016/j.actbio.2009.10.041

Magaz, A., Roberts, A. D., Faraji, S., Nascimento, T. R. L., Medeiros, E. S., Zhang, W., et al. (2018). Porous, aligned, and biomimetic fibers of regenerated silk fibroin produced by solution blow spinning. *Biomacromolecules* 19, 4542–4553. doi: 10.1021/acs.biomac.8b01233

Malay, A. D., Sato, R., Yazawa, K., Watanabe, H., Ifuku, N., Masunaga, H., et al. (2016). Relationships between physical properties and sequence in silkworm silks. *Sci. Rep.* 6:27573. doi: 10.1038/srep27573

Ming, J., Pan, F., and Zuo, B. (2015). Influence factors analysis on the formation of silk I structure. *Int. J. Biol. Macromol.* 75, 398–401. doi: 10.1016/j.ijbiomac.2015.02.002

Morán, J. I., Alvarez, V. A., Cyras, V. P., and Vázquez, A. (2008). Extraction of cellulose and preparation of nanocellulose from sisal fibers. *Cellulose* 15, 149–159. doi: 10.1007/s10570-007-9145-9

Mozumder, M. S., Zhang, H., and Zhu, J. (2011). Mimicking lotus leaf: development of micro-nanostructured biomimetic superhydrophobic polymeric surfaces by ultrafine powder coating technology. *Macromol. Mater. Eng.* 296, 929–936. doi: 10.1002/mame.201100080

Nagarkar, S., Nicolai, T., Chassenieux, C., and Lele, A. (2010). Structure and gelation mechanism of silk hydrogels. *Phys. Chem. Chem. Phys.* 12:3834. doi: 10.1039/b916319k

Nisal, A., Trivedy, K., Mohammad, H., Panneri, S., Sen Gupta, S., Lele, A., et al. (2014). Uptake of azo dyes into silk glands for production of colored silk cocoons using a green feeding approach. *ACS Sustainable Chem. Eng.* 2, 312–317. doi: 10.1021/sc400355k

Numata, K., Yamazaki, S., and Naga, N. (2012). Biocompatible and biodegradable dual-drug release system based on silk hydrogel containing silk nanoparticles. *Biomacromolecules* 13, 1383–1389. doi: 10.1021/bm300089a

Omenetto, F. G., and Kaplan, D. L. (2010). New Opportunities For An Ancient Material. *Science* 329, 528–531. doi: 10.1126/science.1188936

Pandey, A., Jalihal, D., Kalra, D., Mn, D., and Prabhu, D. (2015). Estimation of adiponectin levels in diabetic, non-diabetic fatty liver diseases and healthy controls. *Int. J. Res. Med. Sci.* 3, 140–146. doi: 10.5455/2320-6012.ijrms20150124

Peng, Z., Yang, X., Liu, C., Dong, Z., Wang, F., Wang, X., et al. (2019). Structural and Mechanical properties of silk from different instars of *Bombyx mori*. *Biomacromolecules* 20, 1203–1216. doi: 10.1021/acs.biomac.8b01576

Pommet, M., Juntaro, J., Heng, J. Y. Y., Mantalaris, A., Lee, A. F., Wilson, K., et al. (2008). Surface modification of natural fibers using bacteria: depositing bacterial cellulose onto natural fibers to create hierarchical fiber reinforced nanocomposites. *Biomacromolecules* 9, 1643–1651. doi: 10.1021/bm800169g

Saba, N., Mohammad, F., Pervaiz, M., Jawaid, M., Alothman, O. Y., and Sain, M. (2017a). Mechanical, morphological and structural properties of cellulose nanofibers reinforced epoxy composites. *Int. J. Biol. Macromol.* 97, 190–200. doi: 10.1016/j.ijbiomac.2017.01.029

Saba, N., Safwan, A., Sanyang, M. L., Mohammad, F., Pervaiz, M., Jawaid, M., et al. (2017b). Thermal and dynamic mechanical properties of cellulose nanofibers reinforced epoxy composites. *Int. J. Biol. Macromol.* 102, 822–828. doi: 10.1016/j.ijbiomac.2017.04.074

Saleem, M., Pirzada, T., and Qadeer, R. (2007). Sorption of acid violet 17 and direct red 80 dyes on cotton fiber from aqueous solutions. *Colloid Surf. APhysicochem. Eng. Asp.* 292, 246–250. doi: 10.1016/j.colsurfa.2006.06.035

Sanjay, M. R., Madhu, P., Jawaid, M., Senthamaraikannan, P., Senthil, S., and Pradeep, S. (2018). Characterization and properties of natural fiber polymer composites: a comprehensive review. *J. Cleaner Prod.* 172, 566–581. doi: 10.1016/j.jclepro.2017.10.101

Shah, D. U., Porter, D., and Vollrath, F. (2014). Can silk become an effective reinforcing fibre? A property comparison with flax and glass reinforced composites. *Compos. Sci. Technol.* 101, 173–183. doi: 10.1016/j.compscitech.2014.07.015

Shao, Z., and Vollrath, F. (2002). Surprising strength of silkworm silk. *Nature* 418, 741–741. doi: 10.1038/418741a

Shubhra, Q. T. H., Alam, A. K. M. M., and Beg, M. D. H. (2011). Mechanical and degradation characteristics of natural silk fiber reinforced gelatin composites. *Mater. Lett.* 65, 333–336. doi: 10.1016/j.matlet.2010.09.059

Song, R., Ino, H., and Kimura, T. (2009). Mechanical property of silk/bamboo composite paper for effective utilization of waste silk. *J. Text. Eng.* 55, 85–90. doi: 10.4188/jte.55.85

Song, R., Kimura, T., and Ino, H. (2010). Papermaking from waste silk and its application as reinforcement of green composite. *J. Text. Eng.* 56, 71–76. doi: 10.4188/jte.56.71

Tayeb, A., Amini, E., Ghasemi, S., and Tajvidi, M. (2018). Cellulose nanomaterials—binding properties and applications: a review. *Molecules* 23:2684. doi: 10.3390/molecules23102684

Theng, D., Arbat, G., Delgado-Aguilar, M., Vilaseca, F., Ngo, B., and Mutjé, P. (2015). All-lignocellulosic fiberboard from corn biomass and cellulose nanofibers. *Ind. Crops Prod.* 76, 166–173. doi: 10.1016/j.indcrop.2015.06.046

Theng, D., El Mansouri, N.-E., Arbat, G., Ngo, B., Delgado-Aguilar, M., Pèlach, M. À, et al. (2017). Fiberboards made from corn stalk thermomechanical pulp and kraft lignin as a green adhesive. *Bio Resour.* 12, 2379–2393. doi: 10.15376/biores.12.2.2379-2393

Toprakcioglu, Z., Levin, A., and Knowles, T. P. J. (2017). Hierarchical biomolecular emulsions Using 3-D microfluidics with uniform surface chemistry. *Biomacromolecules* 18, 3642–3651. doi: 10.1021/acs.biomac.7b01159

Urreaga, J. M., and de la Orden, M. U. (2006). Chemical interactions and yellowing in chitosan-treated cellulose. *Eur. Polym. J.* 42, 2606–2616. doi: 10.1016/j.eurpolymj.2006.05.002

Vogler, E. A. (1998). Structure and reactivity of water at biomaterial surfaces. *Adv. Coll. Interface Sci.* 74, 69–117. doi: 10.1016/S0001-8686(97)00040-7

Vollrath, F., Porter, D., and Holland, C. (2013). The science of silks. *MRS Bull.* 38, 73–80. doi: 10.1557/mrs.2012.314

Wang, Y., Cheng, Z., Liu, Z., Kang, H., and Liu, Y. (2018a). Cellulose nanofibers/polyurethane shape memory composites with fast water-responsivity. *J. Mater. Chem. B* 6, 1668–1677. doi: 10.1039/C7TB03069J

Wang, Y., Wen, J., Peng, B., Hu, B., Chen, X., and Shao, Z. (2018b). Understanding the mechanical properties and structure transition of *Antheraea pernyi* Silk fiber induced by its contraction. *Biomacromolecules* 19, 1999–2006. doi: 10.1021/acs.biomac.7b01691

Xiao, L., Liu, S., Yao, D., Ding, Z., Fan, Z., Lu, Q., et al. (2017). Fabrication of silk scaffolds with nanomicroscaled structures and tunable stiffness. *Biomacromolecules* 18, 2073–2079. doi: 10.1021/acs.biomac.7b00406

Yazawa, K., Malay, A. D., Ifuku, N., Ishii, T., Masunaga, H., Hikima, T., et al. (2018). Combination of amorphous silk fiber spinning and postspinning crystallization for tough regenerated silk fibers. *Biomacromolecules* 19, 2227–2237. doi: 10.1021/acs.biomac.8b00232

Yin, Y., Zhao, X., and Xiong, J. (2019). Modeling analysis of silk fibroin/poly(ε-caprolactone) nanofibrous membrane under uniaxial tension. *Nanomaterials* 9, 1149. doi: 10.3390/nano9081149

Yuan, Q., Yao, J., Chen, X., Huang, L., and Shao, Z. (2010). The preparation of high performance silk fiber/fibroin composite. *Polymer* 51, 4843–4849. doi: 10.1016/j.polymer.2010.08.042

Zhang, Y., Zuo, Y., Wen, S., Hu, Y., and Min, Y. (2018). Distinctive stress-stiffening responses of regenerated silk fibroin protein polymers under nanoscale gap geometries: effect of shear on silk fibroin-based materials. *Biomacromolecules* 19, 1223–1233. doi: 10.1021/acs.biomac.8b00070

Conflict of Interest: The authors declare that the research was conducted in the absence of any commercial or financial relationships that could be construed as a potential conflict of interest.

frontiers in Materials

ORIGINAL RESEARCH
published: 19 May 2020
doi: 10.3389/fmats.2020.00135

Green Pathway for Processing Non-mulberry *Antheraea pernyi* Silk Fibroin/Chitin-Based Sponges: Biophysical and Biochemical Characterization

Simone S. Silva[1,2]*, *Joana M. Gomes*[1,2], *Ana Catarina Vale*[1,2], *Shenzhou Lu*[3], *Rui L. Reis*[1,2,4] *and Subhas C. Kundu*[1,2]*

[1] 3B's Research Group, I3Bs- Research Institute on Biomaterials, Biodegradables and Biomimetics, University of Minho, Headquarters of the European Institute of Excellence on Tissue Engineering and Regenerative Medicine, AvePark, Parque da Ciência e Tecnologia, Zona Industrial da Gandra, Braga, Portugal, [2] ICVS/3B's- PT Government Associate Laboratory, Braga, Portugal, [3] National Engineering Laboratory for Modern Silk, College of Textile and Clothing Engineering, Soochow University, Suzhou, China, [4] The Discoveries Centre for Regenerative and Precision Medicine, Headquarters at University of Minho, Guimarães, Portugal

OPEN ACCESS

Edited by:
Nicola Maria Pugno,
University of Trento, Italy

Reviewed by:
Walter Caseri,
ETH Zürich, Switzerland
Dongyan Liu,
Institute of Metals Research (CAS), China

***Correspondence:**
Simone S. Silva
simonesilva@i3bs.uminho.pt
Subhas C. Kundu
kundu@i3bs.uminho.pt

Specialty section:
This article was submitted to Polymeric and Composite Materials, a section of the journal Frontiers in Materials

Received: 22 October 2019
Accepted: 21 April 2020
Published: 19 May 2020

Citation:
Silva SS, Gomes JM, Vale AC, Lu S, Reis RL and Kundu SC (2020) Green Pathway for Processing Non-mulberry Antheraea pernyi Silk Fibroin/Chitin-Based Sponges: Biophysical and Biochemical Characterization. Front. Mater. 7:135. doi: 10.3389/fmats.2020.00135

Silk protein fibroin (SF)-based matrices from non-mulberry, and mulberry silkworms are used for different applications in regenerative medicine. Silk fiber spun by the wild non-mulberry silkworm *Antheraea pernyi* (Ap) is also a promising biomedical material, due to the presence of the inherent tripeptide sequence of Arginine-Glycine-Aspartic acid (RGD) on the protein fibroin sequences. However, SF derived from the Ap cocoons still lacks exploitation in the healthcare field due to its poor solubility in the conventional solvents. This work addresses the application of green chemistry principles, namely the use of ionic liquids (ILs, 1-butyl-imidazolium acetate) and renewable resources such as *Antheraea pernyi* silk fibroin (ApSF) and chitin (Ch), for the fabrication of sponges from the blends of ApSF and Ch (APC). The formation of β-sheet in different contents during ApSF/Ch/IL was acquired by exposing gels to methanol/water and ethanol/water. The sponges were then obtained by freeze-drying. This approach promotes the formation of both stable and ordered ApSF/Ch-based sponges. The developed sponges show the suitable porosity and interconnectivity, appreciable swelling degree, and tuneable viscoelastic compressive properties for tissue engineering applications. Collectively, the structural properties of these ApSF/Ch-based sponges make them promising candidates for biomedical applications, namely cartilage regeneration.

Keywords: ***Antheraea pernyi*, ionic liquids, biomaterials, sponges, chitin, silk fibroin**

INTRODUCTION

Silk protein fibroin-based matrices from mulberry silkworms have already shown a broad range of applications in tissue engineering and regenerative medicine due to its versatility, non-toxicity, and biocompatibility as well as their exceptional structural and mechanical properties (Silva et al., 2016; Singh et al., 2016; Woloszyk et al., 2016).

In particular, silk fibroin from the silkworm *Antheraea pernyi* (ApSF) is known to contain a tripeptide sequence of Arginine-Glycine-Aspartic acid (RGD) on the fibroin sequences, which make it a promising biomedical material (Kang et al., 2018; Silva et al., 2019). Despite this value-added and tunable mechanical advantages, the biomedical potential of Ap silk fibroin (ApSF) is underexplored, since ApSF fibers have a strong resistance to chemicals due to its extended antiparallel β-sheet structure and hydrogen bonds among the chains (Zhang et al., 2016; Silva et al., 2019). Ionic liquids (ILs), have emerged as a class of solvents, capable of providing effective platforms to enhance the processability of natural macromolecules (Swatloski et al., 2002; Silva et al., 2012, 2013a, 2017; Chakravarty et al., 2018; Yang et al., 2019). By definition, ILs are known as poorly coordinated salts, liquids at room temperature (Freire et al., 2012; Vekariya, 2017; Gomes et al., 2019). Matrices with different shapes and sizes, e.g., films, hydrogels, sponges, microspheres, have been produced. Their applications as drug delivery systems and tissue regeneration have been investigated (Silva et al., 2013a,b; Singh et al., 2013; Kim et al., 2015; Bendaoud et al., 2017). For instance, chitin, a natural polymer with appealing properties for biomedical applications, presents a high degree of crystallinity and strong hydrogen-bonding, which complicates its processing (Silva et al., 2011, 2013b). Some ILs showed to be able to disrupt the structure of chitin, and dissolve it at concentrations up to 10 wt%, expanding the use of this polymer into a broader range of fields. The ability of ILs to dissolve chitin has enabled its further processing as nanofibers (Barber et al., 2013; Shamshina et al., 2018), microspheres (Silva et al., 2013a), and sponges/porous scaffolds (Silva et al., 2011, 2013b).

As described for the chitin, the silk protein-based matrices were obtained earlier through the dissolution of cocoons from mulberry silkworm, Bombyx mori, non-mulberry silkworms *Antheraea mylitta*, *Samia ricini,* and *Antheraea assamensis* in ILs (Phillips et al., 2004; Silva et al., 2012, 2013, 2016; Goujon et al., 2013; Lozano-Pérez et al., 2014). On these works, the alternative approaches were made by using the ILs particularly for non-mulberries to overcome the restricted uses of fibroins from the silk glands of live silkworms, as their cocoons were insoluble in usual organic solvents used to dissolve mulberry cocoons. The IL platform allowed the fabrication of non-mulberry silk-based hydrogels (Silva et al., 2013) and sponges (Silva et al., 2016) with required properties, namely appreciable swelling degree, suitable porosity and interconnectivity, good mechanical stability and biological performances for tissue engineering applications.

The present work focuses on the creation of green and sustainable strategies for the fabrication of ApSF/Ch-based sponges to be used in biomedical applications in immediate future. To the best of our knowledge, there are no investigations to develop ApSF/Ch-based sponges. Herein, the sponges produced using the green chemistry principles by employing the IL 1-butyl-3-methyl-imidazolium acetate (BMIMAc) as a common solvent to dissolve both the ApSF and Ch. The solutions are further combined to fabricate the blended matrices. The mixtures of the solvents and freezing temperature variations are also applied during the processing to modulate the physical features of the matrices.

MATERIALS AND METHODS

Materials

Chitin from crab shells (Ch; practical grade; Sigma Aldrich) with a degree of N-acetylation of 57.9%, determined by elemental analysis, were ground through a Wiley Mill (model 4, Thomas) and stored in plastic bottles. Ground chitin (106 μm) was used throughout the experiments to obtain reproducible results. *Antheraea pernyi* cocoons and fibers were purchased from Mayrin Group Co., Ltd; China. The ionic liquid (IL), 1-butyl-3-methyl imidazolium acetate (BMIMAc) was purchased from Sigma Aldrich (St. Louise USA) and was used as a solvent and used without further purification. All other chemicals were reagent grade and were used as received.

Methods

Degumming Process on Antheraea Pernyi Cocoons

The degumming process was achieved by boiling the 5 g of silk filaments for 1 h in water containing 1.1 g/L of Na_2CO_3, followed by 30 min in water with 0.4 g/L of Na_2CO_3. Finally, the resulting fibroin filaments were extensively rinsed in boiling distilled water and air-dried at room temperature (RT).

Preparation of the Antheraea Pernyi/chitin IL Solutions and Structures Formation

The degummed fibers of Ap were dissolved in BMIMAc at 80°C in a concentration of 2% (w/v). In parallel, chitin powder was also dissolved in BMIMAc at 90°C in a concentration of 1% (w/v). The system was kept under stirring for 2 h (Ap) and 4 h (Ch).

After the dissolution, the solutions were blended in a ratio of 1:1, and they were transferred to cylinder molds, followed by frozen at −80°C and −20°C/−80°C for 2 h. Afterward, the gelation of the blended solutions was acquired by exposing the gels to B—methanol (MeOH): water (80/20), or C- ethanol (EtOH): water (80/20) solution, followed by the IL removal using the same solutions B and C. The non-solvent (EtOH) was changed periodically, and the conductivity of the aliquots was made using a conductivimeter (INOLAB, Multilevel 3) with a SondaWTWTetraCon 325, at room temperature. Then, samples were washed with distilled water and frozen at −80°C, while others were frozen at −20°C for 4 h and at −80°C overnight. Throughout the paper, the chitin/ApSF sponges are referred to as APC80B, APC80C, APC20B, APC20C (see details in **Table 1**).

TABLE 1 | Sample identification used throughout the paper.

Sample identification	Preparation condition	
	Frozen temperature	Solvent gelation
APC80B	−80°C	MeOH: H_2O 80/20
APC80C	−80°C	EtOH: H_2O 80/20
APC20B	−20°C/−80°C	MeOH: H_2O 80/20
APC20C	−20°C/−80°C	EtOH: H_2O 80/20

Characterization

FTIR Spectroscopy

The infrared spectra were recorded using a Shimadzu-IR, Prestige 21 spectrometer, in the spectral region of 4,000–650 cm^{-1}, with a resolution of 2 cm^{-1} at 32 scans. The data was acquired using the KBr mode, and, to this end, the samples were powdered, mixed with KBr, and processed into pellets. Fourier self-deconvolution (FSD) of the infrared spectra covering the amide I region (1,595–1,705 cm^{-1}) was performed using the Origin 9.0 Software. To measure the related areas of the amide I components, FSD spectra were curve fitted to Gaussian line shape profiles. The deconvoluted amide I spectra area was normalized, and the relative areas of the single bands were used to determine the fraction of the secondary structural elements. The band assignments and the detailed procedure to determine b-sheet crystallinity were described previously (Hu et al., 2006).

SEM

The different freeze-dried samples were fixed using mutual carbon adhesive tape on aluminum stubs and coated with a conductive gold layer, and their morphology was observed using a NanoSEM-FEI Nova 200 with an integrated microanalysis X-ray system (EDS—energy dispersive spectrometer).

Micro-Computed Tomography (μ-CT)

Non-Destructive characterization of the microstructure of distinct samples was performed through micro-computed tomography (micro-CT) that was performed on a high-resolution device, SkyScan 1272 scan (v1.1.3, Bruker, Boston, USA). The acquisition was conducted under the conditions of intensity 140 μA, a voltage of 71 kV, and a voxel size of 11 μm. The obtained projection images were reconstructed in about 200 slices along the ZZ axis (software NRecon, SkyScan). Then, using the CTAn software (SkyScan), the selected projection images were binarized through a global thresholding (value adjusted to the minimum of the global grayscale histogram from each sample), the reconstructed slice images were processed and through the 3D rendering, the main 3D structural parameters were determined: mean pore size (μm); mean wall thickness (μm); porosity (%); and interconnectivity (%). Finally, the 3D reconstructions were built using CTVox software (version 3.3.0 r1412, Skyscan). At least three samples were analyzed for each condition, and the average value and standard deviation were presented.

Swelling

The swelling tests were performed by immersing the sponges in phosphate buffer solution (PBS) up to 24 h, at 37°C. The weight of the swollen samples was determined after removing the excess surface water by gently tapping the surface with filter paper. The percentage of water uptake was calculated using Equation (1), where W_s is the weight of the swollen sample, and W_d is the weight of the dry sample. Each experiment was repeated three times, and the average value was considered to be the water uptake value.

$$Water\ uptake = \left[\frac{Ws - Wd}{Wd}\right] \times 100 \quad (1)$$

Dynamic Mechanical Analysis (DMA)

Dynamic mechanical analysis was performed using a TRITEC2000B equipment (Triton Technology, UK) equipped with the compressive mode, to evaluate possible alterations on the viscoelastic properties of the developed sponges, when subjected to cyclic loading and immersed in physiologic fluids. Samples were previously soaked in PBS solution up to their equilibration (accordingly to their swelling behavior), and they presented regular geometry, being cylinders with similar dimensions. After equilibration at 37°C, samples were clamped in the DMA apparatus with the total immersion of samples in a reservoir containing PBS solution at 37°C. DMA spectra were obtained using compressive mode cycles of increasing frequency from 0.1 to 20 Hz (5 points per decade) and under constant strain amplitude, corresponding to ∼1% of the height of the samples. At least, five samples were tested for each condition, and the average value and standard deviation obtained for storage modulus (E') and loss factor (tan δ) were plotted in function of the loading frequency.

Statistical Analysis

All quantitative experiments were run in triplicate, and the results are expressed as means ± standard deviation for $n = 3$, and $n = 5$ for the DMA analysis. Statistical analysis of the data was conducted by two-way ANOVA with Bonferroni's post-test using GraphPadPrism v. 8.0 for Windows (GraphPad Software, San Diego, http://www.graphpad.com). Differences between the groups at $p \leq 0.05$ were considered to be statistically significant.

RESULTS AND DISCUSSION

Efficient dissolution and processing of both *Antherarea pernyi* silk fibroin (ApSF) and chitin (Ch) were reached using BMIMAc at concentrations of 2 and 1% (w/v), respectively. Both solutions were yellow and viscous (**Scheme 1**), and they also showed excellent stability (1–2 weeks in an inert atmosphere). Previous studies, made in our laboratory, revealed that ApSF/BMIMAc gels at a concentration below 5% (w/v) were fragile (data not shown). However, ApSF/BMIMAc solution combined with chitin/BMIMAc at low concentration (1% w/v), resulted in APC/BMIMAc gels with good mechanical stability. The preparation of the APC matrices was achieved, as depicted in (**Scheme 1**). Earlier studies described that strategies involving combinations of proteins and polysaccharides could be used to process matrices that may mimic the naturally occurring environment of certain tissues (Silva et al., 2008; Singh et al., 2016; Rosellini et al., 2018). Following these research lines, ApSF and chitin are excellent natural raw materials for the design of porous matrices with potential advantages in terms of chemistry versatility, biocompatibility, and controlled degradability. By its turn, similar to *Bomby mori* SF, *Antheraea pernyi* SF has broad applicability mainly due to the presence of Arg-Gly-Asp (RGD) peptide sequences, which promote cell adhesion and proliferation in ApSF filaments from which the sericin coating has been removed by degumming (Silva et al., 2019). However, the degummed fibers have a lack of solubility in common solvents like lithium bromide, probably due to strong hydrogen bonding.

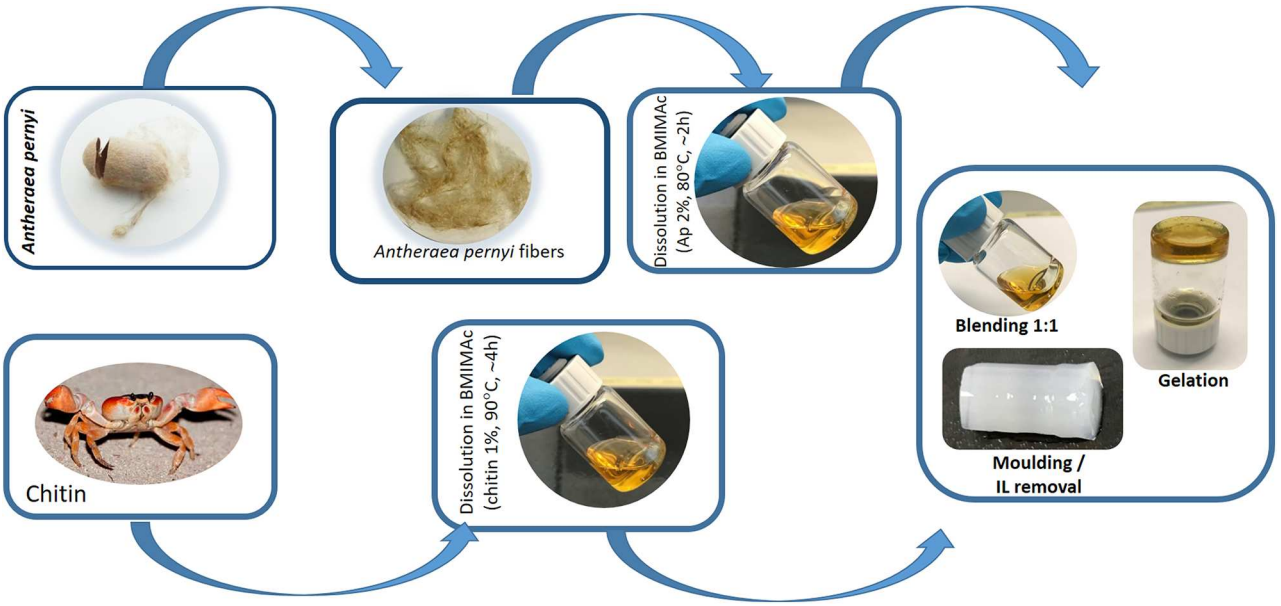

SCHEME 1 | Schematic representation of the fabrication of APC hydrogels using BMIMAc as a solvent from silk cocoon of non-mulberry origin *Antherarea pernyi and* chitin from crab.

In this sense, some ILs such as BMIMAc, have emerged as a suitable solvent not only for mulberry SF but also for non-mulberry SF ones like Eri silk, *Samia/Philosamia ricini*, tropical tasar, *Antheraea mylitta* (Silva et al., 2013, 2016). However, to date, the use of BMIMAc in the dissolution of ApSF cocoons is still limited. On the other hand, the processability of natural polymers such as chitin, chitosan, cellulose, and agarose in different shapes has been successfully described (Tejwant et al., 2010; Silva et al., 2011, 2013a,b; Barber et al., 2013; Nunes et al., 2017), expanding their potential uses in biomedical field.

Upon cooling, both viscous APC/IL solutions resulted in the formation of gels (ionogels), which were molded into a cylindrical shape. Similar behavior was also observed in previous studies during the cooling of the Eri silkworm, *Samia i ricini* SF/BMIMAc solutions (Silva et al., 2016). By definition, in an ionogel, the IL is immobilized in a pathway that involves the formation of a 3D network that is responsible for the solid-like behavior of the matrices (Néouze et al., 2006; Le Bideau et al., 2011). Methanol/ethanol solutions or even ethanol vapor were often used to induce the β-sheet content through structural rearrangement of chains to form covalent bonds (Silva et al., 2016); thus, we hypothesized that the immersion of the APC/IL gels not only in MeOH:H_2O (solvent B) and EtOH:H_2O (solvent C) would provide valuable paths for β-sheet formations and also tune the properties of the resulting materials. Our results demonstrated that the samples treated with solvent B produced architectures with good mechanical stability, while those treated with solvent C were weaker when compared to others treated with solvent B. As mentioned before, these findings could be associated with β-sheet formations, which are discussed in the later sections.

Several toxicity assays have proved that some commonly used ILs exhibit toxicity (Gomes et al., 2019). With this in mind, the use of an IL in the fabrication of a biomaterial demands its removal from the final product. Taking into account that BMIMAc, IL, has inherent high conductivity, the monitoring of IL removal was carried out through conductivity measurements during the immersion of the gels into solvent B and C for 3 days. (**Figure 1**) shows the progressive decrease in conductivity during the IL removal process. The samples were assumed to be completely free from the BMIMAc when the conductivity of the aliquots was below 1.5 μS/cm. This finding suggests that the produced gels have a low level of toxicity, as evidenced in other studies, including cell culture (Silva et al., 2016).

All the samples exhibited peaks centered at 1,221, 1,521, and 1,667 cm^{-1}, corresponding to amide I, II, and III, respectively (**Figure 2**). These peaks constitute the typical random coil conformation. After dissolution/processability and stabilization treatment using MeOH: H_20 (solvent B) and EtOH: H_20 (solvent C), the APC samples showed peaks at 1,624–1,621 cm^{-1} (amide I) and 1,521 cm^{-1} (amide II); which are related to intermolecular β-sheet bands (Um et al., 2001). The absence of the characteristic peaks of BMIMAC (Silva et al., 2016) indicated that this solvent was eliminated from the structures. Therefore, the observed structural features of the APC samples revealed that the use of BMIMAc did not affect the typical β-sheet formation induced by stabilization treatment.

By analyzing the curve fitting of the FTIR spectra (data not shown) of the amide I region between 1,595 and 1,705 cm^{-1} for all APC samples, and taking into account that the regions of 1,600–1,640 cm^{-1} and 1,690–1,705 cm^{-1} were associated with intermolecular β-sheet bands (Um et al., 2001; Silva et al.,

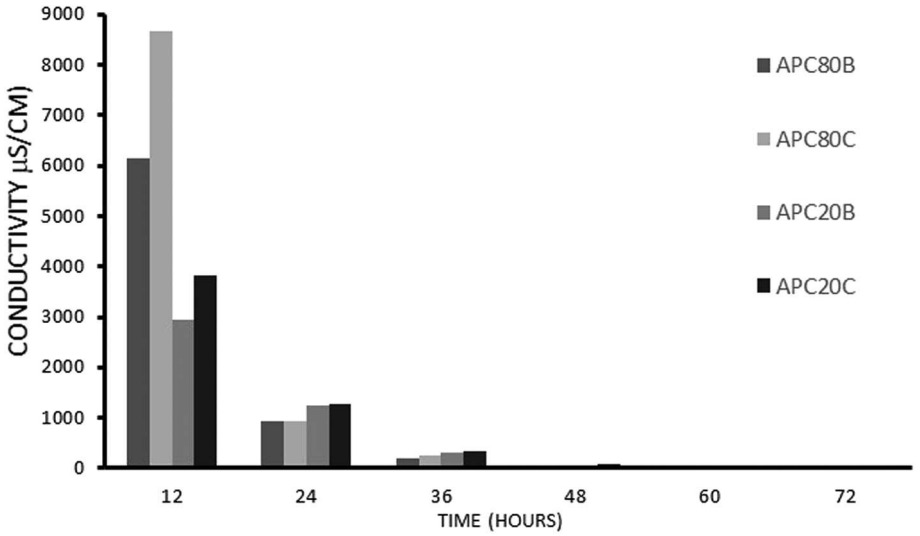

FIGURE 1 | The conductivity measurements on the aliquots of solvent obtained after immersion of the structures in methanol/water, B, or ethanol/water, C.

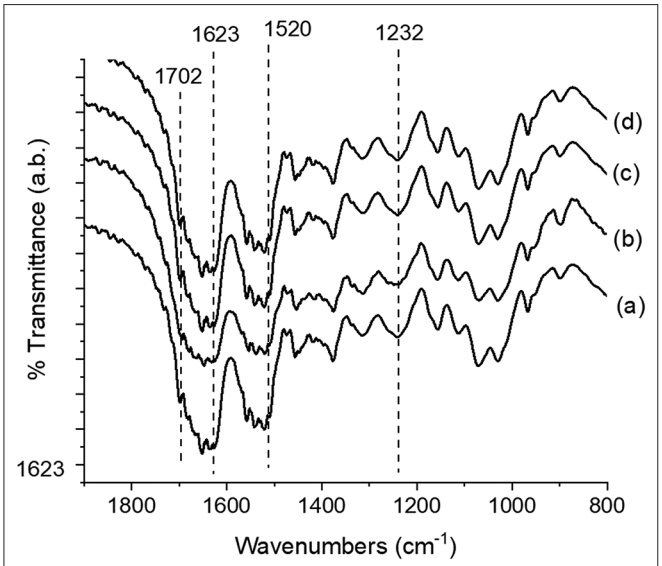

FIGURE 2 | FTIR spectra of the *Antheraea pernyi* silk fibroin/chitin-based structures; (a) APC80B, (b) APC20C, (c) APC20B, and (d) APC80C.

2016), the amount of secondary structure in APC samples was determined. The β-sheet content found for APC samples was: 38.03% (APC80B), 42.69% (APC80C), 20.82% (APC20B), and 17.89% (APC20C). These findings suggest that the gelation temperature step and the use of different solvents influenced the β-sheet content on the different contents.

All APC gels were freeze-dried to produce sponges, whose morphologies were investigated by SEM (see **Figure 3**). By analyzing the morphology of the cross-sections of the produced APC sponges (**Figure 3**), it was possible to verify that all samples have an open structure with pore sizes between 100 and 150 µm, independently of the solvent used in the stabilization step. Also, a quantitative analysis of the 3D morphometric parameters of the produced sponges was performed by micro-CT analysis. The 3D images of the scaffolds obtained from digital geometry processing from a series of two-dimensional X-ray images are illustrated (**Figure 4**). Through these images, the mean pore size, mean wall thickness, porosity, interconnectivity were quantified (**Table 1**). The data revealed that the APC-based sponges have pore sizes ranging between 95 and 137 µm, while the porosity values were between 86 and 88%, and interconnectivity values range from 75 to 88%. It seems that the different freezing temperatures used could explain the morphological variations observed in the samples. Comparing the morphological features of the earlier developed APC-based sponges with similar studies where BMIMAc was used to dissolution/processing of non-mulberry Eri silk (*Samia/Philosamia ricini*) into sponges (Silva et al., 2016); we conclude that the porosity and interconnectivity values found for APC-based sponges are superior. Those developed structures exhibited porosity, pore size, and interconnectivity that may allow not only the successful seeding of cells but also their proliferation into the developed structures.

Swelling Behavior

The swelling degree of the developed sponges after immersing in PBS at 37°C (**Figure 5**). All the sponges have considerable swelling degrees (up to 900% after 24 h), probably due to their high porosities (from 86.4 to 89.1%). Moreover, all APC-based sponges were able to keep their stability along with the assay, which is in accordance with the already published data stating that the stability of the structures was strongly associated with the β-sheet crystalline contents (Silva et al., 2016). However, no statistical differences were observed among the different time points at the four different conditions. In the same condition, there were also no significant differences among the different time points.

DMA experiments were performed to evaluate the variations of the viscoelastic properties of the sponges under compressive

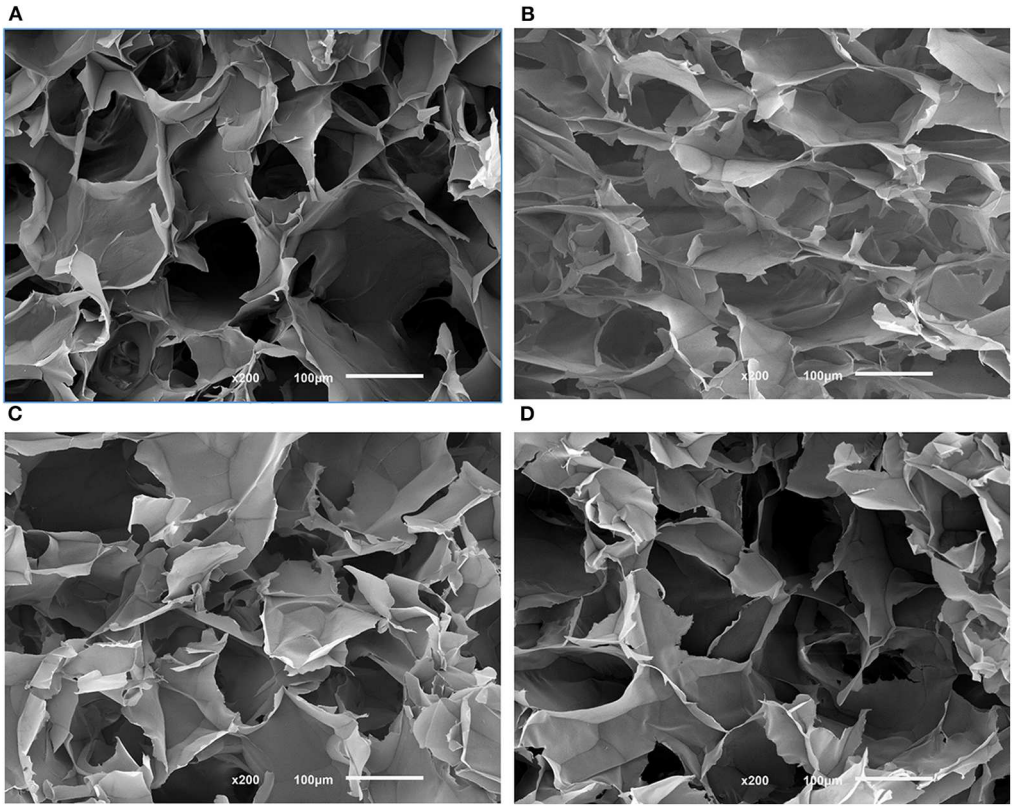

FIGURE 3 | Morphological features of different SEM images of the cross-sections of the APC80B **(A)**, APC80C **(B)**, APC20B **(C)**, and APC20C **(D)** scaffolds. Scale bars represent 100 μm.

loading and immersed in PBS solution at 37°C, trying to simulate the physiological environment (**Figure 6**). Variations of both storage modulus (E') and loss factor (tan δ) during frequency scans are shown in (**Figure 5**). Besides, (**Tables 2**, **3**) summarized the viscoelastic properties obtained at a physiological frequency (1 Hz). These DMA results showed a small increase in E' with the increasing frequency for all samples, varying between 70 and 110 kPa for APC80B and APC 80C, and between 50 and 70 kPa for APC 20B and APC 20C. The results indicated that the mechanical properties of the APC sponges could be modulated by the formation of an organized structure, richer in β-sheet content. Moreover, studies on silk fibroin-based scaffolds described the β-sheet formation as a critical factor that determines the mechanical properties of any particular SF (Silva et al., 2013, 2016). Therefore, it seems that the differences in β-sheet content within the matrices, determined by the deconvolution of the FTIR spectra of the samples, could be useful to modulate the storage modulus of the samples. In fact, the highest β-sheet content, calculated for APC80B (38.03%) and APC80C (42.69%), may have a significant role in the formation of a more rigid network, evidenced by their highest storage modulus (**Table 2**). In a similar study, higher E'(range of 233-797 kPa) were found in non-mulberry Eri silk-based sponges (Silva et al., 2016). The differences between the studies could be associated with the preparation conditions, which in turn affected the porosity and β-sheet content on silk-based matrices. Regarding the variation of the tan δ, for all sponges, it was observed a slight increase with the frequency increasing, evidencing that these materials became viscous and less elastic, and presenting more ability to dissipate energy. However, since the loss factor values were lower than 1, it should be assumed that all sponges can recover due to their higher elastic component.

CONCLUSIONS

The present work provides an innovative and sustainable strategy to produce blended sponges composed of silk protein fibroin derived from *Antheraea pernyi* cocoons and chitin from crab shells. Moreover, the structural features of the developed structures such as the differences in β-sheet contents, suitable porosity, interconnectivity, appreciable swelling degree, and tuneable viscoelastic compressive properties suggest that they can be good candidates for tissue engineering approaches. The formation of ApSF/chitin/BMIMAc gels also demonstrated to be flexible, which allows adapting the shape of the resulting matrices according to the defect sites where it would be implanted for tissue regenerations. In the immediate future, *in vitro* biological performance tests of the sponges with primary

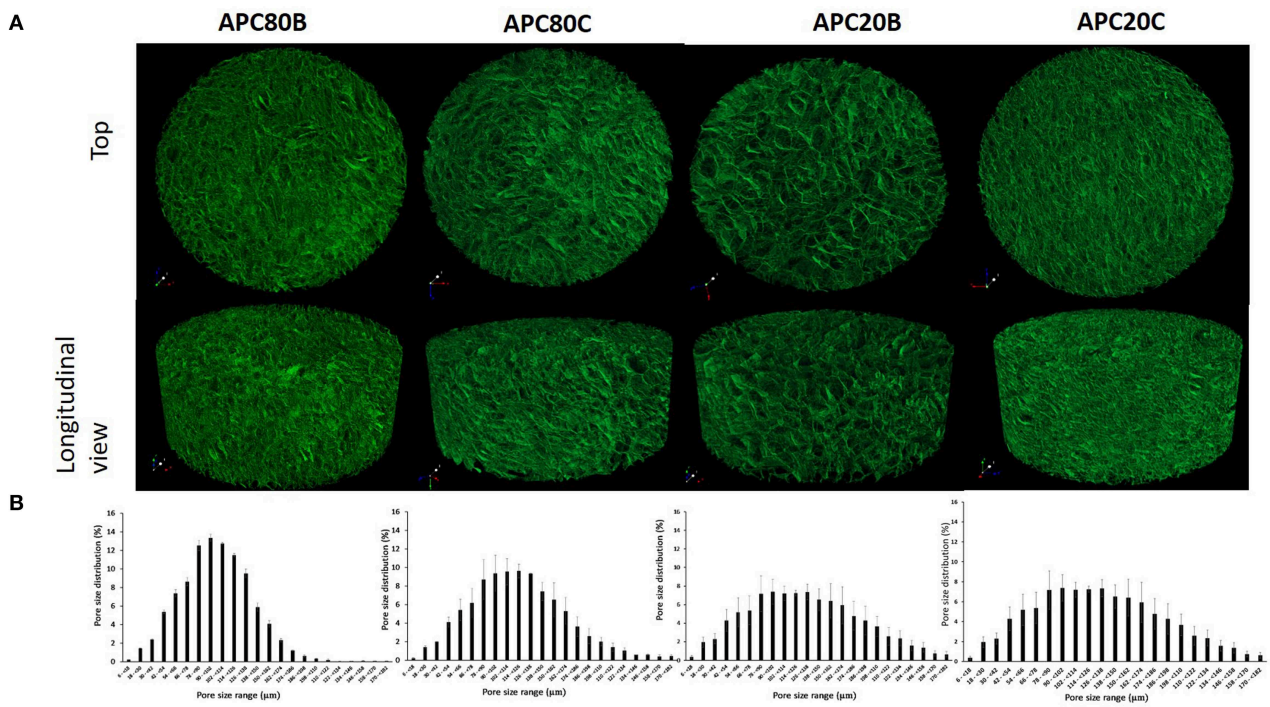

FIGURE 4 | Representative images obtained from the 3D reconstructions of the ApSF/chitin-based sponges by micro-CT **(A)** top and longitudinal views and **(B)** the mean pore size distributions.

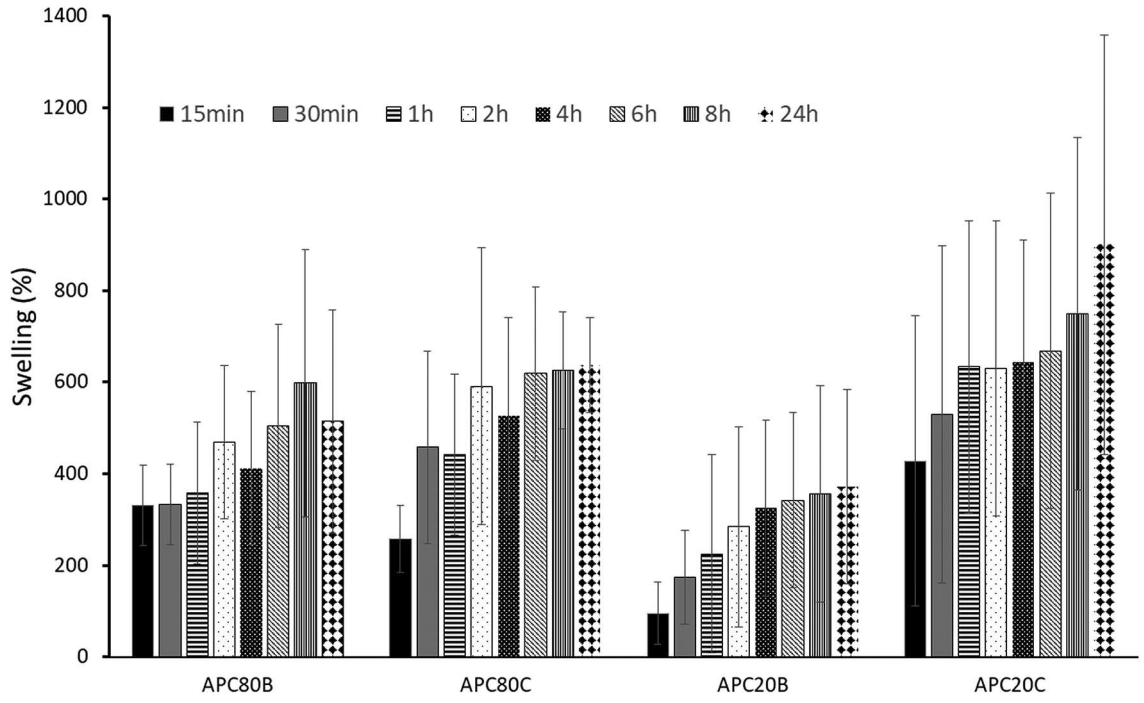

FIGURE 5 | Swelling profiles for APC-based sponges. All samples were immersed in PBS under stirring at 37°C.

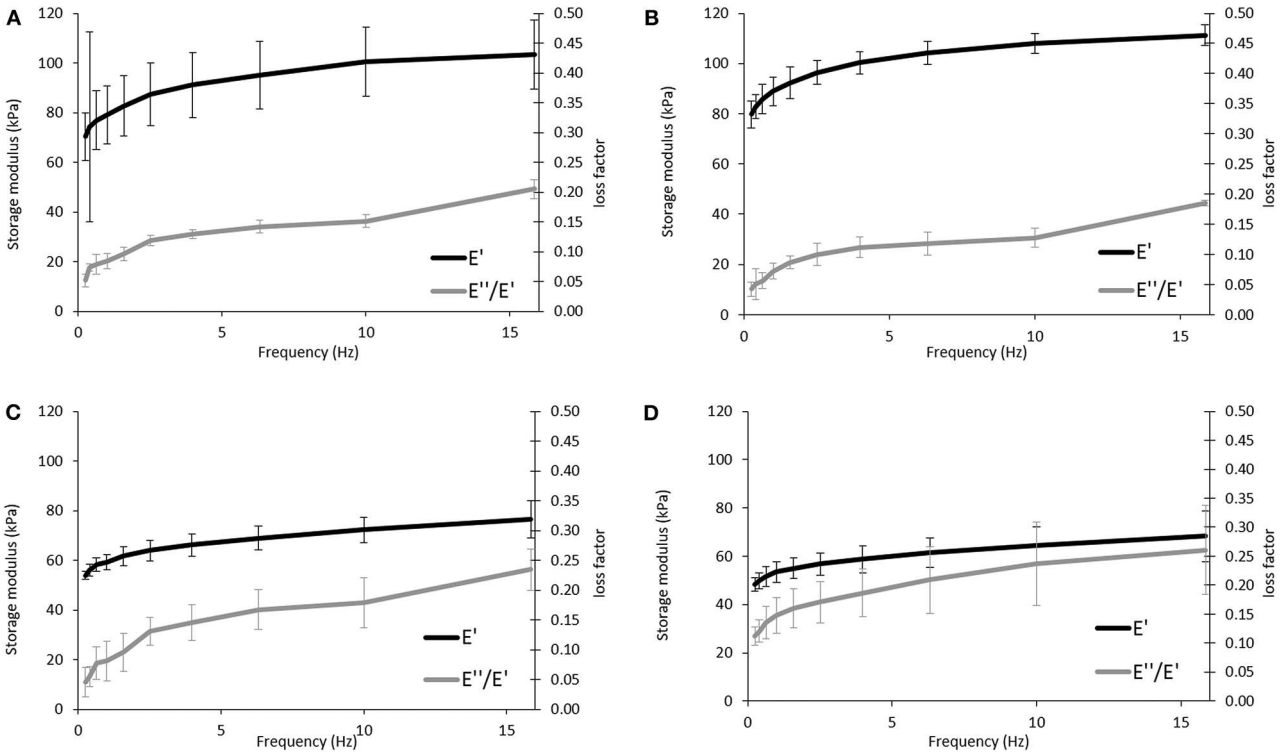

FIGURE 6 | Evaluation of the viscoelastic properties of the APC-based sponges: APC80B **(A)**, APC80C **(B)**, APC20B **(C)**, and APC20C **(D)** using DMA. Frequency scans were performed in the range 0.1–10 Hz under wet conditions at 37°C.

TABLE 2 | Microstructural features of the APC-based sponges obtained by micro-CT.

Sample	Mean pore size (μm)	Thickness (μm)	Porosity (%)	Interconnnectivity (%)
APC80B	101.82 ± 1.64	14.80 ± 0.05	88.39 ± 0.43	86.81 ± 3.54
APC80C	124.13 ± 15.13	15.04 ± 0.38	89.17 ± 0.99	88.20 ± 5.17
APC20B	137.55 ± 8.36	15.12 ± 0.43	88.77 ± 1.03	75.93 ± 4.62
APC20C	110.41 ± 6.18	14.33 ± 0.06	86.46 ± 5.07	88.57 ± 4.13

TABLE 3 | Viscoelastic properties of the APC based-sponges under compressive loading at a physiological frequency (1 Hz).

Sample	Storage modulus (kPa)	tanδ
APC80B	79.01 ± 11.8	0.08 ± 0.01
APC80C	88.91 ± 5.7	0.07 ± 0.01
APC20B	59.3 ± 3.11	0.08 ± 0.03
APC20C	53.4 ± 4.24	0.15 ± 0.03

cells will be performed to elucidate the biological behavior of the APC-based sponges. This strategy allows overcoming the limited use of silk fibroin from *Antheraea pernyi* cocoons as 3D-based structures, which open the prospects for its use for biomedical applications.

DATA AVAILABILITY STATEMENT

The datasets generated for this study are available on request to the corresponding author.

AUTHOR CONTRIBUTIONS

Each author played a major role in the development of the work and writing the manuscript. RR and SK supervised the work. SS (an Assistant Researcher) and JG (Ph.D. student) were involved in all aspects of experimentation and have contributed equally to this manuscript. AV is is a Junior researcher who undertook the DMA work. SL provided the silk of *Antheraea pernyi* and contributed to the experiments and discussion of the manuscript.

FUNDING

We thank the Portuguese FCT (PD/BD/135247/2017) to JG; Ph.D. programme in Advanced Therapies for Health (PATH) (PD/00169/2013) and R&D&I Structured Projects with reference NORTE-01-0145-FDER-000021 to SS; and European Union Framework Programme for Research and Innovation Horizon 2020 under grant agreement n° 668983—FoReCaST to SK and RR.

REFERENCES

Barber, P. S., Griggs, C. S., Bonner, J. R., and Rogers, R. D. (2013). Electrospinning of chitin nanofibers directly from an ionic liquid extract of shrimp shells. *Green Chem.* 15, 601–607. doi: 10.1039/c2gc36582k

Bendaoud, A., Maigret, J. E., Leroy, E., Cathala, B., and Lourdin, D. (2017). Cellulose-xyloglucan composite film processing using ionic liquids as co-solvents. *AIP Conf. Proc.* 1914:070008. doi: 10.1063/1.5016735

Chakravarty, J., Rabbi, M. F., Bach, N., Chalivendra, V., Yang, C.-L., and Brigham, C. J. (2018). Fabrication of porous chitin membrane using ionic liquid and subsequent characterization and modelling studies. *Carbohydr. Polym.* 198, 443–451. doi: 10.1016/j.carbpol.2018.06.101

Freire, M. G., Cláudio, A. F. M., Araújo, J. M. M., Coutinho, J. A. P., Marrucho, I. M., Lopes, J. N. C., et al. (2012). Aqueous biphasic systems: a boost brought about by using ionic liquids. *Chem. Soc. Rev.* 41, 4966–4995. doi: 10.1039/c2cs35151j

Gomes, J. M., Silva, S. S., and Reis, R. L. (2019). Biocompatible ionic liquids: fundamental behaviours and applications. *Chem. Soc. Rev.* 48, 4317–4335. doi: 10.1039/C9CS00016J

Goujon, N., Rajkhowa, R., Wang, X., and Byrne, N. (2013). Effect of solvent on ionic liquid dissolved regenerated antheraea assamensis silk fibroin. *J. Appl. Poly. Sci.* 128, 4411–4416. doi: 10.1002/app.38666

Hu, X., Kaplan, D., and Cebe, P. (2006). Determining beta-sheet crystallinity in fibrous proteins by thermal analysis and infrared spectroscopy. *Macromolecules* 39, 6161–6170. doi: 10.1021/ma0610109

Kang, Z., Wang, Y., Xu, J., Song, G., Ding, M., Zhao, H., et al. (2018). An RGD-containing peptide derived from wild silkworm silk fibroin promotes cell adhesion and spreading. *Polymers* 10, 1193–1205. doi: 10.3390/polym10111193

Kim, S. Y., Hwang, J.-Y., Seo, J.-W., and Shin, U. (2015). Production of CNT-taxol-embedded PCL microspheres using an ammonium-based room temperature ionic liquid: as a sustained drug delivery system. *J. Colloid Interface Sci.* 442, 147–153. doi: 10.1016/j.jcis.2014.11.044

Le Bideau, J., Viau, L., and Vioux, A. (2011). Ionogels, ionic liquid based hybrid materials. *Chem. Soc. Rev.* 40, 907–925. doi: 10.1039/C0CS00059K

Lozano-Pérez, A., Montalbán, M. G., Aznar-Cervantes, S., Cragnolini, F., Cenis, J., and Víllora, G. (2014). Production of silk fibroin nanoparticles using ionic liquids and high-power ultrasounds. *J. Appl. Poly. Sci. 13*2, 41702–41710. doi: 10.1002/app.41702

Néouze, M.-A., Le Bideau, J., Gaveau, P., Bellayer, S., and Vioux, A. (2006). Ionogels, new materials arising from the confinement of ionic liquids within silica-derived networks. *Chem. Mater.* 18, 3931–3936. doi: 10.1021/cm060656c

Nunes, C. S., Rufato, K. B., Souza, P., de Almeida, E. A. M. S., da Silva, M. J. V., Scariot, D. B., et al. (2017). Chitosan/chondroitin sulfate hydrogels prepared in [Hmim][HSO4] ionic liquid. *Carbohydr. Polym.* 170, 99–106. doi: 10.1016/j.carbpol.2017.04.073

Phillips, D. M., Drummy, L. F., Conrady, D. G., Fox, D. M., Naik, R. R., Stone, M. O., et al. (2004). Dissolution and regeneration of bombyx mori silk fibroin using ionic liquids. *J. Am. Chem. Soc.* 126, 14350–14351. doi: 10.1021/ja046079f

Rosellini, E., Zhang, Y. S., Migliori, B., Barbani, N., Lazzeri, L., Shin, S. R., et al. (2018). Protein/polysaccharide-based scaffolds mimicking native extracellular matrix for cardiac tissue engineering applications. *J. Biomed. Mater. Res. A* 106, 769–781. doi: 10.1002/jbm.a.36272

Shamshina, J. L., Zavgorodnya, O., Choudhary, H., Frye, B., Newbury, N., and Rogers, R. D. (2018). In search of stronger/cheaper chitin nanofibers through electrospinning of chitin–cellulose composites using an ionic liquid platform. *ACS Sustain. Chem. Eng.* 6, 14713–14722. doi: 10.1021/acssuschemeng.8b03269

Silva, S. S., Duarte, A., Oliveira, J., Mano, J. F., and Reis, R. L. (2013b). Alternative methodology for chitin–hydroxyapatite composites using ionic liquids and supercritical fluid technology. *J. Bioact. Compat. Pol.* 28, 481–491. doi: 10.1177/0883911513501595

Silva, S. S., Duarte, A. R. C., Carvalho, A. P., Mano, J. F., and Reis, R. L. (2011). Green processing of porous chitin structures for biomedical applications combining ionic liquids and supercritical fluid technology. *Acta Biomater.* 7, 1166–1172. doi: 10.1016/j.actbio.2010.09.041

Silva, S. S., Duarte, A. R. C., Mano, J. F., and Reis, R. L. (2013a). Design and functionalization of chitin-based microsphere scaffolds. *Green Chem.* 15, 3252–3258. doi: 10.1039/c3gc41060a

Silva, S. S., Kundu, B., Lu, S., Reis, R. L., and Kundu, S. C. (2019). Chinese oak tasar silkworm antheraea pernyi silk proteins: current strategies and future perspectives for biomedical applications. *Macromol. Biosci.* 19:1800252. doi: 10.1002/mabi.201800252

Silva, S. S., Mano, J. F., and Reis, R. L. (2017). Ionic liquids in the processing and chemical modification of chitin and chitosan for biomedical applications. *Green Chem.* 19, 1208–1220. doi: 10.1039/C6GC02827F

Silva, S. S., Motta, A., Rodrigues, M. T., Pinheiro, A. F. M., Gomes, M., Mano, J. F., et al. (2008). Novel genipin-cross-linked chitosan/silk fibroin sponges for cartilage engineering strategies. *Biomacromolecules* 9, 2764–2774. doi: 10.1021/bm800874q

Silva, S. S., Oliveira, N. M., Oliveira, M. B., da Costa, D. P. S., Naskar, D., Mano, J. F., et al. (2016). Fabrication and characterization of Eri silk fibers-based sponges for biomedical application. *Acta Biomater.* 32, 178–189. doi: 10.1016/j.actbio.2016.01.003

Silva, S. S., Popa, E., Gomes, M., Oliveira, M., Nayak, S., Subia, B., et al. (2013). Silk hydrogels from non-mulberry and mulberry silkworm cocoons processed with ionic liquids. *Acta Biomater.* 9, 8972–8982. doi: 10.1016/j.actbio.2013.06.044

Silva, S. S., Santos, T., Cerqueira, M. T., Marques, A. P., Reys, L. L., Silva, T. H., et al. (2012). The use of ionic liquids in the processing of chitosan/silk hydrogels for biomedical applications. *Green Chem.* 14, 1463–1470. doi: 10.1039/c2gc16535j

Singh, N., Koziol, K. K., Chen, J., Patil, A. J., Gilman, J., Trulove, P., et al. (2013). Ionic liquids-based processing of electrically conducting chitin nanocomposite scaffolds for stem cell growth. *Green Chem.* 15, 1192–1202. doi: 10.1039/c3gc37087a

Singh, Y., Bhardwaj, N., and Mandal, B. (2016). Potential of agarose/silk fibroin blended hydrogel for *in vitro* cartilage tissue engineering. *ACS Appl. Mater. Interfaces* 8, 21236–21249. doi: 10.1021/acsami.6b08285

Swatloski, R., Spear, S., Holbrey, J., and Rogers, R. (2002). Dissolution of cellose with ionic liquids. *J. Am. Chem. Soc.* 124, 4974–4975. doi: 10.1021/ja025790m

Tejwant, S., Trivedi,. J. T., and Kumar, A. (2010). Dissolution, regeneration and ion-gel formation of agarose in room-temperature ionic liquids. *Green Chem.* 12, 1029–1035. doi: 10.1039/b927589d

Um, I., Kweon, H., Park, Y., and Hudson, S. (2001). Structural characteristics and properties of the regenerated silk fibroin prepared from formic acid. *Int. J. Biol. Macromol.* 29, 91–97. doi: 10.1016/S0141-8130(01)00159-3

Vekariya, R. (2017). A review of ionic liquids: applications towards catalytic organic transformations. *J. Mol. Liqu.* 227, 44–60. doi: 10.1016/j.molliq.2016.11.123

Woloszyk, A., Buschmann, J., Waschkies, C., Stadlinger, B., and Mitsiadis, T. (2016). Human dental pulp stem cells and gingival fibroblasts seeded into silk fibroin scaffolds have the same ability in attracting vessels. *Front. Physiol.* 7, 140–147. doi: 10.3389/fphys.2016.00140

Yang, Y. J., Ganbat, D., Aramwit, P., Bucciarelli, A., Chen, J., Migliaresi, C., et al. (2019). Processing keratin from camel hair and cashmere with ionic liquids. *Express Polym. Lett.* 13, 97–108. doi: 10.3144/expresspolymlett.2019.10

Zhang, C., Chen, X., and Shao, Z. (2016). Sol–gel transition of regenerated silk fibroins in ionic liquid/water mixtures. *ACS Biomater. Sci. Eng.* 2, 12–18. doi: 10.1021/acsbiomaterials.5b00149

Conflict of Interest: The authors declare that the research was conducted in the absence of any commercial or financial relationships that could be construed as a potential conflict of interest.

frontiers in Materials

ORIGINAL RESEARCH
published: 10 June 2020
doi: 10.3389/fmats.2020.00138

Strong and Tough Silk for Resilient Attachment Discs: The Mechanical Properties of Piriform Silk in the Spider *Cupiennius salei* (Keyserling, 1877)

Gabriele Greco[1], *Jonas O. Wolff*[2] *and Nicola M. Pugno*[1,3]*

[1] *Laboratory of Bio-Inspired, Bionic, Nano, Meta, Materials & Mechanics, Department of Civil, Environmental and Mechanical Engineering, University of Trento, Trento, Italy,* [2] *Department of Biological Sciences, Macquarie University, Sydney, NSW, Australia,* [3] *Queen Mary University of London, London, United Kingdom*

Spiders are able to produce different types of silk with different mechanical and biological properties. Piriform silk is produced to secure spiders and their webs to surfaces by using a nano-fibril network embedded in a cement-like matrix. Despite their fundamental role, the mechanical properties and function of these anchorages are still poorly understood due to the practical difficulties in nano-fibril sample preparation, the complexity of the system, and the high variation of attachment disc structures. Here we estimated the mechanical properties of this nano-fibril silk and those of the whole silk membrane in the large wandering spider *Cupiennius salei* through a combination of nanoindentation and nanotensile techniques and with the support of a simple analytical model. The results highlight the mechanical properties of the piriform silk, facilitating the modeling of silk composite mechanics. This could inspire the design of more efficient bio-inspired adhesives and fabrics.

Keywords: spider silk, piriform silk, attachment disc, mechanical properties, nanoindentation

OPEN ACCESS

Edited by:
Giuseppe Saccomandi, University of Perugia, Italy

Reviewed by:
Giuseppe Puglisi, Politecnico di Bari, Italy
Gaetano Napoli, University of Salento, Italy

***Correspondence:**
Nicola M. Pugno
nicola.pugno@unitn.it

Specialty section:
This article was submitted to Mechanics of Materials, a section of the journal Frontiers in Materials

Received: *30 January 2020*
Accepted: *21 April 2020*
Published: *10 June 2020*

Citation:
Greco G, Wolff JO and Pugno NM (2020) Strong and Tough Silk for Resilient Attachment Discs: The Mechanical Properties of Piriform Silk in the Spider Cupiennius salei (Keyserling, 1877). Front. Mater. 7:138. doi: 10.3389/fmats.2020.00138

INTRODUCTION

Silk is produced by spiders to fulfill various functions such as for hunting, for locomotion, and to build robust cocoons and webs (Foelix, 2011). In 400 million years of evolution, the optimization of the properties of the spider silk has been achieved through the diversification of this protein-based material (Brunetta and Craig, 2010). Each of the different silk types is equipped with a unique combination of physical, chemical, and biological properties (Brunetta and Craig, 2010). In particular, the outstanding mechanical and biological properties of the dragline (Agnarsson et al., 2010; Lepore et al., 2017) (mainly produced by the ampullate glands) have been intensely studied in the last two decades, inspiring and developing novel technologies (Eisoldt et al., 2011; Wolff et al., 2017a; Dellaquila et al., 2019).

Although the dragline silk is in the main focus of the applied silk science, it is only one representative of the silk family among the huge variety of silk types that exist. If the number of species of spiders on Earth (more than 48,000, Foelix, 2011) and the fact that each one of them is able to spin from two to seven types of silk (Vollrath and Knight, 2001) are considered, there might be more than 150,000 different types of spider silk, each one with different properties tailored for a specific need (Basu, 2015). Among them, the silk produced by the piriform gland

has been one of the least studied, although it is one of the most common types of spider silk with a fundamental function: the attachment of silk threads to substrates.

The first studies that reported a histological analysis of the piriform glands were conducted by Kovoor and Zylberberg (1980) and Kovoor and Zylberberg (1982). They informed about the shapes and the dimensions of these glands and highlighted their position close to the spinnerets that also host the duct of the major ampullate gland. In comparison to the latter, the piriform glands are much smaller and numerous.

Blasingame et al. (2009) associated the protein of the piriform gland to the silk family due to the revealed conservation of the C-terminal region. The predicted aminoacidic composition of the piriform silk (the fibrous component) revealed a high amount of alanine in comparison to the other types of silk produced by the same spider (Blasingame et al., 2009; Geurts et al., 2010). Alanine can be associated with crystal-forming polyalanine chains, which contribute to a high Young's modulus and strength of the silk material (Yarger et al., 2018). Moreover, a recent study (Chaw et al., 2017) predicted the molecular weight of the PySp1 (the main protein of the piriform fibers) to be 578 kDa, which is larger than that of the dragline (between 200 and 300 kDa Vollrath and Knight, 2001). The molecular weight has been demonstrated to be directly correlated with the strength of fibers both in native and artificial silks (Xia et al., 2010; Bowen et al., 2018).

Piriform silk is used by spiders to create robust and efficient anchorages and adhesive systems that have been optimized during the evolution of spiders (Wolff et al., 2019). These affix the dragline to a surface, securing the arachnid in the event of a fall (Foelix, 2011; Asakura and Miller, 2014) (**Figures 1A–C**). Moreover, they are used to anchor the supporting threads of a cobweb to a surface or to join ampullate silk threads inside a web (Foelix, 2011; Asakura and Miller, 2014; Basu, 2015; Greco et al., 2019). The attachment discs are spun very fast and create a durable, efficient adhesive anchorage (Wolff and Gorb, 2016).

The adhesive membrane ("attachment disc") is composed of a multi-fibril system embedded in a cement-like matrix (**Figures 1D–F**) that creates a structure able to bear high loads (Blasingame et al., 2009; Cranford et al., 2012). Spiders can adjust the morphology of the attachment disc and thus its overall mechanical behavior. For example, the attachment discs used to secure the supporting lines of cobwebs are different from the ones used in pre-stressed trapping lines (Sahni et al., 2012). Moreover, it has been demonstrated that spiders spin larger attachment discs if their weight is experimentally increased (Wolff et al., 2018).

The sectioning of attachment discs revealed that the relative proportion of the cement-like glue and the fiber content of the attachment discs differs between spiders of different ecology and evolutionary history; and that the piriform fibers and the dragline are not in contact with the substrate (Denny, 1976; Wirth

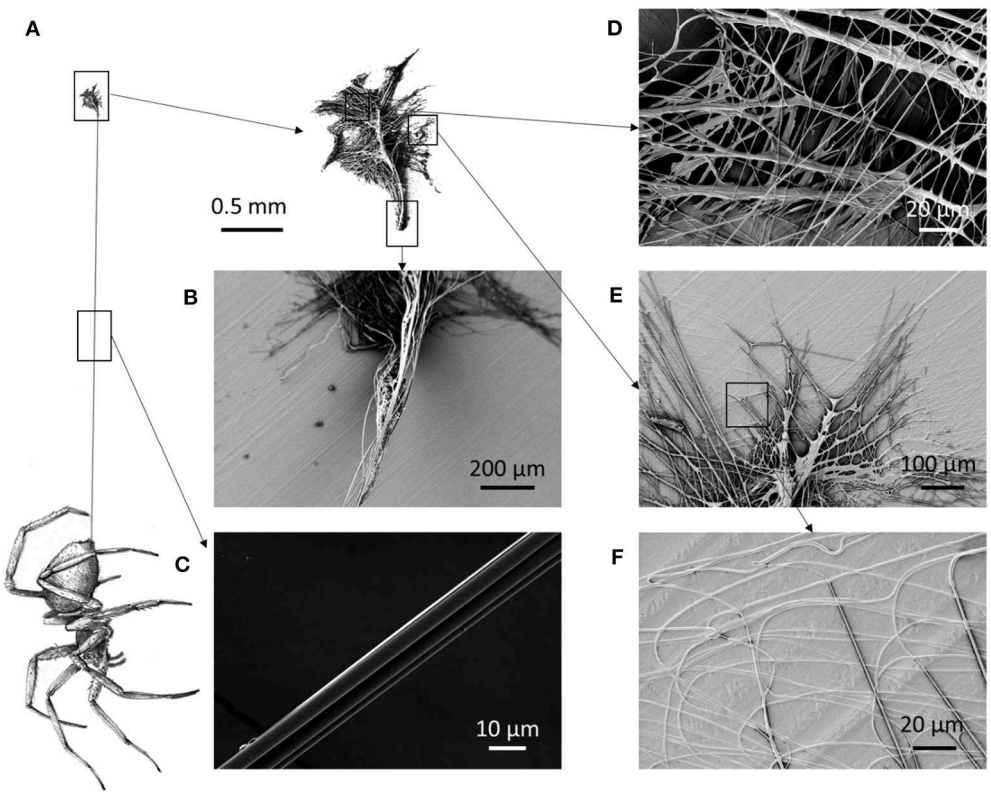

FIGURE 1 | (A) Schematic of a spider that spins its dragline, anchored to the substrate by means of an attachment disc. **(B)** The initial part of the dragline is composed of more threads than the **(C)** distal part of the dragline. **(D)** Scanning electron microscopy (SEM) picture of the median part of the attachment disc, **(E)** the lateral part, and **(F)** an enlargement of the lateral part, which shows fibrils attached to the surface.

et al., 2019). Accordingly, the fibers are not directly involved in the attachment disc's adhesion, yet they may modulate the mechanical properties of the surrounding glue layer. Whereas the ultrastructure of the piriform fibers is rather constant across species, the ultrastructure of the glue is very different (Wirth et al., 2019).

In order to understand the mechanical behavior of attachment discs under load, several approaches have been used. The multiple peeling theory (Pugno, 2011) has been used as a key model in order to explain the relationship between structure, material properties, and adhesive performance of the attachment discs and anchorages by means of multiple contacts points (Pugno et al., 2013; Brely et al., 2015; Liprandi et al., 2019; Greco et al., 2020). From the experimental point of view, the load to detach these membranes from surfaces has been measured by varying the surface's conditions, demonstrating a strong dependence on the type of used substrate (Grawe et al., 2014).

All these aspects, together with the structural hierarchical analysis that has been done on the piriform attachment discs (Wolff et al., 2015; Wirth et al., 2019), could be used for the development and the design of bio-inspired adhesives with superior mechanical performances (Jain et al., 2014).

However, several knowledge gaps have to be filled in the modeling and characterization of the piriform silk and the attachment discs before achieving possible bio-inspired solutions. Among these, there is the need for an understanding of the effects of attachment disc geometry on its load-bearing capabilities (Wolff et al., 2017b). Moreover, the understanding of the mechanical properties of the piriform silk is crucial in order to model the mechanical behavior of attachment discs. The first tensile tests of piriform silk have been performed on isolated piriform silk fibers (including their glue layer) of a hunting spider (*Drassodex* sp.) that were carefully peeled off an anti-adhesive polymer substrate (Wolff et al., 2017c). In this work, an extensibility of 0.5 mm/mm, a strength of 511 MPa, a toughness modulus of 141 MPa, and a Young's modulus of 5.6 GPa were measured. However, in attachment discs, single piriform fibers are not used in isolation, but it is their assembly into a multi-fiber compound material that makes up its full-scale properties. It is therefore indispensable to generate a model to understand the mechanical properties of attachment discs on multiple hierarchical levels.

In this work, we empirically determined the mechanical properties of the single piriform silk fiber and of the whole attachment disc of the species *Cupiennius salei* through nanoindentation and nanotensile techniques. We developed a simple model in order to explain the overall mechanical behavior of the membrane under traction composed of piriform silk and the dragline. With this work, we aim to create a comprehensive understanding of the mechanical properties of piriform silk and its spinning product (the attachment disc), with the potential to inspire the design of novel bio-inspired adhesives and fabrics with superior properties.

ANALYTICAL MODEL

Evaluation of the Spacing Among Fibrils

Determining the mechanical properties of piriform silk from attachment disc membranes creates difficulties due to the chaotic distribution of the fibers in the membrane-like silk film (**Figure 2**). Based on the observation that piriform fibers form a layered network in the attachment disc (**Figures 1**, **2**), we model the silk membrane as a lattice of a glue–fiber material (**Figure 3**).

As modeling the complexity of natural attachment discs is analytically unfeasible, for the purpose to calculate the tensile properties of piriform silk, we simplify the structure as a parallelepiped lattice. The spacing between the fibers (i.e., the porosity of the membrane) was estimated by determining the mean mass and dimension of the membranes through precise measurements.

Based on the observation of Wirth et al. (2019) that in *C. salei* the glue fraction of piriform silk is much smaller (i.e., mean thickness of ∼20 nm) than the fiber fraction (thickness of ∼0.5–1.5 μm), we neglected the presence of the glue (third phase) in the calculation of the volume. We assume that the density of the piriform silk is similar to that of major ampullate silk ($\rho_p \sim \rho_{silk} \sim 1.3\frac{\mathrm{g}}{\mathrm{cm}^3} = \rho$). The nominal volume of the membrane V_n ($= w \cdot l \cdot t$) multiplied by the mean density of the membrane (ρ_m) is equal to the mass m of the membrane:

$$\rho_m V_n = m$$

from which we can obtain the mean density of the membrane. The membrane mass is also given by the real density of the silk multiplied by the real volume of the silk fibrils in the membrane. By following the schematic in **Figure 3**, we can thus write:

$$\rho_m V_n = \rho V \Rightarrow \frac{\rho_m}{\rho} = \frac{A_d l + \frac{2A_p wtl}{s^2}}{wtl} \Rightarrow$$

$$\Rightarrow s = \sqrt{\frac{2A_p wtl}{\frac{\rho_m}{\rho} wtl - A_d l}} \tag{1}$$

where A_d is the cross-sectional area of the dragline fiber of length l, and A_p is the cross-sectional area of the piriform fibril network with fibrils of length l and spacing s (**Figure 3**).

Equation (1) can then be used to compute the mean spacing between the fibers in the piriform membrane.

Evaluation of the Stress in the Fibrils in Tensile Tests

In order to evaluate the mechanical properties of the whole membranes through tensile tests, the engineering stress needs

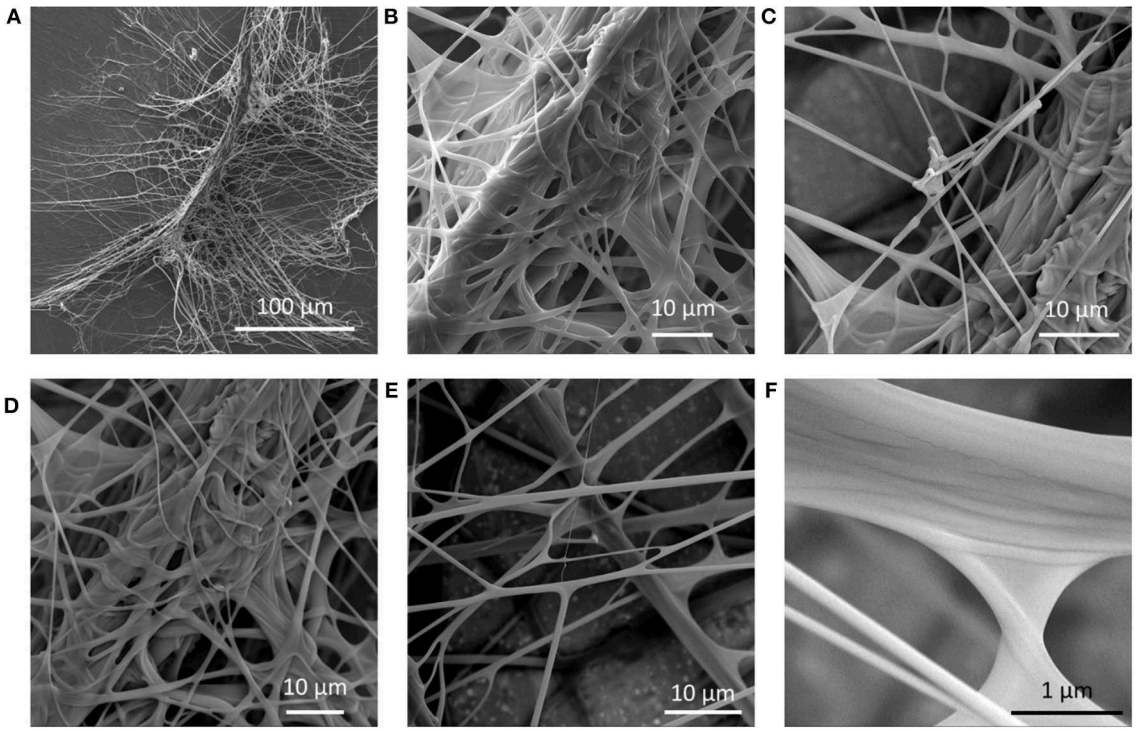

FIGURE 2 | Scanning electron microscopy (SEM) images of an attachment disc of Cupiennius salei. **(A)** The structure is composed of a dragline thread that is suspended in a network of glue-coated fibrils. **(B–F)** Different details of the piriform silk network in the attachment disc.

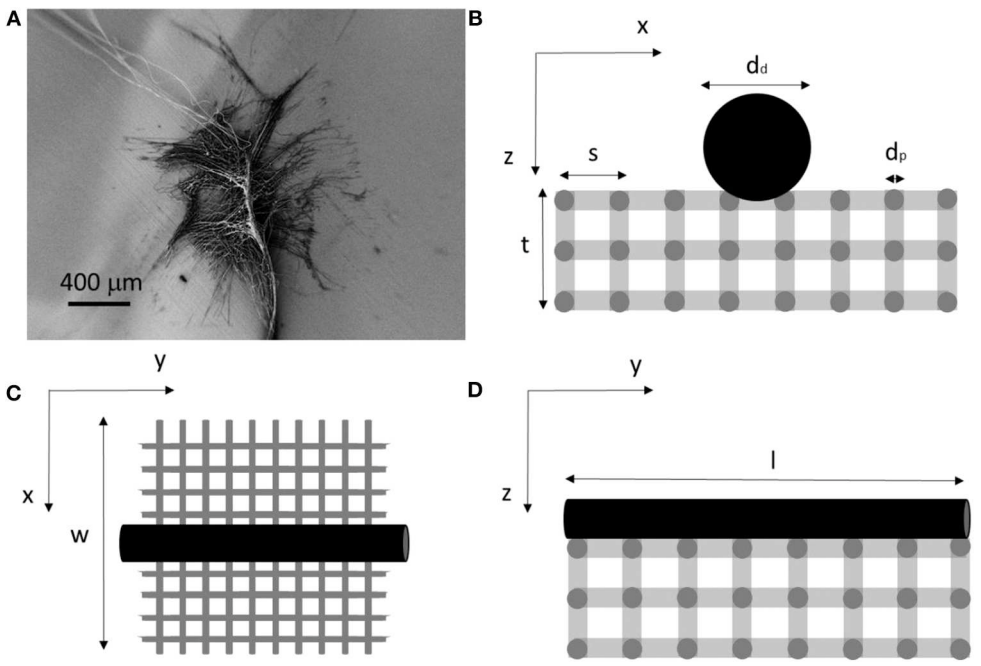

FIGURE 3 | (A) Scanning electron microscopy (SEM) picture of an attachment disc. **(B–D)** Schematic model in the three directions used to compute the mechanical properties of the membrane and composing fibrils.

to be determined. By referring to **Figure 3**, we can estimate it through the measurement of the applied load and section involved. In this approach, we homogenize the layered structure of piriform silk integrating across its glue and fiber fraction.

Along the y direction (**Figure 3B**), we have:

$$\sigma_y = \frac{F_y}{A_y} = \frac{F_y}{A_d + \frac{A_p wt}{s^2}} \tag{2}$$

On the other hand, along the x direction (**Figure 3D**), we have:

$$\sigma_x = \frac{F_x}{A_x} = \frac{F_x}{\frac{A_p tl}{s^2}} \tag{3}$$

It is thus possible to compute the engineering stress on the anisotropic membrane according to Equations (2) and (3).

Interestingly, if we consider the force applied to the membrane in one of the two directions, we find in the y direction that:

$$F_y = F_d + F_p \Rightarrow \sigma_y = \frac{\sigma_d A_d}{A_d + \frac{twA_p}{s^2}} + \frac{\frac{\sigma_p A_p wt}{s^2}}{A_d + \frac{twA_p}{s^2}} \tag{4}$$

whereas in the x direction that:

$$F_x = F_p \Rightarrow \sigma_x = \sigma_p \tag{5}$$

This means that according with our scheme the stress computed along the x direction gives exactly the stress on the piriform silk (since the perpendicular dragline silk does not support any load).

Equation (4) represents also a relation between the strength of the dragline (σ_d), the strength of the piriform silk (σ_p), and the strength of the whole membrane (in this case σ_y). Thus, knowing the strength of the piriform silk measured along x via Equation (5), there is the possibility to check the strength value of the dragline measuring the strength along y with Equation (4) as a control.

Evaluation of the Young's Modulus of the Fibrils in Tensile Tests

In order to estimate the effective Young's modulus of the whole membrane under traction, the topology expressed in **Figure 3** can be applied again.

The membrane is composed of piriform fibrils with the Young's modulus E_p.

The relation between the Young's modulus (E) and the spring constant (k) of a fiber under tensile longitudinal load is in general given by:

$$k = \frac{EA}{L} \tag{6}$$

where A is the section of the fiber and L its length.

During loading parallel to the orientation of the dragline thread (y direction), we have n fibrils in series, N and N' in parallel (x and z direction) that can be obtained by:

$$n = \frac{l}{l_p}$$
$$N = \frac{t}{s}$$
$$N' = \frac{w}{s}$$

where l_p is the mean length of the fibril.

Thus, the stiffness of the piriform fibrils along y is predicted to be:

$$k_{eql'} = \frac{k_p}{n} NN'$$

where $k_p = E_p A_p / l_p$ is the spring constant of the piriform fibril. Moreover, in the y direction, we also have to consider the contribution of the dragline, which is longitudinally attached to the membrane. The total membrane stiffness is thus predicted to be:

$$k_{eqy} = \frac{k_p}{n} NN' + \frac{E_d A_d}{l_d}$$

where E_d is the Young's modulus of the dragline and l_d its length.

We then can estimate the Young's modulus of the whole membrane through Equation (6) and by assuming $l \approx l_d$ as:

$$E_{eqy} = \frac{\pi}{4}\left(\frac{E_p d_p^2}{s^2} + \frac{E_d d_d^2}{tw}\right) \tag{7}$$

where d_p is the diameter of the piriform fibers, and d_d is the diameter of the dragline.

On the other hand, if we consider the membrane pulled along the x direction, we have n' fibrils in series along the x direction, N and N'' in parallel (y and z direction), namely:

$$n' = \frac{w}{l_p}$$
$$N'' = \frac{l}{s}$$

The equivalent membrane stiffness along the x direction is thus:

$$k_{eqx} = \frac{k_p}{n'} NN''$$

and from this, we can estimate the Young's modulus of the whole membrane along the x direction by using Equation (6), i.e.,:

$$E_{eqx} = E_p \frac{\pi d_p^2}{s^2 4} \tag{8}$$

It is possible to notice that Equations (7) and (8) differ only for the contribution of the dragline, which increases the equivalent Young's modulus of the membrane along y with respect to x.

Finally, Equations (7) and (8) are used to estimate the Young's modulus of the single piriform fibers from the mechanical properties of the whole membrane obtained through experimental tensile testing.

MATERIALS AND METHODS

Spiders

The spiders under study were adult females of *C. salei* (Keyserling, 1877) from a captive bred lab stock. They were kept in different plastic boxes and fed with a weekly diet of *Blaptica dubia* or *Acheta domestica (*feed with carrots and fish food). All the plastic boxes were set in a room with controlled environmental parameters. Windows provided natural light, and temperature was about 22°C in the night and 25°C during the day; the humidity rate was controlled in each terrarium to be around 80% with the support of a hygrometer. Each terrarium was provided with a refuge considering the needs of the spider to feel protected and live without stress, according to the Italian regulation on animal protection and EU Directive 2010/63/EU for animal experiments.

Scanning Electron Microscopy

Samples of attachment discs were air-dried and sputter coated with 80:20 Pt/Pd for 5 min in a Q150T.

Scanning electron microscopy (SEM) imaging was performed using a Zeiss−40 Supra.

Measurement of Attachment Disc Mass

The mass of the membranes was measured with a TGA ANALYSIS TA Q5000. We measured the mass of 13 membranes and then the mass of 14 membranes for 3 min (to get stable values). The difference between obtained values represents the average mass of a membrane, of about 5 μg.

Measurement of Attachment Disc Length

We used microphotographs obtained with an optical microscope (Zeiss Axiotech and Axiovert) and analyzed in the ImageJ (Schneider et al., 2012) software. We measured the mean length and the width of the membranes. The thickness was measured through a caliper by sandwiching five membranes between its jaws, this procedure was repeated 100 times. An optical microscope was used to confirm that this procedure was reflecting the native profile of the samples. In particular, by looking laterally at the attachment discs that were produced directly on a quartz substrate, it was possible to get the idea of the profile. For each measurement, 100 samples were measured.

Nanoindentation

The tested samples were prepared by letting the spider walk on a quartz substrate and letting it spin the attachment discs. This quartz substrate was then mounted into an iNano®Nanoindenter (Nanomechanics Inc.). The declared sensitivity of the machine is 3 nN for the load and 0.001 nm for the displacement.

The used mapping method (Nanoblitz 3d, Nanomechanics Inc.) involved a 200 μm × 200 μm square with 400 indentation points inside (each for a maximum of 0.05 mN loads for the piriform and 5 mN for the dragline, which resulted in a below 10% indentation depth). We used a Berkovich tip with a tip radius of about 20 nm for the experiments.

Tensile Testing

Dragline samples were prepared by cutting pieces of the dragline from the attachment disc and sticking them on a paper holder with a window of 1 × 1 cm using double-sided tape. The diameters of the fibers that compose the dragline were measured with an optical microscope (Zeiss Axiotech and Axiovert).

Membrane samples were obtained by detaching attachment discs from the substrate (commercial braplast plastic box, www.braplast.com). The test samples of piriform silk were prepared by fixing the attachment discs (per intended pulling direction, e.g., x or y) on a paper frame provided with a rectangular window with 1 mm height. The sample was fixed to the paper frame with a double-sided tape and by using Loctite super glue (Blackledge et al., 2005). For the y direction, the dragline was included in the membrane.

The tests were performed with the support of the nanotensile machine Agilent UTM T150 (Keysight technology) with a cell load of 500 mN. The displacement speed was 1% of the gauge length per second. The declared sensitivity of the machine is 10 nN for the load and 1 $\dot{A}$ for the displacement in the dynamic configuration. The tests were recorded with a Sony Camera.

The anchorage samples for peeling tests were produced by letting the spider walk on a black paper surface. Once the spider spun the anchorages, we cut the dragline at a length of about 5 mm and stuck the piece of paper (containing the dragline) on a wood block of about 2 cm^3 × 0.5 cm^3 × 0.5 cm^3. This was fixed on the paper frame (1 cm square window) and then fixed on the machine. The testing speed was 6 mm/min.

ANOVA Analysis

Analysis of variance was performed to compare the mean values of the strain at break, strength, Young's modulus, and toughness modulus from x- and y-stress tests (i.e., attachment discs pulled along or perpendicular the dragline direction).

The parameters used to verify the null hypothesis, i.e., all the data sets come from the same distribution and have the same mean value, were:

$$SSQ_a = \sum_{g=1}^{G} n_g \left(m_g - m_u\right)^2$$

$$SSQ_e = \sum_{g=1}^{G} \sum_{j=1}^{n_g} \left(x_{gj} - m_g\right)^2$$

where G is the number of different samples under consideration, n_g is the number of tests of the same sample, m_u is the mean value of all the data, m_g is the mean value within the group (i.e., sample), and x is the single force value. These sums of squares were used to compute the T value:

$$T = \frac{\frac{SSQ_a}{G-1}}{\frac{SSQ_e}{n-G}}$$

that has been compared with the ideal value of the Fisher function F with a significance level of 5%. If $T > F$, we reject the null hypothesis, and thus, we can consider the difference among the data set as significant (i.e., the difference is due to intrinsic differences among the samples and not a consequence of internal variance). The p-value was computed in MatLab®.

Weibull Statistics

In order to analyze the fracture strength distribution, we used Weibull statistics (by following Yang et al., 2020). Weibull cumulative density function is defined by the following relation (we omit the scaling effects here):

$$F(x, m, x_0) = 1 - e^{-\left(\frac{x}{x_0}\right)^c} \quad (9)$$

where x is the fracture strength, c is the shape parameter, and x_0 is the scale parameter. F represents the probability that the sample breaks at the strength lower than x.

In order to obtain the relative probability density distributions of the different samples (i.e., $f(x, c, x_o) = \frac{c}{x_0^m} x^{c-1} e^{-\left(\frac{x}{x_0}\right)^c}$), we obtained the Weibull shape and scale parameters by using the linear regression method. By applying the double logarithm to Equation (9), we obtain the following equation:

$$\ln(\ln\left(\frac{1}{1 - F(x)}\right) = cln(x) - cln(x_0)$$

where F could be estimated through the median rank estimator

$$\hat{F}(x_i) = \frac{i - 0.3}{n + 0.4}$$

where n is the number of the tested specimens, and i is the order of the considered one (after the organization of the samples from the weakest until the strongest). Kolmogorov–Smirnov and R square tests were performed to each set of data to verify (under the 95% of acceptance, MatLab®) that Weibull statistics could be applied to the data set.

RESULTS

When a spider walks, it produces attachment discs where it secures the dragline (**Figure 1A**). Close to the attachment disc, the dragline is composed of more fibers (**Figure 1B**) than in its distal portion (i.e., close to the spinnerets; **Figure 1C**). The attachment discs are complex structures composed of multiple fibers with a mean diameter of 1.2 ± 0.5 μm and coated with a glue (**Figures 1**, **2**). The thickness, the width, and the length of the membranes are, respectively, 5 ± 1 μm, 1.8 ± 0.4 mm, and 3.3 ± 0.6 mm (**Figure S1**). The mass of the membranes (**Figure S2**) has been measured as about 5 μg, which gives us by Equation (1) the mean fibril spacing of about 4.6 μm (**Table S1**).

Nanoindentation Tests

In order to measure the mechanical properties of the piriform silk, we used nanoindentation and nanotensile tests.

We performed a series of experiments to compare the Young's modulus obtained by both nanoindentation and tensile tests (Denny, 1976; Das et al., 2017).

The tests on the dragline attached to the membranes revealed consistent values between the two techniques. With nanoindentation (**Figure S3**, **Table S2**), we measured a Young's modulus of 4.2 ± 0.8 GPa, which was also found with the mapping method (**Figure S4**). In the tensile tests (**Table S3**), we measured a Young modulus of 5.2 ± 4.8 GPa (computed by taking the slope of the fitting regression line in the initial and steepest part of the stress–strain curve), a strain at break of 0.27 ± 0.09 mm/mm, a mean strength of 365 ± 290 MPa, and a mean toughness modulus of 61 ± 47 MJ/m^3. From nanoindentation, we obtained a hardness of 0.33 ± 0.10 GPa for the dragline.

The investigation of the piriform silk through nanoindentation was performed by using both the single indentation method and the mapping method. The single indentation method was performed on different positions along the membrane (**Figure S5**). The obtained Young's modulus of the single fiber was 3.9 ± 1.4 GPa (**Table S4**), and the hardness was 0.09 ± 0.05 GPa. These observations were confirmed by

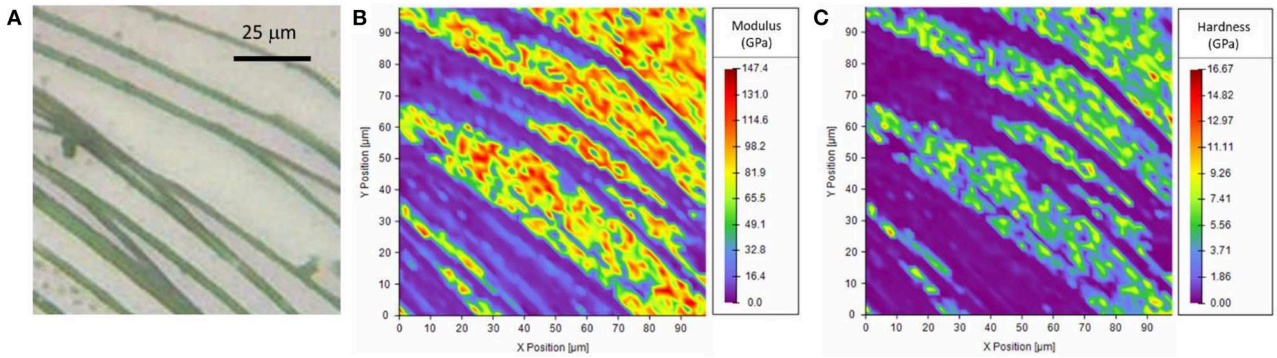

FIGURE 4 | (A) Optical microscopy image of the sample, **(B,C)** Nanoindentation mapping of the mechanical properties of the piriform silk on the border of the attachment disc. Note that high values result from measurements of the quartz substrate exposed between the (softer) silk fibrils.

the mapping method (**Figure 4**, **Figures S6**, **S7**). The results were consistent with the indentation depth (**Figure S8**), which was kept >10% of the thickness of the fibers (Hay et al., 1998; Fischer-Cripps, 2011).

Tensile Tests

In order to measure the overall mechanical properties of the different silk composites, we performed the following nanotensile tests: test of the dragline, the whole membrane pulled along the y direction (**Figure 3B**, Supplementary Video SV1), and the whole membrane pulled along the x direction (**Figure 3D**, Supplementary Video SV2). The obtained stress–strain and load displacement (for the last type of test) curves are depicted in **Figure 5**. The stress on the membrane was computed by using Equations (2) and (3), and related extracted values are reported in **Table S1**.

There was no significant difference in mechanical properties between the x- and y-mounting of attachment disc samples

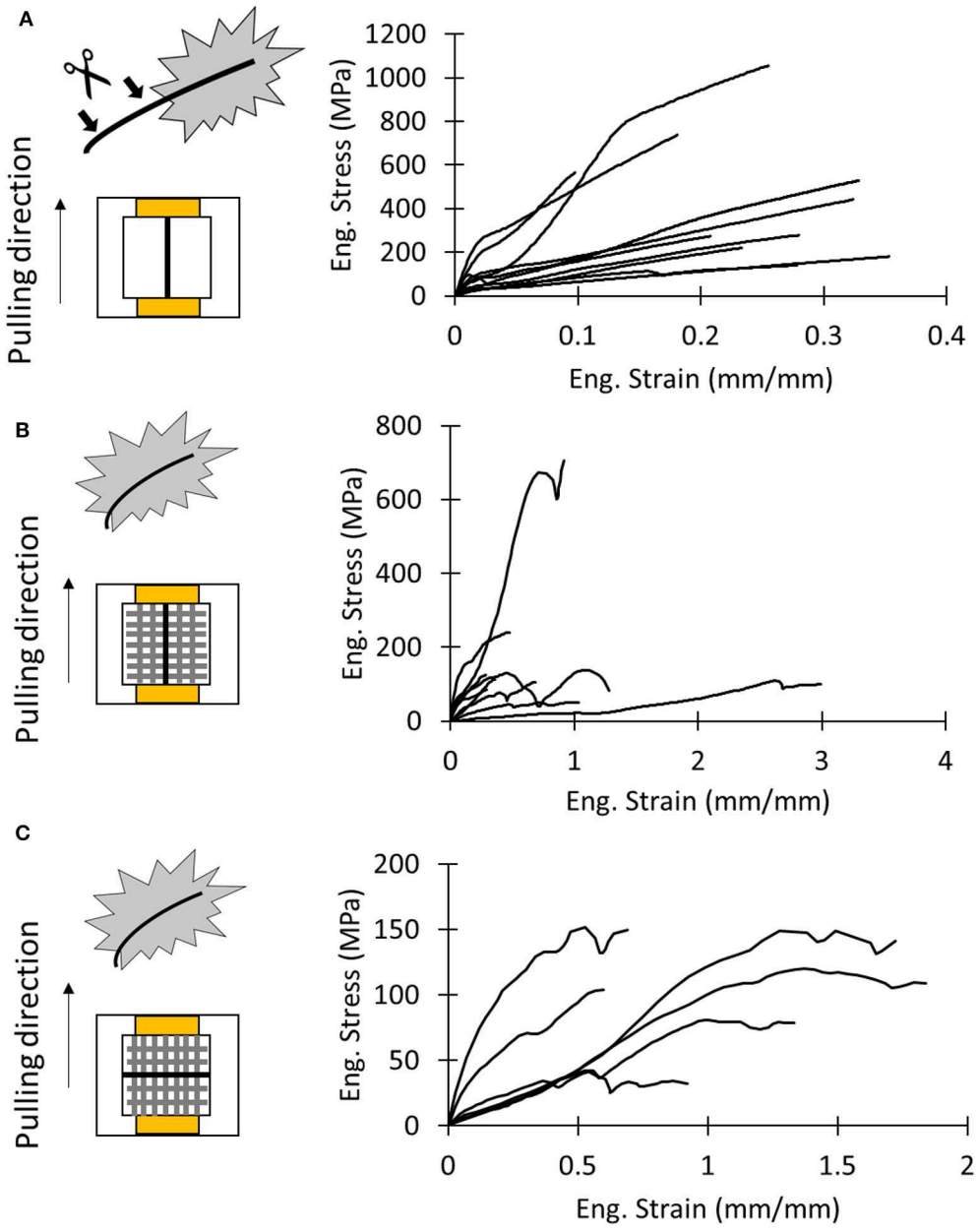

FIGURE 5 | (A) Schematics of test sample and stress–strain curves of dragline samples. **(B)** Schematics of test sample and stress–strain curves of the attachment disc pulled in the dragline direction (y direction). **(C)** Schematics of test sample and stress–strain curves of the attachment disc pulled in the pure fibrils direction (x direction).

TABLE 1 | Values of the mechanical properties of tested silk products obtained in the experimental (tensile tests of the whole membrane and dragline threads and nanoindentation on single fibers) and analytical model compared with literature values (from other species).

Sample	The value is obtained with:	Strain at break (mm/mm)	Strength (MPa)	Young's modulus (GPa)	Toughness (MJ/m^3)
Dragline (near the disc)	Tensile exp	0.26 ± 0.09	365 ± 290	5.2 ± 4.8	60.9 ± 46.6
	Nanoindentation			4.2 ± 0.8	
	Equation		425 equation4	6.1 equation7	
Piriform silk fiber	Tensile exp	0.51 ± 0.26 (Wolff et al., 2017c)	511 ± 124 (Wolff et al., 2017c)	5.59 ± 1.75 (Wolff et al., 2017c)	141 ± 74 (Wolff et al., 2017c)
	Nanoindentation			3.9 ± 1.4	
	Equation		128 equation4	3.45 equation8	
Membrane pulled by x direction	Tensile exp	1.18 ± 0.53	106 ± 42	0.19 ± 0.10	87 ± 53
	Equation		128 equation4	0.21 equation8	
Membrane pulled by y direction	Tensile exp	0.93 ± 0.85	190 ± 180	0.33 ± 0.18	97 ± 90
	Equation		174 equation4	1.19 equation7	

(**Tables S5**, **S6**). For the x and y direction, respectively, we found a strain at break of 1.18 ± 0.53 and 0.93 ± 0.85, a strength of 106 ± 42 MPa and 190 ± 180 MPa, a Young's modulus of 0.19 ± 0.10 MPa and 0.33 ± 0.18 MPa, and a toughness modulus of 87 ± 53 MJ/m^3 and 97 ± 90 MJ/m^3.

In order to evaluate the difference of the mechanical properties between attachment discs and the dragline, we performed a one-way ANOVA test (**Table S7**). Only the strength of the dragline and the membrane pulled along the x direction resulted to be statistically different ($p = 0.00487$, all *post hoc* pairwise comparisons $p < 0.05$). This suggests that the dragline is stronger than the piriform silk membrane.

A better understanding of the difference between the strength of the analyzed samples can be given by looking at Weibull statistics. In this case, the linear regression method was used to compute the Weibull parameters (**Figure 6A**, **Table S8**), and these were used to plot the strength's probability density distributions of the tested samples (**Figure 6B**). The narrower shape of the strength probability distribution of the membranes relative to the dragline indicated their more homogeneous fracture behavior.

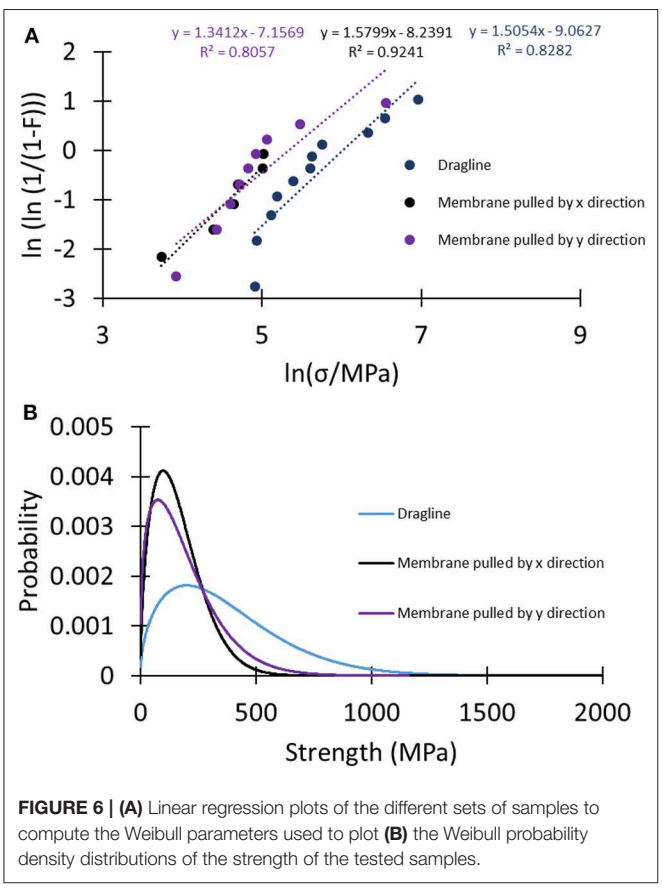

FIGURE 6 | (A) Linear regression plots of the different sets of samples to compute the Weibull parameters used to plot **(B)** the Weibull probability density distributions of the strength of the tested samples.

Comparison With the Model

Table 1 reports mechanical properties of silk fibers and membranes determined in this work and their comparison with values reported in the literature. The Young's modulus estimated with Equations (7) and (8) (i.e., Young's modulus of the whole membrane under traction relative to the Young's modulus of the single fibers) is similar to the one measured by nanoindentation. The values we obtained for single piriform silk fibers are comparable to those previously measured in isolated piriform silk fibers (Wolff et al., 2017c). Equation (7) was also used as a control for estimating the Young's modulus of the dragline, which was found to be comparable to the one directly measured by the dragline tensile test.

Equation (4) gives us the possibility to estimate the strength of the dragline by knowing the measured strength of the membrane along the x and y directions and the strength of the piriform silk. The obtained value is very similar to the one measured in tensile tests, confirming the validity of our simple model.

It is important to understand how the spacing distance *s* can affect the results. We thus plotted the theoretical values obtained with Equations (4), (7), and (8) as functions of the spacing distance *s* in the measured range (**Figure S7**). This confirmed that our results fit well with respect to the obtained *s* values.

Peeling Experiments

In order to quantify the attachment of the whole membrane to the substrate, we performed pull-off tests (**Figure S10**). We found that detachment occurred at displacements of 2.9 ± 1.2 mm, with peak force of 18 ± 10 mN and a membrane stiffness of 6.8 ± 5.8 N/m (**Table S9**). These numbers are comparable to the ones reported in literature (Grawe et al., 2014; Wolff et al., 2015, 2017b,c; Wolff and Gorb, 2016; Wolff and Herberstein, 2017). We found that the failure of the attachment discs occurs mainly at the level of the piriform silk (**Figure S10C**) in our setup, instead of at the dragline's level [see Grawe et al. (2014) for a detailed discussion of the different failure modes resulting from the hierarchical structure of attachment discs]. This was indicated by the observation that detached attachment discs remained almost intact (**Figure S10D**). This supports that the adhesion was measured and not the fracture of the attachment disc.

DISCUSSION

Due to the adhesive nature of piriform silk, it is difficult to obtain native fiber samples for tensile tests. Here, we used a whole-membrane approach, in combination with an analytical model to determine the mechanical properties of piriform silk. When collecting samples, the detachment of the attachment discs from the carrier substrate may create damage or induce a pre-stress that could affect the measurements (Garrido et al., 2002; Perez-Rigueiro, 2005). We therefore backed up our test results by a nanoindentation approach that has been proven a good solution in order to measure the mechanical properties of native attachment discs *in loco* without the requirement of sample manipulation (Das et al., 2017). The combined results from these different approaches are consistent.

The nanoindentation tests revealed that the piriform silk of *C. salei* has a Young's modulus comparable to its dragline. The fact that, in this species, the amount of glue is low if compared to other species (Wirth et al., 2019) partially justifies our approach that neglects the presence of the third phase.

The theoretical model was developed to justify the mechanical properties of the single fibers, obtained by means of nanoindentation, to the mechanical properties of the whole membrane (under tensile tests). Overall, we found consistency in the values obtained from our nanoidentation and tensile test approaches and those reported in the literature (Wolff et al., 2017c). This highlights that anisotropy plays a negligible role in the mechanics of piriform silk. The effect of variation in the spacing parameter s was investigated (**Figure S9**). We note that obtained values for the spacing parameter represent an average of the naturally variable spacing across the lattice.

Another important aspect to consider about the strength of materials is their dimensions. Increasing the size of a material (or in general its dimension) usually leads to a decrease of strength (Carpinteri and Pugno, 2005). This is also valid for spider silk (Greco et al., submitted). Piriform silk is composed of numerous small fibers. This could increase the strength of each fiber and then the strength of the whole membrane.

Regarding the overall mechanical behavior of the membrane, the complexity of the structure and its random shape could be an important cause for the remarkable mechanical properties of attachment discs, as randomization in a system could improve its toughness and ductility (Cranford, 2013).

The parameters determined in this work enable the improvement of numerical models that describe the peeling mechanics and adhesion of composite membranes, which is an important goal in the study of the mechanical function and biomimetics of biological adhesive systems (Liprandi et al., 2019; Wolff et al., 2019).

CONCLUSION

Hundreds of million years have selected attachment systems of spiders to bear high loads (Wolff et al., 2019). Despite their fundamental role, these anchorages are still poorly understood due to the practical difficulties in sample preparation, the complexity of the system, and the high variation of attachment disc structures.

In order to understand the overall mechanical behavior of the whole membrane, knowledge of the mechanical properties of the attachment disc material (piriform silk) is essential.

With this work we delivered some useful information regarding piriform silk mechanical properties. This in our opinion will facilitate the enhancement of numerical models of peeling dynamics for a better understanding of the adhesion function of attachment discs and stimulate the design of new bio-inspired strong adhesives and micro-composite materials.

DATA AVAILABILITY STATEMENT

All datasets generated for this study are included in the article/**Supplementary Material**.

ETHICS STATEMENT

Ethical review and approval was not required for the animal study because, according to the Italian regulation on animal protection and EU Directive 2010/63/EU for animal experiments, no special requirements are necessary for spiders.

AUTHOR CONTRIBUTIONS

GG performed the experiments, acquired the data, and wrote the first draft of the manuscript. JW contributed to the interpretation of the results and the manuscript writing. NP supervised the study, suggested the model and the data analyses, and finalized the paper. All authors were involved

in revising manuscript drafts and viewed and approved the final manuscript.

FUNDING

JW is supported by a Discovery Early Career Researcher Award of the Australian Research Council (DE190101338). NP is supported by the European Commission under the FET Proactive (Neurofibres) grant No. 732344, the FET Open (Boheme) grant No. 863179, as well as by the Italian Ministry of Education, University and Research (MIUR) under the Departments of Excellence grant L. 232/2016.

ACKNOWLEDGMENTS

We would like to thank Lorenzo Moschini, Antonella Motta, Devid Maniglio, and Claudio Migliaresi (Biotech–Mattarello, University of Trento) for their support.

SUPPLEMENTARY MATERIAL

The Supplementary Material for this article can be found online at: https://www.frontiersin.org/articles/10.3389/fmats.2020.00138/full#supplementary-material

REFERENCES

Agnarsson, I., Kuntner, M., and Blackledge, T. A. (2010). Bioprospecting finds the toughest biological material: extraordinary silk from a giant riverine orb spider. *PLoS ONE* 5, 1–8. doi: 10.1371/journal.pone.0011234

Asakura, T., and Miller, T. (2014). *Biotechnology of Silk, Vol. 5*. Dordrecht: Springer.

Basu, A. (2015). *Advances in Silk Science and Technology*. The Textile Institute.

Blackledge, T. A., Cardullo, R. A., and Hayashi, C. Y. (2005). Polarized light microscopy, variability in spider silk diameters, and the mechanical characterization of spider silk. *Invertebr. Biol.* 124, 165–173. doi: 10.1111/j.1744-7410.2005.00016.x

Blasingame, E., Tuton-Blasingame, T., Larkin, L., Falick, A. M., Zhao, L., Fong, J., et al. (2009). Pyriform spidroin 1, a novel member of the silk gene family that anchors dragline silk fibers in attachment discs of the black widow spider, Latrodectus hesperus. *J. Biol. Chem.* 284, 29097–29108. doi: 10.1074/jbc.M109.021378

Bowen, C. H., Dai, B., Sargent, C. J., Bai, W., Ladiwala, P., Feng, H., et al. (2018). Recombinant spidroins fully replicate primary mechanical properties of natural spider silk. *Biomacromolecules* 19, 3853–3860. doi: 10.1021/acs.biomac.8b00980

Brely, L., Bosia, F., and Pugno, N. M. (2015). Numerical implementation of multiple peeling theory and its application to spider web anchorages. *Interface Focus* 5:20140051. doi: 10.1098/rsfs.2014.0051

Brunetta, L., and Craig, C. L. (2010). *Spider Silk: Evolution and 400 Million Years of Spinning, Waiting, Snagging, and Mating*. Yale University Press.

Carpinteri, A., and Pugno, N. (2005). Are scaling laws on strength of solids related to mechanics or to geometry? *Nat. Mater.* 4, 421–423. doi: 10.1038/nmat1408

Chaw, R. C., Saski, C. A., and Hayashi, C. Y. (2017). Complete gene sequence of spider attachment silk protein (PySp1) reveals novel linker regions and extreme repeat homogenization. *Insect Biochem. Mol. Biol.* 81, 80–90. doi: 10.1016/j.ibmb.2017.01.002

Cranford, S. W. (2013). Increasing silk fibre strength through heterogeneity of bundled fibrils. *J. R. Soc. Interface* 10:20130148. doi: 10.1098/rsif.2013.0148

Cranford, S. W., Tarakanova, A., Pugno, N. M., and Buehler, M. J. (2012). Nonlinear material behaviour of spider silk yields robust webs. *Nature* 482, 72–76. doi: 10.1038/nature10739

Das, R., Kumar, A., Patel, A., Vijay, S., Saurabh, S., and Kuma, N., et al. (2017). Biomechanical characterization of spider webs. *J. Mech. Behav. Biomed. Mater.* 67, 101–109. doi: 10.1016/j.jmbbm.2016.12.008

Dellaquila, A., Greco, G., Campodoni, E., Mazzocchi, M., Mazzolai, B., Tampieri, A., et al. (2019). Optimized production of a high-performance hybrid biomaterial : biomineralized spider silk for bone tissue engineering. *J. Appl. Polym. Sci.* 48739, 1–9. doi: 10.1002/app.48739

Denny, M. W. (1976). The physical properties of spider's silk and their role in the design of orb-webs. *J. Exp. Biol.* 65, 483–506.

Eisoldt, L., Smith, A., and Scheibel, T. (2011). Decoding the secrets of spider silk. *Mater. Today* 14, 80–86. doi: 10.1016/S1369-7021(11)70057-8

Fischer-Cripps, A. C. (2011). *Nanoindentation*. New York, NY: Springer.

Foelix, R. (2011). *Biology of Spiders*. New York, NY: Oxford University Press.

Garrido, M. A., Elices, M., Viney, C., and Pérez-Rigueiro, J. (2002). The variability and interdependence of spider drag line tensile properties. *Polymer (Guildf.)*. 43, 4495–4502. doi: 10.1016/S0032-3861(02)00254-9

Geurts, P., Zhao, L., Hsia, Y., Gnesa, E., Tang, S., Jeffery, F., et al. (2010). Synthetic spider silk fibers spun from pyriform spidroin 2, a glue silk protein discovered in orb-weaving spider attachment discs. *Biomacromolecules* 11, 3495–3503. doi: 10.1021/bm101002w

Grawe, I., Wolff, J. O., and Gorb, S. N. (2014). Composition and substrate-dependent strength of the silken attachment discs in spiders. *J. R. Soc. Interface* 11:20140477. doi: 10.1098/rsif.2014.0477

Greco, G., Bosia, F., Tramacere, F., Mazzolai, B., and Pugno, N. M. (2020). The role of hairs in the adhesion of octopus suckers: a hierarchical peeling approach. *Bioinspir. Biomim.* 15:035006. doi: 10.1088/1748-3190/ab72da

Greco, G., Pantano, M. F., Mazzolai, B., and Pugno, N. M. (2019). Imaging, and mechanical characterization of different junctions in spider orb webs. *Sci. Rep.* 9:5776. doi: 10.1038/s41598-019-42070-8

Hay, J. L., O'Hern, M. E., and Oliver, W. (1998). The importance of contact radius for substrate independent property measurement of thin films. *Mat. Res. Soc. Symp. Proc.* 522, 27–32. doi: 10.1557/PROC-522-27

Jain, D., Sahni, V., and Dhinojwala, A. (2014). Synthetic adhesive attachment discs inspired by spider's pyriform silk architecture. *J. Polym. Sci. Part B Polym. Phys.* 52, 553–560. doi: 10.1002/polb.23453

Keyserling, E. (1877). Ueber amerikanische Spinnenarten der Unterordnung Citigradae. *Verhandlungen der Kaiserlich-Königlichen Zoologisch-Botanischen Gesellschaft in Wien* 26, 609–708.

Kovoor, J., and Zylberberg, L. (1980). Fine structural aspects of silk secretion dlademalus. *IN THE. Tissue Cell* 12, 547–556. doi: 10.1016/0040-8166(80)90044-0

Kovoor, J., and Zylberberg, L. (1982). Fine structural aspects of silk secretion in a spider. *Tissue Cell* 14, 519–530. doi: 10.1016/0040-8166(82)90044-1

Lepore, E., Bosia, F., Bonaccorso, F., Bruna, M., Taioli, S., Garberoglio, G., et al. (2017). Spider silk reinforced by graphene or carbon nanotubes. *2D Materials* 4:031013.

Liprandi, D., Bosia, F., and Pugno, N. M. (2019). A theoretical-numerical model for the peeling of elastic membranes. *J. Mech. Phys. Solids* 136:103733. doi: 10.1016/j.jmps.2019.103733

Perez-Rigueiro, J. (2005). The effect of spinning forces on spider silk properties. *J. Exp. Biol.* 208, 2633–2639. doi: 10.1242/jeb.01701

Pugno, N. M. (2011). The theory of multiple peeling. *Int. J. Fract.* 171, 185–193. doi: 10.1007/s10704-011-9638-2

Pugno, N. M., Cranford, S. W., and Buehler, M. J. (2013). Synergetic material and structure optimization yields robust spider web anchorages. *Small* 9, 2747–2756. doi: 10.1002/smll.201201343

Sahni, V., Harris, J., Blackledge, T. A., and Dhinojwala, A. (2012). Cobweb-weaving spiders produce different attachment discs for locomotion and prey capture. *Nat. Commun.* 3, 1106–1107. doi: 10.1038/ncomms2099

Schneider, C. A., Rasband, W. S., and Eliceri, K. W. (2012). NIH Image to ImageJ: 25 years of image analysis. *Nat. Methods* 9, 671–675. doi: 10.1038/nmeth.2089

Vollrath, F., and Knight, D. P. (2001). Liquid crystal spinning of spider silk. *Nature* 410, 541–548. doi: 10.1038/35069000

Wirth, M., Wolff, J. O., Appel, E., and Gorb, S. N. (2019). Ultrastructure of spider thread anchorages. *J. Morphol.* 280, 534–543. doi: 10.1002/jmor.20962

Wolff, J. O., and Gorb, S. N. (2016). *Attachment Structures and Adhesive Secretions in Arachnids*. Cham: Springer, 184.

Wolff, J. O., Grawe, I., Wirth, M., Karstedt, A., and Gorb, S. N. (2015). Spider's super-glue: thread anchors are composite adhesives with synergistic hierarchical organization. *Soft Matter* 11, 2394–2403. doi: 10.1039/C4SM02130D

Wolff, J. O., and Herberstein, M. E. (2017). Three-dimensional printing spiders: back-and-forth glue application yields silk anchorages with high pull-off resistance under varying loading situations. *J. R. Soc. Interface* 14:20160783. doi: 10.1098/rsif.2016.0783

Wolff, J. O., Jones, B., and Herberstein, M. E. (2018). Plastic material investment in load-bearing silk attachments in spiders. *Zoology* 131, 45–47. doi: 10.1016/j.zool.2018.05.002

Wolff, J. O., Paterno, G. B., Liprandi, D., Ramírez, M. J., Bosia, F., van der Meijden, A., et al. (2019). Evolution of aerial spider webs coincided with repeated structural optimization of silk anchorages. *Evolution* 73, 2122–2134. doi: 10.1111/evo.13834

Wolff, J. O., Rez,áč, M., Krejčí, T., and Gorb, S. N. (2017c). Hunting with sticky tape: functional shift in silk glands of araneophagous ground spiders (Gnaphosidae). *J. Exp. Biol.* 220, 2250–2259. doi: 10.1242/jeb.154682

Wolff, J. O., Van der Meijden, A., and Herberstein, M. E. (2017b). Distinct spinning patterns gain differentiated loading tolerance of silk thread anchorages in spiders with different ecology. *Proc. R. Soc. B Biol. Sci.* 284:20171124. doi: 10.1098/rspb.2017.1124

Wolff, J. O., Wells, D., Reid, C. R., and Blamires, S. J. (2017a). Clarity of objectives and working principles enhances the success of biomimetic programs Clarity of objectives and working principles enhances the success of biomimetic programs. *Bioinspir. Biomim.* 12:051001. doi: 10.1088/1748-3190/aa86ff

Xia, X.-X., Qian, Z.-G., Ki, C. S., Park, Y. H., Kaplan, D. L., and Lee, S. Y. (2010). Native-sized recombinant spider silk protein produced in metabolically engineered Escherichia coli results in a strong fiber. *Proc. Natl. Acad. Sci.* 107, 14059–14063. doi: 10.1073/pnas.1003366107

Yang, Y., Greco, G., Maniglio, D., Mazzolai, B., Migliaresi, C., Pugno, N., et al. (2020). Spider (Linothele megatheloides) and silkworm (Bombyx mori) silks: Comparative physical and biological evaluation. *Mater. Sci. Eng. C* 107:110197. doi: 10.1016/j.msec.2019.110197

Yarger, J. L., Cherry, B. R., and Van Der Vaart, A. (2018). Uncovering the structure-function relationship in spider silk. Nat. Rev. Mater. 3:18008. doi: 10.1038/natrevmats.2018.8

Conflict of Interest: The authors declare that the research was conducted in the absence of any commercial or financial relationships that could be construed as a potential conflict of interest.

frontiers in Materials

ORIGINAL RESEARCH
published: 24 June 2020
doi: 10.3389/fmats.2020.00197

Doubling the Mechanical Properties of Spider Silk by C_{60} Supersonic Molecular Beam Epitaxy

Maria F. Pantano[1], *Roberta Tatti*[2†], *Lucrezia Aversa*[2], *Roberto Verucchi*[2] *and Nicola M. Pugno*[1,3*]

[1] *Laboratory of Bio-Inspired, Bionic, Nano, Meta Materials and Mechanics, Department of Civil, Environmental and Mechanical Engineering, University of Trento, Trento, Italy,* [2] *Trento Unit C/O Fondazione Bruno Kessler, IMEM-CNR Institute of Materials for Electronics and Magnetism, Trento, Italy,* [3] *School of Engineering and Materials Science, Queen Mary University of London, London, United Kingdom*

OPEN ACCESS

Edited by:
Seunghwa Ryu,
Korea Advanced Institute of Science and Technology, South Korea

Reviewed by:
Dongchan Jang,
Korea Advanced Institute of Science and Technology, South Korea
Arun Nair,
University of Arkansas, United States

****Correspondence:***
Nicola M. Pugno
nicola.pugno@unitn.it

†Present address:
Roberta Tatti,
Laboratory of Biomarker Studies and Structure Analysis for Health, Fondazione Bruno Kessler, Trento, Italy

Specialty section:
This article was submitted to Mechanics of Materials, a section of the journal Frontiers in Materials

Received: *02 December 2019*
Accepted: *26 May 2020*
Published: *24 June 2020*

Citation:
Pantano MF, Tatti R, Aversa L, Verucchi R and Pugno NM (2020) Doubling the Mechanical Properties of Spider Silk by C_{60} Supersonic Molecular Beam Epitaxy. Front. Mater. 7:197. doi: 10.3389/fmats.2020.00197

Spider silk is one of the most fascinating natural materials, owing to its outstanding mechanical properties. In fact, it is able to combine usually self-excluding properties, like strength and toughness that synthetic fibers fail to replicate. Here, we report a method to further enhance the already excellent mechanical properties of spider's silk, producing nanocomposite fibers where the matrix of spider silk is reinforced with C_{60} molecules. These are deposited by Supersonic Molecular Beam Epitaxy (SuMBE) and are able to efficiently interact with silk, as evidenced by XPS analysis. As a consequence, upon proper adjustment of the fullerene kinetic energy, the treated fibers show improved strength, Young's modulus and toughness.

Keywords: spider silk, mechanical properties, fullerene, SuMBE, composites

INTRODUCTION

Spider silk is one of the most fascinating structural materials offered by nature owing to its unique capability of combining usually self-excluding properties, like load standing (e.g., strength) and energy dissipation (e.g., toughness). In particular, for long time spider's silk was believed to be the strongest among all natural materials (Vollrath, 2000) and only recently this was discovered to be surpassed by the limpet teeth (Barber et al., 2015).

The secret to spider silk's outstanding properties lies into the selection of its constituent macromolecules and their hierarchical supramolecular organization (Thiel et al., 1997), which has been the subject of intense studies that allowed mapping silk genetic sequence (Hayashi and Lewis, 2000). This provided useful information for the further improvement of spider silk properties or the development of novel bio-inspired materials. In fact, in order to overcome issues related to upscaling of spiders farming to a massive industrial level (Altman et al., 2003), transgenic silkworms were created encoding chimeric silkworm/spider silk genes able to produce composite fibers with improved mechanical properties (Teule et al., 2012). Another example was a recombinant protein that allowed mixing of the mechanical properties of spider silk with the capability of controlled nucleation and hydroxyapatite growth typical of dentin (Huang et al., 2007).

Unfortunately, the knowledge of the basic building blocks is not sufficient for a completely artificial yet efficient replication of silk fibers that would require also copying of the spider's spinning process. In fact, such process is characterized by significant complexity that is hard to be replicated by manufacturing tools currently available to humans (Vollrath and Knight, 2001). For this reason, there was a recent attempt to exploit spiders' spinning ability for production of composite silk fibers

reinforced with carbon nanotubes (CNTs) or graphene (Lepore et al., 2017). In that case, spiders after being exposed to CNT/graphene aqueous solutions were able to produce silk that resulted to contain those nanomaterials.

However, if spider silk cannot be fully reproduced artificially, it is possible to produce instead bio-inspired materials that take advantage of some of its features. For example, synthetic/natural ribbons and fibers with enhanced toughness were reported incorporating either dissipative structures in the form of slip knots (Pugno, 2014; Berardo et al., 2016; Bosia et al., 2016; Pantano et al., 2016) or looped metastructures (Koebley et al., 2017). Under application of a tensile load, loops unravel providing fibers/ribbons with an additional length (e.g., hidden length) that mimics the presence of sacrificial bonds in proteins structures (Fantner et al., 2006), thus allowing the possibility to accommodate large strain with consequent toughness improvement.

Apart from genetic engineering and bio-inspired design, spider silk can be exploited as raw material for production of functionalized composites by different techniques. For example, spider silk fibroin was blended with poly-DL-lactide (PDLLA) and electrospun in order to obtain biodegradable mats to be used for tissue engineering applications (Zhou et al., 2008). Alternatively, spider silk fibers were turn magnetic by superparamagnetic magnetite nanoparticles that covered their surfaces after immersion into colloidal sols (Mayes et al., 1998).

Here, we report on the design, fabrication and characterization of spider silk fibers reinforced with fullerenes (C_{60}). C_{60} molecules are well-characterized carbon allotropes, consisting of a cluster of 60 sp^2-bonded carbon atoms, which were shown to have interesting chemical and physical properties (Hedberg et al., 1991; Ruoff and Ruoff, 1991; Pawlak et al., 2011). Previous attempts of incorporation of fullerenes into other materials, such as aluminum (Tokunaga et al., 2008), proved their efficacy in improving the mechanical properties of the host matrix. However, different from other carbon allotropes, such as graphene or carbon nanotubes, its use as reinforcement material, especially in biological host matrices, such as spider silk, has been much less explored.

One of the common challenges to face when producing composites regards the homogeneous dispersion of the reinforcement materials. In this study, we do not use conventional mechanical methods, based on mixing and sonication. Instead, the composite fiber is prepared by depositing C_{60} onto silk fibers through an innovative approach for thin films deposition in Ultra High Vacuum (UHV) conditions, the Supersonic Molecular Beam Epitaxy (SuMBE). Such technique is based on the supersonic expansion in vacuum of a highly diluted gas mixture of a light gas carrier (usually noble gas), seeded by a heavier organic precursor. In case of fullerene, sublimation by thermal heating can be easily achieved and controlled, without introducing defects, degradation or decomposition. The C_{60} molecules, seeding the generating gas beam, experience an aerodynamic acceleration that, depending on the mass ratio between gas carrier and precursor, leads to a kinetic energy (KE) as high as several tens of eV and to a freezing of the molecular roto-vibrational modes. The large amount of translational kinetic energy reached by the precursor molecules in the beam can induce and activate chemical processes and surface diffusion. The possibility to control the thin film properties by changing the precursors kinetics in terms of beam source parameters, makes this approach particularly useful to (i) control the coalescence and diffusion process in the organic thin film growth (Wu et al., 2007; Nardi et al., 2010a); (ii) improve the crystallinity of inorganic material (Verucchi et al., 2012); (iii) synthesize carbon-based nanostructure (Verucchi et al., 2012; Tatti et al., 2016) and hybrid materials (Nardi et al., 2009; Tatti et al., 2017).

Studies conducted on C_{60} supersonic molecular beam have demonstrated that it is possible to break the fullerene cage at room temperature, during the collision of the organic molecule with the substrate, in order to synthesize a highly ordered silicon carbide. Exploiting the high KE of the C_{60} supersonic beam by SuMBE (about 30 eV), it was possible to synthesize high quality nanocrystalline 3C-SiC at room temperature using a C_{60} supersonic beam as precursor and Si(111) as substrate (Verucchi et al., 2012). Moreover, the SuMBE approach can give rise also to a strong chemical interaction between C_{60} and the Cu(111) substrate. The excess of energy, supplied by the C_{60} supersonic beam at a KE of 35 eV, induces a rearrangement of the C_{60} on the metal surface, promoting the fullerene cage breaking after thermal treatment and the formation of graphene flakes (Tatti et al., 2016).

In this work we show the possibility to extend these concepts also for the insertion of reinforcement nanoparticles in silk for the production of composite fibers with improved mechanical properties.

RESULTS AND DISCUSSION

In order to verify the beneficial effects that the addition of C_{60} molecules can play on the mechanical properties of spider silk, we took 18 samples from the dragline silk produced by the same spider that belongs to *Meta menardi* species. Three of these were used as control sample that provided reference values for the mechanical properties, while the remaining 15 specimens were divided in 5 groups and functionalized by C_{60} supersonic beams at different KE. In order to preserve the integrity of the C_{60} molecule during the deposition process, the C_{60} beam was used in a range of KE between 5 and 14 eV, and more specifically at 5, 8, 10, 12, and 14 eV. Particle arrival rate was kept constant for all depositions.

Silk specimens, fixed on a support to maintain fibers straight, were inserted in the analysis chamber, directly connected with the SuMBE apparatus, and decorated with a C_{60} film with an equivalent thickness of 5 monolayers (ML), as measured on a Cu surface used as reference (**Figure 1A**).

The mechanical behavior of the considered samples (**Figure 1B** shows an example spider silk fiber imaged by Scanning Electron Microscopy, SEM) was evaluated through tensile tests carried out on single fibers. **Figure 1C** reports one example curve for each sample type (see **Figure S1** for further details) while **Figure 2** collects the average values of strength, ultimate strain, Young's modulus and toughness for all tested samples. For the sake of comparison, these are reported as a function of SuMBE C_{60} KE. The histograms show that the deposition of C_{60} molecules has a significant influence on all

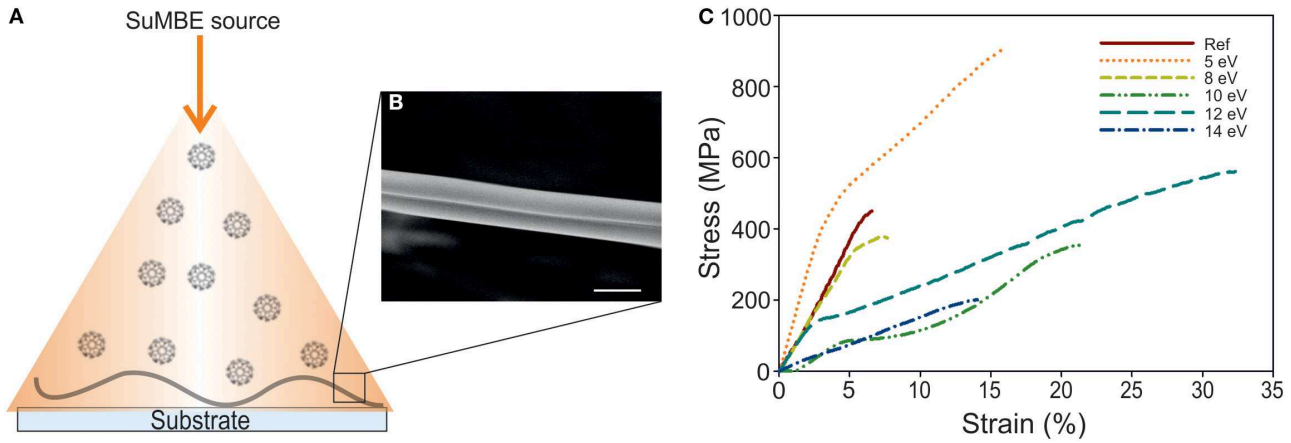

FIGURE 1 | (A) Schematic of the SuMBE process for C_{60} molecules deposition onto a spider silk fiber [detailed in the SEM image **(B)**. Scale bar: 2 μm]. During implantation, 5 ML of fullerenes were deposited. **(C)** Comparison between example stress-strain curves derived from tensile tests on raw fibers and SuMBE processed fibers at different KE (5, 8, 10, 12, and 14 eV). The example stress-strain curves here reported were selected as representative of their mean behavior and all are reported in the **Supplementary Material**.

the mechanical properties. Such effect can be clearly observed in spite of some data dispersion, which is not unexpected in the case of biological material samples, such as spider silk. Indeed, it is common to observe a certain variability across the stress-strain curves of spider silk fibers belonging to the same sample [as visible from the curves reported in **Figure S1A** or in other previous reports (Madurga et al., 2016)], which then causes variability in the values of the mechanical properties extracted from such curves.

With respect to reference, the smallest C_{60} KE (5 eV) corresponds to the highest increase possible of strength (1.7 times the reference value), Young's modulus (2.2 times the reference) and toughness (i.e., toughness modulus, defined as the area under the stress-strain curve; 2.7 times the reference); a significant increase of ultimate strain (1.6 times the reference) is also produced. Such simultaneous enhancement of the mechanical properties of our treated spider silk fibers is very interesting, in line with previous reports on the production of bio-inspired nanocomposite materials reinforced with carbon allotropes. For example, bionic spider silk incorporating carbon nanotubes showed an average increase in fracture strength, Young's modulus and toughness between 80 and 220%, while for bionic spider silk incorporating graphene the average increase was 15 and 60% (Lepore et al., 2017). For artificial nacre-like nanocomposites of copper and reduced graphene oxide, the addition of the graphene-based filler allowed an increase in the strength and Young's modulus of about 41% and 12%, respectively, with a toughness increase of up to 1.8 times (Xiong et al., 2015).

The strength increase observed in our treated silk fibers could be related to the increased number of hard crystal domains contained in the fibers after C_{60} deposition, which improves the already good load standing capability of the fibers, without however affecting their elongation capability. Such beneficial effect is however partially lost at higher KE levels, where probably the impinging supersonic beam causes some modification to the silk structure. This is particularly evident in the case of the highest KE that corresponds to the smallest values of both strength and ultimate strain, even if the reduction is not dramatic, especially in the case of strain (reduced by about 10%, while the strength is reduced to 1/3 of the reference vale). Thus, SuMBE treatment results not to compromise too much the silk structure, as it also emerges from imaging by SEM that does not reveal significant difference on the fibers after C_{60} implantation at different KE (**Figure S2**). Furthermore, it is interesting to notice that intermediate KEs of 10 and 12 eV have a slight negative effect on the strength, but beneficial effects in terms of ultimate strain that results to be 1.6 or 1.8 bigger than the reference value.

In order to clarify the chemical-physical process at the silk—C_{60} interface and evaluate the electronic properties of the bare silk after the deposition of C_{60}, X-ray photoelectron spectroscopy (XPS) analysis was performed on the two borderline cases: the silk "as it is" and after the deposition of 5 ML at the highest kinetic energy (14 eV). A cocoon produced by *Meta menardi* species, same spider used for the production of the dragline silk fibers, was used as reference silk sample. The cocoon was cut in half and mounted on a copper substrate, with the inner part exposed to the analysis and further C_{60} deposition (**Figure S3**).

The XPS characterization performed before and after the C_{60} SuMBE deposition reveals that the predominant elements in the silk are carbon, oxygen and nitrogen, leading also to a quantitative analysis of the chemical composition in terms of surface atomic percentage, as summarized in **Table 1**.

As expected, following the C_{60} deposition, the amount of carbon increases from 58.1 to 73.8%: 46.3% is related to the fullerene and the remaining 27.5 % is due to the silk. With reference to the latter component only, the evaluation of the silk related carbon content is highly influenced by the large fullerene signal, leading to its possible underestimation with lower C/N and C/O ratios, as indeed observed (see **Table 1**). Differently, the N/O ratio remains constant after C_{60} deposition suggesting that

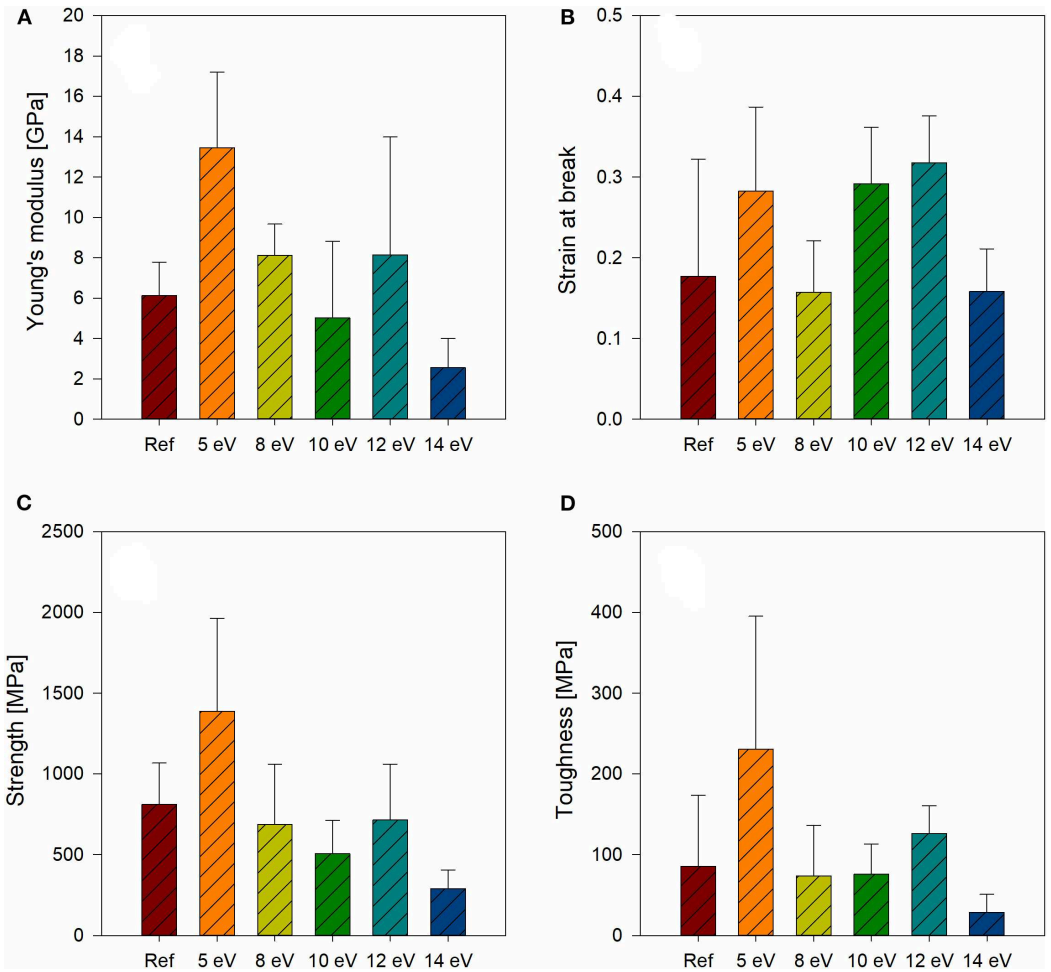

FIGURE 2 | Dependence of the Young's modulus **(A)**, strain at break **(B)**, strength **(C)** and, toughness **(D)** of spider silk fibers on the Kinetic Energy (KE) of Supersonic Molecular Beam Epitaxy (SuMBE) implantation of C_{60} molecules. A KE of 5 eV allows to almost double the Young's modulus, the strain at fracture and strength, while almost triple the toughness (here reported as the area under the stress-strain curve).

no contamination occurs during the SuMBE process. Thus, every eventual modification of the silk chemical/physical properties can be due only to the interaction with fullerene at 14 eV KE.

In order to get further insight about the interaction of silk and C_{60} molecules, we then investigated the lineshape and components of the C1s, O1s, and N1s core levels as shown in **Figure 3**. The features of all the components for the C1s, N1s, and O1s core levels, in terms of binding energy (BE), Full Width at Half Maximum (FWHM) and percentage calculated with respect to the total core level area, are summarized in **Table S1**. It is worth noting that all peaks show a shift toward higher binding energies, typically due to a charging effect related to the insulating character of these organic materials.

The C1s spectrum of the bare silk is characterized by four different components (see **Figure 3A**, upper panel), which reflect the chemical composition of the material. Indeed, silk is constituted by spidroin, a protein which is rich of glycine (Gly), alanine (Ala) and residues of other amino acids. This silk protein folds in a secondary structure characterized by crystalline regions, packed in β-sheets, interlocking with the adjacent chain via hydrogen bonds, and amorphous domains (**Figure 4**) (Hayashi et al., 1999; Hakimi et al., 2007).

TABLE 1 | Atomic percentage of all the chemical species present in the samples.

	C %	N %	O %	C*/N	C*/O	N/O
Spider Silk	59.7	22.8	17.5	2.6	3.4	1.3
C_{60} + Silk	73.8	15.4	10.8	1.8	2.6	1.4

Carbon considered in C/N and C/O ratios refers only to silk species. C only from silk.*

According to this description, the most intense component at 288.56 eV is related to carbon in the amide bond of the peptide chain, the latter being involved in hydrogen bonds between the oxygen and the nitrogen atom of the parallel amino acidic chains. As a matter of fact, the presence of the H bond increases the BE of the electronegative atoms (N, O), with the consequent decreasing of the carbon BE (Kerber et al., 1996; Garcia-Gil et al., 2013). The C-OH and amide groups not involved in hydrogen bonds,

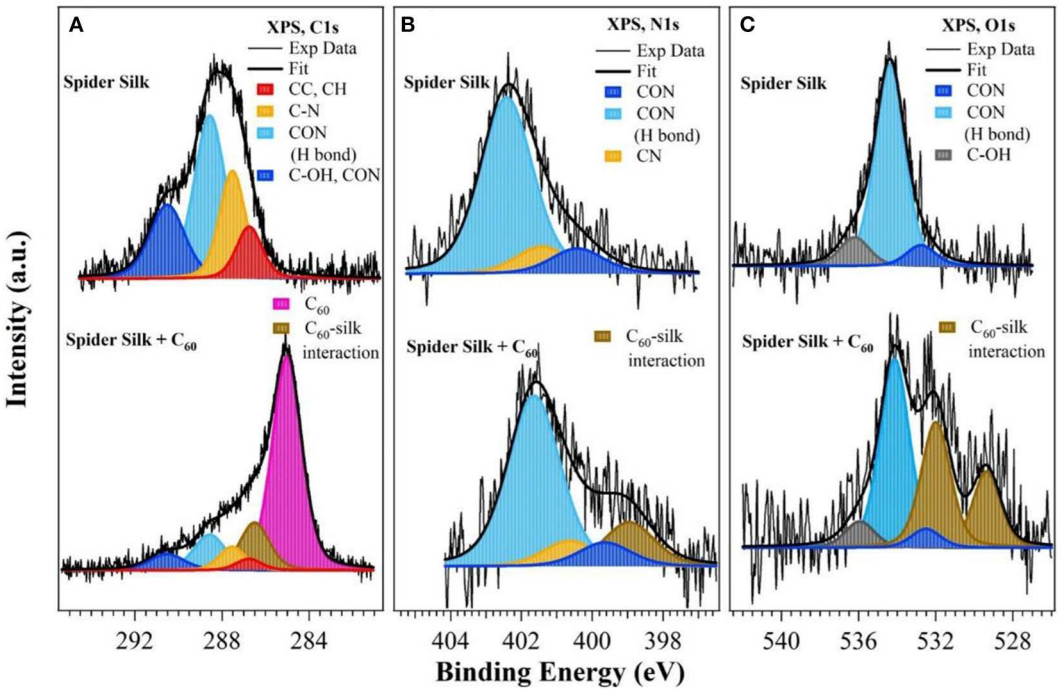

FIGURE 3 | Core level spectra (background subtracted): **(A)** C1s core level, **(B)** N1s core level and **(C)** O1s core level of the silk "as it is" and after the C_{60} deposition, from the top to the bottom, respectively.

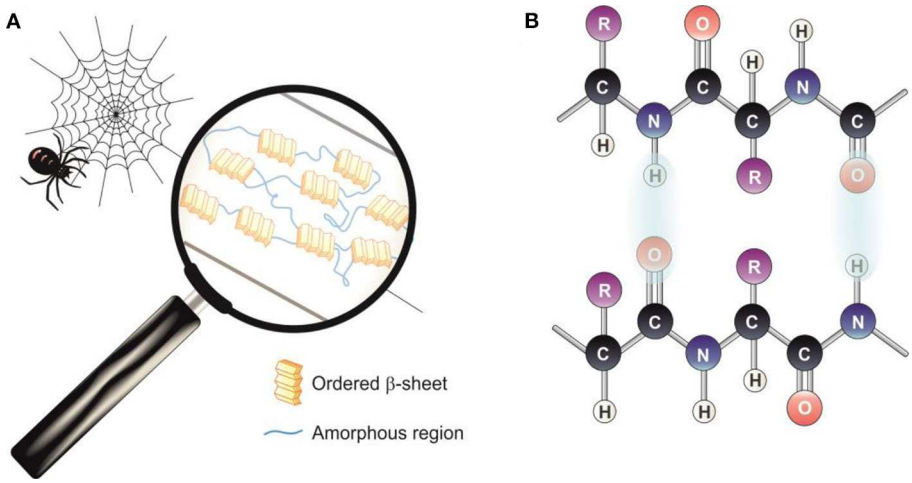

FIGURE 4 | (A) Schematic structure of spider silk. The yellow blocks are the highly ordered crystalline regions, joined by amorphous linkages. **(B)** Hydrogen bonds between parallel protein chains.

such as the substituents in the main chain and the components in the amorphous region, are located at higher BE (290.51 eV). The components at lower BE, 286.75 and 287.52 eV, are related, respectively, to the CC, CH, and CN groups of the substituents of the amino acids.

After the deposition of C_{60}, the deconvolution of the C1s core level lineshape is a superposition of the four features previously identified for silk, and the contribution stemming from the C_{60} (285.00 eV). Moreover, a new component is present at 286.50 eV (**Figure 3A**, bottom panel, brown color). It is not possible to exclude the presence of other peaks associated to this interaction overlapping the C_{60} signal, as indeed suggested by the large FWHM of this peak (1.6 eV), however their introduction would be merely a speculation, due to the complexity of the fitting and to the high number of species in the silk structure. What is worth is the presence of a new peak, suggesting this component belongs

to the interaction of silk chemical groups with the fullerene cages, and could justify the observed underestimation of silk carbon content (see **Table 1**).

The N1s core level of bare silk (**Figure 3B**, top panel) is constituted by a main component at higher BE (402.42 eV) related to the amidic group CON involved in hydrogen bond, a peak at 401.42 eV due to the CN groups of the substituents of the amino acids (Ariza et al., 2000), and a third component related to the CON groups not involved in hydrogen bonds, as observed for the C1s (**Figure 3B**, upper panel). The deposition of C_{60} on silk gives rise to a significant variation of the N1s lineshape (**Figure 3B**, bottom panel). The components related to silk shift by about −0.7 eV (401.64, 400.64, and 399.64 eV, respectively), and a new component is present at 398.95 eV (brown color). As for C1s lineshape analysis, this feature can be associated to the interaction of the C_{60} with the silk.

The O1s core level (**Figure 3C**, upper panel) of silk before the functionalization presents three features that can be related to the CON groups involved (534.38 eV) or not (532.76 eV) in hydrogen bonds, and the C-OH of the substituents (536.20 eV). After C_{60} deposition, these three contributions shift toward lower BE by about −0.3 eV. Moreover, two new peaks at lower BE (529.37 and 532.00 eV) are present, in agreement with what previously observed in C1s and N1s.

Being the N/O ratio constant in bare and C_{60} deposited silk, we can argue that all the new features observed in presence of C_{60} are related to silk chemical groups that suffered a significant modification with respect to the pristine material, while the presence of fingerprints of the original silk structure for all elements suggests modifications are related to specific protein sites. Concerning N1s and O1s analysis, the appearance of new peaks at lower BE suggests breaking of H bonds between CO and N-H, probably due to impingement of the C_{60} cage at 14 eV, a process leading to reduction of silk mechanical properties. Due to the low concentration of nitrogen and oxygen, such an effect cannot be identified in C1s peak analysis. Conversely, the new intense peak at 286.5 eV, very close to the C_{60} main one, could be due to formation of chemical bonds between fullerene and silk chains thanks to the molecule high electronegativity, e.g., promoting link with amide group (López et al., 2011; Umeyama and Imahori, 2013). The balance between the two processes probably determines the increase or decrease of mechanical properties at the different C_{60} KEs.

CONCLUSIONS

In conclusion, we have shown an alternative method for producing spider silk composite fibers with improved mechanical properties requiring no genetic engineering. Raw spider silk fibers were in fact reinforced with C_{60} molecules via a high energy well assessed technique, like SuMBE. Upon optimization of the process parameters, thus of the fullerene translational KE, it is possible to obtain an almost 2-fold increase of strength and an almost 3-fold increase of toughness. Such method could be used in future also for fabrication of other high-performance nanocomposites considering different fibers as matrix.

A cocoon of spider silk was analyzed *ex situ* by XPS, before and after functionalization with C_{60} at high KE (14 eV). The analysis demonstrated the presence of fullerenes in silk, and the formation of new chemical species between silk and C_{60}, confirming the efficiency of the SuMBE approach for the functionalization of spider silk. Moreover, the deep analysis of the C1s, O1s, and N1s core levels put in evidence that the C_{60} deposition reflects in a structural modification of the silk itself. Indeed, new components are present in all the analyzed core levels, suggesting that this interaction affects the whole silk structure and constituents.

It is difficult to interpret the origin of the new components appearing after the deposition. Their intensity and presence in all silk elemental constituents suggest a strong and diffused functionalization, involving all groups and related connections. The mechanical properties show a modification of the silk structure, an evidence that can be interpreted, from a chemical point of view, as the rupture of specific chemical bonds, as well as the formation of other bonds with C_{60} molecules. The interplay of these two effects (the breaking and formation of new species/bonds) is guided by the C_{60} KE as well as by the number of deposited molecules and leads to the observed silk changed mechanical properties. Further experiments will be devoted to study in details the interplay between all parameters.

MATERIALS AND METHODS

Film Deposition and Analysis Apparatus

The deposition of C_{60} and the characterization by X-ray photoelectron spectroscopy of only the spider cocoon, were performed using an experimental setup devoted to the thin film growth and *in-situ* analysis in UHV conditions.

The SuMBE apparatus consists of two chambers at different stages of vacuum (10^{-4} and 10^{-7} mbar, respectively). The supersonic source is located in the first chamber (source chamber) and it is essentially made of a quartz tube (12 cm length) with a nozzle (50 μm of diameter) at the front closed end, whereas in the back end the carrier gas is injected (Helium). The source is resistively heated by a Ta foil, which can reach a maximum temperature of about 1,000°C. The second chamber, instead, acts as an interface between the beam chamber and the final UHV deposition chamber, working as a differential pumping stage. The beam geometry and axis is defined by two collimators (skimmers), one positioned between the first and the second chamber on the axis of the vacuum system, and the other one between the second chamber and the analysis chamber. The first skimmer allows to extract the supersonic "molecular" beam out of the zone of silence of the supersonic expansion, working as a diaphragm between the two vacuum chambers. The second skimmer, maintains a differential vacuum between the second chamber and the analysis chamber and defines the size of the beam spot downstream of the generation apparatus (Nardi et al., 2010b).

The kinetic energy of the fullerene beam is tuned changing the pressure of the buffered gas and the source temperature to which the fullerene is evaporated, ranging from 5 to 14 eV. The

typical organic arrival rate on the substrate was about 1Å/min, as evaluated from a quartz microbalance, and was kept constant during all the experiments. A film of about 5 ML was deposited on the material, with a nominal thickness of about 4 nm. The C_{60} material was supplied by Sigma Aldrich, with a nominal purity of 99.9%.

The source chamber is directly connected by a valve to a μ-metal chamber (pressure $7x10^{-11}$ mbar), where the film deposited on the silk cocoon can be characterized by XPS *in situ*, avoiding air contamination. XPS is performed using the Mg-Kα emission at 1253.6 eV as X-ray photon source. The photoelectrons are analyzed by a VSW HA100 electron energy analyzer, leading to a total energy resolution of 0.86 eV. Core level BEs are referred to the Au 4f7/2 core level signal (at 84.0 eV), obtained from a sputtered gold surface. The photoemission core levels of all elements are analyzed through Voight lineshape deconvolution, after background subtraction of a Shirley function. The typical precision for energy peak position is ±0.05 eV, while uncertainty for FWHM is $< \pm 5\%$ and for area evaluation it is ±5%.

Mechanical Characterization

Tensile tests on single spider silk fibers were carried out through the Nanotensile Tester UTM150 by Agilent at room temperature and at a strain rate of 0.001 s^{-1}. Tested fibers length was about 10 mm.

DATA AVAILABILITY STATEMENT

All datasets generated for this study are included in the article/**Supplementary Material**.

AUTHOR CONTRIBUTIONS

NP designed and coordinated the study. MP analyzed the data from the mechanical tests. RT, LA, and RV performed SuMBE and XPS analysis. All the authors discussed the results and approved the manuscript.

ACKNOWLEDGMENTS

The authors thank E. Lepore for the help in the mechanical characterization. NP is supported by the European Commission under the FET Proactive (Neurofibres) grant no. 732344, as well as by the Italian Ministry of Education, University and Research (MIUR) under the ARS01-01384-PROSCAN and the PRIN-20177TTP3S grants.

SUPPLEMENTARY MATERIAL

The Supplementary Material for this article can be found online at: https://www.frontiersin.org/articles/10.3389/fmats.2020.00197/full#supplementary-material

REFERENCES

Altman, G. H., Diaz, F., Jakuba, C., Calabro, T., Horan, R. L., Chen, J., et al. (2003). Silk-based biomaterials. *Biomaterials* 24, 401–416. doi: 10.1016/S0142-9612(02)00353-8

Ariza, M. J., Rodriguez-Castellon, E., Rico, R., Benavente, J., Munoz, M., and Oleinikova, M. (2000). X-Ray photoelectron spectroscopy analysis of Di-(2-ethylhexyl) phosphoric acid activated membranes. *J. Colloid Interface Sci.* 226, 151–158. doi: 10.1006/jcis.2000.6805

Barber, A. H., Lu, D., and Pugno, N. (2015). Extreme strength observed in limpet teeth. *J. Roy. Soc. Interf.* 12:1326. doi: 10.1098/rsif.2014.1326

Berardo, A., Pantano, M. F., and Pugno, N. (2016). Slip knots and unfastening topologies enhance toughness without reducing strength of silk fibroin fibres. *Interf. Focus* 6:60. doi: 10.1098/rsfs.2015.0060

Bosia, F., Lepore, E., Alvarez, N. T., Miller, P., Shanov, V., and Pugno, N. (2016). Knotted synthetic polymer or carbon nanotube microfibres with enhanced toughness, up to 1400 J/g. *Carbon* 102, 116–125. doi: 10.1016/j.carbon.2016.02.025

Fantner, G. E., Oroudjev, E., Schitter, G., Golde, L. S., Thurner, P., Finch, M. M., et al. (2006). Sacrificial bonds and hidden length: unraveling molecular mesostructures in tough materials. *Biophys. J.* 90, 1411–1418. doi: 10.1529/biophysj.105.069344

Garcia-Gil, S., Arnau, A., and Garcia-Lekue, A. (2013). Exploring large O 1s and N 1s core level shifts due to intermolecular hydrogen bond formation in organic molecules. *Surf. Sci.* 613, 102–107. doi: 10.1016/j.susc.2013.03.017

Hakimi, O., Knight, D. P., Vollrath, F., and Vadgama, P. (2007). Spider and mulberry silkworm silks as compatible biomaterials. *Composites* 38, 324–337. doi: 10.1016/j.compositesb.2006.06.012

Hayashi, C. Y., and Lewis, R. V. (2000). Molecular architecture and evolution of a modular spider silk protein gene. *Science* 287, 1477–1479. doi: 10.1126/science.287.5457.1477

Hayashi, C. Y., Shipley, N. H., and Lewis, R. V. (1999). Hypotheses that correlate the sequence, structure, and mechanical properties of spider silk proteins. *Int. J. Biol. Macromol.* 24, 271–275. doi: 10.1016/S0141-8130(98)00089-0

Hedberg, K., Hedberg, L., Bethune, D. S., Brown, C. A., Dorn, H. C., Johnson, R. D., et al. (1991). Bond lengths in free molecules of buckminsterfullerene, C_{60}, from gas-phase electron diffraction. *Science* 254, 410–412. doi: 10.1126/science.254.5030.410

Huang, J., Wong, C., George, A., and Kaplan, D. L. (2007). The effect of genetically engineered spider silk-dentin matrix protein 1 chimeric protein on hydroxyapatite nucleation. *Biomaterials* 28, 2358–2367. doi: 10.1016/j.biomaterials.2006.11.021

Kerber, S. J., Bruckner, J. J., Wozniak, K., Seal, S., Hardcastle, S., and Barr, T. L. (1996). The nature of hydrogen in x-ray photoelectron spectroscopy: general patterns from hydroxides to hydrogen bonding. *J. Vacuum Sci. Technol.* 14:1314. doi: 10.1116/1.579947

Koebley, S. R., Vollrath, F., and Schniepp, H. C. (2017). Toughness-enhancing metastructure in the recluse spider's looped ribbon silk. *Mat. Horiz.* 4, 377–382. doi: 10.1039/C6MH00473C

Lepore, E., Bonaccorso, F., Bruna, M., Bosia, F., Taioli, S., Garberoglio, G., Ferrari, A. C., and Pugno, N. M. (2017). Silk reinforced with graphene or carbon nanotubes spun by spiders. *2D Materials* 4:031013. doi: 10.1088/2053-1583/aa7cd3

López, A. M., Mateo-Alonso, A., and Prato, M. (2011). Materials chemistry of fullerene C60 derivatives. *J. Mater. Chem.* 21, 1305–1318. doi: 10.1039/C0JM02386H

Madurga, R., Plaza, G. R., Blackledge, T. A., Guinea, G. V., Elices, M., and Perez-Rigueiro, J. (2016). Material properties of evolutionary diverse spider silks described by variation in a single structural parameter. *Sci. Rep.* 6:18991. doi: 10.1038/srep18991

Mayes, E. L., Vollrath, F., and Mann, S. (1998). Fabrication of magnetic spider silk and other silk-fiber composites using inorganic nanoparticles. *Adv. Mater.* 10, 801–805.

Nardi, M., Verucchi, R., Aversa, L., Casarin, M., Vittadini, A., Mahne, N., et al. (2010a). Electronic properties of tetrakis(pentafluorophenyl)porphyrin. *New J. Chem.* 37:1036. doi: 10.1039/c3nj40910d

Nardi, M., Verucchi, R., Corradi, C., Pola, M., Casarin, M., Vittadini, A., et al. (2010b). Tetraphenylporphyrin electronic properties: a combined theoretical

and experimental study of thin films deposited by SuMBD. *Phys. Chem. Chem. Phys.* 12, 871–880. doi: 10.1039/B914847G

Nardi, M., Verucchi, R., Tubino, R., and Iannotta, S. (2009). Activation and control of organolanthanide synthesis by supersonic molecular beams: erbium-porphyrin test case. *Phys. Rev. B* 79:125404. doi: 10.1103/PhysRevB.79.125404

Pantano, M. F., Berardo, A., and Pugno, N. (2016). Tightening slip knots in raw and degummed silk to increase toughness without losing strength. *Sci. Rep* 6:18222. doi: 10.1038/srep18222

Pawlak, R., Kawai, S., Fremy, S., Glatzel, T., and Meyer, E. (2011). Atomic-scale mechanical properties of orientated C_{60} molecules revealed by noncontact atomic force microscopy. *ACS Nano* 5, 6349–6354. doi: 10.1021/nn201462g

Pugno, N. (2014). The "Egg of Columbus" for making the world's toughest fibres. *PLoS ONE* 9:e93079. doi: 10.1371/journal.pone.0093079

Ruoff, R. S., and Ruoff, A. L. (1991). Is C_{60} stiffer than diamond? *Nature* 350, 663–664. doi: 10.1038/350663b0

Tatti, R., Aversa, L., Verucchi, R., Cavaliere, E., Garberoglio, G., Pugno, N. M., et al. (2016). Synthesis of single layer graphene on Cu(111) by C_{60} supersonic molecular beam epitaxy. *RSC Adv.* 6:37982. doi: 10.1039/C6RA02274J

Tatti, R., Timpel, M., Nardi, M. V., Fabbri, F., Rossi, R. L., Pasquardini, A., et al. (2017). Functionalization of SiC/SiOx nanowires with a porphyrin derivative: a hybrid nanosystem for X-ray induced singlet oxygen generation. *Mol. Syst. Des. Eng.* 2, 165–172. doi: 10.1039/C7ME00005G

Teule, F., Miao, Y.-G., Sohn, B.-H., Kim, Y.-S., Hulla, J. J., Fraser, M. J. Jr., Lewis, R. V., and Jarvis, D. L. (2012). Silkworms transformed with chimeric silkworm/spider silk genes spin composite silk fibers with improved mechanical properties. *Proc. Natl. Acad. Sci. U.S.A.* 109, 923–928. doi: 10.1073/pnas.1109420109

Thiel, B. L., Guess, K. B., and Viney, C. (1997). Non-periodic lattice crystals in the hierarchical microstructure of spider (major ampullate) silk. *Biopolymers* 41, 703–719.

Tokunaga, T., Kaneko, K., Sato, K., and Horita, Z. (2008). Microstructure and mechanical properties of aluminum–fullerene composite fabricated by high pressure torsion. *Scr. Mater.* 58, 735–738. doi: 10.1016/j.scriptamat.2007.12.010

Umeyama, T., and Imahori, H. (2013). Photofunctional hybrid nanocarbon materials. *J. Phys. Chem. C* 117, 3195–3209. doi: 10.1021/jp309149s

Verucchi, R., Aversa, L., Nardi, M. V., Taioli, S., Beccara, S. A., Alfˌè, D., et al. (2012). Iannotta, epitaxy of nanocrystalline silicon carbide on Si(111) at room temperature. *J. Am. Chem. Soc.* 134:17400. doi: 10.1021/ja307804v

Vollrath, F. (2000). Strength and structure of spiders' silks. *Rev. Mol. Biotechnol.* 74, 67–83. doi: 10.1016/S1389-0352(00)00006-4

Vollrath, F., and Knight, D. P. (2001). Liquid crystalline spinning of spider silk. *Nature* 410, 541–548. doi: 10.1038/35069000

Wu, Y., Toccoli, T., Koch, N., Iacob, E., Pallaoro, A., Rudolf, P., and Iannotta, S. (2007). Controlling the early stages of pentacene growth by supersonic molecular beam deposition. *Phys. Rev. Lett.* 98:076601. doi: 10.1103/PhysRevLett.98.076601

Xiong, D.-B., Cao, M., Guo, Q., Tan, Z., Fan, G., Li, Z., et al. (2015). Graphene-and-copper artificial nacre fabricated by a preform impregnation process: bioinspired strategy for strengthening-toughening of metal matrix composite. *ACS Nano* 9, 6934–6943. doi: 10.1021/acsnano.5b01067

Zhou, S., Peng, H., Yu, X., Zheng, X., Cui, W., Zhang, Z., et al. (2008). Preparation and characterization of a novel electrospun spider silk fibroin/Poly(D,L-lactide) composite fiber. *J. Phys. Chem. B* 112, 11209–11216. doi: 10.1021/jp800913k

Conflict of Interest: The authors declare that the research was conducted in the absence of any commercial or financial relationships that could be construed as a potential conflict of interest.

frontiers in Materials

ORIGINAL RESEARCH
published: 25 June 2020
doi: 10.3389/fmats.2020.00116

Tumor-Stroma Interactions Alter the Sensitivity of Drug in Breast Cancer

Virginia Brancato[1,2]*, *Banani Kundu*[1,2], *Joaquim Miguel Oliveira*[1,2,3], *Vitor Manuel Correlo*[1,2,3], *Rui Luis Reis*[1,2,3] *and Subhas C. Kundu*[1,2]*

[1] 3B's Research Group, I3Bs—Research Institute on Biomaterials, Biodegradables and Biomimetics, Headquarters of the European Institute of Excellence on Tissue Engineering and Regenerative Medicine, University of Minho, Guimarães, Portugal, [2] ICVS/3B's–PT Government Associate Laboratory, Guimarães, Portugal, [3] The Discoveries Centre for Regenerative and Precision Medicine, Headquarters at University of Minho, Guimarães, Portugal

Flat cell cultures or xenografts are inadequate tools to unravel cancer complex biology. 3D *in vitro* tumor models garnered interest since they recapitulate better dynamic mechanisms of cancer, but a gold standard model that faithfully mimics solid cancer is not available yet. 3D breast cancer model is fabricated using freeze-dried silk fibroin scaffolds. Breast cancer cell lines (MCF-7 and MDA-MB231) are seeded with normal mammary fibroblasts onto silk fibroin scaffold (1 and 2 mm thick). Cells proliferation is monitored by means of Alamar blue assay. 3D breast cancer models morphology is observed by confocal microscopy. Gene expression modulation concerning extracellular matrix markers is evaluated. Further, 3D bioengineered breast cancer models are treated with doxorubicin. Silk fibroin scaffolds allow the proliferation of cancer cells and fibroblasts. Cells growth is enhanced when cancer cells and fibroblasts are seeded together. Histological staining shows 3D cell organization. MMP-1, MMP-2, MMP-3, Col-1, and Fibronectin expression is upregulated in co-culture. After doxorubicin treatment, stronger reduction in cell activity is observed in 2 mm SF scaffold in comparison to 1 mm. The 3D *in vitro* breast cancer model obtained can easily be scaled-up and translated to the preclinical testing of novel chemotherapeutics.

Keywords: tumor stroma, silk fibroin, 3D cancer models, drug testing, tumor microenvironment

OPEN ACCESS

Edited by:
Antonella Motta,
University of Trento, Italy

Reviewed by:
Yong Yang,
University of North Texas, United States
Lia Rimondini,
University of Eastern Piedmont, Italy

***Correspondence:**
Virginia Brancato
virginia.brancato@i3bs.uminho.pt
Subhas C. Kundu
kundu@i3bs.uminho.pt

Specialty section:
This article was submitted to Biomaterials, a section of the journal Frontiers in Materials

Received: *22 October 2019*
Accepted: *15 April 2020*
Published: *25 June 2020*

Citation:
Brancato V, Kundu B, Oliveira JM, Correlo VM, Reis RL and Kundu SC (2020) Tumor-Stroma Interactions Alter the Sensitivity of Drug in Breast Cancer. Front. Mater. 7:116. doi: 10.3389/fmats.2020.00116

INTRODUCTION

Breast cancer is still a leading cause of death for the European women, especially in Eastern Europe countries. European Commission report states that the death rate for breast cancer was 32.6 per 100000 inhabitants for women in 2014 (European Commission, 2016). Recent studies predict that the number of breast cancer new cases will reach about 3.2 million per year by 2050 (Tao et al., 2015). A massive campaign has promoted prevention and awareness toward this disease in the high-income country. Improved chemotherapeutic treatments are helping to decrease the mortality rate for breast cancer (European Commission, 2016). However, the incidence is increasing throughout Europe due to the spread of some risk factors as sedentary lifestyle, obesity, increased average age of women having their first child and the reduced number of child for each woman. Despite the progress in the chemotherapeutic treatment, breast cancer remains the main cause of cancer-related deaths in Europe (Senkus et al., 2015).

The challenge to defeat breast cancer is also related to the understanding the complexity of the tumor microenvironment (Soysal et al., 2015). Tumor "stroma" is an umbrella term that takes into account the non-tumor cells and extracellular matrix (ECM), while excluding probably the immune cells (Spill et al., 2016). The interplay among different cell types imparts the complexity to the disease (Stadler et al., 2015). Besides cancer cells, the activated fibroblasts (well-known as myofibroblasts or cancer activated fibroblasts, CAFs) are the key cellular component of breast cancer stroma (Miles and Sikes, 2014). The CAFs over-express several ECM proteins including collagens, fibronectin and tenascin C that leads to the ECM stiffening (Madar et al., 2013). The stiffer matrix prompts the invasion of cancer cells into the surrounding tissues (Conklin and Keely, 2012; Klein-Goldberg et al., 2014). Hence, the reactive stroma is actively involved in cancer progression. It is also considered a key regulator of drug sensitivity of cancer cells as reported by recent publications (Östman, 2012; Yuan et al., 2016; Fiori et al., 2019; Qu et al., 2019). Though the research focus in past decade involves the development of therapeutics targeting tumor microenvironment, there is still a lack of understanding how the tumor stromal architecture affect the response of chemotherapeutics. Very limited is known about the relation between cancer stromal architecture and response of anticancer therapeutics, in space and time (Altrock et al., 2018). Hence, in the present work we have employed scaffolds of various thickness to engineer a 3D *in vitro* breast cancer model to investigate the direct effect of scaffold thickness on tumorigenicity and drug response. Silk protein fibroin scaffolds are already used to develop tumor models of breast and hepatocarcinoma, which serve as preclinical *in vitro* platform for drug testing (Talukdar and Kundu, 2012; Kundu et al., 2013a). However, these models do not include the contribution of stromal cells such as fibroblasts or the physical parameters like variable ECM thickness. It is already mentioned that CAFs are of utmost importance for the tumoral progression. An attempt is made to include fibroblasts in 3D *in vitro* tumor model (Dondajewska et al., 2018). This model is used as screening platform for chemotherapeutics. The breast cancer model reported in the work is composed of murine cell lines. It is known that mouse-derived cells cannot be considered as relevant to human cells for the screening of chemotherapeutics for human treatment. A heterotypic breast cancer model based on silk fibroin scaffold is developed by incorporating epithelial and fibroblast cells (Wang and Kaplan, 2012). The same group also investigates the interaction among the breast cancer cells, fibroblasts and adipose cells (Wang et al., 2010). Silk fibroin is also used in combination with other biomaterials (Li et al., 2018). Those breast cancer *in vitro* models can recapitulate the complexity of the tumor microenvironment and the crosstalk among the cells. In this work, we propose a heterotypic breast cancer tumor model, which is obtained by seeding human mammary fibroblasts and two different breast cancer cells lines (MCF-7 and MDA-MB-231) on silk fibroin freeze-dried scaffolds of two different thickness. The morphology and distribution of the cells throughout the silk fibroin scaffolds are detected by mean of scansion electron microscopy, hematoxylin and eosin staining and confocal microscopy. The tumorigenicity of these models are further compared by gene analysis. The engineered 3D *in vitro* breast cancer model is then used as testing platform using cancer drug doxorubicin. The results obtained with homotypic and heterotypic cultures are then compared.

Abbreviations: CAF, Cancer associated fibroblasts; ECM, Extracellular matrix; TGF-β, Tumor growth factor-β; TNF-α Tumor necrosis factor-α; 2D, two-dimensional; 3D, three-dimensional; HMF, Human mammary fibroblasts; 3D-BCM, Three-dimensional breast cancer model; SF, silk fibroin; MMPs, metalloproteinases.

MATERIALS AND METHODS

Materials

Fresh mulberry silkworm (*Bombyx mori*) cocoons were obtained from Portuguese Association of Parents and Friends of Mentally Disabled Citizens (APPACDM, CasteloBranco, Portugal). All other products are purchased from Sigma-Aldrich Company (St. Lewis, USA), if not stated specifically.

Silk Fibroin Scaffold Preparation

Silk protein fibroin was extracted from the silk cocoons. The cocoons after removing the pupae, were cut into pieces before the degumming procedure. To remove glue protein sericin from the silk fibers, the cocoon cut pieces were boiled in a solution of 0.02 M sodium carbonate for an hour. The silk fibers were then washed three times with distilled water to remove sericin residues (Talukdar and Kundu, 2012; Kundu et al., 2013a). Silk fibers were dissolved in a solution of 9.3 M lithium bromide for 1 h at 70°C in an oven. The obtained silk fibroin (SF) solution was dialyzed against distilled water for 48 h using benzoylated dialysis tubing (MWCO: 2 kDa). The final concentration was obtained by measuring the dry weight of SF solution after drying at 70°C in an oven for 24 h. 2 wt % (w/v) SF solution was poured into each well of 96-well plate, which was serving as mold and frozen at −20°C for 48 h. Two different scaffold thicknesses (6 mm in diameter and 1 or 2 mm thickness) were fabricated by pouring 50 or 100 μL of 2 wt% SF solution in each well, respectively. SF scaffolds were obtained after freeze-drying (LyoAlfa 10/15, Telstar, Spain).

Morphological Characterization

Micro-Architectures of 3D Scaffold

The non-porous "skin/ layer" formed at the top surface of each scaffold was removed by simply peeling the skin away immediately post-freeze-drying by using fine-forceps prior to scanning electron microscopy analysis (Rnjak-Kovacina et al., 2015). The morphology of the fabricated scaffold was analyzed by mean of scanning electron microscopy (SEM) (JEOL JSM-6010PLUS/LV). Before the observation, all the samples were sputter-coated with a 3 nm layer of platinum (Sputter Coater SC502, Cressington) and the micrographs were taken at an accelerating voltage of 10 kV at different magnifications. To confirm the interconnectivity of the scaffolds, X-ray microtomography was performed (μCT1272, SkyScan 1272, Belgium). The samples were scanned dry in air with a nominal resolution of ∼2 μm at an intensity of 200 μA, energy of

50 kV and integration time of 1 s. NRecon programme was used to reconstruct the 3D structure, which further investigated morphometrically (CT Analyzer v1.17.0.0, SkyScan, Belgium) for distribution of pores, porosity and pore wall thickness ($n = 3$) (Arya et al., 2012).

Qualitative (Morphological) and Quantitative Characterization: Diffusion

To illustrate the transport of biomolecules or therapeutics within porous SF scaffolds, doxorubicin HCl (DOX, Carbosynth, UK) was prepared in phosphate-buffered saline (PBS) at a concentration of 1 mg/mL and the porous sponges were then placed into the suspension. The diffusion phenomenon was imaged immediately after soaking using an inverted confocal microscope TCS SP8 (Leica Microsystems, Germany). The images are represented as *Z*-stack maximum projection with 50 μm of *Z*-size. To compare the loading and release ability of scaffolds, they were immersed in doxorubicin HCl (500 μg/mL in PBS) and incubated overnight under continuous stirring at 37°C (Cacicedo et al., 2016). The scaffolds were then taken out and the concentration of DOX in supernatant was assayed spectro-fluorometrically. The loading efficiency was evaluated as follows:

$$DOX\ loading\ (\%) = (DOXo - DOXs|DOXo) \times 100$$

Where, $DOXo$ = concentration of DOX at time zero, $DOXs$ = concentration of DOX in supernatant after incubation.

The release of DOX from silk fibroin scaffolds was monitored as a function of time for 7 days in PBS at 37°C. Cumulative drug release was investigated by measuring doxorubicin-associated fluorescence (excitation wavelength 485 nm, emission wavelength 590 nm; Seib et al., 2013).

In vitro Cell Culture

Cells Types

Primary human mammary fibroblasts (HMF) were purchased at Innoprot (Bizkaia, Spain) and grown in fibroblast culture medium supplemented with 1% fibroblast growth factor, 1% antibiotic/antimicotic and 2% FBS (Innoprot). MCF-7 and MDA-MB-231 were purchased from ATCC (Virginia, USA) and cultivated in DMEM high glucose (4.5 g/mL) (Sigma-Aldrich, St. Lewis, USA), 10% (v/v) fetal bovine serum (FBS; Gibco, GB) and 1% (v/v) antibiotic/antimycotic solution (final concentration of penicillin 100 units/mL and streptomycin 100 μg/mL; Gibco, GB). The cells were cultured until 80% confluence at 37°C in 5% CO_2 incubator.

Cell Seeding Onto 3D Silk Fibroin Scaffolds

After the freeze-drying process, the SF scaffolds were soaked in ethanol to induce β-sheet crystallization and insolubility in water (5 min in absolute ethanol). To sterilize the scaffolds, they were soaked in 70% ethanol for 30 min. The scaffolds were washed twice in sterile PBS 1X and sterilized by UV light treatment before the seeding of cells under laminar hood. The day before the seeding, the SF scaffold were transferred in 48 multi-well TCPS plate, soaked in the cell culture medium and left overnight in the CO_2 incubator. Confluent HMF, MCF-7 and MDA-MB231 were detached from the cell culture flasks with TrypLE Express (1X) (Life Technologies, Carlsbad, CA, USA). To carry out monoculture (HMF, MCF-7 and MDA-MB-231), a suspension of 10 μL containing 2×10^5 of each cell type was seeded on the entire top of each scaffold evenly. The seeded scaffolds were allowed to adhere to the scaffold for 3 h at 37°C and 5% CO_2 and then 500 μL of cell culture medium was added in each well. Medium was changed each 3 days and ascorbic acid (50 μg/mL) was added to the HMF culture. The cultures were maintained for 14 days and samples were collected for further analysis at different time point (Day 1, 3, 7, 9, 14). For co-culture models of breast cancer cells and fibroblast, MCF-7 and MDA-MB231 were added at day 7 on the previously HMF seeded scaffold. The density of HMF was 5×10^4 when the co-culture was carried out. To maintain 1:3 ratio between HMF and MCF-7 or MDA-MB-231, the cancer cells were seeded at the density of $1.5x10^5$ cells, at day 7 of the culture. The constructs are referred as 3D-BCM (tridimensional breast cancer model), namely as 3D-HMF, 3D-MCF7, 3D-231, 3D-HMF/MCF7, 3D-HMF/231. Moreover, we classify the 3D-HMF, 3D-MCF7, 3D-231 mono-culture with the term homotypic and the 3D-HMF/MCF7, 3D-HMF/231 co-culture with the term heterotypic.

TABLE 1 | Human primers pairs.

Gene	Primer sequences	Amplicon (bp)	Annealing T (°C)	ID
COL1	Rv–GGCAGTTCTT GGTCTCGTCA	156	59	XM_005257058.4
	Fw–GCCAAGACG AAGACATCCCA			
MMP-1	Rv–TTCAATCCTG TAGGTCAGATGTGTT	248	59	NM_002421.3
	Fw–ACCTGGAAAA ATACTACAA CCTGAA			
MMP-2	Rv – TCAGGTA TTGCACTGCCAACT	169	59	NM_004530.5
	Fw – GCTACGATG GAGGCGTAAT			
MMP-3	Rv–AGTCAGGG GGAGGTCCATAG	81	61	NM_002422.4
	Fw–CACTCACAG ACCTGACTCGG			
Fibronectin	Rv–GCTCATC ATCTGGCCATTTT	230	53	NM_001365524.1
	Fw–ACCAACCTA CGGATGACTCG			
GAPDH	Rv–GTCATGA GTCCTTCCACGA	101	-	NM_001289745.2
	Fw–AGCCTCAA GATCATCAGCAA			
β-actin	Rv—AAGGGACT TCCTGTAACAA	140	-	NM_001101.4
	Fw–CTGGAACG GTGAAGGTGACA			

Cell Viability Assay

The cell viability in the 3D-BCM was assessed by Alamar blue assay (Biorad). 3D-BCM at different time point (Day 1, 3, 7, 9, 14) were incubated with 20% (v/v) Alamar blue solution in DMEM High Glucose without FBS for 4 h at 37°C. The fluorescence was measured using a microplate reader (Synergy HT, BIO-TEK) at an excitation wavelength of 530 nm and an emission wavelength of 590 nm. SF scaffold without cells were used as control.

Cell Morphology in the 3D Silk Fibroin Scaffolds

Confocal Imaging

3D-BCMs were observed by mean of confocal laser microscopy at different time points (1, 7, and 14 days). 3D-BCMs were washed in PBS twice and fixed with 10% (v/v) neutral buffered formalin (Richard-Allan Scientific™, ThermoFisher Scientific, Portugal) for 20 min, permeabilized with 0.2% (v/v) Triton X-100 for 15 min. Actin microfilaments were stained with Phalloidin–Tetramethylrhodamine B isothiocyanate (1:200 in PBS; Sigma-Aldrich, USA) for 45 min and nuclei were counterstained with DAPI (1:1000 in PBS; Sigma-Aldrich, USA) for 10 min. The stained cells were observed by inverted confocal microscope (TSC-SP8, Leica Microsystems, Germany) with diode (405 nm) and HeNe (534 nm) lasers. The samples were observed by using $\lambda_{ex} = 415$ nm and $\lambda_{em} = 461$ nm to observe cells' nuclei fluorescence, and using $\lambda_{ex} = 560$ nm and $\lambda_{em} = 630$ nm to observe actin filaments.

Scanning Electron Microscopy

The cell morphology in the 3D-BCM was observed at day 14 by mean of SEM. The constructs were washed in PBS and fixed with a 2.5% (v/v) glutaraldehyde solution overnight at 4°C. Samples were further dehydrated through increasing ethanol concentrations (30, 50, 70, 90, 100% v/v) for 1 h, and left in ethanol absolute overnight. The samples were undergone a cycle of critical point drying (Critical Point Dryer, Autosandri-815, Series A, Tourisms). Before SEM observation, all the samples were sputter coated with gold (Sputter Coater

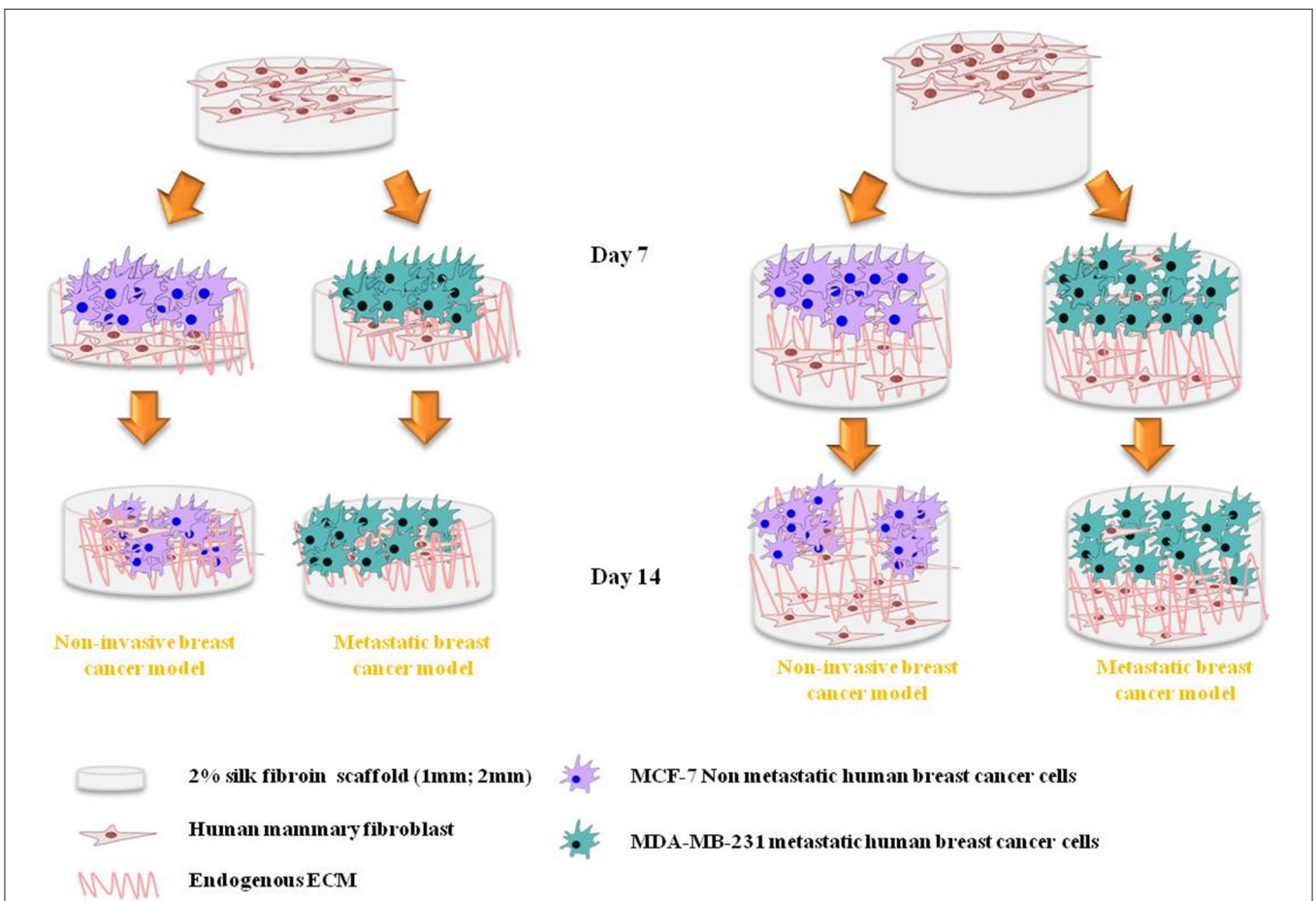

FIGURE 1 | Schematic representation of the *in vitro* cell culture approach using silk protein fibroin (SF) biomaterial to obtain 3D breast cancer model. Silk fibroin scaffolds of two different thicknesses support the growth of breast cancer cells co-cultured with mammary fibroblasts. The cancer cells were seeded 7 days after the fibroblasts seeding. Four different co-cultured conditions were analyzed in this work: 3D-HMF/MCF7 in 1 mm and 2 mm SF scaffold, 3D-HMF/231 in 1 mm and 2 mm SF scaffolds.

SC502, Cressington) and the microphotographs were taken at an accelerating voltage of 10 kV at different magnifications under SEM (JEOL JSM-6010PLUS/LV).

Hematoxylin/Eosin Staining of Silk Fibroin-Cell Scaffold Constructs

To investigate the cell distribution in the 3D-BCM, hematoxylin/eosin staining was carried out. Briefly, the constructs were washed twice in PBS 1X and fixed with 10% (v/v) neutral buffered formalin (Richard Allan Scientific^{TM}, ThermoFisher Scientific, Portugal) for 20 min. The samples were maintained in PBS 1X, dehydrated through increasing ethanol concentrations and embedded in paraffin using an automatized process (EC350-2, Microm, Thermo Scientific, Waltham, MA, USA). Successively, the samples were sectioned at a thickness of 7 μm using a microtome (HM355S, Microm, Thermo scientific, Portugal). Hematoxylin/eosin (Bio-optica, Italy) staining was carried out according to manufacturer's procedure through an automatized process (HMS, Microm, Thermo Scientific, Portugal). The stained structures were mounted with Entellan® (Inopat) and visualized under the microscope with an attached camera (Leica DM750, Germany).

RNA Isolation and Real-Time RT-PCR

SF scaffolds with 1 mm and 2 mm thickness were seeded with $2x10^5$ cells, as described in the section 2.4.2. 3D-BCMs were collected at day 14 to investigate the mRNA expression of the genes of interest. Total mRNA was extracted using TRI Reagent® RNA Isolation Reagent (ThermoFisher Scientific, Portugal), according to the manufacturer's guidelines. RNA concentration and purity were measured by mean of Nanodrop® ND-1000 spectrophotometer (ThermoFisher Scientific, Portugal). The synthesis of cDNA was carried out from 100 ng of mRNA using qScriptTM cDNA Synthesis Kit (Quanta BioSciences, USA). Briefly, a reaction mixture consisting of 4 μL qScript Reaction Mix, 1 μL qScript Reverse Transcriptase (RT), RNA template (100 ng total RNA) and nuclease-free water was prepared in 20 μL of final volume. The single-strand cDNA synthesis occurred by incubating the complete reaction mixture for 5 min at 22°C, followed by 30 min at 42°C and terminated with an incubation of 5 min at 85°C. RT-PCR was performed using PerfeCTA® SYBR Green FastMix (Quanta BioSciences, USA), following manufacturer's instructions, on RT-PCR Mastercycler Realplex machine (Realplex, Eppendorf, Germany). Primer sequences (Eurofins Genomics, UK) were designed using Primer-BLAST tool (**Table 1**). Livak's method ($2^{\Delta\Delta Ct}$) was used to quantify the relative gene expression (Livak and Schmittgen, 2001). The mRNA expression was first normalized to the average expression of multiple internal control genes [glyceraldehyde-3-phosphate dehydrogenase (*GAPDH*) and β-actin (*ACTB*)]. Three samples of each condition were considered and the results are represented as fold change toward the gene expression in the 3D-HMF.

Drug Testing and Cytotoxicity on 3D-BCM

Scaffolds with 1 and 2 mm thickness were seeded with 2×10^5 cells, as described in the section Cell Seeding Onto 3D Silk Fibroin Scaffolds. At day 14, 3D-BCMs (3D-HMF, 3D-MCF7, 3D-231, 3D-HMF/MCF7; 3D-HMF/231) were treated with 15 and 30 μg/mL of DOX (Carbosynth, UK). After the DOX treating for 24, 48, and 72 h at 37°C and 5% CO_2, metabolic activity and cell proliferation were assayed. To evaluate the metabolic activity of the cells in the 3D-BCMs after doxorubicin treatment, Alamar blue assay was performed according to the protocol described in the section Cell Viability Assay. To evaluate cell proliferation in the 3D-BCM after DOX treatment, the amount of DNA of each was quantified by Quant-iT^{TM} PicoGreen® dsDNA assay (Thermofisher scientific, Portugal), according to the manufacturer's guidelines. At each time point, the 3D-BCMs used for the Alamar blue assay were washed twice with PBS, incubated in 1 ml of ultrapure water for 1 h at 37°C and kept at −80°C for further analysis. The constructs were thawed at RT and sonicated 20 min to trigger the membrane lysis. The samples were incubated 10 min in the dark with fluorescent Picogreen® dye. The fluorescence of the supernatant was measured using a microplate reader at 485 and 530 nm excitation and emission wavelength, respectively. SF scaffolds without cells were used as control. To calculate the DNA amount in each sample, the data obtained from the assay were plotted together with the values of DNA concentration and fluorescence of a standard curve ranging between 0 and 2 μg/mL.

Statistical Analysis

To determine statistical significance, the data were analyzed using GraphPad Prism v5.01 software (GraphPad Software, La Jolla, CA). All statistics were reported as mean ± standard deviation. One-way ANOVA test was used to compare the data, followed by Tukey's test. All the experiments were performed in triplicate and statistical significance was considered at $p<0.05$.

RESULTS

The aim of this work is the development of an *in vitro* 3D breast cancer model based on co-cultured primary normal human mammary fibroblasts (HMF) and two different types of breast cancer cells (MCF-7 and MDA-MB231). Two cell types were chosen to mimic different stages of breast cancer like early stage and invasive phenotypes. The chosen scaffold type is 2 wt% silk fibroin (SF) freeze-dried scaffolds of two thickness (1 or 2 mm). The schematic representation (**Figure 1**) shows the approach followed for the development of the 3D-BCM. Briefly, normal mammary fibroblasts were seeded on the SF scaffold. At day 7 of culture, breast cancer cells, MCF-7 and MDA-MB231, respectively, were added into the fibroblast-laden scaffolds and cultured until day 14. Mono-cultures (3D-HMF, 3D-MCF7, 3D-231) were used as control to investigate how the interplay between the cancer cells and fibroblasts could affect the tumor growth or the response to Doxorubicin treatment.

Silk Fibroin Scaffold Preparation and Characterization

Porous SF scaffolds of different thickness were obtained by freeze-drying of different volumes of silk solution (2 wt%) (**Figures 2A,B**). **Figures 2B,C** represent the side and top views, respectively, which reveal highly porous interconnected nature

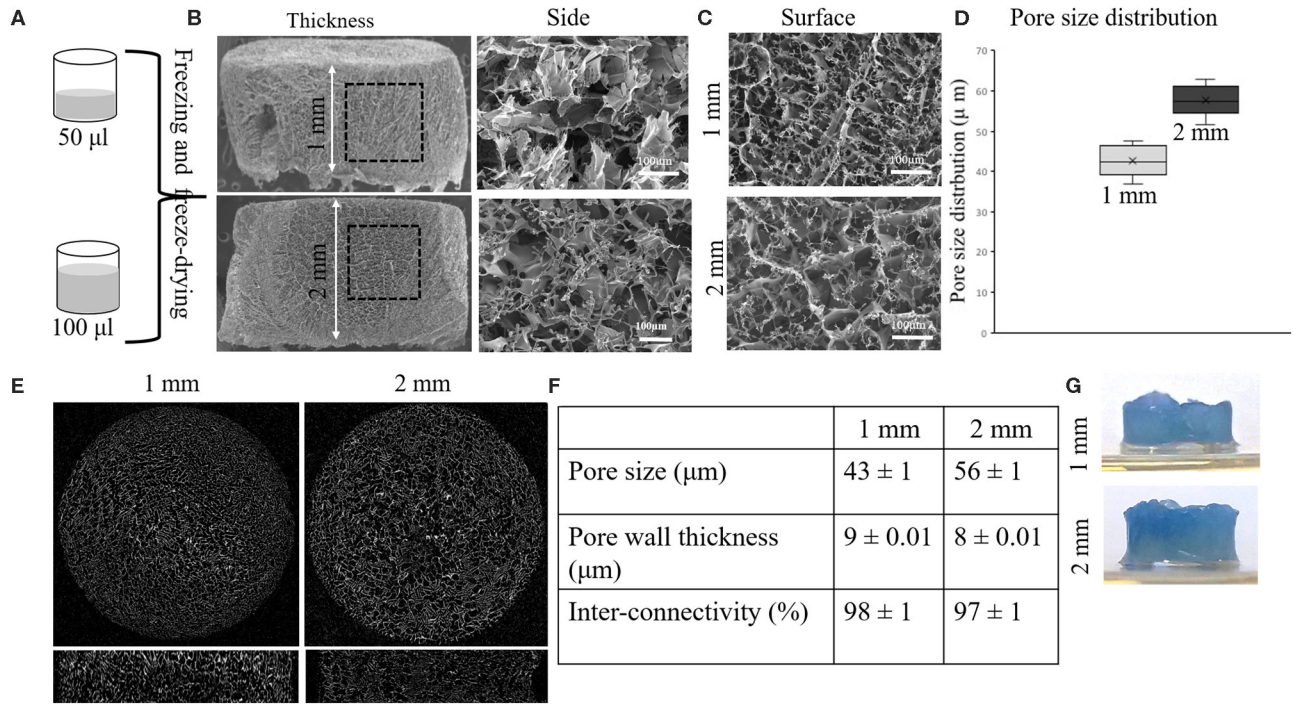

	1 mm	2 mm
Pore size (µm)	43 ± 1	56 ± 1
Pore wall thickness (µm)	9 ± 0.01	8 ± 0.01
Inter-connectivity (%)	98 ± 1	97 ± 1

FIGURE 2 | Silk fibroin (SF) scaffolds' morphological characterization and diffusion. SF scaffolds are obtained pouring 50 µL and 100 µL of silk fibroin solution (2 wt %) in a 96 TCPS well plate **(A)**. Full side **(A,B)** and high view (200× magnification, scale bar 100 µm) of SF 1 and 2 mm scaffolds are shown, respectively. Micrographs **(C)** show the surface profile of the SF scaffolds. The graphs represent the pore size distribution in the two types of SF scaffolds (1 mm and 2 mm). **(D)** The pore size distribution is plotted in the graph. Micrographs **(E)** exhibit the interconnectivity of the porous network in the scaffold with the relative value **(F)** for the pore size, pore wall thickness and inter-connectivity obtained by means of Micro CT analysis ($n = 3$). Alamar blue dye is used to demonstrate liquid diffusion within the scaffolds **(G)**.

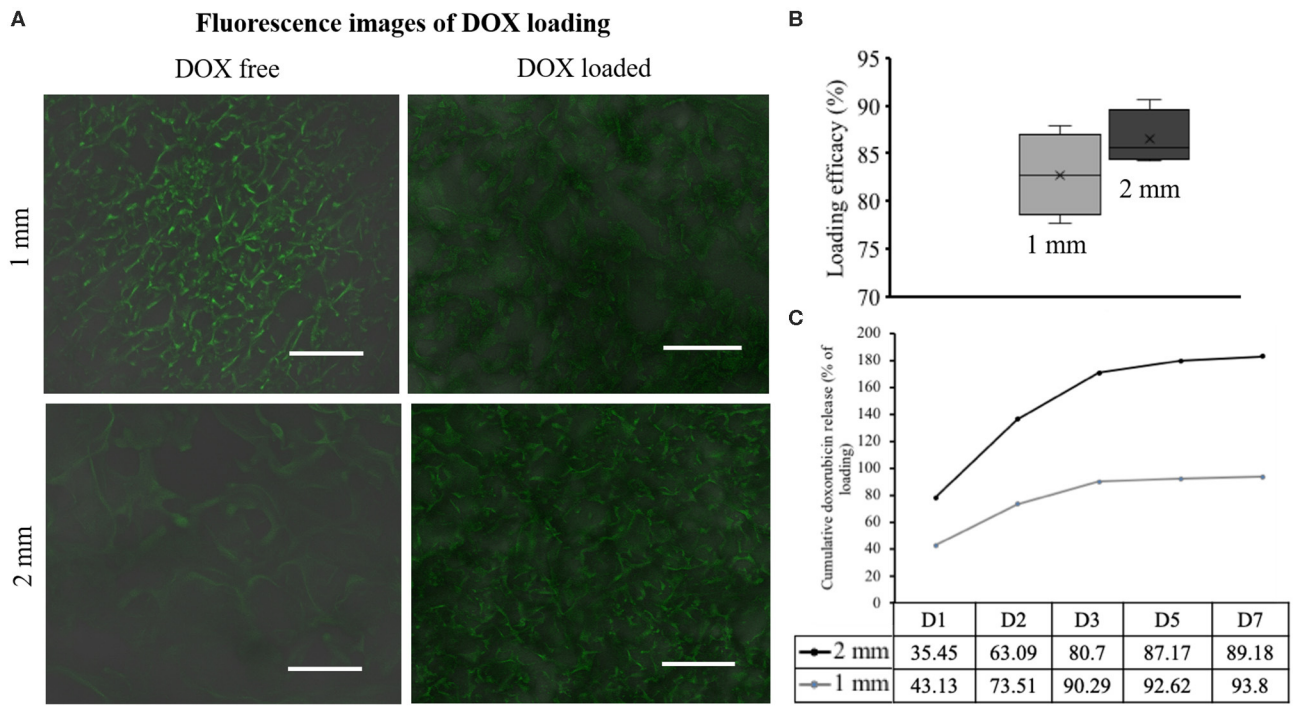

	D1	D2	D3	D5	D7
2 mm	35.45	63.09	80.7	87.17	89.18
1 mm	43.13	73.51	90.29	92.62	93.8

FIGURE 3 | Diffusion profile of doxorubicin (DOX) in the Silk fibroin (SF) scaffolds. DOX is loaded in the SF scaffold and the confocal images are shown together with a DOX free scaffold. It is evident from the SF auto-fluorescence **(A)**. Loading efficiency in both 1 and 2 mm scaffolds is evaluated **(B)**. Cumulative DOX release curve represents the DOX release along 7 days, which is measured by mean of spectrophotometric technique ($n = 3$) **(C)**.

of SF scaffolds. The gradient distribution of pores across the scaffold thickness was due to ice crystal formation and freeze-drying process (Arya et al., 2012). The pore sizes obtained from Micro CT were 43 ± 1 μm and 56 ± 1 μm, respectively (**Figure 2**). The thickness of pore wall was decreased with the increased pore size. Both the scaffolds exhibited well-interconnectivity (> 95%) (**Figure 2F**). To further demonstrate the pore interconnectivity, the SF scaffolds were rehydrated in PBS and placed within a dish containing Alamar blue dye (Rnjak-Kovacina et al., 2015). Instantly upon contact with Alamar blue dye, the scaffolds appeared blue despite being hydrated in PBS (**Figure 2G**). The uptake of dye readily by the scaffolds indicated the interconnectivity within sponges. **Figure 3A** shows the representative confocal microscopy images of porous SF scaffolds with or without doxorubicin (DOX). In order to measure the diffusion properties of scaffolds, the loading of DOX was carried out (for easy visualization due to auto-fluorescence nature of DOX). The diffusion of DOX immediately after immersion was imaged (**Figure 3A**), which indicated the diffused fluorescence signal throughout the porous scaffolds. However, the time-dependent quantitative analysis of DOX diffusion into the porous matrix was not possible to perform due to high loading efficacy. The loading efficacy can be defined as the percentage amount of DOX loaded/entrapped within porous silk fibroin scaffold after initial exposure to free drug and was observed > 80% for both sponges (**Figure 3B**) that corresponding to excessive fluorescence signal (the autofluorescence of silk also provided some background). The release of DOX from scaffolds was defined in relation with their thickness. The release was relatively slow for 2 mm scaffolds, resulting a cumulative release of 89%

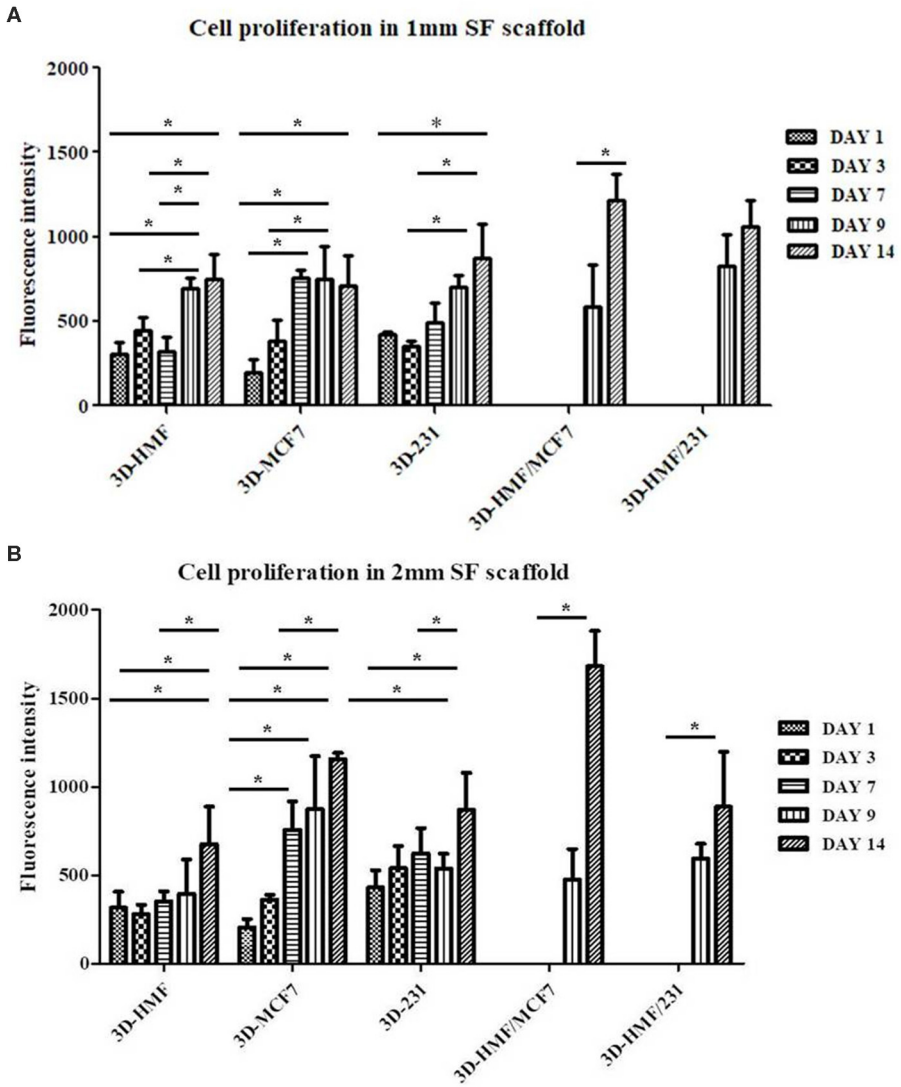

FIGURE 4 | Cell proliferation profile in 1 **(A)** and 2 mm **(B)** Silk fibroin (SF) scaffolds. The cells proliferation is investigated at different time points (Day 1, 3, 7, 9, 14) for both homotypic and heterotypic 3D-BCMs by mean of Alamar blue assay. *$P < 0.05$ is considered as statistically significant ($n = 3$).

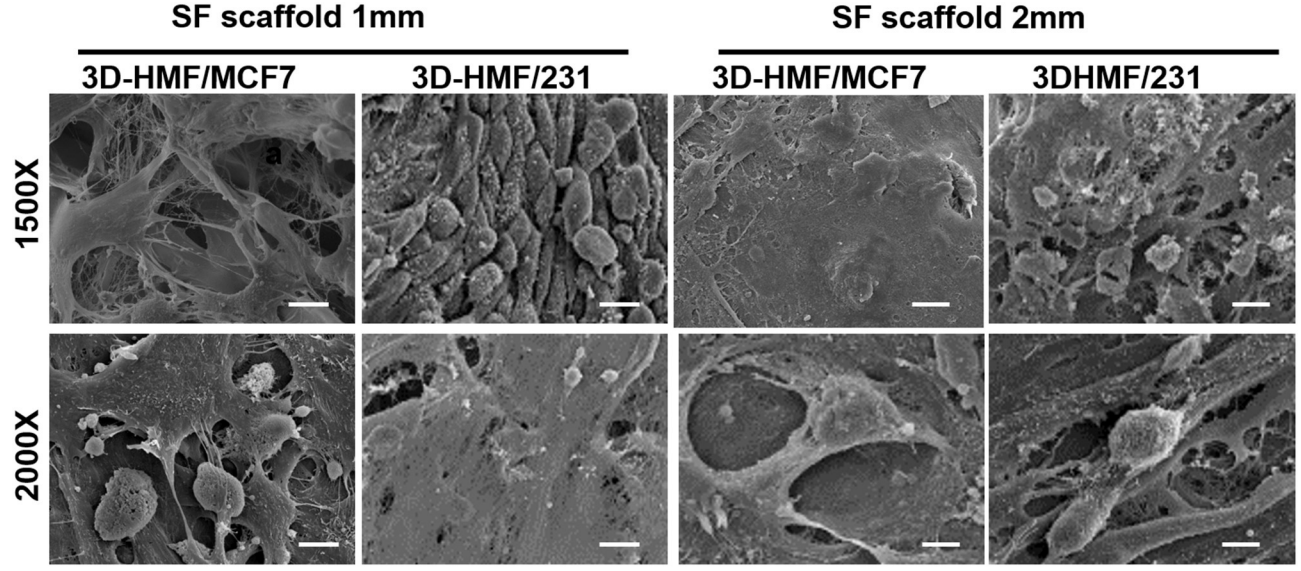

FIGURE 5 | Scanning electron micrographs of the developed 3D tumor models. 3D-HMF/MCF7 and 3D-HMF/231 in 1 mm and 2 mm SF scaffolds are fixed in 2.5% glutaraldehyde at day 14 of co-culture. The scale bar is 10 μm for the 1,500× magnification and 15 μm for the 2,000× magnification micrographs.

after 7 days compared to 1 mm ones, ∼93% (**Figure 3C**). For both types of scaffolds the rapid release of DOX was observed over the first 48 h and this was 73 and 63% of total cumulative release from 1 or 2 mm, respectively. The release was dropped over the remaining period of study.

Cell Viability and Distribution Within Silk Fibroin Scaffolds

Alamar blue assay was carried out to assess the viability and metabolic activity of the cells within the scaffold at different time point (Day 1, 3, 7, 9, 14). The metabolic activity of cells increased along with the time when cells were cultured in both 1 mm and 2 mm silk fibroin scaffolds. In both cases, the heterotypic model showed a higher proliferation rate in comparison to the homotypic one (**Figure 4**), with high growth peak at day 14 for 3D-HMF/MCF7 in 2 mm SF scaffold. We do not observe a significant difference in cell growth when the cells were seeded in 1 or 2 mm thickness scaffolds. The cells showed a rounded shape in the SF scaffold according to the SEM micrographs (**Figure 5**). The cell morphology and distribution were further investigated by mean of Hematoxylin/Eosin staining. Both SEM micrographs and micro-tumor sections revealed a 3D rearrangement of the tumor cells in the scaffolds (**Figure 6A**). The HMF/MCF-7 cells formed compact aggregate in the SF scaffold resembling the 3D architecture of a tumor mass. The HMF/MDAMB231 cells were more spread in the SF scaffolds of both thicknesses (1 mm and 2 mm). Confocal images showed the higher cellular density in the heterotypic 3D-BCM, which also confirmed by the metabolic activities increments. HMF maintained a more spread and elongated shape while the cancer cells (MCF-7 and MDAMB-231) exhibited rounded shape (**Figure 6B**). The Z-scanning of the constructs (i.e. cell laden silk scaffolds of different thickness) indicated the invasion of cells within the interconnective porous scaffolds. Moreover, the cells penetrated both scaffolds irrespective of their thickness. The morphology and dissemination of the cells throughout the scaffolds were also confirmed by micrographs from SEM observation.

Cytotoxicity of DOX in 3D-BCM

At day 15 of culture, the 3D-BCM were challenged with two different concentrations of DOX (15 and 30 μg/mL) as illustrated by the experimental timeline (**Figure 7A**). The DOX cytotoxicity against the 3D-BCM was evaluated at three different time points (24, 48, 72 h). Cell metabolism was evaluated by mean of Alamar Blue assay. In 1 mm SF scaffold, we observed a reduction of the cell metabolism in the 3D-HMF/MCF7 and 3D-HMF/231 co-culture in comparison to the respective 3D-MCF7, 3D-231 monoculture at day 14 (**Figures 7B,C**). Moreover, it is interesting to observe that the 3D-HMF/231 metabolism both in 1 mm and 2 mm SF scaffold was slightly higher than the 3D-HMF/MCF7 one at the three time-points selected for the analysis (**Figures 7B–G**). It is interesting to report that we obtain a time/dose-related response when heterotypic 3D-BCM were treated with DOX at the concentration of 30 μg/mL in the 2 mm SF scaffold (**Figures 7F,E**). In the 2 mm SF scaffolds, the metabolic activity of the 3D-HMF/231 is higher than the 3D-231 monoculture. Double-stranded DNA content was evaluated after DOX treatment in co-cultures (**Figures 7D,E** for 1 mm scaffold and **Figures 7H,I** for 2 mm SF scaffolds) by mean of PicoGreen DNA assay. However, if the percentage of DNA content is calculated, the reduction is not strong when we compared the monocultures and cocultures in 1 mm SF scaffolds (**Figures 7D,E**). The results demonstrated a stronger reduction in DNA content when cells were cultured in 2 mm SF scaffolds in comparison to 1 mm. The results were

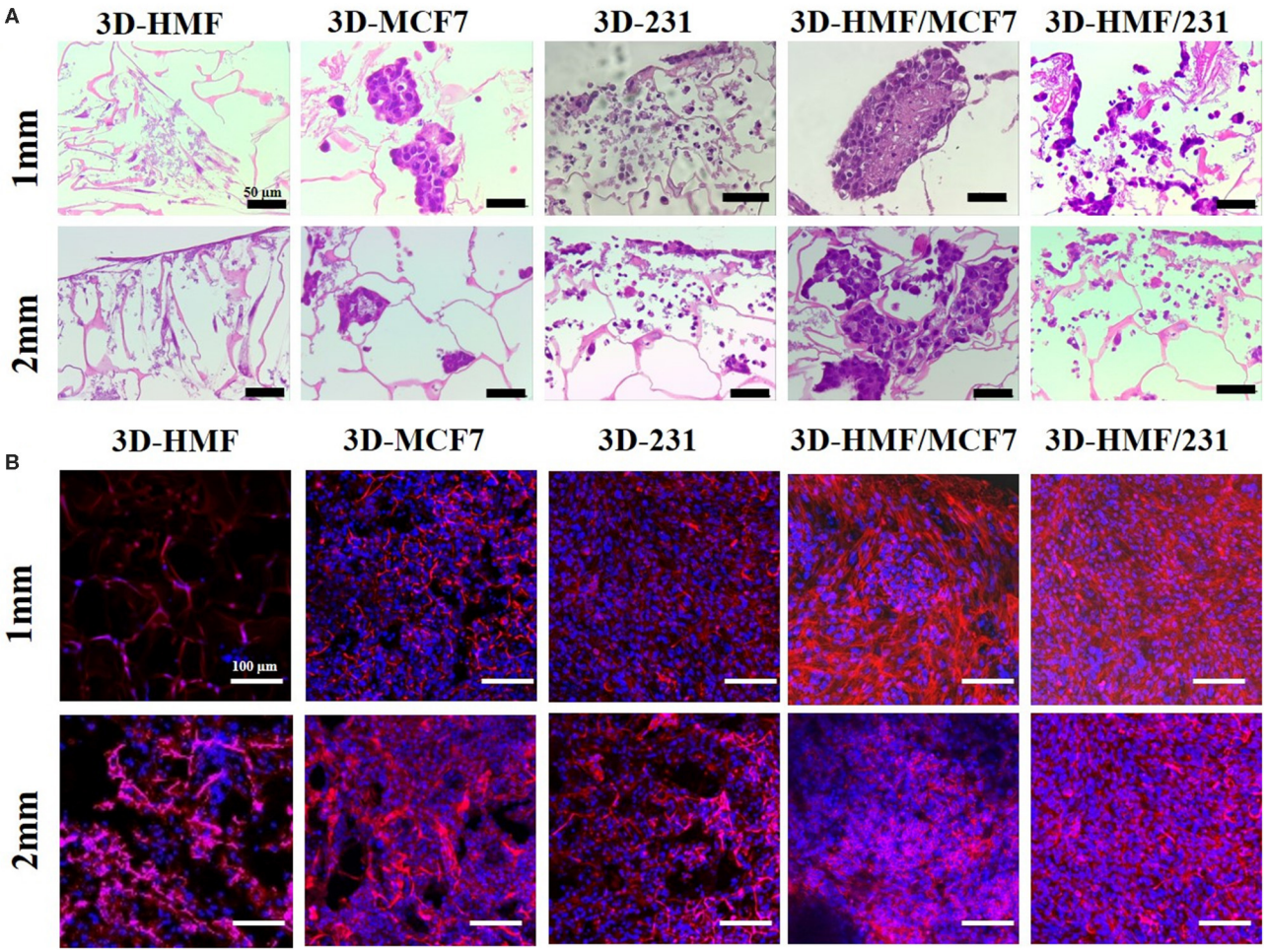

FIGURE 6 | Hematoxylin/eosin staining of developed 3D tumor models constructs at day 14 in both homotypic and heterotypic condition. **(A)** Shows representative images of the 3D-BCM: tumor cells are arranged in spheroid-like architecture (3D-MCF7 and 3D-HMF/MCF7). MDAMB-231 cells spread along the scaffold and do not show an acinar structure (Scale bar 50 µm). **(B)** Representative image of nuclei and cytoskeleton, respectively, stained by DAPI (blue) and Phalloidin (red) (Scale bar 100 µm). The images showed a higher density of cells in heterotypic 3D-HMF/MCF7 and 3D-HMF/231. All the images refer to day 14 of cell culture.

also dose-dependent, showing more decrease in heterotypic cultures in 2 mm SF scaffolds treated with 30 µg/mL of DOX (**Figure 7I**). In 2 mm SF scaffolds, the DNA content is higher in cocultures than in monocultures (**Figures 7H,I**). If only monocultures are considered, both cell metabolism and DNA content decreased in 3D-MCF7, and 3D-231 cultured onto 1 mm SF scaffold. Reduction in DNA content in 2 mm SF scaffolds was higher than in 1 mm SF scaffold (**Figures 7F–I**). The highest decrease in DNA content is reached when 3D-231 in 2 mm SF scaffold is challenged with 30 µg/mL for 72 h (**Figure 7I**).

Gene Expression Profiling in 3D *in vitro* Breast Cancer Model

The expression of genes related to the tumor microenvironment was analyzed. Gene expressions in tumor homotypic and heterotypic cultures were normalized to the homotypic culture of normal mammary fibroblasts (3D-HMF) (**Figure S1**). The up-regulation of Col-I and Fibronectin in the 3D-HMF/MCF-7 and 3D-HMF/231 in comparison to 3D-MCF-7 and 3D-231, both in 1 mm and 2 mm thickness SF scaffolds, is quite relevant. An interesting trend is observed for fibronectin modulation: in 1 mm SF scaffolds, fibronectin level is lower in 3D-HMF/231 when compared to 3D-HMF/MCF-7, while this difference is not statistically significant in 2 mm SF scaffold. MMP-2 is upregulated in both 1 mm and 2 mm SF scaffolds, where 3D-HMF/MCF-7 showed a higher fold change when compared to 3D-HMF/231. In 1 mm SF scaffold, we observed a downregulation of MMP-1 and MMP-3 in co-cultures in comparison to mono-culture, while MMP-2 expression is higher in 3D-HMF/MCF-7 and 3D-HMF/231 in comparison to mono-culture. Regarding the 2 mm SF scaffold, the expression of MMP-1, MMP-2, MMP-3, Col-1 and Fibronectin is slightly higher in co-culture than in mono-culture. If we compare

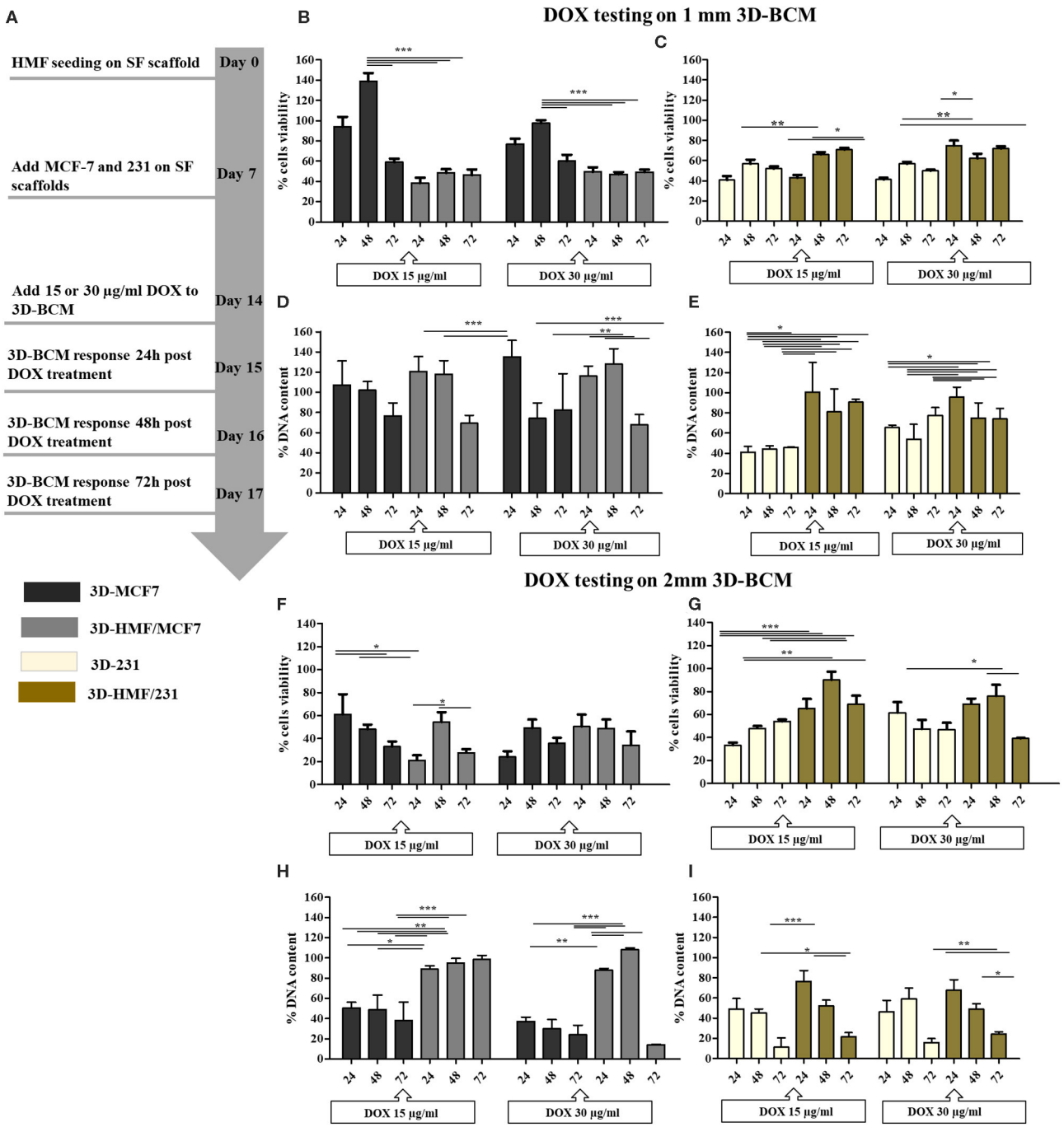

FIGURE 7 | DOX treatment on heterotypic 3D breast cancer model. **(A)** Schematic experimental workflow for the drug testing set-up. The DOX activity is evaluated at 24, 48, and 72 h, starting on day 14 of 3D culture. Anti-proliferative effects of DOX on 3D-MCF7 and 3D-HMF/MCF7 **(B,F)** and 3D-231 and 3D-HMF/231 **(C,G)** was measured by mean of Alamar blue assay in 1 and 2 mm SF scaffolds, respectively. Graphical representation of the amount of double stranded DNA (dsDNA) detected in 3D-MCF7 and 3D-HMF/MCF7 as well as in 3D-231 and 3D-HMF/231 after 24, 48, and 72 h of DOX treatment [**(D,E)** for 1 mm plus **(H,I)** for 2 mm SF scaffolds]. $P < 0.05$ (*) is considered as statistically significant. $^{**}p < 0.01$, $^{***}p < 0.001$ ($n = 3$).

the fold change of the MMP-1 and MMP3 expression in 3D-HMF/MCF-7 and 3D-HMF/231 is higher when the cells were seeded onto 2 mm thickness SF scaffolds in comparison to 1 mm ones.

DISCUSSION

Reliable 3D *in vitro* models can unravel cancer complexity, since they may recapitulate the interactions among the cells of

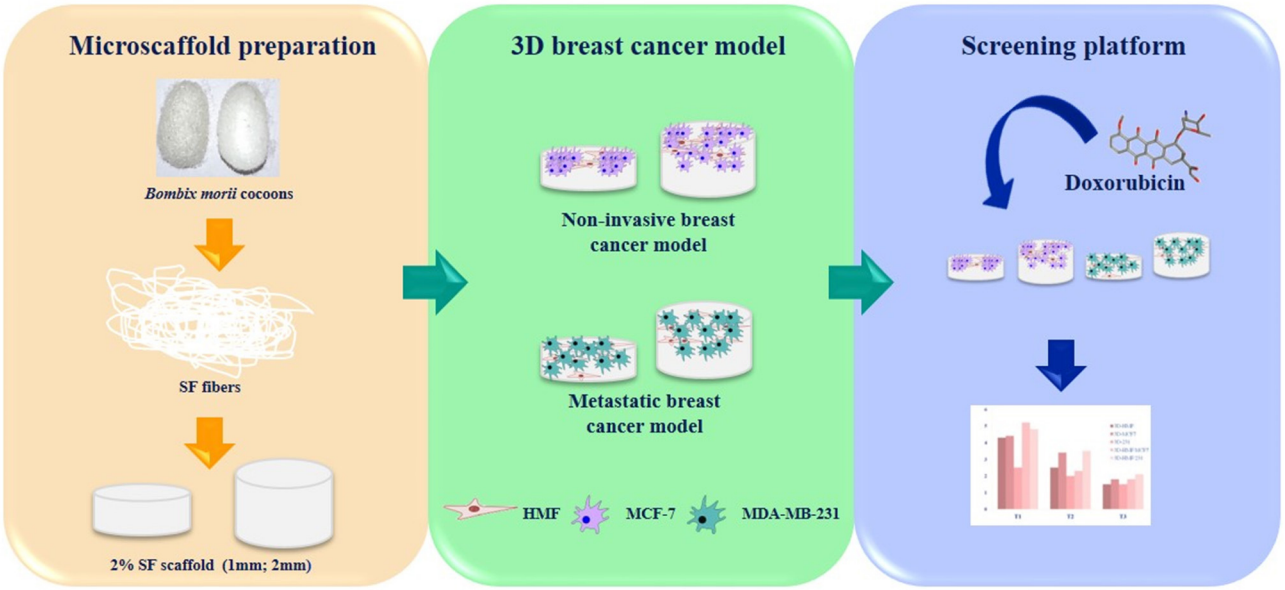

FIGURE 8 | Graphical summary of the experimental setting. Silk fibroin scaffolds are used as matrix to grow different breast cancer cells lines together with mammary fibroblast. The 3D tumor models are challenged with doxorubicin to demonstrate the effect of tumor - stroma cells to the drug response.

the tumor microenvironment (Caballero et al., 2017; Ferreira et al., 2018; Rodrigues et al., 2018; Brancato et al., 2020). The pharmaceutical companies require novel approach to face the lack of efficacy of the current models to assess the anti-cancer agents (Hickman et al., 2014; Lovitt et al., 2016). The present model aims to be a leap toward the adoption of 3D *in vitro* model as platform for drug testing in the preclinical studies. In this work, we propose a 3D-BCM (3D-breast cancer model) where breast cancer cells and mammary normal fibroblasts are seeded together on a tridimensional scaffold. Co-culturing different types of cells gives the opportunity to analyze the interaction between tumor and stroma counterpart. In this work, we exploited the potential of silk fibroin from mulberry silkworm as biomaterial to build a support for tumor cells growth. We have developed an off-the-shelf scaffold that maintains its features for long periods and the work has been focused to investigate how the thickness of the scaffolds effects the re-creation of tumor micro-niche and drug sensitivity (**Figure 8**). Natural silk protein fibroin is an interesting and versatile biomaterial. The process to obtain silk fibroin is straightforward and standardized, which makes this biomaterial quite appealing for biomedical applications (Kundu et al., 2014). Different matrices can be obtained in aqueous solution. Fibroin is used for different range of tissue engineering, regenerative medicine and stem cell research applications, due to its certain important features being protein biopolymer like robust mechanical properties, resilient, biodegradable, low immunogenic response and biocompatibility (Vepari and David Kaplan, 2007; Omenetto and Kaplan, 2010; Kundu et al., 2014; Benam et al., 2015; Rnjak-Kovacina et al., 2015; Pradhan et al., 2016; Yan et al., 2016; Holland et al., 2019). For the fabrication of different scaffolds silk fibroin can be used alone (Talukdar and Kundu, 2012) or in combination with collagen (Khoo et al., 2019), chitosan (She et al., 2008), gellan gum (Kundu et al., 2019) in order to fabricate scaffolds and recapitulate the tumor microenvironment. In addition, the natural source of fibroin is obtained from the mulberry silkworm cocoons (*Bombyx mori*), which are available abundantly and cost-effective in comparison to collagen or other exogenous extracellular matrices used to prepare scaffolds. Silk fibroin is widely used to fabricate *in vitro* different disease models (Kundu et al., 2013a, 2019; Sitarski et al., 2018) including breast cancer one (Wang et al., 2010; Talukdar and Kundu, 2012; Khoo et al., 2019). The tunings of the certain properties like mechanical and degradation are possible (Koh et al., 2015; Holland et al., 2019) as well as the regenerations of different types of tissues (Kundu et al., 2013b; Li et al., 2020). The porosity of the scaffold allows the cancer cell to grow as cluster in a three dimensional structure, resembling the tumor niche (Kundu et al., 2019). Ice-crystals act as porogen during the preparation of silk fibroin scaffolds. The large volume of solution takes more time to freeze, imparting a relatively large crystal size in thicker scaffolds (2 mm) compared to thinner one (1 mm). However, the pore-micro-architecture of both scaffolds is in well-agreement with the porous network of collagen-derived matrices, which is popularly used to investigate breast cancer cells invasion (Sapudom et al., 2015). The aforementioned study indicates least impact of pore sizes on morphology and behavior of breast cancer cells in 3D. Interconnectivity of sponges is linked with cellular distribution and is imparted by the interlocking phenomena of ice-crystals during freezing of silk fibroin solution. By adjusting the concentration of silk solution into designed biomaterials, the release of the drug can be manipulated (Seib et al., 2013). However, to our best of knowledge, this is the first report depicting the different release of drugs based on the thickness

of silk materials. The adsorption of doxorubicin is facilitated by the hydrophobic core of silk as indicated by the binding affinity, which in turn depends on crystallinity (Omenetto and Kaplan, 2010). Therefore, the higher the amount of β-sheet within the porous silk sponges, greater is the loading efficacy and slower is the release. This is observed in our present findings (**Figure 3A**). Silk fibroin being autofluorescent in nature also appear green in DOX free samples (Amirikia et al., 2018). The incorporation of DOX increase the noise, leading to blur fluorescent images. The systematic release of DOX from silk fibroin hydrogels is previously investigated (Seib et al., 2013). It has indicated the impact of weight percentage of silk on drug release. It suggests that 2 wt % of silk provide the highest cumulative release. Therefore, the choice of 2 wt % of SF sponge to model the drug screening platform in the present study is rational. DOX is considered as a model drug in the present study in order to interpret the diffusion of therapeutic molecules through the silk fibroin scaffold, which is further envisioned as low-cost drug screening platform. However, the cross-reactivity of the therapeutic molecules with silk fibroin is needed to be considered and should be investigated systematically for each case.

In this model, commercially available human breast cancer cells and mammary primary fibroblasts are seeded onto 1 or 2 mm silk fibroin scaffolds. In particular, the human mammary primary fibroblasts mimic the tumor stromal counterpart in the 3D-BCM. Two breast cancer cell lines types (luminal and basal phenotype) (Holliday and Speirs, 2011) are coupled with normal fibroblasts in order to recapitulate different subtype of breast cancer microenvironment. The proposed model is not the first in terms of co-culture of tumor and stromal cells (Wang et al., 2010; Hickman et al., 2014; Santo et al., 2016; Brancato et al., 2017a; Dondajewska et al., 2018). However, it shows that the heterotypic model is in the right roadmap toward the fabrication of a functional and efficient 3D tumor model. Other 3D tumor models based on solid porous scaffolds do not take into account of the stromal component (Talukdar and Kundu, 2012; Kundu et al., 2013a; Brancato et al., 2017b). Recently, myofibroblasts or cancer activated fibroblasts (CAF) are considered important player in triggering tumoral progression (Beacham and Cukierman, 2005; Cirri and Chiarugi, 2012; Lovitt et al., 2016; Alguacil-Núñez et al., 2018). Fibroblasts have dual role in tissues. In normal condition, fibroblasts protect the tissues from the cancer cells invasion and proliferation (Werb and Lu, 2016). In stress condition caused by wound or during tumorigenesis, the paracrine loop between cancer cells and fibroblasts triggers the stromal cells transformation, activating the fibroblasts. This phenomenon is known as stromagenesis and runs in parallel with the tumor progression (Castelló-Cros and Cukierman, 2009; Lu et al., 2012; Werb and Lu, 2016). The 3D-BCM proposed in this work is able to capture the evolution of the tumor microenvironment from the initial step where the cancer cells modify the tumor surrounding. Further investigations should assess if the tumor microenvironment transformation is due to the direct contact of the cells or mediated by soluble factors. Our results in terms of cell proliferation in the scaffold are aligned with other previous results where the cells in the scaffolds are metabolically active during the period of 14 days chosen for the model (Brancato et al., 2017a). It is also noteworthy to highlight that the cells in homotypic models are less proliferative when compared to the heterotypic conditions. This shows an interaction among the cell type in the promotion of cell viability and proliferation. Breast cancer cells in the 3D scaffold show a rounded shape, and fibroblast are less elongated than the usual morphology they exhibit in 2D culture. This is highlighted by the SEM and fluorescence images. Histological staining shows that cancer cells copycat the acinar spheroid-like structure. This morphological profile has already recapitulated in previous works (Wang et al., 2010; Talukdar and Kundu, 2012; Wang and Kaplan, 2012; Kundu et al., 2013a). The spheroid architecture is the most resembling tumor spatial organization *in vivo*. ECM secreted by CAF has also a peculiar profile characterized by the over-expression of MMP's, Col I, and fibronectin among the others. Those genes are hallmark for fibrotic phenotype in solid cancers (Bornstein and Sage, 2002; Wong and Rustgi, 2013). Our results state the overexpression of tumor microenvironment markers when the fibroblasts are co-cultured with cancer cells. The up-regulation of MMPs is extremely important features to recapitulate as they play a relevant role in the remodeling of tumor microenvironment. Moreover, our model showed that cancer cells could stimulate the production of collagen by fibroblasts. The CAFs are also investigated as target for anti-cancer agents due to their sophisticated crosstalk between cancer cells and stroma (Zhuo et al., 2009; Conklin and Keely, 2012; Quail and Joyce, 2013). It has also been demonstrated that 3D *in vitro* tumor platform recapitulate better the drug-response. This has been shown when stroma or tumor microenvironment is included in the models (Ridky et al., 2010; Peck and Wang, 2013; Lovitt et al., 2016; Brancato et al., 2017c, 2018). In this work, the use of two different thicknesses to fabricate 3D-BCM also affects the drug response. Based on previous studies (Brancato et al., 2018; Dondajewska et al., 2018) and considering the morphology and thickness of the scaffolds, we selected two different DOX concentrations to carry out our drug-response tests. We have found that 2 mm SF scaffold has retained DOX for a longer time and the release has been slower as compared to the 1 mm SF scaffold. The 2 mm scaffold's behavior has affected the inhibition of proliferation and metabolic activity after DOX treatment. It may be postulated that DOX is entrapped in the scaffold for a longer period, which might have been available for the cells during the 72 h of treatment. The differences in DOX release may be referred to the size of scaffold and the capability to embed more liquid solution. In our opinion, the scaffold thickness is relevant to recapitulate the tumor microenvironment and to make the drug-screening tool more reliable. In this work, the 2 mm scaffold can be considered the best choice for further investigation because allows a slower DOX release and it is able to reduce the cellular metabolic activity and proliferation, better than the 1 mm SF scaffold. 3D-BCM proposed in this work is suitable for drug screening. This model may also support the possibility to perform proliferation assays as well as an easy histological sample preparation along with the gene expression analysis. These are strong advantages of this model toward further characterization for the use as testing platform for anti-cancer drug screening. Bioengineered

cancer models are a valid support to preclinical studies. In this work, we demonstrate that heterotypic 3D *in vitro* cancer model may unravel the crosstalk between cancer cells and tumor microenvironment. We consider that the sample size of the experimental set-up is less, however, previous works demonstrate the reproducibility of the results when SF freeze-dried matrices are used (Talukdar and Kundu, 2012; Kundu et al., 2013a). In future, other cancer types characterized by a fibrotic stroma can be recapitulated using SF scaffolds as lung, colon or pancreatic cancer. The system can be improved by adding endothelial or immune cells in order to investigate the complexity of the tumor microenvironment. In the near future, patient-derived cancer and stromal cells can be seeded onto silk fibroin scaffold to fabricate a 3D-BCM for personalized drug testing. In conclusion, the developed 3D breast cancer model makes closer for the complete understanding of the mechanisms underpinning breast cancer progression.

CONCLUSION

The proposed *in vitro* breast cancer model aims to be used as a tool for drug screening or for investigating tumor microenvironment. Silk protein fibroin scaffold allows us to grow both fibroblasts and cancer cells, which can facilitate the investigation of the tumor-stroma crosstalk as well as cell-extracellular matrix interactions. These interactions are necessary for tumor growth and invasion. This model enlightens the mechanism of tumor migration, cancer associated fibroblast transformation and extracellular matrix remodeling. The model is also a straightforward 3D platform for drug testing due to its easy-to-use and cost-effective features. The interconnectivity and stability of the platform is envisioned to study the invasion of cancer cells over prolong time. The 3D breast cancer model proposed may also be useful for better understanding of the mechanisms behind chemoresistance and metastatic spread.

DATA AVAILABILITY STATEMENT

The datasets generated for this study are available on request to the corresponding author.

AUTHOR CONTRIBUTIONS

VB and SK designed and coordinated the study. VB performed the experiments, analysis of data, and wrote the manuscript. BK performed silk fibroin extraction, scaffold preparation, analyses, and participated in writing the manuscript. All authors read, revised, and approved the final manuscript.

FUNDING

This work was supported by EU-Horizon 2020 grant FoReCaST—Forefront Research in 3D Disease Cancer Models as *in vitro* Screening Technologies (H2020-WIDESPREAD-2014-668983). The authors also acknowledge the FRONTHERA project (Frontiers of technology for theranostics of cancer, metabolic and neurodegenerative diseases) (NORTE-01-0145-FEDER-0000232) and Fundaçao ciencia e tecnologia (FCT grant agreement: PTDC/BTM-ORG/28168/2017 to VB and SK).

ACKNOWLEDGMENTS

We acknowledge the excellent technical assistance provided by Ms. Teresa Oliveira for sectioning and staining of the silk fibroin scaffold for this work. We also thank Dr. Elsa Ribeiro and Dr. Isabel Leonor for the precious support for the SEM microscopy.

SUPPLEMENTARY MATERIAL

The Supplementary Material for this article can be found online at: https://www.frontiersin.org/articles/10.3389/fmats.2020.00116/full#supplementary-material

REFERENCES

Alguacil-Núñez, C., Ferrer-Ortiz, I., García-Verd,ú, E., López-Pirez, P., Llorente-Cortijo, I. M., and Sainz, B. (2018). Current perspectives on the crosstalk between lung cancer stem cells and cancer-associated fibroblasts. *Crit. Rev. Oncol. Hematol.* 125, 102–110. doi: 10.1016/j.critrevonc.2018.02.015

Altrock, P. M., Yoon, N., Bull, J. A., Wu, H., Ruiz-Ramírez, J., Miroshnychenko, D., et al. (2018). The impact of tumor stromal architecture on therapy response and clinical progression. *BioRxiv*. 451047. doi: 10.1101/451047

Amirikia, M. S.,Shariatzadeh, M. A. S., Jorsaraei, G. A., and Mehranjani, M. S. (2018). Auto-fluorescence of a silk fibroin-based scaffold and its interference with fluorophores in labeled cells. *Eur. Biophys. J.* 47, 573–581. doi: 10.1007/s00249-018-1279-1

Arya, N., Sardana, V., Saxena, M., Rangarajan, A., and Katti, D. S. (2012). Recapitulating tumour microenvironment in chitosan – gelatin three-dimensional scaffolds: an improved in vitro tumour model. 9, 3288–3302. doi: 10.1098/rsif.2012.0564

Beacham, D. A., and Cukierman, E. (2005). Stromagenesis: The changing face of fibroblastic microenvironments during tumor progression. *Semin. Cancer Biol.* 15, 329–341. doi: 10.1016/j.semcancer.2005.05.003

Benam, K. H., Dauth, S., Hassell, B., Herland, A., Jain, A., Jang, K.-J., (2015). Engineered in vitro disease models. *Annu. Rev. Pathol. Mech. Dis.* 10, 195–262. doi: 10.1146/annurev-pathol-012414-040418

Bornstein, P., and Sage, H. (2002). Matricellular proteins : extracellular modulators of cell function, Curr. *Opin. Cell Biol.* 14, 608–616. doi: 10.1016/S0955-0674(02)00361-7

Brancato, V., Comunanza, V., Imparato, G., Cor,à, D., Urciuolo, F., Noghero, A., et al. (2017a). Bioengineered tumoral microtissues recapitulate desmoplastic reaction of pancreatic cancer. *Acta Biomater.* 49, 152–166. doi: 10.1016/j.actbio.2016.11.072

Brancato, V., Gioiella, F., Imparato, G., Guarnieri, D., Urciuolo, F., and Netti, P. A. (2018). 3D Breast Cancer Microtissue reveals the role of tumor microenvironment on the transport and efficacy of free-Doxorubicin in vitro. *Acta Biomater.* 75, 200–212. doi: 10.1016/j.actbio.2018.05.055

Brancato, V., Gioiella, F., Profeta, M., Imparato, G., Guarnieri, D., Urciuolo, F., et al. (2017c). 3D tumor microtissues as an in vitro testing platform for microenvironmentally-triggered drug delivery systems. *Acta Biomater.* 57, 47–58. doi: 10.1016/j.actbio.2017.05.004

Brancato, V., Oliveira, J. M., Correlo, V. M., Reis, R. L., and Kundu, S. C. (2020). Could 3D models of cancer enhance drug screening? *Biomaterials* 232:119744. doi: 10.1016/j.biomaterials.2019.119744

Brancato, V., Ventre, M., Imparato, G., Urciuolo, F., Meo, C., and Netti, P. A. (2017b). A straightforward method to produce decellularized dermis-based matrices for tumour cell cultures. *J. Tissue Eng. Regen. Med*. 12, e71–e81. doi: 10.1002/term.2350

Caballero, D., Kaushik, S., Correlo, V. M., Oliveira, J. M., Reis, R. L., and Kundu, S. C. (2017). Organ-on-chip models of cancer metastasis for future personalized medicine: From chip to the patient. *Biomaterials*. 149, 98–115. doi: 10.1016/j.biomaterials.2017.10.005

Cacicedo, M., León, I. E., Gonzalez, J. S., Porto, L., et al. (2016). Modified bacterial cellulose scaffolds for localized doxorubicin release in human colorectal HT-29 cells. *Colloids Surfaces B Biointerfaces*. 140, 421–429. doi: 10.1016/j.colsurfb.2016.01.007

Castelló-Cros, R., and Cukierman, E. (2009). Stromagenesis during tumorigenesis: characterization of tumor- associated fibroblasts and stroma-derived 3D matrices. *Methods Mol Biol.* 522, 275–305. doi: 10.1007/978-1-59745-413-1_19

Cirri, P., and Chiarugi, P. (2012). Cancer-associated-fibroblasts and tumour cells: a diabolic liaison driving cancer progression. *Cancer Metastasis Rev*. 31, 195–208. doi: 10.1007/s10555-011-9340-x

Conklin, M. W., and Keely, P. J. (2012). Why the stroma matters in breast cancer. *Cell Adhes. Migr*. 6286, 249–260. doi: 10.4161/cam.20567

Dondajewska, E., Juzwa, W., Mackiewicz, A., and Dams-Kozlowska, H. (2018). Heterotypic breast cancer model based on a silk fibroin scaffold to study the tumor microenvironment. *Oncotarget* 9, 4935–4950. doi: 10.18632/oncotarget.23574

European Commission (2016). *Cancer Statistics - Specific Cancers*. Brussels: European Commission, 1–16.

Ferreira, L. P., Gaspar, V. M., and Mano, J. F. (2018). Design of spherically structured 3D in vitro tumor models -Advances and prospects. *Acta Biomater*. 75, 11–34. doi: 10.1016/j.actbio.2018.05.034

Fiori, M. E., Di Franco, S., Villanova, L., Bianca, P., Stassi, G., and De Maria, R. (2019). Cancer-associated fibroblasts as abettors of tumor progression at the crossroads of EMT and therapy resistance. *Mol. Cancer*. 18, 1–16. doi: 10.1186/s12943-019-0994-2

Hickman, J. A., Graeser, R., de Hoogt, R., Vidic, S., Brito, C., Gutekunst, M., et al. (2014). Imi Predect consortium, Three-dimensional models of cancer for pharmacology and cancer cell biology: Capturing tumor complexity in vitro/ex vivo. *Biotechnol. J*. 9, 1115–1128. doi: 10.1002/biot.201300492

Holland, C., Numata, K., Rnjak-Kovacina, J., and Seib, F. P. (2019). The biomedical use of silk: past, present. *Future, Adv. Healthc. Mater*. 8:e1800465. doi: 10.1002/adhm.201800465

Holliday, D. L., and Speirs, V. (2011). Choosing the right cell line for breast cancer research. *Breast Cancer Res*. 13:215. doi: 10.1186/bcr2889

Khoo, A. S., Valentin, T. M., Leggett, S. E., Bhaskar, D., Bye, E. M., Benmelech, S., et al. (2019). Breast cancer cells transition from mesenchymal to amoeboid migration in tunable three-dimensional silk-collagen hydrogels. *ACS Biomater. Sci. Eng*. 5, 4341–4354. doi: 10.1021/acsbiomaterials.9b00519

Klein-Goldberg, A., Maman, S., and Witz, I. P. (2014). The role played by the microenvironment in site-specific metastasis. *Cancer Lett*. 352, 54–58. doi: 10.1016/j.canlet.2013.08.029

Koh, L. D., Cheng, Y., Teng, C. P., Khin, Y. W., Loh, X. J., Tee, S. Y., et al. (2015). Structures, mechanical properties and applications of silk fibroin materials. *Prog. Polym. Sci*. 46, 86–110. doi: 10.1016/j.progpolymsci.2015.02.001

Kundu, B., Kurland, N. E., Bano, S., Patra, C., Engel, F. B., Yadavalli, V. K., et al. (2014). Silk proteins for biomedical applications: Bioengineering perspectives. *Prog. Polym. Sci*. 39, 251–267. doi: 10.1016/j.progpolymsci.2013.09.002

Kundu, B., Rajkhowa, R., Kundu, S. C., and Wang, X. (2013b). Silk fibroin biomaterials for tissue regenerations. *Adv. Drug Deliv. Rev*. 65, 457–470. doi: 10.1016/j.addr.2012.09.043

Kundu, B., Saha, P., Datta, K., and Kundu, S. C. (2013a). A silk fibroin based hepatocarcinoma model and the assessment of the drug response in hyaluronan-binding protein 1 overexpressed HepG2 cells. *Biomaterials*. 34, 9462–9474. doi: 10.1016/j.biomaterials.2013.08.047

Kundu, B. A., Bastos, R. F., Brancato, V., Cerqueira, M. T., Oliveira, J. M., Correlo R. L., et al. (2019). Mechanical property of hydrogels and the presence of adipose stem cells in tumor stroma affect spheroid formation in the 3D osteosarcoma model. *ACS Appl. Mater. Interfaces*. 11, 14548–14559. doi: 10.1021/acsami.8b22724

Li, C., Guo, C., Fitzpatrick, V., Ibrahim, A., Zwierstra, M. J., Hanna, P., et al. (2020). Design of biodegradable, implantable devices towards clinical translation. *Nat. Rev. Mater*. 5, 61–81. doi: 10.1038/s41578-019-0150-z

Li, J., Zhou, Y., Chen, W., Yuan, Z., You, B., Liu, Y., et al. (2018). A novel 3D in vitro tumor model based on silk fibroin/chitosan scaffolds to mimic the tumor microenvironment. *ACS Appl. Mater. Interfaces.* 10, 36641–36651. doi: 10.1021/acsami.8b10679

Livak, K. J., and Schmittgen, T. D. (2001). Analysis of relative gene expression data using real-time quantitative PCR and the 2-ΔΔCT method. *Methods* 25, 402–408. doi: 10.1006/meth.2001.1262

Lovitt, C. J., Shelper, T. B., and Avery, V. M. (2016). Cancer drug discovery: recent innovative approaches to tumor modeling. *Expert Opin. Drug Discov*. 11, 885–894. doi: 10.1080/17460441.2016.1214562

Lu, P., Weaver, V. M., and Werb, Z. (2012). The extracellular matrix: a dynamic niche in cancer progression. *J. Cell Biol*. 196, 395–406. doi: 10.1083/jcb.201102147

Madar, S., Goldstein, I., and Rotter, V. (2013). "Cancer associated fibroblasts" - more than meets the eye. *Trends Mol. Med*. 19, 447–453. doi: 10.1016/j.molmed.2013.05.004

Miles, F. L., and Sikes, R. A. (2014). Insidious changes in stromal matrix fuel cancer progression. *Mol. Cancer Res*. 12, 297–312. doi: 10.1158/1541-7786.MCR-13-0535

Omenetto, F. G., and Kaplan, D. L. (2010). New opportunities for an ancient material. *Science* 329, 528–531. doi: 10.1126/science.1188936

Östman, A. (2012). The tumor microenvironment controls drug sensitivity. *Nat. Med*. 18, 1332–1334. doi: 10.1038/nm.2938

Peck, Y., and Wang, A.-D. (2013). Three-dimensionally engineered biomimetic tissue models for *in vitro* drug evaluation: delivery, efficacy and toxicity. *Expert Opin. Drug Deliv*. 10, 369–383. doi: 10.1517/17425247.2013.751096

Pradhan, S., Hassani, I., Clary, J. M., and Lipke, E. A. (2016). Polymeric biomaterials for in vitro cancer tissue engineering and drug testing applications. *Tissue Eng. Part B Rev*. 22, 470–484. doi: 10.1089/ten.teb.2015.0567

Qu, Y., Dou, B., Tan, H., Feng, Y., Wang, N., and Wang, D. (2019). Tumor microenvironment-driven non-cell-autonomous resistance to antineoplastic treatment. *Mol. Cancer*. 18, 1–16. doi: 10.1186/s12943-019-0992-4

Quail, D. F., and Joyce, J. A. (2013). Microenvironmental regulation of tumor progression and metastasis. *Nat. Med*. 19, 1423–1437. doi: 10.1038/nm.3394

Ridky, T. W., Chow, J. M., Wong, D. J., and Khavari, P. A. (2010). Invasive three-dimensional organotypic neoplasia from multiple normal human epithelia. *Nat. Med*. 16, 1450–1456. doi: 10.1038/nm.2265

Rnjak-Kovacina, J., Wray, L. S., Burke, K. A., Torregrosa, T., Golinski, J. M., Huang, W., et al. (2015). Lyophilized silk sponges: a versatile biomaterial platform for soft tissue engineering. *ACS Biomater. Sci. Eng*. 1, 260–270. doi: 10.1021/ab500149p

Rodrigues, T., Kundu, B., Silva-Correia, J., Kundu, S. C., Oliveira, J. M., Reis, R. L., et al. (2018). Emerging tumor spheroids technologies for 3D in vitro cancer modeling. *Pharmacol. Ther*. 184, 201–211. doi: 10.1016/j.pharmthera.2017.10.018

Santo, V. E., Estrada, M. F., Rebelo, S. P., Abreu, S., Silva, I., Pinto, C., et al. (2016). Adaptable stirred-tank culture strategies for large scale production of multicellular spheroid-based tumor cell models. *J. Biotechnol*. 221, 118–129. doi: 10.1016/j.jbiotec.2016.01.031

Sapudom, J., Rubner, S., Martin, S., Kurth, T., Riedel, S., Mierke, C. T., et al. (2015). The phenotype of cancer cell invasion controlled by fibril diameter and pore size of 3D collagen networks. *Biomaterials* 52, 367–375. doi: 10.1016/j.biomaterials.2015.02.022

Seib, P., Pritchard, E. M., and Kaplan, D. L. (2013). Self-assembling doxorubicin silk hydrogels for the focal treatment of primary breast cancer. *Adv. Funct. Mater*. 23, 56–58. doi: 10.1002/adfm.201201238

Senkus, E., Kyriakides, S., Ohno, S., Penault-Llorca, F., Poortmans, P., Rutgers, E., et al. (2015). Primary breast cancer: ESMO Clinical Practice Guidelines for diagnosis, treatment and follow-up. *Ann. Oncol*. 26, v8–v30. doi: 10.1093/annonc/mdv298

She, Z., Jin, C., Huang, Z., Zhang, B., Feng, Q., and Xu, Y. (2008). Silk fibroin/chitosan scaffold: Preparation, characterization, and culture with HepG2 cell. *J. Mater. Sci. Mater. Med*. 19, 3545–3553. doi: 10.1007/s10856-008-3526-y

Sitarski, A. M., Fairfield, H., Falank, C., and Reagan, M. R. (2018). 3D tissue engineered in vitro models of cancer in bone. *ACS Biomater. Sci. Eng*. 4, 324–336. doi: 10.1021/acsbiomaterials.7b00097

Soysal, S. D., Tzankov, A., and Muenst, S. E. (2015). Role of the tumor microenvironment in breast cancer. *Pathobiology* 82, 142–152. doi: 10.1159/000430499

Spill, F., Reynolds, D. S., Kamm, R. D., and Zaman, M. H. (2016). Impact of the physical microenvironment on tumor progression and metastasis. *Curr. Opin. Biotechnol*. 40, 41–48. doi: 10.1016/j.copbio.2016.02.007

Stadler, M., Walter, S., Walzl, A., Kramer, N., Unger, C., Scherzer, M., et al. (2015). Increased complexity in carcinomas: Analyzing and modeling the interaction of human cancer cells with their microenvironment. *Semin. Cancer Biol*. 35, 107–124. doi: 10.1016/j.semcancer.2015.08.007

Talukdar, S., and Kundu, S. C. (2012). A non-mulberry silk fibroin protein based 3D in vitro tumor model for evaluation of anticancer drug activity. *Adv. Funct. Mater*. 22, 4778–4788. doi: 10.1002/adfm.201200375

Tao, Z. Q., Shi, A., Lu, C., Song, T., Zhang, Z., and Zhao, J. (2015). Breast cancer: epidemiology and etiology. *Cell Biochem. Biophys*. 72, 333–338. doi: 10.1007/s12013-014-0459-6

Vepari, C., and David Kaplan, L. (2007). Silk as biomaterial. *Prog. Polym. Sci*. 100, 130–134. doi: 10.1016/j.progpolymsci.2007.05.013

Wang, X., and Kaplan, D. L. (2012). Hormone-responsive 3D multicellular culture model of human breast tissue. *Biomaterials* 33, 3411–3420. doi: 10.1016/j.biomaterials.2012.01.011

Wang, X., Sun, L., Maffini, M., and V., Soto, A. (2010). Sonnenschein, C., Kaplan, D. L., A complex 3D human tissue culture system based on mammary stromal cells and silk scaffolds for modeling breast morphogenesis and function. *Biomaterials* 31, 3920–3929. doi: 10.1016/j.biomaterials.2010.01.118

Werb, Z., and Lu, P. (2016). The role of stroma in tumor development. *Cancer J*. 21, 250–253. doi: 10.1097/PPO.0000000000000127

Wong, G. S., and Rustgi, A. K. (2013). Matricellular proteins: Priming the tumour microenvironment for cancer development and metastasis. *Br. J. Cancer*. 108, 755–761. doi: 10.1038/bjc.2012.592

Yan, P.-L., Silva-Correia, J., Ribeiro, V. P., Miranda-Gonçalves, V., Correia, C., da Silva Morais, A., et al. (2016). Tumor growth suppression induced by biomimetic silk fibroin hydrogels. *Sci. Rep*. 6:31037. doi: 10.1038/srep31037

Yuan, Y., Jiang, Y. C., Sun, C. K., and Chen, Q. M. (2016). Role of the tumor microenvironment in tumor progression and the clinical applications (Review). *Oncol. Rep*. 35, 2499–2515. doi: 10.3892/or.2016.4660

Zhuo, S., Chen, J., Xie, S., Hong, Z., and Jiang, X. (2009). Extracting diagnostic stromal organization features based on intrinsic two-photon excited fluorescence and second-harmonic generation signals. *J. Biomed. Opt*. 14, 020503. doi: 10.1117/1.3088029

Conflict of Interest: The authors declare that the research was conducted in the absence of any commercial or financial relationships that could be construed as a potential conflict of interest.

frontiers in Materials

ORIGINAL RESEARCH
published: 17 July 2020
doi: 10.3389/fmats.2020.00211

3D Structure and Mechanics of Silk Sponge Scaffolds Is Governed by Larger Pore Sizes

Betina M. P. Ferreira[1], *Niklas Andersson*[1], *Erik Atterling*[1], *Jonas Engqvist*[2], *Stephen Hall*[2,3] *and Cedric Dicko*[1,3]*

[1] Division for Pure and Applied Biochemistry, Department of Chemistry, Lund University, Lund, Sweden, [2] Division for Solid Mechanics, Lund University, Lund, Sweden, [3] Lund Institute for Advanced Neutron and X-ray Science, Lund, Sweden

Three-dimensional scaffolds play an essential role in tissue engineering. Although essential, the tunability of the 3D scaffolds mechanical and transport properties remains a challenge. In this work, we present new approaches to advance the field. First, we applied our progressive pH acidification to mimic the natural silk gelation process before ice-templating (−20 and −80°C); second, we fitted the mechanical properties using a connectivity model; third, we fitted the scaffolds mechanical relaxation to understand the transport properties; and fourth we used micro-CT to correlate the process parameters to the scaffolds' performances. Our results suggested that the free shrinkage of the scaffolds determined their final properties. We found, however, that the porosity (above 90%) was anisotropic, similarly the tortuosity (between 1 and 1.3). We identified two major pore dimensions, the first one between 10 and 20 μm, and the second between 50 and 130 μm. Mechanically, our model suggested that the bulk modulus captured the elastic contribution and was controlled predominantly by the silk concentration. We tentatively associated the fractional modulus 1 to the collapse of the larger pores structures and was controlled mostly by the process temperature. We assigned the slow relaxation to the transport of fluid in the silk sponge scaffolds; and the fast relaxation with a viscoelastic relaxation. The silk concentration and process temperatures did not influence the latter. Overall, our use of the tomography, mechanical test, and detailed statistical analysis provides inroads into the interplay between process parameters (silk concentration and process temperature) and the multiple responses of the silk sponge scaffolds. The development of a new mechanical fitting for the compression test helped capture simply the different failure modes in the sponge scaffolds as well as correlating those events to relaxation and eventually transport properties.

Keywords: micro-CT, porous silk scaffolds, ice templating, progressive acidification, compression, stress relaxation, dynamic compression

OPEN ACCESS

Edited by:
Nicola Maria Pugno, University of Trento, Italy

Reviewed by:
Domenico De Tommasi, Politecnico di Bari, Italy
Shangchao Lin, Shanghai Jiao Tong University, China

***Correspondence:**
Cedric Dicko
cedric.dicko@tbiokem.lth.se

Specialty section:
This article was submitted to Mechanics of Materials, a section of the journal Frontiers in Materials

Received: *21 October 2019*
Accepted: *09 June 2020*
Published: *17 July 2020*

Citation:
Ferreira BMP, Andersson N, Atterling E, Engqvist J, Hall S and Dicko C (2020) 3D Structure and Mechanics of Silk Sponge Scaffolds Is Governed by Larger Pore Sizes. Front. Mater. 7:211. doi: 10.3389/fmats.2020.00211

INTRODUCTION

Scaffolds are one of the three main components of tissue engineering, along with cells and bioactive molecules (Yang et al., 2001; O'Brien, 2011). A scaffold serves to mimic extracellular matrix (ECM) environments, which provides a surface/volume for cells to attach, and promotes the desirable interactions between them. The challenge, however, is in mimicking the complexity of

the human machinery that builds tissues and organs (Langer and Vacanti, 2016). The associated high demands (functional and regulatory) placed on scaffolds have limited their success. Indeed, a scaffold (Griffith and Naughton, 2002; DeBari and Abbott, 2019) need to be biocompatible, have suitable mechanical properties, be permeable to fluids, and easy to manufacture to be commercially successful (Howard et al., 2008). Additionally, the scaffolds must facilitate angiogenesis (the ingrowth of blood vessels) once implanted (Varley et al., 2016).

The fabrication of 3-dimensional (3D) scaffolds are central to tissue engineering, and several process strategies already exist. For example: rapid prototyping, gas foaming, salt leaching, fiber bonding, and ice-templating, to name a few (Yang et al., 2001; Elahi et al., 2017). A judicious combination of the processes and the polymers help to address most applications (Yang et al., 2001; Langer and Vacanti, 2016). Nevertheless, the ice-templating technique (Deville et al., 2006) is the most promising one; only for it can use water as the porogen to generate safe and tunable scaffolds for cell culture and *in vivo* implants (Wegst et al., 2010; Deville, 2013; Elahi et al., 2017).

Ice templating is a technique used to form a highly complex and porous material from a solution of proteins or other macromolecules. The method uses a solution of the macromolecule, called a "slurry," that is frozen to a solid. The growing ice crystals form gaps in the slurry, free from the solute, which is the basis of porosity. The forming of crystals is assumed to be randomly distributed and yields a highly complex structure. The frozen solid is immediately freeze-dried. At this step, the solvent is sublimated from the scaffold to produce a foam-like structure (Deville, 2013). By altering the process of the ice template, one can change the outcome of the material properties like different pore sizes and structures (Wegst et al., 2010). Materials obtained by ice-templating are referred to as cryogels (Okay and Lozinsky, 2014). With cryogelation, the scaffold properties (mechanics and transport) are tuned by altering the temperature of the process (freezing regime), the concentration of the polymer, and the solvent used in the process (Okay and Lozinsky, 2014).

The interaction with cells requires, however, more than just correct structures and morphologies. Synthetic polymers cryogels fall short by a lack of favorable interactions with cells; natural polymers, on the other hand, can provide a favorable milieu for the cells to thrive (Tamada, 2005; Reis et al., 2008); and, among them, silk.

Silks, from spiders and insects, has been heavily researched as biomaterials (Vepari and Kaplan, 2007; Holland et al., 2019). On top of being mechanically superior to most other materials, silk is also biodegradable (Vepari and Kaplan, 2007; Rockwood et al., 2011); silk has lower inflammatory responses than other materials (Meinel et al., 2005). Because of its many desirable properties, silk scaffolds have successfully been produced for many different applications, including wound dressings, bone, and cartilage (Vepari and Kaplan, 2007; Rockwood et al., 2011; Holland et al., 2019). The need for degradation *in vivo* is yet to be quantified, and the scaffold needs to make way for the natural growth of new ECM to form healthy tissue.

Nazarov et al. were the pioneers in preparing 3D scaffolds using regenerated silk fibroin (RSF) and the cryogelation technique (Nazarov et al., 2004). They obtained sponges through three different methods, with one being freeze-drying. They used methanol and propanol to induce β-sheet structures formation, silk natural crosslinking mechanism. Several improvements to their initial process followed (Makaya et al., 2009; Min et al., 2009; Rajkhowa et al., 2010; Kadakia et al., 2016; Ming et al., 2016). For example, Tamada et al. prepared different 3D silk scaffolds by freezing with different solvents as a porogen and letting them thaw at room temperature (Tamada, 2005). Cho et al. prepared new silk fibroin scaffolds by freeze-drying and studied the effect on the pore microstructure by altering the pH during the gelation step (Cho et al., 2012). Together, the efforts have been toward greater control of the morphologies (porosity and tortuosity) and the associated mechanics. Until recently, the 3D scaffolds were mechanically weak (in the kPa range); Ak et al. used ethylene glycol diglycidyl ether to prepare RSF scaffolds with a very high compressive modulus of 50 MPa (Ak et al., 2013). The counterpart was poor transport properties. Mallepally et al. in 2015, prepared RSF aerogels with CO_2 as a volatile acidifying sol-gel accelerator; and obtained mechanically tunable scaffolds (up to 174 kPa) with a very high surface area (Mallepally et al., 2015).

Although successful in achieving higher mechanical properties or high transport, accessing scaffolds with high mechanical and high transport properties remains elusive. A measure of success is the level and quality of the scaffold vascularization.

The vascularization in the 3D scaffolds is one of the essential features in a scaffold (Reis et al., 2008; Lovett et al., 2009). For porous biomaterials, the porosity has to be higher than 40% (Wegst et al., 2010), and the material needs to have sufficient stiffness. Still, strength and toughness to mimic the required function for a certain amount of time, depending on the application (Wegst et al., 2010). For each purpose, there are unique associated requirements to be fulfilled (Reis et al., 2008). In regenerative medicine, vascularization is crucial for the cells; 200 μm is the maximum distance from the nearest capillary needed for a cell to survive for an extended period (Lovett et al., 2009; Zhang et al., 2015). For the cartilage and bone tissue engineering field, a wide range of pores and interconnectivity are necessary for a successful scaffold implantation (Griffon et al., 2006; Ribeiro et al., 2019). Generally, larger interconnected pores (300–500 μm) promotes good exchange of nutrients, but not necessarily an adequate cellular growth, while smaller pores (<50 μm) can promote adequate cell adhesion and short-term proliferation (Griffon et al., 2006; Ribeiro et al., 2018, 2019). The interconnection and orientation of the pores are yet to be achieved and understood (Zhu et al., 2014; Qi et al., 2017; DeBari and Abbott, 2019). Mathematical modeling is also a challenge. Only a few articles include numerical analysis in their studies. In 2017, from a query search for "hydrogels and characterization" in the Web of Science database, only 1% of the articles used mathematical models to describe their results (Caccavo et al., 2018).

In 2017, Panda et al. obtained RSF sponges with oriented porous channels using a freeze-casting method (Panda et al., 2017). The mechanical properties (experimental and predicted) did not, however, correlate with the microstructure of the sponges (Panda et al., 2018). Kolahreez and Morshed concluded similarly (Kolahreez and Morshed, 2018). The new commonality with those studies is the lack of accurate 3D structures. In a bid to quantify transport and mechanics, Maniglio et al. used N_2O foaming (Maniglio et al., 2018) to prepare 3D RSF hydrogel scaffolds *in vivo*. They investigated them by micro-computed tomography (micro-CT). They found a correlation between the 3D architecture and the mechanical properties when they controlled the RSF β-sheet structures content. Ribeiro et al. used a salt-leaching and freeze-drying approach to produce 3D scaffolds and correlated the morphology (micro CT) to the mechanics and cell performance (Ribeiro et al., 2019). The study highlighted a gradient in porosity and subsequent gradient in functional responses.

In this work, we present new approaches to advance the field. First, we applied our progressive pH acidification to mimic the natural silk gelation process before ice-templating; second, we fitted the mechanical properties using a connectivity model; third, we fit the scaffolds mechanical relaxation to understand the transport properties; and fourth we use micro-CT to correlate the process parameters to the scaffolds' performances.

MATERIALS AND METHODS

Degummed silk fibers from Mulberry (*Bombyx mori),* were obtained from an online silk supplier (Wild Fibres, http://www.wildfibres.co.uk). Glucono-δ-lactone (GDL) was purchased from Sigma Aldrich and used directly.

Sponge Scaffold Preparation

Regenerated Silk fibroin (RSF) was prepared using a modified protocol described by Rockwood et al. (2011). Briefly, 1 g of degummed silk fibers were dissolved in 9 M LiBr (Sigma-Aldrich) at 70°C for 15 min. After dissolution, the solution was left to cool for 5 min and then immediately transferred to a cellulose dialysis tube (Sigma-Aldrich) with a molecular weight cut-off of 12 kDa. The silk solution was dialyzed for 3 days against 10 mM phosphate buffer at pH 7.2. The dialysis buffer was changed once a day. After dialysis, the solution of silk is recovered in a 50 ml falcon tube and centrifuged at 4,000 rpm for 15 min. The final concentration of the solution was determined by oven drying an aliquot.

The gelation of silk was induced using GDL (Del Giudice et al., 2017; Dicko and Del Giudice, in preparation). The acidification using 0.5% GDL mimics the stable cross-links found in *Bombyx mori*; besides, the progressive acidification allows for a homogeneous gelling of the silk solution.

For sponge scaffold fabrication, 1 ml Henke Sass Wolf Luer syringes with an inner diameter of 4.69 mm, were chosen as the most suitable container to yield the correct form factor, as well as the best alternative to perform the various experimental characterization methods needed. Immediately after mixing the GDL and the silk solutions (**Table 1**), a small volume of air was drawn into the syringe to prevent the silk solution from touching the syringe plunger; and, ∼200 µl silk solution was then withdrawn in the syringe. Lastly, the plunger was moved further up to make sure no silk solution was present in the syringe tip; the samples gelled for 18 h. After gelation, the syringes were placed into freezers at −80 and −20°C, according to **Table 1**, for 24 h. After freezing, the samples were loaded into a freeze-drier (Labconco Freezone 4.5 L) for 24 h to sublimate the water. The temperature in the desiccator was −45°C, and the pressure was 5 mbar.

TABLE 1 | Factorial design for the scaffold preparation.

Run order	Target silk conc. [mg/ml]	Temperature [°C]
1	30	−80
2	30	−20
3	15	−20
4	25	−20
5	5	−80
6	10	−80
7	15	−80
8	20	−20
9	10	−20
10	5	−20
11	20	−80
12	25	−80

The sponge scaffolds were weighed and imaged after each preparation step. Dimensions of the sponge scaffolds were extracted from images using ImageJ. The calculations were performed in the image processing software Fiji (Schindelin et al., 2012).

Factorial Analysis

Sponge scaffolds were prepared using a full factorial design (Minitab, Minitab Inc.). We used six different silk concentrations and two different end freezing temperatures, summarized in a 2 × 6 factorial table of 12 samples (**Table 1**). The samples in **Table 1** were randomized to eliminate systematic errors occurring during the experiments, and every step in the preparation and characterization of the samples was conducted in this order. For each run, we prepared seven samples.

The analysis of the factorial design consisted of an ANOVA and regression. Briefly, the *p*-value indicated if a factor has a significant effect on the observable. The factor had a significant impact if the *p*-value is lower than 0.05. The *F*-value provided a ranking for the strength of the effects relative to one another. The larger the *F*-value, the stronger the effect of the factor on the observable. In addition to this, a linear regression combining the factors to explain the observable (a.k.a. response) was computed and reported as Pearson coefficient (R^2). The closer the R^2 was to 100%, the better the linear fit of the factors to explain the observable. The predictability of the regression was measured by the predicted R^2. The closer to 100%, the better for the

predicted R^2. Interestingly a poor R^2 predicted is indicative of a regression model that is not representative of the variance of the observable. The responses from all the characterization methods were evaluated using the Minitab software (Minitab, Inc.).

X-Ray Tomography and Image Analysis

X-ray tomography data were acquired using a Zeiss Xradia XRM520, at the 4D Imaging Lab at Lund University, with a source voltage of 50 kV with 1,601 radiographs over 360 degrees. Tomographic reconstruction provided 3D image volumes of 1,000 × 992 × 1,014 voxels. Voxel dimensions were 3 × 3 × 3 μm^3. In the following, 2D sections through the volumes perpendicular to the vertical axis of 992 × 1,014 pixels are referred to as "slices." We imaged every scaffold in the dry state, the top 100 and bottom 100 slices were discarded from the analysis to minimize edge effects. The remaining 800 slices were analyzed using Fiji (ImageJ, NIH) and TauFactor (Cooper et al., 2016). The method of pre-processing the images (Fiji) consisted of (i) adjusting the brightness, (ii) applying a threshold, and (iii) removing noise using the "remove outliers" function. The porosity and tortuosity of the stack of 2D images were calculated using TauFactor.

Fast Fourier Transform (FFT) Processing

FFT processing of the images was carried out to obtain quantitative information about the average size of the objects exhibiting an absorption contrast in the scaffold. The FFT was performed on the thresholded images and averaged through the stack (Blaise et al., 2010). Before the FFT, the images were truncated to 822 × 844 pixels to avoid any edge effects. The average FFT images were then radially averaged to produce a one-dimensional radial profile. The analysis was performed using the conventional 2D FFT routine of Matlab. The one-dimensional profile was then interpreted as a small- and wide-angle X-ray scattering. Here we reported the various correlation lengths found in the scaffold.

Permeability

The experimental setup used a modified version of the falling head gravity-based method with the adapted Darcy's law of Pennella et al. (2013). By using this modified setup, the hydraulic conductivity, K, and permeability, k, could be calculated, see (2), (3). Hydraulic conductivity is a measure of how easily water flows through a porous medium, whereas permeability measures how well a material can transmit a fluid. Thus, the permeability has nothing to do with the liquid itself; instead, it is an intrinsic property of the material.

The volumetric flow through the porous medium is given by (1),

$$Q = KiA = \frac{KH}{L} = -a\frac{dH}{dt} \tag{1}$$

where Q is the volumetric flow throw the porous medium, $i = \frac{H}{L}$ is the hydraulic gradient, A is the cross-sectional area of the scaffold, H is the distance between two free water surfaces, and L is the height of the scaffold. With a moving water column, H translates to H_1 (H at time $t = 0$) and H_2 (H at time $t = T$) after integration of (1), which yields the expression for the hydraulic conductivity, K:

$$K = \frac{a}{A}\frac{L}{t}ln\frac{H_1}{H_2} \tag{2}$$

In (2), a is the cross-sectional area of the standpipe, t is the duration of the experiment (i.e., the time it takes for the water column to move from H_1 to H_2). The time (t) was measured in the experiment, as well as the height of each scaffold. The other parameters in (2) were kept constant.

Once we obtained the hydraulic conductivity K, we calculated the permeability k as follows:

$$k = \frac{K\mu}{\rho g} \tag{3}$$

μ is the viscosity of water, ρ is the density of water, and g is the gravitational constant.

Fourier-Transform Infrared Spectroscopy (FTIR)

FTIR spectra of the sponge scaffolds were acquired using a Nicolet iS5 FTIR Spectrometer. We collected three spectra for each sponge scaffold: at the bottom, middle, and top. Rapid comparison of the three positions allowed us to examine the anisotropic properties of the samples. Each spectrum was the average of 32 scans from 550 to 4,000 cm^{-1} at a resolution of 4 cm^{-1}.

The FTIR-ATR spectra were further processed to extract four structural parameters, namely: the crystallinity degree, the tyrosine ratio, and the amide I/II ratio. We calculated the crystallinity degree (Bhat and Nadiger, 1980) of silk fibers by comparing the peaks' intensities at 1,263 and 1,230 cm^{-1} as follows:

$$Crystallinity\ degree\ (\%) = \frac{A_{1263}}{A_{1230} + A_{1263}} * 100 \tag{4}$$

Where A_{1263} and A_{1230} are the intensities of the peaks at 1,263 and 1,230 cm^{-1} respectively.

The tyrosine ratio was calculated by estimating the area under the tyrosine peaks at ± 830 and ± 850 cm^{-1} and computing the ratio of intensities at 850 / 830 cm^{-1}. The weak features at ± 850 and ± 830 cm^{-1} make a doublet attributed to Fermi resonance of the aromatic side chain of the tyrosine residue. The ratio is indicative of the local environment of tyrosine residues within the fibers and by extension, the local environment of the amorphous regions of the silks (Monti et al., 1998).

Further, the ratio of the maximum intensities of amide I (at around 1,640 cm^{-1}) and II (at about 1,540 cm^{-1}) peaks was calculated to estimate the total change in secondary structure upon treatment (Ishida and Griffiths, 1993; Boulet-Audet et al., 2015). Also, the amide I region (1,600–1,700 cm^{-1})

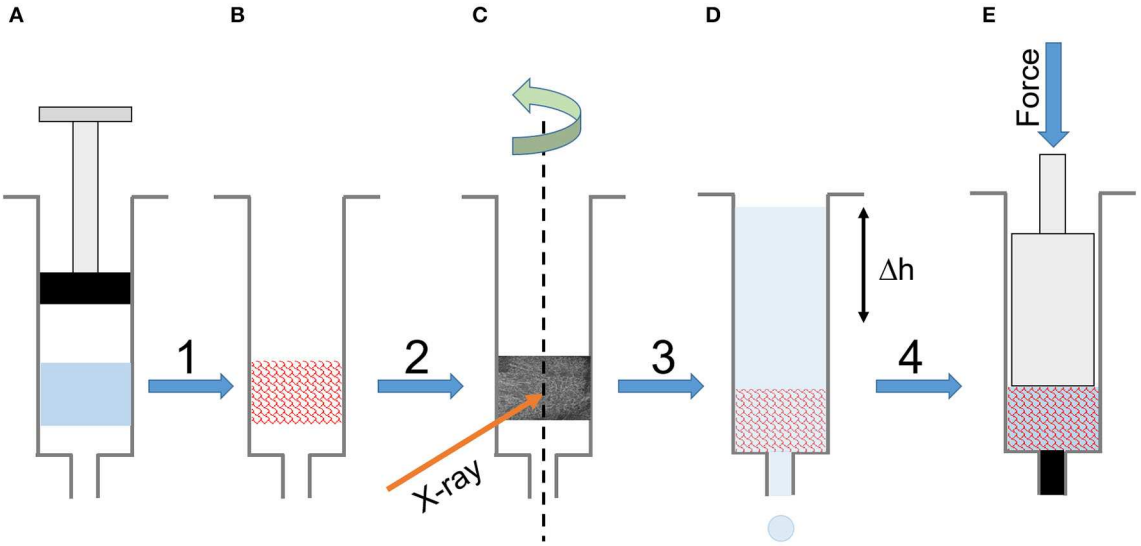

FIGURE 1 | Experimental workflow. **(A)** The silk solution gelled in a 1 mL syringe. **(B)** The final scaffold after freezing and freeze-drying. **(C)** Tomography of the dry scaffold in the syringe. **(D)** Permeability measurement in the syringe using a timed water column elution. **(D)** The mechanical compression of the wet scaffold in the syringe.

was deconvoluted to extract the secondary structure composition of the silks.

Mechanical Tests and Analysis

For the mechanical tests, we used a Mach-1 System model V500c from Biomomentum. The load cell had a nominal maximum load of 1.5 N and a resolution of 75 μN. The mechanical tests were performed in the same syringes that the sponges were cast in, to avoid any destruction or alteration of the intricate architecture of the sponge. The measurements were performed on the wet sponge scaffolds. Initial measurements showed that in the dry state, the sponges were too brittle for any reliable analysis. We conducted a compression test with a 3 mm cylindrical flat-ended indenter. In the low strain regime (<10%), we assumed that the compression was unconfined. For each sample, we equilibrated the sponge scaffolds in double-distilled water for 48 h; then, the samples were compressed at a velocity of 0.005 mm/s and relaxed. We applied three cycles of compression and relaxation consecutively. After each relaxation ramp (changes in force < 0.001 gf/min), the samples were dynamically compressed at 0.5 Hz with an oscillatory amplitude of 0.1 mm. The procedure was repeated two times at 1 and 2 mm depth. The initial contact criterion was 0.1 gf with a stage velocity of 0.02 mm/s.

Compression Test Analysis

To analyze the stress-strain curve, we use the approach developed by Chen et al. (2010). The model was initially derived to relate silk cocoon connectivity and mechanical properties. Briefly, the model describes a shared feature, namely the apparent control of mechanical properties by loss of connectivity of bonding between component materials. The model assumes several different activation effects (i.e., with fractional contribution f_i). The relation between stress, σ, and the initial composite modulus Y becomes:

$$\sigma = Y\varepsilon\left\{1 - \sum_i f_i exp\left[-\left(\frac{\varepsilon_{ai}}{\varepsilon}\right)^2\right]\right\} \quad (5)$$

Where $f_i = \frac{Y_i}{Y}$, with Y_i and ε_{ai} the associated modulus and activation strains, respectively. The force-displacement curve was transformed into stress and strain by normalizing with the cross-sectional area and the initial length of the scaffold, respectively. We determined the number of activations by a brute force method to obtain the Y_i and ε_{ai}. The experimental data were fitted using one, two, or three activations; and the outcome of each model (χ^2) in a pair-wise manner (F-test) to determine which of the model did not overfit the experimental data.

Stress Relaxation Analysis

We use here a simple framework inspired by Meghezi et al. (2017). We modeled the load (L) relaxation by a sum of three exponential decays; with a short, intermediate, and long-time decay contributions as follows:

$$L(t) = L_{short}\exp\left(-\frac{t}{\tau_{short}}\right) + L_{intermediate}\exp\left(-\frac{t}{\tau_{intermediate}}\right) + L_{long}\exp\left(-\frac{t}{\tau_{long}}\right) \quad (6)$$

Where $\tau = \frac{\eta}{G}$, with η being the viscosity and G the modulus of the material.

Not to overfit the data, we fitted the relaxation curves with one, two, and three decay curves; and the outcome of

each model (χ^2) in a pair-wise manner (F-test) to determine which of the model did not overfit the experimental data. All the calculations were performed using custom Matlab (The Mathworks Inc.) scripts.

Dynamic Tests

the dynamic test (sinusoid) was analyzed using the Mach-1 Analysis software (Biomomentum SOP04). We extracted the elastic modulus E, storage modulus E', loss modulus E", and the Phase. The relation between moduli was as follows:

$$E = E' + iE'' \tag{7}$$

TABLE 2 | Shrinkage of the sponges in different silk concentration and temperature.

Concentration [mg/ml]	Temperature [°C]	Shrinkage [%]
5	−80	56.76
5	−20	58.59
10	−80	33.05
10	−20	33.57
15	−80	30.61
15	−20	26.95
20	−80	15.46
20	−20	33.57
25	−80	20.46
25	−20	21.82
30	−80	24.19
30	−20	31.89

RESULTS

For consistency, but with some restrictions, we prepared all the samples (gelled and freeze-dried) in 1 mL syringes. The unique form factor allowed us to perform all the characterizations (except FTIR-ATR) with a minimum of sample handling. The sample preparation resulted in 84 silk sponge scaffolds, cylindrically shaped of ∼1 cm in height. **Figure 1** summarizes the experimental workflow.

Remarkably, all of the scaffolds exhibited shrinkage, noticeable to the naked eye, which led to a quantification of this shrinkage (**Table 2**). The shrinkage proved to be significantly affected by silk concentration ($p = 0.006 < 0.05$) but not statistically by temperature ($p = 0.221$), see **Table 3** for details. Henceforth, we included the shrinkage as a covariate in all the ANOVA analysis.

X-Ray Tomography and Image Analysis

Figure 2 shows a typical 3D X-ray tomography image of a sponge scaffold.

The image slices from the tomography were then pre-processed using the Fiji software (Schindelin et al., 2012). **Figure 3** illustrates the steps.

Analysis of Correlation Features

For determining the average size of the objects, images obtained perpendicularly to the z-axis were used (see materials and methods). **Figures 4A,B** illustrate the one-dimensional radial profiles at −20 and −80°C, respectively. Although featureless, the curves presented three distinct regions (for a pairwise comparison, see **Figures S1–S6**). First, in the higher q region (i.e., smaller size in real space), all curves regardless of temperature and concentration displayed a small peak. The dimensions were between 4 and 5 μm. We assigned this feature to the thickness

TABLE 3 | ANOVA[a] and regression analysis of the factorial design responses.

Responses	Factors	p-value	F-value	R^2 (%)	R^2 predicted (%)
Permeability	Concentration	**0.014**	23.01	96.57	75.62
	Temperature	**0.029**	15.47		
Total Porosity	Concentration	**0.000**	68.44	98.59	91.88
	Temperature	0.043	7.27		
Tortuosity XY	Concentration	**0.001**	36.68	97.46	85.37
	Temperature	**0.034**	8.42		
Tortuosity Z	Concentration	**0.000**	110.11	99.11	94.87
	Temperature	**0.061**	5.82		
Amide I/II ratio	Concentration	**0.003**	18.97	95.03	71.4
	Temperature	0.404	0.83		
Tyrosine ratio	Concentration	**0.004**	16.11	94.16	66.38
	Temperature	0.74	0.12		
Crystallinity index	Concentration	0.708	0.6	40.57	0.00
	Temperature	0.539	0.44		
Shrinkage[b]	Concentration	**0.006**	13.37	93.23	60.99
	Temperature	0.221	1.95		

The significant factors are in bold.
[a] *The ANOVA was run with shrinkage (**Table 2**) as a covariate.*
[b] *Independent ANOVA for shrinkage to estimate its impact.*

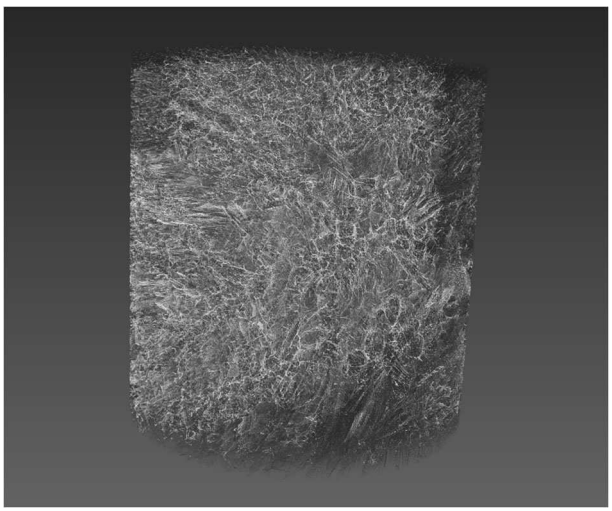

FIGURE 2 | 3D rendering of a silk sponge scaffold reconstructed from computer tomography (CT) slice images. A typical silk sponge scaffold image consisted of 1,000 slices of 992 × 1,014 pixels, at 3 × 3 × 3 μm^3 voxel size. The z-axis is along the page vertical direction and the syringe direction.

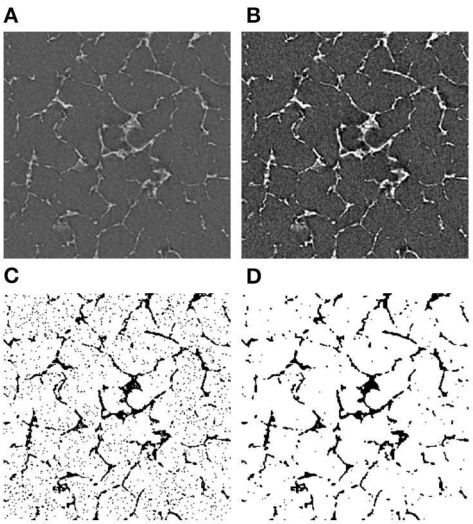

FIGURE 3 | Image processing algorithm for CT images. **(A)** The original image, **(B)** the adjusted brightness, **(C)** the thresholded image, and **(D)** the final noise-free image. The bright areas represent the silk in **(A,B)**. In the binarized images **(C,D)**, the dark areas represent the silk.

of the silk layers in the scaffold. Second, in the mid-q region, we found a broad peak with a varying position. The associated dimensions were between 10 and 20 μm. Third, at low q, we found a mixture of broad and sometimes defined peak.

The associated dimensions were between 50 and 130 μm. The two last correlation lengths were assigned to pore sizes in the scaffold. **Figure 4C** shows the dependence of the three correlation lengths with silk concentration and temperature. The inaccuracy in the peak positions in **Figures 4A,B** precluded any ANOVA. Nevertheless, we found that the silk thickness and the small pore sizes were independent of silk concentration and temperature. In contrast, the larger pore sizes were independent of the silk concentration at −80°C, and decreased in size with silk concentration at −20°C. Note that at concentrations above 25 mg/ml no peaks were discernable in the low q region. The absence of peak could be that the feature was larger than the instrument measurement range, or that the feature simply disappeared in the sample.

Porosity and Tortuosity

The thresholded stack (1,000 slices of **Figure 3B** type binary images) was then analyzed using TauFactor (Cooper et al., 2016) to extract the total porosity and the tortuosities in the XY plane normal to the z-axis (syringe direction), and the z-axis direction. **Figure 5** summarizes the results.

Panel A in **Figure 5** illustrates the dependence of the total porosity with silk concentration and process temperature. The ANOVA was significant for both silk concentration ($p = 0.00$, $F = 68.44$) and process temperature ($p = 0.043$, $F = 7.27$). Interestingly the effect of the silk concentration on the total porosity was almost 10 times stronger than process temperature. The high regression coefficients confirmed the importance of the two factors in explaining the variance of the total porosity. The tortuosity was defined by the ratio of the real open paths through the sponge scaffolds to its physical dimensions. The tortuosity in the XY plane was defined relative to the diameter of the sponge scaffold; the tortuosity in the Z-direction was defined relative to the sponge scaffold height. The ANOVA was significant for both tortuosities for silk concentration, but only significant in the XY-plane for the process temperature.

Similarly, to the porosity, the silk concentration had a stronger effect as compared to the process temperature (F-values). The regression coefficients were high, as well. **Figure 5B** goes further with a plot of the anisotropy in tortuosity; with increasing silk concentration, the sponge scaffolds were more tortuous in the Z-direction compared to the XY-plane.

We captured the transport properties by computing the hindrance factor [i.e., λ^2/ε (the tortuosity squared divided by the porosity)]. The hindrance factor reflects the resistance to flow in a porous matrix (Epstein, 1989; Moreira and Coury, 2004). We combined the hindrance at −20 and −80°C in the XY plane (**Figure 4C**) and the Z-direction (**Figure 4D**). We tentatively fitted the change in hindrance factor using a sigmoid function with upper bounds (three and six) from the *Bombyx mori* cocoons (Horrocks et al., 2013). We found that in the XY-plane, the hindrance was lower than the lowest hindrance factor found for the *Bombyx mori* cocoons. In contrast, in the Z-direction at 30 mg/mL of silks, the hindrance factor was comparable to the lowest hindrance factor found for the *Bombyx mori* cocoons.

Permeability

The permeability of a fluid through a porous scaffold is dependent on porosity, as well as pore size and inter-connectivity of the pores (Horrocks et al., 2013). A permeability test, therefore, describes many different aspects of the scaffold properties that are important to its success once under operation. The results from the scaffold permeability test showed obvious correlations to both

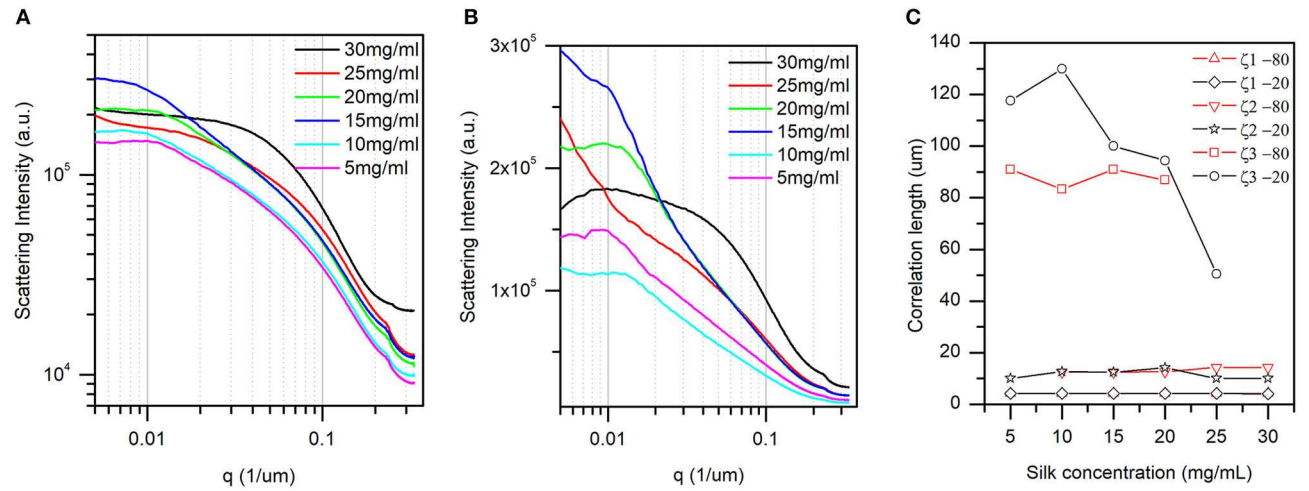

FIGURE 4 | The one-dimensional radial average of the 2D Fourier transform slices (see materials and methods for details). **(A)** At −20°C, and **(B)** at −80°C. The pairwise comparison is found in **Figures S1–S6**. **(C)** Correlation lengths found at −80°C and −20°C and their dependence with silk concentration. Briefly, the peak positions identified in panel **(A,B)** are converted to representative dimensions (correlation lengths) in the sponge scaffolds (see text for details). Only correlation length 3 (x3) at −20°C displayed an inverse linear dependence with silk concentration.

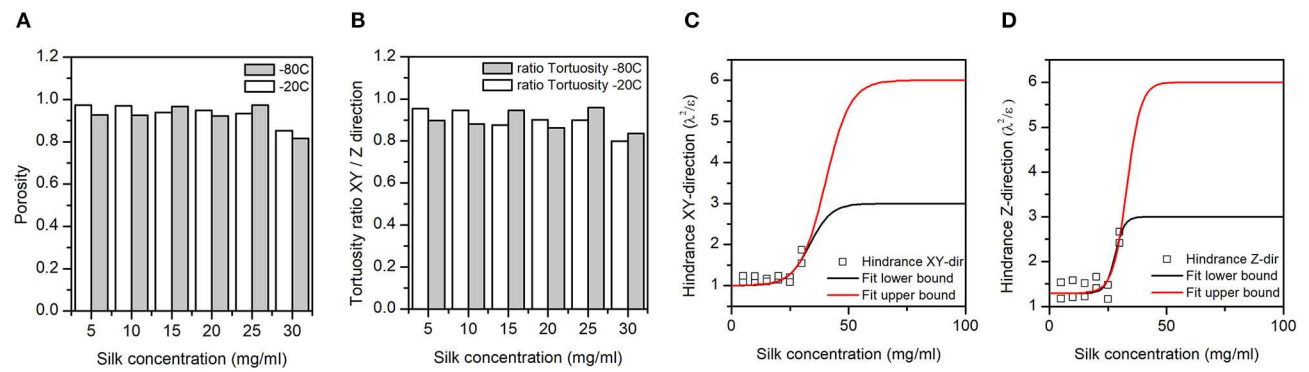

FIGURE 5 | (A) Silk sponge scaffolds' fractional porosity (ε). **(B)** The ratio of the silk sponge scaffold XY plane to Z-direction tortuosities (λ). A ratio of 1 meant no anisotropy in the tortuosity; a ratio < 1 meant a higher tortuosity in the Z-direction as compared to the XY plane. **(C,D)** Hindrance factor (λ^2/ε) in the XY and Z-directions, respectively. The hindrance, or resistance to flow, is tentatively fitted to a sigmoid with lower and upper bounds (three and six) defined by *Bombyx mori* cocoon hindrance (Horrocks et al., 2013). Note that we pulled the −20 and −80°C hindrance together for the fit.

the concentration and the end freezing temperature (**Figure 6**). We excluded the 5 and 10 mg/ml sponge scaffolds because they did not laterally fill the syringe sufficiently. Nevertheless, we observed that the permeability was significantly affected by the concentration of silk ($p = 0.014$, $F = 23.01$) and by the temperature ($p = 0.029$, $F = 15.47$). The marginally higher F-value for concentration suggested that the silk concentration was more important than the temperature. The regression analysis showed a sufficiently high predicted R^2 (75.62%) to predict the permeability.

Fourier-Transform Infrared Spectroscopy (FTIR)

Figures S7, S8 summarize the raw FTIR-ATR spectra and the extracted parameters (amide I/II ratio, crystallinity degree, tyrosine ratio). **Table 3** summarizes the statistical analysis of the FTIR responses. We observed that the concentration had a significant impact on the amide I/II ratio ($p = 0.003$, $F = 18.97$), and tyrosine ratio ($p = 0.004$, $F = 16.11$); but no significant effect for the process temperature. We found that neither the silk concentration or temperature significantly affected the crystallinity degree. To interpret the observation, we need to understand the interplay between amide I/II ratio, crystallinity degree, and tyrosine ratio. Briefly, the assumption was that a change of structure (i.e., changes in the amide I/II ratio) would be reflected by a change in the amorphous domains of the silk sponge scaffolds (i.e., the tyrosine ratio); and, or by a change in the crystallinity (i.e., crystallinity degree). In our case, we observed a significant effect of concentration on the amide I/II ratio and a significant effect only in the tyrosine ratio. We interpreted, therefore, that the concentration of silk

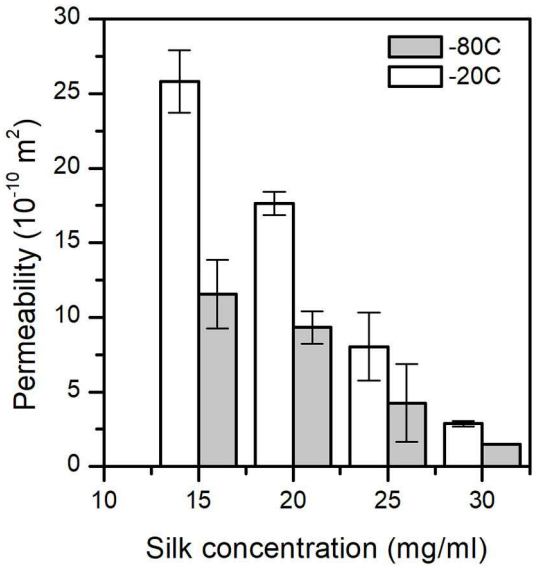

FIGURE 6 | Sponge scaffolds' permeability ($n = 3$) at different process temperatures and silk concentrations.

mainly affected the amorphous domains. The high R^2 and R^2 predicted supported the fact that the concentration predicted a change in structure (Amide I/II ratio). The weaker R^2 predicted for the tyrosine ratio suggested instead that another underlying effect was needed to predict the tyrosine ratio from solely the concentration.

Mechanical Properties: Compression Test

The mechanical properties of a sponge scaffold are dependent on its architecture on a macroscale as well as on a microscale. We can extract from a compression test, important parameters to the mechanical properties, such as bulk modulus and relaxation times. From the dynamic compression test (sinusoid), we obtain the loss and storage moduli. Note that although not performed, we would expect a difference in the mechanical properties in the Z-direction, and normal to the Z-direction, as found from the tomography results.

For the analysis of the compression test, we went beyond state of the art and proposed a new application to the model developed by the Oxford silk group (Chen et al., 2010). We noted that our sponge scaffolds materials had stress-strain profiles that had the same form as those of silkworm silk cocoons (Chen et al., 2010). The main feature shared was the apparent control of mechanical properties by loss of connectivity of bonding between the component materials. Such loss occurs either via fiber-fiber bonding for random fiber in cocoons or via particle-matrix bonding for particulate composites. Here, we apply the cocoon connectivity model to describe the loss of connectivity between layers and pores within the sponge scaffold.

Figures 7A,B illustrate that the cocoon connectivity model fits the sponge scaffolds' compression tests. We observed a good agreement of the model to the experimental data.

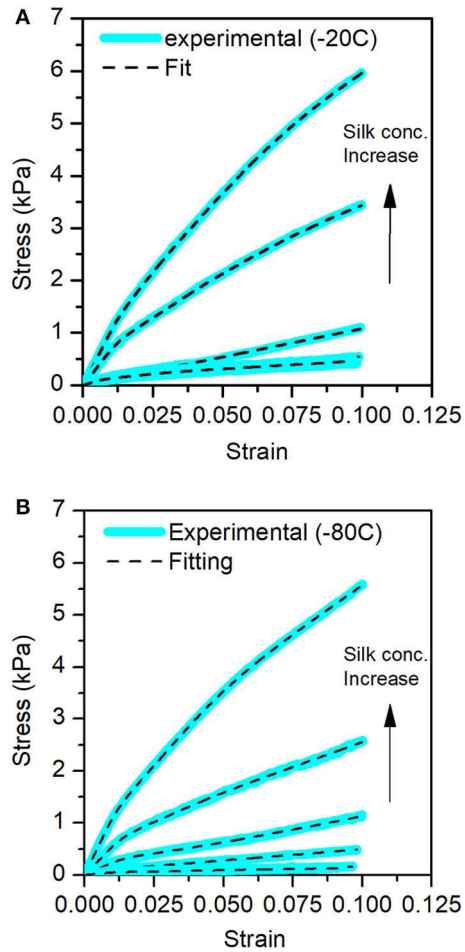

FIGURE 7 | Stress-Strain curves for the different sponge scaffolds obtained from the compression tests. In blue, the experimental data and the fits in the dashed lines. **(A)** At −20°C and **(B)** at −80°C.

Table 4 summarizes the bulk, first, second, and third moduli values of the sponge scaffolds (see materials and methods section for model selection). For the sponge scaffolds prepared at −20°C, the bulk modulus varied from 15.6 kPa for 5 mg/ml to 107.3 kPa for 30 mg/ml of silk concentration. For the sponge scaffolds prepared at −80°C, this variation was from 5.4 kPa for 5 mg/ml of silk concentration to 112 kPa for 30 mg/ml.

The statistical analysis (**Table 5**) showed that silk concentration ($p = 0.000$, $F = 60.56$) and process temperature ($p = 0.01$, $F = 21.61$) had a significant influence on the bulk modulus. When we compared the F-values (i.e., the strength of the effects), we found that the effect of silk concentration was six times stronger than the one of the process temperature. The high R^2 and R^2 (predicted) from the regression model confirmed the predictability of the bulk modulus with both factors. The "Modulus 1" showed similar significant effects with silk concentration ($p = 0.012$, $F = 14.3$) and process temperature ($p = 0.01$, $F = 103.84$). Interestingly the process temperature was seven times stronger than the silk concentration. The R^2 and R^2 predicted were also high. "Modulus 2" showed

TABLE 4 | Moduli obtained from the fit of the sponge scaffold compression test.

Sample conc. (−20°C) [mg/ml]	Bulk modulus [kPa]	Modulus 1 [kPa]	Modulus 2 [kPa]	Modulus 3 [kPa]	Sample conc. (−80°C) [mg/ml]	Bulk modulus [kPa]	Modulus 1 [kPa]	Modulus 2 [kPa]
5	15.60	0.08	3.24	–	5	5.36	3.68	0.45
10	11.63	0.06	1.92	–	10	5.34	3.51	0.53
15	18.31	0.08	4.77	0.018	15	10.24	4.77	0.81
20	10.78	7.4E-08	–	–	20	24.05	13.23	–
25	71.15	0.29	10.67	0.16	25	55.83	26.53	7.43
30	107.31	0.31	11.73	0.24	30	111.98	42.70	25.15

TABLE 5 | ANOVA[a] and regression analysis of the factorial responses.

Response	Factor	*p*-value	*F*-value	R^2 (%)	R^2 predicted (%)
Bulk Modulus	Concentration	**0.000**	121.47	99.50	95.68
	Temperature	**0.010**	21.61		
Modulus 1	Concentration	**0.012**	14.33	98.77	87.11
	Temperature	**0.001**	103.84		
Modulus 2	Concentration	**0.02**	17.43	97.14	35.78
	Temperature	0.066	8.0		
Fast Relaxation time	Concentration	0.834	0.35	0	0
	Temperature	0.994	0.00		
Slow Relax. Time	Concentration	**0.007**	19.35	97.03	42.86
	Temperature	0.287	1.51		
Elastic modulus E	Concentration	**0.001**	**66.48**	97.81	92.97
	Temperature	**0.011**	**20.37**		
Storage modulus E'	Concentration	**0.001**	51.29	98.94	90.64
	Temperature	0.137	3.44		
Loss modulus E"	Concentration	**0.001**	62.44	99.66	95.12
	Temperature	0.068	6.14		

Significant results are in bold text.
[a] *The ANOVA was run with shrinkage (**Table 2**) as a covariate.*

only a significant effect for silk concentration ($p = 0.02$, $F = 17.43$); the R^2 predicted was 35.78%, suggesting that the "Modulus 2" effect was probably circumstantial. "Modulus 3" was not analyzed because only a few sponge scaffolds had it.

The mechanical model consisted of fractional contributions; therefore, an appropriate representation of the effects observed was a plot of the ratio of modulus 1 and 2 by the bulk modulus. **Figure 8A** illustrates the dependencies of bulk modulus and modulus 1 with silk concentration and temperature. It is important to remember here that the moduli were significantly affected by the two factors, we explained the lack of strong visual evidence by the fact that the shrinkage was a significant covariate for the ANOVA and regression analysis. Modulus 2 was not plotted for clarity (see **Figure S9**).

Figure 8B shows the ratio of modulus 1 by the bulk modulus, (i.e., the importance of modulus 1). We observed that for the samples prepared at −20°C, the contribution of modulus 1 was low and constant with silk concentration. Whereas, for the samples prepared at −80°C, we observed a stronger effect of modulus 1 at low silk concentration, monotonously decreasing to weaker effects got modulus 1 at high silk concentration.

Mechanical Properties: Stress Relaxation

For each compression step, we performed a stress-relaxation measurement to evaluate the recovery of the sponge scaffolds. **Figure 9** shows the stress-relaxation curves as a function of silk concentration and process temperature. The higher the concentration of silk, the longer it took to relax the materials.

The fit of the stress-relaxation yielded three possible relaxation times: a fast relaxation time, an intermediate relaxation time, and a slow relaxation time. Not all samples showed the three relaxations. **Table 6** summarizes the numerical values obtained from the fits.

Looking at the statistical analysis (**Table 5**) we found that only the slow relaxation was significantly affected by silk concentration ($p = 0.07$, $F = 19.35$) and not by the process temperature ($p = 0.287$, $F = 1.51$). The R^2 was high at 97.03%, but the R^2 predicted was low at 42.86%, suggesting that the effect was not fully captured by solely the silk concentration. The fast

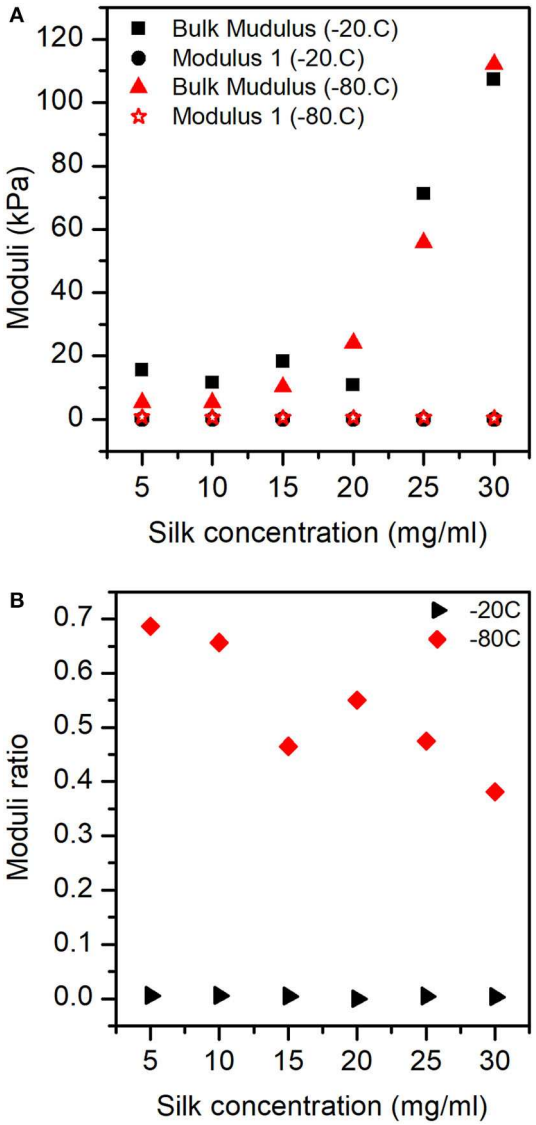

FIGURE 8 | Moduli responses for the sponges in different concentrations of silk and process temperature: **(A)** Bulk modulus and Modulus 1. **(B)** Ratio between Modulus 1 and Bulk modulus.

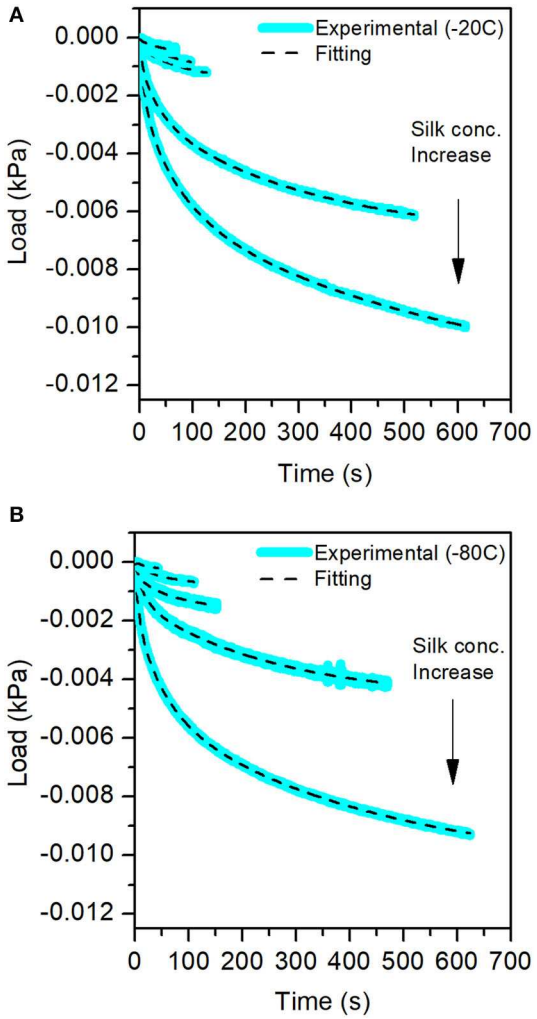

FIGURE 9 | Stress-Relaxation curves obtained from the mechanical test for the different sponge scaffolds. In blue, the experimental data, and in the dash lines, the fits. **(A)** At −20°C and **(B)** at −80°C.

relaxation, on the other hand, was not at all influenced by the design factors.

Figure 10 shows the plot of fast and slow relaxation times.

Mechanical Properties: Dynamic Compression Test

At the end of the stress relaxation step, we applied a 0.5 Hz oscillatory compression of 0.1 mm in amplitude. We extracted from the analysis the elastic modulus (E), the storage modulus (E'), the loss modulus (E"), and the phase (**Figure S10**). **Table 7** summarizes the numerical findings.

The ANOVA analysis (**Table 5**) shows that E ($p = 0.001$, $F = 66.48$), E' ($p = 0.001$, $F = 0.137$), and E" ($p = 0.001$, $F = 62.44$) are significantly affected by the silk concentration. Only the elastic modulus was significantly affected by the process temperature ($p = 0.01$, $F = 20.37$). When we compared the strength of the effect (F-values), we found that the silk concentration had three times more effective than the process temperature on the elastic modulus. Remarkably, the regression analysis for all three moduli had a high R^2 and R^2 predicted.

Figure 11A shows the exponential like increase of the elastic modulus (E) as a function of silk concentration and process temperature. **Figure 11B** illustrates the interplay (phase) between the storage and loss modulus. We found that as a function of silk concentration, the phase increased monotonously for the samples prepared at −80°C. Whereas, for the samples made at −20°C, the phase appeared to rise from low silk concentration and then decreased toward high silk concentration.

TABLE 6 | Different Relaxation Times for the sponges in different silk concentration and temperatures.

Sample conc. (−20°C) [mg/ml]	Fast relaxation time (−20°C) [s]	Intermediate relaxation time (−20°C) [s]	Slow relaxation time (−20°C) [s]	Sample conc. (−80°C) [mg/ml]	Fast relaxation time (−80°C) [s]	Intermediate relaxation time (−80°C) [s]	Slow relaxation time (−80°C) [s]
5	–	–	–	5	–	–	–
10	18.86	–	68.48	10	3.28	–	16.23
15	15.11	48.79	82.33	15	22.40	–	110.06
20	8.23	–	86.97	20	9.33	–	84.22
25	6.75	41.27	325.27	25	19.52	–	259.39
30	11.09	72.19	614.11	30	8.09	52.07	417.42

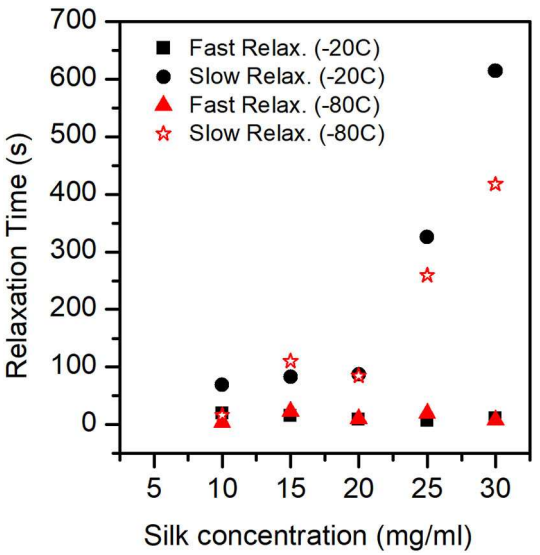

FIGURE 10 | Relaxation Times (Fast mode and Slow mode) for the different sponges. In the ANOVA analysis we found that only the slow relaxation was significantly affected by silk concentration (p-value = 0.07, F-value = 19.35) and not by the process temperature (p-value = 0.287, F-value = 1.51). The fast relaxation was independent of concentration and process temperature.

DISCUSSION

Macroscopic Organization

We prepared RSF sponge scaffolds by ice templating with six different concentrations of silk and two different freezing temperatures. A surprising result of the sample preparation was that the scaffolds exhibited shrinkage. Therefore, the scaffolds used for tomography analysis were chosen based on a visual inspection where the most homogeneous and representative scaffolds were analyzed. The resolution of the images was sufficient to perform the porosity and tortuosity calculations.

The result showed a significant relationship between the concentration of the silk solution and the porosity. This relation was somewhat expected, as the higher the protein concentration, the more material, and the less void space. This behavior has also been observed with other materials (Wegst et al., 2010) and in silks (Min et al., 2009; Zhu et al., 2014; Kadakia et al., 2016). We also found that the process temperature had an impact on the porosity ($p = 0.043$). Other studies have also shown that freezing temperature had an effect on the pore size (O'Brien et al., 2007) and could be the reason for the increased permeability. However, porosity is not sufficient. Now using tomography and image processing, we were able to estimate the sponge scaffolds tortuosity, the path taken by the fluid. The silk concentration had significant effects, but the processed temperature was significant only for the tortuosity in the XY plane (normal to the syringe axis). We interpreted this anisotropy by the fact that the freezing of the samples most likely happened laterally (side of the syringe) from outside to inside, thus not affecting the tortuosity in the z-direction. We also noted that the tortuosity values were very close to 1, (i.e., a direct flow path). Those values should further be scrutinized. Indeed, any calculation depended on the thresholding and binarization processes. In our case, the poor contrast (**Figure 3**) may have yielded a less than optimal binarized image. Nevertheless, the changes within the sample should still be valid. For example, when combing the tortuosity (λ) and porosity (ε) using $\frac{\lambda^2}{\varepsilon}$, the hindrance factor. We found that the hindrance was higher in the Z-direction compared to the XY-plane. The effect appeared to be driven by the geometry and design of the surfaces exposed to the freezing planes (Panda et al., 2017).

The ice nucleation was critical when frozen at −20°C, the ice nucleation takes place slower than it does when frozen at −80°C, due to the temperature being very close to the glass transition temperature of the water-silk proteins between −20 and −80°C (Guan et al., 2016), and estimated at −62°C in fibers (Guan et al., 2016); thus allowing ice crystals to grow larger and create larger voids in the sponge scaffolds. At −80°C, the pore sizes were no longer affected by the water-silk glass transition. Nazarov et al. (2004) already observed this decorrelation. With our current tomography data, and the correlation length analysis we confirmed Nazarov et al. findings and showed specifically that temperature and concentration affected only the large pores (see **Figure 4C**). No conclusion could be drawn about their connectivity and distribution.

Nevertheless, looking at the permeability of some tissues, for example, cartilage permeability ranges from 0.1×10^{-18} to 2×10^{-18} m^2 and $\sim 10^{-9}$ m^2 for trabecular bone (O'Brien et al., 2007). We found that the silk sponge scaffolds permeability was far from the cartilage and neared to the trabecular bone.

TABLE 7 | Elastic modulus (E), Storage modulus (E') and Loss modulus (E") obtained for the different sponges from the dynamical mechanical test.

Sample conc. [mg/ml]	E (−20°C) [kPa]	Phase (−20°C)	E' (−20°C) [kPa]	E" (−20°C) [kPa]	E (−80°C) [kPa]	Phase (−80°C)	E' (−80°C) [kPa]	E" (−80°C) [kPa]
5	1.94	2.7	1.37	0.07	0.43	7.2	0.43	0.05
10	1.89	4.6	1.33	0.11	0.58	9	0.57	0.09
15	3.35	10.4	2.33	0.43	2.06	8.1	2.04	0.29
20	6.13	7.5	4.29	0.57	4.46	8.1	4.41	0.63
25	17.76	9.4	12.39	2.04	9.19	11.4	9.01	1.82
30	26.47	6.7	18.41	2.18	21.73	11.1	21.32	4.18

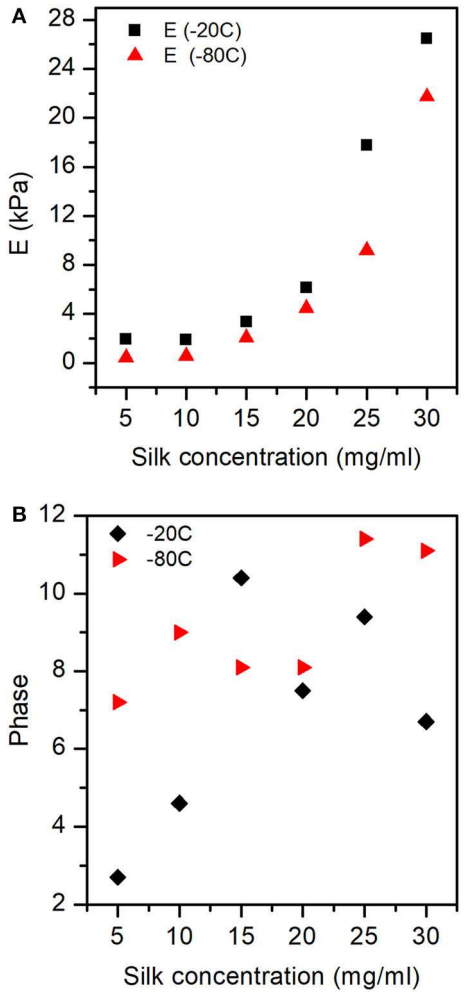

FIGURE 11 | Elastic modulus (*E*), and Phase obtained for the different sponges from the dynamical compression test. **(A)** The elastic modulus was significantly affected by both silk concentration and process temperature. **(B)** The phase shows the interplay between storage and loss modulus with silk concentration and process temperature. See **Figure S4** for the exact values of E, E', and E" at −20 and −80°C.

A higher concentration of silk would not be sufficient to mimic tissue permeability. Still, the control of porosity and tortuosity to insure that the hindrance is kept low (i.e., optimal transport properties).

Mechanical Response

Collectively we found higher bulk moduli and longer relaxation times with increasing silk concentration. Here we tentatively linked the re-organization of the amorphous domains yielding more hydrophobic pockets to slower relaxation. Interestingly, only the slow relaxation time variation was statistically influenced by silk concentration. We further interpreted the slow relaxation with the transport of fluid in the silk sponge scaffolds. We tentatively associated the fast relaxation with a viscoelastic relaxation, which was not influenced by the silk concentration and process temperatures. We interpreted this counter-intuitive observation by the fact that we probed the silk sponges in the small strains regime, and at slow strain rates (i.e., conditions at which the faster viscoelastic relaxation would have already taken place). Panda et al. noted that the sponge scaffolds relaxations curves were characteristic of a viscoelastic solid, and although being a biphasic system, behaved almost like a Newtonian fluid, and relaxing almost instantaneously (Panda et al., 2017).

The interplay of the bulk and modulus 1 provided new insights to explain the transport (slow relaxation) and possible failures of the materials. The mechanical model consisted of fractional contributions from "failure events." The bulk modulus captured the elastic contribution and was controlled predominantly by the silk concentration. We tentatively associated modulus 1 to the collapse of the pores structures and were controlled mostly by the process temperature. At −20°C, the fractional contribution of modulus 1 was low and independent of silk concentration (**Figure 8B**), suggesting the existence of critical pore size and connectivity above which the sponge scaffolds responses appeared elastic. At −80°C, on the other hand, we observed a dependence of the fractional contribution of modulus 1 with silk concentration (**Figure 8B**). The increase of the fractional amount of modulus 1 suggested more collapsible pores, thus a compromised mechanics and transport.

Figure 12 illustrates the three correlation lengths ($\xi_{1,2,3}$) found from the tomography analysis, and the collapse of the larger pore networks (ξ_3). Dynamically, we found unremarkably that the elastic modulus (E) was predominantly dependent on the concentration of silk. Interestingly, when we looked at the interplay between the storage (E') and loss moduli (E"), we found no cross-over (**Figure S4**). We discovered that E' was systematically higher than E", and the difference was more pronounced at higher silk concentrations. By analogy with the rheology, the silk sponge scaffolds behaved like an elastic solid, although not an ideal one because some of the mechanical

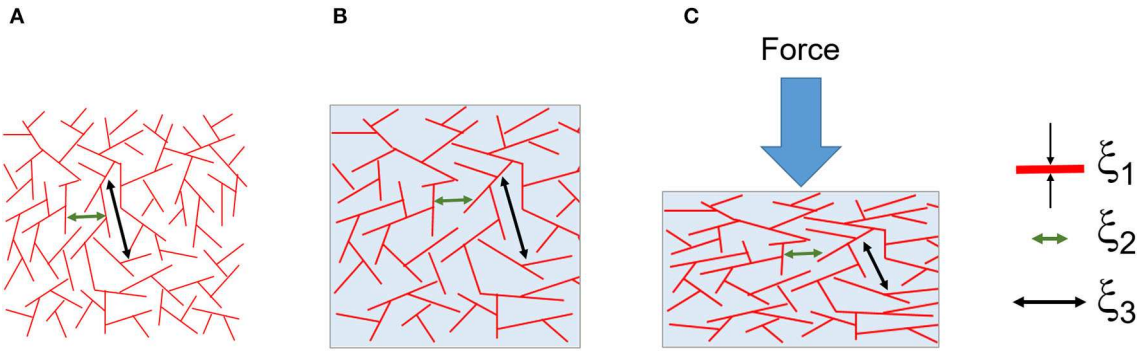

FIGURE 12 | Composite illustration of the results from the tomographic analysis and mechanics. **(A)** The dry foam with a distribution of three correlation lengths ξ_1, ξ_2, and ξ_3. The correlation lengths were assigned to the silk thickness (at around 4 μm), the small pores (between 10 and 20 μm) and the large pores (between 50 and 130 μm), respectively. **(B)** The wet and swollen scaffold. **(C)** The compressed scaffold and the collapse of the larger pores (ξ_3).

energy was dissipated. Looking at the phase (**Figure 11B**), we found that at −80°C the phase increased monotonously with silk concentration. The linear dependence of the phase with silk concentration suggested that at −80°C, the sponge scaffolds were more and more viscous. Paradoxically, since we observed no cross-over between E' and E" we proposed that the effect stemmed from a strong coupling between the matrix and the fluid present. At −20°C, we observed an increase followed by a decrease in the phase. The change indicated a more viscous silk sponge scaffold at low concentrations of silk and a more elastic silk sponge scaffold at higher silk concentrations. The effect was most likely related to the marked decrease of the larger pores as seen in **Figure 4C**. A better understanding of the fluid coupling and transport is needed, however, to resolve the dynamics of the sponge scaffolds.

Molecular Origin of Scaffold Morphology and Mechanical Response

The results from the FTIR analysis indicated that the silk structure had been affected by the manufacturing process, revealed by the amide I/II ratio, which exhibited a significant dependence on concentration. By further analyzing the crystallinity index (specific to rigid domains) and tyrosine ratio (specific to amorphous domains), we found that the crystalline/rigid domains of the silk stayed intact during the manufacturing. Instead, the amorphous domains changed significantly. We interpreted the organization of the amorphous domains with concentration, as re-orientation toward more hydrophobic interfaces (ratio changed from about 1.1 to 0.9). Others have described the network structure of silk scaffolds as heterogeneous with β-sheet and fibrillar structures (Numata et al., 2011). The interpretation, however, does not translate into mechanical effects. Recently two approaches to explain protein-based materials mechanics from its structural organization and thermodynamics have been put forward (Puglisi et al., 2017) and (Panda et al., 2018). Still the roles of the silk secondary structures, their organization and the strong fluid coupling to the mechanics remain unclear. On-going work combining mechanical deformation with spectroscopy and scattering might reveal the underlying mechanisms.

SUMMARY

We used a factorial design analysis to decouple the effects of silk concentration and freezing temperature (for cryogel formation). In summary

- We found that the scaffolds suffered from shrinkage upon freeze drying. Although not controlled, the effect was included in the ANOVA analysis of the subsequent responses
- We derived three correlation lengths (ξ) that we assigned to the silk thickness (around 4 μm), small pores (between 10 and 20 μm) and large pores (50 and 130 μm). Interestingly only ξ_3 decreased at −20°C with increasing silk concentration
- The permeability, porosity, and tortuosity were high, and mostly dependent on the silk concentration for the last two. In contrast for the permeability, the silk concentration and temperature had a similar effect
- Structurally, by FTIR, the silk proteins amorphous organization only was affected by the protein concentration and process temperature. The β-sheet structures were not affected
- Mechanically, using a fracture model, the scaffolds were dominated by the collapse of the larger pores
- We considered the scaffolds as biphasic (silk and aqueous solvent) material. We assigned the slow stress relaxation to the fluid displacement, and the fast stress relaxation to a coupled viscoelastic response from the silk-fluid
- Dynamically, the scaffolds behaved as viscoelastic solids with a strong dependence on silk concentration for the −20°C process temperature. We tentatively explained the effect from the larger pores sizes more affected at −20°C than at −80°C.

CONCLUSION

Overall, our results are in line with previous studies (Nazarov et al., 2004; Panda et al., 2017; Ribeiro et al., 2019). Our use of

the tomography, mechanical test, and detailed statistical analysis provides inroads into the interplay between process parameters (silk concentration and process temperature) and the multiple responses of the silk sponge scaffolds. The development of a new mechanical fitting for the compression test helped capture simply the different failure modes in the sponge scaffolds as well as correlates those events to relaxation and eventually transport properties. We could link the macroscopic responses to specific pore sizes distribution in the scaffolds. We are further investigating the advantages of our progressive acidification method as well as improving the tomography characterization with *in-situ* characterization.

DATA AVAILABILITY STATEMENT

The datasets generated for this study are available on request to the corresponding author.

AUTHOR CONTRIBUTIONS

CD, BF, NA, EA, and SH contributed conception and design of the study. BF, NA, EA, and JE collected the data. CD performed the data analysis. NA, EA, and BF wrote the first draft of the manuscript. BF, NA, EA, JE, SH, and CD wrote sections of the manuscript. All authors contributed to manuscript revision, read, and approved the submitted version.

FUNDING

The Olle Engkvist Foundation (Stiftelsen Olle Engkvist Byggmastare grant number 189–0280) and the Crafoord Foundation (Crafoordska Stiftelsen grant number 20180927) are kindly acknowledged for their financial support. The Lund Institute for Advanced Neutron and X-ray Science (LINXS) is recognized for partial funding.

ACKNOWLEDGMENTS

X-ray tomography was performed at the 4D Imaging Lab at Lund University.

SUPPLEMENTARY MATERIAL

The Supplementary Material for this article can be found online at: https://www.frontiersin.org/articles/10.3389/fmats.2020.00211/full#supplementary-material

REFERENCES

Ak, F., Oztoprak, Z., Karakutuk, I., and Okay, O. (2013). Macroporous silk fibroin cryogels. *Biomacromolecules* 14, 719–727. doi: 10.1021/bm3018033

Bhat, N. V., and Nadiger, G. S. (1980). Crystallinity in silk fibers: partial acid hydrolysis and related studies. *J. Supercrit. Fluids* 25, 921–932. doi: 10.1002/app.1980.070250518

Blaise, A., Baravian, C., André, S., Dillet, J., Michot, L. J., and Mokso, R. (2010). Investigation of the mesostructure of a mechanically deformed HDPE by synchrotron microtomography. *Macromolecules* 43, 8143–8152. doi: 10.1021/ma101033b

Boulet-Audet, M., Vollrath, F., and Holland, C. (2015). Identification and classification of silks using infrared spectroscopy. *J. Exp. Biol.* 218, 3138–3149. doi: 10.1242/jeb.128306

Caccavo, D., Cascone, S., Lamberti, G., and Barba, A. A. (2018). *Hydrogels: experimental characterization and mathematical modelling of their mechanical and diffusive behaviour. Chem. Soc. Rev*. 47, 2357–2373. doi: 10.1039/C7CS00638A

Chen, F., Porter, D., and Vollrath, F. (2010). Silkworm cocoons inspire models for random fiber and particulate composites. *Phys. Rev. E Stat. Nonlin. Soft Matter Phys.* 82:041911. doi: 10.1103/PhysRevE.82.041911

Cho, S. Y., Heo, S., and Jin, H. J. (2012). Controlling microstructure of three-dimensional scaffolds from regenerated silk fibroin by adjusting pH. *J. Nanosci. Nanotechnol.* 12, 806–810. doi: 10.1166/jnn.2012.5364

Cooper, S. J., Bertei, A., Shearing, P. R., Kilner, J. A., and Brandon, N. P. (2016). TauFactor: an open-source application for calculating tortuosity factors from tomographic data. *SoftwareX* 5, 203–210. doi: 10.1016/j.softx.2016.09.002

DeBari, M. K., and Abbott, R. D. (2019). Microscopic considerations for optimizing silk biomaterials. *Wiley Interdiscip. Rev. Nanomed. Nanobiotechnol.* 11:e1534. doi: 10.1002/wnan.1534

Del Giudice, A., Dicko, C., Galantini, L., and Pavel, N. V. (2017). Time-dependent pH scanning of the acid-induced unfolding of human serum albumin reveals stabilization of the native form by palmitic acid binding. *J. Phys. Chem. B* 121, 4388–4399. doi: 10.1021/acs.jpcb.7b01342

Deville, S. (2013). Ice-templating, freeze casting: beyond materials processing. *J. Mater. Res.* 28, 2202–2219. doi: 10.1557/jmr.2013.105

Deville, S., Saiz, E., Nalla, R. K., and Tomsia, A. P. (2006). Freezing as a path to build complex composites. *Science* 311, 515–518. doi: 10.1126/science.1120937

Elahi, M. F., Wang, F., Li, Y., and Wang, L. (2017). "Porous structures from biobased synthetic polymers via freeze-drying," in *Porous Lightweight Composites Reinforced with Fibrous Structures*, eds Y. Yang, J. Yu, H. Xu, and B. Sun (Berlin; Heidelberg: Springer), 179–206. doi: 10.1007/978-3-662-53804-3_8

Epstein, N. (1989). On tortuosity and the tortuosity factor in flow and diffusion through porous media. *Chem. Eng. Sci.* 44, 779–781. doi: 10.1016/0009-2509(89)85053-5

Griffith, L. G., and Naughton, G. (2002). Tissue engineering–current challenges and expanding opportunities. *Science* 295, 1009–1014. doi: 10.1126/science.1069210

Griffon, D. J., Sedighi, M. R., Schaeffer, D. V., Eurell, J. A., and Johnson, A. L. (2006). Chitosan scaffolds: Interconnective pore size and cartilage engineering. *Acta Biomater.* 2, 313–320. doi: 10.1016/j.actbio.2005.12.007

Guan, J., Wang, Y., Mortimer, B., Holland, C., Shao, Z., Porter, D., et al. (2016). Glass transitions in native silk fibres studied by dynamic mechanical thermal analysis. *Soft Matter* 12, 5926–5936. doi: 10.1039/C6SM00019C

Holland, C., Numata, K., Rnjak-Kovacina, J., and Seib, F. P. (2019). The biomedical use of silk: past, present, future. *Adv. Healthcare Mater.* 8:e1800465. doi: 10.1002/adhm.201800465

Horrocks, N. P. C., Vollrath, F., and Dicko, C. (2013). The silkmoth cocoon as humidity trap and waterproof barrier. *Comp. Biochem. Physiol. A Mol. Integr. Physiol.* 164, 645–652. doi: 10.1016/j.cbpa.2013.01.023

Howard, D., Buttery, L. D., Shakesheff, K. M., and Roberts, S. J. (2008). Tissue engineering: strategies, stem cells and scaffolds. *J. Anat.* 213, 66–72. doi: 10.1111/j.1469-7580.2008.00878.x

Ishida, K. P., and Griffiths, P. R. (1993). Comparison of the amide I/II intensity ratio of solution and solid-state proteins samples by transmission, attenuated total reflectance, and diffuse reflectance spectrometry. *Appl. Spectrosc.* 47, 584–589. doi: 10.1366/0003702934067306

Kadakia, P. U., Jain, E., Hixon, K. R., Eberlin, C. T., and Sell, S. A. (2016). Sonication induced silk fibroin cryogels for tissue engineering applications. *Mater. Res. Express* 3:055401. doi: 10.1088/2053-1591/3/5/055401

Kolahreez, D., and Morshed, M. (2018). Fabrication of porous three-dimensional fibroin structures through a freezing process. *J. Appl. Polymer Sci.* 135:46537. doi: 10.1002/app.46537

Langer, R., and Vacanti, J. (2016). Advances in tissue engineering. *J. Pediatr. Surg.* 51, 8–12. doi: 10.1016/j.jpedsurg.2015.10.022

Lovett, M., Lee, K., Edwards, A., and Kaplan, D. L. (2009). Vascularization strategies for tissue engineering. *Tissue Eng. B Rev.* 15, 353–370. doi: 10.1089/ten.teb.2009.0085

Makaya, K., Terada, S., Ohgo, K., and Asakura, T. (2009). Comparative study of silk fibroin porous scaffolds derived from salt/water and sucrose/hexafluoroisopropanol in cartilage formation. *J. Biosci. Bioeng.* 108, 68–75. doi: 10.1016/j.jbiosc.2009.02.015

Mallepally, R. R., Marin, M. A., Surampudi, V., Subia, B., Rao, R. R., Kundu, S. C., et al. (2015). Silk fibroin aerogels: potential scaffolds for tissue engineering applications. *Biomed. Mater.* 10:035002. doi: 10.1088/1748-6041/10/3/035002

Maniglio, D., Bonani, W., Migliaresi, C., and Motta, A. (2018). Silk fibroin porous scaffolds by N2O foaming. *J. Biomater. Sci. Polymer Edn.* 29, 491–506. doi: 10.1080/09205063.2018.1423811

Meghezi, S., Drouin, B., and Mantovani, D. (2017). "*Collagen hydrogel-based scaffolds for vascular tissue regeneration: Mechanical and viscoelastic characterization,*" *in Characterization of Polymeric Biomaterials*, eds. M.C. Tanzi and S. Farè (Woodhead Publishing).

Meinel, L., Hofmann, S., Karageorgiou, V., Kirker-Head, C., McCool, J., Gronowicz, G., et al. (2005). The inflammatory responses to silk films *in vitro* and *in vivo*. *Biomaterials* 26, 147–155. doi: 10.1016/j.biomaterials.2004.02.047

Min, S., Gao, X., Liu, L., Tian, L., Zhu, L., Zhang, H., et al. (2009). Fabrication and characterization of porous tubular silk fibroin scaffolds. *J. Biomater. Sci. Polym. Edn.* 20, 1961–1974. doi: 10.1163/156856208X396056

Ming, J., Li, M., Han, Y., Chen, Y., Li, H., Zuo, B., et al. (2016). Novel two-step method to form silk fibroin fibrous hydrogel. *Mater. Sci. Eng. C* 59, 185–192. doi: 10.1016/j.msec.2015.10.013

Monti, P., Freddi, G., Bertoluzza, A., Kasai, N., and Tsukada, M. (1998). Raman spectroscopic studies of silk fibroin from bombyx mori. *J. Raman Spectrosc.* 29, 297–304. doi: 10.1002/(SICI)1097-4555(199804)29:4<297::AID-JRS240>3.0.CO;2-G

Moreira, E. A., and Coury, J. R. (2004). The influence of structural parameters on the permeability of ceramic foams. *Braz. J. Chem. Eng.* 21, 23–33. doi: 10.1590/S0104-66322004000100004

Nazarov, R., Jin, H. J., and Kaplan, D. L. (2004). Porous 3-D scaffolds from regenerated silk fibroin. *Biomacromolecules* 5, 718–726. doi: 10.1021/bm034327e

Numata, K., Katashima, T., and Sakai, T. (2011). State of water, molecular structure, and cytotoxicity of silk hydrogels. *Biomacromolecules* 12, 2137–2144. doi: 10.1021/bm200221u

O'Brien, F. J. (2011). Biomaterials and scaffolds for tissue engineering. *Mater. Today* 14, 88–95. doi: 10.1016/S1369-7021(11)70058-X

O'Brien, F. J., Harley, B. A., Waller, M. A., Yannas, I. V., Gibson, L. J., and Prendergast, P. J. (2007). The effect of pore size on permeability and cell attachment in collagen scaffolds for tissue engineering. *Technol. Health Care* 15, 3–17. doi: 10.3233/THC-2007-15102

Okay, O., and Lozinsky, V. I. (2014). Synthesis and structure–property relationships of cryogels. *Adv. Polym. Sci.* 263, 103–157. doi: 10.1007/978-3-319-05846-7_3

Panda, D., Konar, S., Bajpai, S. K., and Arockiarajan, A. (2017). Synthesis and viscoelastic characterization of microstructurally aligned Silk fibroin sponges. *J. Mech. Behav. Biomed.* 71, 362–371. doi: 10.1016/j.jmbbm.2017.03.029

Panda, D., Konar, S., Bajpai, S. K., and Arockiarajan, A. (2018). Thermodynamically-consistent constitutive modeling of aligned Silk fibroin sponges: theory and application to uniaxial compression. *Int. J. Solids Struct.* 138, 144–154. doi: 10.1016/j.ijsolstr.2018.01.006

Pennella, F., Cerino, G., Massai, D., Gallo, D., Falvo D'Urso Labate, G., Schiavi, A., et al. (2013). A survey of methods for the evaluation of tissue engineering scaffold permeability. *Ann. Biomed. Eng.* 41, 2027–2041. doi: 10.1007/s10439-013-0815-5

Puglisi, G., De Tommasi, D., Pantano, M. F., Pugno, N. M., and Saccomandi, G. (2017). Micromechanical model for protein materials: from macromolecules to macroscopic fibers. *Phys. Rev. E* 96:042407. doi: 10.1103/PhysRevE.96.042407

Qi, Y., Wang, H., Wei, K., Yang, Y., Zheng, R. Y., Kim, I. S., et al. (2017). A review of structure construction of silk fibroin biomaterials from single structures to multi-level structures. *Int. J. Mol. Sci.* 18:237. doi: 10.3390/ijms18030237

Rajkhowa, R., Gil, E. S., Kluge, J., Numata, K., Wang, L., Wang, X., et al. (2010). Reinforcing silk scaffolds with silk particles. *Macromol. Biosci.* 10, 599–611. doi: 10.1002/mabi.200900358

Reis, R. L., Neves, N. M., Mano, J. F., Gomes, M. E., Marques, A. P., and Azevedo, H. S. (2008). *Natural-Based Polymers for Biomedical Applications*. Woodhead Publishing.

Ribeiro, V. P., da Silva Morais, A., Maia, F. R., Canadas, R. F., Costa, J. B., Oliveira, A. L., et al. (2018). Combinatory approach for developing silk fibroin scaffolds for cartilage regeneration. *Acta Biomater.* 72, 167–181. doi: 10.1016/j.actbio.2018.03.047

Ribeiro, V. P., Pina, S., Costa, J. B., Cengiz, I. F., García-Fernández, L., Fernández-Gutiérrez, M. D. M., et al. (2019). Enzymatically cross-linked silk fibroin-based hierarchical scaffolds for osteochondral regeneration. *ACS Appl. Mater. Interf.* 11, 3781–3799. doi: 10.1021/acsami.8b21259

Rockwood, D. N., Preda, R. C., Yücel, T., Wang, X., Lovett, M. L., and Kaplan, D. L. (2011). Materials fabrication from *Bombyx mori* silk fibroin. *Nat. Protoc.* 6, 1612–1631. doi: 10.1038/nprot.2011.379

Schindelin, J., Arganda-Carreras, I., Frise, E., Kaynig, V., Longair, M., Pietzsch, T., et al. (2012). Fiji: an open-source platform for biological-image analysis. *Nat. Methods* 9, 676–676. doi: 10.1038/nmeth.2019

Tamada, Y. (2005). New process to form a silk fibroin porous 3-D structure. *Biomacromolecules* 6, 3100–3106. doi: 10.1021/bm050431f

Varley, M. C., Neelakantan, S., Clyne, T. W., Dean, J., Brooks, R. A., and Markaki, A. E. (2016). Cell structure, stiffness and permeability of freeze-dried collagen scaffolds in dry and hydrated states. *Acta Biomater.* 33, 166–175. doi: 10.1016/j.actbio.2016.01.041

Vepari, C., and Kaplan, D. L. (2007). Silk as a biomaterial. *Prog. Polym. Sci.* 32, 991–1007. doi: 10.1016/j.progpolymsci.2007.05.013

Wegst, U. G. K., Schecter, M., Donius, A. E., and Hunger, P. M. (2010). Biomaterials by freeze casting. *Philos. Trans. Royal Soc. A* 368, 2099–2121. doi: 10.1098/rsta.2010.0014

Yang, S., Leong, K.-F. E., Du, Z. M. E., and Chua, C.-K. (2001). The design of scaffolds for use in tissue engineering. Part I. traditional factors. *Tissue Eng.* 7, 679–689. doi: 10.1089/107632701753337645

Zhang, W., Wray, L. S., Rnjak-Kovacina, J., Xu, L., Zou, D., Wang, S., et al. (2015). Vascularization of hollow channel-modified porous silk scaffolds with endothelial cells for tissue regeneration. *Biomaterials* 56, 68–77. doi: 10.1016/j.biomaterials.2015.03.053

Zhu, M., Wang, K., Mei, J., Li, C., Zhang, J., Zheng, W., et al. (2014). Fabrication of highly interconnected porous silk fibroin scaffolds for potential use as vascular grafts. *Acta Biomater.* 10, 2014–2023. doi: 10.1016/j.actbio.2014.01.022

Conflict of Interest: The authors declare that the research was conducted in the absence of any commercial or financial relationships that could be construed as a potential conflict of interest.

frontiers in Bioengineering and Biotechnology

ORIGINAL RESEARCH
published: 18 August 2020
doi: 10.3389/fbioe.2020.00973

Phase Diagram and Estimation of Flory-Huggins Parameter of Interaction of Silk Fibroin/Sodium Alginate Blends

Laise Maia Lopes[1†], Mariana Agostini de Moraes[2†] and Marisa Masumi Beppu[1†]*

[1] School of Chemical Engineering, University of Campinas, Campinas, Brazil, [2] Department of Chemical Engineering, Federal University of São Paulo, Diadema, Brazil

Silk fibroin (SF) and sodium alginate (SA) are natural polymers used to produce biomaterials. One of the strategies to improve the properties of these products is to prepare blends with them, which are partially miscible. Phase separation is observed, therefore, the thermodynamic analysis of this system is important to predict the final state and composition of this blends. This study explored blends with a different initial composition of SF, SA, and water (WA) at 25°C and neutral pH. After phase separation, two phases were identified, one rich in SF and other rich in SA. The Flory-Huggins parameters of interaction of polymer-solvent and polymer-polymer were estimated using the extended equation and data of phase equilibrium, their values indicates the partial miscibility of the polymers.

Keywords: silk fibroin, sodium alginate, phase separation, blends, thermodynamic, biomaterials

OPEN ACCESS

Edited by:
Nicola Maria Pugno, University of Trento, Italy

Reviewed by:
Narendra Pal Singh Chauhan, Bhupal Nobles University, India
Claudio Della Volpe, University of Trento, Italy

***Correspondence:**
Marisa Masumi Beppu
beppu@unicamp.br

† These authors have contributed equally to this work

Specialty section:
This article was submitted to Biomaterials, a section of the journal Frontiers in Bioengineering and Biotechnology

Received: *15 October 2019*
Accepted: *27 July 2020*
Published: *18 August 2020*

Citation:
Lopes LM, de Moraes MA and Beppu MM (2020) Phase Diagram and Estimation of Flory-Huggins Parameter of Interaction of Silk Fibroin/Sodium Alginate Blends. Front. Bioeng. Biotechnol. 8:973. doi: 10.3389/fbioe.2020.00973

INTRODUCTION

Blends of Silk fibroin (SF) and sodium alginate (SA) have been studied since the beginning of the 90's years (Liang and Hirabayashi, 1992). Most of the works with these two polymers explore the potential of the blends as a biomaterial due to their characteristics such as biocompatibility, biodegradability and low toxicity (de Moraes and Beppu, 2013; de Moraes et al., 2014; Ming and Zuo, 2014; Zhang et al., 2015; Wang et al., 2016). Despite that, the commercialization of these products is not a reality due to the complexity of the system formed by these polymers.

Silk fibroin is a protein produced by arthropods like spiders, mites, bees and silkworms, the last one is more used due to the facility of domestication (Kundu et al., 2013), the main producer worldwide is *Bombyx mori* silkworm (Koh et al., 2015). It has good mechanical properties with high tensile strength and high thermal resistance with a temperature of degradation close to 300°C (Kundu et al., 2013; Koh et al., 2015). SF has been explored to develop new materials such as porous materials, scaffolds, wound dressings, hydrogels, nano-particles and as a substrate in optics and sensors (Kim et al., 2005; Nogueira et al., 2011; Wenk et al., 2011; Calamak et al., 2014; Li et al., 2017; Wang et al., 2020).

One of the challenges of working with SF is its metastable solution behavior. The transition of α-helix conformation to β-sheet occurs spontaneously and can speed up by temperature, mechanical treatments and changes in solvent and salt concentration (Sohn et al., 2004; Matsumoto et al., 2006). This transition in SF chain conformation is widely studied in literature because it can clarify the self-assembly mechanism and nanofibrils formation of SF (Lu et al., 2012; Bai et al., 2013;

Zhong et al., 2015; Li et al., 2018). This information is important for designing new materials. It is reported that it depends on thermodynamic and, also, kinetic variables (Lu et al., 2012; Bai et al., 2013).

Another important parameter to be investigated is the behavior of SF in aqueous solution. SF is a non-water soluble protein, to obtain its solution it is necessary to use a saline solution, usually containing LiBr or $CaCl_2$. The dialysis process could influence the SF conformation by changing the osmotic pressure, the temperature and the salt concentration after dialysis (Sohn et al., 2004; Nogueira et al., 2011; Yang et al., 2013; Ribeiro et al., 2014). The knowledge about how SF conformation can be adjusted in SF solution is fundamental since it could influence the self-assembly process and consequently the properties of new materials.

Sodium alginate is a polysaccharide extracted from brown seaweeds and some bacteria (Agulhon et al., 2014). It is a copolymer formed by the α-L guluronic acid (block G) and β-D mannuronic acid (block M), their fraction and sequence in SA chain depend on the species of brown seaweeds that SA was extracted and can influence in the properties of the products developed (Draget et al., 1997). It is a natural polymer very explored in the development of different products, from the food industry, as an emulsifier, to the biomaterials field due to its facility to form films and hydrogels. Some SA applications are as cell encapsulation, wound dressing and drug delivery (Meng et al., 2010; Brachkova et al., 2011; Feng et al., 2014; Leung et al., 2014; Bhutani et al., 2015; Sarker et al., 2015).

Due to its use in the food industry, some studies investigated the phase separation of systems composed by alginate and other proteins, such as gelatin, casein and pea protein (Antonov et al., 1996; Panouillé and Larreta-Garde, 2009; Antonov and Moldenaers, 2011; Mession et al., 2012). Although SF and those proteins have different characteristics, the results could be useful to understand the SF-SA system. In those studies, phase separation is observed, as well as the presence of globular structures even in low concentration of polymers (Antonov and Moldenaers, 2011; Mession et al., 2012). These structures are also observed by scanning electron microscopy in our previous study of SF-SA blends (de Moraes et al., 2014; Lopes et al., 2018), which investigated the physical-chemical behavior of the blends.

Protein-polysaccharide systems are complex and in many cases, phase separation is observed (Pacek et al., 2000; Mession et al., 2012). Miscible blends are rare, being considered almost an exception in systems with macromolecules (Utracki and Manias, 2014). A miscible blend must attempt two conditions, Eqs 1 and 2:

$$\Delta G_m = \Delta H_m - T\Delta S_m < 0 \quad (1)$$

$$\left(\frac{\partial^2 \Delta G_m}{\partial \varphi_i^2}\right)_{T,P} > 0 \quad (2)$$

where ΔG_m is the Gibbs free energy of mixing, ΔH_m is the enthalpy of mixing, T is the temperature, ΔS_m is the entropy of mixing, ϕ_i is the volumetric fraction.

For polymers, the entropic contribution is small due to the low probability of molecular rearrangement (Mishra et al., 2017). Thus, the enthalpic contribution plays an important role in polymeric systems. So, macromolecules that interact through strong bonds, for example, hydrogen bonds, can form partially miscible systems. The interaction between SF and natural polysaccharides is well established in the literature and it can occur by hydrogen bonds and covalent bonds (de Moraes et al., 2014; Zhang et al., 2015; Wang et al., 2019). In protein-polysaccharide aqueous systems, intermolecular complexes are formed and macroscopically phase separation occurs by thermodynamic incompatibility (Mession et al., 2012). In a recent study, we focused on understanding the mechanism of phase separation of SF-SA system and the physical-chemical characteristics of those blends (Lopes et al., 2018). The literature presents just a few studies about the application of SF-SA blends and there is a lack of literature about the phase behavior of these blends.

In the present study, the phase separation and equilibrium of the ternary system composed by SF, SA, and water (WA) was experimentally investigated at 25°C and neutral pH. The quantification of each phase was made using different methods. The identification of the region rich in SF or SA is necessary to predict the behavior of blends with different initial conditions that will influence the final state of the blend and consequently the process and final product.

MATERIALS AND METHODS

Preparation of Solutions: Silk Fibroin and Sodium Alginate

Silk fibroin solution was prepared following the method previously published (de Moraes et al., 2014). Briefly, *Bombyx mori* silkworm cocoons (Bratac, Brazil) were degummed using 1 $g.L^{-1}$ Na_2CO_3 solution in a thermostatic bath at 85°C (Nova Analitica, Brazil) for 30 min, the process was repeated other two times. The fibers obtained were washed with deionized water and maintained at room temperature until completely dry. They were milled using a sieve with 10 mesh of diameter and then solubilized in a solution of $CaCl_2$: Ethanol: water (1:2:8 molar ratio). To remove the salts, the solution was dialyzed using a dialysis membrane (MWCO 3.5 kDa, Thermo Fisher Scientific, EUA) in ultrapure water (1:10 ratio). To remove the insoluble parts that are formed during dialysis, the solution was centrifuged for 30 min and 2300 relative centrifugal force (RCF). The final concentration was calculated by gravimetry and was around 4% (w/v).

Sodium alginate (Sigma-Aldrich, United States) extracted from *Macrocystis pyrifera* were dissolved in deionized water with a concentration of 2% (w/v). The solution was kept 3 days, so the water could solvate the powder, then the solution was homogenized by stirring.

Blend Preparation

The SF and SA blends were prepared in seven different mass proportions, as shown in **Table 1**. These compositions were

TABLE 1 | Initial mass fraction (%) of each component in the SF and SA blend.

Blend	SF	SA	WA
$SF_{0.5}/SA_{0.5}/WA_{99}$	0.5	0.5	99
$SF_{1.5}/SA_{0.5}/WA_{98}$	1.5	0.5	98
$SF_{1.0}/SA_{1.0}/WA_{98}$	1.0	1.0	98
$SF_{0.5}/SA_{1.5}/WA_{98}$	0.5	1.5	98
$SF_{1.5}/SA_{1.5}/WA_{97}$	1.5	1.5	97
$SF_{1.0}/SA_{2.0}/WA_{97}$	1.0	2.0	97
$SF_{0.5}/SA_{2.5}/WA_{97}$	0.5	2.5	97

chosen following previous studies (Lopes et al., 2018) which showed that for more concentrated systems, i.e., with less water, hydrogel formation would occur. Thus, it would not be possible to make a quantitative analysis of each phase. To prepare the blends, SF was slowly added to SA solution under stirring, the system was kept in a thermostatic bath at 25°C (Nova Analitica, Brazil). After 8 days, each phase was collected and the components were quantified. The notation used to refer the blends was $SA_{x\%}/SF_{y\%}/WA_{z\%}$ where x, y, and z are the mass fraction of each component in the blend.

Zeta Potential

Zeta potential was performed using Malvern Zetasizer Nano ZS (Malvern, United Kingdom). It was measured using a zeta universal dip cell and polystyrene cuvettes. The polymers concentration was 1 $g.L^{-1}$ and the samples were measured three times. The values of the refractive index and absorbance used were 1.33 and 0.001 a.u for SA and 1.45 and 0.001 a.u for SF. The absorbance was measured using the Varioskan LUX multimode microplate reader (Thermo Fisher Scientific, United States) and the refractive index was measured using a refractometer (Instrutherm, Brazil). The pH of SF and SA solution was 6.77 and 7.63, respectively. Zeta potential was performed to analyze the blends by mixing the SF and SA solution with the same concentration in different volume proportions, 75–25, 50–50 and 75–25 (SA-SF).

Optical Microscopy

The optical microscopy was used to analyze the morphology of microparticles formed after blend preparation. The optical microscopy was performed using the E200 optical microscope (Nikon, Japan). The image was analyzed using ImageJ software.

Phase Quantification

After phase separation, the blends were centrifuged for 15 min and 2300 RCF, the final state of SA/SF blends is a liquid phase and a "solid" one that looks like a hydrogel and it is mostly composed by SF with water trapped in the structure. The analysis used to quantify each phase is described in **Figure 1**.

Water was quantified gravimetrically by solvent evaporation in the liquid and solid phase in an oven until the weight was constant. SF in the liquid phase was quantified by Bradford assay (Bradford, 1976), a consolidated method to quantify proteins using the Coomassie Blue G-250 stain with maximum absorbance in the range between 465 and 595 nm. This method was chosen because carbohydrates do not interfere with the results. It was prepared a calibration curve from 0 to 100 μg/mL using Bradford reagent (Amresco, United States) that was analyzed at 590 nm using a 24 plate-well in a spectrophotometer (Tecan M200 Pro, Switzerland). In the solid-like phase, it was not possible to use the same method because SF was insoluble, so it was quantified by mass balance using Eq. 3.

$$m_{sfsp} = m_{msp} - m_{wasp} - m_{masp} \tag{3}$$

where m_{msp} is the total mass of solid phase, m_{sfsp} is the SF mass in the solid-like phase, m_{wasp} is the water mass in the solid-like phase and m_{sasp} is the SA mass in the solid-like phase.

The SA was quantified by mass balance in both phases using Eqs 4 and 5.

$$m_{salp} = m_{mlp} - m_{sflp} - m_{walp} \tag{4}$$

where m_{salp} is the SA mass in the liquid phase, m_{mlp} is the total mass of liquid phase, m_{sflp} is the SF mass in the liquid phase (determinate by Bradford assay) and m_{walp} is the water mass in the liquid phase.

$$m_{sasp} = (m_t * a) - m_{salp} \tag{5}$$

where m_{sasp} is the SA mass in the solid phase, m_t is the blend mass, α is the SA mass fraction in the blend, and m_{salp} is the SA mass in the liquid phase.

Flory-Huggins Parameter of Interaction

The Flory-Huggins model is a classic mathematical approach for polymer systems. It uses the balance between the entropic and enthalpic contributions (Eqs 6 and 7), regarding the size and form effect and the intermolecular interactions.

$$\frac{\Delta S}{R} = \Sigma \; x_i \; \ln \varphi_i \tag{6}$$

$$\frac{\Delta H}{RT} = \left(\sum {}_i x_i \frac{V_i}{V_s}\right) \sum {}_i \sum {}_{j>i} \frac{\chi_{ij}}{T} \varphi_i \varphi_j \tag{7}$$

where R is the gas constant, T is the temperature, x_i is the molar fraction of component i, V_i e V_s are the volume per amount of matter of pure component i and for solvent, respectively; χ_{ij} is the Flory-Huggins parameter of interaction for component i and j, φ_i and φ_j are the volumetric fractions of component i and j.

By replacing Eqs 6 and 7 in Eq. 1, the extended expression of the Flory-Huggins equation is obtained, which is usually simplified for use in a polymer-solvent system. The Flory-Huggins parameter can be, also, calculated using the activity value of each component in each phase. This is useful because in the equilibrium the chemical potential of each component in each phase is equal, and using the data of equilibrium is possible to calculated Flory-Huggins parameter solving a non-linear equation system, described by Eqs 8–10 for a ternary system (Favre et al., 1996).

$$lna_1 = \ln \varphi_1 + (1 - \varphi_1) - \left(\frac{V_1}{V_2}\right) \varphi_2 - \left(\frac{V_1}{V_3}\right) \varphi_3 +$$

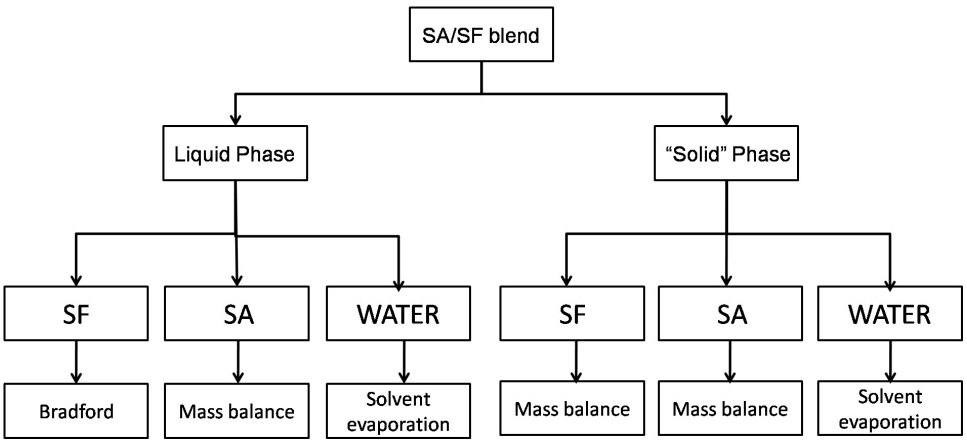

FIGURE 1 | Scheme showing the methodology used to quantify the different substances in liquid and solid-like phase.

$$((\chi_{12}\varphi_2 + \chi_{13}\varphi_3)(\varphi_2 + \varphi_3)) - \chi_{23}(\frac{V_1}{V_2})\varphi_2\varphi_3 \quad (8)$$

$$lna_2 = \ln\ \varphi_2 + (1 - \varphi_2) - \left(\frac{V_2}{V_1}\right)\ \varphi_1 - \ \left(\frac{V_2}{V_3}\right)\ \varphi_3 +$$

$$\left((\chi_{12}\varphi_1(\frac{V_2}{V_1}) + \chi_{23}\varphi_3)(\varphi_1 + \varphi_3)\right) - \chi_{13}(\frac{V_2}{V_1})\varphi_1\varphi_3 \quad (9)$$

$$\varphi_1 + \varphi_2 + \varphi_3 = 1 \quad (10)$$

where a_1 and a_2 are the activity of component 1 and 2, respectively; V_1, V_2 and V_3 are the volume per amount of matter of component 1, 2, and 3, respectively; χ_{12}, χ_{13}, and χ_{23} are the Flory-Huggins parameter of component 1–2, 1–3, and 2–3, respectively.

The Flory-Huggins model is used to describe various polymeric systems, due to its simplicity and the possibility of its interaction parameter being determined experimentally by calorimetric techniques or, osmotic pressure, for example (Safronov et al., 2009; Kim et al., 2010). The extended equation can be used as an initial model to describe and understand the forces involved in polymer-polymer and polymer-solvent interactions.

RESULTS

Physical Aspects of the SA/SF Blends

After the addition of silk fibroin in sodium alginate solution, for blend preparation, it was possible to notice that the solution became cloudy immediately, even in blends with low polymer concentration, for instance, $SF_{0.5}SA_{0.5}WA_{99}$. When observing the blend in optical microscopy, microstructures with a diameter of 0.247 ± 0.120 mm were detected (**Figure 2A**). The formation

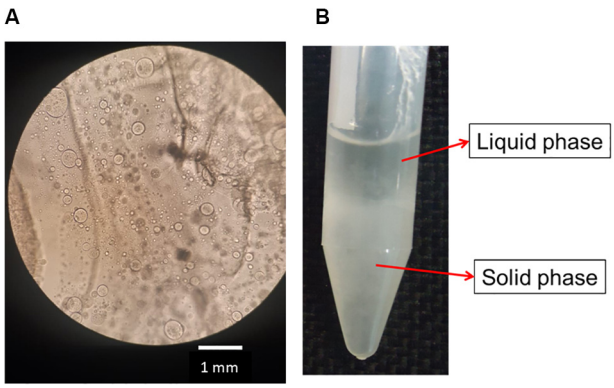

FIGURE 2 | Image of optical microscopy of silk fibroin and sodium alginate blend after preparing **(A)**. Photo of the $SA_{0.5}/SF_{0.5}/WA_{99}$ blend showing phase separation and formation of a liquid and solid-like phase **(B)**.

of these structures, like drops, was also verified in other protein-polysaccharide systems, such as alginate-casein and alginate-pea protein (Pacek et al., 2000; Antonov and Moldenaers, 2011; Mession et al., 2012). After 1 day, it was possible to notice two phases, shown in **Figure 2B**. The proportion of each phase changes over the days, the solid-like phase becomes denser, indicating that even if phase separation started after 1 day (macroscopically), the system was not in thermodynamic equilibrium. The evolution of this phenomenon was investigated by static light scattering (Lopes et al., 2018) and the system was considered in equilibrium when changes in the scattering profile were not observed anymore, which happened after the eighth day. It is possible that over time, the microstructures observed in the microscope, collapse and precipitate forming the solid-like phase (**Figure 3**).

The hydrogel formation, here called the solid-like phase, is a spontaneous phenomenon. It could happen due to the hydrophobic interaction and intra and intermolecular hydrogen bonds, changing the SF conformation from α-helix to β-sheet,

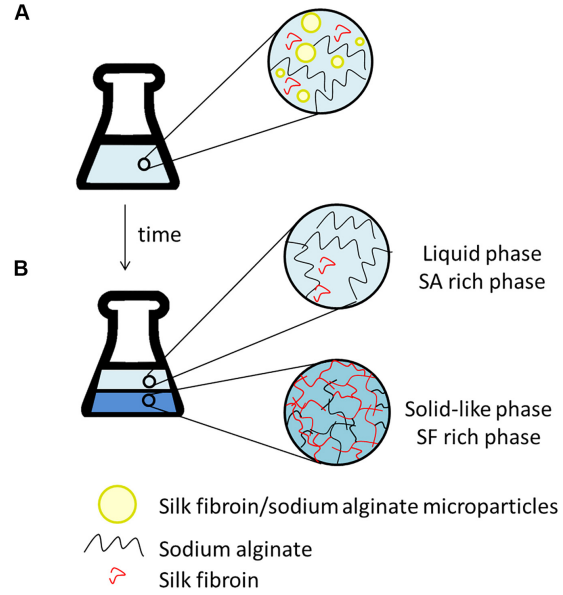

FIGURE 3 | Scheme illustrating the time evolution of phase separation that could be occurring in the silk fibroin/sodium alginate blends. **(A)** After preparing the blends: microparticles formation (observed in microscope). **(B)** After some days: liquid phase enriched with SA, coalescence of globules and hydrogel (solid-like phase) formation. The water is present in both stages **(A,B)** and represented by the blue background.

precipitating the protein and turning it stable in water (Matsumoto et al., 2006). Some parameters can contribute to the hydrogel formation, such as protein concentration, decreasing pH, chemical crosslinking and temperature (Nogueira et al., 2011; Yin et al., 2017). In previous studies, it was observed that the increase in temperature could accelerate the hydrogel formation from SF solution, as well as, the presence of poly(ethylene oxide) (PEO), a water-soluble polymer (Kim et al., 2004; Nogueira et al., 2011; Zhong et al., 2015; Yin et al., 2017). Based on the literature, SA may have the same influence, accelerating the formation of the solid-like phase.

Zeta Potential

Table 2 shows the values of zeta potential. that was negative for both polymers. For SF this parameter is close to zero, showing a balance of charges between the amino and carboxyl groups. The pI for SF is around 4, so in neutral pH, there is a predominance of negative charges, which justify the value obtained (Wenk et al., 2011). This zeta potential value also indicates that the SF solution is unstable, based on DLVO theory (Derjaguin and Landau, 1941), which could explains the spontaneous hydrogel formation after some days. The SA zeta potential value was −57.9 mV. At neutral pH, the carboxyl groups are deprotonated (pKa = 3.4–3.6) (Draget et al., 1997), so the polymer chain will be negatively charged.

Analyzing the zeta potential values of each polymer is reasonable to conclude that there will be an electrostatic repulsion between the polymers. At the same time, there will be also an interaction between the amino groups from SF and the carboxyl groups of SA. The results of blends zeta potential show that for the ones with more SF in the composition, the zeta potential is higher showing charge compensation phenomenon.

TABLE 2 | Values of zeta potential (mV) of SF, SA, and blends. Solution concentration for both polymers was 1 g/L and solution pH was 6.77 for SF and 7.63 for SA.

	Zeta potential (mV)
SF	−12.7 ± 0.3
SA	−57.9 ± 0.4
SA_{75}/SF_{25}	−64.0 ± 2.8
SA_{50}/SF_{50}	−50.0 ± 2.3
SA_{25}/SF_{75}	−29.4 ± 0.5

Phase Quantification and Estimation of Flory-Huggins Parameter of Interaction

After phase separation, a phase rich in SA (liquid) and another rich in SF (solid-like) are observed, the experimental results for the composition of each phase are shown in **Table 3** and plotted in the ternary graph shown at **Figure 4**. Water is the most predominant component of the phases, even in the solid-like one, where water is probably entrapped between the polymer chains, and then the hydrogel formation occurs, as proposed in **Figure 3**. The tie lines are very close to each other and it was observed that each blend presents some variability, that is expected due to the characteristics of SF and SA solutions, which form a dispersion and may have a small variation in the same sample. Besides, there is inherent variability in the measurements, therefore, the establishment of this region is important.

The phase diagram can be analyzed by the method presented by Popova et al. (2008) that is based on two major principles. The first one is that the protein-rich phase is not a single phase but a mixture of two: a supernatant and a "true" precipitate, which cannot be separated. The other is that the extension of the tie lines would converge to one point, which represents the "true" precipitate that in this case would be composed mostly by SF. The phase diagram shows that the tie-lines converge to a point with a high concentration of SF (5.4 wt% of SF, 1.25 wt% of SA, and 93.35 wt% of water). In practice, the "true" precipitate could not be obtained, because, at this concentration, the system would be in the "hydrogel" zone, therefore, it would not be possible to observe two distinguished phases.

It was observed that, for blends with the same SF initial concentration, the increase of SA initial concentration resulted in a higher concentration of this polymer in solid-like phase (**Figure 5**). It was expected that an increase in the polysaccharide concentration would lead to a more concentrated SF solid-like phase since the SA has more affinity to the solvent and would stay in solution. Thus, probably part of the SA rich phase could be entrapped within the SF rich phase, as observed in **Figure 5**, as a consequence of SA viscosity (Mession et al., 2012). This behavior is observed in other protein-polysaccharide systems, such as alginate-pea protein and soy protein-κ- carrageenan (Li et al., 2008; Mession et al., 2012).

TABLE 3 | Average mass fraction (%) of feed, SF rich phase (solid) and SA rich phase (liquid) at 25°C, $n = 3$.

Mass fraction (%) of each component in feed			Mass fraction (%) of SF rich phase (solid)			Mass fraction (%) of SA rich phase (liquid)		
SF	**SA**	**WA**	**SF**	**SA**	**WA**	**SF**	**SA**	**WA**
0.5	0.5	99	2.12 ± 0.47	0.82 ± 0.39	97.06 ± 0.08	0.01 ± 0.01	0.44 ± 0.08	99.55 ± 0.08
1.5	0.5	98	3.50 ± 0.23	0.59 ± 0.14	95.91 ± 0.09	0.06 ± 0.02	0.44 ± 0.11	99.50 ± 0.11
1.0	1.0	98	2.96 ± 0.10	1.30 ± 0.23	95.74 ± 0.32	0.05 ± 0.03	0.88 ± 0.10	99.07 ± 0.10
0.5	1.5	98	2.74 ± 0.33	1.27 ± 0.13	95.99 ± 0.04	0.04 ± 0.03	1.55 ± 0.03	98.41 ± 0.03
1.5	1.5	97	3.04 ± 0.12	1.62 ± 0.36	95.34 ± 0.52	0.05 ± 0.02	1.44 ± 0.29	98.50 ± 0.29
1.0	2.0	97	3.71 ± 0.03	1.58 ± 0.26	94.71 ± 0.33	0.07 ± 0.02	2.18 ± 0.08	97.75 ± 0.08
0.5	2.5	97	1.93 ± 0.22	2.04 ± 0.05	96.03 ± 0.18	0.09 ± 0.01	2.62 ± 0.03	97.29 ± 0.03

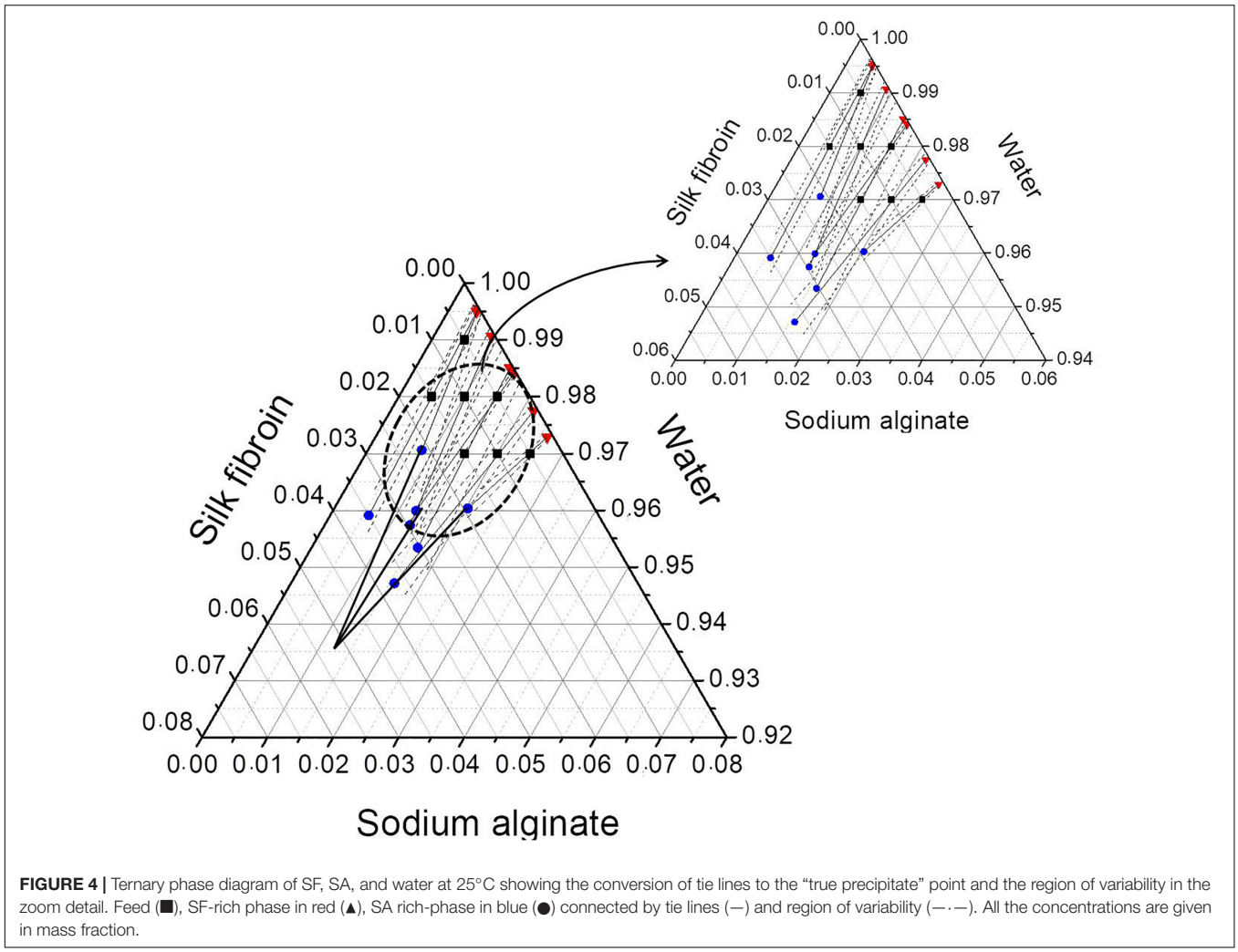

FIGURE 4 | Ternary phase diagram of SF, SA, and water at 25°C showing the conversion of tie lines to the "true precipitate" point and the region of variability in the zoom detail. Feed (■), SF-rich phase in red (▲), SA rich-phase in blue (●) connected by tie lines (—) and region of variability (—·—). All the concentrations are given in mass fraction.

The three Flory-Huggins parameters of interaction were estimated by solving the non-linear equation system described by Eqs 8–10, the values are reported in **Table 4**. Using those values and the equilibrium data, new mass fractions were calculated by fixing the composition of two values and using Eq. 8 for both phases. The theoretical mass fractions for each component in liquid and solid-like phases are shown in **Table 5**, and the ternary phase diagram with the calculated and experimental data is shown in **Figure 6**. The binodal curve was plotted using the Flory-Huggins model. It was not possible to obtain the experimental binodal curve, because this is, usually, obtained by cloudy point experiments. As previously described, when mixing the silk fibroin solution in sodium alginate solution, the formation of microstructures (like drops) is observed, even in blend with low polymer concentration, which makes it difficult to determinate the cloudy point.

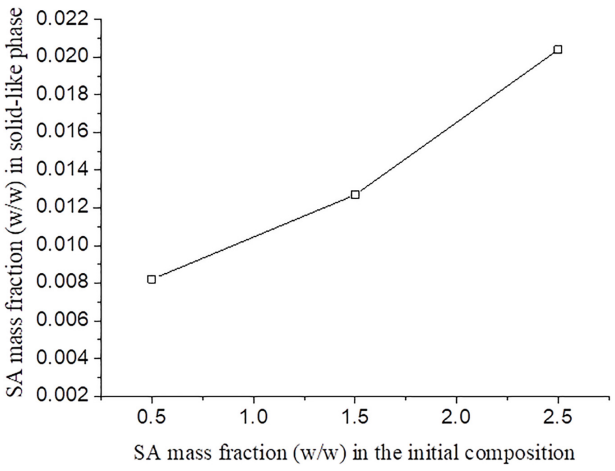

FIGURE 5 | SA mass fraction in the solid-like phase after phase separation for different SF initial concentration as function of the SA initial concentration.

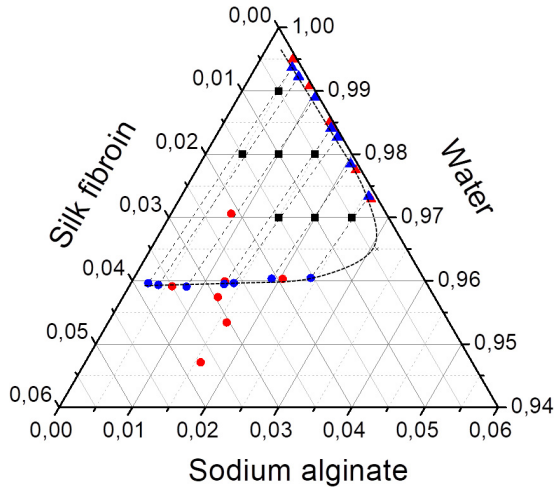

FIGURE 6 | Ternary phase diagram of SF, SA, and water at 25°C with the feed composition (■), experimental (red), and calculated data (blue) of liquid (▲) and solid-like phase (●). Binodal curve plotted with calculated data (– –).

TABLE 4 | Values of Flory-Huggins parameters of interaction (χ_{SAWA}, χ_{SFWA}, and χ_{SFSA}) for silk fibroin-sodium alginate-water system at 25°C.

χ_{SAWA}	χ_{SFWA}	χ_{SFSA}
−0.004	0.015	−0.424

DISCUSSION

The system formed by SF, SA, and water is complex and partially miscible. That is a common phenomenon observed in protein-polysaccharide systems. A study conducted by Grinberg and Tolstoguzov (1997) showed almost a hundred different systems considered thermodynamically incompatible. After blend preparation, it was observed the formation of microstructures, like drops, in solution, indicating that phase separation occurs almost instantly. After some days, the polymers formed two phases, one liquid and rich in SA, another solid-like and rich in SF. It was observed that the kinetics of phase separation is slow; it takes 8 days to the system to reach equilibrium. The zeta potential showed that at the pH used for blends preparation, SF and SA are negatively charged, which favors the electrostatic repulsion. Despite that, the chemical interaction is observed, with a charge compensation between the polymers, because the SF has groups positively charged, NH^{+}_{3}, and SA has groups negatively charged, COO^{-}, which could interact through hydrogen bonds (Shang et al., 2013). The system with more quantity of SF presented zeta potential closer to zero, due to the interaction between carboxyl and amino groups.

In systems containing biopolymers, two different types of phase separation can be observed: associative phase separation or segregated phase separation, it depends on the interactions between the biopolymer and the solvent (Doublier et al., 2000). The first one occurs when the polymer has more affinity to the solvent than to the other polymer; generally, the Flory-Huggins parameter is positive. The second one occurs when the polymer-polymer interactions are favored, and normally the Flory-Huggins parameter is negative (Doublier et al., 2000). It is observed the formation of complexes or polymer coacervate. The experimental results for the system studied and the interpretation from the point of view of phase equilibrium thermodynamics showed that the solid-like phase seems to be a mixture between SF and a supernatant formed by alginate water that coacervates,

TABLE 5 | Mass fraction of silk fibroin, sodium alginate, and water calculated using the parameter of Flory-Huggins estimated by the non-linear system of Eqs. 8, 9, and 10.

Mass fraction (%) of each component in feed			Mass fraction (%) of SF rich phase (solid)			Mass fraction (%) of SA rich phase (liquid)		
SF	**SA**	**WA**	**SF**	**SA**	**WA**	**SF**	**SA**	**WA**
0.5	0.5	99	3.80	0.24	95.96	0.13	0.50	99.37
1.5	0.5	98	3.68	0.39	95.93	0.11	0.66	99.23
1.0	1.0	98	3.31	0.79	95.90	0.05	1.05	98.90
0.5	1.5	98	2.77	1.28	95.95	0.08	1.51	98.41
1.5	1.5	97	2.63	1.41	95.96	0.07	1.67	98.27
1.0	2.0	97	2.08	1.89	96.03	0.09	2.06	97.84
0.5	2.5	97	1.54	2.42	96.04	0.10	2.57	97.33

forming a hydrogel. The formation of a "true precipitate" could not be possible in this system because it requires a high amount of SF, which in practice leads to hydrogel formation. Due to the characteristics of the system, the formation of a coacervate and negative Flory-Huggins parameter of interaction, probably the type of phase separation observed in silk-alginate system is the segregated one. Another fact that corroborates is that segregated phase separation usually occurs when anionic polysaccharide is mixed with proteins with a negative charge (close to neutrality), which is the case of silk-alginate blends.

The value of the Flory-Huggins parameter of SF-SA interaction is negative, while SA-water and SF-water parameters of interaction are negative and positive, respectively. If we analyze the Equation 7 the Flory-Huggins parameter is related to the enthalpic contribution, which for polymers is more significant than the entropic contribution since the polymers chains have low mobility and fewer possibilities of molecular configuration. Generally, the enthalpic term is also unfavorable to the establishment of a miscibility system, mainly for polymers that interact through van der Walls bond (Kim et al., 2010). However, for polymers that interact by ionic bonds, dipole-dipole, or hydrogen bonds, miscibility can be achieved. Therefore, if the polymers have a good chemical interaction, represented by the negative F-H parameter, it is reasonable to expect a miscible or semi-miscible blend, which occurs in the SF-SA blend. The polymer-polymer parameter is very important, but the phase separation phenomenon takes into account the polymer-solvent interaction, and depending on this balance of forces, phase separation will be favored or not. That is why it is important to use the F-H extended equation, so this analysis can be done more accurately.

The Flory-Huggins model is widely used due to the facility to obtain experimentally the parameter of interaction. It is based on three hypotheses (Schmid, 2011):

1. The polymer conformation is considered an ideal chain, independent on the composition;
2. The polymers are considered incompressible and the monomers occupy equal volumes;
3. The local composition fluctuations are neglected.

In practice, none of them is valid, since the polymer conformation depends on composition, the monomers volumes are not equal and the composition fluctuation has an important influence in phase separation. These variations can have a significant influence on the real Flory-Huggins parameter, especially for natural polymers that already have intrinsic variability in their composition. Despite the limitations, the model presented an acceptable correlation, mainly in the liquid phase, and can give important information about the studied system. It can be used for initial studies and its physical-chemical interpretation must take into account all the limitations.

The understanding of a complex system, such as those formed by protein and polysaccharides, is important because they have been used extensively in our daily life. Therefore, fundamental studies are important, to predict and understand the system behavior, allowing the products made by these polymers to be produced and available in the market.

DATA AVAILABILITY STATEMENT

The datasets generated for this study are available on request to the corresponding author.

AUTHOR CONTRIBUTIONS

MB conceived of the presented idea. LL performed the experiments and analyzed the data. MM and MB verified the analytical methods. and supervised the findings of this work. All authors discussed the results and contributed to the final manuscript.

FUNDING

This study was financed by the Coordenação de Aperfeiçoamento de Pessoal de Nível Superior – Brazil (CAPES – Finance Code 001).

ACKNOWLEDGMENTS

The authors acknowledge the grant that allowed the development of this work (CAPES – Finance Code 001).

REFERENCES

Agulhon, P., Robitzer, M., Habas, J.-P., and Quignard, F. (2014). Influence of both cation and alginate nature on the rheological behavior of transition metal alginate gels. *Carbohydr. Polym.* 112, 525–531. doi: 10.1016/j.carbpol.2014.05.097

Antonov, Y. A., Lashko, N. P., Glotova, Y. K., Malovikova, A., and Markovich, O. (1996). Effect of the structural features of pectins and alginates on their thermodynamic compatibility with gelatin in aqueous media. *Food Hydrocoll.* 10, 1–9. doi: 10.1016/S0268-005X(96)80047-6

Antonov, Y. A., and Moldenaers, P. (2011). Structure formation and phase-separation behaviour of aqueous casein-alginate emulsions in the presence of strong polyelectrolyte. *Food Hydrocoll.* 25, 350–360. doi: 10.1016/j.foodhyd.2010.06.013

Bai, S., Liu, S., Zhang, C., Xu, W., Lu, Q., Han, H., et al. (2013). Controllable transition of silk fibroin nanostructures: an insight into in vitro silk self-assembly process. *Acta Biomater.* 9, 7806–7813. doi: 10.1016/j.actbio.2013.04.033

Bhutani, U., Laha, A., Mitra, K., and Majumdar, S. (2015). Sodium alginate and gelatin hydrogels: viscosity effect on hydrophobic drug release. *Mater. Lett.* 164, 76–79. doi: 10.1016/j.matlet.2015.10.114

Brachkova, M. I., Marques, P., Rocha, J., Sepodes, B., Duarte, M. A., and Pinto, J. F. (2011). Alginate films containing lactobacillus plantarum as wound dressing for prevention of burn infection. *J. Hosp. Infect.* 79, 375–377. doi: 10.1016/j.jhin.2011.09.003

Bradford, M. M. (1976). A rapid and sensitive method for the quantitation of microgram quantities of protein utilizing the principle of protein-dye binding. *Anal. Biochem.* 72, 248–254. doi: 10.1016/0003-2697(76)90527-3

Calamak, S., Erdoğdu, C., Ozalp, M., and Ulubayram, K. (2014). Silk fibroin based antibacterial bionanotextiles as wound dressing materials. *Mater. Sci. Eng. C* 43, 11–20. doi: 10.1016/j.msec.2014.07.001

de Moraes, M. A., and Beppu, M. M. (2013). Biocomposite membranes of sodium alginate and silk fibroin fibers for biomedical applications. *J. Appl. Polym. Sci.* 130, 3451–3457. doi: 10.1002/app.39598

de Moraes, M. A., Silva, M. F., Weska, R. F., and Beppu, M. M. (2014). Silk fibroin and sodium alginate blend: miscibility and physical characteristics. *Mater. Sci. Eng. C* 40, 85–91. doi: 10.1016/j.msec.2014.03.047

Derjaguin, B., and Landau, L. D. (1941). Theory of the stability of strongly charged lyophobic sols and of the adhesion of strongly charged particles in solutions of electrolytes. *Acta Physicochimica U.R.S.S.* 14, 633–662.

Doublier, J. L., Garnier, C., Renard, D., and Sanchez, C. (2000). Protein-polysaccharide interactions. *Curr. Opin. Colloid Interface Sci.* 5, 202–214. doi: 10.1201/9780203755617

Draget, K. I., Skjåk-Bræk, G., and Smidsrød, O. (1997). Alginate based new materials. *Int. J. Biol. Macromol.* 21, 47–55. doi: 10.1016/S0141-8130(97)00040-8

Favre, E., Nguyen, Q. T., Clement, R., and Neel, J. (1996). Application of flory-huggins theory to ternary polymer-solvents equilibria: a case study. *Eur. Polym. J.* 32, 303–309. doi: 10.1016/0014-3057(95)00146-8

Feng, C., Song, R., Sun, G., Kong, M., Bao, Z., Li, Y., et al. (2014). Immobilization of coacervate microcapsules in multilayer sodium alginate beads for efficient oral anticancer drug delivery. *Biomacromolecules* 15, 985–996. doi: 10.1021/bm401890x

Grinberg, V. Y., and Tolstoguzov, V. B. (1997). Thermodynamic incompatibility of proteins and polysaccharides in solutions. *Food Hydrocoll.* 11, 145–158. doi: 10.1016/S0268-005X(97)80022-7

Kim, S. D., Chakravarti, S., Tian, J., and Bell, P. (2010). The phase behavior and the flory-huggins interaction parameter of blends containing amorphous poly(resorcinol phthalate-block-carbonate), poly(bisphenol-a carbonate) and poly(ethylene terephthalate). *Polymer* 51, 2199–2206. doi: 10.1016/j.polymer.2010.03.018

Kim, U.-J., Park, J., Kim, H. J., Wada, M., and Kaplan, D. L. (2005). Three-dimensional aqueous-derived biomaterial scaffolds from silk fibroin. *Biomaterials* 26, 2775–2785. doi: 10.1016/j.biomaterials.2004.07.044

Kim, U. J., Park, J., Li, C., Jin, H. J., Valluzzi, R., and Kaplan, D. L. (2004). Structure and properties of silk hydrogels. *Biomacromolecules* 5, 786–792. doi: 10.1021/bm0345460

Koh, L. D., Cheng, Y., Teng, C. P., Khin, Y. W., Loh, X. J., Tee, S. Y., et al. (2015). Structures, mechanical properties and applications of silk fibroin materials. *Prog. Polym. Sci.* 46, 86–110. doi: 10.1016/j.progpolymsci.2015.02.001

Kundu, B., Rajkhowa, R., Kundu, S. C., and Wang, X. (2013). Silk fibroin biomaterials for tissue regenerations. *Adv. Drug Deliv. Rev.* 65, 457–470. doi: 10.1016/j.addr.2012.09.043

Leung, V., Hartwell, R., Elizei, S. S., Yang, H., Ghahary, A., and Ko, F. (2014). Postelectrospinning modifications for alginate nanofiber-based wound dressings. *J. Biomed. Mater. Res. B. Appl. Biomater.* 102, 508–515. doi: 10.1002/jbm.b.33028

Li, S., Li, L., Guo, C., Qin, H., and Yu, X. (2017). A Promising Wound dressing material with excellent cytocompatibility and proangiogenesis action for wound healing: strontium loaded silk fibroin/sodium alginate (SF/SA) blend films. *Int. J. Biol. Macromol.* 104, 969–978. doi: 10.1016/j.ijbiomac.2017.07.020

Li, X., Hua, Y., Qiu, A., Yang, C., and Cui, S. (2008). Phase behavior and microstructure of preheated soy proteins and κ-carrageenan mixtures. *Food Hydrocoll.* 22, 845–853. doi: 10.1016/j.foodhyd.2007.04.008

Li, X., Yan, S., Qu, J., Li, M., Ye, D., You, R., et al. (2018). Soft freezing-induced self-assembly of silk fibroin for tunable gelation. *Int. J. Biol. Macromol.* 117, 691–695. doi: 10.1016/j.ijbiomac.2018.05.223

Liang, C. X., and Hirabayashi, K. (1992). Improvements of the physical properties of fibroin membranes with sodium alginate. *J. Appl. Polym. Sci.* 45, 1937–1943.

Lopes, L. M., De Moraes, M. A., and Beppu, M. M. (2018). Study of phase separation in blends of silk fibroin and sodium alginate in solution and in solid state. *J. Polym. Res.* 25, 198. doi: 10.1007/s10965-018-1594-3

Lu, Q., Zhu, H., Zhang, C., Zhang, F., Zhang, B., and Kaplan, D. L. (2012). Silk self-assembly mechanisms and control from thermodynamics to kinetics. *Biomacromolecules.* 13, 826–832. doi: 10.1021/bm201731e

Matsumoto, A., Chen, J., Collette, A. L., Kim, U. J., Altman, G. H., Cebe, P., et al. (2006). Mechanisms of silk fibroin Sol-Gel transitions. *J. Phys. Chem. B* 110, 21630–21638. doi: 10.1021/jp056350v

Meng, X., Tian, F., Yang, J., He, C. N., Xing, N., and Li, F. (2010). Chitosan and alginate polyelectrolyte complex membranes and their properties for wound dressing application. *J. Mater. Sci. Mater. Med.* 21, 1751–1759. doi: 10.1007/s10856-010-3996-6

Mession, J. L., Assifaoui, A., Lafarge, C., Saurel, R., and Cayot, P. (2012). Protein aggregation induced by phase separation in a pea proteins-sodium alginate-water ternary system. *Food Hydrocoll.* 28, 333–343. doi: 10.1016/j.foodhyd.2011.12.022

Ming, J., and Zuo, B. (2014). A novel silk fibroin/sodium alginate hybrid scaffolds. *Polym. Eng. Sci.* 54, 129–136. doi: 10.1002/pen.23542

Mishra, J., Tiwari, S. K., Abolhasani, M. M., Azimi, S., and Nayak, G. C. (2017). "Fundamental of polymer blends and its thermodynamics," in *Micro and Nano Fibrillar Composites (MFCs and NFCs) from Polymer Blends*, ed. S. Thomas (Amsterdam: Elsevier Ltd). doi: 10.1016/B978-0-08-101991-7.00002-9

Nogueira, G. M., De Moraes, M. A., Rodas, A. C. D., Higa, O. Z., and Beppu, M. M. (2011). Hydrogels from silk fibroin metastable solution: formation and characterization from a biomaterial perspective. *Mater. Sci. Eng.* 31, 997–1001. doi: 10.1016/j.msec.2011.02.019

Pacek, A. W., Ding, P., Nienow, A. W., and Wedd, M. (2000). Phase separation and drop size distributions in ' Homogeneous ' Na-alginate / Na-caseinate mixtures. *Carbohydr. Polym.* 42, 401–409.

Panouillé, M., and Larreta-Garde, V. (2009). Gelation behaviour of gelatin and alginate mixtures. *Food Hydrocoll.* 23, 1074–1080. doi: 10.1016/j.foodhyd.2008.06.011

Popova, E., Watanabe, E. O., Pessôa Filho, P. A., and Maurer, G. (2008). Phase equilibria for salt-induced lysozyme precipitation: effect of salt concentration and PH. *Chem. Eng. Process.* 47, 1026–1033. doi: 10.1016/j.cep.2007.02.005

Ribeiro, M., De Moraes, M. A., Beppu, M. M., Monteiro, F. J., and Ferraz, M. P. (2014). The role of dialysis and freezing on structural conformation, thermal properties and morphology of silk fibroin hydrogels. *Biomatter* 4:e28536. doi: 10.4161/biom.28536

Safronov, A. P., Blyakhman, F. A., Shklyar, T. F., Terziyan, T. V., Kostareva, M. A., Tchikunov, S. A., et al. (2009). The influence of counterion type and temperature on flory-huggins binary interaction parameter in polyelectrolyte hydrogels. *Macromol. Chem. Phys.* 210, 511–519. doi: 10.1002/macp.200800495

Sarker, B., Rompf, J., Silva, R., Lang, N., Detsch, R., Kaschta, J., et al. (2015). Alginate-based hydrogels with improved adhesive properties for cell encapsulation. *Int. J. Biol. Macromol.* 78, 72–78. doi: 10.1016/j.ijbiomac.2015.03.061

Schmid, F. (2011). "Theory and simulation of multiphase polymer systems," in *Handbook of Multiphase Polymer Systems*, eds A. Boudenne, L. Ibos, Y. Candau, and S. Thomas (New Jersey: John Wiley & Sons Ltd), 31–80. doi: 10.1002/9781119972020.ch3

Shang, S., Zhu, L., and Fan, J. (2013). Intermolecular interactions between natural polysaccharides and silk fibroin protein. *Carbohydr. Polym.* 93, 561–573. doi: 10.1016/j.carbpol.2012.12.038

Sohn, S., Strey, H. H., and Gido, S. P. (2004). Phase behavior and hydration of silk fibroin. *Biomacromolecules* 5, 751–757. doi: 10.1021/bm0343693

Utracki, L. A., and Manias, E. (2014). "Thermodynamics of polymer blends," in *Polymer Blends Handbook*, eds L. A. Utracki and C. A. Wilkie (Dordrecht: Springer), 517–675. doi: 10.1007/978-94-007-6064-6

Wang, Y., Fan, S., Li, Y., Niu, C., Li, X., Guo, Y., et al. (2020). Silk fibroin/sodium alginate composite porous materials with controllable degradation. *Int. J. Biol. Macromol.* 150, 1314–1322. doi: 10.1016/j.ijbiomac.2019.10.141

Wang, Y., Wang, X., Shi, J., Zhu, R., Zhang, J., Zhang, Z., et al. (2016). A biomimetic silk fibroin/sodium alginate composite scaffold for soft tissue engineering. *Sci. Rep.* 6:39477. doi: 10.1038/srep39477

Wang, Z., Yang, H., and Zhu, Z. (2019). Study on the blends of silk fibroin and sodium alginate: hydrogen bond formation, structure and properties. *Polymer* 163, 144–153. doi: 10.1016/j.polymer.2019.01.004

Wenk, E., Merkle, H. P., and Meinel, L. (2011). Silk fibroin as a vehicle for drug delivery applications. *J. Control. Release* 150, 128–141. doi: 10.1016/j.jconrel.2010.11.007

Yang, Y., Kwak, H. W., and Lee, K. H. (2013). Effect of residual lithium ions on the structure and cytotoxicity of silk fibroin film. *Int. J. Indust. Entomol.* 27, 265–270.

Yin, Z., Wu, F., Xing, T., Yadavalli, V. K., Kundu, S. C., and Lu, S. (2017). A silk fibroin hydrogel with reversible sol-gel transition. *RSC Adv.* 7, 24085–24096. doi: 10.1039/c7ra02682j

Zhang, H., Liu, X., Yang, M., and Zhu, L. (2015). Silk fibroin/sodium alginate composite nano-fibrous scaffold prepared through thermally induced phase-separation (TIPS) method for biomedical applications. *Mater. Sci. Eng. C* 55, 8–13. doi: 10.1016/j.msec.2015.05.052

Zhong, J., Liu, X., Wei, D., Yan, J., Wang, P., Sun, G., et al. (2015). Effect of incubation temperature on the self-assembly of regenerated silk fibroin: a study using AFM. *Int. J. Biol. Macromol.* 76, 195–202. doi: 10.1016/j.ijbiomac.2015.02.045

Conflict of Interest: The authors declare that the research was conducted in the absence of any commercial or financial relationships that could be construed as a potential conflict of interest.

frontiers in Materials

ORIGINAL RESEARCH
published: 13 November 2020
doi: 10.3389/fmats.2020.504642

Progress in Silk Fibroin Based Composite Scaffold/Hydrogel: Silk Fibroin/PEG Hydrogel for the RPE Regeneration a Promising Biomaterial for Clinical Application

*Yong Woon Jeong, Han Sol Kim, Muthukumar Thangavelu, Min Joung Choi, Gi Won Lee, Cheol Ui Song, Jeong Eun Song and Gilson Khang**

Department of BIN Convergence Technology, Polymer Nano Science & Technology, Polymer Materials Fusion Center, Jeonbuk National University, Jeonju, South Korea

OPEN ACCESS

Edited by:
Nicola Maria Pugno, University of Trento, Italy

Reviewed by:
Pasquale Vena, Politecnico di Milano, Italy
Domenico De Tommasi, Politecnico di Bari, Italy

***Correspondence:**
Gilson Khang
gskhang@jbnu.ac.kr

Specialty section:
This article was submitted to Mechanics of Materials, a section of the journal Frontiers in Materials

Received: *14 October 2019*
Accepted: *13 August 2020*
Published: *13 November 2020*

Citation:
Jeong YW, Kim HS, Thangavelu M, Choi MJ, Lee GW, Song CU, Song JE and Khang G (2020) Progress in Silk Fibroin Based Composite Scaffold/Hydrogel: Silk Fibroin/PEG Hydrogel for the RPE Regeneration a Promising Biomaterial for Clinical Application. Front. Mater. 7:504642. doi: 10.3389/fmats.2020.504642

Retinal pigment epithelium (RPE) plays a decisive role in the normal function of the retina, especially in the maintenance of photoreceptors. RPE dysfunction, loss of sight, and degeneration has been implicated as the cause of many retinal diseases including pigmented retinitis and age-related macular degeneration (AMD). Silk fibroin (SF) is a biodegradable natural polymer with biocompatibility, non-toxic, and non-immunological properties. In this study, hydrogel material was prepared by mixing it with PEG [poly (ethylene glycol)] a synthetic polymer. SF hydrogel (SH) and with PEG (SPH) were prepared with different sonication times. The SH and SPH were prepared with different sonication time (20s SH, 30s SH, 20s SPH, and 30s SPH were prepared, respectively. The prepared SH and SPH were physio chemically characterized by SEM, FTIR, compressive strength, porosity, and *in vitro* biocompatibility were analyzed using MTT assay along with cell adhesion and cell proliferation, their gene expression was analyzed using RT-PCR. As a result, the 20s SPH hydrogel exhibited superior biocompatibility, cell adhesion, and improved cell growth compared to pure SH. Their respective genes expression for retinal function and matrix production was also positively influenced by 20s SPH with an increase in gene expression folds of RPE65, CRALBP. The obtained results suggest that the 20s SPH hydrogel can be used as an alternative material for the application of retinal regeneration and delivery.

Keywords: silk fibroin, polyethylene glycol, retinal pigment epithelial, hydrogel, gene expression, porosity

INTRODUCTION

Retinal pigment epithelial cells (RPE) are the outermost layer of retina consisting of ten layers (Hageman et al., 2001). RPE cells nourish the retinal visual cells and are firmly attached to the choroid and retinal visual cells. RPE is composed of a single layer of hexagonal cells with dense pigment granules characterized by a dark color with melanin pigment (Bok, 1993; Strauss, 2005, 2009). RPE has several functions and plays an important role in maintaining the normal visual function of the retina (Simo et al., 2010). Degeneration of the RPE causes various retinal diseases.

Diseases of retinal and retinal functions can lead to permanent loss of visual function without any definitive treatment. The adverse effects of quality of life and poor vision on daily living activities affect the entire age range. Age-related macular degeneration (AMD) is a major cause of blindness and that cannot be reversed (Bressler et al., 1988; Liang and Godley, 2003). In the United States, there are 200,000 new cases a year. Death or malfunction of irreversible photoreceptors is common to all these pathologies. The rate of visual loss due to retinal degeneration is expected to increase due to aging. Currently, there was a lack of a cure for this, and studies are carried out to make a suitable scaffold that supports cell transplantation (Mandelcorn et al., 1975; Algvere et al., 1997; Lu et al., 2009; Bhutto and Lutty, 2012).

Natural polymers that can be used as a substrates for RPE regeneration including collagen, alginate, hyaluronic acid, gellan gum, gelatin, and silk fibroin (SF) and synthetic polymers including PLGA, PCL, and PEG (Lee et al., 2017; Wang and Han, 2017; Park et al., 2018; Kim et al., 2019; Shin et al., 2019). As a carrier that delivers RPE cells, it should have good cell adhesion, survival rate, invasiveness and biocompatible properties that helps in binding to other tissues of the retina. In addition, to increase cell efficiency, it should be an injectable and biodegradable material (Santin et al., 1999; Vepari and Kaplan, 2007; Binder, 2011). Among them, SF occupies 70–80% that is an excellent biomaterial with better mechanical, excellent water, and oxygen permeability properties; it is also used as a support material for cell adhesion, proliferation, and expression of the extracellular matrix (Wang et al., 2008; Yucel et al., 2009; Chao et al., 2010). PEG is a hydrophilic polymer having long linear chains and does not interact with biological chemicals. Therefore, PEG is widely used in medical instruments and materials for improving its physical properties (Zustiak and Leach, 2010; Kim et al., 2019).

Therefore, in this study, SH and SPH hydrogels were prepared and optimized to evaluate the suitability of new hydrogels for RPE cell regeneration. 4% SF and SFH were prepared by sonicating for the 20s and 30s, respectively. Porosity, biodegradability, FT-IR, and hygroscopicity were measured to characterize the hydrogel physiochemical properties. Cell attachment and proliferation rate of RPE cells were confirmed using MTT assay.

MATERIALS AND METHODS

Materials

Bombyx mori was purchased from Kyebong Farm (Korea) and polyethylene glycol (MW 10,000, Sigma-Aldrich) and Trizol (Invitrogen, Life Technologies Co, Groningen, Netherlands) were used in this study. The reagents required for cell culture were purchased from Gibco (United States), all other chemicals and organic solvents used were of HPLC grade.

Silk Fibroin Extract

The cocoon was cut into 1 cm × 1 cm pieces and SF solution was prepared by removing the sericin from the cocoons, by boiling them in 0.02 M sodium carbonate solution (Na_2CO_3, Showa chemical, Japan) for a minimum of 30 min and rinsed five times with double distilled water (dDW). The purified SF was dissolved in a 9.3 M lithium bromide (LiBr, Kanto Chemical, Japan) solution at 60°C for around 4 h. The obtained SF solution was dialyzed using a cellulose dialysis membrane (Snakeskin® Dialysis Tubing, 3.5K Mw, Thermo science, United States) in distilled water for 48 h. During the dialysis, the distilled water was replaced frequently, and the dialyzed aqueous solution was filtered and stored in the refrigerator until further use. The final concentration of the SF aqueous solution was concentrated to 8%.

Preparation of Silk Fibroin/PEG Hydrogel

For the preparation of SPH, PEG (10% v/v) was dissolved in distilled water and they were slowly added to the aqueous solution of SF and finally diluted to 4%. For the preparation of SH and SPH, the aqueous solution was added to the vial and tip sonication was performed for a period of 20s and 30s separately for each batch. 1ml of each solution was dispensed into a 24-well plate and stored in the refrigerator until further use (Samal et al., 2013). The hydrogel for the physicochemical characterization was prepared by lyophilization (using freeze dry method) by pouring them in a 15 mm diameter petri dish, followed by refrigerating, freezing for 4 h and quenching at −80°C, finally, they were lyophilized and stored for further use. The material sizes of 8 mm were cut using a biopsy.

Surface Morphology and Pore Size

Scanning electron microscopy (SEM, Hitachi Co, Model S-2250N, Japan) was performed to confirm the surface morphology and porosity of 20s and 30s SH and SPH samples. Plasma-palladium coating was performed using a plasma sputter (Emscope, Model SC500K, United Kingdom) under argon gas. The samples ware observed at an accelerating voltage of 1.5 kV. To measure the pore size of each scaffold, image J program tools were used by taking the cross-sectional images and calculating their average pore size.

Change in the Functional Group Using FTIR

The change in the functional group of SF aqueous solution, PEG powder, and prepared hydrogels was confirmed by FT-IR analyzed using ATR mode with the lyophilized samples (FT-IR Spectroscopy- FT-IR, GX, Perkin Elmer, Connecticut, United States). All the spectrums were observed between 4,000 and 400 cm^{-1} at a resolution of 4 cm^{-1} with a minimum of 50 scans.

Compressing Test Properties of the Hydrogel

A universal physical property meter (TMS-Pro, Food Technology Corporation, Sterling, United States) was used to measure the compressive strength of the prepared hydrogels in compressive mode at a constant speed of 5 mm/min and the measurement distance was set to be 3 mm. The as prepared hydrogels are cut into cylindrical shape with the height 50 mm. The analysis was carried out at 25°C and the test are repeated at least 5 times for each samples.

Porosity of the Prepared Hydrogel

The porosity of the prepared hydrogels was evaluated by the principle of Archimedes via fluid displacement measurement technique. Before the analysis, the test sample was immersed in the known volume of distilled water (V_1) for 10 min. The total volume of distilled water containing the scaffold after 10 min was referred to as V_2. The hydrated scaffold was removed and the remaining volume of distilled water was recorded as (V_3). The porosity of the scaffold was estimated by using the following equation with the average of 4 measurements.

$$\text{Porosity } (\%) = \frac{V_1 - V_3}{V_2 - V_3} \times 100$$

Degradation of the Hydrogel

Freeze-dried hydrogel scaffold (W_f) was immersed in 1M phosphate-buffered saline (PBS, pH 7.4) and their percentage of weight loss was analyzed on 7, 14, 21, and 28 days over time. Briefly, the scaffold was immersed in PBS and incubated at 37 ± 0.5°C, after specific time intervals the PBS was carefully removed and the scaffolds are dried and their weight (W_d) was measured after 7, 14, 21, and 28 days. PBS was changed every day (n = 3). The degradability was calculated using the following equation.

$$\textit{Degradation}\,(\%) = \frac{W_f - W_d}{W_f} \times 100$$

Isolation and Culturing of RPE Cells

All the animal experiments were performed in accordance with the guidelines and the approval of the Jeonbuk National University Animal Care Committee (CBNUACC), Jeonju, South Korea. The protocol was approved by the CBNUACC. The RPE cells were isolated from a 3 weeks old female New Zealand white rabbit (Hanil laboratory animal center, Wanju, South Korea). The eyes of the rabbits were harvested using sterile surgical scissors and unwanted surrounding tissues (anterior eye and vitreous body were removed) were removed, washed several times with PBS, and stored in PBS. For RPE isolation the specimen was incubated in 0.2% collagenase A (Roche Diagnostics, Germany) for 60 min followed by filtering using 70 μm filter, and the content were centrifuged at 15,000 rpm for 5 min. The cell pellets were suspended using 1 mL RPE medium (DMEM/F-12 (Dulbecco's Modified Eagle's Media, Gibco, United States)/Ml streptomycin, Gibco) adding FBS (Gibco) with 1% penicillin-streptomycin (PS, 100 units/mL penicillin and 100 μg/mL penicillin-streptomycin) in a cell culture dish. The cells were placed inside the incubator at 37°C in 5% CO_2, and the culture medium was changed every 2 days until it reaches as confluency. After that, the cells (2×10^5 cells) were seeded on the surface of the hydrogel and each well was filled with medium after seeding the cells for 30 min and incubated at 37°C in 5% CO_2. The culture medium was changed every 2 days until the specified time intervals.

Initial Attachment and Proliferation of RPE Cell

In order to confirm the initial adhesion of the retinal pigment epithelial cells, 1×10^5 cells were seeded on each hydrogel and cultured in an incubator for 30 min. After that, the culture solution was removed, and 2.5% glutaraldehyde was added, and the cells were fixed by refrigerated storage for 24 h. Nuclei were then stained with UltraCruz™ Mounting Medium (Santa Cruz, United States) and photomicrographs were taken using a fluorescence microscope (Eclipse TE 2000-U, Nikon, Japan) to determine cell density per square mm^2. The photographed images were quantified using the Image J program.

Biocompatibility of the Hydrogels Using MTT

Biocompatibility of the prepared SF and SF/P hydrogels were analyzed using MTT (dimethylthiazol-2-yl-2,5-diphenyltetrazolium bromide) assay to determine cell viability on each hydrogel. 2×10^5 RPE cells were seeded on each hydrogel and filled with the media, after respective time point the media was removed and they were treated with 0.1 mL of MTT solution (50 μg/mL) each on day 1, 3, 7, and 14 of the experimental period and kept in an incubator for 3 h at 37°C in 5% CO_2. After the incubation period, 1 mL of dimethylsulfoxide (DMSO, Sigma, United States) was added to completely dissolve the purple crystals, then the solution was dispensed into fresh 96-well plates and absorbance was measured at 570 nm.

Reverse Transcription-Polymers Chain Reaction (RT-PCR)

In order to confirm the specific gene expression level of RPE cells seeded on SF and SF/P hydrogel, RT-PCR was performed on 7 day cultured cells on the hydrogel. RNA was extracted from RPE cells by centrifugation at 12,000 rpm for 15 min at 4°C using 1 mL of trizol (Invitrogen™ Life Technologies Co., Groningen, Netherlands) and 0.2 mL of chloroform (Sigma, United States). The expression of mRNA in the sample was confirmed by RPE-specific 65 kDa (RPE65), natriuretic peptide-A receptor (NPRA), and cellular retinaldehyde -binding protein (CRALBP) markers. All samples were denatured at 95°C for 30 s followed by annealing at a specific temperature of the primer and amplified at 72°C for 1 min/kb to synthesize complementary DNA (cDNAs). The expression were confirmed by running the samples through the electrophoretic gel and imaged at 360 nm using an ultraviolet-transilluminator tester (Flourchem® HD2, Alpha Innotech, San Leandro, United States). The images were quantified using the Image J program. The primers used in this study are listed in **Table 1**.

Statistical Analysis

Data are presented as means ± SD (SD), n = 3. Statistical analysis of each experiment was considered to be significant when

TABLE 1 | The primer for β-actin, RPE65, NPR-A, and CRALBP mRNA.

Gene		Primer sequences
β-actin	F	5′-GCCATCCTGCTCCGTCTGGACCTGGCT-3′
	R	5′-GTGATGACCTGGCCGTCAGGCAGC-3′
RPE65	F	5′-GCCCTCCTGCACAAGTTTGACTTT-3′
	R	5′-AGTTGGTCTCTGTGCAAGCGTAGT-3′
NPRA	F	5′-GTTGAGCCCAGTAGCCTTGAG-3′
	R	5′-CCCAAGGAGCCAGTAGGTCCG-3′
CRALBP	F	5′-TTCCGCATGGTACCTGAAGAGGAA-3′
	R	5′-ACTGCAGCCGGAAATTCACATAGC-3′

$^{*}p < 0.5$, $^{**}p < 0.05$, and $^{***}p < 0.01$ by Student's *t*-test (Excel 2013, Microsoft).

RESULTS AND DISCUSSION

Surface Morphology of the Hydrogel Scaffold

Surface morphology along with the pore size, shape, and thickness of the interconnecting pore walls of the prepared freeze-dried SF/SPH hydrogels was observed using SEM. It was confirmed that the SF/SPH hydrogel had a relatively small pore size in all groups, and the pore size was observed to be decreasing as the PEG content increases. As mentioned above, increasing the sonication time of the hydrogels results in the decrease of the pore size due to the formation of smaller molecules, smaller crystal structure, and smaller pore size as mentioned in **Figure 1**.

Change in Functional Group Analyses Using FT-IR

The change in the functional group analysis of the prepared SF, PEG, and SH/SPH hydrogels was carried out using FT-IR for qualitative analysis in the range of 4,000 ∼ 400 cm^{-1}. The results were shown in **Figure 2A**. FT-IR analysis results of SF and SPH showed the characteristic amide I, II, and III peaks at 1,621, 1,515, and 1,231 cm^{-1}, respectively. The characteristic peak of -OH was observed at 2900–3,300 cm^{-1}, and the characteristic peak of PEG -CH was observed at 2880 cm^{-1}, and the peak of -COC-group was observed at 1101 cm^{-1} (Ohno et al., 1992). It was observed that the sonication time of SH and SPH did not change the functional properties or structural change of the hydrogels, indicating that the chemical structure of SF and SPH did not change during the preparation process. In addition, SPH was confirmed to show a physical bond, not a chemical bond, when the PEG was mixed with SF. The peak intensity and respective peaks of SF did not change during the whole sonication process.

Compressive Strength of the Hydrogels

Compressive strength was measured to evaluate the physical properties of the 20s and 30s sonicated SF and SF/P hydrogels. The compressive strength values of the 20s, 30s SF, and SF/P hydrogels were observed to be 19.71 ± 0.28, 21.62 ± 0.56, 20.65 ± 0.78, and 22.5 ± 0.13 MPa, respectively. The obtained results clearly confirm that increasing the sonication time of the hydrogels increases its compressive strength due to the increase in the viscosity of the SF due to the addition of PEG. This change in the compressive strength of the SF material is due to

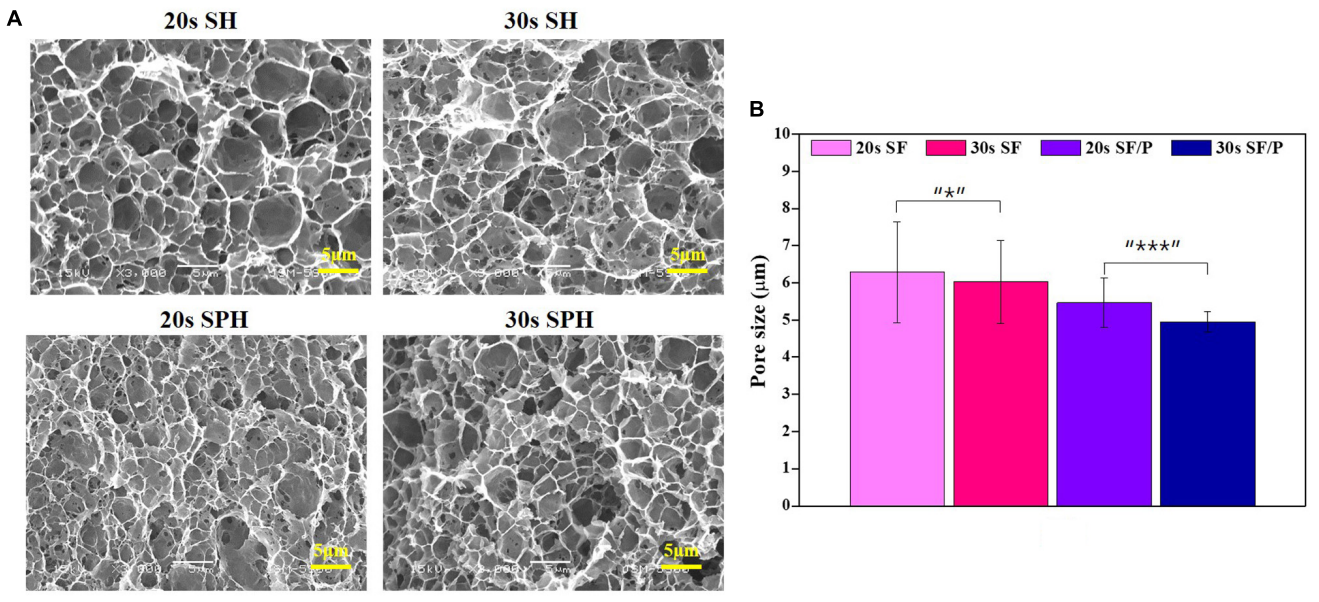

FIGURE 1 | (A) SEM microphotographs to insert gross image of SF, SF/P hydrogels (magnification with 3,000×, scale bar = 5 μm). **(B)** Pore size of freeze dried SF and SF/P hydrogels ($n = 3$ in each group; $^{*}p < 0.05$ and $^{***}p < 0.001$).

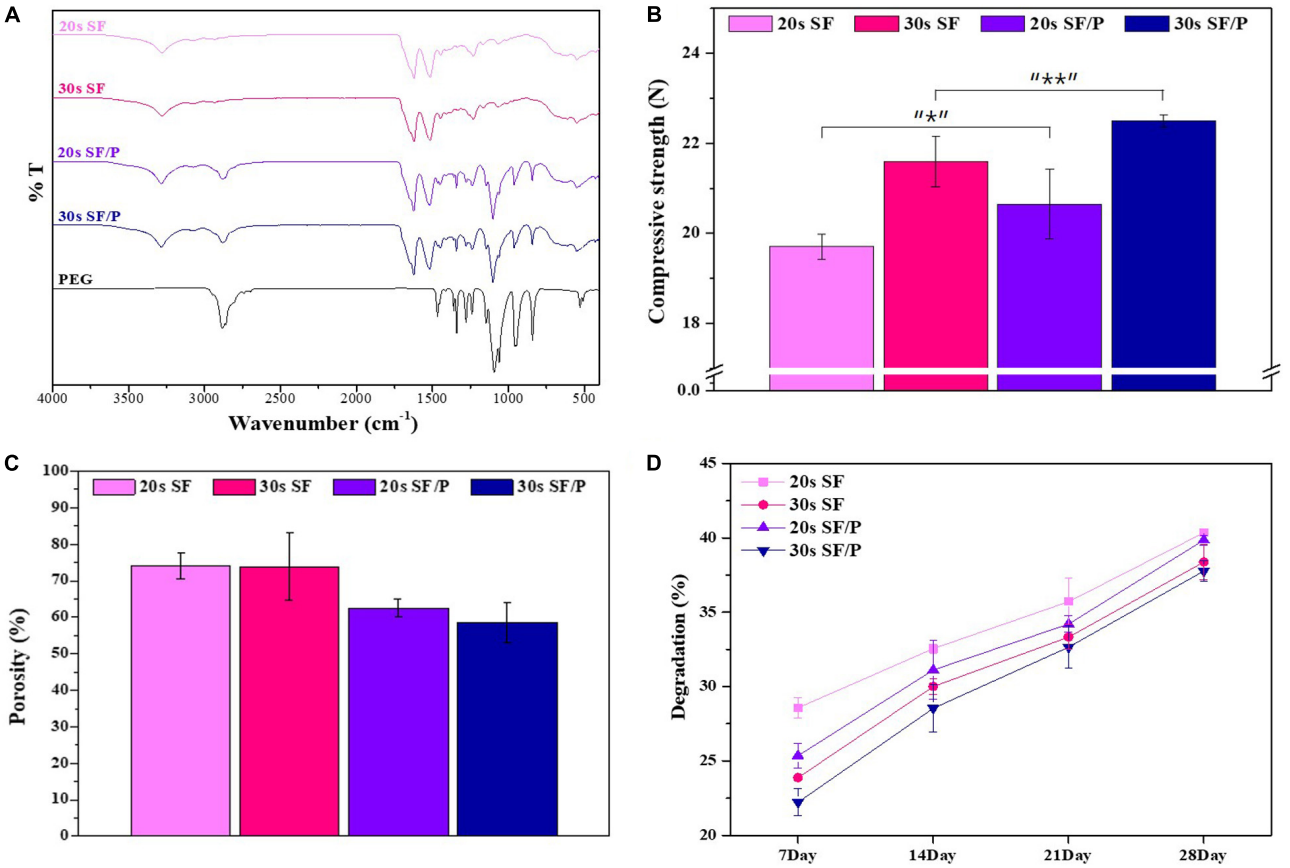

FIGURE 2 | (A) FT-IR spectra of SF, SF/P hydrogels, and PEG powder. Graphs showing **(B)** compressive strength, **(C)** porosity, and **(D)** degradation test of 20s SF, 30s SF, 20s SF/P, and 30s SF/P hydrogels ($n = 3$; $^{*}p < 0.5$, $^{**}p < 0.05$, and $^{***}p < 0.01$).

changing the viscosity of the final hydrogel along with the sonication time.

Porosity Measurements of Hydrogels

The porosity characteristic properties of the material are crucial for hydrogel scaffold because it helps in cell adhesion, penetration, proliferation, and nutrient and oxygen exchange (Li et al., 1996). The obtained results of the prepared SF and SF/P hydrogel sonicated for the 20s and 30s results were shown in **Figure 2B**. The 20s SF/P hydrogel showed more than 60% porosity compare to other studied hydrogels including 20s SF, 30s SF, and 30s SF/P, and the results were similar to the pore size (**Figure 2C**). The results show that the addition of PEG results in increased viscosity that results in decreased porosity, and reduced pore size with increasing the sonication time. As a result, the size of the pores is generated by the size of the ice crystals, and thus it is confirmed that the friendliness is formed by combining with PEG to form smaller pores.

Degradation Properties of Hydrogels

The degradation rate was evaluated to confirm the biodegradability of the prepared SF and SPH hydrogel. Hydrogels are problematic even if they are not degraded quickly or decomposed. Therefore, hydrogels should provide adequate biodegradability property for RPE cell proliferation (Sung et al., 2004; Lu et al., 2011). The results show that the degradation rate of SF, SPH hydrogel for 28 days are shown in **Figure 2D**. Similar degradation rates were observed in all groups and 20s hydrogel degradation occurred well. This is because the shorter the time of the sonication, the lesser the binding of the hydrogel, and the higher the porosity, as shown in **Figure 2B**.

Initial Attachment and Proliferation of RPE Cells

In order to evaluate the initial cell adhesion and proliferation and viability percentage rate of the 20s and 30s sonicated SF and SF/P hydrogel were analyzed using MTT assay and nuclear stain, by culturing RPE cells on the surface of the material. The initial adhesions of the cells are affected by the surface roughness and hydrophilicity of the material (Hallab et al., 2001; Chanasakulniyom et al., 2015). The higher the rate of adhesion, the shorter the cell diffusion time, which helps in the increased cell proliferation. The initial cell adhesion on the surface of the 20s, 30s SF, and SF/P hydrogels after 30 min of sowing were calculated to be 619 ± 39.11, 587 ± 35.32, 680 ± 27.29, and 631 ± 61.33 cell/mm^2, respectively, that were calculated from

the respective images from **Figure 3**. The initial cell adhesion was significantly ($p < 0.05$) increased in the 20s SF/P hydrogels compared with other hydrogels. The cell viability was analyzed using MTT assay studied on 1, 3, 7, and 14 days on the 20s, 30s SF, and SF/P hydrogels (**Figure 4A**). Initial cell viability rate on day 1 and 3 were observed to be same whereas, the proliferation and viability of the RPE cells were observed to be significantly increased on all the samples/When compared between the samples studied, it was confirmed that 20s SF/P hydrogel had significantly increased ($p < 0.05$) cell proliferation rate compared with 20s and 30s SF hydrogel group. Moreover, the cell viability was observed to significantly increased on days 7 and 14 in the 20s SF/P hydrogel followed by 30s SF/P which is due to the addition of PEG that resulted in their decreased porosity and well-interconnected walls compared to 20s and 30s SF samples. This result clearly confirms that the material physical property and their porosity play an evident role in the increased cell adhesion.

Gene Expressions in Hydrogels Using RT-PCR

The effect of prepared 20s and 30s SF and SF/P hydrogels were evaluated for its ability to support RPE cell growth by studying mRNA expression taking RPE related gene marker genes. *In vitro*, RPE cells were cultured on the 20s and 30s SF and SF/P hydrogels for a period of 1, 3, and 7 days, followed by RNA isolation and RT-PCR to confirm specific gene expressions (Liao et al., 2010). Based on the overall genetic marker Beta-actin, RPE65 provides guidelines for making proteins essential

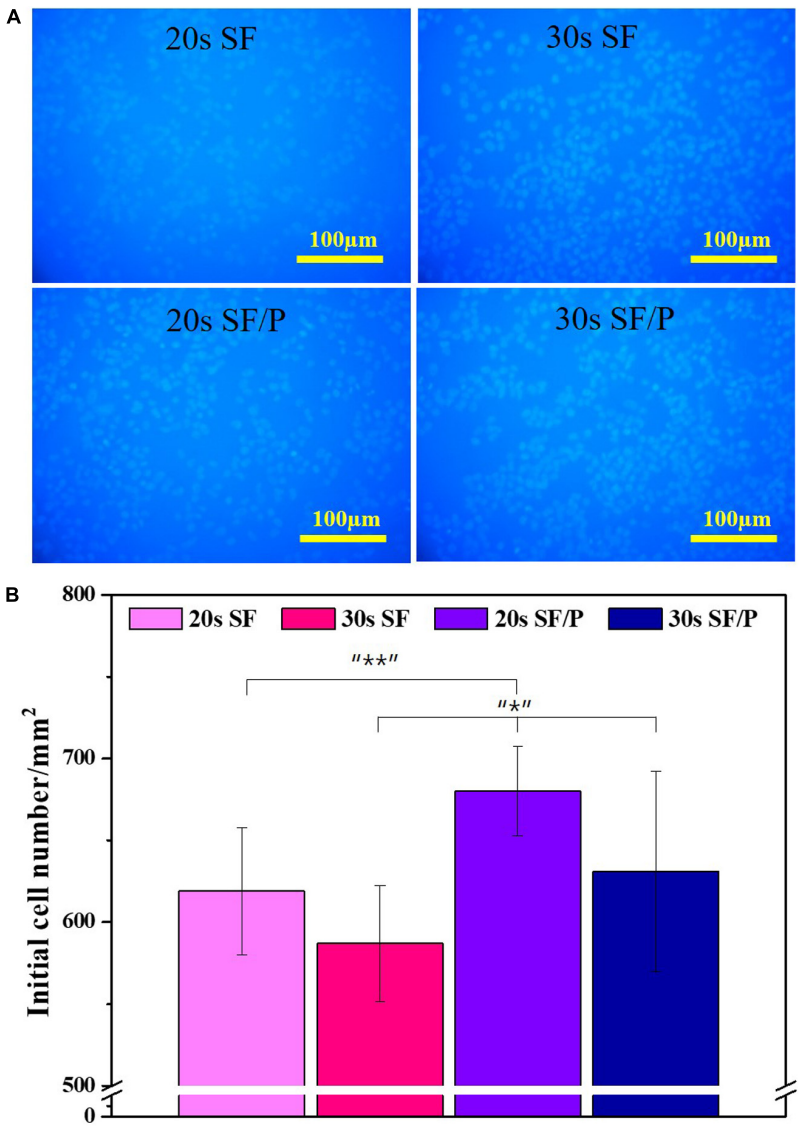

FIGURE 3 | (A) Initial attachment Nuclear stain photograph, **(B)** initial attachment cell number graph on SF and SF/P hydrogels (Magnification is 200×; scale bar = 100 µm; $n = 3$ in each group; $^{*}p < 0.5$, $^{**}p < 0.05$, and $^{***}p < 0.01$).

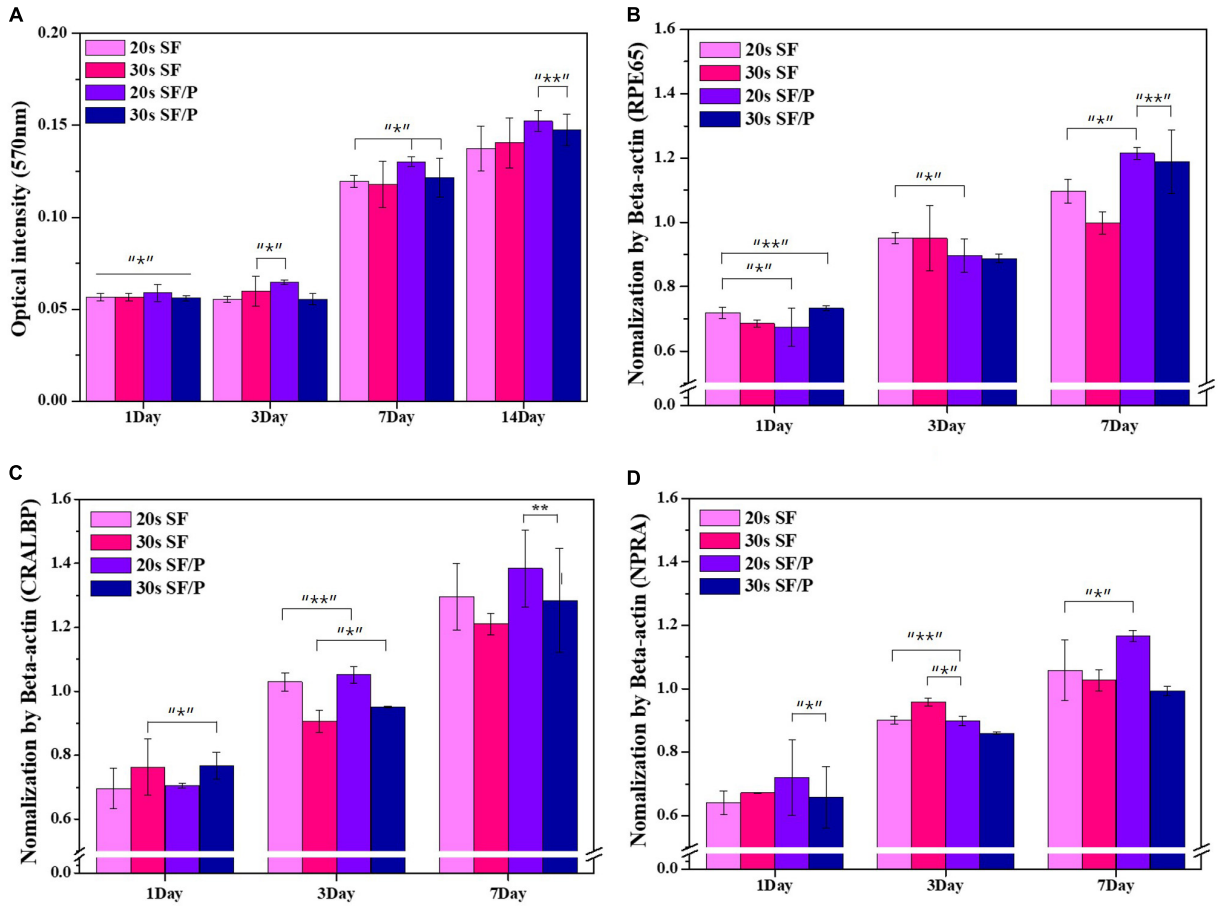

FIGURE 4 | (A) Cell proliferation result by MTT assay of RPE cell on SF and SF/P hydrogels ($n = 3$ in each group; $^{*}P < 0.05$, $^{**}P < 0.01$). Gene expression of RPE on SF/P hydrogels was analyzed by RT-PCR after 1, 3, and 7 days. Quantitative analysis of RPE65 **(B)**, NRPA **(C)**, and CRALBP **(D)** by normalization of ß-actin ($n = 3$; $^{*}p < 0.5$, $^{**}p < 0.05$, and $^{***}p < 0.01$).

for normal vision, produced in the retina, and is a visual cycle in which photoreceptor optical pigments can maintain the sight and absorb light. It is a retinol isomerase enzyme of RPE involved in important steps. CRALBP is a 36 kDa soluble protein found in the retina that transports the physiological ligand 11-cis-retinol or 11-cis-retinaldehyde. NPR-A regulates gene expression associated with RPE cell proliferation or retinal fluid uptake. RPE65, NPR-A, and CRALBP gene expression were observed to be higher in the 20s SF/P hydrogel compared to 20s and 30s SF and 30 s SF/P hydrogels (**Figures 4B,D**). On day 3, the gene expression profile was observed to be the 20s and 30s SF hydrogel compared with the 20s and 30s SF/P hydrogels for all the marker genes. While the marker gene expression were observed to be significantly increased on day 7 in the 20s and 30s SF/P hydrogels. The expression of the marker gene in the fold was in the order of CRALB > RPE65 > NPR-A as a result. The obtained results clearly infer that the 20s SF/P hydrogel was biocompatible and helps in RPE cell adhesion and proliferation and it was also confirmed that RPE cell proliferation was inhibited when the sonication time exceeds a certain level here it was 20s. This is in agreement with the MTT assay results as mentioned above, confirming that RPE cell proliferation is actively progressing in the 20s SF/P hydrogel.

CONCLUSION

In this study, the 20s and 30s SF and SF/P hydrogels were prepared by sonication for a period of 20s and 30s, respectively. The 20s sonicated SF7P hydrogel sample can be used for transplantation of retinal pigment epithelial cell regeneration. The prepared SF/P hydrogel was observed to have smaller porosity depending on their sonication time and the presence of PEG concentration. It was also confirmed that the compression strength of SF hydrogels without PEG decreases with decreasing sonication time. In addition, FT-IR confirmed that there were no observed changes in the intrinsic components and functional group changes of SF, SF/P, and PEG. The MTT and nuclear stain results confirmed that the cell proliferation rate was higher in the 20s SF/P hydrogel compared with SF seeded cells. Also, the RPE marker gene expression of RPE65, NPRA, and CRALBP, were found to be expressed in higher amounts in the 20s SF/P hydrogel

than that of the other groups (30s SF and SF/P hydrogels). Based on the obtained results of this study, 20s SF/P hydrogel has a positive effect on the proliferation of RPE cells compared with the 30s SF and SF/P hydrogels. Thus, 20s SF/PEG hydrogel can be used as an alternative material in the tissue engineering field, especially for retinal regeneration applications.

DATA AVAILABILITY STATEMENT

The datasets generated for this study are available on request to the corresponding author.

ETHICS STATEMENT

All the animal experiments were performed in accordance with the guidelines and the approval of the Chonbuk National University Animal Care Committee (CBNUACC), Jeonju, South Korea. The protocol was approved by the (CBNUACC).

AUTHOR CONTRIBUTIONS

YJ and HK performed the experiments and wrote the manuscript. MT designed the experiments and wrote the manuscript. MC, GL, CS, and JS performed the *in vitro* studies. GK designed the experiments and proofread the manuscript. All authors contributed to the article and approved the submitted version.

FUNDING

This research was supported by the Basic Science Research Program through the National Research Foundation of Korea (NRF) funded by the Ministry of Science, ICT and Future Planning (NRF-2017R1A2B3010270).

REFERENCES

Algvere, P. V., Berglin, L., Gouras, P., Sheng, Y. H., and Kopp, E. D. (1997). Transplantation of RPE in age-related macular degeneration: observations in disciform lesions and dry RPE atrophy. *Graefes Arch. Clin. Exp. Ophthalmol.* 235, 149–158. doi: 10.1007/Bf00941722

Bhutto, I., and Lutty, G. (2012). Understanding age-related macular degeneration (AMD): relationships between the photoreceptor/retinal pigment epithelium/Bruch's membrane/choriocapillaris complex. *Mol. Aspects Med.* 33, 295–317. doi: 10.1016/j.mam.2012.04.005

Binder, S. (2011). Scaffolds for retinal pigment epithelium (RPE) replacement therapy. *Br. J. Ophthalmol.* 95, 441–442. doi: 10.1136/bjo.2009.171926

Bok, D. (1993). The retinal-pigment epithelium - a versatile partner in vision. *J. Cell Sci.* 17, 189–195. doi: 10.1242/jcs.1993.supplement_17.27

Bressler, N. M., Bressler, S. B., and Fine, S. L. (1988). Age-related macular degeneration. *Survey Ophthalmol.* 32, 375–413. doi: 10.1016/0039-6257(88)90052-5

Chanasakulniyom, M., Glidle, A., and Cooper, J. M. (2015). Cell proliferation and migration inside single cell arrays. *Lab Chip* 15, 208–215. doi: 10.1039/c4lc00774c

Chao, P. H. G., Yodmuang, S., Wang, X. Q., Sun, L., Kaplan, D. L., Vunjak-Novakovic, G., et al. (2010). Silk hydrogel for cartilage tissue engineering. *J. Biomed. Mater. Res. Part B Appl. Biomater.* 95, 84–90. doi: 10.1002/jbm.b.31686

Hageman, G. S., Luthert, P. J., Chong, N. H. V., Johnson, L. V., Anderson, D. H., and Mullins, R. F. (2001). An integrated hypothesis that considers drusen as biomarkers of immune-mediated processes at the RPE-Bruch's membrane interface in aging and age-related macular degeneration. *Prog. Retinal Eye Res.* 20, 705–732. doi: 10.1016/S1350-9462(01)00010-6

Hallab, N. J., Bundy, K. J., O'Connor, K., Moses, R. L., and Jacobs, J. J. (2001). Evaluation of metallic and polymeric biomaterial surface energy and surface roughness characteristics for directed cell adhesion. *Tissue Eng.* 7, 55–71. doi: 10.1089/107632700300003297

Kim, H. S., Kim, D., Jeong, Y. W., Choi, M. J., Lee, G. W., Thangavelu, M., et al. (2019). Engineering retinal pigment epithelial cells regeneration for transplantation in regenerative medicine using PEG/Gellan gum hydrogels. *Int. J. Biol. Macromol.* 130, 220–228. doi: 10.1016/j.jbiomac.2019.01.078

Lee, G. Y., Kang, S. J., Lee, S. J., Song, J. E., Joo, C. K., Lee, D., et al. (2017). Effects of small intestinal submucosa content on the adhesion and proliferation of retinal pigment epithelial cells on SIS-PLGA films. *J. Tissue Eng. Regenera. Med.* 11, 99–108. doi: 10.1002/term.1882

Li, R. H., Altreuter, D. H., and Gentile, F. T. (1996). Transport characterization of hydrogel matrices for cell encapsulation. *Biotechnol. Bioeng.* 50, 365–373. doi: 10.1002/(Sici)1097-0290(19960520)50:4<365::Aid-Bit3>3.0.Co;2-J

Liang, F. Q., and Godley, B. F. (2003). Oxidative stress-induced mitochondrial DNA damage in human retinal pigment epithelial cells: a possible mechanism for RPE aging and age-related macular degeneration. *Exp. Eye Res.* 76, 397–403. doi: 10.1016/S0014-4835(03)00023-X

Liao, J. L., Yu, J. H., Huang, K., Hu, J., Diemer, T., Ma, Z. C., et al. (2010). Molecular signature of primary retinal pigment epithelium and stem-cell-derived RPE cells. *Hum. Mol. Genet.* 19, 4229–4238. doi: 10.1093/hmg/ddq34.1

Lu, B., Malcuit, C., Wang, S. M., Girman, S., Francis, P., Lemieux, L., et al. (2009). Long-term safety and function of RPE from human embryonic stem cells in preclinical models of macular degeneration. *Stem Cells* 27, 2126–2135. doi: 10.1002/stem.149

Lu, Q. A., Zhang, B., Li, M. Z., Zuo, B. Q., Kapan, D. L., Huang, Y. L., et al. (2011). Degradation mechanism and control of silk fibroin. *Biomacromolecules* 12, 1080–1086. doi: 10.1021/bm101422j

Mandelcorn, M. S., Machemer, R., Fineberg, E., and Hersch, S. B. (1975). Proliferation and metaplasia of intravitreal retinal-pigment epithelium cell autotransplants. *Am. J. Ophthalmol.* 80, 227–237. doi: 10.1016/0002-9394(75)90137-3

Ohno, K., Mandai, Y., and Matsuura, H. (1992). Vibrational-spectra and molecular-conformation of taurine and its related-compounds. *J. Mol. Struct.* 268, 41–50. doi: 10.1016/0022-2860(92)85058-O

Park, J. H., Shin, E. Y., Shin, M. E., Choi, M. J., Carlomagno, C., Song, J. E., et al. (2018). Enhanced retinal pigment epithelium (RPE) regeneration using curcumin/alginate hydrogels: in vitro evaluation. *Int. J. Biol. Macromol.* 117, 546–552. doi: 10.1016/j.ijbiomac.2018.05.127

Samal, S. K., Kaplan, D. L., and Chiellini, E. (2013). Ultrasound sonication effects on silk fibroin protein. *Macromol. Mater. Eng.* 298, 1201–1208. doi: 10.1002/mame.201200377

Santin, M., Motta, A., Freddi, G., and Cannas, M. (1999). In vitro evaluation of the inflammatory potential of the silk fibroin. *J. Biomed. Mater. Res.* 46, 382–389. doi: 10.1002/(Sici)1097-4636(19990905)46:3<382::Aid-Jbm11>3.0.Co;2-R

Shin, E. Y., Park, J. H., Shin, M. E., Song, J. E., Thangavelu, M., Carlomagno, C., et al. (2019). Injectable taurine-loaded alginate hydrogels for retinal pigment epithelium (RPE) regeneration. *Mater. Sci. Eng. C Mater. Biol. Appl.* 103:109787. doi: 10.1016/j.msec.2019.109787

Simo, R., Villarroel, M., Corraliza, L., Hernandez, C., and Garcia-Ramirez, M. (2010). The retinal pigment epithelium: something more than a constituent of the blood-retinal barrier-implications for the pathogenesis of diabetic retinopathy. *J. Biomed. Biotechnol.* 2010:15. doi: 10.1155/2010/190724

Strauss, O. (2005). The retinal pigment epithelium in visual function. *Physiol. Rev.* 85, 845–881. doi: 10.1152/physrev.00021.2004

Strauss, O. (2009). The role of retinal pigment epithelium in visual functions. *Ophthalmologe* 106, 299–304. doi: 10.1007/s00347-008-1869-x

Sung, H. J., Meredith, C., Johnson, C., and Galis, Z. S. (2004). The effect of scaffold degradation rate on three-dimensional cell growth and angiogenesis. *Biomaterials* 25, 5735–5742. doi: 10.1016/j.biomaterials.2004.01.066

Vepari, C., and Kaplan, D. L. (2007). Silk as a biomaterial. *Prog. Polym. Sci.* 32, 991–1007. doi: 10.1016/j.progpolymsci.2007.05.013

Wang, K., and Han, Z. C. (2017). Injectable hydrogels for ophthalmic applications. *J. Control. Release* 268, 212–224. doi: 10.1016/j.jconrel.2017.10.031

Wang, X. Q., Kluge, J. A., Leisk, G. G., and Kaplan, D. L. (2008). Sonication-induced gelation of silk fibroin for cell encapsulation. *Biomaterials* 29, 1054–1064. doi: 10.1016/j.biomaterials.2007.11.003

Yucel, T., Cebe, P., and Kaplan, D. L. (2009). Vortex-induced injectable silk fibroin hydrogels. *Biophys. J.* 97, 2044–2050. doi: 10.1016/j.bpj.2009.07.028

Zustiak, S. P., and Leach, J. B. (2010). Hydrolytically degradable poly(Ethylene Glycol) hydrogel scaffolds with tunable degradation and mechanical properties. *Biomacromolecules* 11, 1348–1357. doi: 10.1021/bm100137q

Conflict of Interest: The authors declare that the research was conducted in the absence of any commercial or financial relationships that could be construed as a potential conflict of interest.

frontiers in Bioengineering and Biotechnology

ORIGINAL RESEARCH
published: 02 December 2020
doi: 10.3389/fbioe.2020.523949

Effects of Chemical Post-treatments on Structural and Physicochemical Properties of Silk Fibroin Films Obtained From Silk Fibrous Waste

*Melissa Puerta[1], Maria S. Peresin[2] and Adriana Restrepo-Osorio[1,3]**

[1] Grupo de Investigación Sobre Nuevos Materiales, Universidad Pontificia Bolivariana, Medellín, Colombia, [2] Forest Products Development Center, School of Forestry and Wildlife Sciences, Auburn University, Auburn, AL, United States, [3] Facultad de Ingeniería Textil, Escuela de Ingenierías, Universidad Pontificia Bolivariana, Medellín, Colombia

Silk fibroin (SF) is a protein polymer claimed to have outstanding potential for medical applications. However, because of the manufacturing process, materials from regenerated SF exhibit a higher percentage of amorphous structures. The amorphous structures cause the material to be water soluble and can significantly limit its applications in wet biological environments. In order to increase the amount of crystalline structures and decrease the water solubility of SF materials, post-treatment with alcohols is usually employed. SF can be obtained from silk fibrous wastes (SFW), usually discarded in silk textile processes. This represents an opportunity to produce materials with high added value from low-cost natural sources. In this study, SF was obtained from SFW, and films were made thereof followed by a post-treatment by immersion or in a saturated atmosphere of methanol (MeOH) or ethanol (EtOH), using different exposure times. The resulting films were analyzed according to crystallinity, the percentage of crystalline and amorphous structures, and thermal stability. Also, water absorption and weight loss in aqueous media were determined. The results showed a significant increase in crystalline structures in all treated samples, varying according to the type and time of exposure to post-treatment conducted. The highest increase was shown in the case of the post-treatment by immersion in MeOH for 1 h, with a 23% increase over the untreated sample. This increase in crystallinity was reflected in an increase in the degradation temperature and a degradation rate of 5.3% on day 7. The possibility of tuning the degree of crystallinity, as well as thermal stability and aqueous integrity of thin films of SFW, can be applied to adjust these materials to the requirements of specific biomedical applications.

Keywords: silk fibroin, silk fibrous waste, alcohol post-treatment, secondary structure, water stability

OPEN ACCESS

Edited by:
Antonella Motta,
University of Trento, Italy

Reviewed by:
PaYaM ZarrinTaj,
Oklahoma State University, United States
Simone Silva,
University of Minho, Portugal

***Correspondence:**
Adriana Restrepo-Osorio
adriana.restrepo@upb.edu.co

Specialty section:
This article was submitted to Biomaterials, a section of the journal Frontiers in Bioengineering and Biotechnology

Received: *01 January 2020*
Accepted: *03 November 2020*
Published: *02 December 2020*

Citation:
Puerta M, Peresin MS and Restrepo-Osorio A (2020) Effects of Chemical Post-treatments on Structural and Physicochemical Properties of Silk Fibroin Films Obtained From Silk Fibrous Waste. Front. Bioeng. Biotechnol. 8:523949. doi: 10.3389/fbioe.2020.523949

INTRODUCTION

Silk fibroin (SF) is a protein that can be extracted from the silk produced by the *Bombyx mori* silkworms. In recent years, SF has been studied for medical applications such as cutaneous wound healing (Bhardwaj et al., 2015; Panico et al., 2018), bone tissue regeneration (Ko et al., 2016), and vascular implants (Bonani et al., 2011; Wu et al., 2018), among others. This has been made possible

thanks to its biocompatibility (Adali and Uncu, 2016), biodegradability, adequate mechanical performance (Fukayama et al., 2015), ability to promote cell growth and interaction (Unger et al., 2004), and its hemocompatibility and cytocompatibility (Fukayama et al., 2015; Adali and Uncu, 2016). SF is usually extracted from cocoons of high-quality silkworms (Rockwood et al., 2011; Tao et al., 2012; Huang et al., 2017) but there are other sources such as silk fibrous wastes (SFW). In Colombia, this waste is widely available as raw material and is provided by a few small-scale sericulture production units. Many of these production units are interested in finding alternative uses to increase the value of this waste stream. Such is the case of the Corporation for the Development of Sericulture of Cauca (CORSEDA), which produces about 20 tons/year of cocoons. It is estimated that the amount of fibrous by-products of silk can reach up to 30% by weight of the cocoons produced, in which SF is the predominant protein (Babu, 2013; Jaramillo-Quiceno and Restrepo-Osorio, 2019). The development of new value-added products from waste streams, such as the manufacture of materials from SF for medical applications, may represent an alternative solution for increasing the sustainability of the sericulture chain.

On the other hand, one of the most relevant factors for materials used for biomedical purposes is their controlled biodegradability, as this defines the possible functions and durability according to the specific application of a biomaterial (Kim et al., 2012). Due to processing methods, materials manufactured from regenerated SF may have a higher percentage of amorphous structures including random coil, α helix, side chains, turns, and bends. These structures are less orderly and have weak bonds, making the material water soluble and giving the SF reduced mechanical properties (Kim et al., 2012; Babu, 2013). Therefore, post-treatments are required to enrich and control the quantity of crystalline structures of the SF, known as β sheets and β-turns, which allows for tuning of properties including thermal stability and integrity in aqueous media. Some SF post-treatments include vapor or immersion of solvents such as EtOH and MeOH, separated or mixed, to modify its crystalline structure and decrease its water solubility (Jeong et al., 2006; Zhang et al., 2009; Kim et al., 2012; Terada et al., 2016).

There are few reports of SFW as raw materials for biomaterials fabrication. Also, no further literature reports the post-treatment methods presented here, immersion and atmospheric saturation with ethanol (EtOH) and methanol (MeOH) as solvents, and their comparative effect on SF properties. In this work, we investigate the effect of post-treatment of SFW using EtOH and MeOH. The followed methodology was immersion and exposure of SFW to atmosphere saturated in EtOH and MeOH for 15 min and 1 h, independently for each treatment. Morphological, thermal, and chemical properties of the materials, in addition to crystallinity, were investigated by X-ray diffraction (XRD), Fourier transform infrared spectroscopy with attenuated total reflectance (FTIR-ATR), scanning electron microscopy (SEM), differential scanning calorimetry (DSC), weight loss, and water absorption.

MATERIALS AND METHODS

Silk Fibroin Extraction

Silk fibroin was extracted from fibrous wastes, provided by CORSEDA, following previously published procedures (Rockwood et al., 2011; Jaramillo-Quiceno et al., 2017; Jaramillo-Quiceno and Restrepo-Osorio, 2019). Briefly, the fibrous waste was degummed twice in a 0.5% w/w aqueous solution of Na_2CO_3 (MERK, Germany) at boiling point for 30 min. The obtained SFW was dried at 60°C for 24 h and subsequently dissolved using LiBr (Sigma-Aldrich, St. Louis, MO, United States, > 99% purity), 9.3 M at 60°C. The solution was dialyzed and finally microfiltered obtained an SFW aqueous solution at 5.6% w/w. Subsequently, films were prepared by solvent casting and dried at 35°C until constant weight was reached. The obtained films had thicknesses 115 ± 2 μm, determined with a micrometer device. The isolation process is illustrated in **Figure 1**.

Post-treatments of Silk Fibroin Films

Post-treatment of the SFW films was performed using EtOH (SIGMA ALDRICH > 99.8% purity) and MeOH (EMSURE > 99.9% purity), by (i) immersing the films in or (ii) exposing them to a saturated atmosphere with vapors of each of the solvents. The samples will be referred to as the following: films immersed in MeOH (IMeOH), exposed to MeOH vapor (VMeOH), immersed in EtOH (IEtOH) and exposed to EtOH vapor (VEtOH). To determine the effect of post-treatment time, the properties were evaluated after 15 min and 1 h of immersion/vapor exposure. These times were chosen according to previous reports (Mandal et al., 2009; Bie et al., 2015; Srivastava et al., 2015; Zhou et al., 2016; Bagrov et al., 2017).

Crystallinity

To determine the crystallinity of the samples with and without post-treatments, an XPert PANalytical Empyrean Series II diffractometer was used with a Cu source. XRD patterns were obtained in a range (2θ) between 5 and 50°, with a step of 0.026° and time per step of 50 s.

Chemical Structure

The effect of post-treatments on the chemical structure of SFW films with and without post-treatments was evaluated by means of the FTIR technique (Nicolet 6700 Series). 64 scans and a resolution of 4 cm^{-1} were recorded in a range of the absorption spectrum between 4,000 and 400 cm^{-1}. OMNIC software was used to deconvolute the spectra in the region of amide I (1,700–1,600 cm^{-1}) as detailed in previous work (Jaramillo-Quiceno and Restrepo-Osorio, 2019). This spectral region was selected as it is the most sensitive to changes in the secondary structures of the protein which originate from the C = O stretch vibration of the amide groups together with the phase flexion of the N-H bond and C-N bond stretch (Yang et al., 2015).

Thermal Behavior

To measure the thermal behavior of the films with and without post-treatments, DSC technique was used in a Q2000 TA

Instruments unit. The samples were subjected to a temperature scan from 30 to 320°C and a heating rate of 10°C/min. In order to remove the water content in the samples and improve the baseline of thermogram, an isotherm at 120°C was performed prior to measurement in all cases.

Absorption Water and Weight Loss in Aqueous Medium

The integrity of films in an aqueous medium was determined by absorption water and weight loss of the SF films with and without post-treatments. The assay was carried out through deposition of dry pieces, with a known weight and with an area approximately 1 cm^2, in distilled water at 37°C. After 1 and 7 days, the samples were removed from the water, cleared of excess water, and weighed. The weight loss was determined by percentage of solubilized mass, according to Eq. 1.

$$\%WL = (W_0 - W_f)/W_0 \quad (1)$$

where, W_0: initial weight, W_f: final weight after water medium exposure of dried samples.

Morphology

The effect of post-treatments and exposure to aqueous medium on morphology of the surface, and the cross-section of the films was observed with an SEM, JEOL JSM–6490 LV. Samples were cryofractured and sputtered with gold prior to the imaging. The acceleration voltage was 15 kV and approaches were made to ×2,000, ×5,000 for surface, and ×1,500 for cross-section images.

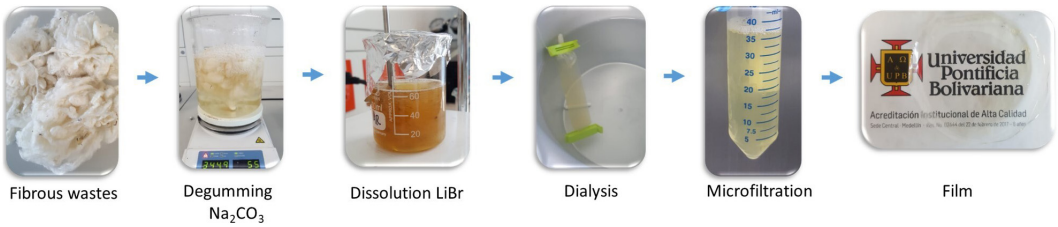

FIGURE 1 | SFW extraction porcess.

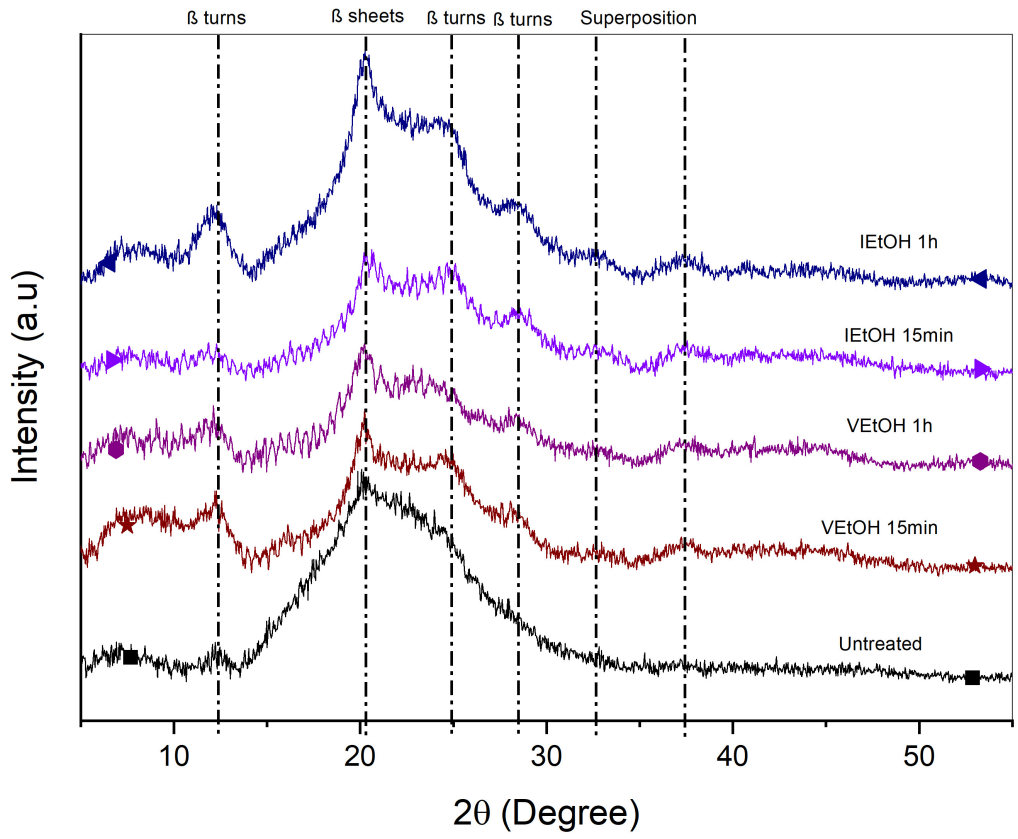

FIGURE 2 | XRD untreated and treated films with EtOH.

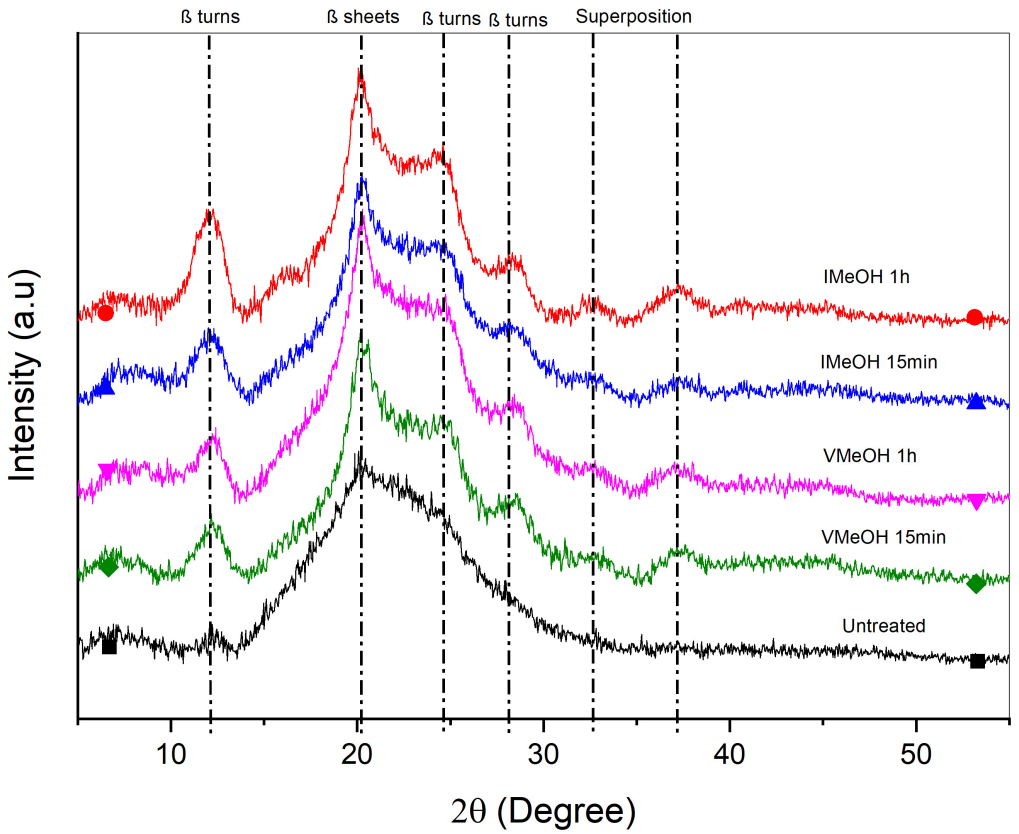

FIGURE 3 | XRD untreated and treated films with MeOH.

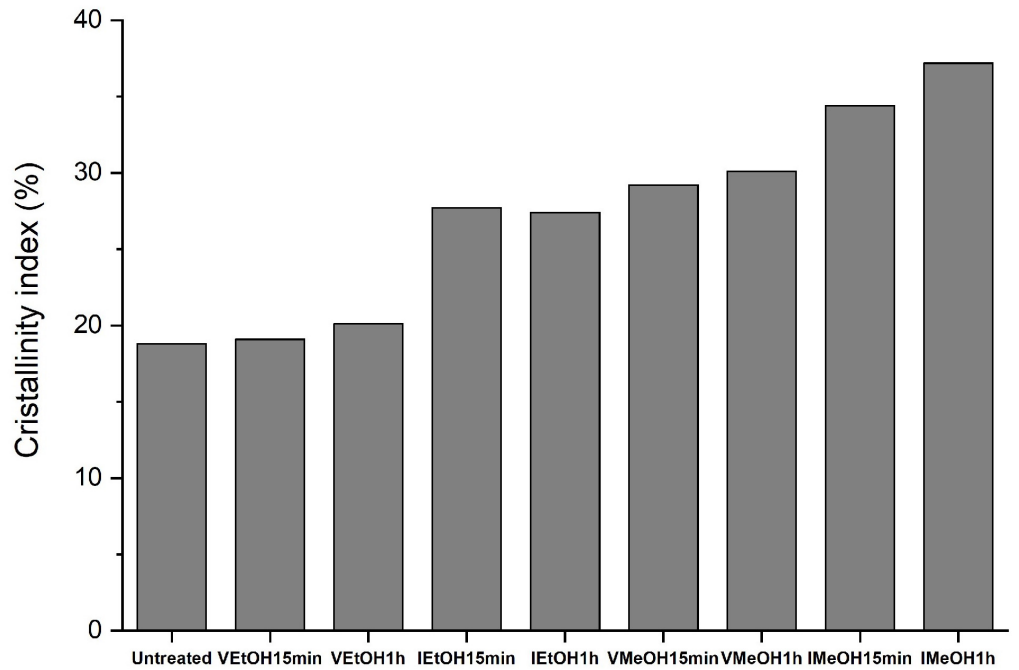

FIGURE 4 | XRD crystallinity index of untreated and treated films.

Statistical Analysis

The effect of post-treatments on films crystallinity (FTIR-ATR), absorbed water and weight loss in water media test was assessed by applying ANOVA one way, with $n = 3$ for each assessed condition.

RESULTS AND DISCUSSION

Crystallinity

X-ray diffraction was utilized to determine changes in crystallinity ratio attributed to post-treatment. **Figures 2**, **3** show the diffractograms of the films treated with EtOH and MeOH, respectively. Untreated films present a broad peak and low intensity at $2\theta = 19.9°$ representative of random coil structures consistent with that reported in the literature (Nogueira et al., 2010). On the other hand, samples treated with MeOH and EtOH exhibit a defined peak at $2\theta = 20.1°$ associated with β sheets (silk II) (Yan et al., 2012) and attenuated peaks at $2\theta = 12.2°$, 24.7°, and 28.6°corresponding to β turns (silk I) (Ha et al., 2005; Wongpanit et al., 2007; Yan et al., 2012; Zhou et al., 2016). In addition, there are two other peaks at $2\theta = 32°$ and 37°, which can be attributed to the superposition of other specific peaks of the SF around $2\theta = 24.71°$ (silk I), 18.40° (silk II), 20.14° (silk I), 21.54° (silk I), or 27.77° (silk I) (Jin and Kaplan, 2003; Stefan et al., 2019). The peaks in the samples treated with MeOH and EtOH have higher intensities compared to those observed in untreated samples, with the intensities in films treated with MeOH being relatively more pronounced. This suggests a higher degree of crystallinity in MeOH samples. The same behavior was presented in the work of Nogueira et al. (2010), where they compared the intensities of the untreated samples and those treated with EtOH.

The crystallinity index of the SFW films was calculated using the ratio of the area of the crystalline regions to the total diffraction area (Amiraliyan et al., 2010; Jaramillo-Quiceno and Restrepo-Osorio, 2019) and the results are present in **Figure 4**. According to the literature, the enrichment of crystalline structures was achieved through post-treatments, resulting in a greater effect on those samples treated with MeOH. This is attributable to the changes from amorphous structures such as random coil to β sheet reported for SF films treated by immersion in EtOH (Kaewprasit et al., 2018), MeOH (Çetin Altındal et al., 2019), and saturated vapor from both solvents (Jeong et al., 2006).

Chemical Structure

Structural changes, attributable to different post-treatments, were studied by FTIR spectra analysis in the region within 1,700–1,200 cm^{-1} (**Supplementary Figures 1**, **2**). This region is assigned to absorption of the peptide backbones of the Amide I (1,700–1,600 cm^{-1}), the Amide II (1,600–1,500 cm^{-1}), and the Amide III (1,350–1,200 cm^{-1}). All treated samples showed a displacement of the evaluated bands (**Table 1**), indicating a change in the secondary structures from random coils to β sheets.

Additionally, the analysis of Amide I was performed using deconvolution of the peak to determine the proportions in the percentages of the secondary structures of the SFW films without treatment and when treated with EtOH and MeOH (**Tables 2**, **3**). **Figure 5** presents the total percentages of amorphous and crystalline structures in samples with and without post-treatments. The results obtained from the treated films indicate that all the post-treatments lead to an increase in crystallinity with respect to the untreated films. In all cases, p-values are <0.05, indicating statistically significant differences. The results obtained by FTIR confirm those found by means of XRD analysis. Specifically, a greater increase in crystallinity was observed due to post-treatment by immersion compared to with vapor saturated atmosphere. This can be attributed to the greater surface-to-surface interaction of film to solvent. Similarly, a higher percentage of crystalline structures was observed in samples treated by immersion in MeOH. This can be attributed to the greater polarity of MeOH in comparison to EtOH; as the formation of β sheets is favored by the contact of SFW with the solvent of greatest polarity (MeOH) (Jeong et al., 2006). The hydrogen bonds between the water molecules and SFW are rearranged into intermolecular hydrogen bonds within the SFW chains, due to the interaction between water and the organic solvent. EtOH has a lower affinity with water molecules than MeOH, so there is less formation of β sheets (Yazawa et al., 2018). Regarding the time of the post-treatments, it was found that 1 h caused a greater enrichment of crystalline structures. It is suggested that this is caused by a prolonged interaction between the solvents and the SF.

TABLE 1 | Location of the peaks associated with the secondary structures in the SFW samples and the different treatments.

	Random coil	β Turn	β Sheet
Untreated	1,652, 1,538, and 1,240		
VEtOH 15 min	1,640, 1,525, and 1,236		
VEtOH 1 h	1,240	1,646 and 1,537	
lEtOH 15 min	1,642, 1,529, and 1230		1,618 and 1,512
lEtOH 1 h	1,242		1,622 and 1,515
VMeOH 15 min	1,642, 1,529, and 1,236		
VMeOH 1 h	1,510 and 1,231	1,618	
lMeOH 15 min	1,236		1,650 and 1,520
lMeOH 1 h	1,231		1,622 and 1,515

These findings are comparable with those reported by Chankow (2016) and Callone et al. (2016) who found increases in β sheets between 10 and 12% in SFW films treated with EtOH and MeOH. This behavior is attributed to the transformation of random coil into β sheets with post-treatments applied (Yali et al., 2014; Maghdouri-White et al., 2016). This is evidenced in the reduction of random coils in the treated samples compared with those untreated.

Thermal Behavior

To examine the thermal properties, the DSC thermograms for the samples with and without treatment using EtOH or MeOH, are presented in **Supplementary Figures 3, 4**, respectively. The temperature values corresponding to the glass transition

TABLE 2 | Secondary structures percentages of SFW treated with EtOH and untreated films.

	Untreated	VEtOH 15 min	VEtOH 1 h	IEtOH 15 min	IEtOH 1 h
Side chains	14.3 ± 0.1	12.5 ± 1.8	12.8 ± 1.2	13.4 ± 0.2	14.8 ± 2.3
β Sheet	24.8 ± 0.8	29.0 ± 0.1	29.6 ± 0.4	33.7 ± 0.9	32.2 ± 3.1
Random coil	21.1 ± 0.4	17.8 ± 5.5	14.7 ± 2.1	11.1 ± 0.3	9.8 ± 2.3
α Helix	6.7 ± 0.0	7.5 ± 2.6	6.4 ± 1.9	8.9 ± 0.6	6.6 ± 2.4
β Turn	8.4 ± 0.0	11.9 ± 0.8	13.5 ± 1.2	10.3 ± 0.8	13.1 ± 3.5
Turns and bends	24.4 ± 0.1	21.0 ± 4.4	22.8 ± 1.5	22.5 ± 1.1	23.1 ± 1.9

TABLE 3 | Secondary structures percentages of SFW treated with MeOH and untreated films.

	Untreated	VMeOH 15 min	VMeOH 1 h	IMeOH 15 min	IMeOH 1 h
Side chains	14.3 ± 0.1	7.3 ± 0.8	6.5 ± 0.2	6.9 ± 0.7	9.1 ± 0.8
β Sheet	24.8 ± 0.8	33.1 ± 0.3	35.7 ± 0.1	39.6 ± 0.9	42.4 ± 0.2
Random coil	21.1 ± 0.4	11.1 ± 0.9	11.0 ± 0.3	13.3 ± 0.5	9.1 ± 1.5
α Helix	6.7 ± 0.0	10.4 ± 1.4	10.0 ± 0.9	10.3 ± 0.1	6.9 ± 0.7
β Turn	8.4 ± 0.0	15.2 ± 0.5	18.0 ± 0.7	15.9 ± 0.8	14.6 ± 1.0
Turns and bends	24.4 ± 0.1	22.6 ± 1.1	18.5 ± 0.5	13.8 ± 0.2	17.6 ± 1.3

temperature (T_g), the crystallization temperature, and the degradation temperature of the samples studied are included in **Table 4**. The exothermic recrystallization peak can be evidenced only in the samples without post-treatment and in VEtOH 15 min. In all the samples, the glass transition and endothermic degradation peaks occurred. In the treated samples there are two endothermic degradation peaks. The first peak is attributed to the degradation of amorphous structures while the second peak is attributed to the crystalline structures present in the material. In a sample without post-treatment, these two events are not completely differentiated.

The T_g occurs at a higher temperature in the treated samples compared to the samples without post-treatment. The highest one corresponding to IMeOH (165.92°C) compared to the untreated SFW (144.30°C), which in turn are the samples with highest and lowest crystallinity, respectively (McGill et al., 2018). This can be explained because, in the samples showing higher crystallinity, the protein chains are in a more compact state and need more energy for the molecular movement of the glass transition to occur (Park et al., 2011). The T_g values obtained in this study are relatively lower than those reported in the literature (Lu et al., 2010) which evaluates SF films obtained from silk cocoons and treated with immersion in MeOH. This can be due to the different raw material used in this work as compared to high quality cocoons used in the literature. SFW presents a secondary structure different from that obtained from silk cocoons, on account of the textile transformation processes to which it is subjected (Jaramillo-Quiceno et al., 2017).

As mentioned before, untreated films have a recrystallization peak and the film treated with VEtOH for 15 min showed a lower recrystallization peak than the untreated films, both near 230°C. This indicates that there are amorphous secondary structures that can crystallize due to the temperature treatment in the DSC. In other samples the recrystallization peak was not observed, indicating the formation of β sheets after post-treatment with both EtOH and MeOH in all the other conditions. These results agree with those found in the FTIR ATR analysis.

Degradation peaks of the untreated films appear in the range of 270–272°C and for the treated films between 273–277°C, showing a slight increase in degradation temperatures in the treated samples. This can be attributed to the aforementioned increase in the percentage of crystalline structures in the treated samples, which is consistent with data reported in the literature (Um et al., 2001; Nogueira et al., 2010). These reports indicate a peak of degradation at lower temperatures in untreated samples compared to the degradation peaks of samples treated with solvents. This is due to the higher percentage of amorphous structures in the samples without treatment.

Absorption Water and Weight Loss in Aqueous Medium

The weight loss and the water absorption in aqueous media of SFW films with and without post treatment were obtained. The results are shown in **Table 5**. Regarding weight loss, all samples show a greater mass loss on day 7 compared to day 1, as expected. However, the percentages are less than 10% in both cases. In addition, there is a statistically significant difference for days 1 and 7 in the weight loss of the treated samples compared to the untreated ones with a p value <0.05. The weight loss results on day 7 for the untreated samples (9.5%) were higher with regards to VEtOH 15 min (8.9%) followed by VEtOH 1 h (8.7%), IEtOH 15 min (8.4%), IEtOH 1 h (7.8%), VMeOH 15 min (7.4%), VMeOH 1 h (7.2%), IMeOH 1 min (6.2%), and finally IMeOH 1 h (5.3%). The values obtained for the untreated samples, and samples treated with IMeOH for 1 h are similar to those reported in the literature by Srivastava et al. (2015). Moreover, Mandal et al. (2009) and Zhou et al. (2016) reported a non-significant loss in IMeOH and 10% in untreated films. On the other hand, samples treated with EtOH showed a mass

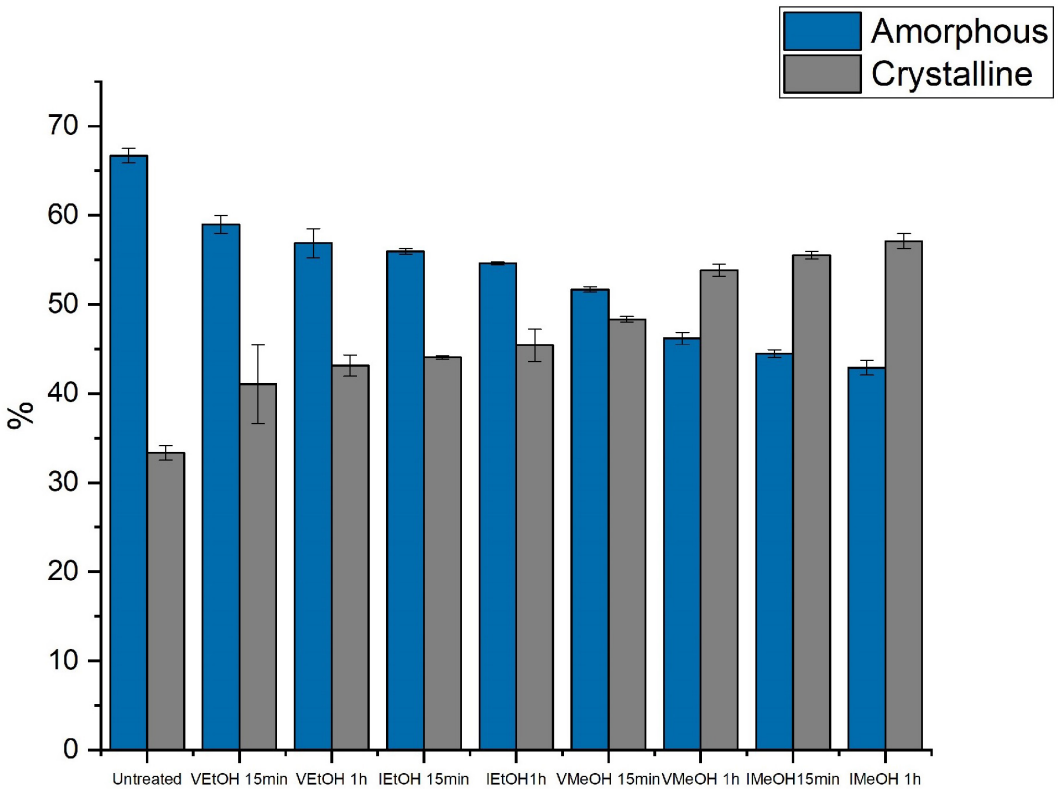

FIGURE 5 | FTIR amorphous and crystalline structures of treated and untreated SFW films.

TABLE 4 | Summary of DSC data obtained from films with different post-treatments.

	T_g (°C)	$T_{crystallization}$ (°C)	$T_{degradation\ 1}$ (°C)	$T_{degradation\ 2}$ (°C)
Untreated	144.30	229.59	255.80	272.98
VEtOH 15 min	151.20	231.80	258.13	273.47
VEtOH 1 h	151.61	–	256.65	273.05
IEtOH 15 min	152.75	–	258.00	275.32
IEtOH 1 h	153.11	–	258.11	273.12
VMeOH 15 min	153.90	–	256.72	274.37
VMeOH 1 h	160.73	–	259.47	274.29
IMeOH 15 min	164.45	–	257.01	274.82
IMeOH 1 h	165.92	–	260.10	276.73

TABLE 5 | Results of weight loss films and water absorption films of SFW.

	Weight loss (%)		Water absorption (%)	
	D1	D7	D1	D7
Untreated	8.52 ± 0.56	9.55 ± 0.32	30.65 ± 0.94	34.91 ± 0.39
VEtOH 15 min	7.70 ± 0.92	8.91 ± 0.11	29.32 ± 0.79	32.16 ± 0.51
VEtOH 1 h	7.15 ± 0.55	8.74 ± 0.20	27.66 ± 0.77	30.12 ± 0.04
IEtOH 15 min	6.47 ± 0.18	8.43 ± 0.19	25.47 ± 0.71	28.15 ± 0.57
IEtOH 1 h	5.88 ± 0.43	7.82 ± 0.53	22.26 ± 1.46	25,46 ± 0.26
VMeOH 15 min	4.47 ± 0.02	7.40 ± 0.22	19.23 ± 0.51	22.83 ± 0.34
VMeOH 1 h	4.13 ± 0.14	7.25 ± 0.28	16.82 ± 0.67	19.82 ± 0.95
IMeOH 15 min	2.82 ± 0.19	6.26 ± 0.29	14.14 ± 0.92	17.21 ± 0.64
IMeOH 1 h	1.64 ± 1.64	5.38 ± 5.38	12.70 ± 0.41	15.03 ± 0.05

loss between 7 and 8%, a percentage comparable to that reported by Rajkhowa et al. (2011).

The water absorption results show a similar trend to that which was previously observed, corresponding to degradation. There was a higher absorption of water observed in untreated samples (34.9%), followed by VEtOH 15 min (32.1%), VEtOH 1 h (30.1%), IEtOH 15 min (28.1%), IEtOH 1 h (25.4%), VMeOH 15 min (22.8%), VMeOH 1 h (19.8%), IMeOH 15 min (17.2%), and finally IMeOH 1 h (15%). This can be attributed to the fact that samples treated with MeOH have a higher percentage of crystalline structures, which makes them more hydrophobic compared to those treated with vapor and untreated samples. There is a statistically significant difference on day 7 in the treated samples compared to the untreated ones, with a p value <0.05. Srivastava et al. (2015), Bagrov et al. (2017), and Bie et al. (2015) reported absorption in samples treated with 15% MeOH and untreated between 36 and 46%, respectively. These values are similar to those obtained in this study.

Scanning Electron Microscopy

Scanning electron microscopy micrographs (**Figure 6**) showed a change in the surface morphology of films

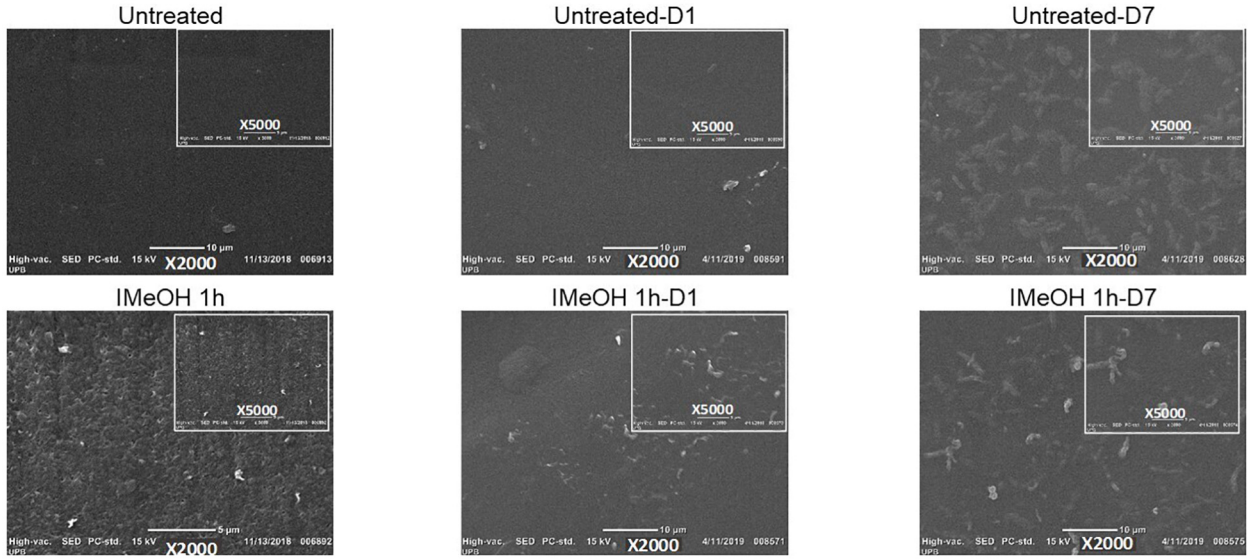

FIGURE 6 | SEM untreated, treated films IMeOH 1 h, before and after the degradation.

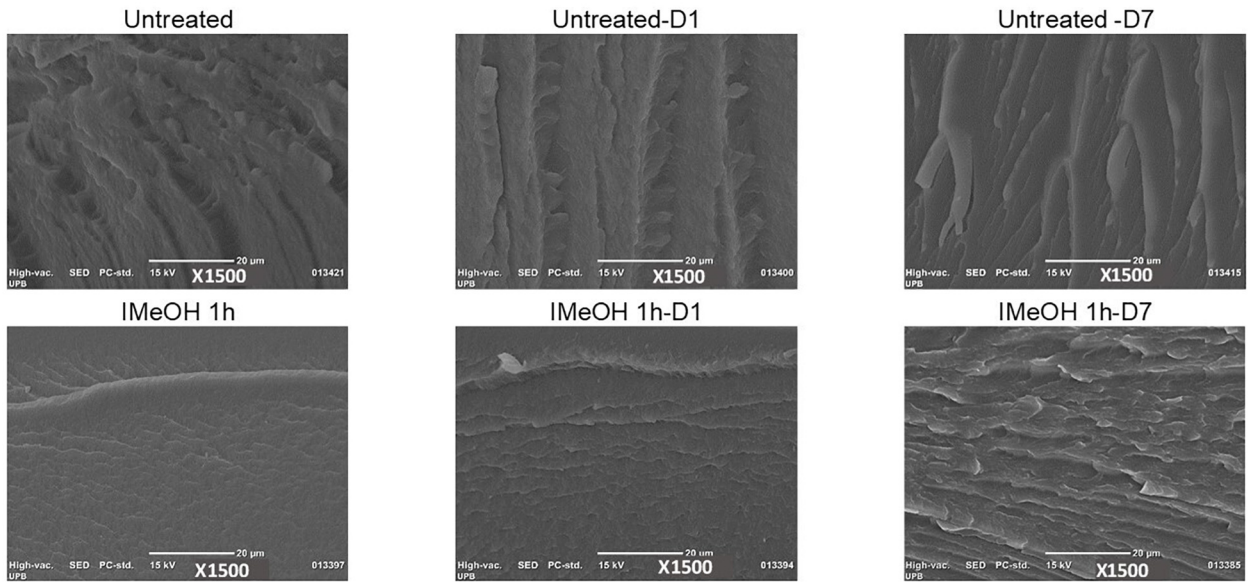

FIGURE 7 | SEM cross-section untreated, treated films IMeOH 1 h, before and after the degradation.

treated by immersion in MeOH for 1 h, changing from a smooth to a rough surface, due to the contraction of the proteinaceous material. This phenomenon can be explained by the hydrophobic dehydration that occurs due to molecular interactions between protein chains and the polar solvent (Chen et al., 2009). These results are in agreement with those reported in the literature by Terada et al. (2016) and Wongpanit et al. (2007) who reported a rougher surface when using immersion post-treatments with more than 90% EtOH and MeOH respectively, which could potentially rebound in the cell adhesion (Wongpanit et al., 2007; Terada et al., 2016).

In addition, SFW films treated by immersion (**Supplementary Figures 5, 6**) show a higher roughness compared to those treated by saturated vapor (**Supplementary Figures 7, 8**), given the large density of molecules of solvent in the liquid state. This could suggest higher interaction between the SF film and the solvent. On the other hand, post-treatments with MeOH (**Supplementary Figures 5, 7**) cause a more noticeable change due to the higher polarity of MeOH compared to that of EtOH (**Supplementary Figures 6, 8**). This allows for easier interactions

between water molecules and the solvent with higher polarity. The change in morphology is related to the structural and thermal changes discussed above. This is because the films that presented a greater apparent roughness in the SEM images are the same that presented a higher percentage of crystalline structures, along with a higher degradation temperature. Thus, this indicates that the immersion treatment with MeOH provides greater changes in the properties evaluated when compared to the other treatments.

The films morphology was also studied after the exposure of samples for 1 and 7 days, in the corresponding SEM images (**Figure 6** and **Supplementary Figures 5–8**). It can be observed on day 1 what appears to be the swelling of the surface with a decrease in roughness, which can be attributed to the water absorption of the films. Moreover, on day 7, erosion is evident on the surface, showing some cavities and surface agglomerations caused by swelling and potentially by the solubilization process, which is consistent with results reported in the literature (Zhou et al., 2016; Wang et al., 2019). According to the content of secondary structures present in SFW films, there are significant changes in morphology (Minoura et al., 1990; Lu et al., 2010), with films post-treated with EtOH having the most evident differences. Those films show a higher content of amorphous structures, compared to those treated with MeOH, which favors higher weight loss values, as presented above.

The images obtained by SEM (**Figure 7** and **Supplementary Figures 9–12**) of the cross-section show changes in the striations of the samples, with narrower filaments/striations and more compacting in the samples with a higher percentage of crystallinity (IMeOH, **Supplementary Figure 9**). In contrast, as the samples decrease in their percentage of crystallinity, the size of striae become wider (EtOH treated samples, **Supplementary Figures 11, 12**). These results confirm our observations regarding the dependence on the morphology of the films cross-sections and the percentage of the crystalline structures, and are also consistent with those previously reported (Zhang et al., 2012). Zhang et al. (2012) had shown that films with greater crystallinity present a more regular compact morphology.

CONCLUSION

The effects of post-treatment with EtOH and MeOH at different times, by immersion and saturated atmosphere on the SFW films, were evaluated. The change in the percentage of secondary structures and their influence on degradation rates and thermal properties were determined. The results obtained indicate that the treatments evaluated in this study are effective in increasing the content of the crystalline structure, evidenced in the reduction of random coils and the increase of β sheets as demonstrated by XRD and FTIR. Therefore, treatments with organic solvents present an effective mechanism to regulate the crystallinity, water integrity and thermal stability of the material.

Among the post-treatments studied, immersion in MeOH for 1 h provided the highest increase in percentage of crystalline structures with a value of 57.1% compared to 33.3% of the sample without treatment. This increase also indicates that films with higher percentage of crystalline structures also show higher degradation temperatures, as well as decreased degradation and water absorption rates when compared to untreated samples.

These results are relevant for applications of SF from SFW in biomedicine, such as cellular scaffolding, as regulated degradation rates and mechanical and thermal stability are required to allow adhesion, cell proliferation, and durability of scaffolding.

Films obtained from fibrous wastes showed similar properties to those reported for SF extracted from cocoons, indicating that materials manufactured from wastes have the potential to be used in biomedical applications. Additionally, the results obtained from this study can aid in improving the sustainability of the sericultural chain, especially regarding small scale production, allowing for better utilization of resources and increased value of the material.

DATA AVAILABILITY STATEMENT

The datasets generated for this study are available on request to the corresponding author.

AUTHOR CONTRIBUTIONS

MP developed the materials and performed the experiments and characterizations. MP, MSP, and AR-O contributed to the conceptualization, data analysis, and writing of the manuscript. All authors listed have made a substantial, direct and intellectual contribution to the work, and approved it for publication.

FUNDING

This research received financial support to Ministerio de Ciencia y Tecnología (MINCIENCIAS) of the research project 121080762864. Additional support from the Alabama Experimental Station, the HATCH Program (ALA013-1-17003), and the McIntire Stennis Program (ALAZ00076) of the National Institute of Food and Agriculture, United States Department of Agriculture.

ACKNOWLEDGMENTS

Acknowledgments to Centro de Investigación para el Desarrollo y la Innovación (CIDI) of the Universidad Pontificia Bolivariana for financial the advanced training scholarship for the master's student to MP.

SUPPLEMENTARY MATERIAL

The Supplementary Material for this article can be found online at: https://www.frontiersin.org/articles/10.3389/fbioe.2020.523949/full#supplementary-material

REFERENCES

Adali, T., and Uncu, M. (2016). Silk fibroin as a non thrombogenic biomaterial. *Int. J. Biol. Macromol.* 90, 11–19. doi: 10.1016/j.ijbiomac.2016.01.088

Amiraliyan, N., Nouri, M., and Kish, M. H. (2010). Structural characterization and mechanical properties of electrospun silk fibroin nanofiber mats. *Polym. Sci. Ser. A* 52, 407–412. doi: 10.1134/S0965545X10040097

Babu, K. M. (2013). *Silk: Processing, Properties and Applications*. Sawston: Woodhead Publishing Limited. doi: 10.1533/9781782421580

Bagrov, D., Zhuikov, V., Chudinova, Y., Yarisheva, A., Kotlyarova, M., and Arkhipova, A. (2017). Mechanical properties of films and three-dimensional scaffolds made of fibroin and gelatin. *Mol. Biophys.* 62, 17–23. doi: 10.1134/S0006350917010031

Bhardwaj, N., Sow, W. T., Devi, D., Ng, K. W., Mandal, B. B., and Cho, N. J. (2015). Silk fibroin-keratin based 3D scaffolds as a dermal substitute for skin tissue engineering. *Integr. Biol. (United Kingdom)* 7, 53–63. doi: 10.1039/c4ib00208c

Bie, S., Ming, J., Zhou, Y., Zhong, T., Zhang, F., and Zuo, B. (2015). Rapid formation of flexible silk fibroin gel-like films. *J. Appl. Polym. Sci.* 41842, 2–9. doi: 10.1002/app.41842

Bonani, W., Maniglio, D., Motta, A., Tan, W., and Migliaresi, C. (2011). Biohybrid nanofiber constructs with anisotropic biomechanical properties. *J. Biomed. Mater. Res. Part B Appl. Biomater.* 96 B, 276–286. doi: 10.1002/jbm.b.31763

Callone, E., Dire, S., Hu, X., and Motta, A. (2016). Processing influence on molecular assembling and structural conformations in silk fibroin: elucidation by solid-state NMR. *ACS Biomater. Sci. Eng.* 2, 758–767. doi: 10.1021/acsbiomaterials.5b00507

Çetin Altındal, D., James, E. N., Kaplan, D. L., and Gümüşderelioğlu, M. (2019). Melatonin-induced osteogenesis with methanol-annealed silk materials. *J. Bioact. Compat. Polym.* 34, 291–305. doi: 10.1177/0883911519847489

Chankow, S. (2016). "Conformational transitions of thai silk fibroin secondary structures," in *Biomedical Engineering International Conference (BMEiCON-2016)*, Vol. 89, Laung Prabang, 25–34.

Chen, X., Knight, D. P., and Shao, Z. (2009). B -turn formation during the conformation transition in silk fibroin. *R. Soc. Chem.* 5, 2777–2781. doi: 10.1039/b900908f

Fukayama, T., Takagi, K., Tanaka, R., Hatakeyama, Y., Aytemiz, D., Suzuki, Y., et al. (2015). Biological reaction to small-diameter vascular grafts made of silk fibroin implanted in the abdominal aortae of rats. *Ann. Vasc. Surg.* 29, 341–352. doi: 10.1016/j.avsg.2014.10.008

Ha, S. W., Tonelli, A. E., and Hudson, S. M. (2005). Structural studies of Bombyx mori silk fibroin during regeneration from solutions and wet fiber spinning. *Biomacromolecules* 6, 1722–1731. doi: 10.1021/bm050010y

Huang, Y., Bailey, K., Wang, S., and Feng, X. (2017). Silk fibroin films for potential applications in controlled release. *React. Funct. Polym.* 116, 57–68. doi: 10.1016/j.reactfunctpolym.2017.05.007

Jaramillo-Quiceno, N., Álvarez-López, C., and Restrepo-Osorio, A. (2017). Structural and thermal properties of silk fibroin films obtained from cocoon and waste silk fibers as raw materials. *Proc. Eng.* 200, 384–388. doi: 10.1016/j.proeng.2017.07.054

Jaramillo-Quiceno, N., and Restrepo-Osorio, A. (2019). Water—annealing treatment for edible silk fibroin coatings from fibrous waste. *J. Appl. Polym. Sci.* 137:48505. doi: 10.1002/app.48505

Jeong, L., Lee, K. Y., Liu, J. W., and Park, W. H. (2006). Time-resolved structural investigation of regenerated silk fibroin nanofibers treated with solvent vapor. *Int. J. Biol. Macromol.* 38, 140–144. doi: 10.1016/j.ijbiomac.2006.02.009

Jin, H. J., and Kaplan, D. L. (2003). Mechanism of silk processing in insects and spiders. *Nature* 424, 1057–1061. doi: 10.1038/nature01809

Kaewprasit, K., Kobayashi, T., and Damrongsakkul, S. (2018). Thai silk fibroin gelation process enhancing by monohydric and polyhydric alcohols. *Int. J. Biol. Macromol.* 118, 1726–1735. doi: 10.1016/J.IJBIOMAC.2018.07.017

Kim, J. H., Park, C. H., Lee, O. J., Lee, J. M., Kim, J. W., Park, Y. H., et al. (2012). Preparation and in vivo degradation of controlled biodegradability of electrospun silk fibroin nanofiber mats. *J. Biomed. Mater. Res. Part A* 100 A, 3287–3295. doi: 10.1002/jbm.a.34274

Ko, Y. G., Lee, M., Park, W. H., Cho, D., Kwon, O. K., and Kwon, O. H. (2016). Guiding bone regeneration using hydrophobized silk fibroin nanofiber membranes. *Macromol. Res.* 24, 824–828. doi: 10.1007/s13233-016-4109-2

Lu, Q., Hu, X., Wang, X., Kluge, J. A., Lu, S., Cebe, P., et al. (2010). Water-insoluble silk films with silk I structure. *Acta Biomater.* 6, 1380–1387. doi: 10.1016/j.actbio.2009.10.041

Maghdouri-White, Y., Bowlin, G. L., Lemmon, C. A., and Dréau, D. (2016). Bioengineered silk scaffolds in 3D tissue modeling with focus on mammary tissues. *Mater. Sci. Eng. C* 59, 1168–1180. doi: 10.1016/j.msec.2015.10.007

Mandal, B. B., Mann, J. K., and Kundu, S. C. (2009). Silk fibroin/gelatin multilayered films as a model system for controlled drug release. *Eur. J. Pharm. Sci.* 37, 160–171. doi: 10.1016/j.ejps.2009.02.005

McGill, M., Holland, G. P., and Kaplan, D. L. (2018). Experimental methods for characterizing the secondary structure and thermal properties of silk proteins. *Macromol. Rapid Commun.* 40, 1–14. doi: 10.1002/marc.201800390

Minoura, N., Tsukada, M., and Nagura, M. (1990). Physico-chemical properties of silk fibroin membrane as a biomaterial. *Biomaterials* 11, 430–434. doi: 10.1016/0142-9612(90)90100-5

Nogueira, G. M., Rodas, A. C. D., Leite, C. A. P., Giles, C., Higa, O. Z., Polakiewicz, B., et al. (2010). Preparation and characterization of ethanol-treated silk fibroin dense membranes for biomaterials application using waste silk fibers as raw material. *Bioresour. Technol.* 101, 8446–8451. doi: 10.1016/j.biortech.2010.06.064

Panico, A., Paladini, F., and Pollini, M. (2018). Development of regenerative and flexible fibroin-based wound dressings. *J. Biomed. Mater. Res. B Appl. Biomater.* 107, 7–18. doi: 10.1002/jbm.b.34090

Park, S., Kaplan, D. L., Hu, X., Shmelev, K., Sun, L., Gil, E., et al. (2011). Regulation of silk material structure by temperature-controlled water vapor annealing regulation of silk material structure by temperature-controlled water vapor annealing. *Biomacromolecules* 12, 1686–1696. doi: 10.1021/bm200062a

Rajkhowa, R., Levin, B., Redmond, S. L., Li, L. H., Wang, L., Kanwar, J. R., et al. (2011). Structure and properties of biomedical films prepared from aqueous and acidic silk fibroin solutions. *J. Biomed. Mater. Res. A* 97, 37–45. doi: 10.1002/jbm.a.33021

Rockwood, D. N., Preda, R. C., Yücel, T., Wang, X., Lovett, M. L., and Kaplan, D. L. (2011). Materials fabrication from Bombyx mori silk fibroin. *Nat. Protoc.* 6, 1612–1631. doi: 10.1038/nprot.2011.379

Srivastava, C. M., Purwar, R., Kannaujia, R., and Sharma, D. (2015). Flexible silk fibroin films for wound dressing. *Fibers Polym.* 16, 1020–1030. doi: 10.1007/s12221-015-1020-y

Stefan, N., Miroiu, F. M., and Socol, G. (2019). Degradable silk fibroin – poly (sebacic acid) diacetoxy terminated, (SF-PSADT) polymeric composite coatings for biodegradable medical applications deposited by laser technology. *Prog. Org. Coatings* 134, 11–21. doi: 10.1016/j.porgcoat.2019.04.075

Tao, H., Kaplan, D. L., and Omenetto, F. G. (2012). Silk materials–a road to sustainable high technology. *Adv. Mater.* 24, 2824–2837. doi: 10.1002/adma.201104477

Terada, D., Yokoyama, Y., Hattori, S., Kobayashi, H., and Tamada, Y. (2016). The outermost surface properties of silk fibroin films reflect ethanol-treatment conditions used in biomaterial preparation. *Mater. Sci. Eng. C* 58, 119–126. doi: 10.1016/j.msec.2015.07.041

Um, I. C., Kweon, H., Park, Y. H., and Hudson, S. (2001). Structural characteristics and properties of the regenerated silk fibroin prepared from formic acid. *Int. J. Biol. Macromol.* 29, 91–97. doi: 10.1016/S0141-8130(01)00159-3

Unger, R. E., Peters, K., Wolf, M., Motta, A., Migliaresi, C., and Kirkpatrick, C. J. (2004). Endothelialization of a non-woven silk fibroin net for use in tissue engineering: growth and gene regulation of human endothelial cells. *Biomaterials* 25, 5137–5146. doi: 10.1016/j.biomaterials.2003.12.040

Wang, L., Luo, Z., Zhang, Q., Guan, Y., Cai, J., You, R., et al. (2019). Effect of degumming methods on the degradation behavior of silk fibroin biomaterials. *Fibers Polym.* 20, 45–50. doi: 10.1007/s12221-019-8658-9

Wongpanit, P., Tabata, Y., and Rujiravanit, R. (2007). Miscibility and biodegradability of silk fibroin/carboxymethyl chitin blend films. *Macromol. Biosci.* 7, 1258–1271. doi: 10.1002/mabi.200700074

Wu, T., Zhang, J., Wang, Y., Li, D., Sun, B., El-Hamshary, H., et al. (2018). Fabrication and preliminary study of a biomimetic tri-layer tubular graft based on fibers and fiber yarns for vascular tissue engineering. *Mater. Sci. Eng. C* 82, 121–129. doi: 10.1016/j.msec.2017.08.072

Yali, W., Dan, S., Honggen, Y., and Jiannan, W. (2014). Characterization of a PEG-DE cross-linked tubular silk scaffold. *Text. Res. J.* 84, 959–967. doi: 10.1177/0040517513512401

Yan, L. P., Oliveira, J. M., Oliveira, A. L., Caridade, S. G., Mano, J. F., and Reis, R. L. (2012). Macro/microporous silk fibroin scaffolds with potential for articular cartilage and meniscus tissue engineering applications. *Acta Biomater.* 8, 289–301. doi: 10.1016/j.actbio.2011.09.037

Yang, H., Yang, S., Kong, J., Dong, A., and Yu, S. (2015). Obtaining information about protein secondary structures in aqueous solution using Fourier transform IR spectroscopy. *Nat. Protoc.* 10, 382–396. doi: 10.1038/nprot.2015.024

Yazawa, K., Malay, A. D., Ifuku, N., Ishii, T., Masunaga, H., Hikima, T., et al. (2018). Combination of amorphous silk fiber spinning and postspinning crystallization for tough regenerated silk fibers. *Biomacromolecules* 19, 2227–2237. doi: 10.1021/acs.biomac.8b00232

Zhang, C., Song, D., Lu, Q., Hu, X., Kaplan, D. L., and Zhu, H. (2012). Flexibility regeneration of silk fibroin in vitro. *Biomacromolecules* 13, 2148–2153. doi: 10.1021/bm300541g

Zhang, X., Reagan, M. R., and Kaplan, D. L. (2009). Electrospun silk biomaterial scaffolds for regenerative medicine. *Adv. Drug Deliv. Rev.* 61, 988–1006. doi: 10.1016/j.addr.2009.07.005

Zhou, J., Zhang, B., Liu, X., Shi, L., Zhu, J., Wei, D., et al. (2016). Facile method to prepare silk fibroin/hyaluronic acid films for vascular endothelial growth factor release. *Carbohydr. Polym.* 143, 301–309. doi: 10.1016/j.carbpol.2016.01.023

Conflict of Interest: The authors declare that the research was conducted in the absence of any commercial or financial relationships that could be construed as a potential conflict of interest.

Advantages of publishing in Frontiers

OPEN ACCESS
Articles are free to read for greatest visibility and readership

FAST PUBLICATION
Around 90 days from submission to decision

HIGH QUALITY PEER-REVIEW
Rigorous, collaborative, and constructive peer-review

TRANSPARENT PEER-REVIEW
Editors and reviewers acknowledged by name on published articles

Frontiers
Avenue du Tribunal-Fédéral 34
1005 Lausanne | Switzerland

Visit us: www.frontiersin.org
Contact us: frontiersin.org/about/contact

REPRODUCIBILITY OF RESEARCH
Support open data and methods to enhance research reproducibility

DIGITAL PUBLISHING
Articles designed for optimal readership across devices

FOLLOW US
@frontiersin

IMPACT METRICS
Advanced article metrics track visibility across digital media

EXTENSIVE PROMOTION
Marketing and promotion of impactful research

LOOP RESEARCH NETWORK
Our network increases your article's readership